



**UNIVERSITÀ
DEGLI STUDI
DI TRIESTE**

**UNIVERSITÀ DEGLI STUDI DI TRIESTE
XXXIII CICLO DEL DOTTORATO DI RICERCA IN
NANOTECNOLOGIE**

**HYBRID NANOPARTICLES FOR THERANOSTICS:
DESIGN, SYNTHESIS AND CHARACTERIZATION**

Settore scientifico-disciplinare: CHIM/06 CHIMICA ORGANICA

**DOTTORANDO
STEFANO VALENTE**

**COORDINATORE
PROF. ALBERTO MORGANTE**

**SUPERVISORE DI TESI
PROF.SSA LUCIA PASQUATO**

**CO-SUPERVISORE DI TESI
PROF. PAOLO PENGO**

ANNO ACCADEMICO 2019/2020

“Why by miniaturization?”

“Because the brain clot cannot be reached from the outside. I told you that. So we will miniaturize a submarine, inject it into an artery, and with Captain Owens at the controls and with myself as pilot, journey to the clot. There, Duval and his assistant, Miss Peterson, will operate.”

Mr. Grant & Dr. Michaels

Isaac Asimov – *Fantastic Voyage*, 1966

“Now I’m a scientific expert; that means I know nothing about absolutely everything”

Dr. Heywood Floyd

Arthur C. Clarke – *2001: A Space Odyssey*, 1968

TABLE OF CONTENTS

Table of Contents	5
List of Abbreviations	8
Abstract.....	11
Riassunto.....	13

PART I - Introduction

Chapter 1: Nanomedicine	17
1.1 Introduction to nanomedicine.....	17
1.2 Theranostic nanoplatforms	20
Chapter 2: Aim of the Thesis	26

PART II - SPIO Nanoparticles in Polymeric Structures (SPIONs@Polymer)

Chapter 3: SPIONs@Polymer – Introduction.....	31
3.1 Superparamagnetic Iron Oxide Nanoparticles (SPIONs).....	31
3.1.1 <i>Synthesis</i>	33
3.1.1.1 Iron oxide core.....	34
3.1.1.2 Surface coating	36
3.1.1.3 Functionalization	38
3.1.2 <i>Characterization methods</i>	39
3.1.2.1 Characterization of the core.....	39
3.1.2.2 Characterization of the shell.....	42
3.1.3 <i>Applications in nanomedicine</i>	43
3.2 SPIONs inside polymeric structures	48
3.2.1 <i>Biocompatible polymeric structures and properties</i>	49
3.2.1.1 Polymeric nanogels (nanospheres)	50
3.2.1.2 Polymeric micelles	51
3.2.1.3 Polymersomes (nanocapsules).....	52
3.2.2 <i>Preparation strategies, SPIONs encapsulation, and surface functionalization</i>	54
3.2.3 <i>Characterization methods</i>	59
3.2.3.1 Size and Morphology.....	59
3.2.3.2 Theranostic properties	61

3.2.3.3 Biological interactions.....	62
Chapter 4: SPIONs@Polymer – Results & Discussion	64
4.1 Nanosystem’s Design.....	64
4.2 Synthesis of SPIONs.....	69
4.2.1 Hydrothermal synthesis (microwave heating).....	69
4.2.2 Thermal decomposition (conventional heating).....	71
4.2.3 Thermal decomposition (microwave heating).....	73
4.3 Assembly of the polymeric structure and SPIONs loading.....	81
4.3.1 Assembly of the polymeric structure using PVA with $M_w = 13$ kDa	83
4.3.2 Assembly of the polymeric structure using PVA with $M_w = 57 - 66$ kDa.....	93
4.3.3 Assembly of the polymeric structure using Pluronic F127 and PVA with $M_w = 13$ kDa	102
4.3.4 Assembly of the polymeric structure using Pluronic F127 and PVA with $M_w = 57 - 66$ kDa.....	111
4.4 Drug loading in the polymeric nanosystem	122
4.4.1 Assembly of the polymeric nanosystem – PVA 13kDa + F127 + Riluzole.....	123
4.4.2 Assembly of the polymeric nanosystem – PVA 13kDa + F127 + SF89	131
4.4.3 Assembly of the polymeric nanosystem – PVA 57kDa + F127 + Riluzole.....	133
4.4.4 Assembly of the polymeric nanosystem – PVA 57kDa + F127 + SF89	140
Chapter 5: SPIONs@Polymer – Experimental Part	142
5.1 General information	142
5.2 Synthesis of SPIONs.....	143
5.3 Assembly of the polymeric structure and SPIONs loading.....	146
5.4 Drug loading in the polymeric nanosystem	153
Chapter 6: SPIONs@Polymer: Conclusions & Outlook.....	159

PART III - Fluorinated Gold Nanoparticles

Chapter 7: Fluorinated AuNPs - Introduction.....	165
7.1 Monolayer-protected gold nanoparticles	165
7.1.1 Synthesis of AuNPs	166
7.1.1.1 Gold nanoparticle formation via chemical processes	167
7.1.1.2 Functionalization of gold nanoparticles.....	170
7.1.1.3 Purification of gold nanoparticles.....	173
7.1.2 Characterization of AuNPs.....	174

7.1.2.1 Characterization of the core.....	174
7.1.2.2 Characterization of the organic monolayer.....	175
7.2 Fluorinated ligands	180
7.2.1 <i>Properties</i>	181
7.2.2 <i>Applications</i>	183
7.2.3 <i>Fluorinated gold nanoparticles</i>	187
Chapter 8: Fluorinated AuNPs – Results & Discussion	191
8.1 Nanosystem’s design	191
8.2 Synthesis of gold nanoparticles protected by fluorinated thiolates.....	195
8.2.1 <i>Synthesis of the linear ligand with F-PEG600COOMe</i>	195
8.2.2 <i>Synthesis of AuNPs with F-PEG600COOMe-derivate ligand (Au@SC6NHOF11CONHPEG)</i>	210
8.3 Synthesis of other fluorinated ligands.....	217
8.3.1 <i>Synthesis of the linear ligand with F-PEG600DIOL</i>	217
8.3.2 <i>Synthesis of the branched ligand with F-PEG600COOMe</i>	223
Chapter 9: Fluorinated AuNPs – Experimental Part.....	236
9.1 General information	236
9.2 Synthesis of the linear ligand with F-PEG600COOMe	237
9.3 Synthesis of AuNPs with F-PEG600COOMe-derivate ligand	246
9.4 Synthesis of the linear ligand with F-PEG600DIOL.....	247
9.5 Synthesis of the branched ligand with F-PEG600COOMe.....	249
Chapter 10: Fluorinated AuNPs – Conclusions & Outlook.....	254
Bibliography.....	259
Appendix: NMR Spectra (Chapters 8 - 9)	287

LIST OF ABBREVIATIONS

AAS	Atomic absorption spectroscopy
ADV	Acoustic droplet vaporization
AFM	Atomic force microscopy
APTES	3-aminopropyltriethoxysilane (APTES)
AuNP	Gold nanoparticle
BBB	Blood-brain barrier
CCD	Charge-coupled device
CLSM	Confocal laser scanning microscopy
CMC	Critical micelle concentration
CMT	Critical micelle temperature
CPMG	Carr-Purcell-Meiboom-Gill
CT	Computed tomography
CVD	Chemical Vapour Deposition
DCM	Dichloromethane
DLS	Dynamic light scattering
DMF	Dimethylformamide
DNA	Deoxyribonucleic acid
DOSY	Diffusion ordered spectroscopy
DTG	Differential thermal gravimetry
EDA	Ethylenediamine
EDC · HCl	<i>N</i> -(3-dimethylaminopropyl)- <i>N'</i> -ethylcarbodiimide hydrochloride
EDXS	Energy dispersive X-ray spectroscopy
EMA	European medicines agency
ESION	Extremely small iron oxide nanoparticle
ESR	Electron spin resonance
Et ₂ O	Diethyl ether
EtOH	Ethanol
FDA	Food and Drug administration
FTIR	Fourier transform infrared
HIFU	High intensity focused ultrasound
HLB	Hydrophilic-Lipophilic Balance
HOBt	Hydroxybenzotriazole
HR-IR	High-resolution infrared
HRTEM	High-resolution transmission electron microscopy
ICP-MS	Inductively coupled plasma mass spectrometry
ICP-OES	Inductively coupled plasma optical emission spectroscopy
IM-MS	Ion mobility-mass spectrometry
ION	Iron oxide nanoparticle
LCST	Lower critical solution temperature
MALDI	Matrix-assisted laser desorption/ionization
MDT	Magnetic drug targeting
MFFF	Magnetic field flow fractionation
MHT	Magnetic hyperthermia
MPI	Magnetic particle imaging
MPIO	Micro-sized particles of iron oxide

MPTES	Mercaptopropyltriethoxysilane
MR	Magnetic resonance
MRI	Magnetic resonance imaging
MS	Mass spectrometry
NIMS	Nanostructure imaging mass spectrometry
NIPAAm	<i>N</i> -isopropylacrylamide
NIR	Near-infrared radiation
NMR	Nuclear magnetic resonance
NOESY	Nuclear Overhauser enhancement spectroscopy
NP	Nanoparticle
NTA	Nanoparticle tracking analysis
OI	Optical imaging
ORMOSIL	Organic modified silica nanoparticles
PAI	Photoacoustic imaging
PAMPA	Parallel Artificial Membrane Permeability Assay
PB	Polybutadiene
PBS	Phosphate buffer solution
PCL	Poly(ϵ -caprolactone)
PDI	Polydispersity index
PE	Petroleum ether
PEG	Polyethylene glycol
PEI	Polyethylenimine
PEO	Polyethylene oxide
PET	Positron emission tomography
PFA	Perfluoroalkyl
PFC	Perfluorocarbon
PFPE	Perfluoropolyether
PGA	Polyglutamic acid
PLA	Polylactic acid
PLGA	Poly(lactide-co-glycolide)
Pluronic F127	Block copolymer (PEG ₁₀₀ PPO ₆₅ PEG ₁₀₀)
PDT	Photodynamic therapy
PDMS	Polydimethylsiloxane
PMMA	Polymethylmethacrylate
PPO	Polypropylene oxide
PS	Polystyrene
PSD	Power spectral density
PTFE	Polytetrafluoroethylene
PTT	Photothermal therapy
PVA	Polyvinyl alcohol
P(VBODENA)	Poly(2-[4-vinylbenzyloxy]- <i>N,N</i> -diethylnicotinamide)
PVD	Physical Vapour Deposition
PVP	Polyvinylpyrrolidone
RAFT	Reversible addition-fragmentation chain transfer
RNA	Ribonucleic acid
ROS	Reactive oxygen species
RT	Room temperature
RT	Radio therapy

SAED	Selected area electron diffraction
SAM	Self-assembled monolayer
SANS	Small angle neutron scattering
SAR	Specific absorption rate
SAXS	Small angle X-ray scattering
SDT	Sonodynamic therapy
SEM	Scanning electron microscopy
SI-ATRP	Surface-initiated atom transfer radical polymerization
SLP	Specific loss power
SLS	Static light scattering
SPECT	Single-photon emission computed tomography
SPION	Superparamagnetic Iron Oxide Nanoparticle
SPB	Surface plasmon band
SPR	Surface plasmon resonance
SQUID	Superconductive quantum interference device
SSPIO	Standard superparamagnetic Iron Oxide
STM	Scanning tunnelling microscopy
TEA	Triethylamine
TEG	Triethylene glycol
TEM	Transmission electron microscopy
TFA	Trifluoroacetic acid
TGA	Thermogravimetric analysis
TIPS	Triisopropylsilane
TOAB	Tetrabutylammonium bromide
VSM	Vibrating sample magnetometry
VSPIO	Very small superparamagnetic iron oxide
USPIO	Ultra-small superparamagnetic iron oxide
UV-Vis	Ultraviolet-visible
XANES	X-ray absorption near-edge structure
XPS	X-ray spectroscopy
XRD	X-ray diffraction

ABSTRACT

The last decades have witnessed the foundation and the ascent of a novel discipline that applies the innovation in nanotechnology and material sciences to medicine and biology: nanomedicine. The current trend in nanomedicine is the development of “theranostic” nanosystems, devices designed to be employed both for the diagnosis and the treatment of specific pathologies. Within the context of nanomedicine, this PhD thesis work addressed the topical clinical need for theranostic alternatives and proposed two different designs for hybrid organic-inorganic theranostic nanoplatfoms.

The first one is centered on superparamagnetic iron oxide nanoparticles (SPIONs) enclosed inside polymeric structures. This nanoplatfom was conceived to deliver the so far less exploited positive contrast in ^1H -MRI and to act as a biocompatible and magnetically guided carrier for drug molecules; in perspective, the medical target will be the treatment of amyotrophic lateral sclerosis. This hybrid nanosystem comprises hydrophobic SPIONs that were synthesized with thermal decomposition of iron acetylacetonate, in a pioneering approach that exploits microwave heating to enhance reaction rate and reproducibility. These SPIONs were subsequently loaded inside polymeric micelles made by Pluronic F127 (a block copolymer of polyethylene oxide and polypropylene oxide) and polyvinyl alcohol (PVA) using an emulsion-solvent evaporation approach mediated by ultrasonication. The specific polymeric mixture was selected to induce the micellization of Pluronic F127 in a complex structure useful for different theranostic purposes since it comprises a hydrophobic core for SPIONs and drug hosting and a hydrophilic shell for water dispersibility, which is further covered and stabilized externally by PVA. Along with the magnetic nanoparticles, in collaboration with the group of Prof. Federico, two different types of hydrophobic drug molecules addressing the same pathological target were successfully included for the first time within the nanosystem: they were a commercial benzothiazole drug (riluzole) and a novel synthesized triazole-triazine derivative.

Both SPIONs and the polymeric nanosystems were analyzed by TEM to measure the inorganic core size and vibrating sample magnetometry (VSM) to assess their magnetic properties. Moreover, the final nanosystem was studied with nanoparticle tracking analysis (NTA) and DLS to obtain hydrodynamic diameters. Finally, thermogravimetric analysis (TGA) was employed to extrapolate their organic content, while UV-Vis spectra were recorded to assess the drug loading.

The second nanosystem addressed in this PhD thesis was devised to provide a nanoplatfom intended for the diagnosis and treatment of glioblastoma. This system is based on gold nanoparticles (AuNPs) passivated by PEGylated thiol ligands bearing an innovative perfluoropolyether moiety. This unit has a twofold role that provides a novel theranostic tool,

expanding the possible combinations: it comprises a large number of quasi-equivalent fluorine nuclei, thus making the nanosystem a contrast agent for ^{19}F -MRI and forms a fluorophobic layer within the nanoparticle monolayer for drug hosting and release. In this project, we proposed three different ligand structures, starting from two unique fluorinated symmetrical moieties bearing hydroxyl or methyl esters groups. We outlined three synthetic strategies for linear and branched ligands, managing to complete the preparation of the novel linear ligand derived from methyl ester. The characterization of each step of the syntheses for the different structures was carried out by 1D (^1H , ^{13}C , ^{19}F), 2D (COSY, HSQC, HMBC) NMR spectroscopy, and MS to study their chemical structure and functionalities. Moreover, AuNPs prepared were studied with TEM and DLS to obtain respectively the core and the hydrodynamic diameters, with TGA for the organic percentage and with NMR to confirm the ligand passivation and measure the T1 and T2 relaxation times.

RIASSUNTO

Gli ultimi decenni hanno visto la fondazione e l'ascesa di una nuova disciplina che applica l'innovazione nelle nanotecnologie e nelle scienze dei materiali alla medicina e alla biologia: la nanomedicina. L'attuale tendenza in questo campo è lo sviluppo di nanosistemi "teranostici", dispositivi progettati per essere impiegati sia per la diagnosi, sia per il trattamento di specifiche patologie. Nel contesto della nanomedicina, questo lavoro di tesi di dottorato ha affrontato la necessità clinica di nuove alternative teranostiche e ha proposto due diversi progetti per nanopiatteforme teranostiche ibride organico-inorganico.

La prima è incentrata sulle nanoparticelle di ossido di ferro superparamagnetiche (SPION) racchiuse all'interno di strutture polimeriche. Questa nanopiatteforma è stata concepita per fornire un contrasto positivo nel ^1H -MRI (fino a questo momento poco utilizzato) e per agire come vettore biocompatibile e magneticamente indirizzabile per molecole di farmaci; in prospettiva, l'obiettivo medico sarà il trattamento della sclerosi laterale amiotrofica. Questo nanosistema ibrido comprende nanoparticelle magnetiche idrofobe che sono state sintetizzate con un metodo veloce e riproducibile basato sulla decomposizione termica dell'acetilacetato di ferro, supportata in maniera pionieristica dal riscaldamento a microonde. Queste SPION sono state successivamente caricate all'interno di micelle polimeriche composte da Pluronic F127 (un copolimero a blocchi di ossido di polietilene e ossido di polipropilene) e alcol polivinilico (PVA), utilizzando un approccio di emulsione-evaporazione del solvente mediato dall'ultrasonificazione. La specifica miscela polimerica è stata selezionata per indurre la micellizzazione del Pluronic F127 in una struttura complessa comprendente un nucleo idrofobo per le SPION e l'incapsulamento di farmaci e un guscio idrofilo per la solubilità in acqua, ulteriormente ricoperto e stabilizzato esternamente da PVA. Insieme alle nanoparticelle magnetiche, in collaborazione con il gruppo della Prof.ssa Federico, nel nanosistema sono stati inclusi con successo per la prima volta due diversi tipi di molecole di farmaci idrofobi che si focalizzano sullo stesso bersaglio patologico: un farmaco benzotiazolico commerciale (riluzolo) e un nuovo derivato triazolo-triazina.

Sia le nanoparticelle magnetiche che i nanosistemi polimerici sono stati analizzati sfruttando TEM per la misurazione della dimensione del nucleo VSM per la valutazione delle loro proprietà magnetiche. Inoltre, il nanosistema finale è stato studiato con analisi di tracciamento delle nanoparticelle NTA e DLS per ottenere i diametri idrodinamici. Infine, l'analisi termogravimetrica (TGA) è stata impiegata per estrapolare il contenuto organico dei nanosistemi, mentre sono stati registrati gli spettri UV-Vis per valutare il carico del farmaco.

Il secondo nanosistema affrontato in questa tesi di dottorato è stato ideato per fornire una nanopiatteforma destinata alla diagnosi e al trattamento del glioblastoma. Questo sistema è basato

su nanoparticelle d'oro passivate da ligandi tiolici PEGilati innovativi contenenti una frazione di perfluoropolietere. Questa unità ha un duplice ruolo: fornisce un gran numero di nuclei di fluoro quasi equivalenti, rendendo così il nanosistema un agente di contrasto per la ^{19}F -MRI e forma uno strato fluorofobico all'interno del monostrato di nanoparticelle per l'hosting e il rilascio del farmaco. In questo progetto abbiamo proposto tre diverse strutture di ligandi, a partire da due diverse porzioni simmetriche fluorurate contenenti gruppi ossidrilici o esteri metilici. Abbiamo delineato tre strategie sintetiche per ligandi lineari e ramificati, riuscendo a completare la preparazione del ligando lineare derivato dall'estere metilico.

La caratterizzazione di ogni fase delle sintesi per le diverse strutture è stata effettuata mediante spettroscopia NMR 1D (^1H , ^{13}C , ^{19}F), 2D (COSY, HSQC, HMBC) e spettrometria di massa per studiarne la struttura chimica e le funzionalità. Inoltre, le nanoparticelle d'oro sono state studiate con TEM e DLS per ottenere rispettivamente il diametro del nucleo e quello idrodinamico, con TGA per la percentuale di organico e con NMR per confermare la passivazione del ligando e misurare i tempi di rilassamento T1 e T2.

PART I



INTRODUCTION

In order to pursue chemotherapy successfully we must look for substances which possess a high affinity and high lethal potency in relation to the parasites, but have a low toxicity in relation to the body, so that it becomes possible to kill the parasites without damaging the body to any great extent. We want to hit the parasites as selectively as possible. In other words, we must learn to aim and to aim in a chemical sense.

— Paul Ehrlich¹

1.1 INTRODUCTION TO NANOMEDICINE

Nanotechnology is the study and the **manipulation of matter at nanometric scale**. Despite being introduced by Richard Feynman in December 1959², it still continues to be an engaging and flourishing research area: over the last decades we have set some astonishing steps forward in both the comprehension of increasingly smaller phenomena and the precise handling and model of different materials, even at atomic resolutions³.

A more recent scientific field that stemmed from nanoscience and nanotechnology is **nanomedicine**. Its definition can be deduced from the words that constitute the whole term: nano and medicine. Indeed, this field is considered the **application of advanced nanotechnologies to medicine**. Within this general description, nanomedicine hides a highly multi-disciplinary area that bridges and takes advantage of concepts related to physics, chemistry, biotechnology, engineering, and more⁴.

The interaction between these disciplines is fundamental to overcome the challenges that nanomedicine has been called to face; human health is threatened by a huge variety of pathologies and for some of which we have become only very recently aware of their biological mechanisms or even their existence. Among them, the major causes of infirmity and death in modern times are related to pathologies affecting the cardiovascular system (stroke, arteriosclerosis, ischemia), the nervous system (Parkinson, Alzheimer, ALS) or they concern oncological diseases (prostate and breast cancer *in primis*), communicable disease (hepatitis, AIDS) or genetic mutations.

Each of these illnesses represents a medical need that nanomedicine has the potential to address, with the recent literature focusing prevalently on cancer treatment through nanotechnological materials⁵. Notably, some remarkable achievements are already tangible and available to the people: by the year 2016, the Food and Drug Administration (FDA) had approved

51 nanomedicines⁶ such as Doxil[®], the first nanodrug accepted in 1995 to treat Kaposi's sarcoma and now ovarian cancer or multiple myeloma and consisting of doxorubicin liposomal-PEG nanoformulation^{7,8}, or Gastromark[™] (ferumoxsil, an aqueous suspension of silicone-coated superparamagnetic iron oxide nanoparticles (SPIONs) used as an MRI contrast agent for the gastrointestinal tract^{9,10} approved in 2001).

The clinical translation path of nanomedicines is organized in rigorous phases for the assessment of their safety and efficacy; in addition to the above-mentioned accepted nanodrugs, other promising nanomaterials and formulations are currently under investigation¹¹. For example, Genexol[®]-PM consists of polymeric micelles made of polyethylene glycol (PEG) and polylactic acid (PLA) loaded with Paclitaxel that is currently in clinical phase III test for breast cancer¹² or a particular type of Cornell Dots ("C-Dots", PEGylated silica nanoparticles¹³) labeled with ¹²⁴I which is under testing for the imaging of metastatic melanoma through positron emission tomography (PET)¹⁴.

These examples highlight the advantages of nanomedicine in respect to classic pharmacology or underline the technical problems related to the diagnostic instruments that could be overcome using a more efficient nanoscale contrast agent.

As a matter of fact, there are many favorable aspects (**Figure 1.1**) that explain why the researchers are so prone to find a nanotechnological strategy to boost the imaging and sensing power of current techniques and to improve the efficacy of novel or well-established treatments, even with drugs in clinical use¹⁵. Starting with the advantages in diagnostics, the great innovation is **multiplexing**, meaning the ability to detect simultaneously many different molecular signals or biomarkers. Moreover, for many analytical techniques, several nanomaterials have demonstrated striking contrast or **signal enhancement** capacity¹⁶.

Continuing with the improvements in the formulation of drugs in **nanovectors**, the proper combinations, and structuring of specifically designed nanomaterials allows even hydrophobic components, like many drugs, to be dispersed in aqueous biological fluids. Furthermore, the nanovector structure may **protect the active ingredient** from the biological environment. The size of the nanosystem increases their circulation time, helping to reach the site in which the drug should act, without losing the possibility to cross biological barriers. Another advantage of the nanovector resides in the possibility to insert **targeting elements** for the recognition by certain tissues or cell populations, therefore allowing selectivity for accumulation. Moreover, the structure containing the drug could feature a **trigger mechanism** that allows a controlled release. Eventually, the structure containing the active agents should be degraded and excreted without toxic effects to the organism:

for this reason, an important branch of nanomedicine aims to study the intrinsic hazards that these nanomaterials might bring^{17,18} and the biophysical interaction at the nano-bio interface¹⁹. Several of the advantages just described allow reducing the drug dose to be administered, with enormous benefits on limiting adverse or collateral effects on the patient.

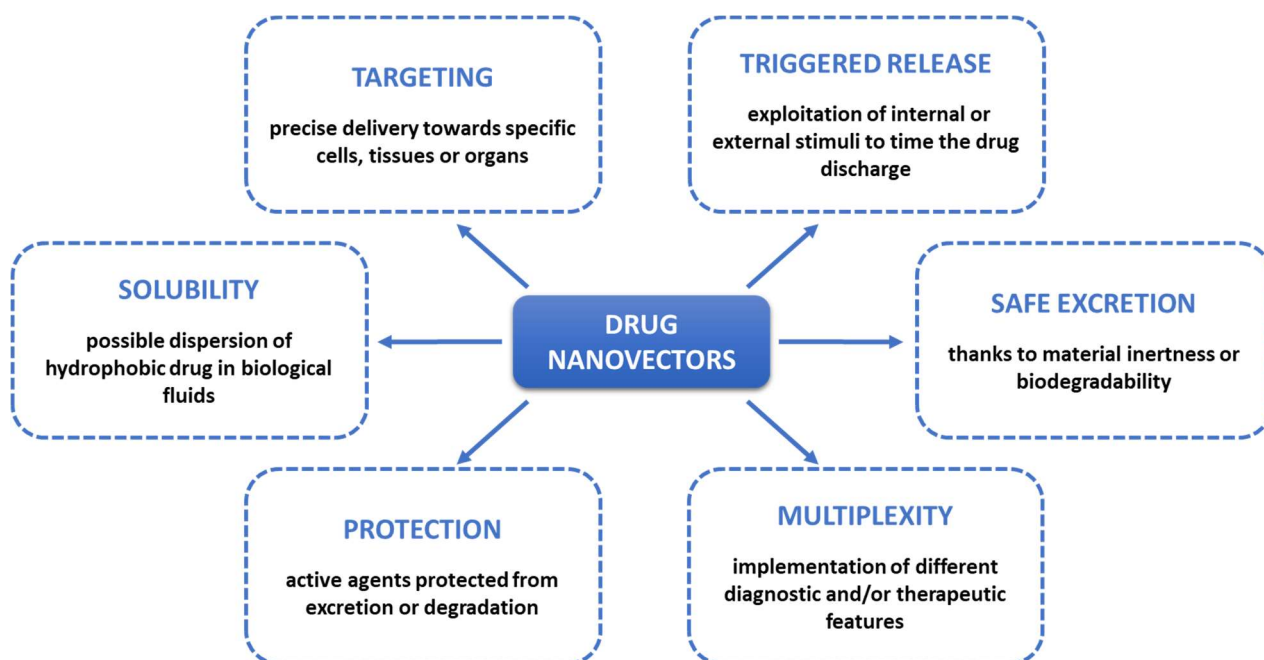


Figure 1.1: Scheme illustrating the main advantages of using nanovectors as formulations for drug administration.

The commercially available materials mentioned before are just few examples among many. Indeed, in many years of efforts in the nanomedicine field, a wide plethora of materials have been designed or reinvented (**Figure 1.2**). Typically, the nanomaterials are primarily divided in organic, inorganic, and hybrid materials: to the first class belong **carbon nanostructures** such as nanotubes, nanodots, fullerenes, graphene dots^{20,21}, the **polymeric nanoparticles** made of linear polymers as in PEG or PLA or block co-polymers²², lipids (for liposomes, vesicles, micelles)^{23,24}, **protein nanosystems** like albumin as in the formulation of Abraxane^{®25} or polysaccharides such as guar gum²⁶.

The second type of nanoparticle consists of **metals** (gold, silver, copper, and alloys), **metal oxide** (iron oxide, titanium oxide, zinc oxide), **silica** (derived from silicon tetraalkoxides or ORMOSIL, organic modified silica), **semiconductors** (silicon, ceramics, quantum dots generally made of CdSe or GaAs) or lanthanides (such as Ho³⁺, Er³⁺, Tm³⁺ or Yb³⁺ dispersed in a dielectric lattice).

The progress in nanotechnology has given us the possibility to obtain both types with a plethora of methodologies, generally divided in “**top-down**” approaches, in which the bulk material is progressively broken or eroded in nanometric pieces (generally with laser ablation, milling,

homogenization, physical or chemical vapor deposition) and “**bottom-up**” approaches, which uses atomic or molecular precursors to form nanosized materials through reactions in an appropriate synthetic environment¹⁵.

Nevertheless, the degree of manipulation reached by nanotechnology these days allows also the design and the preparation of more complex nanostructures with composite nanomaterials that exploit multi-core or multi-layer structures and **organic-inorganic hybrid nanoparticles**.

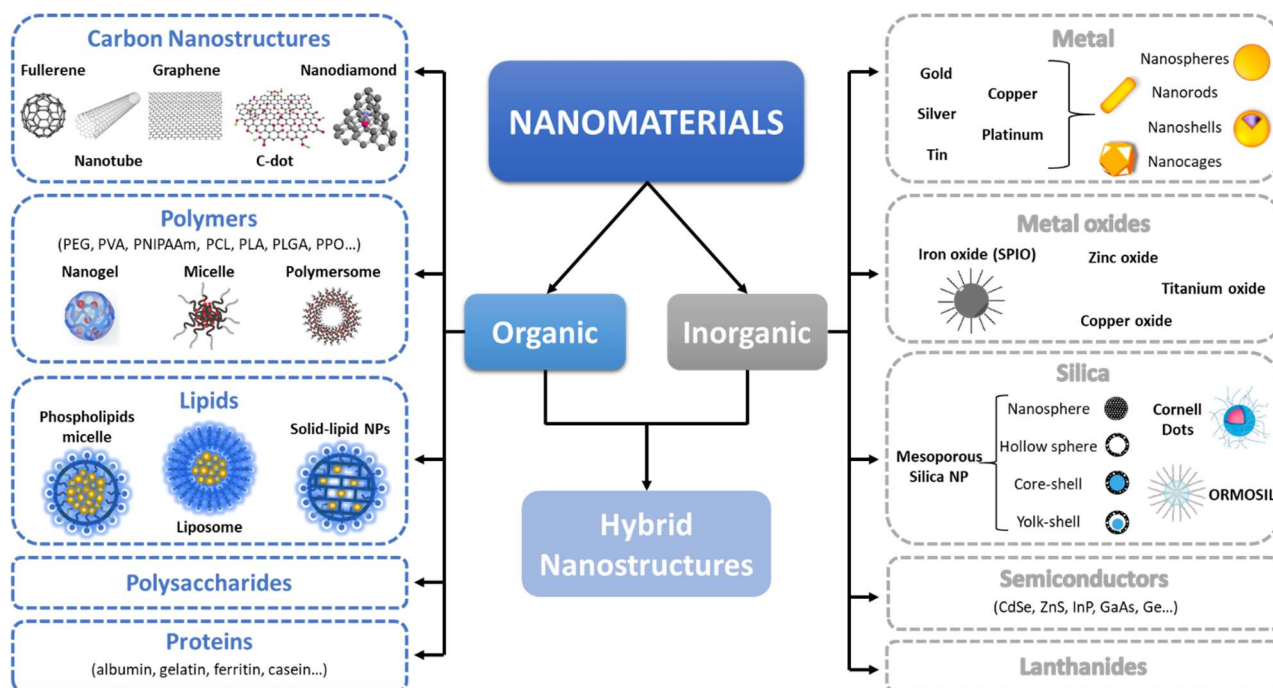


Figure 1.2: Scheme illustrating the principal groups of nanomaterials and structures adopted in the preparation of advanced nanosystems.

1.2 THERANOSTIC NANOPLATFORMS

In the early years of nanomedicine, the aims were primarily to explore the possibilities of these new nanomaterials, to integrate the drugs already available, and to implement target elements to exploit the properties of the material in the nanoscale both for therapy and diagnosis.

The complexity of nanocarriers has increased in the last years thank to the improvement of synthetic methodologies and characterization techniques. Indeed, nowadays, scientists propose more platforms with properties suitable for multiple and even complementary diagnostic techniques or multimodal drug delivery and approaches for therapy.

At the present time, what is pursued at most is the devising of **theranostic nanosystems**: a single device that is able to work as a **nanodrug for therapy** and as a **contrast agent for diagnostics**. This revolutionary approach, first conceived in 1998 by John Funkhouser^{27,28}, relies on the

possibility to localize the disease and treat it on the spot and has been favored by the increasing availability of different matching alternatives for diagnoses and treatments of diverse pathologies.

In terms of therapeutic approaches, there are eight major types of treatment, which can be also combined in a multimodal synergistic way²⁹ (**Figure 1.3**). The one that is currently the most employed is based on the administration of certain drugs delivered by nanocarriers (**chemotherapy**)^{30,31}, but the various transportation and the targeting methods developed can be used also to favors the intracellular delivery of particular DNA and RNA sequences (**gene therapy**)^{32,33} or antibodies (**immunotherapy**)^{34,35}.

A way to eradicate cancer cells is to use the heat to induce their apoptosis. For example, the **magnetic hyperthermia** (MHT)^{36,37} treatment uses SPIONs while **photothermal therapy** (PTT)³⁸ involves chromophores as conversion agents. Both these species can produce heat upon their excitation with external alternate magnetic fields or near-infrared (NIR) radiation, respectively.

Light can also activate a different form of treatment: in the **photodynamic therapy** (PDT)³⁹, particular compounds called “photosensitizers” are able to convert NIR or X-ray radiation in UV-Vis that generates reactive oxygen species (ROS) which ultimately cause the death of the cancer cell⁴⁰.

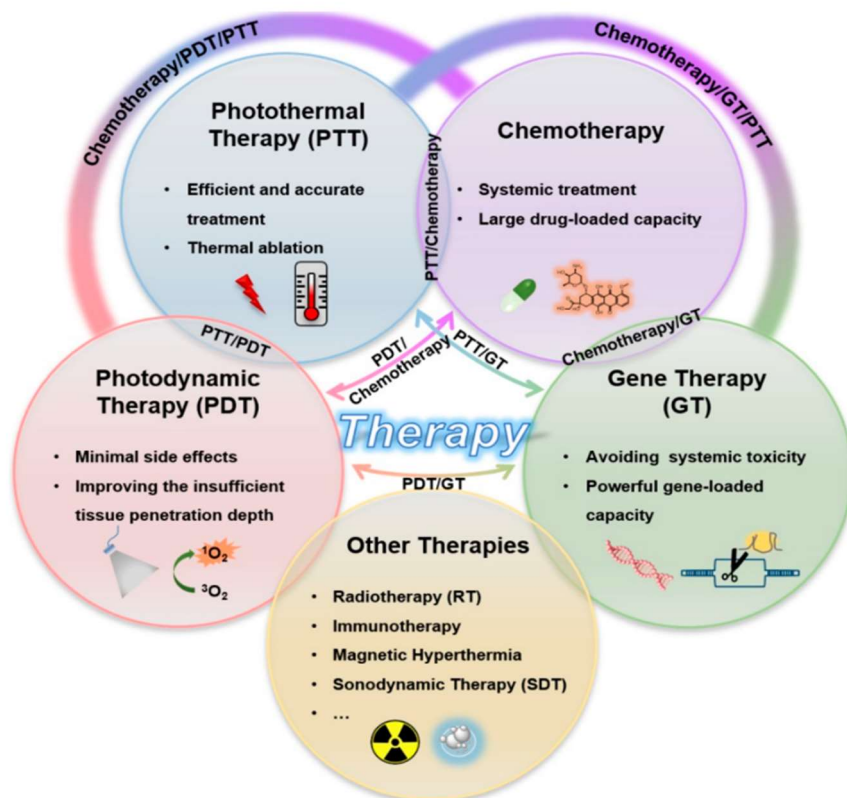


Figure 1.3: Scheme containing the primary therapeutic strategies exploited in nanomedicine with the peculiar advantages of using hybrid nanosystems. Image from reference ⁴¹. Copyright © 2018 American Chemical Society.

Ultrasound waves can act as a mean to trigger two types of therapies: the high intensity focused ultrasound (HIFU)^{42,43} approach or the **sonodynamic therapy** (SDT)⁴⁴. Both are supported by dedicated compounds such as perfluorocarbons⁴⁵, gold⁴⁶, or iron oxide⁴⁷ nanoparticles, which in the case of HIFU help to focus and enhance the ablation following the cavitation, while for SDT “sonosensitizers” molecules work in a similar way to PDT and can be embodied (i.e. TiO₂ itself⁴⁸) or encapsulated (i.e. with mesoporous organosilica⁴⁹) by nanomaterials.

“Radiosensitizers” are molecules or compounds containing heavy metal atoms (such as gold⁵⁰ or tungsten⁵¹) used in the most common form of **radiotherapy** (RT)⁵² that make cancer cells particularly sensitive to the external X-ray radiation that follows the treatment and can be part of a tailored nanosystem⁵³ for an enhance efficacy. An alternative form of this therapy requires the direct administration of specific therapeutic radioisotopes (such as ⁹⁰Y ¹⁶⁶Ho or ¹⁸⁸Re)⁵⁴ that are guided towards the tumor mass where they decay with X-ray emission.

A nanomedicine approach permits to achieve the fundamental requirement that all these different treatments have in common: the selective delivery of the active species. The ultimate objective is to maximize the ratio between the quantities that actually reach the target and the dose originally administrated, while reducing any collateral effects.

Focusing on the diagnostic aspect of nanomedicine (**Figure 1.4**), the most common and available technique is based on **ultrasound** instruments, but there are other methods with a higher level of sensitivity. One of these is **magnetic resonance imaging** (MRI), in which the spins of selected atoms nuclei can be visualized *in vivo* if excited with radiofrequency pulses. MRI has been demonstrated to be very useful for pre-clinical diagnosis, biodistribution, and treatment monitoring.

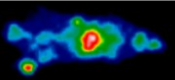
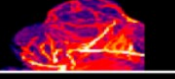
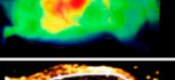
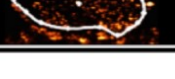
IMAGING	APPLICATIONS	ADVANTAGES	LIMITATIONS
PET SPECT 	<ul style="list-style-type: none"> Drug targeting Biodistribution Blood pool imaging 	<ul style="list-style-type: none"> High sensitivity Quantitative results Unlimited penetration 	<ul style="list-style-type: none"> Limited spatial resolution No anatomical information Radioactive probes
CT 	<ul style="list-style-type: none"> Anatomical information Hybrid imaging Perfusion monitoring 	<ul style="list-style-type: none"> High spatial resolution Dynamic imaging Quantitative results 	<ul style="list-style-type: none"> Low contrast agent sensitivity Poor soft tissue contrast Radiation exposure
MRI 	<ul style="list-style-type: none"> Drug release Drug efficacy Cell tracking 	<ul style="list-style-type: none"> High spatial resolution High soft tissue contrast High versatility 	<ul style="list-style-type: none"> Low throughput Low contrast agent sensitivity Difficult quantification
OI 	<ul style="list-style-type: none"> Drug targeting Hybrid imaging Nucleic acid delivery 	<ul style="list-style-type: none"> High throughput High sensitivity High probe versatility 	<ul style="list-style-type: none"> Poor penetration depth No anatomical information Difficult quantification
US 	<ul style="list-style-type: none"> Drug targeting Perfusion monitoring Sonoporation 	<ul style="list-style-type: none"> High sensitivity High throughput Dynamic imaging 	<ul style="list-style-type: none"> Low probe versatility High user dependency No whole-body imaging

Figure 1.4: Summary of the most diffused imaging techniques with their applications and peculiarities. Adapted from reference ⁵⁵. Copyright © 2015 American Chemical Society.

Light sources are at the basis of the **optical imaging** (OI) and **photoacoustic imaging** (PAI), even if they transduce the incoming radiation differently: in the first case, specific fluorophores are able to emit in a range that can be sensed through the body tissues, while for the second technique the decay is not radiative but produces heat that induces thermoelastic tissue expansion detectable with ultrasound equipment.

Alternative similar diagnostic techniques are **computed tomography** (CT), **positron emission tomography** (PET) and single-photon emission computed tomography (SPECT). While the first relies on the detection of X-rays, the last two use γ -rays coming from substances injected in the patient, but the source is different: for PET a positron is emitted by a radioisotope (positive β decay) and annihilate immediately with an electron, while in SPECT the radiation is a consequence of a radionuclide decay.

For each of these modalities, the contribution of nanomedicine reflects in the sensitivity of the measure: the aim is to increase the signal-to-noise ratio, maximizing the useful output that the instrument collects by means of tailored contrast agents¹⁶.

An example of a nanosystem that works in a theranostic way is the one developed by Huang and co-workers⁵⁶. They designed a nanoplatform for photoacoustic imaging-guided sonodynamic therapy of cancer composed of folate (for tumor targeting), PLGA (for drug protection and delivery), melanin nanoparticles, and hematoporphyrin monomethyl ester. Melanin nanoparticles act as imaging elements since they are a contrast agent for PAI, while hematoporphyrins are species known for their applications in sonodynamic therapy (SDT).

The group of Liu and co-workers has chosen different techniques: they have prepared a multi-layer nanosystem with a gold nanowire core, covered with silica and decorated on the surface with iron oxide nanoparticles restrained by a polycystamine net. Once inside the cell, this network is disassembled by glutathione, and the magnetic nanoparticles can be detected by MRI, while the Au nanowires can be used for PTT upon their excitation with NIR radiation⁵⁷.

Despite the increasing knowledge on nanomaterials and the notable number of nanosystems that are currently in clinical trials, we lack solutions that have actually hit the market and the clinical field: the nanomedicines currently available are very few in respect to the related literature and the efforts put into play. The increasingly widespread realization in the scientific community to explain this shortage is that the nanomedicine approach was biased by some naïve assumptions in the understanding of biology, the nanomaterial design, and its application in tests. Nanomedicine,

more than other fields, is a multidisciplinary field that has to face a series of complex challenges, ranging from biological and technological ones or related to the study design⁵⁸.

To take up the biological challenge means evaluating carefully the nanosystem in terms of biodistribution, targeting, membrane permeation, interaction with proteins, accumulation, efficacy vs. toxicity⁵⁹. These aspects would benefit from a deeper understanding of NPs-bio interactions for different medical targets, which the scientific community is slowly but steadily achieving.

From the technological point of view, what still hampers the spread of nanosystems are issues related to the scale-up of their production and purification, the uncertain long-term stability, the complexity of manufacturing processes, the optimization of their performances, and the lack of standardized protocols⁶⁰. Moreover, clinical imaging still shows its intrinsic limitation in terms of tissue penetration for certain types of applications and for studies of nanodrug dynamics at cellular or molecular levels⁵⁹.

Finally, the study design is another aspect that needs a rethinking: the applications study and the clinical translations have to be better devised and reported in order to overcome what are known as the two “gaps”. The first one, the “*in vivo-in vitro* gap”, means that *in vitro* results are often difficult to translate and compare to *in vivo* experiments and outcomes, since these studies involve very different settings, while the “translational gap” considers that animal models are not always equivalent to human patients, hence clinical results could be even conflicting, and the therapeutic or diagnostic strategies should be reconsidered in some cases⁶¹. Both would be helped by more rigorous standardization of experimentations and protocol design.

All these challenges are particularly tough in relation to cancer nanomedicine, where the variability in morphology, behavior, and response to treatments among different types of tumors and even within the same type but affecting different patients is considerable. For this reason, the heterogeneity in cancer is an aspect that drives the modern research in nanomedicine, which should involve nanosystems specifically designed for a certain kind of tumor and patient stratification.

The conventional nanomedicine approach that limited the efficacy of the nanosystems studied relied more strongly on the EPR effect, ignoring several other fundamental aspects such as the interstitial fluid pressure and the stroma thickness: it is now commonly accepted that EPR is an oversimplified and too general model.

Therefore, delivering NPs to tumors (solid tumors in particular) effectively is an extremely hard process, since it is necessary to take into account new aspects and obstacles which has been discovered only very recently: in a recent meta-analysis of the past literature, it was estimated that

the amount of injected dose of nanoparticles effectively accumulated in the tumor was below 1 % on average⁶².

Finally, the lack of nanosystems to treat human patients successfully and the difficulty to translate them between biological and clinical trials is imputable to the inadequacy of the cellular and animal models adopted so far. This awareness has led to new theories and methods such as comparative oncology and studies that confront new nanodrugs with nanomedicines that are already on the market.

So far, these complications have interfered with the manifestation of the full potential of nanomedicine, but fortunately, the trend is changing, and we start to learn from the former error and embrace new methods (microfluidics, bioprinted 3D models), new approaches (such as theranostic and immuno-oncology) and philosophies, like “working *with* biology and not *against* biology”.

For what concern the nanosystems that will be presented in this thesis, we tried to embrace this new mentality by combining a depth-independent and reliable imaging technique as MRI with drugs known to be effective for particular pathologies in a theranostic approach that will be translated into hybrid organic-inorganic nanocarrier for drug molecules and contrast agents.

We know that even more endeavors and deep comprehension are requested to succeed, so research in nanomedicine has never been so engaging and promising: there is (still) plenty of space for new discoveries.

Considering the current challenges in the nanomedicine field, the endeavors of the research work within the PhD period were dedicated to devise and prepare **innovative hybrid organic-inorganic theranostic nanoplatforms**.

In particular, the focus of the thesis was twofold:

- The *ex-novo* design, synthesis, and characterization of a complex nanosystem constituted by a **polymeric framework** capable of hosting **drug molecules** for the treatment of neurodegenerative disorders and **superparamagnetic iron oxide nanoparticles (SPIONs)** for ^1H -MRI;
- The design, synthesis, and characterization of a series of improved **fluorinated ligands** for the assembly of **gold nanoparticles** and their application in ^{19}F -MRI and drug delivery with possible application in the treatment of glioblastoma.

Accordingly with the objectives of the current nanomedicine research, our goal is to develop a device in which both the therapeutic and the diagnostic functionalities are already implemented and readily accessible: the optimal and most desirable theranostic nanoplatform should enable the delivery of therapeutics in a less toxic and more efficient way respect to common formulations and the possibility to push forward the sensibility and the applicability of current diagnostic techniques.

The first hybrid nanosystem proposed will be properly assembled around a polymeric structure to combine the **chemotherapeutic effect** of the drug payload and the **positive contrast effect on ^1H -MRI**, with the enabled possibility for **magnetic drug targeting**.

Some examples of polymer-based nanoparticles as carriers for drug and contrast agents are already known in literature⁶³ and the thesis work has one of the primary objectives of identifying suitable polymers or blends of them meeting the criteria of biocompatibility, high SPIONs loading, reduced polydispersity, and purity respect to the residual presence of free polymer and SPIONs not included in the nanosystems as well as the absence of nanosystem aggregates.

For what concern the synthesis of SPIONs, the intention is to find an approach that could provide very small nanoparticles made of magnetite for positive contrast in MRI, with a coating that could help their internalization in polymeric compartments without affecting their dimensional and magnetic characteristics.

Subsequently, we aimed to expand the functionality and complexity of this nanosystem, by enclosing selected hydrophobic drug molecules within the polymeric inner compartments.

The second project concerns the development of a theranostic hybrid nanosystem based on gold nanoparticles coated with PEGylated thiols carrying a perfluoropolyether moiety to be used for the **therapeutic function of drug carrier** and act, at the same time, as contrast agent for ^{19}F -MRI. This work is integrated with previous studies on fluorinated gold nanoparticles undertaken by our research group⁶⁴ and constitutes its natural continuation. The objective of this work is to improve both the imaging and the drug delivery features with respect to previous examples.

These enhancements can be achieved simultaneously by increasing the number of fluorine nuclei in the thiol ligand, thus providing both a wider fluorophobic reservoir in which hydrophobic and fluorophilic interactions could be exploited and a stronger NMR signal, hence an increased diagnostic power.

For these reasons, the structure and the synthetic strategy for the preparation of the ligand have to be adjusted to consider the insertion of a different perfluoropolyether moiety, with the related changes in reactivity and solubility. Since we still want to prepare water-soluble species, the synthetic approach should always consider the insertion of PEG units in the ligand structure.

PART II



SPIO NANOPARTICLES IN POLYMERIC STRUCTURES (SPIONs@POLYMER)

3.1 SUPERPARAMAGNETIC IRON OXIDE NANOPARTICLES (SPIONS)

Generally, SPIONS, such as the FDA-approved Feridex IV[®] are normally used as negative contrast agents, resulting in darker areas in MR images. However, it is difficult for radiologists to differentiate the tumor from internal bleeding, air–tissue boundaries or other benign lesions (calcification and cysts). The recently emerged ultrasmall superparamagnetic iron oxide nanoparticles (USPIONS) are promising in acting as T1-weighted contrast agents and are potential candidates for substituting Gd-based contrast agents in T1-weighted MRI.

— from Du et al.⁶⁵, *Journal of Materials Chemistry B*, 2020, 8, 2296-2306

One of the nanomaterials that have been extensively and successfully studied for both therapeutic and imaging applications is **iron oxide**, which can be shaped into nanoparticles. The key properties exploited in medicine, stem from the phenomenon known as **superparamagnetism**, observed for the first time in 1938 by William Cronk Elmore⁶⁶, but named as we know it today only lately by Bean and Livingston⁶⁷. This property rises below a certain dimension from species that are naturally ferromagnetic or ferrimagnetic: as shown in **Figure 3.1**, if the particle is smaller than the critical diameter (D_c , which depends on the magnetic material⁶⁸), then it has a single magnetic domain which can be defined by a unique magnetic moment (called “macro-spin” or “super-spin”) that lies on an “easy axis” of magnetization related to the nanoparticle magnetic anisotropy⁶⁹.

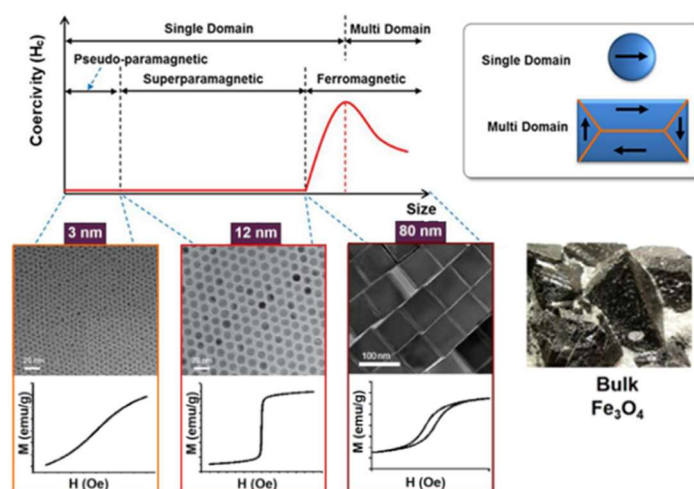


Figure 3.1: Scheme illustrating the magnetic properties in relation to the nanoparticles' size, where the superparamagnetic range and the domains are showed, along with (center row) TEM images and (bottom row) magnetization curves of the corresponding nanoparticles. Adapted from images⁷⁰ and⁷¹. Copyright © Authors of⁷⁰ and © 2015 American Chemical Society.

Due to the thermal energy that exceeds the barriers between superspin's direction states along the same axis, below a certain dimension, this magnetic moment fluctuates spontaneously between them⁷² within a range of time called Néel relaxation time (τ_N), therefore showing zero overall magnetization and acting like a paramagnet⁷³. However, in the presence of an external magnetic field, it is possible to align the spin with a response that is greater in respect to a normal paramagnet; the presence of a superspin, its flipping, and this high magnetic susceptibility define the superparamagnetic state.

Therefore, superparamagnetic nanoparticles can be magnetized with a relatively low magnetic field ($< 0.5 \text{ T}$)⁷⁴ but do not retain the magnetization once the input is interrupted. This behavior is particularly useful in the biomedical field since **high susceptibility and magnetization** are essential to guarantee supreme performances in contrast effect, magnetic guidance, or thermal activation. At the same time, the **absence of initial magnetization** prevents the formation of early coagulation (which occurs only when the external magnetic field is applied), leading to an extended circulation time in the organism, while the **lack of remnant magnetization** favors the successive re-dispersion⁷⁵.

Regarding the size, magnetic NPs are sometimes divided in the following categories:

- Micro-sized particles of iron oxide (MPIO): with a hydrodynamic mean diameter between 1 and $8 \mu\text{m}$ ⁷⁶;
- Standard SPIO (SSPIO): with a hydrodynamic mean diameter between 50 and 150 nm ⁷⁷ and a magnetic core below 20 nm, the upper limit for ION superparamagnetism (ref);
- Ultra-small SPIO (USPIO): with a hydrodynamic mean diameter of 20 - 50 nm ⁷⁸;
- Very small SPIO (VSPIO): with a hydrodynamic mean diameter below 20 nm ⁷⁸;
- Extremely small iron oxide nanoparticles (ESION): with a magnetic core below 5 nm ⁷⁹.

Among iron oxides, there are six non-hydrates phases that have been identified, which are FeO (instable and paramagnetic, contains only Fe^{2+}), Fe_2O_3 (contains only Fe^{3+} and counts 4 polymorphs), and Fe_3O_4 (contains both Fe^{2+} and Fe^{3+})⁸⁰. However, only the $\gamma\text{-Fe}_2\text{O}_3$ (**maghemite, ferrimagnetic**) and Fe_3O_4 (**magnetite, ferrimagnetic**) species have shown structural and magnetic properties that make them suitable for application in biotechnology and medicine^{81,82}.

In particular, what has been proposed during the years are several *in vitro* studies for the separation of cells⁸³, viruses⁸⁴, biochemicals⁸⁵ or metals⁸⁶, along with studies for applications in immunoassays⁸⁷ and enzyme immobilization⁸⁸; the most part of these applications exploits the possibility to retain magnetically SPIONs functionalized with specific ligands, nucleotides, enzymes, or antibodies.

On the side of *in vivo* nanomedicine instead, SPIONs proved themselves to be a very valuable resource for both therapeutic⁸⁹ and diagnostic^{90,91} purposes, with some formulations already approved by FDA^{92,93}, for example to be used specifically in liver imaging like Feridex®⁹⁴. The intrinsic biocompatibility of this type of nanomaterials is certainly a factor that helps their translation towards biological applications. Indeed, iron ions are already present in our organism where they support vital biological processes (cellular respiration, oxygen transport). Furthermore, iron oxide nanoparticles are one of the few examples of nanomaterials that can be naturally taken and employed by the human metabolism after the administration⁹⁵ (for example their incorporation into ferritin by Küppfer cells⁹⁶). Indeed, several iron oxide formulations already on the market are currently prescribed to contrast the iron deficiency in chronic kidney disease (such as Venofer® or Ferrlecit®⁹³). Therefore, they are largely considered **nontoxic and biologically tolerated**, since they can be easily degraded and excreted either through renal⁹⁷ (< 8 nm), hepatic⁹⁸ (10-180 nm), or splenic⁹⁵ pathways based on their dimension and charge.

However, naked iron oxide nanocrystals have been demonstrated to induce the production of reactive oxygen species (ROS) and lead to serious DNA, cytoskeleton, mitochondria, or cell membrane damaging or altering⁹⁹, even if there were no measurable toxic effects for concentration below 200 µg/mL¹⁰⁰. The dangerousness is known to be greater the smaller the nanoparticles are. The way through which this threat has been avoided is to coat the SPION's surface with natural or synthetic species (polymers or small molecules) to prevent agglomeration and enhance biocompatibility¹⁰¹. Furthermore, the coating can be engineered to endow the magnetic particles with targeting, recognition, or other imaging functions.

3.1.1 Synthesis

The synthesis of new core-shell SPIO nanoparticles is generally planned to take into account the formation of both the magnetic core and the protecting coating which can be, if necessary, further functionalized. The nanostructure is therefore divided in (**Figure 3.2**):

- The **iron oxide core**, whose properties can be exploited for magnetic targeting or imaging purposes;
- The **surface coating**, which determines the solubility of the system and the interactions with the other species;
- The **functionalization**, which confers particular features to the nanosystem, such as receptor targeting, molecular recognition elements, or additional imaging features (i.e. fluorophores or radiotracers)

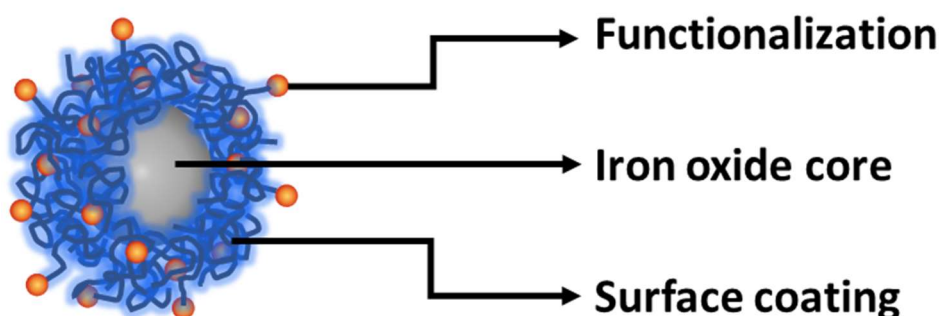


Figure 3.2: Representation of a general core-shell superparamagnetic iron oxide nanoparticle (SPION) with the major structural components.

3.1.1.1 Iron oxide core

For what concerns the first element, the research area on SPIONs has been particularly successful in terms of methods developed for the nucleation of the iron oxide core and strategies to achieve specific size, shapes, dispersion, and magnetic properties.

Moreover, the condition upon which these nanoparticles can be employed in nanomedicine is to have a biocompatible shell molded from suitable ligands. This surface functionalization has many purposes: it prevents the possible nanoparticle degradation that can occur in biological environment, it stabilizes the dispersion, avoiding the aggregation that can be triggered by the magnetic attraction between NPs, and finally it provides a support for functionalization, such as the binding of drugs, targeting compounds or biomolecules⁸².

The most common and versatile pathway for the synthesis of iron oxide nanoparticles is the **wet chemical method**, a “bottom-up” approach that comprises various strategies that have been devised to expand the range of size and functionalization of these magnetic nanosystems: these procedures are synoptically summarised in **Table 3.1**. Furthermore, the wet chemical approach enables the preparation of large quantities of materials in a reproducible way.

The **co-precipitation synthesis** is historically the first reported method and still the most popular one: discovered by Massart and colleagues in 1981¹⁰², it uses a mixture of Fe^{3+} and Fe^{2+} ions (usually in the form of chlorides or sulfates) in a 1:2 molar ratio dispersed in basic aqueous solutions (generally using NaOH or NH_4OH) at room temperature or upon heating. The synthesis can lead to both Fe_2O_3 or Fe_3O_4 nanoparticles, whether it is performed in aerobic or anaerobic conditions respectively. These nanoparticles present many hydroxyl groups on the surface that help their dispersion in water¹⁰³. This is a relatively simple procedure that allows many conditions (molar ratio, counterions, pH, temperature, or stirring rate) to be tuned in order to change the final

properties of the particles. Unfortunately, the size distribution is generally broad and this can affect negatively the magnetic properties.

A commonly used strategy is the **hydrothermal synthesis**: it is performed in aqueous solution at high temperatures (130-250 °C) and high pressures (0.3-4 MPa) to obtain small hydrophilic nanoparticles with a high degree of monodispersity and crystallinity¹⁰⁴ and can be performed either with¹⁰⁵ or without¹⁰⁶ surfactants.

A similar method associated to the hydrothermal procedure is the **solvothermal synthesis** in which the formation of SPIONs occurs in analogous conditions of temperature and pressure, but in organic solvents instead of water¹⁰⁷. This procedure allows the preparation of nanoparticles with hydrophobic coating and the control over size and morphological properties is better than the hydrothermal alternative.

Another procedure that enables the preparation of hydrophobic iron oxide nanoparticles with narrow size distribution and high crystallinity is the **thermal decomposition** of different organometallic precursors (such as $\text{Fe}(\text{cup})_3$, $\text{Fe}(\text{acac})_3$ or $\text{Fe}(\text{CO})_5$)¹⁰⁸ performed in high boiling solvents in the presence of stabilizing surfactants such as oleylamine, oleic acid or other fatty acids¹⁰⁹. This procedure allows achieving the smallest nanoparticle dimension⁸⁹, although a wide variety of size and shape features can be obtained by changing parameters such as the precursors, reagents concentration, solvent, temperature, and the reaction time¹¹⁰. A recent example of this procedure is reported by Khandhar and co-workers with the thermolysis of Fe(III) oleate with oleic acid and octadecene at 318 °C¹¹¹. However, the general disadvantages of this route regard primarily the complicated synthetic conditions, which force to work with very high temperatures and toxic reagents and ultimately the hydrophobic nature of the nanoparticles, that should be further functionalized to disperse them in aqueous environments¹¹².

The last approach that allows obtaining either hydrophilic or hydrophobic iron oxide nanoparticles is the **microemulsion method**, which employs a thermodynamically stable isotropic dispersion of two immiscible liquids (oil-like in water-like, O/W¹¹³ or water-like in oil-like, W/O or reversed micelle¹¹⁴) in the presence of suitable surfactants that stabilized the interfacial film¹¹². The aim is to form “nano-reactors” in which the nucleation and the growth of iron oxide nanocrystals (usually in a co-precipitation fashion) occur in a stable, confined, and protected environment. The confinement of the growth of the nanocrystals has the major benefit of achieving materials with tuneable sizes and morphologies with a lower polydispersity in respect to the classic co-precipitation method, avoiding at the same time their aggregation¹⁰⁴. However, very often there are some notable disadvantages regarding the biosafety of the surfactants used and the long purification steps for their elimination.

Table 3.1: Overview of the characteristics of the principal synthetic methods in SPIONs preparation.

METHOD	CONDITIONS	SIZE DISTRIBUTION	SHAPE CONTROL	DISPERSION	NPs TYPE
Co-precipitation	Ambient, base; minutes	Wide	Not good	Polydisperse	Hydrophilic
Hydrothermal synthesis	High pressure, high temperature; hours	Narrow	Good	Monodisperse	Hydrophilic
Solvothermal synthesis	High pressure, high temperature; hours	Very narrow	Very good	Highly monodisperse	Hydrophobic
Thermal decomposition	High temperature, inert atmosphere; days	Very narrow	Very good	Highly monodisperse	Hydrophobic
Microemulsion	Ambient, surfactants; hours	Narrow	Good	Rather monodisperse	Hydrophilic, hydrophobic

3.1.1.2 Surface coating

Some of the synthetic routes previously described already provide a complete coating layer, but usually, after the core growth completion, the surface remains “naked”: this could lead to issues in terms of colloidal stability or solubility and make the nanoparticles unsuitable for biological applications. The set of different **coating species** used in the syntheses has been considerably enriched during the years, and nowadays include both organic and inorganic materials.

According to their polarity, organic coating agents can be divided in:

- **Oil-soluble**, such as alkanolic acids⁸² or phosphonates¹¹⁵ with long alkyl chains;
- **Water-soluble**, typically small molecules like citric acid¹¹⁶, amino acids¹¹⁷, hydroxamate, or cyclodextrins¹¹⁸;
- **Amphiphilic compounds**, surfactants containing both hydrophobic and hydrophilic functions or biomolecules such as polypeptides¹¹⁹ and proteins¹²⁰.

Among **organic substances**, **polymers** are the most employed for the passivation of the magnetic core thanks to their extreme versatility, hydrophilicity, biocompatibility, and the possibility to prevent the opsonization by plasma proteins¹²¹. The ones that are most commonly used are either **natural polymers** such as the polysaccharides dextran, starch, and chitosan or **synthetic polymers** like polyethylene glycol (PEG)¹²², polyvinyl alcohol (PVA)¹²³, or polylactic acid (PLA)¹²⁴. These species are adsorbed or grafted to the SPION's surface prevalently via hydrogen bonds, hydrophobic interactions, or metal complexation¹²⁵ and once grafted present helpful hydroxyl, amine, or carboxyl acid groups on the exposed surface that paves the way for further shell functionalization.

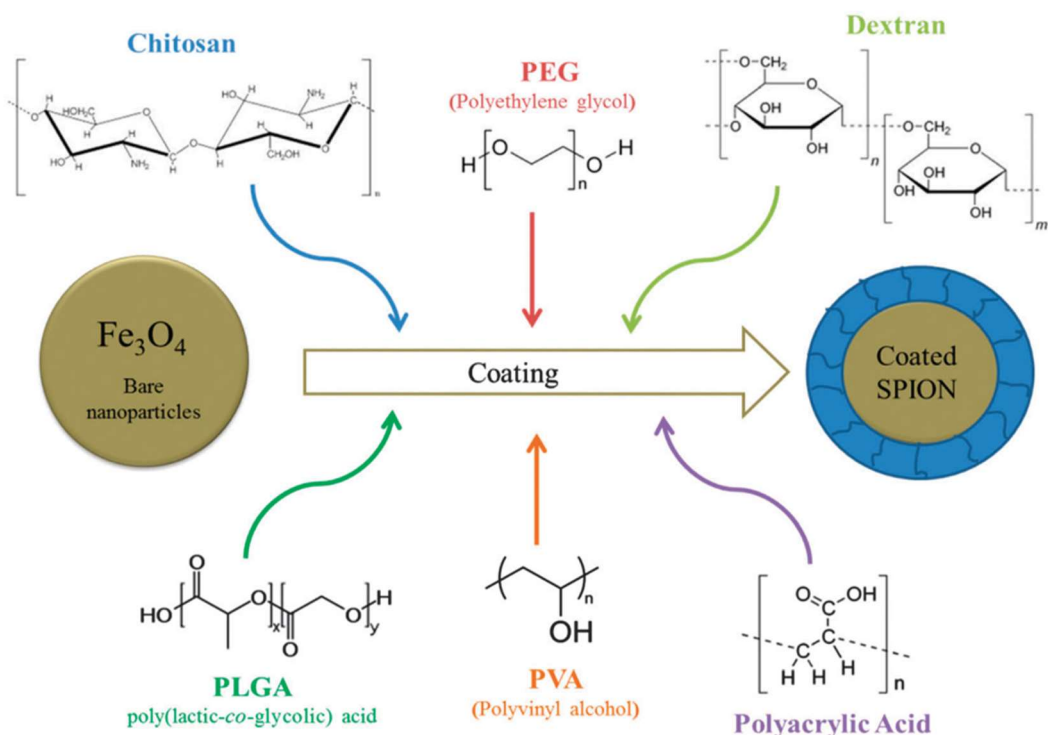


Figure 3.3: Scheme illustrating the principal polymers used for coating bare SPIONs. Image from reference ¹⁰⁴. Copyright © 2015 The Royal Society of Chemistry

Another particular type of organic compounds that are often used for imparting stability to hydrophilic SPIONs are **organosilicon compounds or silanes** (in particular alkyltrialcoxysilanes), described by the general formula $R^1Si(OR^2)_3$, where R^2 can be either H or an alkyl group (usually methyl or ethyl). In the presence of traces of water, the R^2 groups are replaced and the silane derivative forms a network of Si-O bonds with the hydroxyl groups of SPION's surface¹²⁶. On the other hand, the R^1 chain is the one that endows the organic shell with specific properties and/or functional groups. Very common is the use of 3-aminopropyltriethoxysilane (APTES)¹²⁷ and mercaptopropyltriethoxysilane (MPTES)¹²⁸ for further functionalization.

The **inorganic coatings** are prevalently used to protect the naked iron oxide nanoparticles from oxidation and to confer unique properties for applications in catalysis, bio-labeling, and bioseparation¹¹², while maintaining the magnetic properties of the core. The list of inorganic coating materials counts **metals** such as silver¹²⁹, platinum^{130,131} or palladium¹³² and gold, **non-metals** (i.e. carbon¹³³), **metal oxides** (such as Al₂O₃¹³⁴, TiO₂¹³⁵, ZnO¹³⁶, Co₃O₄¹³⁷), and **metal sulfides** (i.e. ZnS).

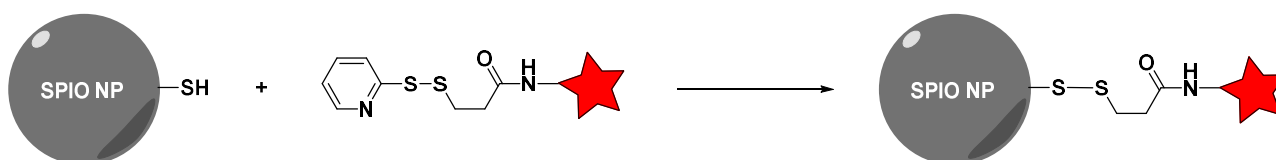
The most commonly used material for this purpose is **silica**, for a great series of useful properties that can provide to the nanosystem, such as chemical stability, aggregation prevention, biocompatibility, hydrophilicity, and surface functional groups versatility¹³⁸. However, the main

limitation is that it is still hard to obtain a homogenous thickness of the shell, and this can affect the magnetic properties of the final nanosystem¹³⁹. With other metal oxides or chalcogenides, it is often hard to achieve a complete covering, so usually the “nanocomposite” or “dumbbell” structure has a main SPIO core from which several protrusions of the other compound stick out.

3.1.1.3 Functionalization

The last optional passage in the preparation of a functional SPION is to implement **tailored ligands** or **specific units** on the coated particles formed during the previous steps. If the coating presents reactive moieties (such as the hydroxyl functions in polysaccharides, the amine functions of chitosan, or the carboxylic functions of citrate), these primary functional groups can be the linking point for further conjugations (for example via click chemistry¹⁴⁰).

The process for the functionalization of SPIONs’ surface using primary or intermediate reactive groups is called “**vectorization**” (**Scheme 3.1**) and can be performed on an extensive list of small molecules (dyes, targeting agents) or macromolecules (proteins, enzymes, antibodies) for different purposes.



Scheme 3.1: Graphical representation of an example of vectorization through S-S bridge between a SPION carrying a thiol group and the pyridyl sulfide moiety of SPDP grafted on a dye (“vector”). Adapted from reference ¹⁴¹.

To fulfill this aim, different strategies may be employed, with either an **activation of the functional groups of the NP coating or the active compound**. In the first case, the intermediate functional group presented before is introduced and used immediately or following its activation, for the conjugation with a natural bioactive substance¹⁴².

In the second case, the bioactive molecule is modified with reactive groups that can interact with the primary functional groups of the coating, as in the case of the commercially available fluorescein isothiocyanate or rhodamine B isothiocyanate that can interact with thiol or amine groups¹⁴³ or analogous structures with terminal epoxides if the coating presents hydroxyl groups¹⁴⁴.

The **ligand exchange** is also a technique that is used to modify the surface properties of the nanosystem in order to achieve biocompatibility, long-term stability, or specific functionalities.

This strategy is usually adopted to **displace the hydrophobic chains** that cover the surface with other hydrophilic molecules containing ending groups with high affinity for it, such as hydroxyl (i.e. in dopamine¹⁴⁵), carboxylic acids¹⁴⁶, amines, silanes¹²⁶, or phosphines¹⁴⁷.

Moreover, these new ligands can already contain bioactive or luminescent species or end with a group that can be further functionalized¹⁴⁸. The ligand exchange strategy can be employed either to replace some chains or to renew the shell completely¹⁰⁹, depending on the concentration of the new ligand that is put in contact with the nanoparticles.

An alternative way to modify the coating, make the nanoparticle biocompatible and introduce additional functionalization is its **total encapsulation** by means of various kinds of amphiphilic (PEG-based¹⁴⁹) or natural (polypeptides or polysaccharides¹⁵⁰) polymers: they self-assemble to form a new coating layer that endows the nanoparticle with completely new or enhanced properties, as in the case of the work of Tong and colleagues that have encapsulated 14 nm SPIO nanoparticles within a 1,2-distearoyl-*sn*-glycero-3-phosphoethanolamine-*N*-[methoxy(polyethylene glycol)] copolymer (DSPE-mPEG) to increase their T2 relaxivity up to 200 fold¹⁵¹.

3.1.2 Characterization methods

The characterization of these nanosystems has mostly the aim of assessing the success of the synthetic procedure employed, the achievement of the desired properties; it is directed towards the study of both the core and the shell components, since they concur to the final application of the theranostic nanosystem, very often in a complementary way.

3.1.2.1 Characterization of the core

The main techniques to gain information about **SPIONs' size and distribution** are **transmission electron microscopy (TEM)**¹⁵² and **small-angle X-ray scattering (SAXS)**¹⁵³. These two techniques rely on different sources and physical phenomena, providing size data related to the number of nanoparticles sampled (TEM case) or weighted on the amount of light that has been scattered (SAXS case)¹⁵²; therefore, for samples that are not monodispersed, the size values obtained with these techniques may be discordant. While both TEM and SAXS give the size dispersion of the sample, HR-TEM can be used to display the shape of NPs.

Electrons or X-ray sources are also what can be used to study the **crystal structure and the composition of the core**, respectively in **selected area electron diffraction (SAED)**¹¹³ or in the **X-ray diffraction (XRD)**¹⁵⁴. Using XRD allows also to evaluate the degree of disorder in the lattice of

the different layers of the nanoparticle's core (especially on or near the surface), which is an essential feature that influences its magnetism¹⁰⁶. Finally, with this method is also possible to estimate the size of the nanoparticles through Scherrer's formula^{155,156}.

Some examples of techniques that can be used for the **elemental analysis** of the magnetic core are the **energy dispersive X-ray (EDX)** analysis¹⁵⁷ or the **inductively coupled plasma optical emission spectroscopy (ICP-OES)**¹⁵², which are very helpful to determine the content of iron and other species, especially if some impurities or other metal components are present in the structure.

An essential part of the characterization of these nanoparticles, which is highly finalized to their applicability, concerns the assessment of their **magnetic properties**. The two principal magnetic parameters that define a superparamagnetic material are the residual magnetization (M_r) and the saturated magnetization (M_s). The former is the magnetization of the material without any external magnetic field, while the latter is the maximum magnetization reached when an increasing field is applied¹⁵⁸. These information can be acquired using instruments called magnetometers, such as in **vibrating sample magnetometry (VSM)**¹⁵⁹ or with a **superconductive quantum interference device (SQUID)**¹⁶⁰. Both can be used to acquire the hysteresis diagram of the core material: this is a graph of the magnetic moment (M) versus the external applied field (H) that generally forms a loop plot if the field is swept from positive to negative values and back¹⁶¹. For superparamagnetic nanoparticles above a certain temperature, this hysteresis diagram should show a maximum magnetization value (M_s) and no residual magnetization (M_r) nor coercitivity (H_c) once the applied field returns to zero and then is inverted, hence the trace should pass through the origin at every cycle¹⁶².

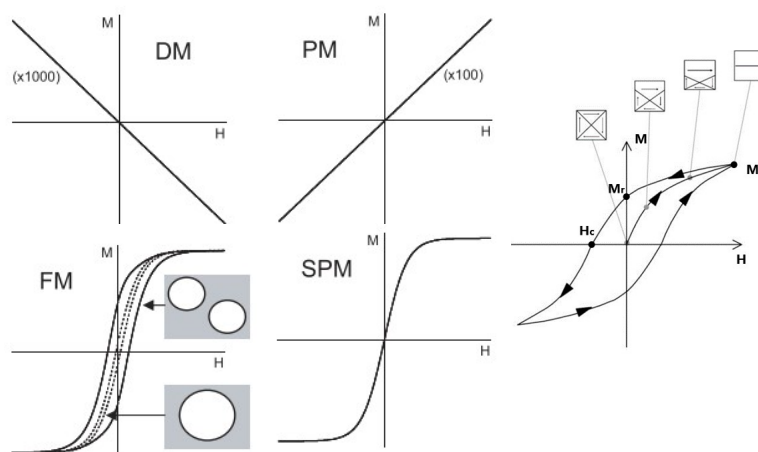


Figure 3.4: Examples of magnetization vs. applied magnetic field (M vs. H) diagrams for different types of materials: diamagnetic (DM), paramagnetic (PM), ferromagnetic (FM), and superparamagnetic (SPM). (Right) Typical hysteresis diagram for ferromagnetic species, indicating the alignment of the internal domains and illustrating the characteristics point of saturation magnetization (M_s), residual magnetization (M_r), and coercitivity (H_c). Images adapted from references ⁸¹ and ¹⁰¹.

Another diagram that offers useful information is the magnetic moment vs. temperature plot, which is recorded applying a fixed magnetic field at the sample while the temperature is gradually changed from low temperature up (zero-field-cooled, ZFC) or from a high temperature down (field-cooled, FC)¹⁶³. The crossing of these plots lead to the estimation of the blocking temperature (T_B)¹⁶⁴, that is the temperature above which the material is not a permanent magnet anymore but starts to manifest superparamagnetic properties for a given measurement time, since the super-spin is no more blocked, but can flip spontaneously¹⁶⁵.

Central parameters for the employment of SPIONs in magnetic resonance imaging are the relaxivities r_1 and r_2 , which are related to the **relaxation times T1 and T2**. These values determine the SPIONs efficiency as positive or negative contrast agents for proton MRI. It is well-known that the particular coating of the magnetic core (being specific ligands, polymers, or the protein corona¹⁶⁶) could influence the relaxation behavior and thus the MRI contrast effect, so it is essential to measure these parameters in the actual conditions of the nanodevice application.

There are instruments specifically built for these measurements (“**NMR relaxometer**”), but the analysis can be also performed with a classic setup for NMR spectroscopy. Alternatively, the relaxation rates R_2 can be calculated differently, knowing the saturation magnetization and some geometrical and physical features of the nanoparticles, exploiting the formula¹⁶⁷:

$$R_2 = \frac{1}{T_2} = \frac{256\pi^2\gamma^2}{405} M_s^2 V \frac{r^2}{D \left(1 + \frac{L}{r}\right)}$$

where T_2 is the transverse relaxation time, γ is the proton gyromagnetic ratio, M_s is the saturation magnetization, D is the diffusion coefficient, and V , r , and L are respectively the volume, the radius, and the surface coating thickness of the magnetic nanoparticle.

For what concern the properties that could be implemented in therapy, what is usually measured is the **specific absorption rate (SAR)**, which is the heat generated per unit gram of SPIONs upon the application of an alternating magnetic field¹⁶⁸ and can be calculated using the formula:

$$SAR = \frac{\mu_0\chi_0 H_0^2}{2\rho\phi} 2\pi f \frac{2\pi f\tau}{1 + (2\pi f\tau)^2}$$

where μ_0 is the permeability of the free space, H_0 is the magnetic field intensity in the material, χ_0 is the equilibrium susceptibility, ϕ is the volume fraction of the magnetic nanostructure, f is the field frequency and τ is the Brown-Neél relaxation time.

Alternatively, the SAR value can be extrapolated from thermal activation plots (T vs. time) of samples subjected to an alternate magnetic field, relying on the formula⁷⁴:

$$SAR = \frac{CV_s}{m} \left(\frac{dT}{dt} \right)$$

where C is the specific heat capacity of the solvent, dT/dt is the initial slope of the plot, V_s is the volume of the sample and m is the mass of the magnetic material.

This heat is exploited directly in hyperthermia treatments or indirectly as a trigger for drug release and depends prevalently on the saturation magnetization of the nanoparticles.

3.1.2.2 Characterization of the shell

Different techniques are required to obtain all the information necessary to understand how the shell is able to interact with the external milieu.

Starting with dimensional studies, even if TEM can be employed to identifying the organic shell upon appropriate staining of the sample, the most preferred technique is the indirect method with **dynamic light scattering** (DLS)¹⁶⁹. DLS allows to obtain the hydrodynamic diameter of the nanoparticle in the dispersion; therefore, if it is combined with the TEM analysis of the core, the thickness of the coating can be extrapolated.

For a deeper and more precise evaluation of the shell structure and the packing density of the coating, along with the nature of the adsorption on the SPION's surface (physical or chemical), other techniques can be employed: the **thermogravimetric analysis** (TGA)¹⁷⁰ that gives the organic percentage and **small-angle neutron scattering** (SANS)¹⁷¹ that gives the hydrodynamic diameter. The chemical composition of the shell can be studied by means of FTIR¹⁷² and XPS¹⁷³, which are useful also to discriminate attached ligands from impurities or free capping agents.

Other features of the shell that can be easily determined are the morphology of the nanosystem and the surface charge density, using respectively the **atomic force microscopy** (AFM)¹⁷⁴ or the DLS equipment for the measurement of the **ζ-potential** through the electrophoretic mobility of the nanoparticle¹⁷⁵. This last parameter is important also to evaluate the colloidal stability of the nanoparticles, since the electrostatic repulsion is one of the factors that limit the aggregation among NPs¹⁷⁶. Another useful information that the ζ-potential can provide, is the amount of drug molecules (charged) firmly loaded within a neutral shell¹⁷⁷.

Considering that the shell is the portion that determines the interaction of the nanosystem with the biological environment, with nanomedicine application in mind, part of the characterization has to include an analysis of the ***in vivo* behavior** of the materials

(pharmacokinetics, biodistribution, cellular uptake). This is greatly influenced by nanoparticles' size, shell composition¹⁷⁸, targeting features¹⁷⁹, and surface charge¹⁸⁰. Besides the relevance of the enhanced permeation and retention effect (EPR)¹⁸¹, the possible bioaccumulation and the excretion route, the studies on animals (generally rats or rabbits) have also to point out if the external magnetic field may be useful to induce a local nanoparticles accumulation against the blood flow¹⁸². Here the parameters to consider are the magnitude of the applied field, the depth, and the nanoparticles' magnetization.

In parallel with these studies, the overall nanosystem should also undergo **toxicity tests** to verify its effective applicability in medicine. These types of core-shell SPIONs are often tested *in vitro* using specific cell lines to evaluate if factors like size, charge, surface chemistry, solubility, and concentration¹⁸³ provoke irreversible effects such as cytoskeleton or mitochondria malfunctions, membrane disruption, and apoptosis. The step forward is then to test these SPIONs *in vivo* to appraise the impact on the overall metabolism and on different organs (lungs, kidney, heart, or liver). The administration route and the dose are additional relevant parameters to consider in the assessment of nanoparticles' toxicity.

3.1.3 Applications in nanomedicine

Coated SPIONs have demonstrated rather early their potential for both therapeutic and imaging purposes (**Table 3.2**).

Table 3.2: Overview of the SPIONs preparation currently present in the clinical field in different stages of approval and use, with the respecting imaging or therapy applications. Adapted from reference ⁶³. Copyright © 2016 American Chemical Society.

	CLINICAL TRIALS	APPROVED	CURRENTLY USED	APPLICATION	
MRI		Abdoscan® Ferristene	Lumirem® GastroMARK® Ferumoxil	Gastrointestinal tract	
		Sinerem® Combidex™ Ferumoxtran-10	Sienna+®	Lymph node biopsy	
		Clariscan™ Feruglose	Feridex® Endorem™ Ferumoxide	Resovist® Cliavist™ Ferucarbotran	Liver lesions
		Feraheme® Ferumoxytol		Brain tumor	
		Sinerem® Combidex™ Ferumoxtran-10		Carotid plaques	
Treatment			Feraheme® Ferumoxytol	Anemia	
	SPIONs-epirubicin	MTC-DOX	NanoTherm®	Hyperthermia Magnetic drug delivery	

The first attempts in designing a **drug delivery system** based on SPIONs are dated back to the 1970s when Widder and colleagues succeeded in developing a magnetically responsive and biodegradable carrier for the chemotherapeutic Adriamycin hydrochloride in the form of albumin microspheres (0.2 – 2 μm) containing magnetite nanoparticles (10 – 20 nm)¹⁸⁴.

Since then the coating methodologies and conjugation strategies to covalently link the drug to the organic shell have made much progress and these nanoparticles have been implemented to deliver their loading either with **passive targeting** (exploiting their size and the EPR effect or the RES uptake) or with **active targeting** (using specific peptides, antibodies, aptamers, proteins or molecules)¹⁸⁵.

One of the features of these magnetic nanoparticles is the possibility to guide them after the injection, with an adequate external magnetic field, in order to have higher concentration of drug molecules at the target site and less elsewhere¹⁸⁶. This opportunity has been exploited since 1966 and applied *in vivo* with iron carbonyl magnetic microspheres guided inside the lymphatic or the vascular systems to reach specific sites¹⁸⁷. Later on, this practice was named magnetophoresis or **magnetic drug targeting** (MDT) and several groups have tried to expand its applicability, spanning from the delivery of an aerosol of SPIONs and plasmid DNA to the lungs (**magnetofection**)¹⁸⁸, to the development of a Janus “nano-bullet” magnetically guided towards liver cancer cells to enhance the endocytosis and the chemotherapeutic effect of doxorubin¹⁸⁹ (**Figure 3.5**).

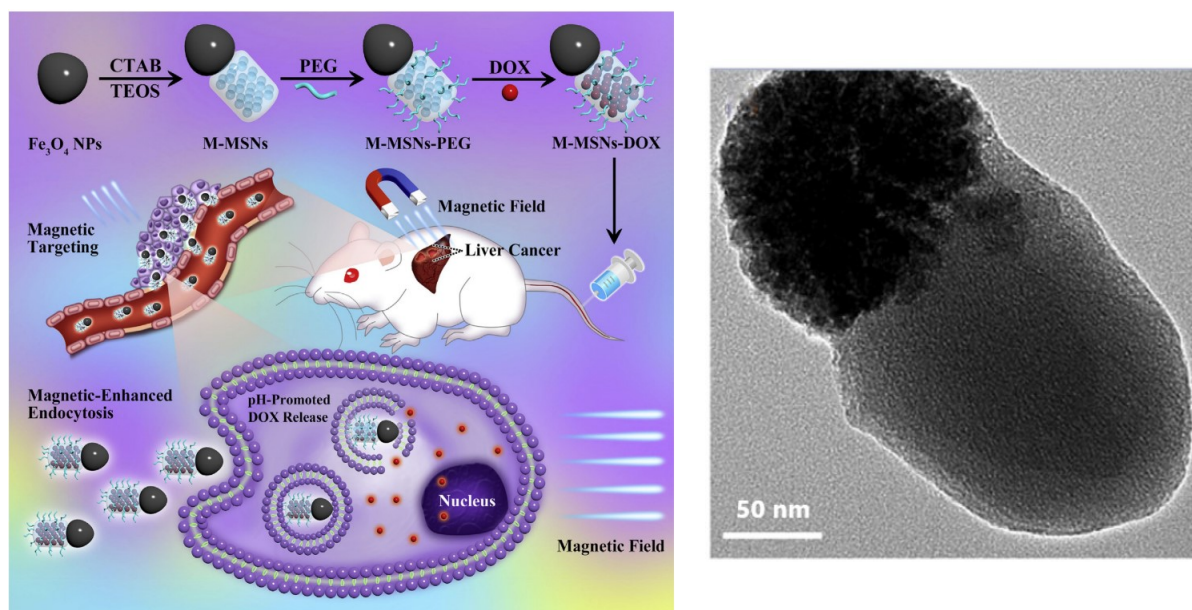


Figure 3.5: (Left) Scheme for the synthetic procedure and in vivo application of a Janus SPIONs-Silica nano-bullet loaded with plasmid DNA and doxorubicin for the treatment of liver cancer, helped with magnetic-enhanced delivery and endocytosis. (Right) HRTEM image of the Janus nano-bullet. Images adapted from reference ¹⁸⁹. Copyright © 2016 Elsevier Ltd-

Magnetic nanoparticles can be also exploited to **trigger the release of the drug** entrapped in the nanocarrier at a specific moment of its pathway throughout the body. The trigger relies on the SPIONs' ability to increase the temperature in the nearby region thanks to the heat that is dissipated upon the relaxation of the core's super-spin while it is quickly flipped by an external alternating field^{190,191}. In this case, the local change of temperature can be used, for example, to increase the permeability of a lipid membrane in which the SPIONs are included, thus releasing the drug cargo release from the liposome¹⁹² or to induce a physical transition on thermo-responsive polymers (such as poly-n-isopropylacrylamide, PNIPAM) promoting a fast ejection of the drug molecules¹⁹³. The generation of heat is also the key point for other therapeutic applications of these SPIONs: based on the final temperature and the effects on the biological tissues, **magnetic hyperthermia** (MHT) or thermal ablation can be achieved¹⁹⁴. In the first case, temperatures from 41 °C to 45 °C are reached and maintained for several hours in order to sensitize tumor cells towards chemotherapy or radiotherapy¹⁹⁵. The **thermal ablation** instead requires a higher temperature (above 50 °C) for few minutes in order to directly kill the tumor cell: for example, Ling and colleagues synthesized a hybrid nanomaterial composed of magnetite nanoparticles coated with polymethylmethacrylate (PMMA) that has been tested on mice bearing human breast cancer cells¹⁹⁶.

From the diagnostic point of view, different types of iron oxide nanoparticles have been tested to be employed in a very wide range of biological targets and diseases¹⁸⁰; the effects of paramagnetic ions on the relaxation times of other nuclei were known and explained since the 40s^{197,198}, but only in 1978 the group of Ohgushi managed to prepare a nanosystem made of magnetite nanoparticles coated with dextran that could act as a relaxation agent for biological NMR measurements, **shortening the T2** of water outside the cells' membrane¹⁹⁹, thus highlighting the area with darker colors (**“negative” contrast**).

Since then, several products that work as negative contrast agents for magnetic resonance imaging (MRI) have hit the market, like Feridex® (ferumoxides, dextran-coated SPIONs)⁹⁴ in 1996 and the cited GastroMark™ (ferumoxsil)¹⁰ in 2001. Recently, researchers have tried to use SPIONs also as a **positive contrast agent**, tuning the physical properties or the composition of the core to obtain the **accelerating effect on the T1 relaxation time**, without using Gd complexes, whose safety has become a concern. One way is to dope the iron oxide core with other metal ions (such as Zn or Ni)¹⁵⁴ to suppress the magnetization effect, but the group of Taboada has achieved this contrast effect using only iron oxide nanoparticles, carefully choosing their size and the ligands on the surface to guarantee a sufficient exposure to the water molecules, producing SPIONs coated with citric acid²⁰⁰.

Moreover, it is also possible to sum the two types of contrast effects in **multimodal T1/T2 agents** that combine both the advantages such as the scan accuracy and the extended detection limit²⁰¹, using two separate types of nanoparticles in the same carrier²⁰² or specifically designed iron oxide nanoparticles^{203,204} (**Figure 3.6**).

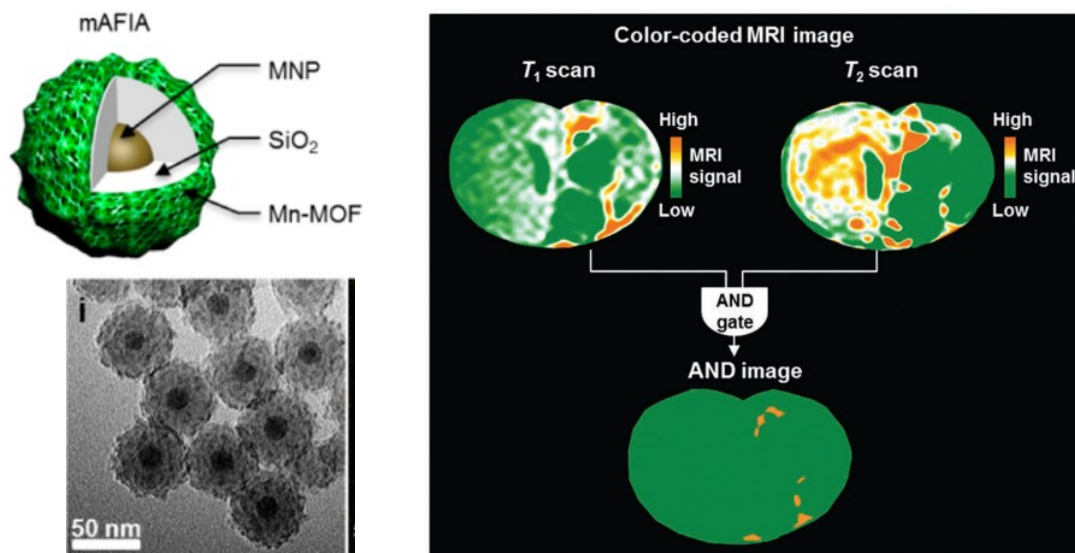


Figure 3.6: (Left) Structural scheme and TEM image of Mn-MOF containing Artifact Filtering Imaging Agent (mAFIA). (Right) Color-coded MRI images of a rat brain after the injection of stem cells labeled with mAFIA, showing single and cumulative T1 and T2 contrasts. Images from reference ²⁰⁴. Copyright © 2014 American Chemical Society.

An alternative imaging technique that employs SPIONs is the **magnetic particle imaging (MPI)**²⁰⁵: instead of evaluating the effect of their presence on the water relaxation times as in MRI, this technique detects directly the magnetic nanoparticles on the spot of interest probing their magnetization with external magnetic fields to generate a tomographic image²⁰⁶.

The main advantages of this type of imaging technique are the depth-independency of the signal, the high contrast, and the great signal-to-noise ratio, since there is no background signal. This fact involves that MPI can be used for the direct quantification of SPIONs tracer, in the whole 3D space of the scanning¹¹¹. The development of this imaging technique has brought also to advanced applications, such as the imaging-guided drug delivery to control the effective delivery and release of the drug payload²⁰⁷ or the cell tracking (stem cells²⁰⁸, macrophages²⁰⁹, bacteria²¹⁰), where the SPIONs are either attached as a label or internalized by the cells to monitor their distribution inside the body, especially in cell-based therapies²¹¹.

Seeking multimodal functionalities, many groups have proposed a **combination of imaging techniques** in the same nanodevice such as supporting the MRI of SPIONs with radionuclides for PET (such as ¹²⁴I)²¹² or fluorescent dyes for optical imaging (like cyanine5.5 that emits in the NIR

region)²¹³. Another step forward in the complexity that is more and more pursued nowadays, is to combine one of the therapeutic and imaging features described so far in a single nanoplatform, thus forming a theranostic nanosystem¹¹⁰. Examples of this design are the system proposed by the group of Santra with SPIONs covered by a PAA folate-derivatized shell for targeted imaging (optical and MRI) and cancer cells treatment²¹⁴ and the one described by Xu and colleagues with SPIONs covered with a multifunctional shell carrying doxorubicin molecules and target molecules, in order to provide a chemotherapeutic treatment and a way for drug monitoring and diagnosis through MRI²¹⁵.

3.2 SPIONs INSIDE POLYMERIC STRUCTURES

Rather than coating individual nanocrystal cores, a different strategy for providing cell accessible iron oxide particles is to encapsulate many nanocrystals within a polymer matrix.

— from Shapiro et al.²¹⁶, *Magnetic Resonance in Medicine*, **2015**, 73, 376-389

In the previous chapter, the focus has been pointed on SPIONs and methods for their synthesis and characterization. However, from the examples of application reported, it has been clear that these nanoparticles have to be further coated: without a proper protection and a biocompatible shell, the SPIONs would aggregate and be detected by the immune system, accumulate in the liver or the spleen, and expelled before reaching the target site in a sufficient amount²¹⁷. Such type of SPIONs is considered the **first generation** of superparamagnetic nanoparticles exploited in nanomedicine, whose aim is mainly to support and boost the diagnostic power of MRI²¹⁸. With a deeper comprehension of the physical properties of these magnetic oxide NPs and the discovery of other nanomaterials, a new generation of multifunctional platforms seems possible. Trying to encounter the nowadays medical needs, the **new generation of SPIONs-based nanomedicines** should be able to **combine both diagnosis and treatment** within a single element.

The strategies adopted to achieve these innovative nanoplatfroms pursue the expansion of the range of functionalization and the complexity of the coating that protects the magnetic core, leading eventually to the assembly of a nanocontainer to carry more SPIONs at the same time.

This kind of construct often mimics natural structures: one of the notable scaffolds that is studied in the last years are liposomes, a vesicle with a thin bilayer constituted by phospholipids that resembles the membrane of eukaryotic cells²¹⁹. However, no materials can assure the same great variability and adaptability of structures, shapes, and functionalization that is given by **polymers**: the exploration of their suitability already started in the early 80s, with the first attempts of using polymeric structures for the controlled delivery of drugs²²⁰, then continued in the following years with even more sophisticated and functional nanostructures²²¹.

Therefore, the combination of the **structural support of polymers in protection and delivery**, with the **imaging properties of magnetic nanoparticles**, foresees a notable breakthrough in nanomedicine and theranostics.

For the first hybrid nanosystem designed in this PhD thesis, the organic part chosen to ensure potential applicability in the medical field consists of a series of well-known polymers that here form the encapsulating and supporting network of the whole structure.

3.2.1 Biocompatible polymeric structures and properties

Based on the structure of the chain, the included functional groups, and the synthetic procedure adopted, polymers assemble with different shapes (**Figure 3.7**):

- **Polymeric nanogels** (or “nanospheres”): constituted by a porous and dispersed matrix composed of cross-linked polymers²²²;
- **Polymeric micelles**: ordered core-shell structures with a hydrophobic nucleus and a hydrophilic surface²²³;
- **Polymersomes** (or “nanocapsules” or “polymeric vesicles”): having a compartmentalization similar to liposomes, composed of two hydrophilic portions with an interposed hydrophobic band²²⁴.

In the following paragraphs, each of these polymeric structures will be briefly analyzed to underline the peculiar characteristics, applications, and related precursors. Some examples referred in particular to magnetic nanoparticles will be presented and critically discussed.



Figure 3.7: Different types and structures of colloidal nanoassemblies exploiting interactions between inorganic magnetic nanoparticles and organic species. (A) Cluster of SPIONs directly functionalized with polymeric ligands. (B) Magnetoliposome. (C) Polymersome with hydrophilic SPIONs. (D) Magnetomicelle. (E) Condensed clusters coated with agarose. (F) Polymersome with hydrophilic SPIONs. Image from reference ⁶³. Copyright © 2016 American Chemical Society.

3.2.1.1 Polymeric nanogels (nanospheres)

Polymeric nanogels are **nanosized networks of hydrophilic and amphiphilic polymer chains**. This network is built with an intertwining of physical and chemical cross-links and has the peculiar ability to swell in aqueous dispersion, forming a structure with hydrophilic compartments like gels. The **swelling** is indeed the major property of these nanogels, and it is determined by internal factors such as the chemical structure of the polymer or the cross-linking degree and external factors like the pH, temperature, and ionic strength. Therefore, the overall size is determined by the balance between the osmotic pressure and the polymer elasticity²²⁵.

Several polymers were discovered during the years as optimal nanomaterials to achieve this degree of swelling and responsiveness: the nanogel production is mainly based on polyethyleneimine (PEI)²²⁶, *N*-isopropylacrylamide (NIPAAm)²²⁷, very often conjugated with polyethylene glycol (PEG) units to provide proper hydrophilicity, dispersibility, and protection towards undesired adhesion²²⁸.

These and other polymers make the nanogel structure porous and flexible, hence very adaptive and versatile in hosting drugs or biomacromolecule, exploiting weak interactions²²⁹ or conjugated covalently²³⁰ for their subsequent release once inside the body by means of different strategies such as diffusion, conformational or dimensional changes, polymer degradation.

The **extremely high loading capacity** of nanogels has been exploited by several research groups to successfully insert SPIONs to achieve magnetic responsiveness²³¹ or advanced theranostic properties. For example, Wang and colleagues have experimented with a polysaccharide cationic polymer glycol chitosan nanogel in which they were able to encapsulate two different ROS-responsive enzymes (catalase and superoxide dismutase) and modified SPIONs used to create a dual-mode contrast agent (US and MRI) for the detection of tumor tissues²³².



Figure 3.8: Examples of drug release mechanisms from nanogels exploiting (Left) passive diffusion, (Centre) change in pH and polymer deionization, and (Right) breakage of biodegradable polymeric chains or cross-links. Adapted from reference ²²². Copyright © 2009 Wiley-VCH.

This type of polymeric nanostructure is abundantly used in nanomedicine as drug- or macromolecule carrier thanks mostly to its **extreme responsiveness to a wide variety of external stimuli (Figure 3.8)** such as pH²³³, temperature²³⁴, and specific chemical or biological conditions²³⁵.

3.2.1.2 Polymeric micelles

Polymeric micelles are another type of material commonly used in nanomedicine and one of the first examples of self-assembled drug carriers. In aqueous media **amphiphilic polymeric chains self-assemble spontaneously**, forming the typical **core-shell structure** at concentrations above the critical micelle concentration (CMC) driven by the tendency of amphiphilic monomers to lower the energy of the interface with water and maximize the van der Waals interactions among hydrophobic chains²³⁶.

The first attempts of polymeric micelles as antitumor agents date back to the early 1980s²²⁰, intending to enhance the beneficial action of localized treatment and reduce the collateral effects of small drug molecules employed in chemotherapy. Since then, the development of this nanosystem has led to the discovery of many options for the delivery of hydrophobic anticancer drugs or bioactive molecules in the field of cancer therapy and diagnosis: several of them have been successfully brought to clinical trials²²³.

The main polymeric chains that are employed in these promising systems are constituted by distinct **hydrophilic and hydrophobic block domains**²³⁷: for the first type of block, PEG, PVP, or NIPAAm are often employed, while for the hydrophobic portion polypropylene oxide (PPO), PLA, poly(lactide-co-glycolide) (PLGA) or poly(ϵ -caprolactone) (PCL) are usually exploited²³⁷.

These polymers have been chosen either for a series of properties useful for an *in vivo* application such as water solubility, aggregation prevention, encapsulation ability, biocompatibility, and biodegradability, but also for their aptitude to respond to external stimuli that brings advancements in the field of precision nanomedicine, since they enable **triggered drug delivery**.

The inclusion of SPIONs inside these micelles allows a particular type of stimulus-driven drug delivery, triggered by an external alternate magnetic field: this input leads to heat emission by the nanoparticles that increases the local temperature, affecting the polymeric structure, especially if constituted by thermo-sensitive polymers²³⁸.

Exploring this possibility, several research groups have implemented iron oxide nanoparticles inside core-shell polymeric structures: for example, Glover and colleagues developed magnetic micelles made of a PEG-PCL di-block copolymer through self-assembly and successfully inserted both chemotherapeutic drug (doxorubicin) and SPIONs²³⁹. They proceeded to verify the heating capacity of the nanosystem and the drug release followed by an increase of temperature, demonstrating the potential to be used as a magnetically-heated drug delivery system.

Beside this, SPIONs included in polymeric micelles have been used successfully also in magnetic transfection, magnetic hyperthermia, and MRI.

3.2.1.3 Polymersomes (nanocapsules)

The most structured polymeric construction that is possible to assemble is the polymersome, a name that refers directly to the analogous liposome used proficiently as drug carrier in many commercial formulations²⁴⁰. The polymersome shares with the lipid vesicle the self-assembly formation mechanism²⁴¹ and the **compartmentalization in hydrophilic shell, the inner hydrophilic pool, and the hydrophobic intermediate layer (Figure 3.9)**; the idea behind its design is to combine the multi-layered structure of the liposome given by amphiphilic lipid molecules, with the versatility and the customizability of polymers²⁴².

Polymersomes present some peculiar differences with respect to liposomes, especially in physical properties that are better suited for their application in drug delivery, starting from the shared possibility to **carry both hydrophobic and hydrophilic species** in separated parts of the same nanosystem²⁴³. Copolymers are usually longer and heavier in molecular weight with respect to lipids, therefore vesicles with a diameter that ranges from 20 nm to more than 1 μm and with a thicker shell (usually from 5 to 50 nm)²⁴⁴ are more common. This reflects drastically on the mechanical properties, the **greater encapsulation ability**, and the **lower permeability** that polymersomes generally have. Moreover, since the number of intermolecular interactions and branches is higher, the intermediate layer is more rigid and contributes to make the **system more stable**²⁴⁵.

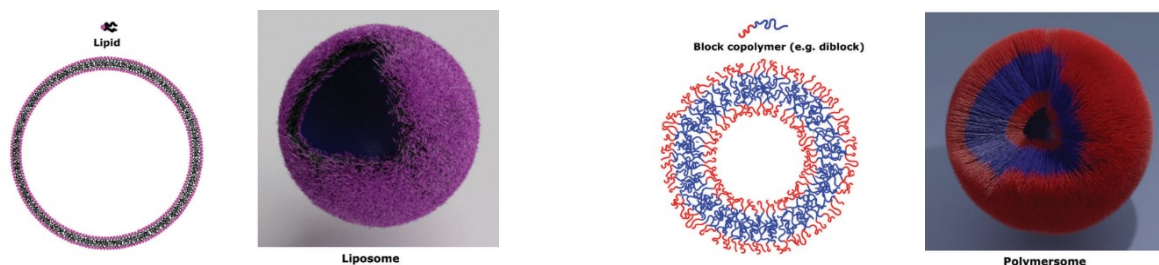


Figure 3.9: Representation of the constitutive unit, 2D structure, and 3D structure of (Left) liposomes and (Right) polymersome. Images from reference ²⁴⁶. Copyright © 2018 The Royal Society of Chemistry.

In literature, the first examples of polymersome were reported in 1995: independently, the two research groups of van Hest and Zhang were working on polystyrene amphiphilic block copolymers to induce supramolecular aggregation. As the hydrophilic polymeric component, they used poly(propylene imine) dendrimers²⁴⁷ and poly(acrylic acid)²⁴⁸ respectively, both succeeding in forming structures of different morphologies, one of those being polymersome.

The difference in respect with the previous micellar structure is principally the number of layers and the compartmentalization of hydrophobic and hydrophilic parts: in the polymeric micelle, the system is assembled starting from a diblock copolymer in order to form two compartments (the

hydrophobic core and the hydrophilic shell), while the formation of the polymersome starts from a grafted²⁴⁹, di-²⁵⁰ or tri-block copolymer²⁵¹ to obtain three different portions: the shell, the core, and the intermediate bilayer.

These complex polymeric chains usually feature polar and non-polar blocks to obtain amphiphilicity: along with the polymers mentioned above, many others are suitable, such as polyethylene oxide (PEO), polydimethylsiloxane (PDMS), or polystyrene (PS). In fact, the versatility stems from the possibility to tune both the composition and the length of each portion of the final chain, to adjust precisely the final characteristics of the polymersome such as size, shape, permeability, and responsiveness.

As in the previous cases, also polymersome can undergo physical modifications upon external or internal stimuli to apply them for **timely drug delivery**^{252,253}.

Due to the three complementary compartments that constitute the polymersome, both hydrophobic- and hydrophilic-coated SPIONs can be successfully included inside it for uses in therapy and imaging. Focusing on the hydrophobic SPIONs, Sanson and co-workers have synthesized SPIONs coated with an anionic surfactant (Beycostat NB09, containing an hydroxyphosphate head that interacts with SPIONs surface) to confer hydrophobicity and include them within the hydrophobic membrane of polymersomes composed of poly(trimethylene carbonate) and poly(L-glutamic acid) for theranostic purposes²⁵⁴. Considering an example of hydrophilic SPIONs, the research group of Kania managed to coat iron oxide nanoparticles with a specific cationic chitosan derivative in order to confer hydrophilicity and enable their storage in polymersomes made by mixing a pair of oppositely charged block copolymers²⁵⁵. The hydrophilic SPIONs are capable of affecting greatly T2, since they can interact more efficiently with water molecules that diffuse inside the polymersome thanks to its semipermeable bilayer. An alternative is to coprecipitate iron oxide directly inside the bilayer of the polymersome, so SPIONs are formed and stabilized directly *in situ*^{256,257}.

Based on a solid literature background, an increased level of structural stability is recognized as going from polymeric micelles, through nanogels to polymersomes and this reflects on both the kinetics of the release (faster for micelles) and the permanence without structural changes inside the body²²².

Several of the nanosystems containing SPIONs presented in this section are very promising and many of them are currently under pre-clinical or clinical investigations.

The strong points that had determined their success relies on the ability to protect efficiently whatever is stored in them, until release is needed: the payload can be either drug molecules or biomacromolecules for the treatment, or contrast elements for imaging. In a biological environment, this means avoiding the interaction with plasma proteins or macrophages, thus prolonging the circulation time in the cardiovascular system and reducing the problem of premature excretion. Moreover, the uptake by tissues and cells and the successive dosage of the drug can be tuned and optimized by introducing particular surface modifications or using polymers that can be physically or chemically modified by the variation of environmental conditions.

3.2.2 Preparation strategies, SPIONs encapsulation, and surface functionalization

The synthetic procedures regarding the formation of these assemblies have always been strictly finalized to assure the achievement of certain physical and chemical properties needed for their final application (especially for drug encapsulation and delivery), which are mostly determined by the choice of the polymers²⁵⁸. The plethora of possible strategies is generally classified whether the constituent polymers are **pre-formed** or should be **synthesized *in situ*** before the assembly.

In the first case, the three nanosystems previously introduced are generally constructed relying on the different water affinity of the polymeric blocks that self-assemble in solution²⁵⁹. This rearrangement can be favored by different experimental setups that usually take advantage of a **preliminary emulsification step**, followed by the removal of the organic solvent through evaporation (**Figure 3.10**), diffusion, or by salting-out²⁶⁰.

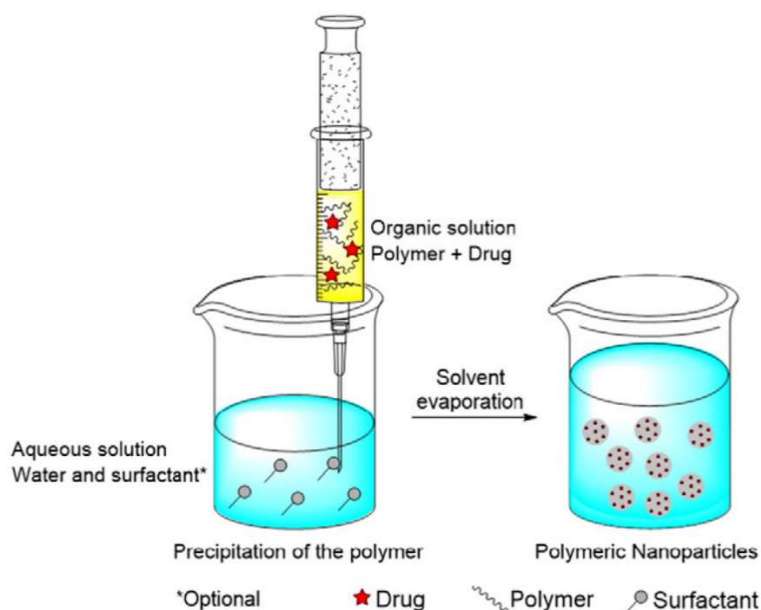


Figure 3.10: Schematic representation of nanospheres preparation using the nanoprecipitation method. Image from reference ²⁶¹. Copyright © 2017 Elsevier B.V.

Alternative techniques that do not require emulsification as the first step such as **nanoprecipitation** (or solvent displacement)²⁵⁴, **film rehydration**²⁶², or the **dialysis** method²⁶³ have been also discovered.

There could be also the case in which the copolymer is not commercially available or it has to possess a specific structure: in these circumstances, it must be synthesized by covalent linkage of the different blocks coupling the functional ends of each block or using a classic **radical polymerization** (ATRP or RAFT in most of the cases)²⁶⁴. Often this polymerization is performed at the interface between the two immiscible solvents where the reactive monomers with opposite polarity can interact (interfacial polymerization) or most commonly in a “nano-reactor” made by emulsifying an aqueous dispersion of the monomer and the initiator thanks to a surfactant (mini- or micro-emulsion polymerization)²⁶⁵. In each case, the following step witnesses the rearrangement of the polymeric chains in the desired nanostructure through self-assembly.

Generally, the polymeric blocks are designed to contain other reactive functional groups for the successive **cross-linking**: the formation of a covalent network helps to control the porosity of the nanogel²⁶⁶ or to ensure a higher colloidal stability of the compartmentalized structure and to reduce the permeability²⁶⁷. The typical species that are coupled together bear carbonyl groups (carboxylic acids, aldehydes), amines, or thiols: in the latter case, the cross-linking enables the formation of redox-responsive disulfide bonds for triggered delivery²⁶⁸.

An alternative synthetic pathway that is exploited usually in the nanogels formation is **the template-assisted nanofabrication** (named also “particle replication in non-wetting templates, PRINT)²⁶⁹, with which is possible to obtain systems with a very narrow dispersity and homogenous shape.

The elements that determine whether a micelle or a polymersome is obtained from the self-assembly step are mainly related to the nature of the different blocks and the **hydrophilic/hydrophobic ratio** between them²⁷⁰, but also specific setups and procedures can favor one or the other.

An example of the first case is provided by the research group of Hickey that, as depicted in **Figure 3.11**, was able to obtain three different morphologies of polymeric nanoparticles with encapsulated SPIONs by modulating both the ratio between the PAA and PS blocks and the type and number of solvent/nanoparticle and polymer/nanoparticle interactions²⁷¹.

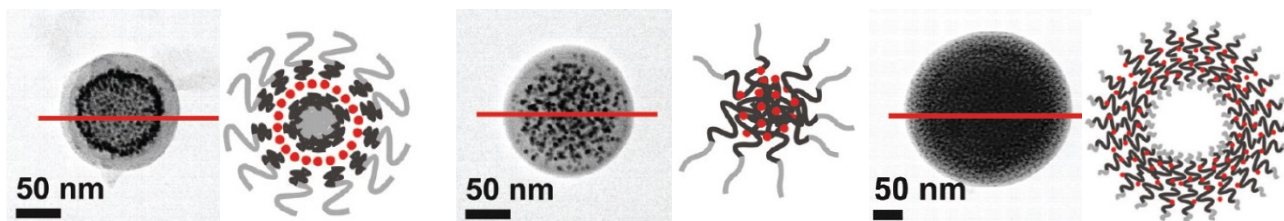


Figure 3.11: Schematic representation and dimensional characterization of three different self-assembly structures, comprising (Left) magneto-core shell (Centre) magneto-micelle and (Right) magneto-polymersome. Adapted from reference ²⁷¹. Copyright © 2011 American Chemical Society.

Polymeric vesicles can be formed exploiting microfluidics: this advanced technique of solvent-displacement supports and controls precisely the two-step formation of a double emulsion (w/o/w) to construct very size homogenous capsules²⁷².

Recently, the group of Poschenrieder unraveled the mechanisms behind the formation of polymersomes in a co-solvent method for a particular type of block copolymer, using TEM, DLS, and UV-Vis analysis²⁷³. Two different proposed mechanisms may occur, both start with the formation of spherical micelles immediately after the polymer dissolution. The following fusion between them forms either intermediate discs or “worms” that grow in more complex forms (baskets, rings, donuts) and ultimately lead to the formation of the bilayer that gives the polymersome’s structure (**Figure 3.12**).

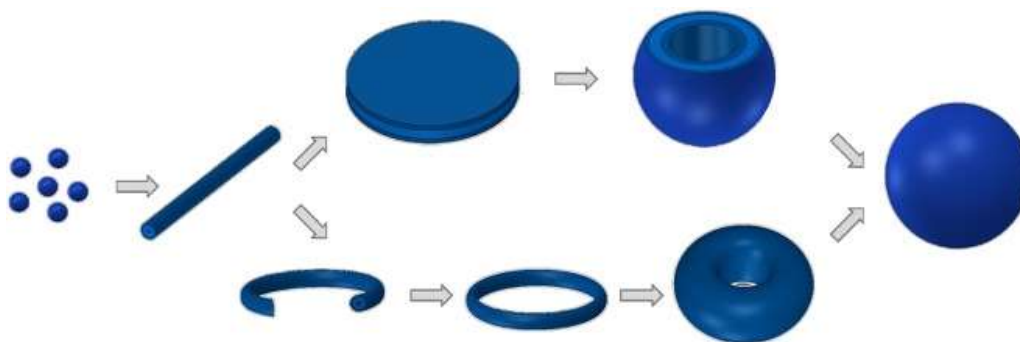


Figure 3.12: Scheme of the polymersome’s formation pathways, involving an intermediate (Top) disc-basket or (Bottom) ring-donut transitions. Image from reference ²⁷³. Copyright © 2017 Wiley Periodicals Inc.

The self-assembly mechanism is primarily dependent on the particular polymeric structure, but the kinetic behind the nanostructure’s formation depends also heavily on the concentration and the agitation speed.

Understanding the ways in which the system can be constructed and its desired final structure is crucial to optimize the **encapsulation** of whatever drug molecules or other species the nanosystem is designed to carry. This could be particularly important when trying to insert SPIONs in a polymeric nanosystem for theranostics purposes, especially considering that is possible to

synthesize both hydrophilic or hydrophobic SPIONs and allocate them in different compartments of the same structure. Besides, the precise placement of the magnetic nanoparticles enables or improves specific applications: trapping them in the nanogel network or within the hydrophilic compartment of a vesicle together with water molecules is important in order to optimize the **T1 or T2 effects for imaging** purposes²⁷⁴. Loading a large amount of them inside a micelle forming what is called a colloidal nanocrystal cluster (CNC), increases its susceptibility in magnetic guide for **drug delivery** applications²⁷⁵, while placing them inside the hydrophobic bilayer of a vesicle can induce a change in shape, permeability or favor its degradation as part of the **triggered delivery** when an external magnetic field is applied²⁵⁴. Generally, SPIONs embedded in polymeric nanosystems can be also exploited as **structural probes** to elucidate the dimension, morphology, and compartmentalization of the nanosystem, thanks to their augmented contrast in respect to organic species²⁷⁶.

As already mentioned above, the assembly of polymers made by the same blocks can provide different morphologies depending on the length of each block so the SPIONs will be distributed inside it accordingly. Lecommandoux and co-workers focused on di-block copolymer PB-*b*-PGA (polybutadiene-*block*-polyglutamic acid) for the formation of nanostructures that could encapsulate a ferrofluid suspension of hydrophobic SPIONs: by varying the length of the PGA block, they were able to obtain micelles with SPIONs encapsulated in the hydrophobic core or vesicles, with SPIONs included in the hydrophobic bilayer²⁷⁶. Structurally and functionally different, these two nanosystems could be used for complementary applications.

The **mechanisms of inclusion of SPIONs** are similar to the ones currently used for the encapsulation of drug molecules inside the same polymeric structures. The crucial aspect to consider in order to understand which procedure could be better applied is the nature of the SPIONs' external coating: besides the solubility factor, the shell nature determines also the type of interactions (usually non-covalent such as coordination, hydrogen bonding, hydrophobic interactions) with the polymeric matrix⁶³.

The first strategy developed and the most common route to encapsulate SPIONs within a polymeric structure is forming an **emulsion** between two immiscible solvents where both the polymeric surfactants and the nanoparticles are dissolved (either in the same or in the two different phases). These two immiscible solvents are then processed with **high-speed homogenization or ultrasonication** to form a dispersion of nanodroplets, which leads to a suspension of nanoparticles after the evaporation of the organic solvent²⁷⁷. Following this methodology, the research group of Hu was able to entrap a great number of magnetic nanoparticles in a soft PVA nanogel,

successively stabilized with a hard silica shell²⁷⁸. Kocbek and colleagues instead, managed to encapsulate SPIONs in a core-shell structure composed by a PLGA inner matrix externally stabilized by PVA²⁷⁹.

In the case of a W/O/W emulsion to form complex capsules, usually the **double emulsion approach** is adopted: the primary oil-in-water dispersion obtained through the sonication of a solution containing the polymeric surfactant, and the SPIONs is placed in contact with an aqueous continuous phase containing the hydrophilic polymeric component and sonicated again, as Fang and colleagues did use only PVA²⁸⁰.

The **nanoprecipitation** method mentioned above is another efficient way to include SPIONs during the assembly: these nanoparticles are mixed together with the polymeric constituents in the same organic solvent, which can be either injected in aqueous solvent²⁸¹ or put in contact with a controlled flow of water²⁵⁴ for example to trigger the formation of polymersomes with a SPIONs-filled hydrophobic membrane.

The same result can be achieved also in successive steps with a **layer-by-layer assembly**: Carregal-Romero and co-workers started with a CaCO₃ template wrapped in successive layers of positive and negative electrolytes (**Figure 3.13**). Using a positive layer of poly(acrylamide-*co*-diallyldimethylammonium chloride) they were able to attach negatively charged SPIONs through electrostatic interactions with the capsule's shell, which was further reinforced and stabilized with the deposition of other polymeric layers²⁸².

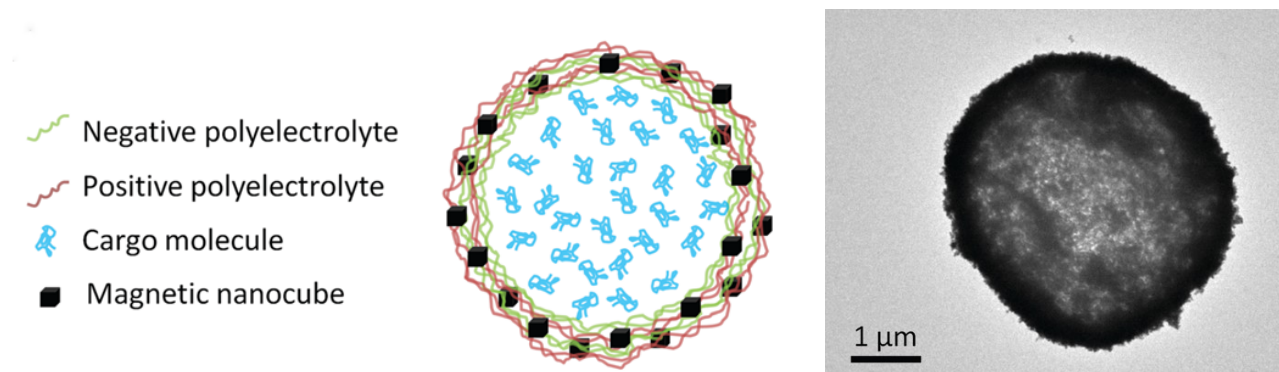


Figure 3.13: (Left) Structure representation of the nanosystem obtained with a layer-by-layer assembly of positive and negative polyelectrolyte to include magnetic nanocubes. (Right) TEM image of the aforementioned nanosystem.

The SPIONs encapsulation can also be implemented in the **dialysis strategy** for the assembly of polymeric nanoparticles: in the organic solvent contained inside a dialysis membrane, both the polymer and the SPIONs are dissolved and the nanosystem forms when the dispersion is dialyzed against a miscible non-solvent, as was done for example with folate-PEG-PCL by Yang and colleagues²⁸³ or with PEG-*b*-P(VBODENA) (poly(2-[4-vinylbenzyloxy]-*N,N*-diethylnicotinamide) block copolymer by Yoon et al²⁸⁴.

There are also few remarkable examples in which the **SPIONs are synthesized directly inside** the portion of the polymeric nanosystem that will host them. For example, Liu and colleagues used a diblock copolymer made of PGA and PCL in order to form a polymersome. They subsequently increased the pH to deprotonate the acid groups and favor the inclusion of Fe^{2+} and Fe^{3+} ions added with an aqueous solution. By heating and increasing the concentration of NaOH in the dispersion, they successfully coprecipitate Fe_3O_4 nanoparticles within the hydrophilic compartments of the structure, which also passivate and stabilize their surface²⁵⁷.

What has been largely observed is that the inclusion of SPIONs greatly affects the polymeric nanocarriers' self-assembly mechanism and the final stability of the system, conveying further solidity and allowing the formation of structures that otherwise would be redispersed in the medium or would eventually precipitate²⁸⁵. This phenomenon is known as the **Pickering solid-stabilized emulsion**, where colloidal particles, SPIONs in this case, are able to stabilize a liquid-liquid interface²²¹.

A further way to tailor the nanosystem towards its final application and enhance its efficiency is to implement specific functions on its surface. This could be desired to improve the theranostic functions both directly (with the introduction of active molecules for therapy or imaging) and indirectly (targeting species to promote the precise delivery of the nanosystem).

All the three different polymeric structures described before (nanogel, micelle, and polymersome) are adequate for **surface functionalization**: in particular, there are several known cases of nanogels decorated with small molecules²⁸⁶ and proteins or polymeric micelles presenting antibodies²⁸⁷ or peptides for tumor targeting. However, polymersomes seem to be the most versatile and functionalized nanostructure, since a wide variety of different small molecules, peptides, aptamers, proteins, and antibodies have been successfully implemented²⁴².

For all of these structural alternatives, the functional species can be implemented either before the self-assembly step (polymer modification, usually for the attachment of small molecules) or after it (surface functionalization, used especially for macromolecules and proteins).

3.2.3 Characterization methods

3.2.3.1 Size and Morphology

The characterization methods for SPIONs@Polymer assemblies require analyses aimed at assessing their size and morphology, their magnetic and surface properties, and stability. This information can

be gathered by the same techniques used in the characterization of SPIONs themselves. However, from the point of view of size characterization, **nanoparticle tracking** analysis (NTA)²⁸⁸ becomes a valuable method to be associated with DLS: both rely on the analysis of the nanoparticles' **Brownian motion** using the scattered light collected after the sample is irradiated with a laser beam. The diffusion behavior is then correlated to the nanoparticle's dimension through the Stokes-Einstein equation²⁸⁹, here presented:

$$D_h = \frac{k_B T}{3\pi\eta D_t}$$

where D_h is the hydrodynamic diameter, k_B is the Boltzmann's constant, T is the temperature, η is the viscosity and D_t is the translational diffusion coefficient (which is the product of the diffusion coefficient D and the time t).

Even if the mathematical background is the same, these two techniques present some basic diversities: while DLS collects the scattered light with a photon detector and process its intensity with an autocorrelation function¹⁶⁹, the NTA setup is equipped with a CCD camera to recognize and follow directly the Brownian motion of each nanoparticle in solution in two dimensions.

Due to these different setups, DLS has the possibility to scan quickly the whole sample but has the disadvantage of size overestimation when even a small amount of aggregates is detected, since the hydrodynamic diameter is related to the light intensity and bigger nanoparticles scatter more light. On the other hand, NTA requires a longer time for the adjustment of the optimal parameters, the measurement, and the processing of data, but guarantees a more accurate estimation of the size distribution and enables to measure NPs concentration; moreover, it permits also to resolve better distinct nanoparticle populations in the same sample²⁹⁰. In terms of size range, these two techniques may be considered complementary: while the DLS equipment is more suitable for small nanoparticles down to 5 nm of hydrodynamic radius²⁹¹, NTA is best indicated for larger nanoparticles, with a reliability within 30 and 1000 nm of hydrodynamic radius, depending on the sample type²⁹².

Another type of properties of the single polymeric nanosystem that results important when considering its distribution and internalization into cells are related to its mechanical behavior, represented by its **stiffness** and **deformability**. In this research field, the AFM technique comes in handy again: by performing indentation experiments using the tip of the cantilever, the Young's modulus can be extracted from force-displacement curves²⁹³.

3.2.3.2 Theranostic properties

From the point of view of the therapy, usually these structures are assembled as a carrier for a specific drug that has to be delivered and then released in a precise site, maximizing the effective dose and overcoming the general problems of the conventional treatment.

The **inclusion of drug molecules** inside the structure or on its surface that takes place during the synthesis and undergoes controls to assess the effective drug content and the kinetics of its release. Both studies can be performed by means of **UV spectroscopy, fluorescence spectroscopy, or high-pressure liquid chromatography (HPLC)**. The strategy for the determination of the drug content can be either an indirect and non-destructive method that analyses the supernatant produced by centrifugation²⁸⁴ or a direct method on a redispersed freeze-dried sample²²⁸.

On the other hand, when the drug release has to be quantified, the procedure mostly adopted is to perform **dialysis** of a known nanoparticles concentration, collecting the dialysate at fixed intervals of time²³⁹.

Considering the encapsulation of SPIONs specifically, the measurement of this quantity often requires the disruption of the nanoparticles and the analyses of the freed content by means of **inductively coupled plasma (ICP)**²⁸⁴ or **atomic absorption spectroscopy (AAS)**²⁸³. Another destructive technique that can be employed is the TGA²⁹⁴, since it can measure the weight of the remaining inorganic content (iron oxide nanoparticles in this case) after burning completely the organic species, the polymer, and other organic parts.

The use of SPIONs is related to their magnetic properties to drive the release of drugs in the biological environment: therefore, ***in vitro***²⁸³ and ***in vivo***²⁸⁰ **distribution studies** are performed also with the help of an external magnet placed in a specific region of the Petri dish or the animal model to test if the nanosystem accumulates properly in the desired position upon application of the magnetic field.

Hybrid SPIONs-polymers nanosystem may be exploited for their ability to generate heat upon the application of an alternate magnetic field, using it, for example, as adjuvant to damage cancer cells in hyperthermia treatment. Additionally, the local temperature increase may trigger the delivery of drugs present on the polymeric shell. There are not conventional instruments to control these effects, but rather some custom-made apparatus; for example, by means of an infrared thermometer Vijayan and colleagues managed to measure the temperature increase of a dispersion of magnetic nanogels placed inside a coil that generated an alternate magnetic field²⁹⁵ and quantify the dissipated energy as **specific loss power (SLP)**, estimated using the formula:

$$SLP = \frac{CV_s dT}{m dt}$$

where C is the volumetric heat capacity of the sample (for example $C_{\text{water}} = 4185 \text{ J}/(\text{L}\cdot\text{K})$), V_s is the sample volume, m is the mass of the magnetic nanocomposite present in the sample volume, and dT/dt indicates the initial slope of the temperature versus time curve ($\text{K} \cdot \text{s}^{-1}$).

Sanson and co-workers performed instead drug release tests putting a dialysis tube filled with vesicles loaded with SPIONs and doxorubicin inside a similar coil crossed by an adequate electric current²⁵⁴.

From the diagnostic side, the aim is to verify that the inclusion of the SPIONs in the polymeric scaffold doesn't affect their response in MRI. Likewise, the hybrid nanosystem is tested in **phantom MRI experiments**²⁵⁶ or directly *in vivo*²¹⁷ using MRI clinical scanners for the collection of T1-weighted or T2-weighted MR images.

3.2.3.3 Biological interactions

Since the ultimate aim of these nanomedicines is to interact with living organisms, before proceeding with the clinical trials, is of the utmost importance to know exactly their interactions in biological media with biological substrates is and what are the eventual modifications of their surface such as **proteins adhesion** or the mechanism of **interaction with cells**.

Therefore, the primary assessment to be carried out must be a **toxicity assay** in order to prove that the nanosystem can be safely administered. There are several types of *in vitro* cytotoxicity assays that can be performed, but the common *modus operandi* is to put in contact the nanosystem with a specific cell line (macrophages, liver cells) and dying the culture with molecules that allows the identification of specific cell compartments and their structural modification (for example membrane disruption, oxidative stress, mitochondria damaged using fluorescence spectroscopy²¹⁷ or specific probes (such as for XTT or MTT tests) whose alteration by the enzymatic activity of viable cells can be detected with a colorimetric assay²⁸¹.

Related to the execution of their theranostic jobs, other biological tests have to be carried out to assess the degree of cell internalization and the distribution throughout the whole organism. For the first case, **confocal laser scanning microscopy (CLSM)**²⁹⁶ or **fluorescence microscopy** may be used (**Figure 3.14**). Regarding the latter analysis, generally, the polymeric nanoparticles are superficially functionalized with a probe that helps to understand whether the nanosystem is inside or outside a cell membrane after the incubation²⁷⁹.

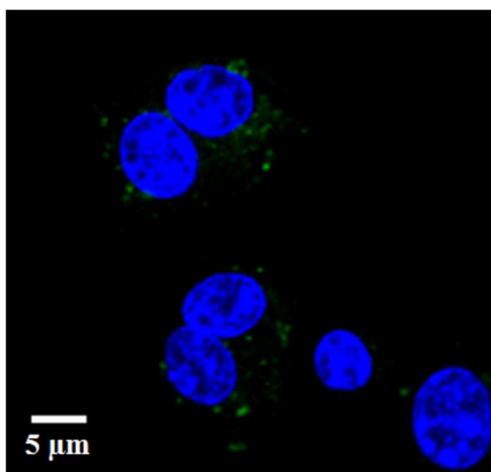


Figure 3.14: Fluorescent microscopy image showing the inclusion of magnetic hybrid nanoparticles labeled with green fluorescent dye within J-774 cells whose nucleus was stained with 4',6-diamidino-2-phenylindole (blue). Image from reference ²¹⁷. Copyright © 2013 Elsevier Ltd.

Hyperspectral inorganic analysis is a powerful method to determine the presence of NPs/nanosystems without the need for modification with fluorescent dyes. The alternative to analyze efficiently a high quantity of cells is to resort to flow cytometry²⁸¹.

To consider the analysis of the bio-distribution and to determine the metabolic pathway of the nanomedicine, ***in vivo* circulation and clearance studies** will be scheduled in the advanced stages of its development. The animal model (usually rats) is injected with the nanomedicine and the blood or the organs collected, treated, and analyzed by common spectroscopic techniques after a certain amount of time²⁹⁷, focusing specifically on the target site to assess the delivery efficiency or on liver, spleen, and kidneys to evaluate the excretion rate. Exploiting the peculiar SPIONs' property of being a contrast agent, another direct and less invasive technique that can be exploited for biodistribution and clearance studies is the **magnetic particle imaging (MPI)**¹¹¹, which enables tomographic detection and quantification of these nanoparticles in a 3D space, with limitations due to SPIONs concentration.

My research project within the nanomedicine field is focused on the development of an innovative nanosystem that could pursue both the therapeutic and diagnostic functionalities at once, making it a promising theranostic device.

The idea is to build a polymeric nanocarrier able to host SPIO nanoparticles and drug molecules to provide a chemotherapeutic solution for the treatment of amyotrophic lateral sclerosis (ALS) and the simultaneous imaging for diagnostic and drug monitoring purposes.

4.1 NANOSYSTEM'S DESIGN

The structure and the elements of the nanosystem have been carefully chosen to provide an effective mean for the diagnosis, the delivery of drugs, and their monitoring while dealing with ALS disease.

From the diagnostic point of view, **MRI** is a known technique that currently begins to be exploited for the early diagnosis of this pathology through the detection of specific biomarkers²⁹⁸ or structural abnormalities in the brain²⁹⁹. Moreover, the use of MRI for monitoring the drug circulation and the therapeutic effect has been theorized, but actual applications of this opportunity are still scarce³⁰⁰.

This need stems from the recent availability of the first drug employable in the pharmacological treatment of ALS patients: **riluzole** is a modified benzothiazole that was approved by the FDA in 1995³⁰¹ and has a strong neuroprotective effect against several types of neurodegenerations³⁰², preventing acute glutamate-induced damages in motoneurons.

The main feature of this novel nanosystem is the implementation of **superparamagnetic iron oxide nanoparticles (SPIONs)**, that have the potential to act as contrast agents for proton MRI, magnetic guides for site targeting, trigger elements for drug release, and devices for heat generation.

The **superparamagnetism** of these nanoparticles is the fundamental property that makes possible all these applications: under certain physicochemical conditions of size and composition, each nanoparticle shows a single magnetic domain (**Figure 4.1**) that responds to an external magnetic field (ferromagnetic behavior) but flips constantly in absence of fields and above a certain temperature, causing no total magnetization (paramagnetic behavior). This is useful for example to exploit magnetism for *in vivo* delivery, without the risk of aggregation caused by magnetic particles that attract each other.

In this research field, the materials that are commonly employed belong to the iron oxides group: in particular, the most common structures are maghemite ($\gamma\text{-Fe}_2\text{O}_3$) and magnetite (Fe_3O_4). Both are ferrimagnetic materials with an inverse spinel oxygen lattice and very similar unit cell dimensions³⁰³. The impaired spins configuration arise due to the particular occupation of tetrahedral and octahedral sites in the crystal structure ($\gamma\text{-Fe}_2\text{O}_3$ that has only Fe^{3+} ions) or to the presence of different ions ($1/3$ of Fe^{2+} and $2/3$ of Fe^{3+} in the Fe_3O_4 structure); however, superparamagnetism manifests when the particles are below 20 nm in diameter³⁰⁴.

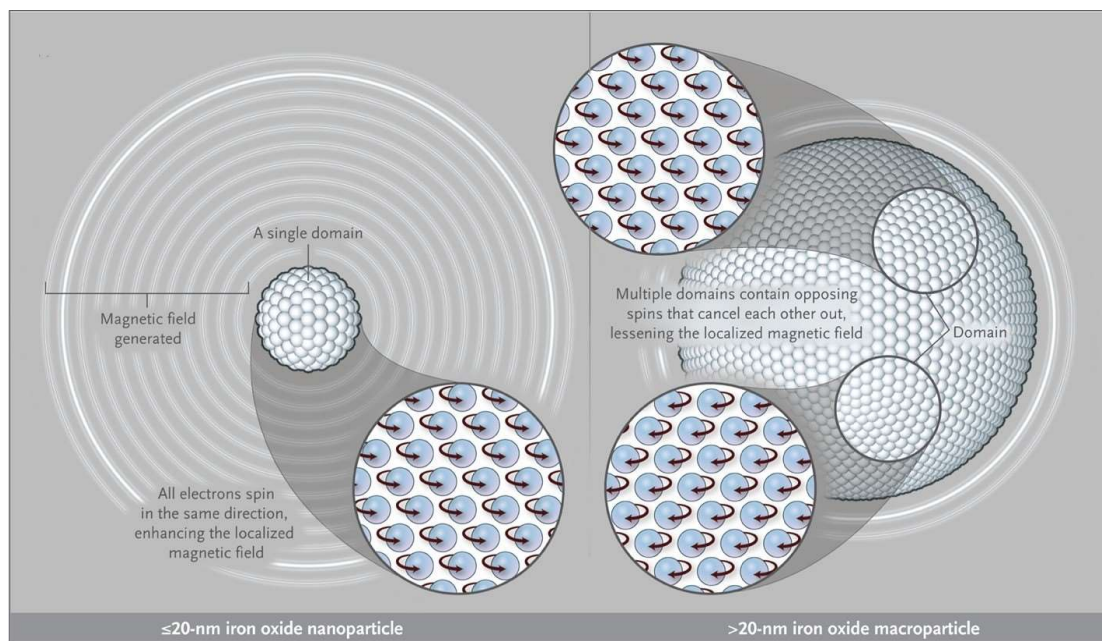


Figure 4.1: Graphical representation of the domains inside magnetic nanoparticles of different size dimensions and the magnetic field generated. Image from reference ³⁰⁵. Copyright © 2010 Massachusetts Medical Society.

From the clinical point of view, these two oxides possess similar useful properties: recent comparative studies have evidenced an almost absolute equivalence in terms of critical particle diameter, low toxicity, MR performance, and stability after cell internalization³⁰³. The only differences reside in the synthetic process (to obtain $\gamma\text{-Fe}_2\text{O}_3$, a further oxidation step is required) and the maximum saturation magnetization for the same size (generally higher for Fe_3O_4 nanoparticles).

Therefore, our primary goal is to **synthesize magnetite (Fe_3O_4) nanoparticles of small dimensions** to achieve a superparamagnetic behavior and improving the synthetic procedure for their preparation with respect to those reported in the literature. Moreover, the precise size we have chosen is determined by the specific imaging application we aim to achieve.

SPIONs are well known to operate as a negative contrast agent for $^1\text{H-MRI}$, meaning they can reduce the T2 of water molecules' protons and make their location site darker than the

surroundings (**Figure 4.2**, on the left), since they possess a high r_2 relaxivity coefficient, along with a big saturation magnetization m_s .

However, this type of contrast results harder to visualize properly if compared with the positive one (**Figure 4.2**, on the right) provided for examples by gadolinium complexes³⁰⁶.

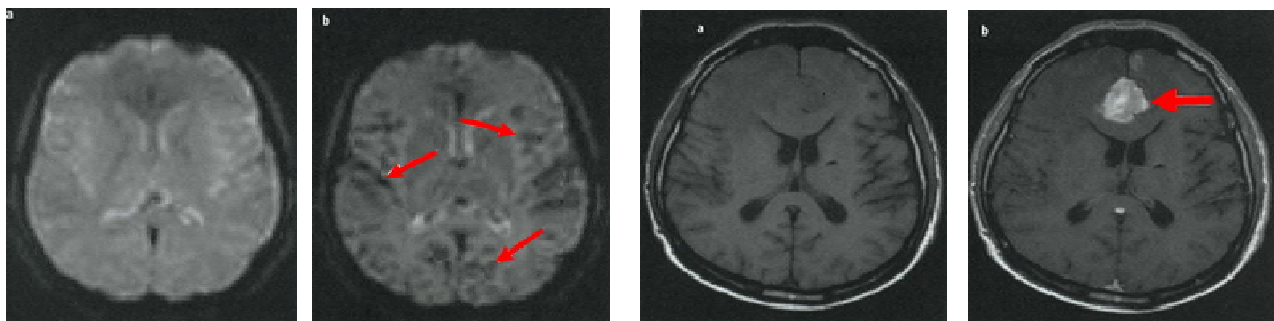


Figure 4.2: (Left) Part of the brain analyzed by MRI before and after the injection of a negative contrast agent. (Right) Part of the brain analyzed by MRI before and after the injection of a positive contrast agent. Images adapted from reference ³⁰⁷. Copyright © 2014 Springer-Verlag Italia.

Nonetheless, recent studies show that peculiar iron oxide nanoparticles could have different magnetic characteristics (high longitudinal relaxivity r_1 and a low r_2/r_1 ratio) that give them the ability to shorten protons' T_1 relaxation time, thus brightening the spot in which they reside and act effectively as a **positive contrast agent**.

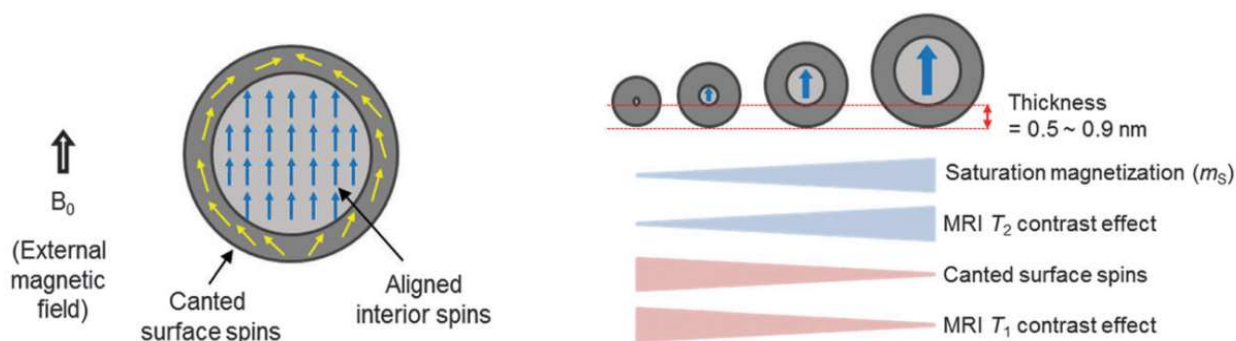


Figure 4.3: (Left) Schematic representation of the different magnetic spins (aligned on the inside, canted, and disordered on the surface) of a SPION under an external magnetic field B_0 . (Right) Diagram illustrating the dependence of the SPION's size and thickness of a canted-spins layer on the relaxation times T_1 , T_2 , and the overall saturation magnetization m_s . Image from reference ³⁰⁸. Copyright © 2015 The Royal Society of Chemistry.

The T_1 spin-lattice relaxation of proton spins is generally accelerated (increase of r_1) by the interaction with magnetically disordered spin layers on the surface of iron oxide nanoparticles (due to the presence of unpaired electrons), which are always around 0.5 – 0.9 nm, regardless of the overall dimension³⁰⁹ (**Figure 4.3** on the left). By producing small NPs (at least smaller than 10 nm³¹⁰), the inner part (light grey in **Figure 4.3**) that is instead ordered and aligned and acts on T_2

relaxation time (increasing r_2 and m_s), can be reduced to the minimum, thus keeping low the ratio r_2/r_1 and producing a bright contrast (**Figure 4.3**, on the right).

Since we aim at keeping the synthesis simple and retain a certain degree of magnetic response given by the magnetization acquirable by the core, the intention is to grow full-magnetite nanoparticles of around 4 nm in diameter, then analyze their magnetic and imaging properties to evaluate a further size reduction. The compromise on the small dimension is the reduction of the magnetic susceptibility, which could be detrimental for magnetic drug targeting purposes. One more advantage of working with small iron-based NPs is that below the range of 6 – 8 nm, the external object can be excreted from the organism via renal route, which is quicker and reduces the risk of bioaccumulation and toxic effects. Moreover, the portion that remains inside the body can be naturally taken by the human metabolism and employed as an iron source for the biosynthesis of vital biomolecules or structures (e.g. red blood cells)^{95,311}.

Freshly produced SPIO NPs present on their surface many hydroxyl groups due to partial oxidation: depending on the synthetic conditions, the post-synthesis modifications, and the final application wanted, they will eventually be covered with either a hydrophilic (e.g. surfactants) or lipophilic (e.g. oleic acid) layer, for stabilization, binding, and further functionalization. Despite the versatility of having a hydrophilic shell, the high synthetic reproducibility, the ease of manipulation and the overall structure of the nanosystem make us adopt a hydrophobic coverage for our SPIONs. In order to disperse the SPIONs in biological environments, these NPs are usually implemented in a **compartmentalized polymeric structure** that can be further modified to provide a series of features for targeting, imaging, or therapy (**Figure 4.4**).

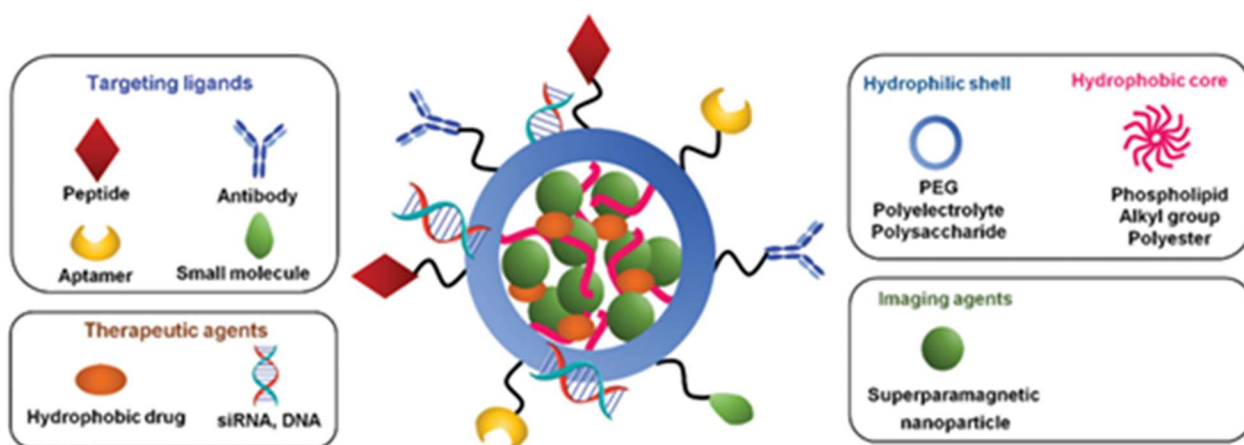


Figure 4.4: Schematic representation of the possible features for a polymeric nanosystem containing SPIONs, based on different structural compartments and surface modifications. Image from reference ⁸⁹. Copyright © 2019 The Royal Society of Chemistry.

The design of our hybrid nanosystem foresees the employment of a similar strategy for the implementation of a **polymeric coating** that:

- Protects and stabilizes the magnetic nanoparticles;
- Presents a hydrophilic surface and impart solubility in aqueous phase;
- Enables to entrap the desired drug acting as a drug carrier.

Consequently, the final nanosystem is suited primarily to combine chemotherapy with MRI in a single complex theranostic nanoplatform. Moreover, the design we devised and the choice of materials makes this structure open to be expanded to additional functionalities and purposes: SPIONs could be exploited also for heat generation, which could be useful for triggered drug delivery or hyperthermia treatment, possibly used synergistically with chemotherapy. Besides, the polymer could present active functionalities which will be used for conjugation with biomolecules in an active targeting scenario.

The biocompatibility of the whole nanosystem will be granted through the employment of non-toxic polymers already used for biological applications which will be screened thoroughly to the optimal combination. The objective is to achieve the possibility to fully degrade the system in small parts after the accomplishment of its function, ensuring rapid renal excretion.

4.2 SYNTHESIS OF SPIONS

The construction of this hybrid polymeric-inorganic nanosystem started from the identification and the optimization of an efficient synthetic strategy for the formation of the SPIONs that will be internalized in the polymeric structure.

The search for the best approach is based on certain characteristics of dimension, solubility, and dispersion of the nanoparticles. Since we want to obtain very small SPIONs with a dispersion that is as low as possible, we will evaluate an adequate synthesis among the ones introduced in the early chapters. The fundamental characteristics we want to achieve regards a core diameter of 4 - 5 nm, suitable for positive contrast in ^1H -MRI, composed prevalently of magnetite (Fe_3O_4) as crystalline phase and with a sufficient susceptibility for magnetic drug targeting applications.

For what concerns the coating and the external stabilization, our objective is to have the possibility to insert these magnetic species either in the hydrophobic or hydrophilic compartment of the complex polymeric structure. However, foreseeing the completion of the entire nanosystem, probably the optimal condition is to have a final nanoparticle that could be prevalently hydrophobic in order to interact better with drug molecules in the late steps of nanosystem's preparation, favoring its internalization in the hydrophobic portion of the nanosystem which will guarantee aqueous dispersibility to both.

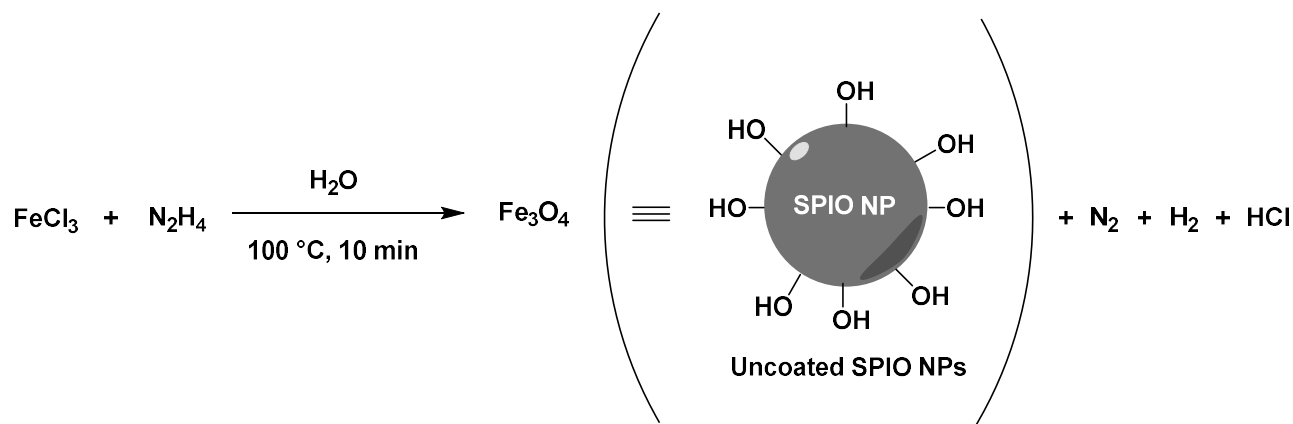
4.2.1 Hydrothermal synthesis (microwave heating)

The first direct method of synthesis that could be adopted to gain access to small SPIONs is the one that exploits hydrothermal conditions with microwave excitation and heating³¹², which is quicker, simpler, and more efficient than conventional heating and is expected to produce homogeneous magnetite nanoclusters.

Preliminary experimental conditions were set up, following a recent work of Osborne³¹³: the synthesis of Fe_3O_4 magnetic nanoparticles coated with dextran was conducted in either one or two separated steps. The group successfully produced SPIO NPs, starting from the precursor ferric chloride and hydrazine hydrated as reducing agent, both dissolved in water. The key point is the microwave heating at fixed temperature and time to decompose the reactants in a precise and reproducible way³¹³. The resulting NPs were fully analyzed, verifying that the iron oxide nanoparticles had a diameter of about 10 – 20 nm and possessed good magnetic properties, compatible with imaging and clinical usage. Considering these results, the aim is to modify their

synthetic conditions in order to obtain uncoated nanoparticles with reduced dimension and with a smaller dispersity, that we further functionalize.

With this aim in mind, we tried some different synthetic conditions and precursors species: the first iron precursor that has been employed was the anhydrous ferric chloride and its partial reduction has been performed as described in **Scheme 4.1**.



Scheme 4.1: Synthetic scheme for the preparation of uncoated SPIO nanoparticles, performed in hydrothermal conditions with the help of microwave heating.

We employed ferric chloride dissolved in water (10 mL), then hydrazine monohydrate was added at room temperature, causing the solution to become immediately orange. The mixture was then shaken and heated by microwave. Different reaction times were explored. In the end, the black magnetic product was washed with water several times and finally the mixture was freeze-dried to obtain a black magnetic powder.

All the syntheses performed with this method were analyzed by TEM and representative images of the materials are reported below in **Figure 4.5**.

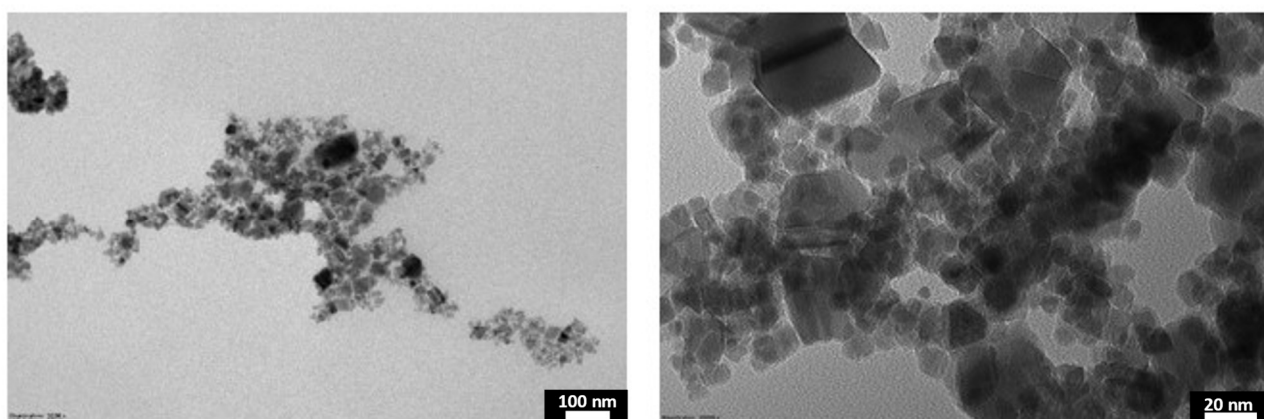


Figure 4.5: Representative TEM images of SPIOs samples prepared with hydrothermal synthesis supported by microwave heating.

The images in the figure above suggest that NPs aggregate during the preparation of the sample for TEM so that only a qualitative analysis can be performed.

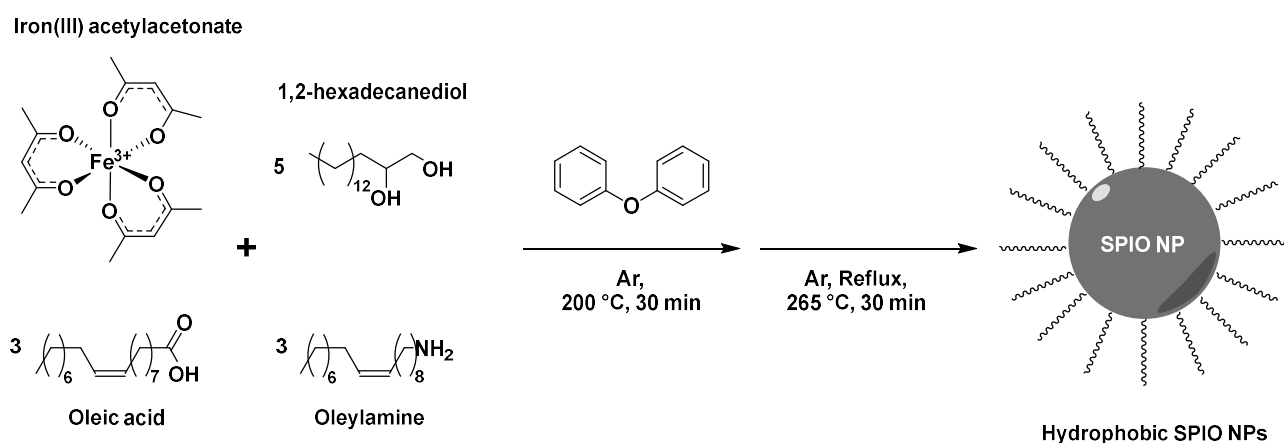
Unfortunately, all the attempts performed varying the iron precursor, the molar ratio, the temperature, and the time of heating, led to unsuitable samples. For all of them, it was not possible to obtain nanoparticles with homogeneous shapes and diameters. Moreover, the nanoparticles' dimension is above the target size (with aggregates even above 25 nm), and it is noted that only the smaller ones are rounded, while the bigger ones are squared or with linear edges. Another important issue is that the dispersion of SPIONs is stable only for few hours.

Despite the results in literature, the cause of these failures in our case is primarily the absence of a coating species that can successfully separate the nanoparticles from each other and maintain them in dispersion. Given the high dispersion and instability of the samples over a short time, even with the variation of synthetic conditions and iron precursors, it has not been possible to obtain the desired SPIONs and this approach has been abandoned for one that is considered more reliable.

4.2.2 Thermal decomposition (conventional heating)

Another synthetic possibility is to exploit a variant of the thermal decomposition method: the high-temperature conversion of iron ions in solution leads to small hydrophobic nanoparticles whose dimensions are easily tunable and can be further modified. For example, these lipophilic nanoparticles can be eventually converted into hydrophilic NPs by adding bipolar surfactants³¹⁴.

We adopted the procedure in **Scheme 4.2** that allows the preparation of 4 nm Fe₃O₄ nanoparticles.



Scheme 4.2: Reaction scheme illustrating the synthesis of hydrophobic SPIO nanoparticles, performed under reflux with conventional heating.

The procedure starts from the species Fe(acac)₃ as the supplier of Fe³⁺ ions that are dispersed in a mixture of 1,2-hexadecanediol, oleic acid, oleylamine, and phenyl ether. The whole mixture is then

pre-heated at 200 °C for 30 minutes and finally heated at reflux, 265 °C for another 30 minutes. This gradient of temperature and the time of each heating step are fundamental to obtain monodisperse nanoparticles of a precise size. The product is cooled down at room temperature and finally, oleic acid and oleylamine are added for stabilization and coating the NPs surface, while the product is dispersed in ethanol. Adopting several steps of precipitation and centrifugation guarantees the purification of the product before its dispersion in hexane.

Even if the general procedure was presented by Sun and colleagues in 2004³¹⁴, the mechanism behind the formation and passivation of the iron oxide core, as well as the role of each reactant are not fully understood. What is known is that the co-precipitation of Fe³⁺ and Fe²⁺ occurs – the latter formed at least for 1/3 of the total – through the reduction of the former, followed by crystallization. This reduction can be attributable to either oleylamine³¹⁵ or the 1,2-alkanediol species³¹⁶. Moreover, since the crystal core derives from conditions and mechanisms similar to co-precipitation, it has been suggested that may present extensive hydroxyl groups on the surface as well. These groups can react with the carboxylic functions of oleic acid, forming a chemically adsorbed layer through an electrostatic acid-base complex³¹⁷ or a coordination bond between Fe³⁺ and oleic acid to give Fe³⁺-oleate³¹⁸ (**Figure 4.6**). These interactions lead to the coating of the nanoclusters with a compact primary layer of oleic acid. Finally, the excess of oleic acid and oleylamine is weakly adsorbed on this primary layer to form a second one presenting the polar heads on the surface. Nonetheless, since the reaction occurs at high reflux temperature, the nanoparticles are characterized by a higher degree of crystal order that guarantees a top-quality material and set the thermal decomposition as one of the most promising routes to obtain magnetic nanoparticles³¹⁹.

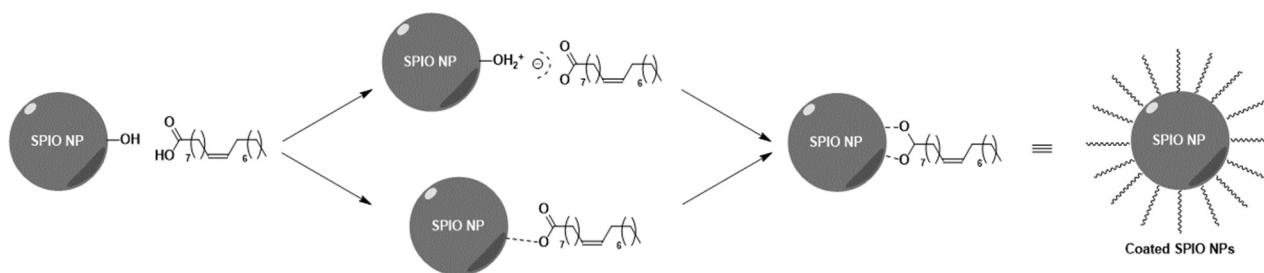


Figure 4.6: Scheme illustrating the possible interaction between the iron oxide surface decorated with hydroxyl groups and the oleic acid molecules that will form the organic monolayer.

Seeking the preparation of this promising nanomaterial, we followed the original procedure, using an apparatus kept under argon atmosphere to bring to reflux the reactant mixture. The SPIONs obtained after the centrifugation and washing steps were analyzed preliminarily with TEM (**Figure 4.7**) to compare our results with the ones reported in literature.

SPIONs_1	
TEM (N = 841)	d = 3.22 ± 1.04 nm (0.324)

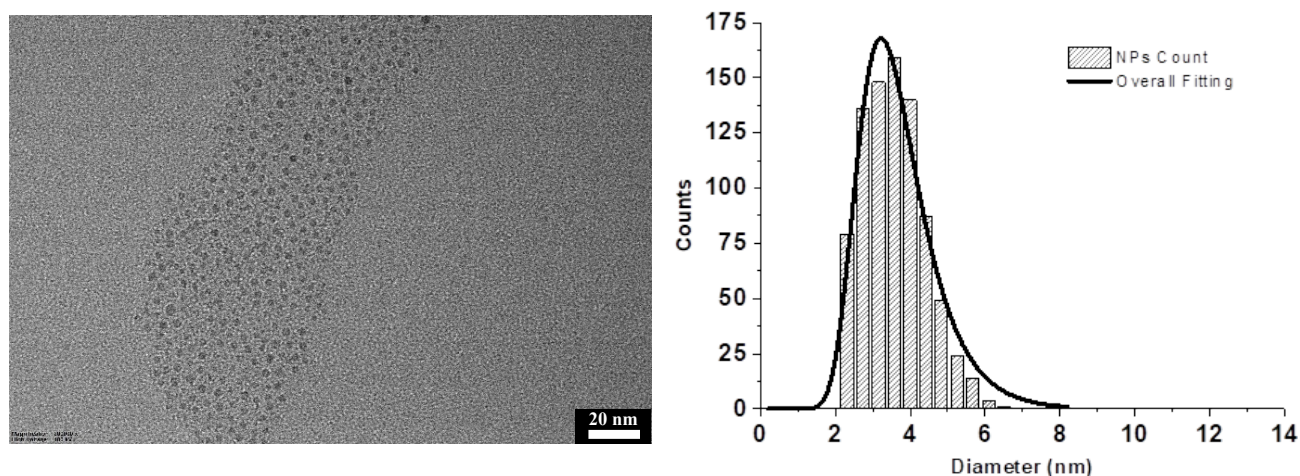


Figure 4.7: (Left) Representative TEM image of SPIONs_1 sample prepared by thermal decomposition with conventional heating. (Right) Histogram and Extreme fitting showing the size distribution of the inorganic core diameter, obtained from the analysis of the TEM images: $d = 3.22 \pm 1.04$ nm.

As can be seen from the image presented, some small hydrophobically-coated nanoparticles have been successfully synthesized and purified. However, another noticeable feature is that the SPIONs' shape is highly irregular as well as their size. The statistical analysis confirms this impression, since we obtained a broad and tailed distribution of diameters centered at 3.22 nm, with a high variance coefficient (0.324).

With this different synthetic approach, the outcome is more encouraging than the nanoparticles obtained with the previous method, since we prepared rounded and well-dispersed SPIONs that strongly responded to the magnet. However, we need to find a way to optimize the synthetic conditions, in particular the reactant dispersion and the heating steps, to guarantee the formation of a homogeneous nanoparticle and meet the desired requirements.

4.2.3 Thermal decomposition (microwave heating)

A variant of the previous procedure relies on the same ensemble of reactants, with the difference that this time the heating is provided by a microwave setting. Unlike the conventional heating process performed with a bath or a DrySyn system, microwave irradiation is characterized by greater speed, simplicity, and high-energy efficiency (**Figure 4.8**). Moreover, with this method many “hot-spots” can be produced at the same time, leading to a uniform seeding process that hence gives very small Fe₃O₄ nanocrystals.

This change is therefore expected to speed up the synthesis and make the heating faster and more uniform and reproducible, preventing the possibility of unwanted parallel reactions of oxidation of the NPs or uneven growth of nanoparticles caused by heating parts of the vessel differently. Thanks to these improvements, the resulting SPIONs should have a more homogeneous composition and better monodispersity and magnetic characteristics.

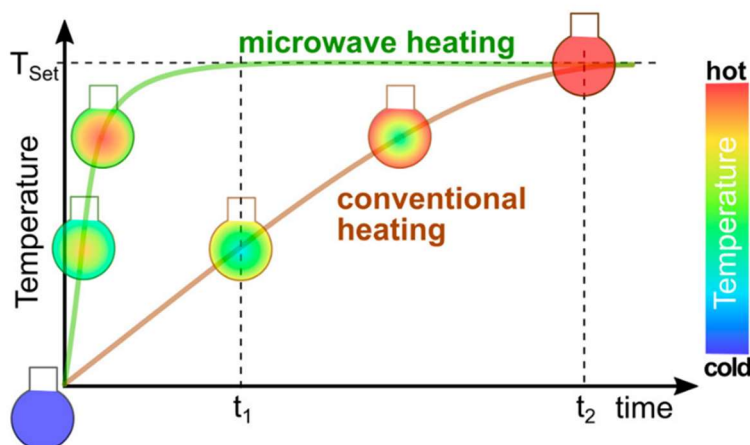
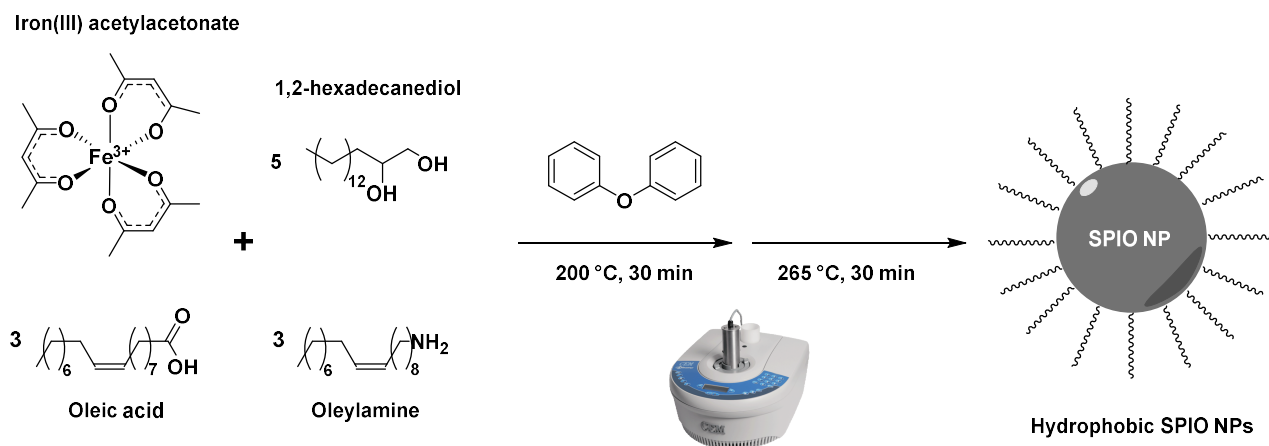


Figure 4.8: Temperature versus time plot confronting the heating profile, heat distribution, and efficiency of conventional and microwave-supported heating. Image from reference ³²⁰. Copyright © 2017 Institute of Materials, Minerals and Mining and ASM International.

Therefore, we started our series of new syntheses using microwave instrumentation (**Scheme 4.3**): for the introduction of the reactants and their solvation in phenyl ether we used a 30 mL microwave vial completed with a pressure-resistant snap cap. The ruby-red mixture was placed inside the microwave instrument that within few minutes heated at the right temperature with the ramp and steady-temperature steps continuously controlled. The resulting dark dispersion was already more homogeneous than the tries with conventional heating and was purified by the same cycles of precipitation in ethanol and redispersion in hexane.



Scheme 4.3: Reaction scheme illustrating the synthesis of hydrophobic SPIO nanoparticles, performed with the help of microwave heating.

The sample has been analyzed only by means of TEM to assess the nanoparticles' dimension and dispersion. The image presented in **Figure 4.9** shows a distribution of well-separated nanoparticles that have a more homogeneous rounded shape and dimension: this made us think that the microwave instrument assured effectively uniform heating and that the nanoparticles were correctly coated and do not aggregate.

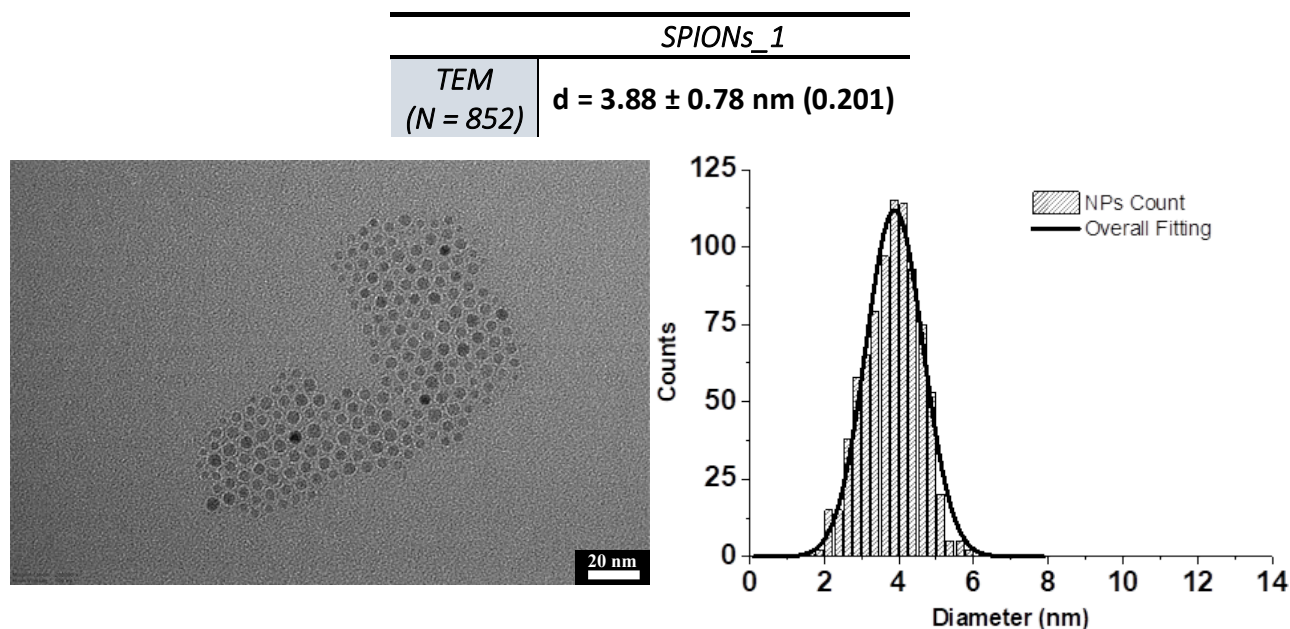


Figure 4.9: (Left) Representative TEM image of SPIONs_1 sample prepared by thermal decomposition with microwave heating. (Right) Histogram and Gaussian fitting showing the size distribution of the inorganic core diameter, obtained from the analysis of the TEM images: $d = 3.88 \pm 0.78$ nm.

The histogram reported in **Figure 4.9** can be fitted with a Gaussian curve centered at 3.88 nm, which indicates a quite monodispersed distribution (variation coefficient = 0.201).

Just at the end of the last purification step and mostly some time after the drying and storage, we observed for all the preparation obtained so far, a change in color from brown-black to brown-orange, likely because of the oxidation to Fe_2O_3 . This is due in the first place to the oxygen that is naturally dissolved in all the solvents used and to oxidation during sample storage. Therefore, the improvements we introduced afterward were the use of de-oxygenated solvents for both the synthesis and the purification cycles. For what concerns the synthesis, argon was bubbled directly in the mixture as soon as the reactants' dissolution in diphenyl ether was completed. Regarding the final washing steps, both ethanol and hexane used for SPIONs precipitation and re-dispersion were de-oxygenated separately with argon and the help of sonication. Moreover, we evaporated the hexane in the intermediate step with a flux of argon, and finally, we stored the dried sample in an inert atmosphere. Already after the first adjustments, we observed a significant change in the color of the SPIONs hexane solution and in the final appearance of solid SPIONs, which maintained a

darker shade of black-brown instead of turning brown-orange as we observed in the previous synthesis where solvent de-oxygenation was not performed.

The sample prepared with this synthesis was characterized by TEM, which gave an even Gaussian distribution, slightly broader (the variance coefficient is 0.238) and with a bigger average diameter of 4.05 nm, which however is still suitable for the purpose we seek for these SPIONs. From the images in **Figure 4.10**, we observed that the nanoparticles are more rounded and still tend to interact with each other through hydrophobic interactions between alkyl chains that constitute the organic passivation shell, but now small groups of SPIONs instead of aggregates are detectable.

SPIONs_2	
TEM (N = 577)	$d = 4.05 \pm 0.97 \text{ nm}$ (0.238)
XANES	$\text{Fe}_3\text{O}_4 = 90 \% (\pm 5 \%)$
	$\text{Fe}_2\text{O}_3 = 10 \% (\pm 5 \%)$
	FeO = negligible

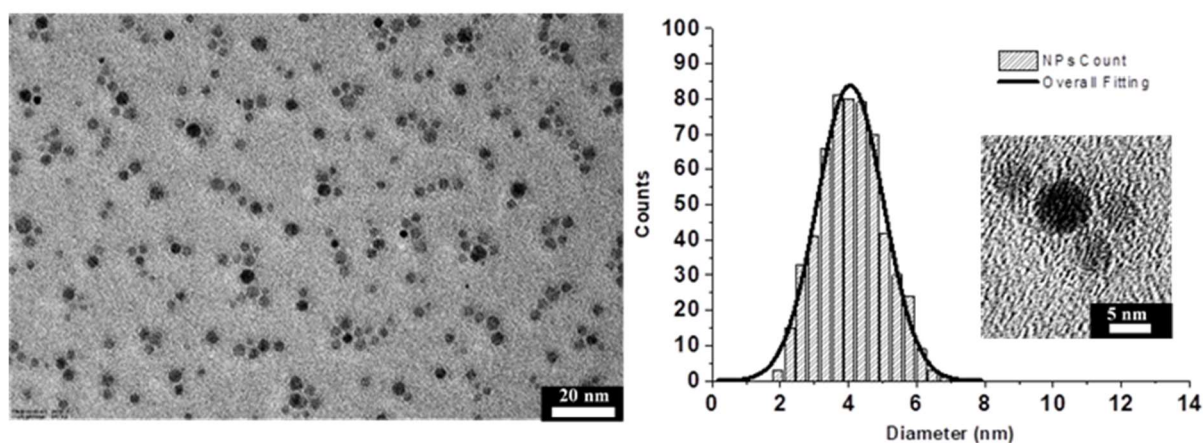


Figure 4.10: (Left) Representative TEM image of SPIONs_2 sample prepared by thermal decomposition with microwave heating and deoxygenated solvents. (Right) Histogram and Gaussian fitting showing the size distribution of the inorganic core diameter, obtained from the analysis of the TEM images with and insert showing some of the SPIONs more in detail: $d = 4.05 \pm 0.97 \text{ nm}$.

To estimate the SPIONs' composition in terms of crystalline phases and oxidation states of the Fe atoms, we analyzed this sample with x-ray absorption near-edge structure (XANES) spectroscopy (**Figure 4.11**). Therefore, we observed the region between 7100 eV and 7200 eV, corresponding to the Fe K-edge of iron oxide nanoparticles and made a comparison with reference spectra³²¹ of magnetite (Fe_3O_4) and maghemite (Fe_2O_3). From the linear combination fit we operated using the reference spectra to reproduce the sample curve, we calculated a percentage of magnetite of 90 %, therefore only the remnant 10 % was constituted by maghemite. The spectrum of FeO was also considered, but its contribution was negligible.

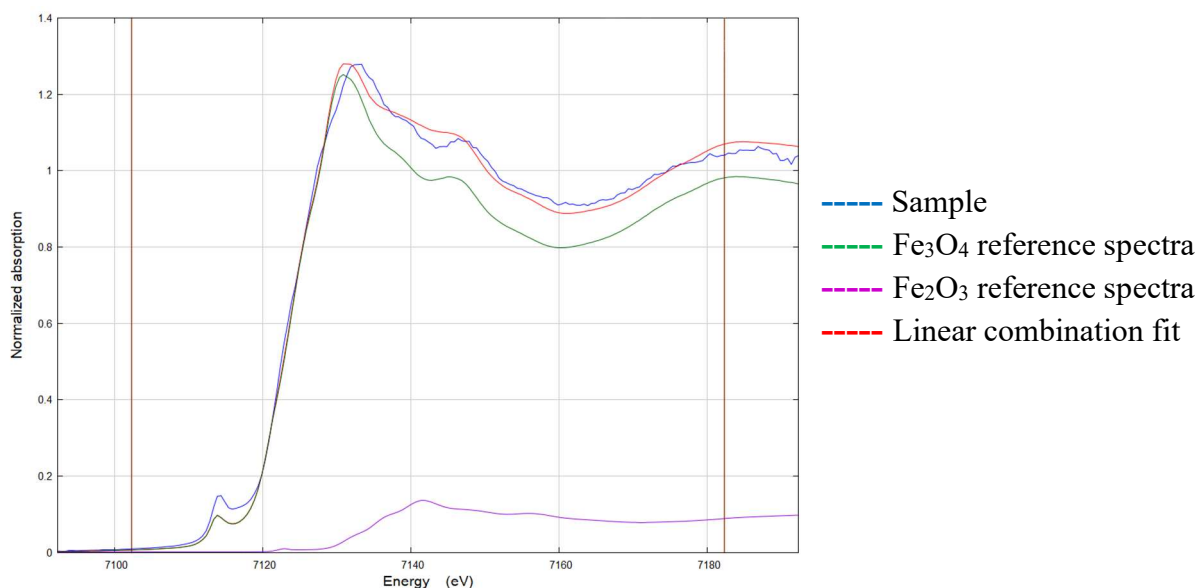


Figure 4.11: XANES spectrum of SPIONs_2 sample obtained by thermal decomposition with microwave heating and deoxygenated solvents, in which the sample line is fitted with the reference spectra of Fe₂O₃ and Fe₃O₄.

The latest test we performed on this synthesis was to increase the reactant scale in order to obtain more SPIONs for the following studies on the polymeric nanosystems. We operated a 3-fold scale-up adapting the procedure and the experimental apparatus for both the synthesis and the cleaning steps to ensure the same outcome in terms of physical-chemical characteristics and degree of purity. The result was controlled through TEM (**Figure 4.12**) which images showed nanoparticles identical in shape to the previous experiments even if slightly smaller, as is indicated by the statistical analysis resulting in a Gaussian distribution centered at 3.47 nm and promisingly less disperse.

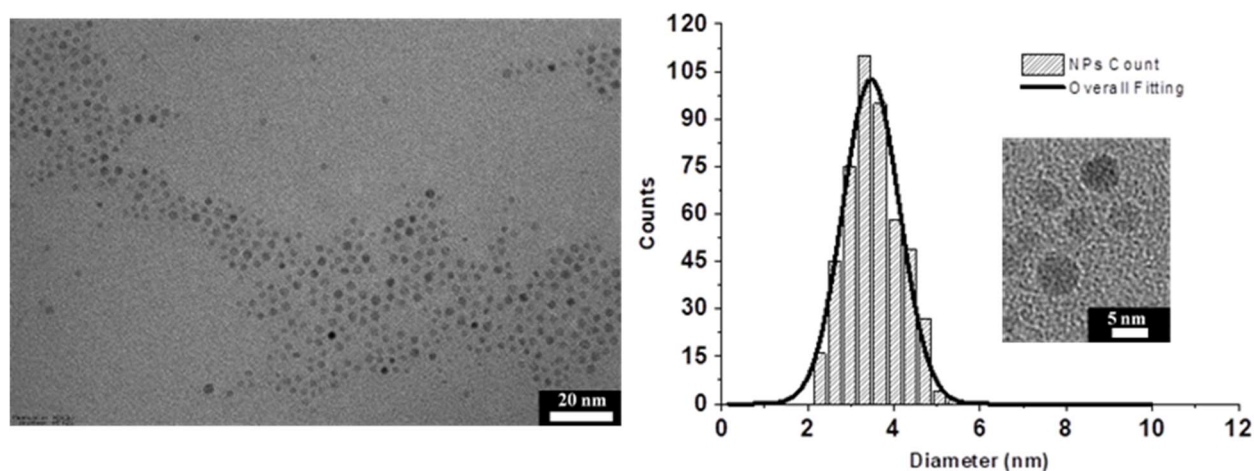


Figure 4.12: (Left) Representative TEM image of SPIONs_3 sample prepared with a 3-fold scale-up. (Right) Histogram and Gaussian fitting showing the size distribution of the inorganic core diameter, obtained from the analysis of the TEM images, with an insert showing some of the SPIONs more in detail: $d = 3.47 \pm 0.66$ nm.

This sample was then submitted to TGA in order to assess the percentage of the organic shell and retrieve the magnetic content of each coated nanoparticle. The plots in **Figure 4.13** illustrate the decreasing mass of the sample (TGA curve, in red) and its first derivative (named differential thermal gravimetry curve, DTG, in blue).

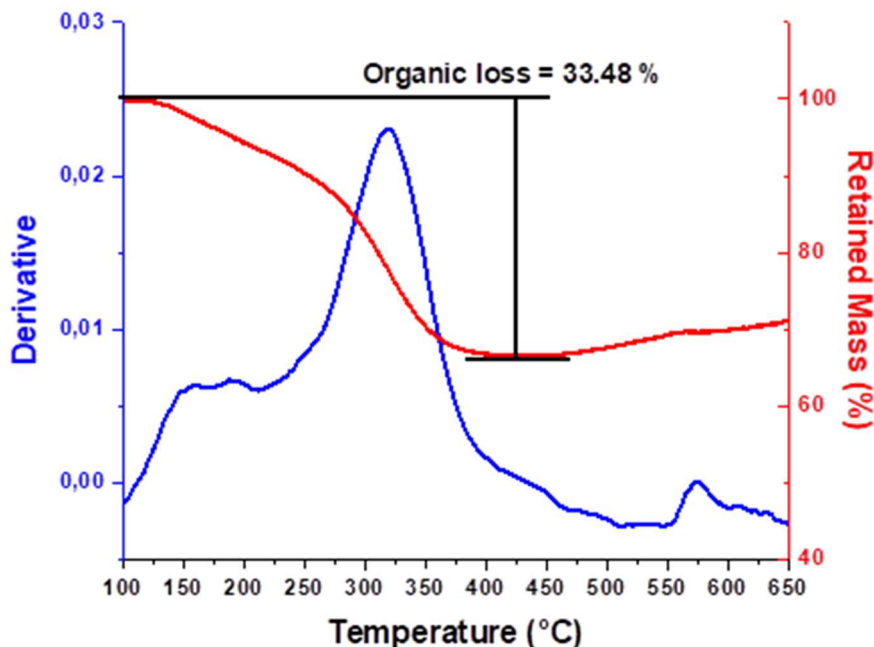


Figure 4.13: TGA plot of SPIONs obtained with the last approach comprising (blue) the derivative of the mass loss and (red) the percentage of the mass that is retained with increasing temperatures.

The analysis of the derivative of this mass loss can provide information about the species that are desorbed at a certain temperature: we can spot two main contributions between 150 °C and 200 °C and a major one around 325 °C. From the literature, it is known that oleic acid is responsible for both these derivative peaks, since they are related to two types of bonding between the COO⁻ groups and Fe that possess different energies³²²: therefore, they are both assigned to the loss of oleic acid coating from the iron oxide surface³²³. The signals detected above 500 °C instead, are related to the reduction of the inorganic Fe₃O₄ core by gases produced during the degradation of oleic acid³²⁴, hence they were not considered in the organic loss calculation. The increase in the retention mass that is detected above that temperature is considered an instrumental deviation.

Finally, in collaboration with Dr. Slavko Kralj of the Jožef Stefan Institute in Ljubljana, we characterized these SPIONs synthesized with the optimized and scaled procedure with vibrating sample magnetometry (VSM) to verify the superparamagnetic behavior and retrieve the principal magnetic parameters of the iron oxide core. This technique gives a magnetization (M) versus magnetic field strength (M-H) plot from which it becomes possible to collect the saturation magnetization (M_s, the maximum value of magnetization reachable by the sample), the remnant magnetization (or retentivity, M_r, the magnetization retained by the sample after the applied

external field returns to 0) and the coercivity (H_c , the required magnetic field to demagnetize the nanoparticles after saturation). The superparamagnetic character of our nanoparticles can be immediately deduced by the peculiar profile of the plot in **Figure 4.14** and verified by calculating a coercivity of 0.23 Oe and a remnant field of $1.76 \cdot 10^{-3}$ emu/g: since both these values are negligible, the sample is considered superparamagnetic.

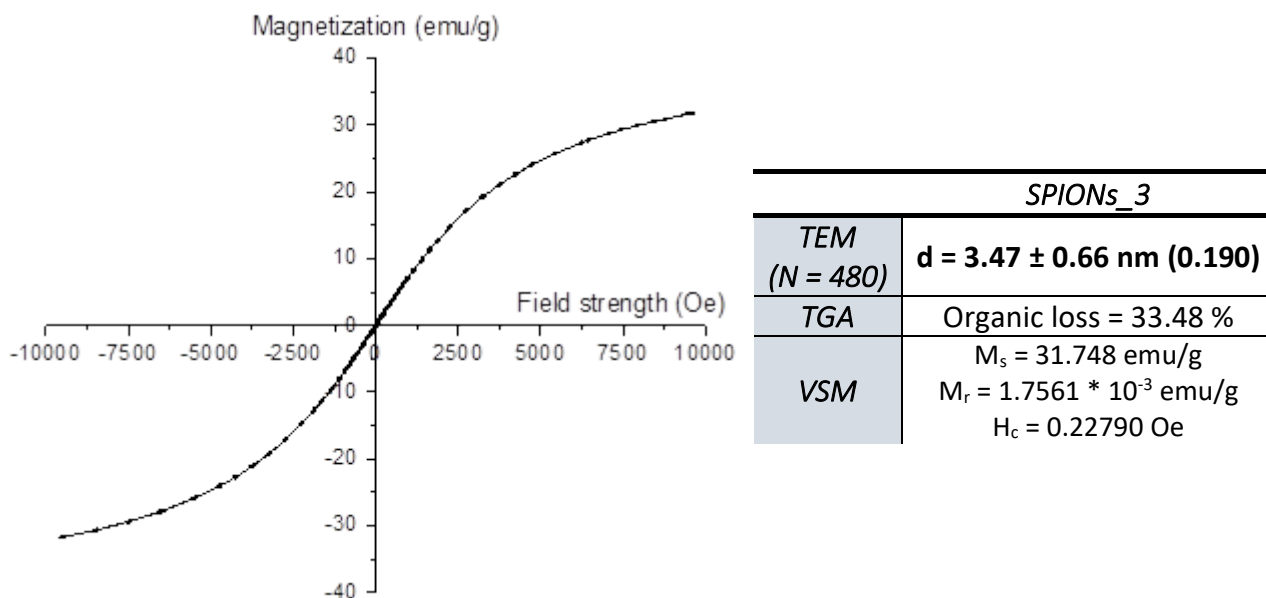


Figure 4.14: (Left) Magnetization vs. applied field plot showing the superparamagnetic character of the SPIONs_3 sample. (Right) Overview of dimensional, organic composition, and magnetic characteristics of the sample.

Moreover, the saturation magnetization was estimated at 31.7 emu/g: this low value is in accordance with the literature³⁰⁹, considering the small dimension of the iron oxide core, its crystalline composition, and the coating made of fatty acids. In fact, the maximum magnetization depends on the internal structure, electronic configuration (bulk Fe_3O_4 has a slightly bigger M_s than γ - Fe_2O_3 ²⁰⁸, calculated around 92 emu/g¹¹⁰), the extent of the superficial canted spin layer (which increases with the reduction of size and lowers M_s ³²⁵) and the type of coating (which can reduce the interaction between nanoparticles³²⁶). In our case, considering the achievement of strong positive contrast in 1H -MRI, a low r_2 value, thus a reduced saturation magnetization are preferable³²⁷. Therefore, we are confident that the value we obtained is a good compromise between the desired effect on T1 and the retained ability to be magnetized and guided by an external field for magnetic drug targeting. Further analyses will be performed on the complete nanosystem to verify that these magnetic characteristics are maintained once SPIONs are encapsulated in the polymeric structure.

Thanks to the microwave setting and the employment of some synthetic adjustments such as the use of deoxygenated solvent and the evaporation with argon, we finally achieved the preparation of SPIONs with the desired size and morphology. Moreover, further analysis evidenced that the inorganic core presents a considerable percentage of magnetite that confers ideal magnetic properties to a system protected by an optimal coverage of alkyl ligands for its proper stabilization and dispersion in organic solvents.

4.3 ASSEMBLY OF THE POLYMERIC STRUCTURE AND SPIONS LOADING

The following subchapter illustrates the different experiments carried out with the scope of preparing a polymeric coating hosting SPIONs.

The choice for the polymers, after a critical literature analysis, was guided by a series of requirements needed for its final application in the biomedical field, like biocompatibility, the right degree of hydrophilicity, and the ability to avoid the triggering of the immune system and the protein corona adsorption. Several polymers were taken into consideration, but the ultimate choice was focused on a combination of polyvinyl alcohol (PVA) and Pluronic. We decided to investigate both PVA at low molecular weight, PVA of 13 kDa and PVA of 57-66 kDa.

The specific synthetic technique that was employed for all the following assemblies was the emulsification-solvent evaporation method (**Figure 4.15**). This was the first method used to prepare polymeric nanoparticles out of preformed polymers³²⁸ and is currently the most employed in the pharmacological and medical fields when polymer dispersion is required. Briefly, polymer dispersions are prepared in aqueous and organic solvents – depending on the solubility of the species – and the two immiscible phases are emulsified. The final aqueous nanoparticles suspension is then achieved through the evaporation of the organic solvent, which is free to diffuse through the continuous phase of the emulsion³²⁹.

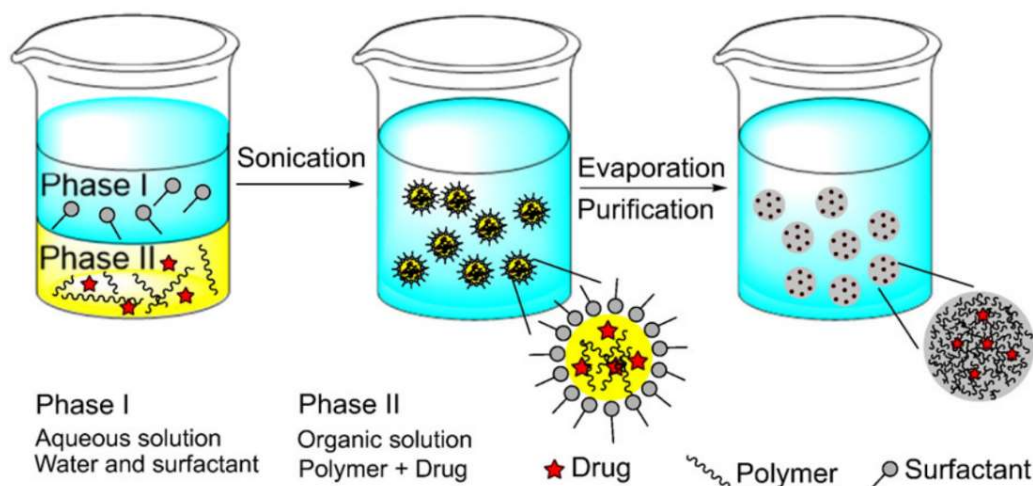


Figure 4.15: Schematic representation of nanospheres preparation using the emulsification-solvent evaporation method. Image from reference ²⁶¹. Copyright © 2017 Elsevier B.V.

This approach allows to prepare both single emulsions (oil-in-water, O/W) and double emulsions (water-in-oil-in-water, W/O/W), depending on the polymers' molecular weight, the reciprocal intra- and intermolecular interactions between the chains, and the number of emulsification steps taken.

The instruments that are usually used to prepare the emulsion are the high-speed homogenizer or the ultrasonicator, and the choice is based on the energy required to mix the two phases, the type of polymers, and the desired final nanoparticles' size.

Once the emulsion is prepared in the form of nanodroplets, the organic and volatile solvent is let to evaporate either under reduced pressure or with magnetic stirring at atmospheric pressure (possibly with the help of heating). The result is a suspension of solidified hydrophilic nanoparticles that are washed and centrifuged to clean the sample and remove impurities and non-assembled polymers. Eventually, the sample could be freeze-dried to guarantee long-term storage and stability and dispersed again in aqueous solutions at need.

In this project, the emulsion-solvent evaporation approach was undertaken using one aqueous phase to dissolve the polymer and one organic phase to disperse the SPIONs. Even if ethyl acetate is more favorable as organic solvent for biomedical applications²⁷⁷, it doesn't solubilize efficiently our hydrophobic SPIONs, therefore we were forced to resort to dichloromethane or chloroform in which they dissolve easily and completely. Accordingly, particular attention has to be paid during the removal of the organic solvent and the washing steps.

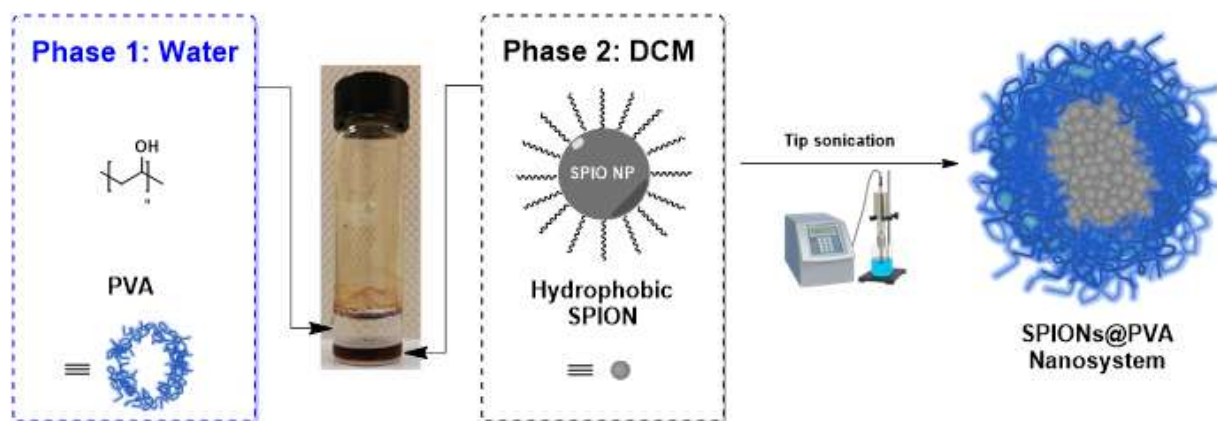
To emulsify the immiscible phases in which the two main components are dispersed, a considerable amount of energy is required. Moreover, we desired to focus the final nanosystem on a diameter size between 100 nm and 300 nm. For these reasons, the source selected was the tip sonicator¹⁶². The physical phenomenon behind this approach is acoustic cavitation: high-frequency sound waves cause pressure variations in the liquid with the subsequent formation of microbubbles that oscillates and expand until the rise of temperature and pressure within them bring to a localized implosive collapse which creates a "hot spot"³³⁰. The result is a powerful mixing and stirring force in that precise region due to microstreaming, shock waves from collapses, and local high temperatures from the gas heating³³¹.

A standard sonication bath for glassware cleaning has insufficient power to mix the phases and form a stable emulsion. For this reason, we will take advantage of a tip sonicator (ultrasonicator), capable of conveying a higher cavitation power in a precise and reduced volume of solution: this is enough to force the formation of an emulsion in which the polymer is assembled in a complex nanostructure. Moreover, we have to eliminate the use of magnetic stirring for homogenization in the first part of the synthesis to avoid the sequestration of SPIONs while they are still in dispersion and not yet included in the polymeric structure.

4.3.1 Assembly of the polymeric structure using PVA with $M_w = 13$ kDa

The first polymer that was experimented in this project was polyvinyl alcohol with an average molecular weight of 13000 Da.

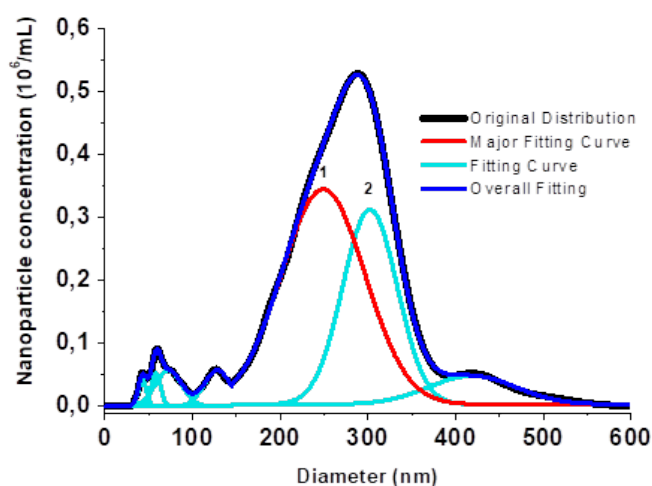
The initial experiments were performed according to the synthetic procedure for the stabilization of core-shell PVA nanocapsules containing SPIONs, published by Shang-Hsiu Hu and coworkers²⁸⁵ and adapting the technique to our reagents. In their paper, the authors claimed that two types of nanocapsules can be prepared starting from the same polymer (PVA), if only the molecular weight (hence the chain length) is changed. The parameter related to this differentiated outcome and the polymer length is the so-called “Hydrophilic-Lipophilic Balance” (HLB), which gives the degree of affinity for polar or non-polar compounds, measured by emulsifying the compound with a series of reference oil with known HLB: if this emulsion is maintained for 24 hours after the ultrasonication, then the sample has the same HLB of the reference used. More in detail, the higher the HLB value is, the more the polymer is hydrophilic: in fact, PVA chains of greater molecular weight tend to possess a low HLB index. The paper describes the same procedure based on ultrasonication of two immiscible phases for four different PVA chains of increasing molecular weight, with the result of forming alternatively a W/O/W structure with the ones with higher HLB and lower molecular weight and an O/W structure with the ones characterized by lower HLB and high molecular weight. Considering the mass of the first PVA we selected (13kDa) and the HLB index of the most similar polymer used by the authors (PVA 16 kDa with HLB = 6 - 15), the polymer should have an even stronger lipophilic character, therefore enabling the formation of a polymersome with a hydrophilic inner chamber surrounded by a hydrophobic layer and covered for its dispersion in aqueous environment. The SPIONs dispersed in an organic solvent at the start, are transferred to the hydrophobic layer during the nanostructure’s formation, thus providing also a structural and joining element that increases the strength of the nanosystem.



Scheme 4.4: Scheme representing the reagents and the general synthetic approach adopted for the formation of SPIONs@PVA nanosystems.

For the very first experiment, the concentrations of the species used by Hu and colleagues²⁸⁵ were strictly reproduced: 20 mg of PVA 13 kDa were dispersed in 1 mL of Milli-Q H₂O, while 8 mg of SPIONs were dispersed in 0.4 mL of chloroform. Also for the assembly and the cleaning steps, the procedure reported in literature²⁸⁵ was followed: a tip sonicator was used to emulsify the two-phases system for 1 minute and then the organic solvent was eliminated mixing and heating the emulsion at 60 °C for 2 hours. Three steps of centrifugation/washing were performed to clean the dispersion from the unassembled polymer, collecting an unexpected orange supernatant that was progressively paler after every centrifugation cycle.

The precipitate has been analyzed with the NTA technique to study preliminarily the dimension of the nanosystem. The resulting overall distribution is reported in **Figure 4.16** as a black line, while the fitting operated using Gaussian distributions (red and cyan lines) is illustrated in blue, with only the major fitting curves reported in the table to the right.



<i>SPIONs@PVA13kDa_1 (Precipitate)</i>	
NTA	1) $d_H = 248.9 \pm 40.5 \text{ nm}$ (0.16)
	2) $d_H = 302.3 \pm 26.4 \text{ nm}$ (0.09)

Figure 4.16: (Left) NTA analysis of SPIONs@PVA13kDa_1 precipitate, showing the original size distribution and data extrapolation curves using Gaussian fitting. (Right) Hydrodynamic diameters of the two principal size populations with the related variation coefficient.

Considering this analysis, even if there are two major distributions (evidenced in red and turquoise), they overlap significantly having a broad extension, thus quite invalidating the distinction. Moreover, there are some other populations of nanoparticles that arise from the distribution, both with smaller – probably unassembled polymer or aggregated SPIONs – and larger – likely polymeric aggregates – diameters.

Overall, the sample doesn't reflect the expectation in terms of dimension and dispersion, being characterized by high values in both parameters.

Based on the results related to the precipitate properties described above, the supernatant was also analyzed to achieve a complete overview of the synthetic and cleaning steps carried out. The better

distribution obtained with the NTA analysis encouraged us to study the sample with TEM (**Figure 4.17**).

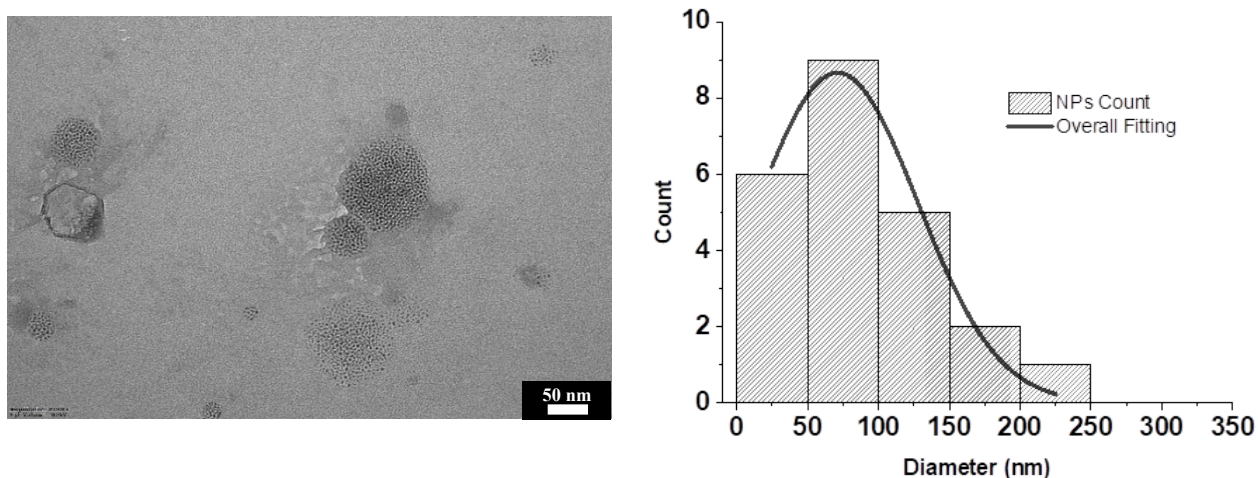


Figure 4.17: (Left) Representative TEM image of SPIONs@PVA13kDa_1 supernatant. (Right) Histogram and Gaussian fitting showing the size distribution of the inner core diameter, obtained from the analysis of the TEM images: $d = 71.4 \pm 48.1$ nm.

The TEM images show a heterogeneous distribution of spherical nanosystems that have successfully included a discrete amount of SPIONs in the hydrophobic reservoir, even if the successive data elaboration evidenced a great size dispersion.

The particular conditions in which the TEM grid is prepared and analyzed are surely responsible for the outcome. Indeed, the NPs solution is dried and consequently, the soft nanosystems deposited are probably spread onto the grid and both the polymeric and core perimeters result visually enlarged in respect to the conditions in solution. Moreover, the TEM sample is kept under high vacuum for the measurement. However, it has to be stressed that the diameter values retrieved from the images and reported in the histogram above are only related to the extension of the core of the nanosystem that is made visible thanks to the clusterization of the SPIONs, while the external shell is almost invisible and cannot be quantified because the polymer is transparent to the electron beam.

The NTA carried out on the supernatant in **Figure 4.18**, depicts the presence of a single broad population centered at 217 nm, which is moderately dispersed and only slightly larger than the expected dimension of 200 nm.

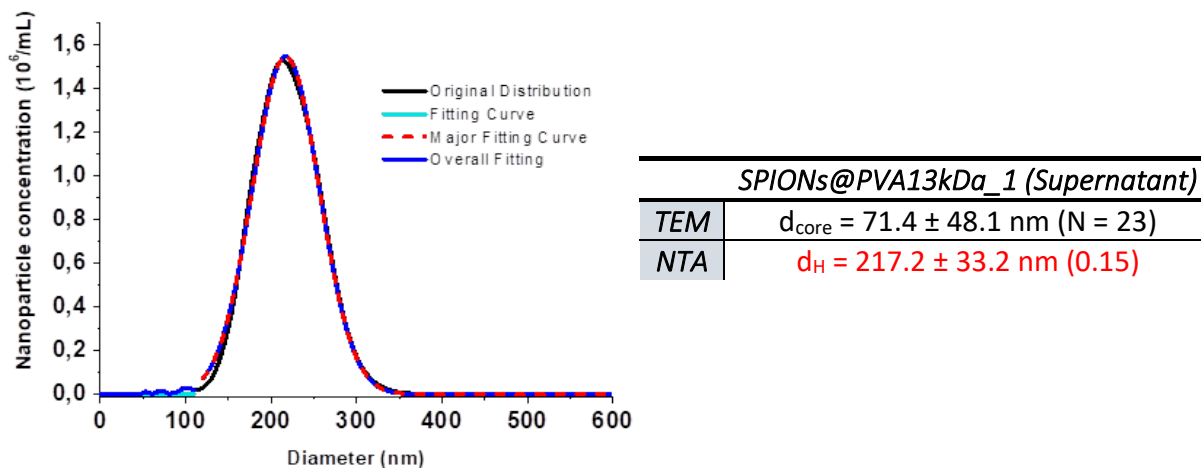
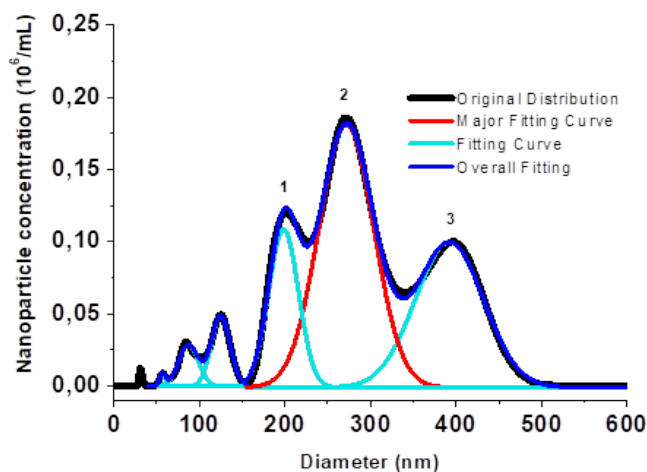
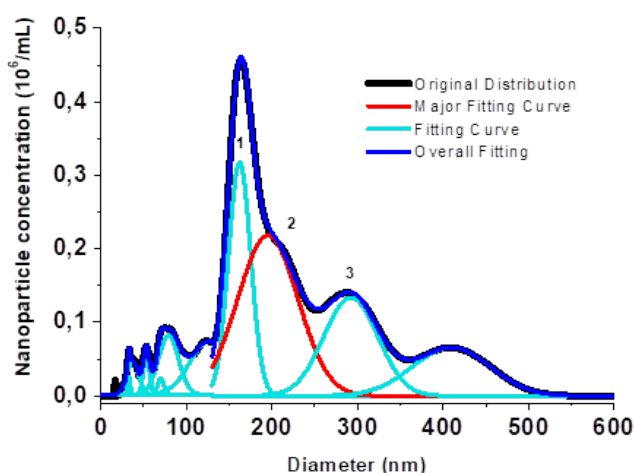


Figure 4.18: (Left) NTA analysis of SPIONs@PVA13kDa_1 supernatant, showing the original size distribution and the data extrapolation curve using Gaussian fitting. (Right) Inner core diameter from TEM and hydrodynamic diameter from NTA with the related variation coefficient.

The hypothesis that can be drawn from the comparison of these two samples is that probably the conditions of purification and centrifugation are too harsh for this type of nanosystem and they cause aggregation and partial precipitation. The fact that this precipitate is not easily dispersible in water once it is separated by centrifugation, could corroborate the aggregation hypothesis. Therefore, in the next set of experiments, the purification steps were carried out in a separated sample for comparison in order to find the most suitable purification procedure for this type of nanosystem. The reagent quantities were maintained constant, as well as the synthetic conditions. At the end of the evaporation step, the dispersion was divided in two aliquots: one was magnetically decanted using an N38 Neodymium-Iron-Boron (NdFeB) magnet with a nominal remanence of 1.22 T, while the other was centrifuged for a smaller period (1 minute) at 8500 rpm. The two samples were preliminarily analyzed with NTA to assess the purification quality, giving the distributions reported in **Figure 4.19**.



<i>SPIONs@PVA13kDa_2 (Decanted)</i>	
NTA	1) $d_H = 198.4 \pm 14.8$ nm (0.07)
	2) $d_H = 271.7 \pm 27.3$ nm (0.10)
	3) $d_H = 392.3 \pm 33.8$ nm (0.09)



<i>SPIONs@PVA13kDa_2 (Centrifuged)</i>	
NTA	1) $d_H = 162.2 \pm 11.0$ nm (0.07)
	2) $d_H = 195.2 \pm 29.9$ nm (0.15)
	3) $d_H = 292.3 \pm 26.8$ nm (0.09)

Figure 4.19: (Top and bottom left) NTA analysis of SPIONs@PVA13kDa_2 precipitate collected with decanting or centrifugation, showing the original size distribution and data extrapolation curves using Gaussian fitting. (Top and bottom right) Hydrodynamic diameters of the principal size populations in the two samples with the related variation coefficient.

From the NTA profiles of **Figure 4.19** the following comments can be drawn: magnetically decanting the sample containing the magnetic nanosystem does not remove the aggregates, but on the contrary, helps to collect a population of larger magnetic nanosystems of aggregates at 392 nm. Interestingly, another distribution centered at 198 nm can be detected: it matches the desired size, therefore further efforts will be invested to isolate this population from the rest. Moreover, the magnetic susceptibility and responsiveness of the SPIONs – and of the polymeric nanosystems that include them – are still interesting properties that have to be better exploited in the successive experiments to achieve a proper separation from the empty polymeric micelles.

The sample that underwent the softer centrifugation step is effectively characterized by a distribution of smaller size, even if nanosystems above 290 nm are still far from being eliminated, either because of the inefficient centrifugation steps or the not optimized assembly procedure. In fact, the solvent evaporation method is known to possibly bring coalescence of the nanodroplets

during the evaporation phase²⁶⁵, hence the need to modify and tune carefully the experimental conditions in the next tries. Centrifuging the sample is still the preferred option for the purification of the magnetic nanosystems.

Considering the result of these experiments, neither of the two samples were studied with TEM, but were kept as a reference for the following experiments performed to pursue a better elimination of both the larger aggregates and the smaller nanoparticles.

For the next set of syntheses, both the assembly procedure and the successive evaporation of the organic solvent were slightly modified to reduce the possible coalescence, polymer degradation, and SPIONs diffusion that provoked the presence of small debris and large aggregates seen in the previous experiments. For this reason, the solvent for the organic phase was changed in favor of dichloromethane, which has a higher vapor tension and can still dissolve the hydrophobic SPIONs properly. Moreover, we wanted to push forward the encapsulation percentage: with this aim in mind, we decided to maintain the weight ratio between the polymer and the SPIONs and the concentration of these two components in their respective phases (20 mg/mL each), but to reduce their volume to favor a more homogeneous and complete sonication that could place better in contact the two phases during the emulsion formation. The degree of encapsulation will be controlled after the centrifugation steps with TEM analyses.

Finally, both the time and the temperature employed during the evaporation of the organic solvent entrapped in the polymeric structure were reduced: a first experiment was performed at room temperature for 3 hours, always under constant slow stirring. In this way, we intended to remove quickly the organic solvent from the emulsion, without the risk of keeping the nanosystem in dispersion too much.

As mentioned, in the following purification step, the nature of the components of the dispersion was assessed: after the first centrifugation, the dispersion still appeared brown-orange with a noticeable brown precipitate. Despite our efforts in mixing, we were not able to disperse again the precipitate in water completely, but it remained as a brown pellet at the bottom of the vessel or as visible brown particulate stable in dispersion only for a short time. After collecting the supernatant, the brown precipitate was washed with water, but only a small fraction passed in dispersion. On the contrary, by adding dichloromethane in the same vessel and the brown precipitate was easily and completely dissolved observing two immiscible phases, one aqueous turbid and beige at the top and one organic brown-orange phase at the bottom.

The conclusion that can be drawn from these experiments is that the assembly process allows the preparation of SPIONs-carrying nanosystems (first brown-orange supernatant), but that

unfortunately not the entire amount of hydrophobic magnetic nanoparticle can be included: a significant portion remains as insoluble aggregates (brown precipitate). However, the centrifugation conditions are optimal to separate them from the desired nanosystem's dispersion: the successive solubility analyses carried out on the precipitate indicated that only a small amount of nanosystems (final beige dispersion) was collected with the magnetic aggregates of SPIONs (final brown-orange dispersion in dichloromethane).

In the following centrifugation steps performed on the first supernatant, we successfully separated a brown-orange precipitate from a clear supernatant: in this case, the precipitate was always dispersible in the fresh water provided to wash the sample. This clearly indicates that, unlike the first precipitate, this one is composed of hydrophobic SPIONs included in a stable polymeric structure, which confers them the sought dispersibility in aqueous environment.

This hypothesis was fully confirmed by analyzing the sample with both TEM and NTA techniques, which results are reported in **Figure 4.20**.

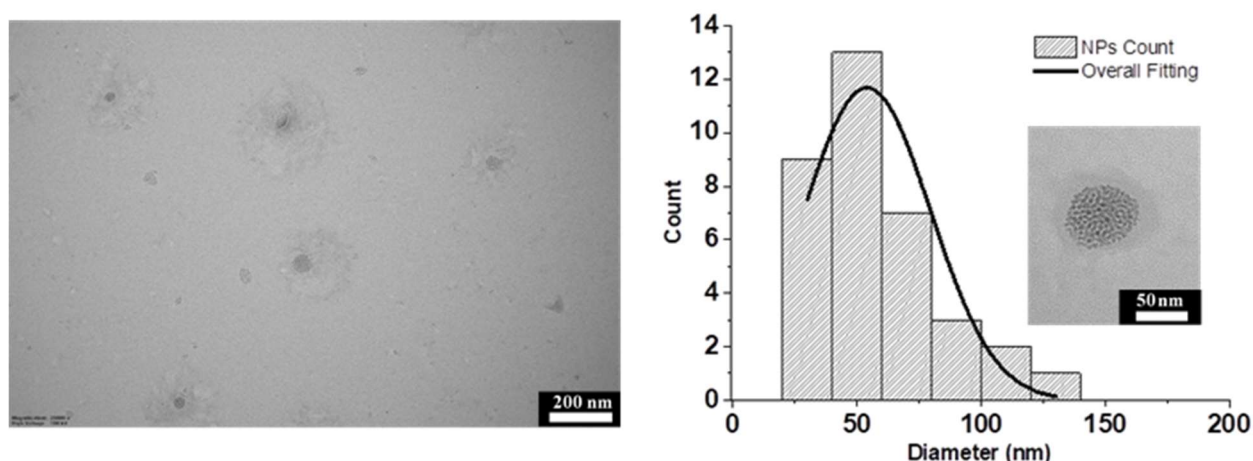


Figure 4.20: (Left) Representative TEM image of SPIONs@PVA13kDa_3 supernatant. (Right) Histogram and Gaussian fitting showing the size distribution of the inner core diameter, obtained from the analysis of the TEM images: $d = 54.0 \pm 21.7$ nm.

The TEM images show indeed some interesting nanosystem presenting SPIONs and a polymeric shadow with likely the desired size.

The difference in polymeric shell dimensions whether the nanosystem is in dispersion or dried on a grid is clearly depicted by the comparison of the TEM images and the NTA results. NTA data are consistent with TEM results displaying NPs diameter of 121 nm with an acceptable dispersion.

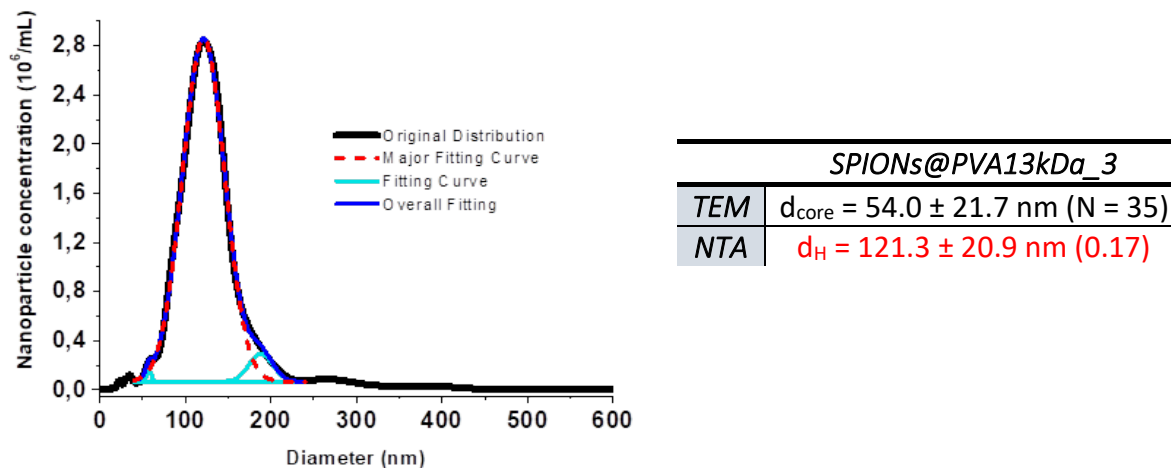


Figure 4.21: (Left) NTA analysis of SPIONs@PVA13kDa_3 sample, showing the original size distribution and data extrapolation curve using Gaussian fitting. (Right) Inner core diameter from TEM and hydrodynamic diameter from NTA with the related variation coefficient.

However, with this synthetic procedure, we obtained a significant amount of not dispersible aggregates.

Nevertheless, the results of the previous set of syntheses indicate that the evaporation and the purification steps used may favor a cleaner sample, avoiding coalescence and leaving undesired aggregates behind: for the next experiments we decided, therefore, to follow this same procedure. Since the encapsulation of SPIONs did not seem to improve with the volume reduction, we took a step back in the assembly procedure, returning to a total dispersion volume, but reducing the final concentration of SPIONs in the dispersion, while maintaining the same initial concentration in the organic phase. If the maximum degree of inclusion for this nanosystem was already reached, we wanted to waste the minimum amount of SPIONs and consequently, a lower amount of aggregates are formed.

Also in this case the different samples obtained after the centrifugation cycles were briefly analyzed. Thus, a brown not dispersible precipitate was separated from a brown-orange supernatant during the first cycle, even if its amount was considerably smaller in mass than in the previous attempts. The addition of dichloromethane could disperse again the precipitate, indicating that it is an aggregation of hydrophobic SPIONs clustered together by the sonication-evaporation process, but not stabilized by PVA.

On the other hand, the purified first supernatant was analyzed with both TEM and NTA to retrieve dimensional information: the results are illustrated in **Figure 4.22** and **Figure 4.23**.

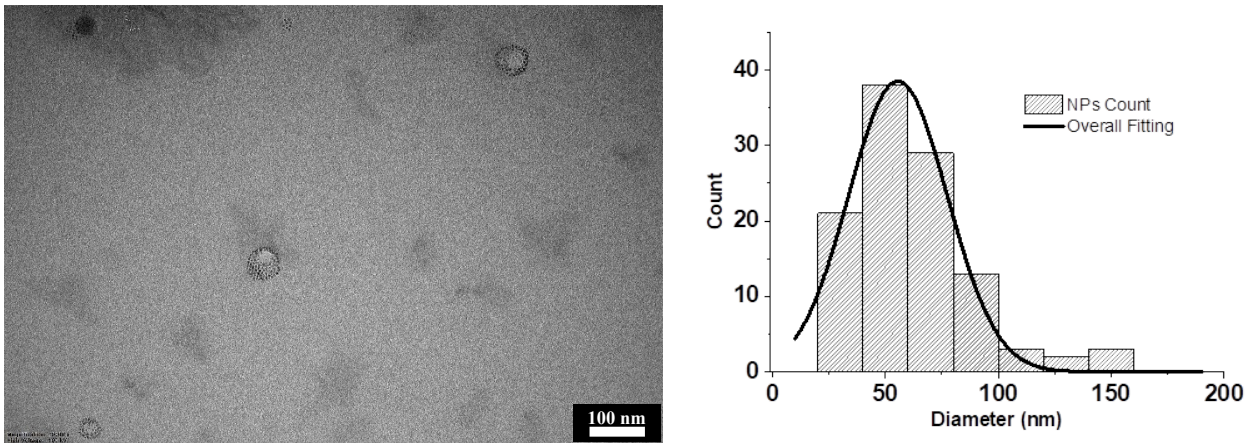


Figure 4.22: (Left) Representative TEM image of SPIONs@PVA13kDa_4 sample. (Right) Histogram and Gaussian fitting showing the size distribution of the inner core diameter, obtained from the analysis of the TEM images: $d = 55.5 \pm 18.6$ nm.

In particular, the TEM analysis of the visible inner portion of the nanosystem displays an inner core of 56 nm with a less disperse distribution of larger structures in respect to the previous measurements, without bigger aggregates. Even if only a part of the sample was retrieved and a certain quantity of SPIONs was discarded, we were able to identify a more well-formed nanosystem within the supernatant dispersion. However, the sample is yet not completely cleaned from the empty polymeric constructs, which are visible as dark grey irregular spots on TEM images. In conclusion, the centrifugation steps may still be improved.

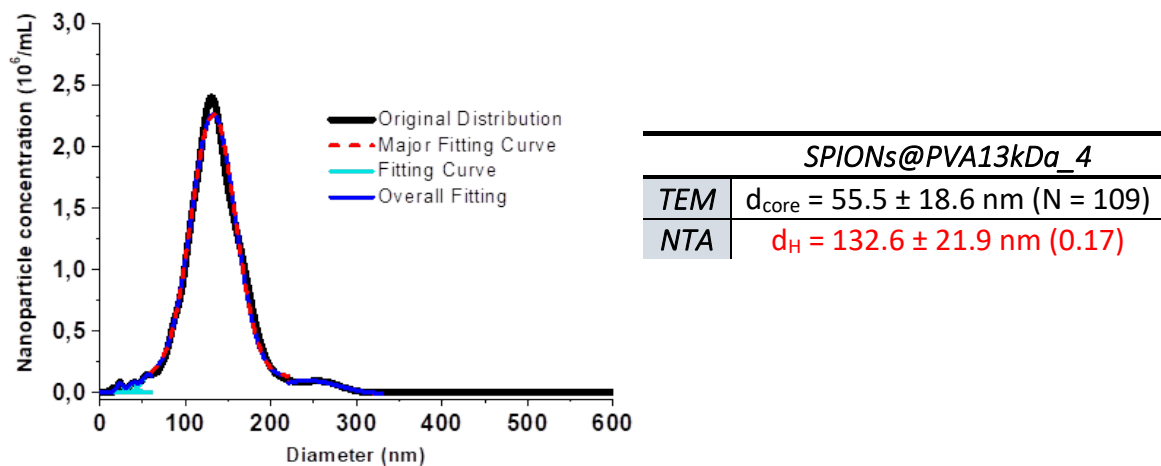


Figure 4.23: (Left) NTA analysis of SPIONs@PVA13kDa_4 sample, showing the original size distribution and data extrapolation curve using Gaussian fitting. (Right) Inner core diameter from TEM and hydrodynamic diameter from NTA with the related variation coefficient.

The absence of aggregates is also verified by the NTA of the sample: in the diagram reported in **Figure 4.23**, only one Gaussian distribution can be identified, centered at 133 nm and with a moderate dispersion. Populations of higher or lower hydrodynamic diameters are negligible. The

reduction of time and temperature for the evaporation step had successfully reduced the coalescence and polymeric aggregates formation phenomena.

We decided to perform the same NTA also on a sample in which we did not include SPIONs: the aim is to understand if this polymeric superstructure would form also in absence of the magnetic content and what are the probable differences between the two types of experiments. We expect that the polymeric micelles without SPIONs should be smaller than the ones containing them^{283,332}. The results are presented in **Figure 4.24**.

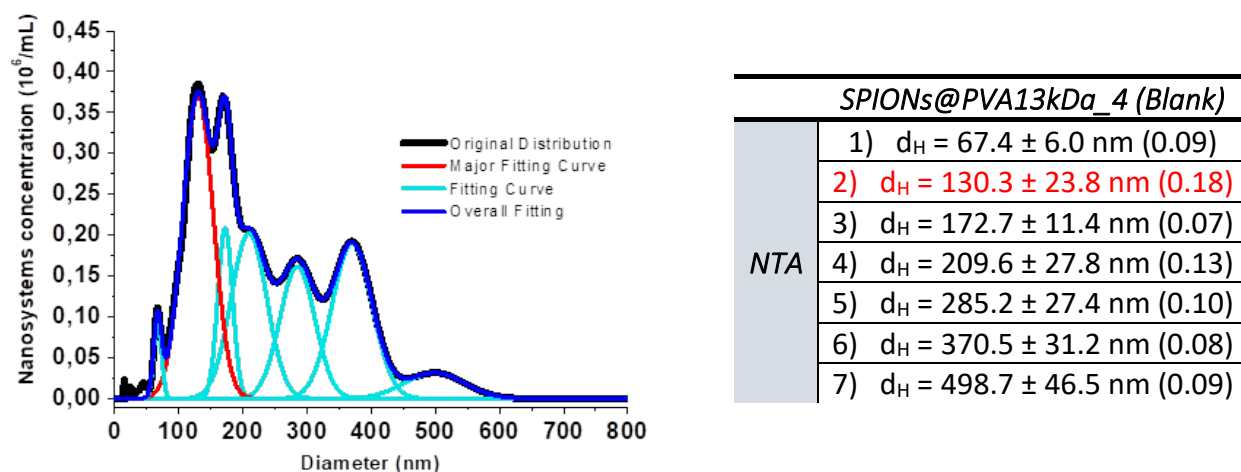


Figure 4.24: (Left) NTA analysis of blank SPIONs@PVA13kDa_4, showing the original size distribution and data extrapolation curves using Gaussian fitting. (Right) Hydrodynamic diameters of all the size populations in the blank sample with the related variation coefficient.

As can be noticed, the sample presents many different broad populations, with the major one centered at 130.3 nm, which is almost identical to the distribution observed preparing the complete nanosystems in the same conditions, with the addition of SPIONs (133 nm). Considering this, we can assume that the procedure adopted for the assembly of the polymeric structure both in presence or in absence of SPIONs leads prevalently to the same type of polymeric NPs in terms of dimension, but in the latter case, it is far from being optimal to produce monodisperse and stable structures.

A remarkable feature that is evident in the TEM images reported in **Figure 4.22**, is that most of the nanosystems present a clear circular portion within the SPIONs cluster that does not include nanoparticles. This is undoubtedly related to the particular superstructure this type of PVA can assume in dispersion and the conditions in which the TEM grid is prepared. Accordingly to the reference literature²⁸⁵, mostly hydrophilic PVA (HLB = 6 - 14) with an average molecular weight in the 16000 - 19000 Da range spontaneously forms a polymersome that stabilizes a W/O/W double-emulsion. Our PVA falls approximately in the same range and is thought to assemble in the same manner, hosting the SPIONs in the intermediate hydrophobic compartment between the hydrophilic

core and shell. Surprisingly, the dry conditions in which the nanosystem are prepared for the TEM analysis, disrupt their structure and allow us to observe this internal compartmentalization: the images show the layers collapse once water is removed and this leaves well exposes both the middle layer – the circular arrangement of SPIONs – and the inner hydrophilic core: the central light grey area.

Overall, this experiment was promising both in terms of nanosystem formation and purification: in particular, we achieve the desired nanosystem size and the internal structure that was previously observed in literature and can be exploited for hosting both hydrophilic and hydrophobic species. Unfortunately, the aspect that has still to be optimized is the encapsulation percentage of SPIONs and the overall yield for the nanosystem assembly: with this type of PVA we had presumably reached the maximum amount of SPIONs that can be stored within the given NPs size, which might be insufficient for the desired clinical applications.

4.3.2 Assembly of the polymeric structure using PVA with $M_w = 57 - 66$ kDa

In parallel with the attempts above illustrated, we employed a different PVA polymer, characterized by a higher average molecular weight, in the range between 57000 and 66000 Da. Considering the HLB parameter and the same diagram we took previously as reference²⁸⁵, this alternative polymer presents an HLB between 5 and 12, thus is lightly more lipophilic than the previous one. Therefore, an enhanced affinity for the hydrophobic SPIONs and a greater encapsulation efficiency are expected.

Since the PVA with molecular weight between 57000 and 66000 Da has an enhanced hydrophobic nature, we expect both a higher number of SPIONs within the inner portion of the structure and a smaller size due to the shrinkage caused by less favored interactions with the solvent.

For the very first experiment, we maintained the ratios and the conditions successfully experimented in the last experiments of SPIO@PVA13kDa assembly. Also, for the assembly and the cleaning steps, the former procedure was followed. Three steps of centrifugation/washing were performed to clean the dispersion from the unassembled polymer, collecting a brown supernatant that was progressively paler after every centrifugation cycle and with an ever-dispersible brown precipitate derived from the first supernatant.

The first series of analyses performed by TEM and NTA aimed at assessing which impact the higher molecular weight PVA has in the nanosystem formation and on the hydrodynamic diameter of the polymeric structure, with respect to the previous PVA used (**Figure 4.25**).

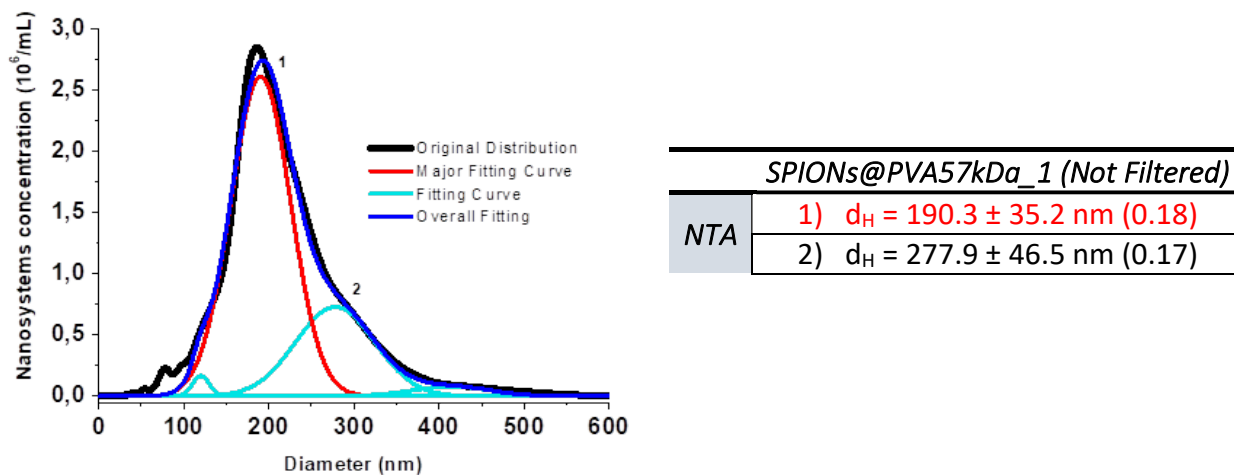


Figure 4.25: (Left) NTA analysis of SPIONs@PVA57kDa_1 sample, showing the original size distribution and data extrapolation curves using Gaussian fitting. (Right) Hydrodynamic diameters of the principal size populations in the two samples with the related variation coefficient.

The NTA shows different and broad overlapping populations of nanosystems with diameters above 400 nm. The major distribution presents a d_H centered at 190 nm, which is a size significantly higher than the average diameter found for the last set of experiments concerning nanosystems prepared with 13 kDa PVA (120 – 130 nm). The larger hydrodynamic diameter could be due to: i) the different types of nanostructure consisting in one hydrophobic core and one hydrophilic shell, ii) the consistently enhanced bulkiness and iii) the mobility that a longer chain has in respect to a shorter one. Another broad population is present with d_H of 280 nm that could represent larger SPIONs@PVA nanosystems or simply polymeric aggregates without magnetic nanoparticles inside. Based on this first analysis, this PVA is a reasonable alternative to low M_w PVA for the construction of our nanosystem, but seems to entail a higher dispersity in respect to the single population of SPIONs@PVA13kDa nanosystems.

To improve the result for the synthesis of this hybrid nanosystem, we tested filtration as a method to eliminate the aggregates and homogenize the size distribution. We used a 0.2 μm PTFE filter to guarantee that the nanosystems we retrieved were below 200 nm, as desired.

A first inspection of the NTA study reported in **Figure 4.26** shows that nanoparticles populations above 200 nm were effectively retained in the filter and eliminated from the final sample, while the distribution at 145 nm is the only one left, even if the dispersity is significant and diameter distribution can be better fitted considering the presence of other, very minor, small populations.

This reduction in size following the filtration could be also due to the polymer's nature: being soft, squashy, and held together by non-covalent forces, when forced through the pores of the filter the structure could be compressed in a smaller shape or some of the outer polymer chains in the shell could be lost due to shear forces.

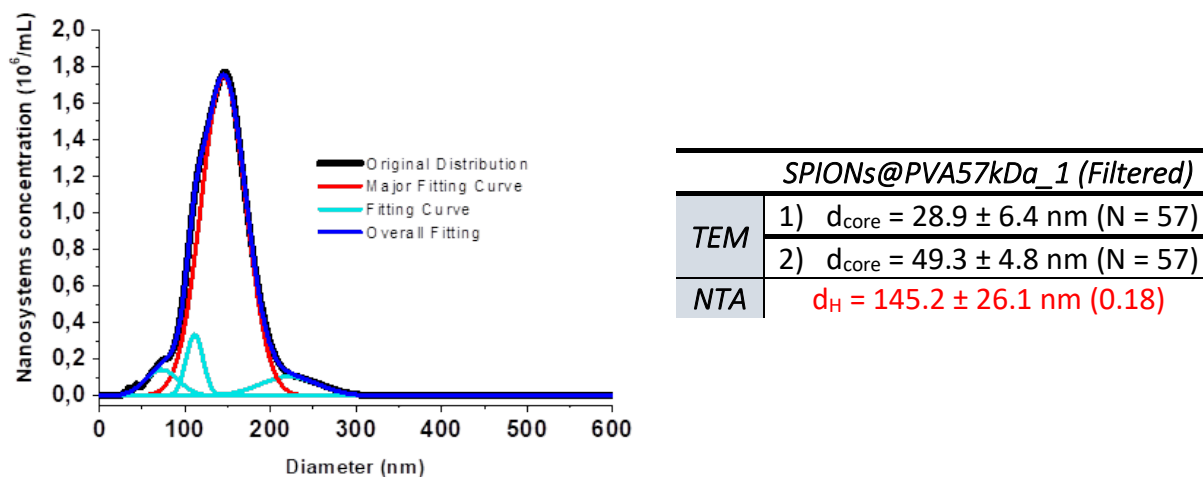


Figure 4.26: (Left) NTA analysis of the filtered SPIONs@PVA57kDa_1 sample, showing the original size distribution and data extrapolation curves using Gaussian fitting. (Right) Inner core diameter from TEM and hydrodynamic diameters of the principal size populations in the filtered sample with the related variation coefficient.

The same sample has been also analyzed with TEM to determine the size of the hydrophobic core containing the magnetic SPIONs and to evaluate the degree of inclusion.

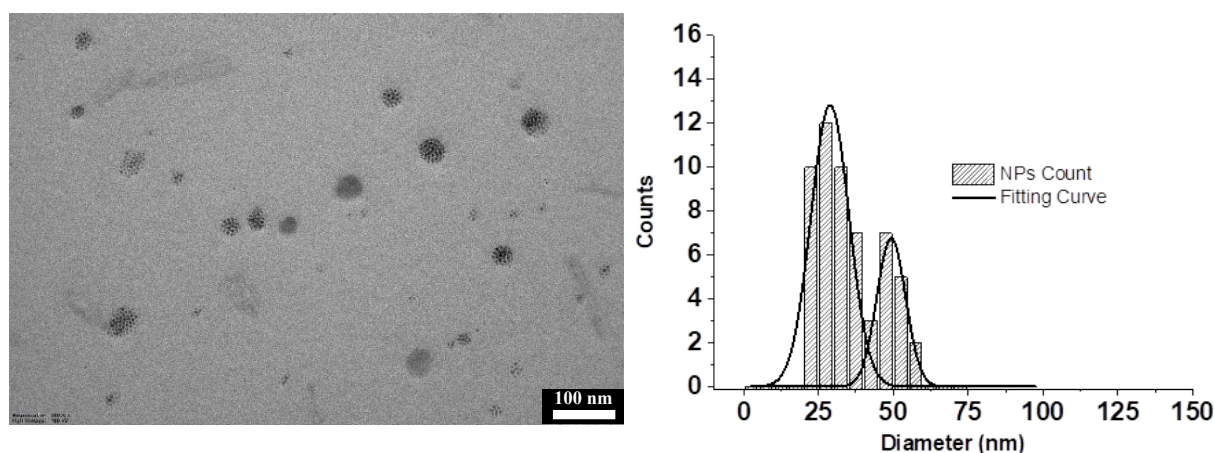


Figure 4.27: (Left) Representative TEM image of the filtered SPIONs@PVA57kDa_1 sample. (Right) Histogram and Gaussian fitting showing the size distributions of different inner core diameters, obtained from the analysis of the TEM images: $d_1 = 28.9 \pm 6.4 \text{ nm}$ and $d_2 = 49.3 \pm 4.8 \text{ nm}$.

TEM images, one representative is reported in **Figure 4.27**, show a distribution of spherical clusters of SPIONs, which are presumably held together by polymer chains – not visible with TEM – forming an O/W nanostructure. Other elements that can be detected in the images are very small

groups of SPIONs, probably not covered by polymer chains (which were not considered in the nanosystem counting, hence in the statistics), and some nanosystems composed only of PVA, without any magnetic nanoparticle inside that are visible as dark grey circular elements. Based on the nanosystems that were detectable from the TEM images, the statistical analysis of the core dimension leads to the identification of two major distributions, both with a diameter that is much smaller than the one found for the previous nanosystem obtained with PVA 13 kDa. This could be due to the increased hydrophobicity of the heavier PVA, that once in water dispersion is not able to establish and sustain the formation of a larger hydrophobic reservoir.

Additionally, a small amount of SPIONs can be seen in the filter after filtration: several nanosystems could be retained in it despite having a diameter lower than the cutoff because of the increasing concentration of polymeric aggregates blocked on the filter's surface. For this reason, it would be better to optimize the centrifugation steps and exploit the filtration just for the final cleaning, only when the sample has been cleaned from the aggregates.

As checked before, we are also interested in understanding the role of superparamagnetic nanoparticles in the polymeric structure formation and stabilization, hence the assembly has been performed also without including SPIONs in the organic phase.

This blank sample was analyzed only with NTA, since the lack of contrasting species like SPIONs makes the TEM analysis unfeasible. The result is illustrated in **Figure 4.28** and overall, the sample presents different populations of nanosystems.

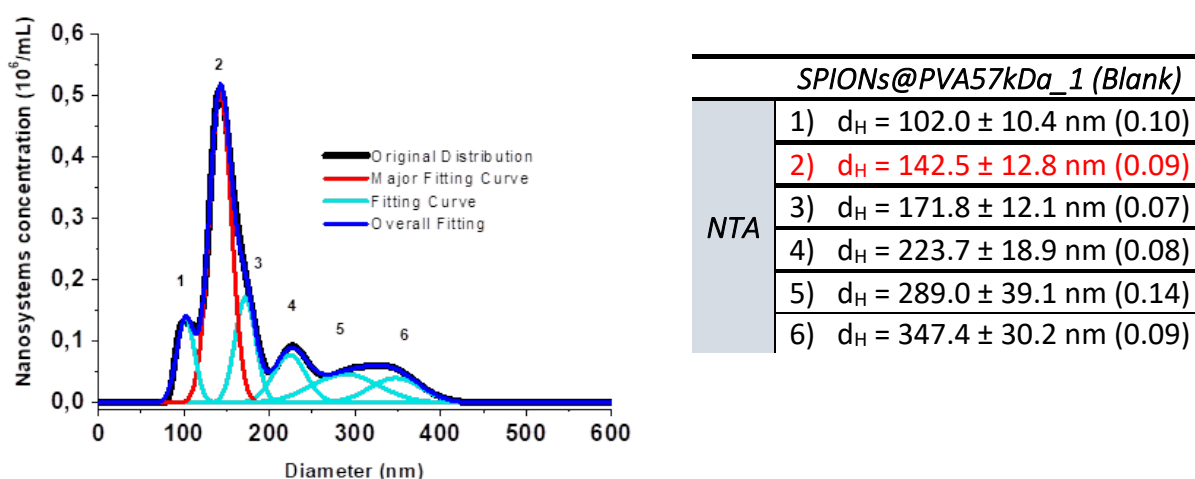


Figure 4.28: (Left) NTA analysis of blank SPIONs@PVA57kDa_1, showing the original size distribution and data extrapolation curves using Gaussian fitting. (Right) Hydrodynamic diameters of all the size populations in the blank sample with the related variation coefficient.

Even if not optimal, unlike the precedent experiment, the dispersity is lower and the different populations can be easily detected, while one of them is prevalent. In fact, the major distribution with d_H centered at 143 nm, which is fairly near to the values we found in filtered SPIONs-

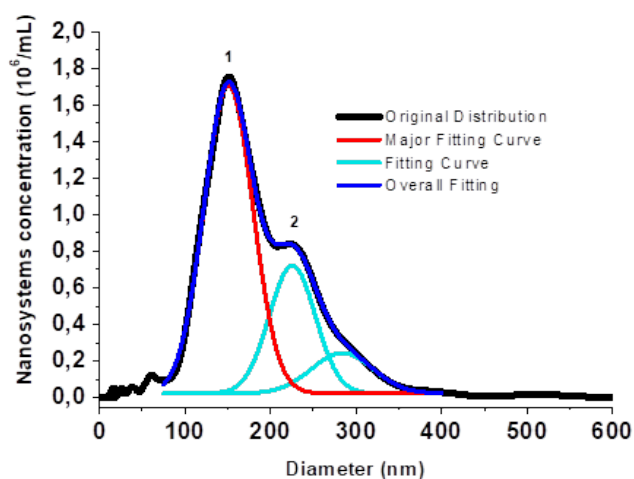
including nanosystem. The slightly lower d_H value could be due to the structure softness and lower rigidity when the iron oxide core is missing. Besides it, many aggregates can be spotted at d_H values above 200 nm, where different broad distributions appear with agglomerates up to 350 nm in diameter. Considering this and the nanosystem distributions found in the unfiltered sample, it is even more clear that the filtration operated after the washing steps is a good method to eliminate the blank polymeric aggregates in all the samples.

The conclusion that can be drawn from this experiment is that the single emulsion O/W which constitutes the polymeric structure with 57-66 kDa PVA can form nanostructures below 200 nm spontaneously. However, the SPIONs inclusion can enhance the structural integrity and its stability, favoring the preparation of structures characterized by a homogeneous d_H size and with a low aggregates content, as they formed for the W/O/W double emulsion using 13 kDa PVA.

One of the problems that arose during the assembly procedure in the previous experiments was the difficult dissolution of the heavier PVA in water, which is even more complicated than in the PVA 13 kDa case because of its increased hydrophobic nature. Consequently, part of the polymer was not available for synthesis during the emulsion formation, with the consequent alteration of the experimental conditions. Not only whether SPIONs are included or not (blank sample), but also the ratio between SPIONs and PVA quantities and concentration is fundamental for the preparation of stable nanosystems with a precise dimension³³³: the last experiment described is clearly the result of a misbalanced interaction between the two components.

To try to overcome this issue, the PVA dissolution was helped by sonication and heating the dispersion until the grains of polymer disappeared. In this way, a higher amount of polymer was effectively brought in solution, being therefore available for the nanosystems formation hopefully with improved inclusion of SPIONs and a better yield of polymeric NPs. However, despite many cycles of sonication, the increased temperature, and an apparent complete and stable dissolution, the polymer re-precipitates as a gel soon after these stimuli ceased. To make sure the nominal concentration within the two phases before the emulsion is guaranteed at the end, the polymeric gel had to be physically transferred to the final vessel where the presence of dichloromethane completed the dissolution.

The results of this improved procedure have been controlled primarily with NTA, which provided a size distribution of the hydrodynamic diameter characterized prevalently by a broad population with d_H centered at 151 nm (**Figure 4.29**), which is smaller in respect to the previous not-filtered sample. Even if some other populations of nanoparticles are detected at higher values, they are clearly distinguishable and have a minor impact on the overall distribution.



<i>SPIONs@PVA57kDa_2 (Not Filtered)</i>	
NTA	1) $d_H = 150.8 \pm 24.2 \text{ nm} (0.16)$
	2) $d_H = 225.6 \pm 23.0 \text{ nm} (0.10)$

Figure 4.29: (Left) NTA analysis of the not filtered SPIONs@PVA57kDa_2 sample, showing the original size distribution and data extrapolation curves using Gaussian fitting. (Right) Hydrodynamic diameters of the principal size populations in the unfiltered sample with the related variation coefficient.

However, considering these small aggregates and bigger nanosystems detected, also in this case we relied on 0.22 μm PTFE filters to narrow the dispersion and select only the major population below 200 nm. The filtrated sample was analyzed by both TEM and NTA in **Figure 4.30** and **Figure 4.31** respectively.

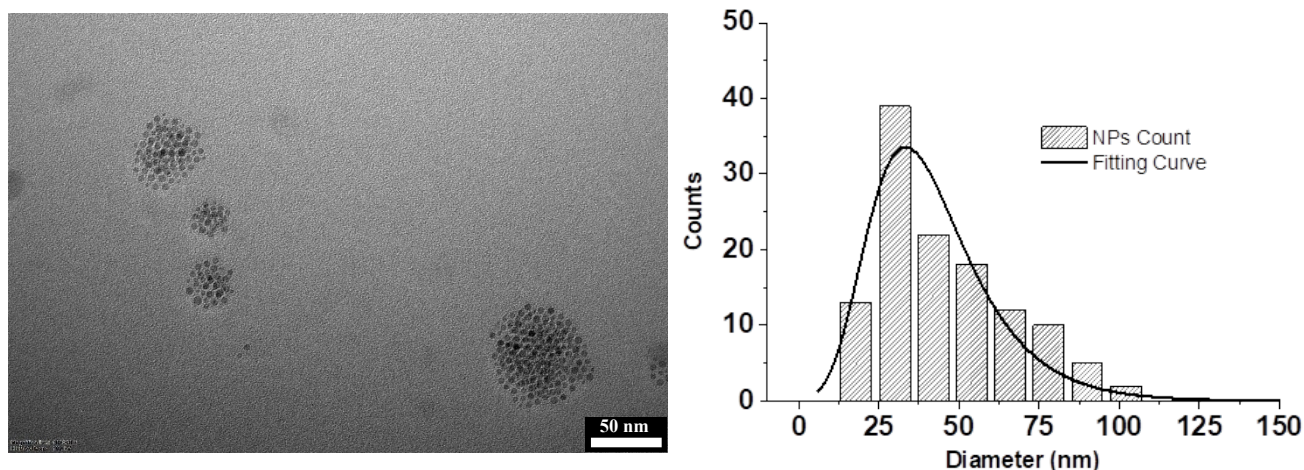


Figure 4.30: (Left) Representative TEM image of the filtered SPIONs@PVA57kDa_2 sample. (Right) Histogram and Extreme fitting showing the broad size distribution of the inner core diameter, obtained from the analysis of the TEM images: $d = 33.3 \pm 19.4 \text{ nm}$.

TEM images as in **Figure 4.30** display nanosystems with a higher amount of SPIONs included in the polymer and a more defined spherical shape but rather dispersed in the diameter of the core size, as it is clearer from the histogram on the right of **Figure 4.30**. The histogram was fitted with an Extreme function instead of a Gaussian, to better consider the distribution tail of bigger diameters. What is evident from TEM images is that in this sample a lower number of small clusters or single

SPIONs are outside the polymeric nanosystems, as they were seen in the previous experiments. This is an encouraging step forward that proves the importance of using the correct ratio of polymer in respect to the magnetic NPs to form a stable dispersion and to avoid the loss of SPIONs, which would precipitate and be wasted if not included in the PVA structure.

Evaluating the hydrodynamic diameter in NTA data reported in **Figure 4.31**, the species with d_H above 300 nm have been successfully removed, allowing to retrieve only the two smaller populations that now are centered at 121 nm and 167 nm. We think that their sudden reduction in size in respect to the not filtered sample (d_H at 151 nm and 226 nm), may be due to the peculiar plasticity and adaptability of the soft polymeric shell around the magnetic core.

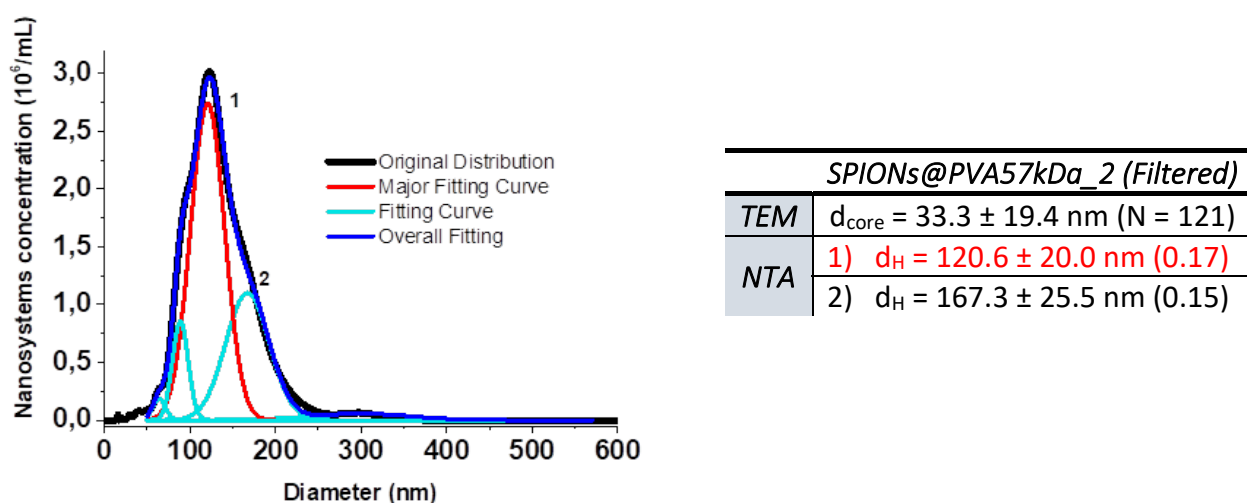


Figure 4.31: (Left) NTA analysis of the not filtered SPIONs@PVA57kDa_2 sample, showing the original size distribution and data extrapolation curves using Gaussian fitting. (Right) Inner core diameter from TEM and hydrodynamic diameters of the principal size populations in the unfiltered sample with the related variation coefficient.

Considering the better results obtained with PVA at higher molecular weight in respect to the 13 kDa PVA and the final purpose of this preparation, we decided to assemble the next set of nanosystems in phosphate buffer solution (PBS), in order to simulate the biological environment. All the other aspects and conditions in the previous procedure were maintained.

This procedure and the following analyses may provide a first – even if limited – indication of the behavior of these nanosystems in terms of size and structure stability once inside buffered solutions. The TEM images in **Figure 4.32** are characterized by the presence of well-defined nanosystems in which the inner magnetic core is clearly visible inside a solvation corona that still is not completely removed from the grid: this feature allows to estimate preliminarily the value of pseudo-hydrodynamic diameter to be compared with the one analyzed with NTA.

In order to have indications of the overall dimension of the polymeric shell, we proceeded to stain the whole grid with uranyl acetate.

However, this treatment is sample-destructive and can only provide a qualitative indication of the polymeric wrapping extension and shape around the inorganic core, along with the information regarding the empty nanosystems.

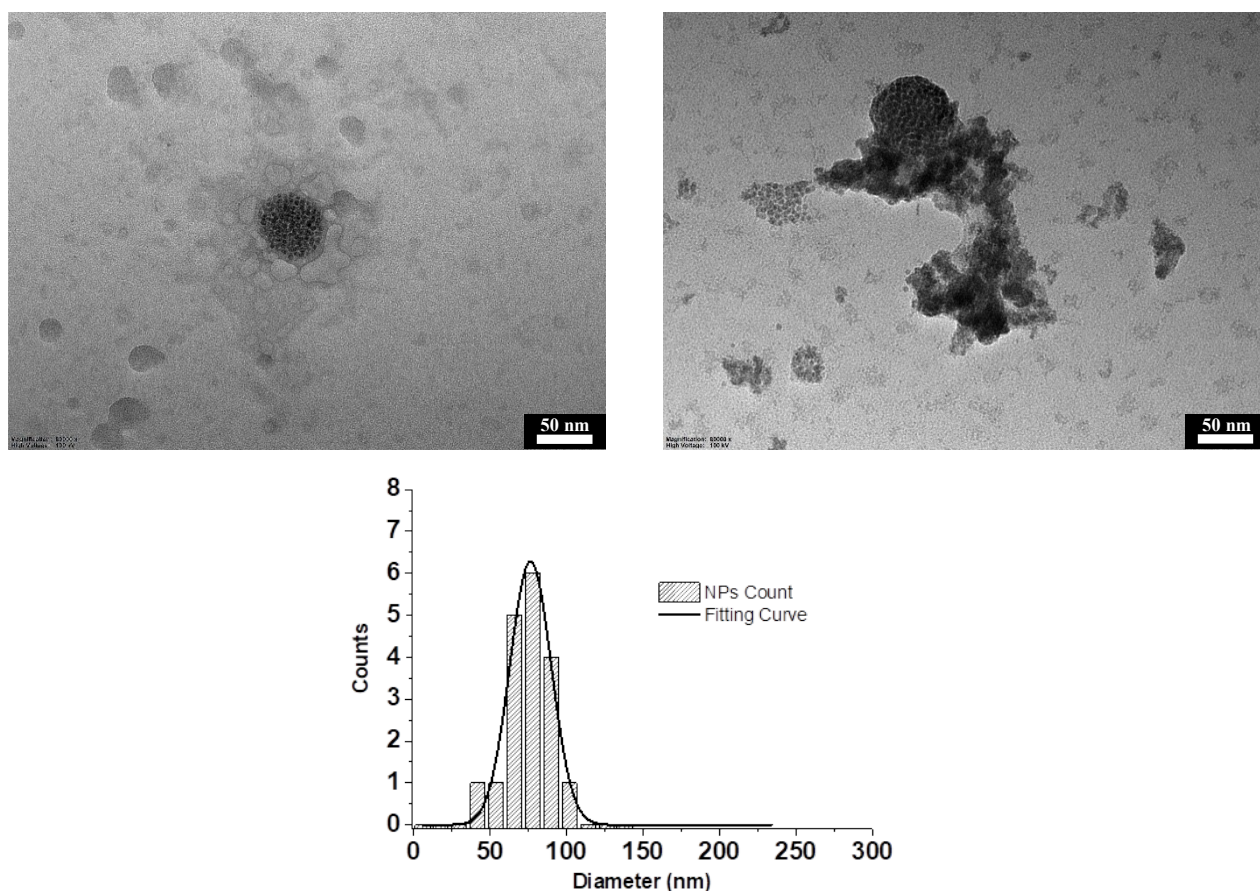


Figure 4.32: (Top) Representative TEM images of SPIONs@PVA57kDa_3 sample. (Bottom) Histogram and Gaussian fitting showing the size distribution of the inner core diameter, obtained from the analysis of the TEM images: $d = 76.5 \pm 13.5$ nm.

The stained TEM images confirm that the nanosystems lose their shape because of the dry conditions and spread onto the grid, sometimes crystallizing around the inorganic core. Moreover, the staining shows the amount of unassembled polymers not removed during the purification steps.

The differences between the core diameter estimated from the above histogram plot and the size of the complete polymeric NP are made available by the NTA reported in **Figure 4.33**. These data display a single very broad distribution centered at 173 nm, by comparison with TEM data in **Figure 4.32**, the inorganic core represents only a small portion in the overall nanosystem.

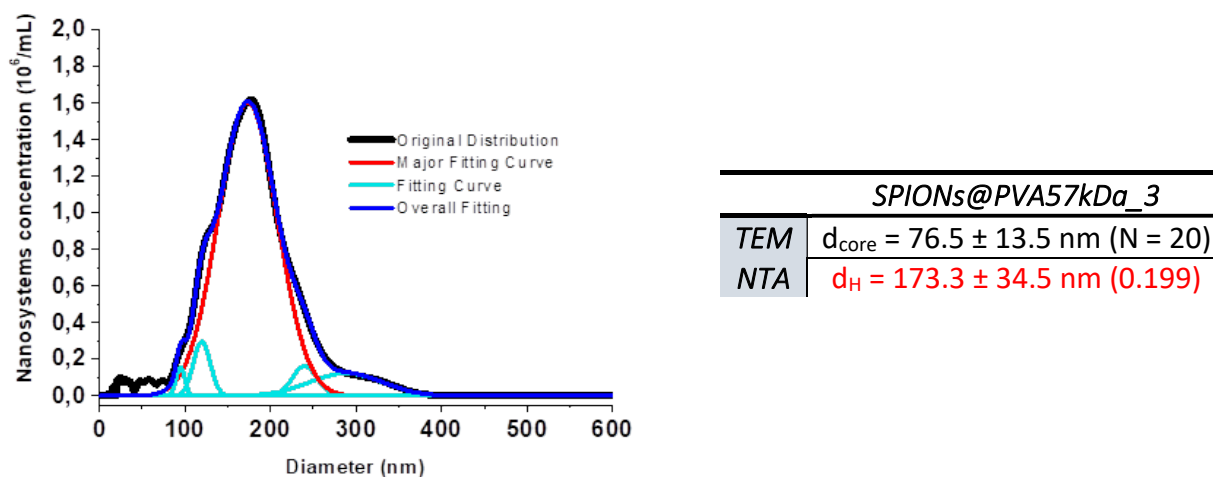


Figure 4.33: (Left) NTA analysis of the SPIONs@PVA57kDa_3 sample, showing the original size distribution and data extrapolation curves using Gaussian fitting. (Right) Inner core diameter from TEM and hydrodynamic diameter of the principal size population with the related variation coefficient.

This set of experiments suggested that for the preparation of these nanosystems using PBS instead of water could be a valid alternative allowing to achieve structures with a larger inner core and overall dimensions, therefore capable of hosting more SPIONs.

However, as determined by the TEM analysis and evidenced by the staining, the amount of free polymer remains very relevant, causing aggregation and a substantial change in the properties of the dispersive medium, even if the centrifugation steps performed are identical to the ones used for the sample prepared in water. Therefore, a compromise should be made between the encapsulation degree and the sample's purity.

For these reasons, it seems reasonable to performed firstly the preparation of the polymeric NPs in the presence of SPIONs in water, remove the supernatant enriched by the free polymer, retrieving only the complete nanosystem which can be re-dispersed in PBS at need.

In conclusion, the experiments with this type of PVA seemed to lead to the same critical points we encountered with the light PVA. Despite the formation of the polymeric structure is evident, the elimination of the unassembled polymer is critical to obtain clean nanosystems. These nanosystems seem a good option to host hydrophobic species, but are not yet optimal to maximize the inclusion of SPIONs and drug molecules, being the hydrophobic reservoir even smaller than the one obtained using PVA of 13 kDa.

4.3.3 Assembly of the polymeric structure using Pluronic F127 and PVA with $M_w = 13$ kDa

The results of the experiments performed with only one type of polymer were promising and led effectively to the assembly of nanosystems with the desired target size and SPIONs hosted in the core, but not yet optimal in terms of synthetic efficiency and purity of the sample.

For these reasons, we decided to keep the PVA 13 kDa and try to stabilize the nanosystem development with the addition of a second biocompatible polymer to induce the formation of an improved structure and to optimize the inclusion of SPIONs. In literature, amphiphilic block copolymers have been extensively used, exploiting their peculiar ability to self-assemble in polymersomes or micelles characterized by a hydrophobic internal region and a hydrophilic shell. Pluronic F127 (or Poloxamer 407) is already employed in the biomedical field³³⁴: it is a tri-block copolymer made of two external polyethylene oxide units and one polypropylene oxide unit in the middle (polyethylene oxide-*b*-polypropylene oxide-*b*-polyethylene oxide, PEO-PPO-PEO). This copolymer has an HLB of 18-23 and is cheap, easily modifiable, biocompatible, and already approved by FDA.

Depending on the concentration, Pluronic F127 possesses a lower critical solution temperature (LCST) between 25 and 37 °C³³⁵, which is suitable for drug delivery purposes. In addition, it has the peculiar ability to self-assemble reversibly in micelle as a result of PPO dehydration above a certain temperature (indicated by the term “critical micelle temperature”, CMT or Krafft temperature), which causes the phase segregation in a core-shell structure once the critical micelle concentration (CMC) has been reached³³⁶.

The thermoreversibility of the structure formation is certainly a useful characteristic for triggered drug delivery, but could be also a disadvantage in terms of stability, since Pluronic gels dissolve rapidly in aqueous solution to return in solvated unimers once the dispersion is cooled and the initial conditions are restored³³³ (**Figure 4.34**).

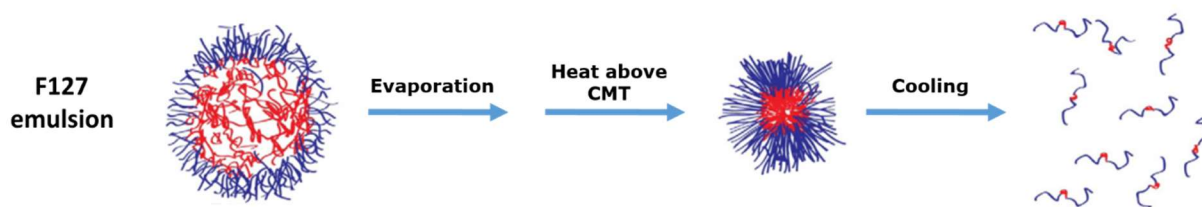


Figure 4.34: Representation of the thermo-reversible passage between micelle formation and complete dissolution of Pluronic F127 in water. Adapted from reference ³³³. Copyright © 2013 Elsevier B.V.

For this reason, it is necessary to stabilize and held together the micelle structure for example modifying the original polymer³³⁷ or mixing it with other species to induce chemical (covalent) or physical (non-covalent) cross-linking³³⁸. In our case, the objective is to stabilize the external

hydrophilic shell of Pluronic F127 with PVA, through non-covalent interactions on the nanosystem's surface.

The synthesis we took as an example for a preliminary experiment was reported by Huang and colleagues³³⁹. They prepared thermally sensitive nanocarriers using ultrasonication, inducing the self-assembly of Pluronic and the successive external H-bonding with PVA, studying their behavior induced by changing temperature and weight ratios. We implemented the key parts of this procedure in our own approach (**Scheme 4.5**) using the same Pluronic, the 13 kDa PVA and our magnetic nanoparticles.



Scheme 4.5: Scheme representing the reagents and the general synthetic approach for the formation of SPIONs@F127/PVA nanosystems.

Unfortunately, following the same procedure with our reagents did not give the desired nanosystem. TEM and NTA studies display some nanosystems encapsulating SPIONs, but the result of microscopy showed that they were very scarce and the NTA indicated they were too much dispersed, with at least four overlapped d_H populations with the principal one centered at 169 nm. Moreover, the reference experiment performed on dispersion in the absence of SPIONs, resulted in void nanosystems that were not stable, difficult to detect by NTA, and prone to form other structures or aggregates of many different sizes.

In fact, in analogy to the case of PVA only, the presence of magnetic nanoparticles is essential to guarantee a stable nanosystem in presence of another polymer such as Pluronic F127 that spontaneously forms a complex structure upon a temperature increase, but is not able to maintain it once the dispersion returns to the original conditions.

For this reason, we have increased the overall amount of SPIONs used in the nanosystem preparation, maintaining the same concentration in the organic solvent, so increasing the volume of the organic phase to ensure complete solubilization.

The aim is to raise the number of hydrophobic magnetic nanoparticles stored in the hydrophobic portion of Pluronic F127 chains, thus providing a denser and rigid internal scaffolding to confer stability to the whole polymeric structure.

The result of this set of experiments was analyzed by TEM and NTA and the data are illustrated in **Figure 4.35** and **Figure 4.36**.

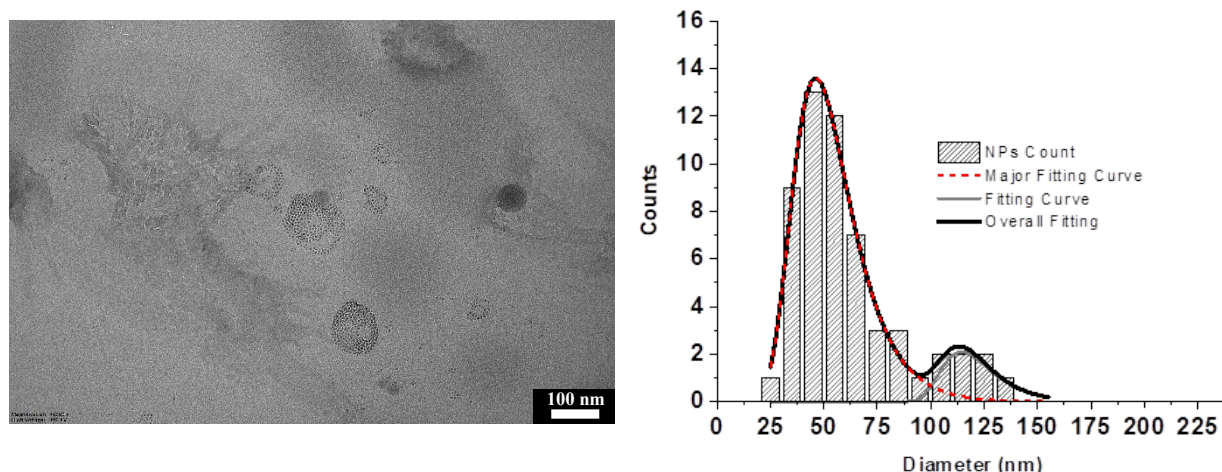


Figure 4.35: (Left) Representative TEM image of SPIONs@F127/PVA13kDa_1 sample. (Right) Histogram and Extreme fitting showing the size distributions of different inner core diameters, obtained from the analysis of the TEM images: $d_1 = 46.2 \pm 17.3$ nm and $d_2 = 114.4 \pm 15.2$ nm.

Interestingly, the new nanosystems' structure is very similar to that of the nanosystem obtained using only 13 kDa PVA. This made us suspect that the Pluronic did not form the micelles correctly or that the PVA could not provide stabilization because the power provided with sonication or the mixing of the phases were not sufficient. Therefore, only the result of SPIONs' clusterization or inclusion in a PVA superstructure are likely obtained. The NTA values of hydrodynamic diameter related to the major populations of the previous sample of SPIONs@PVA13kDa_4 is 133 nm and the comparison with the present sample that is 117 nm corroborates the hypothesis that the two are identical within the experimental errors.

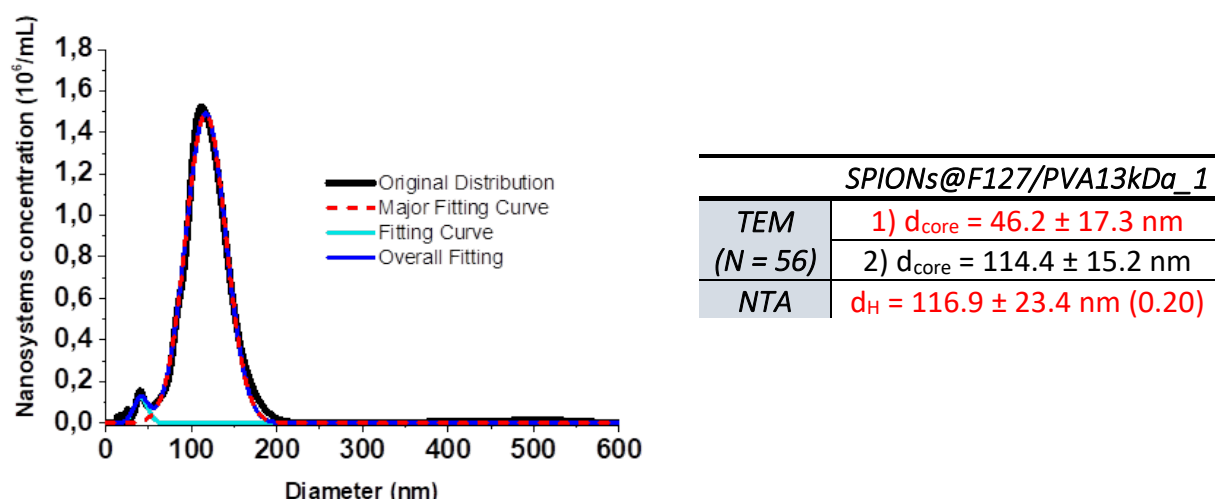


Figure 4.36: (Left) NTA analysis of the SPIONs@F127/PVA13kDa_1 sample, showing the original size distribution and data extrapolation curves using Gaussian fitting. (Right) Inner core diameter from TEM and hydrodynamic diameters of the principal size population with the related variation coefficient.

Overall, the sample still contained a significant amount of polymeric aggregates or unassembled chains that remained in dispersion: this could be due to inefficient purification steps, but we think primarily to failed emulsification and micelle formation. Therefore, the next objective was to involve correctly the Pluronic part of the polymeric mixture as the primary amphiphilic structural element.

What we tried at first was to add and sonicate separately the two polymers that constituted the nanosystem, to form the complex structure by successive steps. Therefore, we first put in contact the organic phase containing SPIONs with the aqueous phase in which Pluronic F127 was completely dissolved and emulsified with 1-minute sonication. As soon as the first cycle ended, we added the aqueous dispersion of PVA to reduce the risk of breaking the emulsion and dissolving the newly-formed micelles because of Pluronic redispersion in water. Then we sonicated again in the same conditions, mixing the previous emulsion with the aqueous phase containing the PVA.

Since the first attempt with this procedure adjustment, we immediately noticed the formation of a supernatant and predominant phase which kept its dark brown color and turbidity – hence its emulsion state – for longer times with respect to the previous experiments. Moreover, the amount of dark precipitate after the second sonication is visibly reduced.

In addition, we also decided to evaporate the organic solvent at 40 °C instead of at room temperature, as reported in literature. This choice was driven by the peculiar behavior of the polymeric coating we saw in the analogous set of experiments with PVA 57 kDa and, in our assumption, the increased temperature of the solvent evaporation step had the double function of

speeding up the evaporation process and keeping the polymeric mixture tight and intertwined. All these variations allowed achieving and maintaining a stable emulsion until the purification steps. During one of these steps, as a further proof of the precipitate's nature after the first centrifugation, we have tested its re-dispersibility by solvating it again with water after the supernatant removal. We observed that the precipitate was completely dispersible in water, giving a brown dispersion. The addition of the same volume of dichloromethane to this aqueous dispersion extracted only a small part of the magnetic content, resulting in a light brown-yellow organic phase: this let us conclude that the major part of the precipitate is composed by SPIONs successfully encapsulated in polymeric structures that confer them water solubility, with probably only some nanoparticles that are not perfectly coated by the polymers and are therefore extracted by the organic solvent. Moreover, we have tested with the same procedure also the supernatant of this first centrifugation, observing that the organic phase did not contain any uncoated SPION.

A sample of the precipitate was analyzed with TEM and NTA to verify SPIONs inclusion and to measure the diameter of the inorganic inner core and the d_H of the polymeric shell. The results are displayed in **Figure 4.37** and **Figure 4.38**.

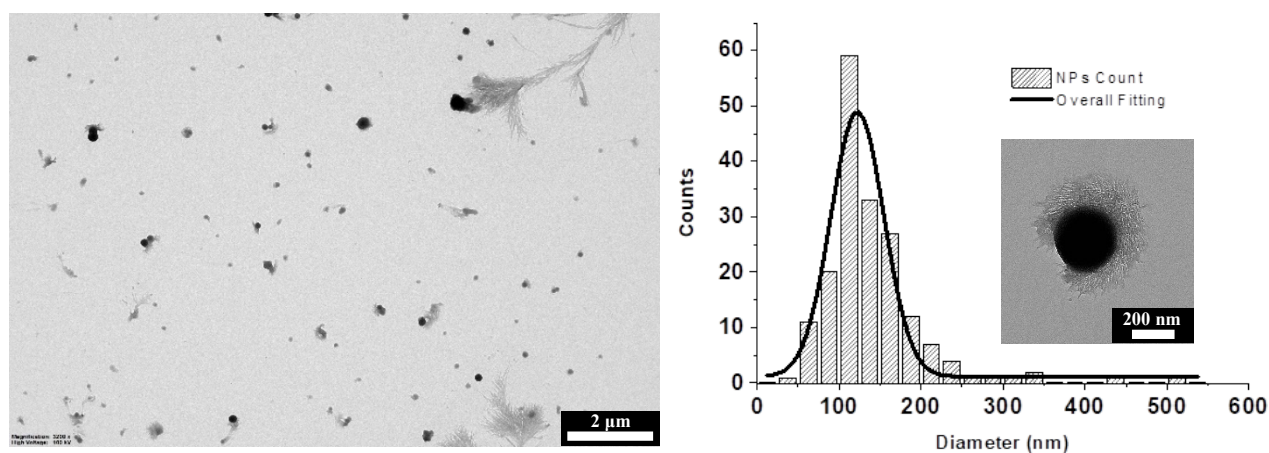


Figure 4.37: (Left) Representative TEM image of SPIONs@F127/PVA13kDa_2 sample. (Right) Histogram and Gaussian fitting showing the size distribution of the inner core, with and insert showing one of the rounded nanosystems prepared, in which the crystalline polymeric corona can be seen fully: $d_1 = 122.3 \pm 32.3$ nm.

The TEM images show an even distribution of nanosystems in which both the inorganic core and the polymeric shell spread around it can be clearly distinguished. Furthermore, for some nanosystems, a peculiar corona with a crystalline appearance is detected (insert in **Figure 4.37**): we believe that this is a visualization of the external PVA, whose chains tend to pack together and form an ordered and hard coating with characteristic shapes. In terms of dispersion, with these experiments we observe a better outcome than the previous ones: even if the standard deviation is

higher, based on the statistical analysis of the nanosystems' core, the sample is characterized by a single population centered at 122 nm, much larger than those detected in SPIO@F127/PVA13kDa_1.

The average hydrodynamic diameter is centered at 250 nm, as we observed with the NTA, but the technique reveals that the dispersion is higher than the expectations, since the overall fitting can be divided into four main distributions.

Combining TEM and NTA data, the average shell thickness can be estimated of about 65 nm. With such an increase in the shell thickness, the SPIONs are surely better protected, but on the other hand, there could be less room for the encapsulation of the magnetic content and more problems regarding the crossing of biological membranes.

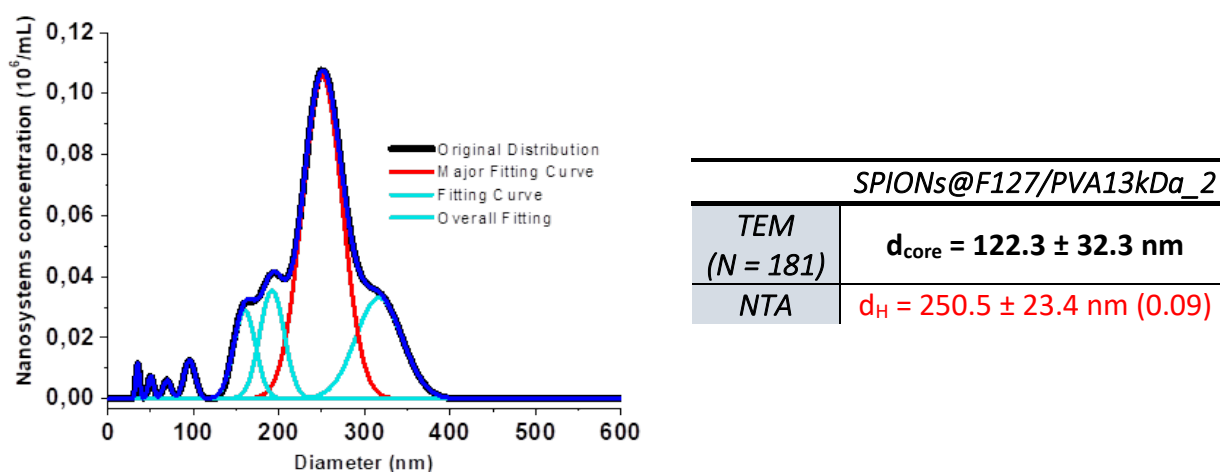


Figure 4.38: (Left) NTA analysis of the SPIONs@F127/PVA13kDa_2 sample, showing the original size distribution and data extrapolation curves using Gaussian fitting. (Right) Inner core diameter from TEM and hydrodynamic diameter of the principal size population with the related variation coefficient.

Even if nanosystems were effectively produced, the SPIONs inclusion and the stability of the emulsion can still be improved, since after the organic solvent evaporation the emulsion seemed to break and a consistent insoluble magnetic precipitate remained. The hypothesis is that one cycle of sonication for each polymeric species added is not sufficient to ensure a strong interaction between the two phases for the entire volume of the dispersion. The consequence is that some SPIONs remained in the organic layer during the emulsification and precipitate once it evaporates, causing a waste of valuable precursors.

Therefore, in the next set of experiments, we aimed to improve the emulsification step by adding more cycles of sonication for each polymer, in order to assure a final stable dispersion in which the interaction between the organic solvent and the hydrophobic part of the micelle and the SPIONs encapsulation within it are maximized. Further improvements that were implemented in the

procedure for this objective were the heating of the polymeric dispersion before the first sonication to induce an early micellization and a vigorous shaking and heating between sonication cycles. The effects of all these adjustments were immediately visible at the end of sonication: the dispersions resulted more homogeneous and of grey color, with less dark precipitate in respect to the previous experiments. Moreover, the dispersion was stable for a longer period, even after the organic solvent evaporation. This is clearly an indication of a more stable emulsion and we assume that a greater number of nanosystems was correctly formed and a higher degree of SPIONs inclusion was reached: furthermore, being the nanosystem more stable and properly intertwined, the magnetic nanoparticles inside are also more protected towards air and the aqueous environment and for this reason, they maintain the greyish color.

Indeed, the change of color from grey to brown is an indication of the oxidation of magnetite to maghemite. In particular, this was observed during the long exposure to air needed for the evaporation step and in samples that were not properly emulsified. Even though the improvement was already promising with the last experiments, we intended to reduce the oxidation even more efficiently by performing the organic solvent evaporation under argon atmosphere. As expected, this led to maintaining the original grey color.

The sample resulting from all these procedure improvements was firstly characterized with TEM: a representing image and the histogram of the inner hydrophobic core are presented in **Figure 4.39**.

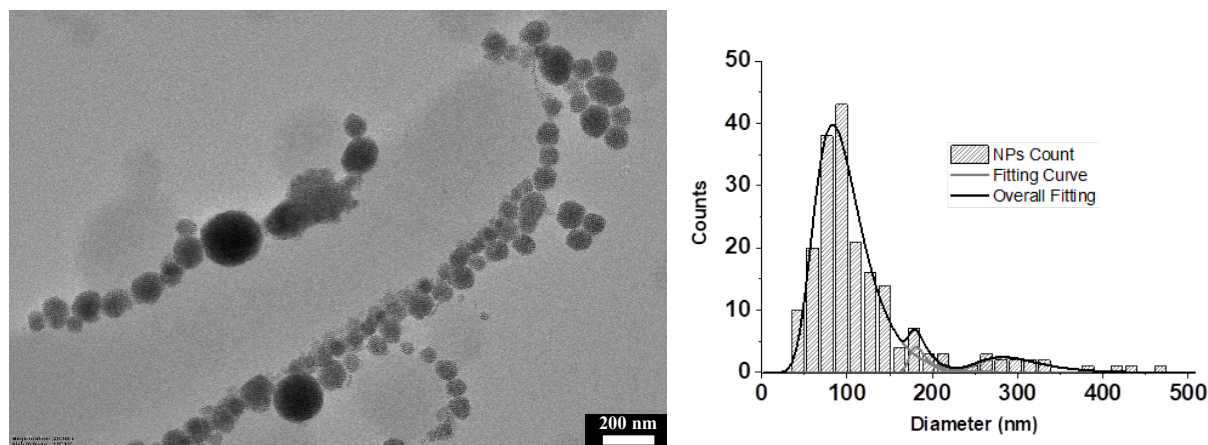


Figure 4.39: (Left) Representative TEM image of the SPIONs@F127/PVA13kDa_3 sample. (Right) Histogram and Extreme fitting showing the size distributions of different inner core diameters, obtained from the analysis of the TEM images: $d_1 = 83.2 \pm 34.2$ nm, $d_2 = 181.0 \pm 12.1$ nm and $d_3 = 283.3 \pm 44.0$ nm.

The TEM images and the core size fitting (performed with an Extreme fitting function), display a distribution of rounded nanosystems of three different components, with the major being the one centered at 83 nm. What is encouraging is the almost complete absence of unassembled polymer chains, empty polymeric nanosystems, and solitary magnetic nanoparticles in the images collected:

this proves the effectiveness of the improved procedure in forming stable nanosystems and reducing the amount of wasted or released SPIONs. The measurement of the hydrodynamic diameter for this particular sample was performed with either NTA and DLS instruments, in order to compare the outcome. The results are shown in **Figure 4.40** and **Figure 4.41**.

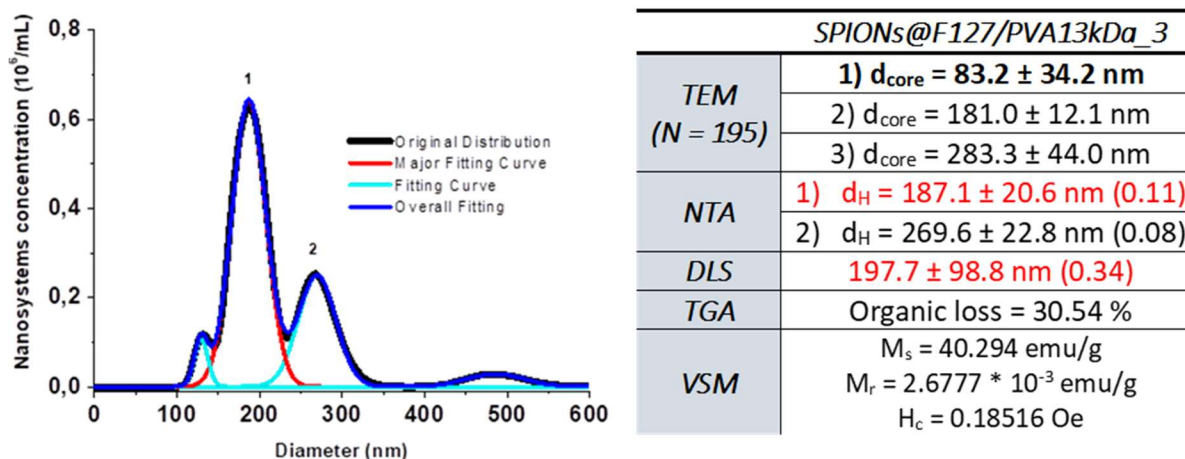


Figure 4.40: (Left) NTA analysis of the SPIONs@F127/PVA13kDa_3 sample, showing the original size distribution and data extrapolation curves using Gaussian fitting. (Right) Inner core diameter from TEM and hydrodynamic diameters of the principal size populations obtained with NTA and DLS.

Upon a quick comparison of NTA with DLS data, the peculiar differences between the two techniques can be appreciated: while with NTA the different populations are distinguished and can be fitted separately, the DLS analysis groups all the different nanoparticle populations, giving a single broad distribution as output that gives a larger d_H and a bigger standard deviation. Nonetheless, the two results are comparable, both indicating a major population of nanosystems with a d_H below 200 nm and larger than the average core dimension retrieved from TEM.

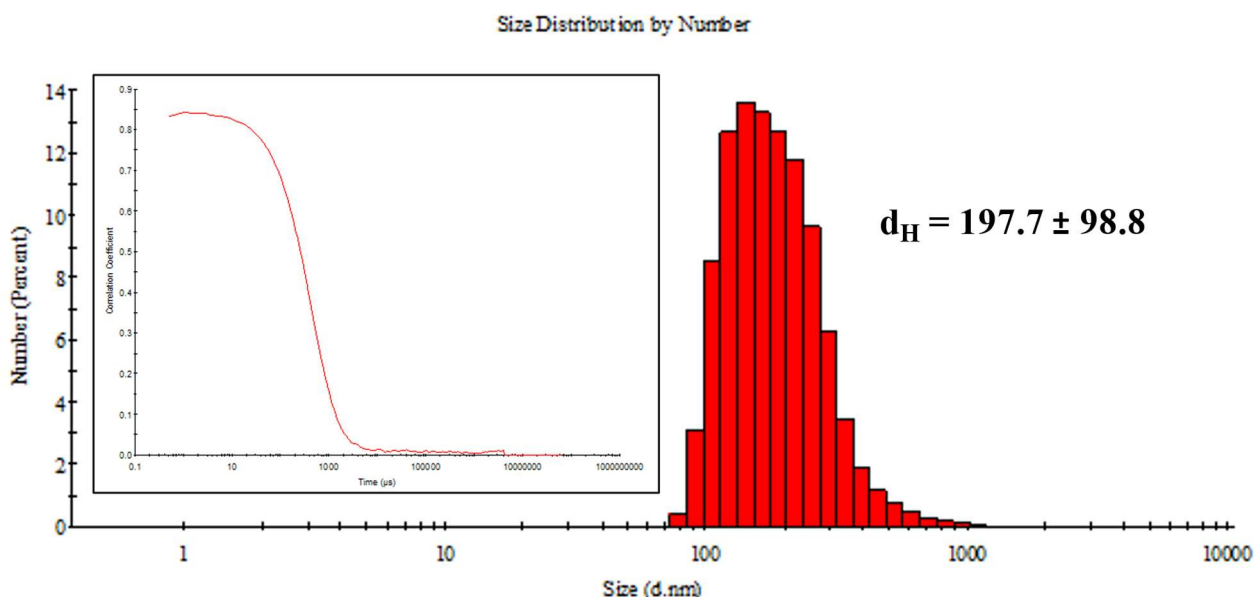


Figure 4.41: DLS analysis of the SPIONs@F127/PVA13kDa_3 sample with the size distribution by number of nanoparticles extrapolated from it and (Insert) the related correlogram.

Therefore, even if some aggregates are still present in the sample and it is still not possible to produce only one population, the nanosystem prepared with the mixture of PVA 13 kDa and Pluronic F127 meets the desired core and shell dimensions.

A further technique that we employed for the characterization of this nanosystem was TGA: it allowed us to calculate the percentages of the organic content and, by difference, the inorganic content. We have performed different runs of analyses and the value reported in the **Figure 4.40** overview is the average percentage calculated, while we report one of the runs on the left side in **Figure 4.42** as representative. In this plot, we detected a first mass loss of 31 % which corresponds to the elimination of the polymeric content of the sample and the organic coating of the SPIONs. This assumption was confirmed with the analysis of the derivative of this mass loss, which gave a maximum at 307 °C that hides a broad distribution between 150 °C and 350 °C: in literature, it is known that the Pluronic decomposition starts at 230 °C and the principal decomposition range is between 240 °C and 410 °C³⁴⁰, while the PVA structure gives a signal between 200 °C and 500 °C attributable to the dehydration reaction of -OH groups and subsequent degradation of PVA releasing CO₂ gas³⁴¹. The other signals detected above 500 °C were not considered in the organic loss calculation, since they are related to the reduction of Fe₃O₄ by gases produced during the degradation of oleic acid³²⁴. With this information, we were able to calculate an inorganic content of 69 %.

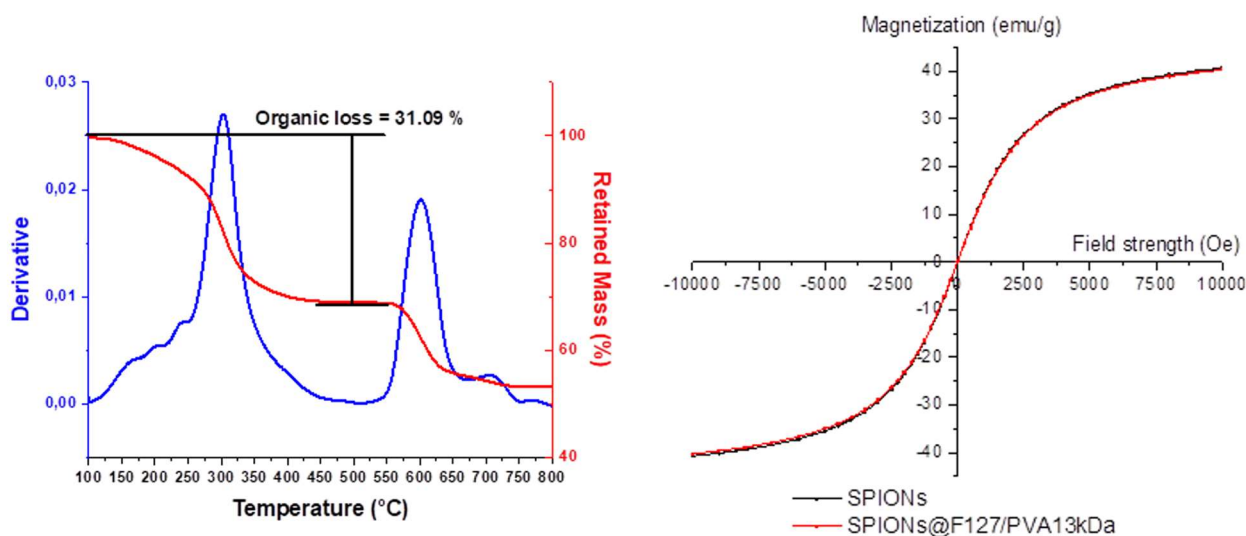


Figure 4.42: (Left) Representative TGA plot of SPIONs@F127/PVA13kDa sample with the derivative of the mass loss and the percentage of the mass that is retained with increasing temperatures. (Right) Magnetization vs. applied field plot showing the superparamagnetic character of (black) the pristine SPIONs and (red) the same SPIONs encapsulated in the polymeric structure.

Finally, in collaboration with Dr. Slavko Kralj of the Jožef Stefan Institute in Ljubljana, we wanted to investigate the magnetic properties of the complete nanosystem to test whether the overall

magnetization measured for the single SPIO is maintained once it is clusterized in the inner core of the polymeric structure. The VSM analysis of the SPIONs@F127/PVA13kDa sample reported in red in **Figure 4.42** and compared with the pristine dispersion of SPIONs in black, shows complete retention of the superparamagnetic characteristics (coercivity of 0.19 Oe and remnant field of $2.7 \cdot 10^{-3}$ emu/g) and the saturation magnetization (M_s of 40.3 emu/g considering a M_s of 40.7 emu/g for the original dispersion). This is a promising result in terms of theranostic applications: thanks to the maintained magnetic characteristics, the polymeric structure can be used as an efficient magnetically-driven drug carrier.

To summarize, the introduction of F127 for the formation of a more complex and compartmentalized structure resulted in an improved nanosystem with respect to the one constituted only by PVA. We overcame the previous flaws regarding the size and the SPIONs inclusion, managing to bring the nanosystem nearer to the desired characteristics. However, only with the improvement of the ultrasonication steps, we were able to obtain stabler structures with an optimized size of both the hydrophobic core and the hydrophilic shell and characterized by organic/inorganic composition and magnetism that were optimal for the theranostic purposes we sought.

4.3.4 Assembly of the polymeric structure using Pluronic F127 and PVA with $M_w = 57 - 66$ kDa

As in the previous cycle of experiments, the higher molecular weight PVA was tested in combination with the amphiphilic copolymer Pluronic F127. The optimization of the synthetic and cleaning procedures to guarantee the most suitable nanosystem followed the same protocol we employed in the case of 13 kDa PVA and Pluronic combination.

For the first set of experiments, we adopted the synthetic procedure reported by Huang and colleagues³³⁹. Even if we employed a different polymer, characterized by a higher average molecular weight, we decided to keep the same weight ratios between the three components of the nanosystem (SPIONs, PVA, and Pluronic F127). Unfortunately, the yield of this first procedure was very low and only a few nanosystems could be detected by TEM. However, the following NTA evidenced a series of large nanosystems with hydrodynamic diameters above 400 nm, probably due to the inefficient purification or the breaking of emulsion, that caused the formation of aggregates of the more insoluble PVA 57 kDa.

Nonetheless, the reference experiment performed to obtain void nanosystems with the same polymeric mixture, led apparently to the preparation of a sample characterized by only one broad population with average d_H of 172 nm, measured by NTA.

Considering this rather unsuccessful outcome, we decided to implement the same approach we used in the SPIONs@F127/PVA13kDa case, by increasing the concentration of magnetic nanoparticles in the dispersion. This was done in order to convey more stability to the polymeric assembly, trying to use SPIONs as a key structural point, in the form of a more rigid and compact core.

A slight change we introduced for the first time with this type of polymeric mixture, then for all the following experiments performed with both the PVA, was to increase the role and the power of magnetic separation during the purification steps. We used an N38 Neodymium-Iron-Boron (NdFeB) magnet with a nominal remanence of 1.22 T to retrieve only the magnetic content of the emulsion and boosting the efficiency of the centrifugation in eliminating the non-magnetic polymeric structures or aggregates.

Also with this series of experiments, we observed a slight improvement in nanosystems' formation and stability: TEM and NTA studies are described below in **Figure 4.43** and **Figure 4.45**.

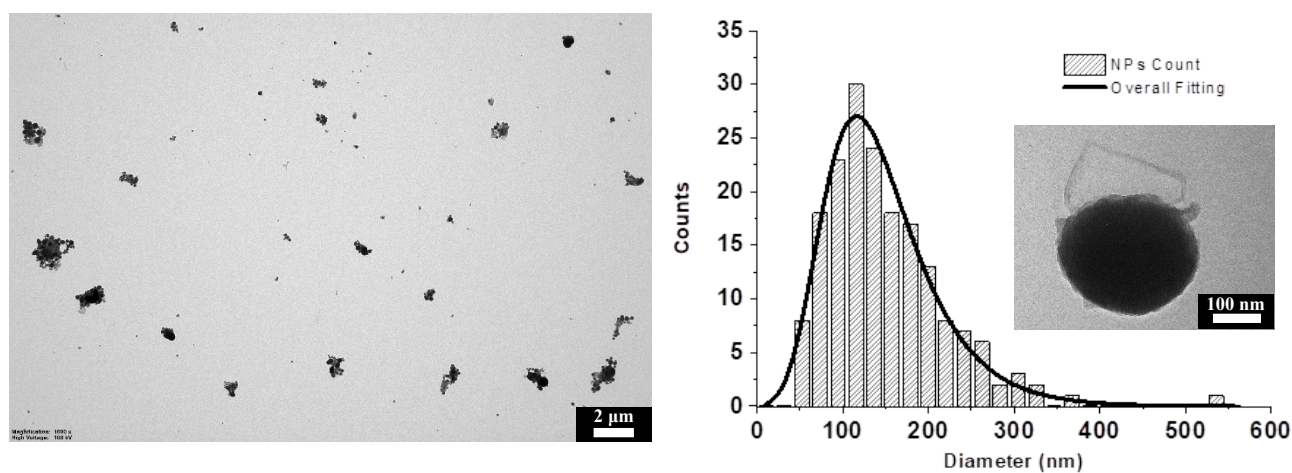


Figure 4.43: (Left) Representative TEM image of SPIONs@F127/PVA57kDa_1 sample. (Right) Histogram and Extreme fitting showing the broad size distribution of the inner core, with an inset showing one of the rounded nanosystems prepared, in which part of the polymeric coating was shrunk by the electron beam: $d_1 = 116.2 \pm 66.1$ nm.

As can be seen from the image reported as example in **Figure 4.43**, the magnetic separation in addition to the centrifugation allowed the almost complete removal of the unassembled polymeric chains. The resulting dispersion is composed of spherical nanosystems partially aggregated due to the water removal, with a significant amount of nanoparticles encapsulated, as can be appreciated by the dark intense color of the inorganic cores. The statistical analysis on these TEM images

indicates that the average diameter is centered at 116 nm, which is significantly different from the size measured for the case of SPIONs@F127/PVA13kDa_1. Regardless of the different PVA adopted, we think that the variation in size can be due only to the modified weight ratio, since the inner core is prevalently determined by the micellization of Pluronic F127. With this adjustment, we think we had favored the formation of less but more stable nanosystems, with a higher content of SPIONs hosted in the polymeric shell and a reduced size dispersion.

Remarkably, we noticed that the heat generated by the electron beam of the TEM instrument hitting the sample, caused the fast dehydration of the polymeric coating and its shrinking onto the surface of the inorganic core, which instead retained its consistency and its shape (**Figure 4.44**).

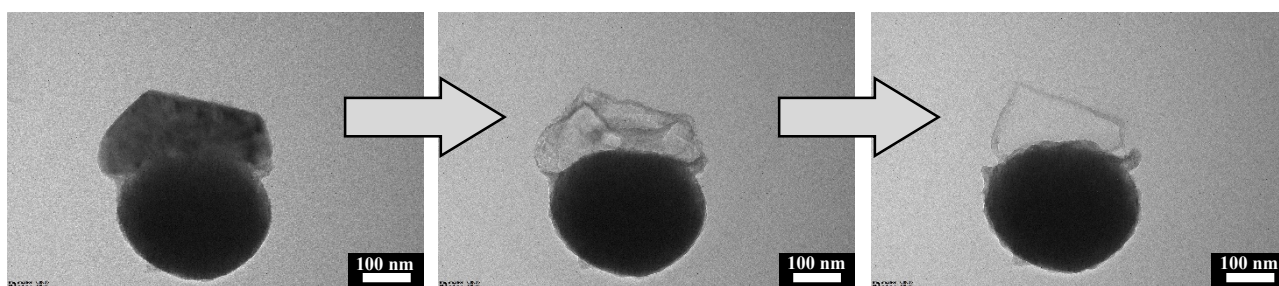


Figure 4.44: Sequence of TEM images of the SPIONs@F127/PVA57kDa_1 sample, showing the dehydration and the shrinkage of the polymeric coating.

This suggests that the inorganic core is indeed a robust structure and an indication of a good synthetic procedure that can be implemented. If the polymer shrinks and holds together better the components, it may be useful to maintain temperatures above room temperature at least for the whole of organic solvent evaporation, which is the longest step of the synthesis.

On the contrary, in respect to the comparison we did for SPIONs@PVA13kDa_4 and SPIONs@F127/PVA13kDa_2 (which were probably the same type of nanosystem, *vide supra*), the present sample and the analogous one assembled without Pluronic F127 (SPIONs@PVA57kDa_3) are significantly different, from both the structural and dimensional points of view. Therefore, we assume that the synthetic method adopted here had successfully taken advantage of the Pluronic F127 for the construction of the hydrophobic core and the first polymeric layer.

We performed also an NTA on the sample collected after centrifugation and magnetic separation: the nanosystems concentration vs. diameter plot is reported in **Figure 4.45**.

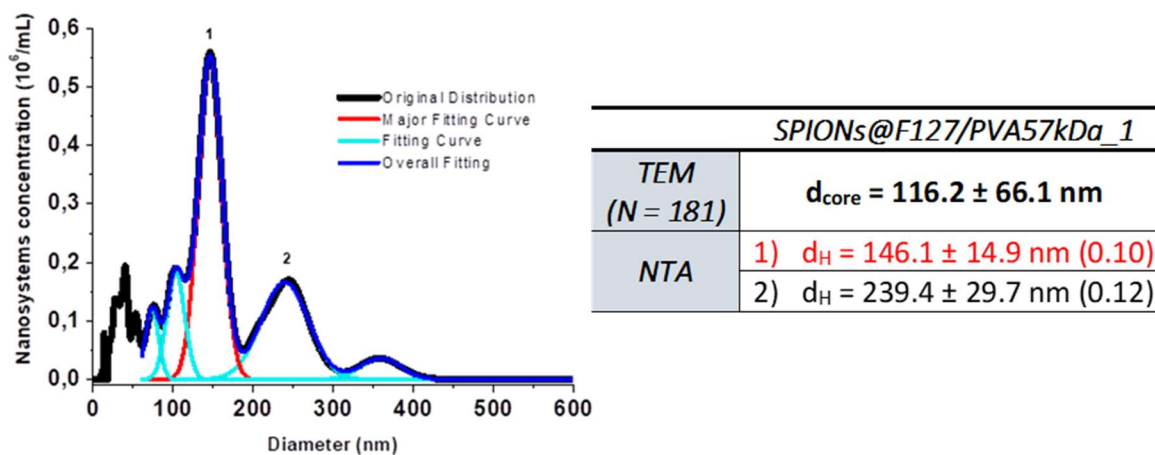


Figure 4.45: (Left) NTA analysis of the SPIONs@F127/PVA57kDa_1 sample, showing the original size distribution and data extrapolation curves using Gaussian fitting. (Right) Inner core diameter from TEM and hydrodynamic diameters of the principal size populations with the related variation coefficient.

The plot shows a series of different populations: the most important ones are the two indicated with 1 and 2 in **Figure 4.45**: the first one is centered at 146 nm and the second one at 239 nm. These distributions are in agreement with the result we obtained with the TEM, characterized by only one but broad populations: in this case, the NTA was revealed to be more accurate in distinguishing different nanosystems populations. The curve above 350 nm could represent a portion of polymeric aggregates that were not completely removed.

Considering the major distribution, the shell thickness that can be calculated is around 15 nm, which is significantly thinner than the one calculated for the shell made of PVA 13kDa: this is in accordance with the lower polarity and water affinity of the heavier PVA that induces a shrinkage to minimize the unfavorable interactions with water molecules.

With the objective to increase the stability and the degree of SPIONs encapsulation, we implemented the double sonication and the evaporation of the organic solvent at 40 °C as described in the previous experiments with PVA 13 kDa, for the Pluronic F127 - PVA 57 kDa mixture. With this aim in mind, we first emulsified the organic phase where SPIONs were dissolved, with the aqueous phase containing Pluronic F127; the intermediate brown-grey emulsion that still had some black undispersed organic bubbles in it was immediately mixed and sonicated with the other aqueous dispersion of 57 kDa PVA we prepared heating the aqueous phase at 70 °C to ensure its complete dissolution. Since the heavier PVA has a more hydrophobic character, this operation has been rather more complex and time-consuming than the solubilization of 13 kDa PVA. Nonetheless, the final emulsion obtained after the second sonication cycle seemed visually even more homogeneous in its turbid brown color and the amount of precipitated SPIONs was

significantly lower than after the single sonication performed on SPIONs@F127/PVA57kDa_1 sample.

In a similar way to SPIONs@F127/PVA13kDa_2, we tested the re-dispersibility of the precipitate collected after the first sonication: we were still able to redisperse it in water. Unfortunately, at variance to the former attempt, the dichloromethane addition extracted a greater amount of magnetic nanoparticles. This could be either due to weak polymeric structures that are disrupted by organic solvents and release the magnetic content or, more likely, to the fact that a considerable part of SPIONs is stored not only on the most internal hydrophobic compartment of the nanosystem, but also within the more hydrophobic PVA that constitutes the external polymeric shell. In the latter case, SPIONs are less protected and more in contact with the external environment: consequently, it is plausible that dichloromethane interactions would replace the weak non-covalent bonds between SPIONs' organic coating and PVA chains.

We proceeded with the characterization of the precipitate after further purification steps to determine the core and shell size of the nanosystems in the precipitate.

The TEM images reported in **Figure 4.46** presents a distribution of nanosystems with heterogeneous shapes. Moreover, what can be appreciated from the TEM images is the presence of PVA, polymer solidified in linear and elongated structures that do not contain magnetic nanoparticles.

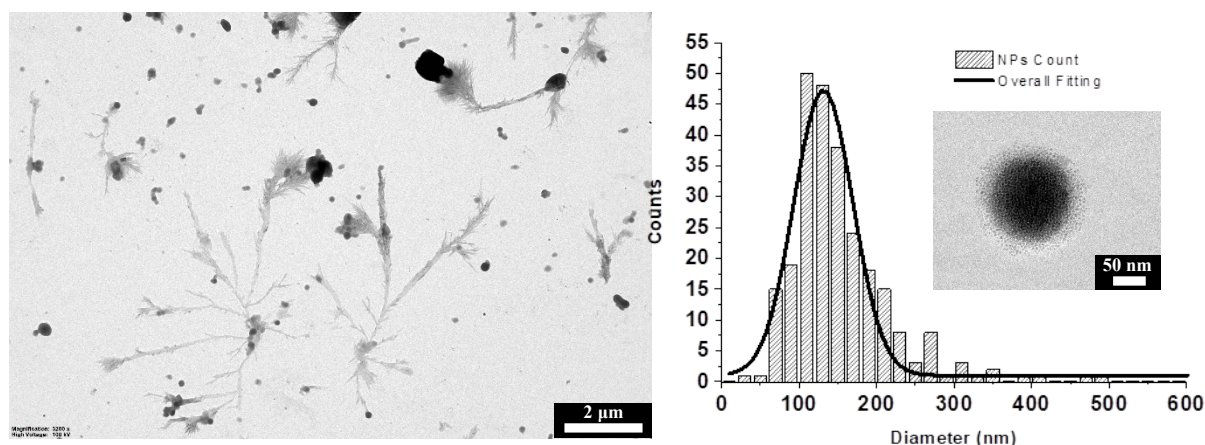


Figure 4.46: (Left) Representative TEM image of SPIONs@F127/PVA57kDa_2 sample. (Right) Histogram and Gaussian fitting showing the size distribution of the inner core, with an insert showing one of the rounded nanosystems prepared, in which part of the magnetic content is spread at the edge of the polymeric coating: $d_1 = 131.4 \pm 38.1$ nm.

Another effect of the water removal is that nanosystems that are already near to each other tend to interact more with the respective polymeric shells and eventually aggregate: this is the reason why it seems that many dark cores are held together by the same polymeric coating. The precipitation and the crystallization of the outer PVA when water is removed are clearly visible also in some of

the images recorded focusing on a single nanosystem. In other images, where the outer PVA did not precipitate, it is possible to notice that part of the SPIONs that are clustered in the outer part of the inorganic core protrude and become more spread the more distant are to the center of the core (insert in **Figure 4.46**). We assume that this is the confirmation that some magnetic nanoparticles are only loosely bonded within the nanosystems' shell and not included in the hydrophobic reservoir made of the polypropylene oxide portion of Pluronic F127. Unfortunately, the TEM images do not answer completely whether this is an effect due to the intrinsic stability of the nanosystem in dispersion and caused by weaker interactions between PEG unities and PVA, or is rather due to the preparation of the sample for the TEM analysis that put the nanosystems under harsh conditions. However, this behavior was not observed in the previous experiments with 13 kDa PVA, since the thicker shell did not contain any SPIONs, but were all clustered and compacted together within the inorganic core even after solvent removal.

Regardless of this overall appearance, the statistical analysis of the inorganic cores shows a narrower distribution centered at 131 nm, without any other populations or size distribution tail broadening. This average core size is similar to the previous value of d_{core} [SPIONs@F127/PVA57kDa_1] of 116 nm and to the d_{core} [SPIONs@F127/PVA13kDa_2] of 122 nm. The low dispersion of core size is likely intrinsic to the Pluronic F127: given a precise weight ratio and concentration in the dispersion, this amphiphilic copolymer will always form micelles of the same size characterized by a narrow dispersion. On the contrary, since the variable element is the length of the PVA, the difference in size and the dispersion broadening are expected only when the hydrodynamic diameters are analyzed. Therefore, NTA data of the same sample are reported in **Figure 4.47**.

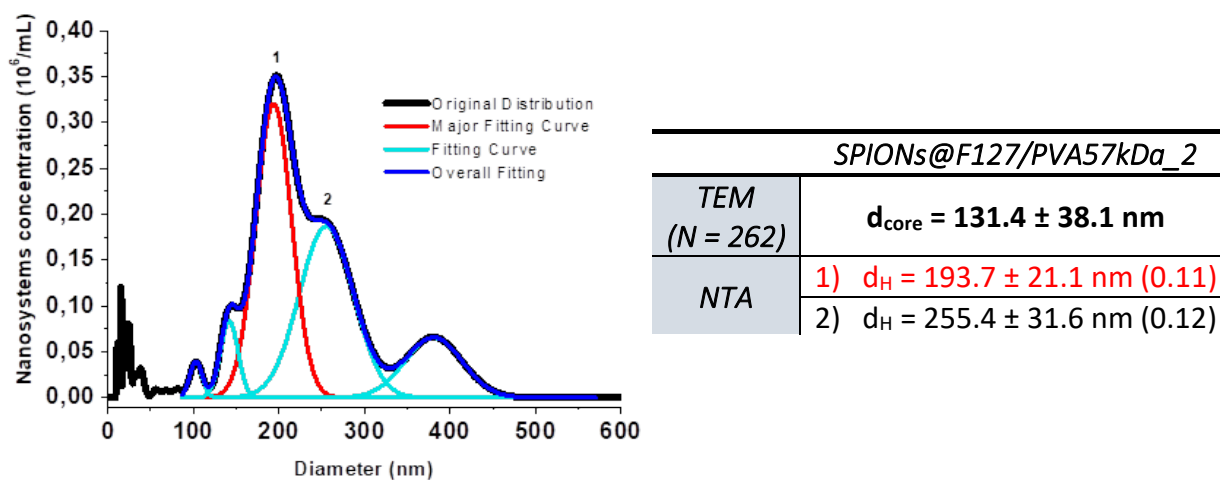


Figure 4.47: (Left) NTA analysis of the SPIONs@F127/PVA57kDa_2 sample, showing the original size distribution and data extrapolation curves using Gaussian fitting. (Right) Inner core diameter from TEM and hydrodynamic diameters of the principal size populations with the related variation coefficient.

This sample is characterized by two major overlapped distributions centered at 194 nm and 255 nm and a minor population of aggregates above 350 nm. While the first two could be nanosystems associated with the same inorganic core, but covered by increasing amounts of PVA (with a difference in shell thickness), the last one could probably be related to aggregates observed also in the TEM images.

Considering the major distributions, the average shell thickness that can be calculated is around 30 nm, which once again is thinner than the analogous SPIONs@F127/PVA13kDa_2.

In conclusion, the addition of a further sonication cycle and the addition of polymers in successive steps had led surely to nanosystems with the correct internal compartmentalization, but large and probably not too stable, considering the weak interactions within the outer polymeric shell and its reduced thickness.

In parallel with the last synthetic procedure described and in analogy with the applied experiments carried out with PVA 13kDa, the Pluronic dispersion was heated above the LCST until reaching the cloud point (the dispersion becomes turbid), to dehydrate the polymer and favored the phase separation that leads to micellization before the first sonication. Moreover, we increased the number of 1-minute cycles of sonication for both the polymer additions until the dispersion gained a more homogeneous appearance and we made sure to limit the separation of the two phases by keeping the mixing in between. The resulting brown-grey dispersion presented only a little magnetic black precipitate and was stable even after the organic solvent evaporation, without losing its turbidity: this indicates that the nanosystems were formed well enough to maintain the micellar structure once the DCM evaporated, sustaining the emulsion state and preventing the Pluronic to redisperse in water with consequent SPIONs release. However, in respect to the analogous experiments with the 13kDa PVA, the color of the dispersion in this case seemed lighter and with a more marked brown shade, which is not enhanced during the evaporation step thanks to the use of argon. This fact could be explained considering PVA 57kDa higher hydrophobicity, which probably prevents it to stabilize the outer shell of the nanosystem and to protect the magnetic content as effectively as PVA 13 kDa.

The sample resulting from this set of experiments was first characterized by TEM: a representative image is reported in **Figure 4.48**, with the statistical analysis of inorganic cores' size.

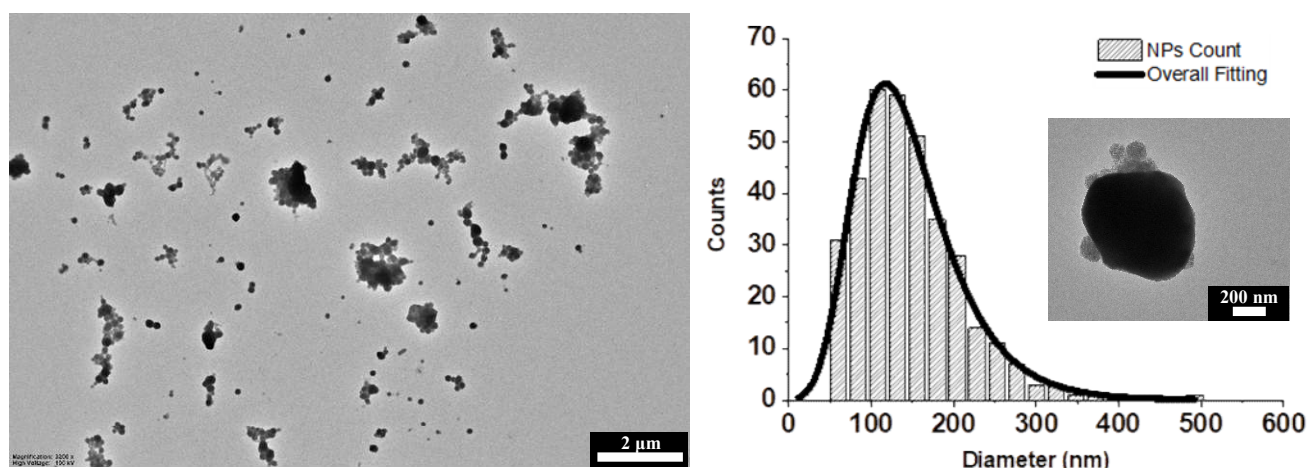
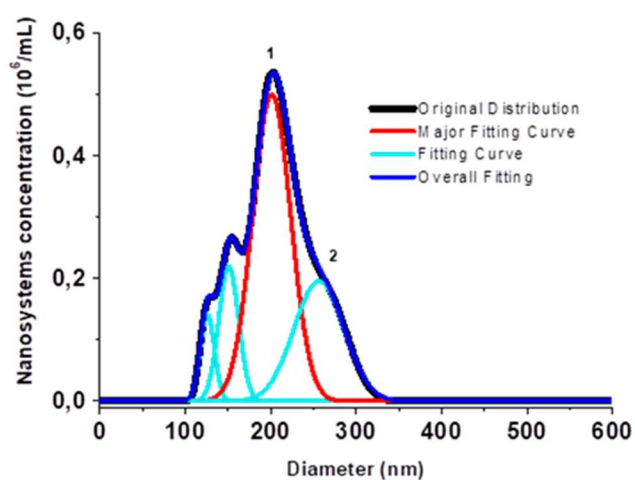


Figure 4.48: (Left) Representative TEM image of SPIONs@F127/PVA57kDa_3 sample. (Right) Histogram and Extreme fitting showing the broad size distribution of the inner core, with and insert showing one of the rounded nanosystems prepared: $d_1 = 117.2 \pm 65.5$ nm.

The TEM image shows a rather spread distribution of single nanosystems or groups of them in which the spherical inorganic core is clearly identified by the darker shade. In some of the nanosystems, it is possible to appreciate the single SPIONs clustered together in a rounded shape. The statistical analysis was performed with an extreme function to consider the tail above 200 nm, which increased the final average size of 117 nm. This diameter is compatible with the size of micelles formed by Pluronic F127 in these conditions and observed in other similar experiments described previously.

In **Figure 4.49** and **Figure 4.50** are reported respectively the results of NTA and DLS analyses.



<i>SPIONs@F127/PVA57kDa_3</i>	
<i>TEM</i> (<i>N</i> = 354)	$d_{\text{core}} = 117.2 \pm 65.5$ nm
<i>NTA</i>	1) $d_H = 201.1 \pm 22.3$ nm (0.11)
	2) $d_H = 256.5 \pm 29.2$ nm (0.11)
<i>DLS</i>	218.8 ± 88.2 nm (0.33)
<i>TGA</i>	Organic loss = 34.47 %
<i>VSM</i>	$M_s = 32.970$ emu/g
	$M_r = 4.1747 \cdot 10^{-3}$ emu/g
	$H_c = 0.35929$ Oe

Figure 4.49: (Left) NTA analysis of the SPIONs@F127/PVA57kDa_3 sample, showing the original size distribution and data extrapolation curves using Gaussian fitting. (Right) Inner core diameter from TEM, hydrodynamic diameters of the principal size populations, organic composition, and magnetic properties.

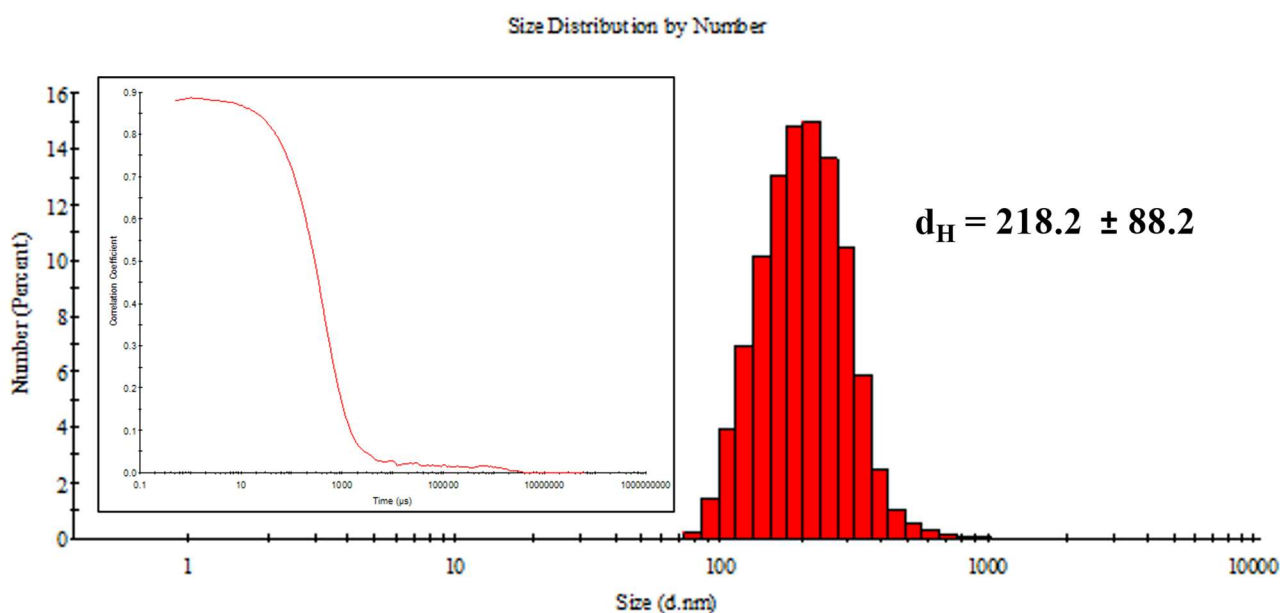


Figure 4.50: DLS analysis of the SPIONs@F127/PVA57kDa_3 sample with the size distribution by number of nanoparticles extrapolated from it and (Insert) the related correlogram.

The NTA displays a major population of nanosystems, with an average size of 201 nm, while with the DLS the d_H is 218 nm, making these values consistent.

Considering SPIONs@F127/PVA13kDa nanosystems, this sample features a bigger hydrodynamic diameter, which we hypothesize may be due to the more than 4-times increase in length of the PVA polymeric chain, regardless of the minor affinity of the heavier PVA for water which is supposed to induce a shell shrinkage. However, the balance between the major physical length and volume of this polymer and the tendency to shrink leads to a slight increase of the overall hydrodynamic diameter but still suitable for biological applications.

The TGA was performed also in this case: in **Figure 4.51** is reported one of the representative plots with which we have calculated the average value of 34 % of organic mass loss and consequently an inorganic content of 66 %. In respect to the TGA of the analogous sample with the lighter PVA (SPIONs@F127/PVA13kDa, organic loss of 31 %), we notice a slight increase in the percentage, consistent with the increased molecular weight of the PVA used, hence the organic content. Moreover, we identified a maximum at 244 °C which is more prominent than in the previous analysis: since it falls in the range assigned to PVA decomposition³⁴¹, this is an indication of the increased significance of PVA in the content ratio between the two polymers. The other maximum above 500 °C is related to the reduction of Fe_3O_4 ³²⁴.

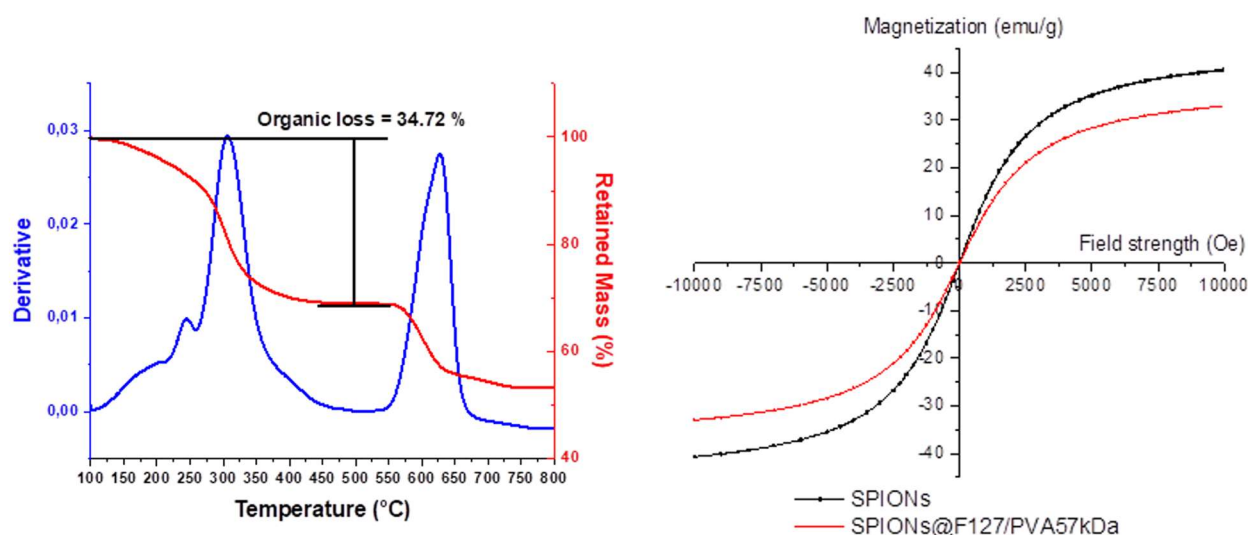


Figure 4.51: (Left) Representative TGA plot of SPIONs@F127/PVA57kDa sample with the derivative of the mass loss and the percentage of the mass that is retained with increasing temperatures. (Right) Magnetization vs. applied field plot showing the superparamagnetic character of (black) the pristine SPIONs and (red) the same SPIONs encapsulated in the polymeric structure.

Considering the magnetic characteristics of the hybrid nanosystem, the VSM analysis of the SPIONs@F127/PVA57kDa sample is reported in red in **Figure 4.51** and compared with the pristine dispersion of the same SPIONs in black. From the extrapolation of the coercivity of 0.36 Oe and the remnant field of $4.2 \cdot 10^{-3}$ emu/g, we can state that the superparamagnetic behavior has been maintained also for these clustered SPIONs. However, we also noticed a decrease in the saturation magnetization from 40.7 emu/g to 33.0 emu/g: this may be the consequence of a series of factors like the magnetite oxidation during the sonication step³⁴² or the coating with a polymeric shell¹²⁴. Considering the second factor, Pluronic should not cause a loss in saturation magnetization¹⁷² (as we observed in the case of SPIONs@F127/PVA13kDa), while the PVA coating can refrain the close contact between SPIONs, with the consequence that the crystallite size is reduced and the saturation magnetization decreases accordingly³⁴¹. The use of the 57 kDa PVA could have led to both the factor we proposed: since it is more hydrophobic than PVA 13 kDa and we have evidence of lower stability of the nanosystem, SPIONs in this structure can be less protected, more exposed to oxidation and a significant part of them may be singularly coated with PVA, instead of being clustered in the hydrophobic moiety of Pluronic. Even if this is desirable for imaging purposes³²⁷, on the other hand, this may be detrimental for magnetic drug targeting, since fewer magnetic SPIONs are less susceptible to the external field and may not respond to it sufficiently to contrast the hydrodynamic drag forces exerted by the blood flow inside the vessels.

The results of the preparation of these nanosystems with the same optimized procedure adopted for the F127/PVA13kDa case using an extended ultrasonication approach and centrifugation steps, led to similar structures in terms of core and shell size, in accordance with the employment of the same Pluronic F127 copolymer as the principal structural constituent. However, the extensive characterization performed on them evidenced features that were less promising in a nanotheranostic view: even if the reduced magnetization could help their application for positive ^1H -MRI, both the nanosystems' stability and the SPIONs inclusion were inferior.

4.4 DRUG LOADING IN THE POLYMERIC NANOSYSTEM

Once the hybrid nanosystem has been demonstrated to be stable and within the desired range of dimensions, the next step is to internalize the selected drug molecules.

Since the nanosystems that demonstrated the most promising results in terms of stability, encapsulation, and dimension were the ones prepared by mixing PVA with Pluronic F127 (SPIONs@F127/PVA13kDa and SPIONs@F127/PVA57kDa), we decided to continue forward the completion of the designed hybrid nanosystem, exploiting these two structures.

The first molecule identified for the inclusion in the polymeric-magnetic composite nanostructure is riluzole (6-trifluoromethoxy benzothiazol-2-amine), a benzothiazole derivative that is currently the only drug approved by FDA³⁰¹ for the treatment of amyotrophic lateral sclerosis (ALS)³⁰². ALS is a neurodegenerative disorder that affects motor neurons and leads to the deterioration of voluntary muscles, eventually resulting in paralysis and long-term disability; riluzole has been demonstrated successful in giving symptomatic relief and interrupting the disease progression³⁴³. This molecule acts as a potent neuroprotective agent, since it prevents acute cell damage: the mechanisms proposed for its pharmaceutical action comprises the inhibition of the release of glutamate (an excitatory amino acid) into the synaptic gap, the inhibition of events following stimulation and activation of glutamate receptors and the stabilization of the inactivated state of voltage-dependent sodium channels³⁴⁴.

Other than this application, riluzole was studied as an agent to contrast anxiety, memory impairment, and oxidative stress³⁴³ and it is also able to protect dopamine neurons in Parkinson's disease³⁴⁵.

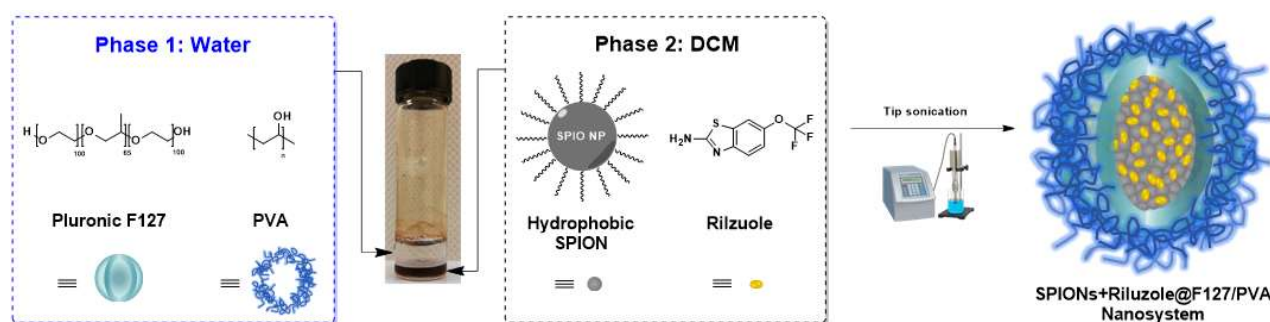
Currently, riluzole is prepared in tablets that are orally administered and rapidly absorbed from the gastrointestinal tract, extensively metabolized primarily by cytochrome P450³⁴⁶. It is very slightly soluble in water, therefore can cross efficiently the blood-brain barrier (BBB), but needs a compatible administration way in aqueous media which our nanosystem may provide.

Another drug molecule whose interaction with the nanosystem will be investigated is named SF89. It is a very active triazole-triazine scaffold compound synthesized by the research group of Prof. Stephanie Federico (UNITS). It showed an IC₅₀ of 0.18 μ M for CK1- δ (enzyme belonging to the family of casein kinases isoform δ). CK1- δ is an interesting target for various neurodegenerative diseases and in particular for Amyotrophic Lateral Sclerosis (ALS) as it is able to promote the cytoplasmic accumulation carried out by TDP-43. In pathological conditions, it is altered and sequestered in hyperphosphorylated cytoplasmic aggregates, therefore enzymatic inhibitors may be

of interest for the treatment of this pathology. The target is therefore the same as that of riluzole, thus in our project this offers the possibility of studying the molecule's inclusion and release from the nanoparticle in question, comparing them with a lead compound now on the market in different formulations.

4.4.1 Assembly of the polymeric nanosystem – PVA 13kDa + F127 + Riluzole

The synthetic procedure employed in the previous section has to be slightly changed in order to consider the insertion of drug molecules (**Scheme 4.6**).



Scheme 4.6: Scheme representing the compounds and the general synthetic approach adopted for the formation of SPIONs+Riluzole@F127/PVA nanosystems.

The simpler approach is to solubilize the apolar drug along with the hydrophobic SPIONs in the organic solvent and then sonicate with the aqueous layer containing the polymer.

In this way, riluzole molecules can interact with the alkyl chains that decorate the iron oxide core, favoring their inclusion in the hydrophobic reservoir of the micelle, following the deposition of PVA on the outer shell to stabilize the structure. In fact, we have maintained the major improvements in the procedure devised until now in the experiments with nanosystems without drugs, pushing forward the optimization with further adjustments.

In the set of experiments presented below the nanosystems were therefore synthesized employing the double sonication method, therefore distinguishing the first emulsification between the organic dispersion of SPIONs and riluzole and the aqueous phase of Pluronic, and the second emulsification between the primary one and the aqueous dispersion of PVA. For the purification steps of the resulting turbid brown-orange dispersion, we decided to perform several cycles of centrifugation aided with magnetic separation, verifying qualitatively the presence of drug molecules and polymer chains in the removed supernatant and the dispersibility of the separated magnetic precipitate. On this basis, we employed three centrifugation cycles, observing that the

second supernatant was already clear, while the precipitate was highly magnetic-responsive and always re-dispersible in Milli-Q water with vigorous shaking after the centrifugation and the supernatant removal.

The precipitate was analyzed with TEM (**Figure 4.52**), finding only one distribution after statistical analysis: the peak is centered at 145 nm, which is a size bigger than the usual average dimension obtained for the unloaded nanosystems. Visually, the sample still presents some unassembled polymer and the nanosystems are stuck together in groups of rounded structures due to the solvent evaporation: however, each of them is clearly distinguishable from the others.

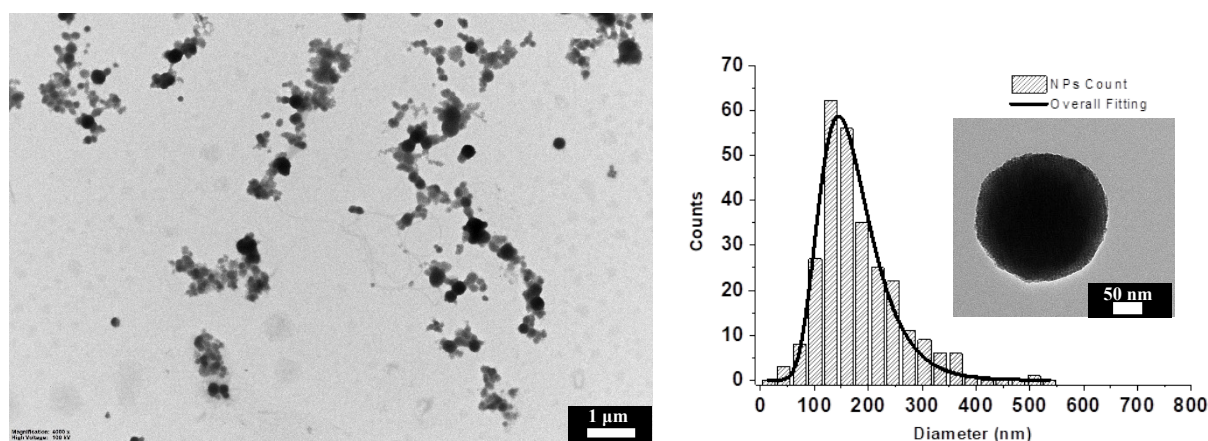


Figure 4.52: (Left) TEM image of SPIONs+Riluzole@F127/PVA13kDa_1 sample. (Right) Histogram and Extreme fitting showing the size distribution of the inner core, with an insert showing one of the rounded nanosystems prepared, in which the compact inorganic core can be seen fully.

One feature that is variable throughout the grid is the appearance of the outer shell: in some nanosystems, there is a compact and almost invisible layer (due to the poor contrast the polymer has toward the electron beam) that held together the inorganic core, while in some other structures we identify protrusions containing SPIONs that we already saw in some SPIO@F127/PVA57kDa nanosystems, suspected to be slightly unstable.

Considering these results, we anticipated also an increase in the hydrodynamic diameter, and the NTA in **Figure 4.53** confirmed this expectation.

In the plot retrieved there is prevalently one population of nanosystem centered at 193 nm, with only some minor ones above 100 nm and below 300 nm. The group of peaks below 100 nm was probably related to the polymer chains still in dispersion that were not removed by centrifugation and assemble in small structures while they are hydrated. The shell thickness is calculated to be around 24 nm.

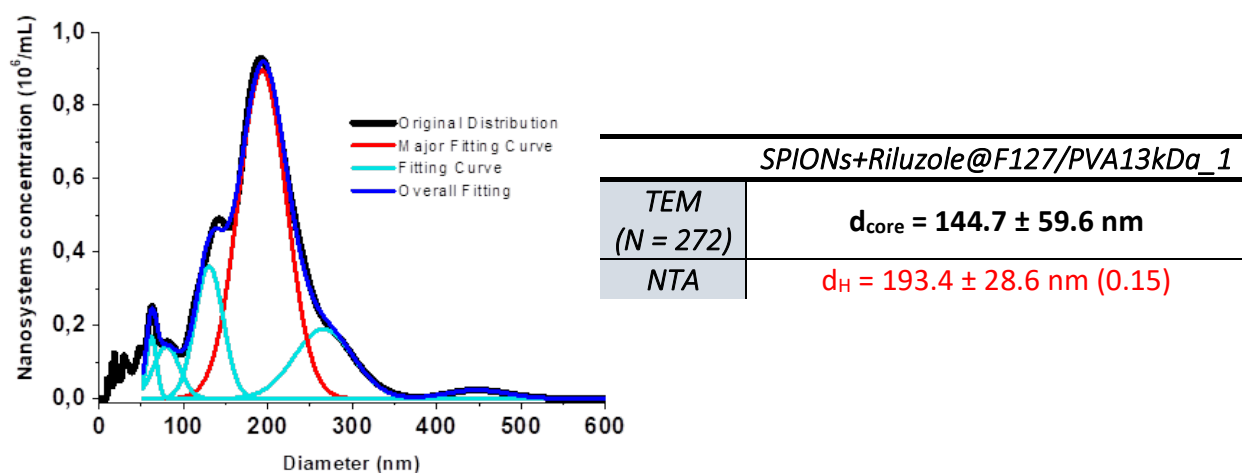


Figure 4.53: (Left) NTA analysis of SPIONs+Riluzole@F127/PVA13kDa_1 sample, showing the original size distribution and the following data extrapolation using Gaussian fitting. (Right) Dimensional characteristics overview for the principal size populations.

In conclusion, also for the nanosystems loaded with riluzole, the improved procedure gave an acceptable size distribution of nanostructures: the bigger inorganic core from the TEM images is promising in terms of available hydrophobic space and therefore in terms of drug molecules encapsulated.

Foreseeing the preliminary experiments in the membrane permeation, we decided to redisperse in PBS the nanosystems synthesized in Milli-Q water in the following attempts. This was done to better simulate the biological environment and verify the stability of our nanosystems.

The techniques we employed to control the result of re-dispersion were always TEM (**Figure 4.54**) and NTA (**Figure 4.55**).

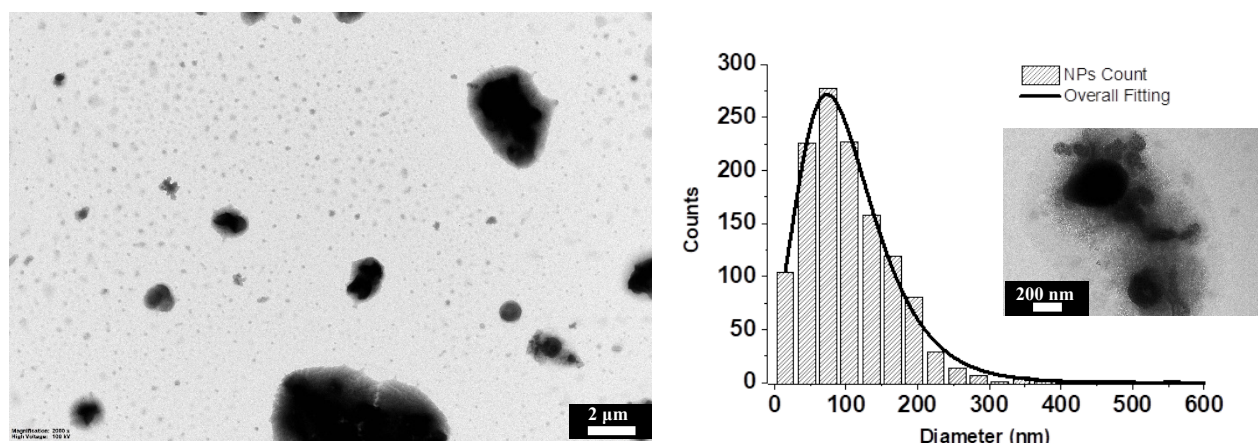


Figure 4.54: (Left) TEM image of SPIONs+Riluzole@F127/PVA13kDa_2 sample re-dispersed in PBS. (Right) Histogram and Extreme fitting showing the size distribution of the inner core, with an insert showing one of the nanosystems prepared, in which the SPIONs in the core are less distinguishable and the outer shell seems to have crystallized.

Regarding the first one, the images show a distribution of nanosystems that is rather different from the ones recorded previously: from a certain point of view, they are well-separated from each other and the aggregation seen in the previous try does not occur, but there are also regions of the grid covered with aggregates above 1 micrometer. However, the major part of the sample is composed of small polymeric nanosystems which form a distribution with a significant tail above 200 nm and centered at 73.5 nm.

Overall, since the contrast is poorer, the nanosystems seem to have lower inorganic content in them and to feature a polymeric coating that is thicker or simply more spread on the grid. To verify one of these two hypotheses, we performed the NTA on the sample, to measure the hydrodynamic diameter in the classic conditions of aqueous dispersion.

The results reported in **Figure 4.55** show no significant differences in size in respect to the previous analyses, only a sample that is a little more complex and heterogeneous. For this reason, we assume that the dispersion in PBS does not affect too much the average size, but helps to separate the nanosystems and avoid aggregation. However, the interaction between phosphate ions and the external PVA coating may weaken it, resulting in the loss of stability and compactness of the polymeric matrix that we observed spread on the grid in the TEM images.

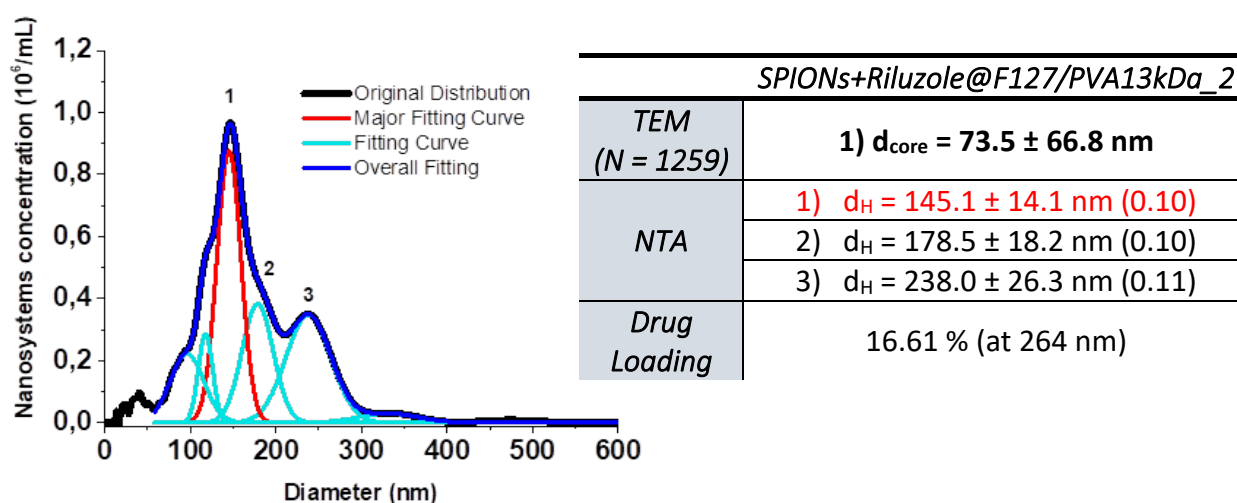


Figure 4.55: (Left) NTA analysis of SPIONs+Riluzole@F127/PVA13kDa_2 sample, showing the original size distribution and the following data extrapolation using Gaussian fitting. (Right) Overview of the dimensional characteristics for the principal size populations and drug loading.

With this set of experiments, we started to assess the percentage of drug molecules successfully encapsulated within the nanosystem. To this aim, we relied on UV-Vis spectroscopy, with analyses performed on all the different supernatant dispersions we collected after each centrifugation step, which might contain a certain amount of riluzole molecules maintained in dispersion by unassembled polymer chains or encapsulated in small polymeric nanosystems without a magnetic core, which we eliminated employing magnetic separation. To correlate the data we needed a

calibration line between the absorbance and riluzole concentration in dispersion: since this drug is a hydrophobic species which we were not able to dissolve in Milli-Q water, we were forced to detect its characteristic UV-Vis peaks – found at 223 nm and 264 nm – and to calculate the respective calibration curve in methanol. The best fitting for these calibrations was the one related to the absorbance at 264 nm and we decided to use it as a matter of comparison for the drug loading calculations. Based on this reference, we estimate a drug loading percentage of 17 %, which is quite low considering the molecule apolar character and the supposed favored interactions with hydrophobic species.

The progression and the last optimization of the assembly procedure implemented for the SPIONs@F127/PVA-type nanosystems was transferred as well to the ones containing riluzole. In particular, we paid more attention to the ultrasonication step to assure the complete emulsification of the two phases and the successful inclusion of both SPIONs and drug molecules within the hydrophobic core. Therefore, we implemented several more cycles of sonication for each of the polymeric species we introduced, obtaining a darker brown-grey and homogeneous dispersion at the end with respect to the one prepared with the previous experiments.

The inclusion and the size of the internal part of these nanosystems were preliminarily assessed by TEM (Figure 4.56). The images recorded show a rather aggregated distribution of rounded nanosystems in many parts of the grid: this is mainly due to the sample concentration used for the preparation of the grid, which was too high and favored the interactions between shells even before the solvent removal.

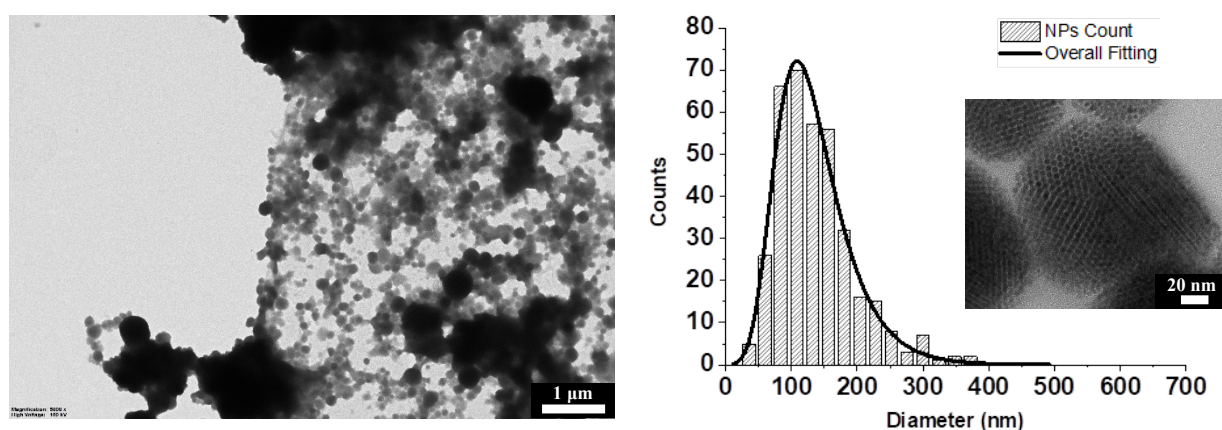


Figure 4.56: (Left) TEM image of SPIONs+Riluzole@F127/PVA13kDa_3 sample. (Right) Histogram and Extreme fitting showing the size distribution of the inner core, with an insert showing one of the nanosystems prepared, in which the SPIONs in the core are packed in different crystalline faces.

Interestingly, a feature that can be detected in many inorganic cores, is that the constituent SPIONs tend to interact and form a crystallized cluster: for example, three different crystalline faces can be detected starting from the center of the nanosystem presented in the insert figure.

The size distribution that can be calculated excluding the superimposed nanosystems, gives a single broad population centered at 109 nm, which is slightly bigger than the inorganic core obtained for the analogous system assembled without riluzole.

These data are compared with the results of the NTA reported in **Figure 4.57**, which indicate the presence of three populations of nanosystems under 300 nm, with the major one centered at 216 nm. Therefore, as observed for the core diameter, also the hydrodynamic one seems to increase in size accordingly, but we do not assume this is directly related to the presence of a considerable amount of riluzole within the hydrophobic core.

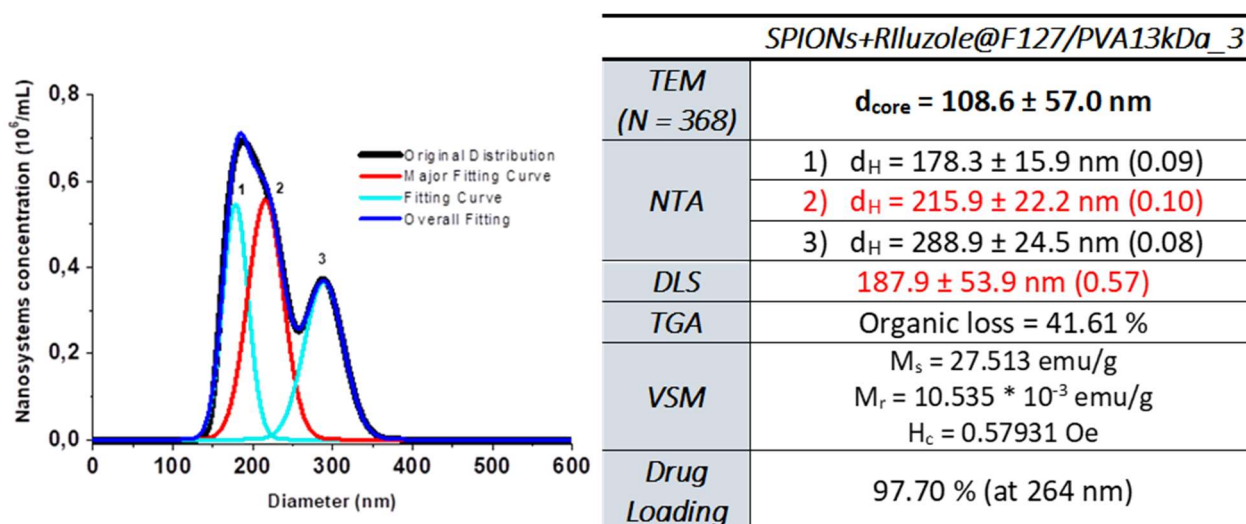


Figure 4.57: (Left) NTA analysis of SPIONs+Riluzole@F127/PVA13kDa_3 sample, showing the original size distribution and the following data extrapolation using Gaussian fitting. (Right) Overview of the dimensional characteristics for the principal size populations, organic content, magnetic properties, and drug loading.

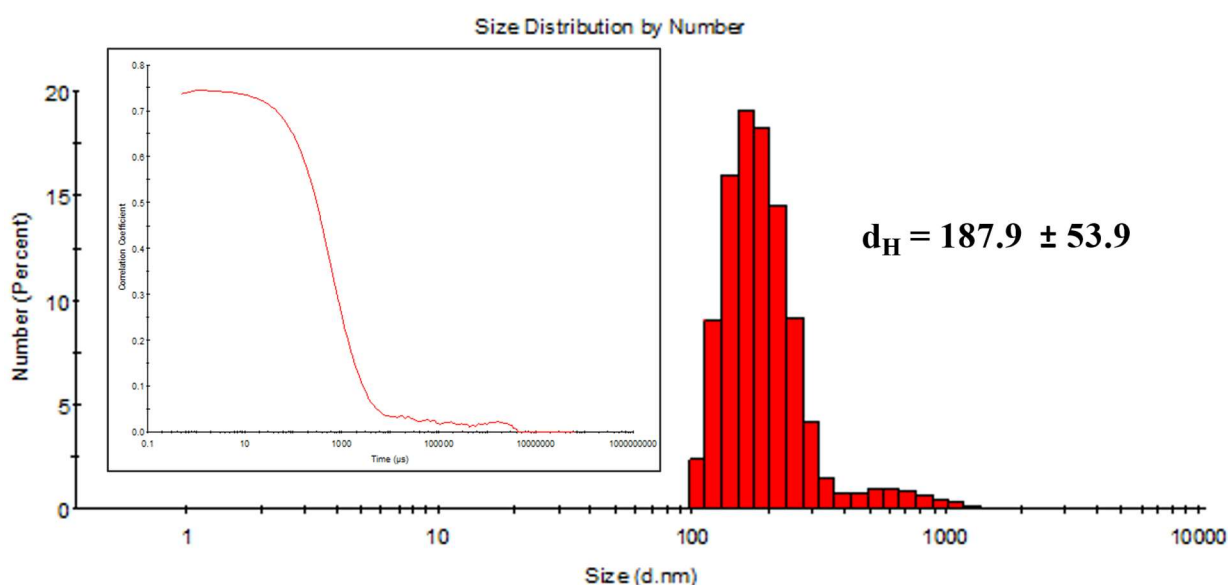


Figure 4.58: DLS analysis of the SPIONs+Riluzole@F127/PVA13kDa_3 sample with the size distribution by number of nanoparticles extrapolated from it and (Insert) the related correlogram.

As a further and alternative method to evaluate the hydrodynamic diameter, we relied on the DLS (**Figure 4.58**). Differently from the NTA, it gave us a single broad and very polydisperse distribution centered at 188 nm that should include all the others detected below 350 nm. Moreover, another small population above 600 nm can be detected at the DLS due to its sensibility for high-scattering species. The results of these three analyses is a polydispersed sample that however maintains size and shape suitable for the biological application we seek, even if the overall core and shell dimensions seem to increase both in respect to previous SPIONs+Riluzole@F127/PVA13 kDa experiments and the last tries performed without riluzole.

The drug loading was significantly improved after the optimization of the procedure: even if the supernatant collected after the first sonication was undoubtedly yellow and substantial in volume, the amount of riluzole lost during the synthesis extrapolated from the UV-Vis spectra was very low. We obtained a drug encapsulation of almost 98 % in respect to the amount of riluzole introduced in the early steps of the assembly, using the same calibration line relative to the absorbance at 264 nm. Notably, with the increased loading percentage in respect to the previous experiments, we noticed that riluzole is indeed a hydrophobic drug easily and almost completely stored inside the hydrophilic polypropylene compartment.

In addition, we have performed the TGA on the portion of the sample that was freeze-dried immediately after the purification (**Figure 4.59**). We observed a total loss of organic content of 42 % up to 500 °C, related to the presence of both the polymeric mixture and riluzole molecules. Interestingly, with respect to the TGA profile of the analogous SPIONs@F127/PVA13kDa nanosystem, the organic loss percentage for this sample is sensibly higher (11 % of difference, considering the previous percentage of 31 %): since the core and the hydrodynamic diameter are well comparable, this significant difference hints to the effective encapsulation of riluzole molecules. Moreover, also the TGA plot profile is significantly different in the range of temperatures between 200 °C and 300 °C: it features an additional spike centered at 275 °C after the one around 250 °C related to the presence of PVA³⁴¹ and the major peak at 310 °C that is detectable in all the measurements and can be referred to Pluronic F127³⁴⁰. We assume that this new peak in the plot corresponds to the desorption and vaporization of riluzole molecules from the polymeric matrix.

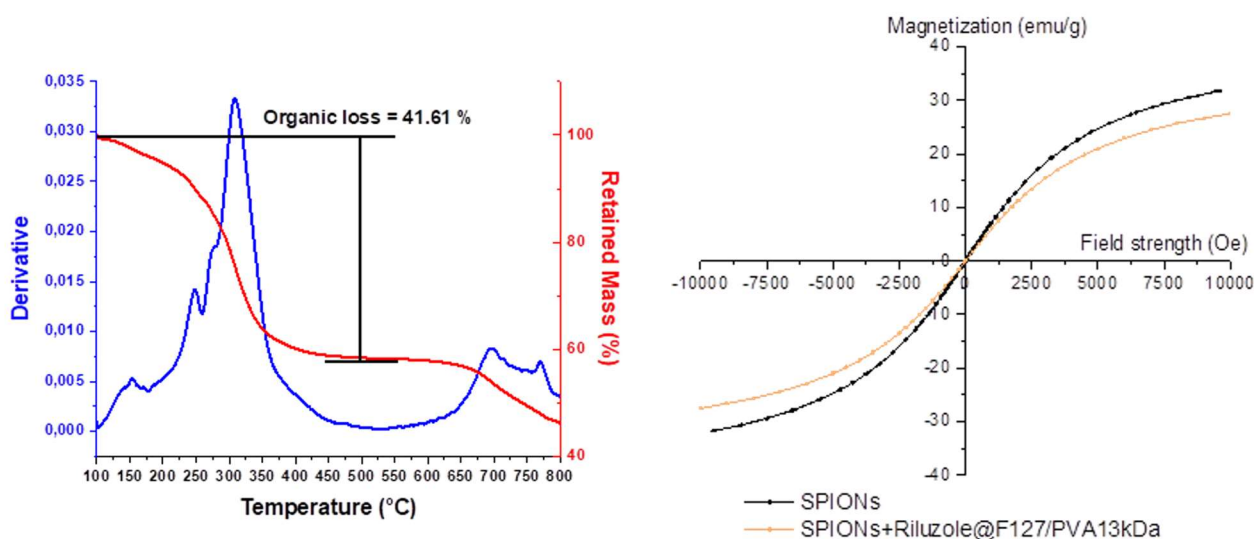


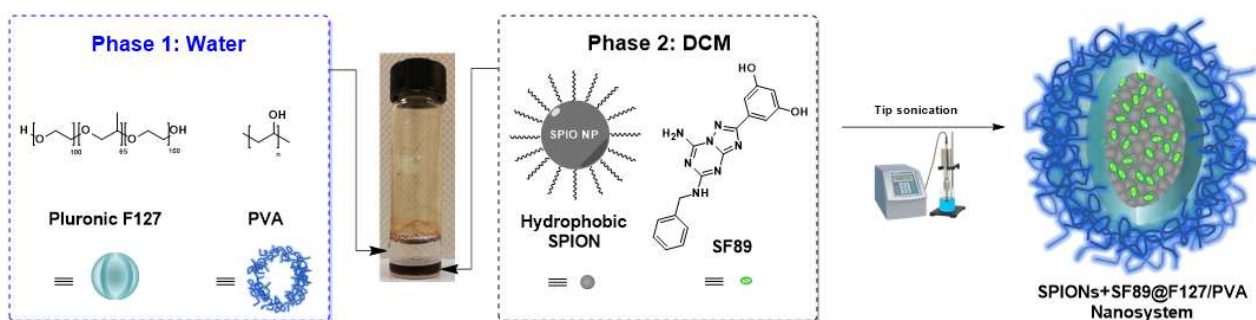
Figure 4.59: (Left) Representative TGA plot of SPIONs+Riluzole@F127/PVA13kDa sample with the derivative of the mass loss and the percentage of the mass that is retained with increasing temperatures. (Right) Magnetization vs. applied field plot showing the superparamagnetic character of (black) the pristine SPIONs and (orange) the same SPIONs encapsulated in the polymeric drug-loaded structure.

The VSM reported in **Figure 4.59** confirms that the polymeric nanosystems containing both SPIONs and riluzole are still superparamagnetic (both 0.58 Oe and remnant field of $10.5 \cdot 10^{-3}$ emu/g are low), hence apparently suitable for the application we devise. The aspect that could possibly bring an issue is the reduction of the saturation magnetization to the pristine value of 31.7 emu/g (black line) to 27.5 emu/g (orange line). A hypothesis to explain this phenomenon may regard the presence of riluzole, since it is the only difference with respect to the SPIONs@F127/PVA13kDa sample in which we noticed negligible M_s reduction. Considering the SPIONs distancing factor as a possible cause, we can imagine that the hydrophobic riluzole molecules tend to interact and – favored by the sonication treatment – being inserted between the alkyl chains that passivate SPIONs, separating them from each other. However, since we noticed from TEM images that the inorganic core still maintains a high degree of crystallinity (insert in **Figure 4.56**), what we suspect is that the major contribution to M_s decrease is the magnetite oxidation and its conversion to Fe_2O_3 .

To summarize, all the series of experiments performed for the inclusion of riluzole in the F127/PVA13kDa nanosystem started with the optimized ultrasonication approach and we focused more on the drug inclusion and sample purification. In the end, with slight variations to the dispersion approach and while maintaining almost unaltered the size with respect to the previous experiments, we obtained nanosystems with an excellent riluzole loading, which is in accordance with the increased organic content measured.

4.4.2 Assembly of the polymeric nanosystem – PVA 13kDa + F127 + SF89

Considering the encouraging results in nanosystem formation and riluzole encapsulation, we decided to move from this model molecule to the second drug adopted for the identical clinical target. The intermediate synthetic procedure employed in the previous section was maintained unaltered for the inclusion of SF89 in the same polymeric mixture (**Scheme 4.7**): both the double step of sonication and the rapid evaporation at 40 °C should let us obtain stable nanosystems properly protecting the drug payload, while reducing at the same time the risk of undesired early release. The purification steps have been also kept identical for the same reasons.



Scheme 4.7: Scheme representing the compounds and the general synthetic approach adopted for the formation of SPIONs+SF89@F127/PVA nanosystems.

The samples from this set of experiments were characterized by TEM (**Figure 4.60**) and NTA (**Figure 4.61**) to assess if the size of these nanosystems is still compatible with the biological tests and applications we foresee and to compare them with the previous nanosystems. The TEM images show a rich distribution of rounded nanosystems that had successfully included a significant amount of SPIONs even if, in accordance with the statistical data, the size distribution is slightly broad (an extreme function instead of a Gaussian one was needed to take into account the distribution tail) and two nanoparticles populations can be detected, with the major one centered at 85 nm.

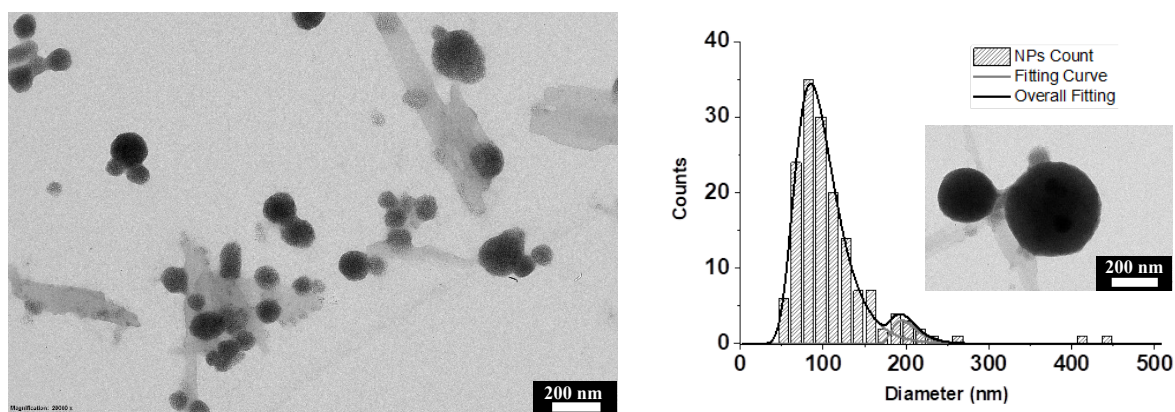


Figure 4.60: (Left) TEM image of SPIONs+SF89@F127/PVA13kDa_1 sample, showing crystal of unassembled polymer. (Right) Histogram and Gaussian fitting showing the size distribution of the inner core, with an insert showing two of the nanosystems prepared, interacting through their outer shells.

The other feature that can be observed in the images is the presence of many low-contrast crystal formations among or linking the nanosystems: we assume that they derive from the deposition of the unassembled PVA in dispersion and this suggests that the washing steps for the removal of the excess polymer should be optimized.

The same sample was subjected to NTA revealing that, regardless of the compact inorganic core, the overall hydrodynamic diameter is much larger due to the external polymer coating.

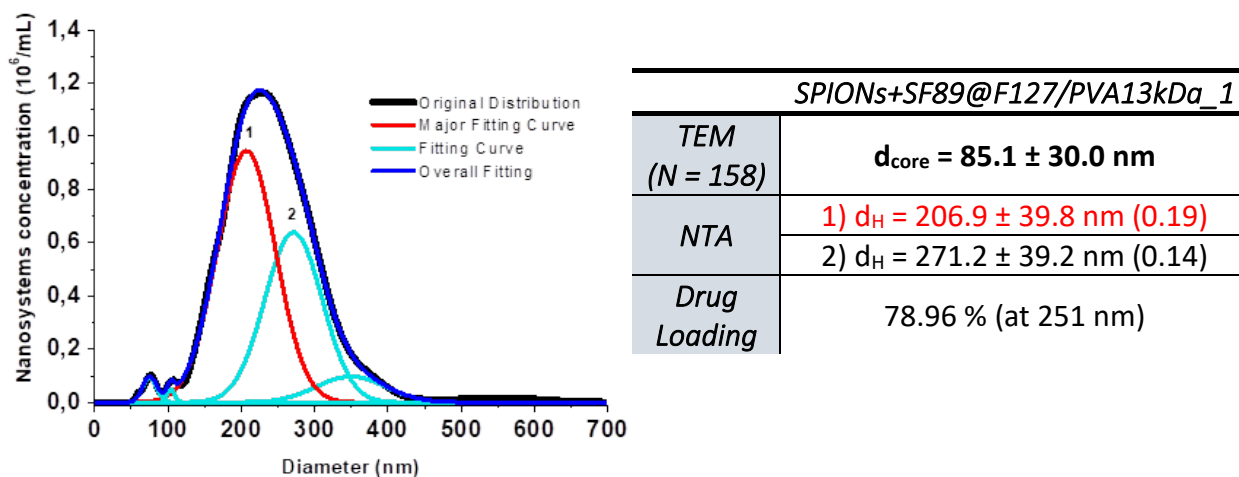


Figure 4.61: (Left) NTA analysis of SPIONs+SF89@F127/PVA13kDa_1 sample, showing the original size distribution and the following data extrapolation using Gaussian fitting. (Right) Overview of the dimensional characteristics for the principal size populations and drug loading.

However, this size is quite comparable with all the previous nanosystems prepared using the same procedure: the inclusion of SF89 within the polymeric structure does not affect in a notable way the assembly and the final dimension of the nanosystem.

To assess the amount of SF89 successfully included, we performed a UV-Vis of the supernatant solutions collected after each cycle of centrifugation, during nanosystems' purification. Notably, the supernatant has a more intense yellow shade in comparison to all the samples' supernatants obtained in the previous experiments. Initially, we recorded a series of UV-Vis spectra of SF89 in Milli-Q water, finding the characteristics absorption peaks of this molecule at 214 nm, 251 nm, and 286 nm: for each of this maximum, we plotted a calibration absorption vs. concentration curve, finding the characteristic molar absorptivity ϵ for each wavelength. On the basis of the best fitting, we decided to compare the absorbance of our sample with the SF89 reference at 251 nm, obtaining by difference a good drug loading value of 79 %. Interestingly, this heads in the opposite direction with respect to our initial idea: since SF89 is less hydrophobic than riluzole, we expected an even lower encapsulation. The explanation could be that the major part of the drug content is placed not inside the inorganic core, but in the hydrophilic shell or within the interface between the two.

Also in this case the double sonication method adopted at the end of all the previous experiments provided nanosystems with comparable hydrophobic core and hydrophilic shell size. Similar adjustment in terms of drug dispersion before the sonication guaranteed a good inclusion of SF89 molecules within the polymeric nanosystems. The difference we observed as a lower loading percentage was imputable to the different hydrophobicity of this drug, which influenced its placing in the nanosystems' compartments.

4.4.3 Assembly of the polymeric nanosystem – PVA 57kDa + F127 + Riluzole

In parallel with the experiments performed with the first polymeric mixture (PVA M_w = 13 kDa and Pluronic F127), we synthesized also the analogous nanosystem with the heavier PVA, to assess which one is the most valid alternative for the riluzole encapsulation and protection. We do not expect major changes in the size and shape of the inorganic core, since – as we already showed and demonstrated – this is mainly determined by the presence of Pluronic and its weight ratio in respect to SPIONs. What probably would change is the polymeric coating and the consequent stability of the whole nanosystem on the basis of the shell thickness and the density of the absorbed PVA that interacts with the hydrophilic layer of the Pluronic micelle.

For what concern the synthesis, the same conditions used for the different experiments in the case of SPIONs+Riluzole@F127/PVA13kDa (**Scheme 4.6**), were identically employed for this system.

The implementation of the double sonication in the procedure led also in this case to a stable turbid emulsion with no much magnetic precipitate that eventually escaped the encapsulation. Here in **Figure 4.62**, the TEM analysis on the purified sample is reported.

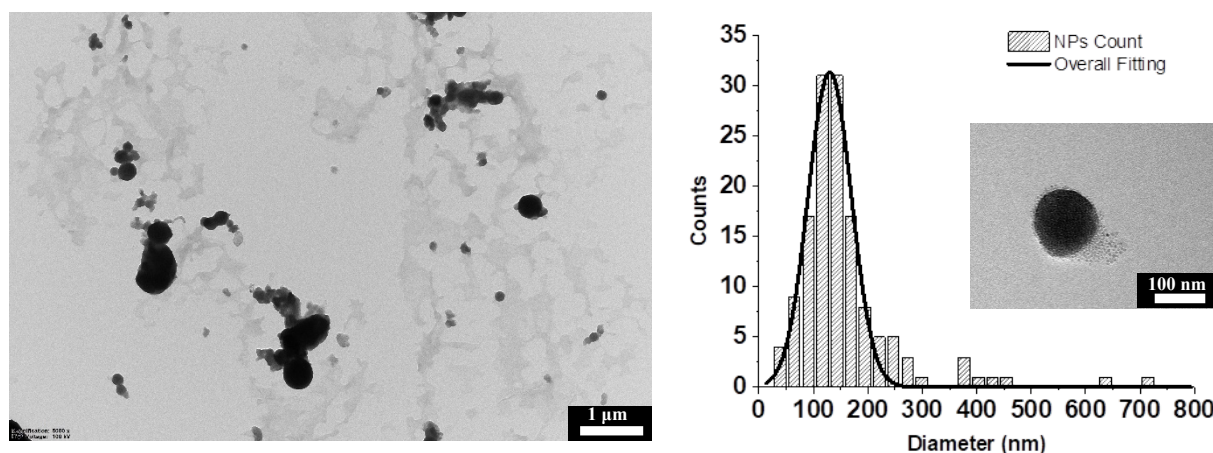


Figure 4.62: (Left) TEM image of SPIONs+Riluzole@F127/PVA57kDa_1 sample. (Right) Histogram and gaussian fitting showing the size distribution of the inner core, with an insert showing one of the nanosystems prepared, in which the outer shell can be seen fall apart a little.

Regardless of the three cycles of centrifugation and the magnetic separation, a considerable amount of unassembled polymer is visible in the grid. This may be related to strong interactions between the PVA that covers the nanosystem and the excess of PVA in dispersion, which survives the washing steps, or to the fact that some part of the coating may be released in dispersion, either following the purification or due to the dry conditions on the TEM grid. Another characteristic of this nanosystem that can be inferred from the images is that the coating could not be as tightly packed or as dense as it was for the SPIONs+Riluzole@F127/PVA13kDa nanosystem. This hypothesis comes to our mind when analyzing structures like the one in the insert in (Figure 4.62), where the SPIONs that constitute the inorganic core are protruded in one direction as if the polymeric coating that held them together was disrupted, causing their release.

However, the statistical distribution retrieved from the other images shows a good Gaussian distribution centered at 130 nm with only some bigger species around 400 nm.

The NTA performed on the sample to retrieve the hydrodynamic diameter showed the presence of two major overlapped populations, the principal centered at 175 nm and moderately broad. Also in this case we observe some small assemble of free polymer chains below 100 nm.

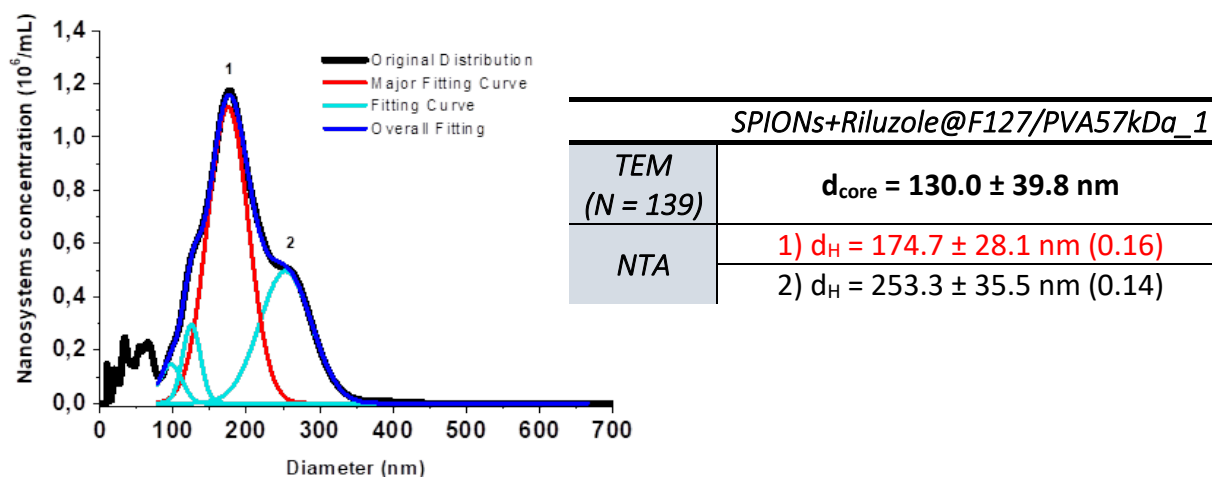


Figure 4.63: (Left) NTA analysis of SPIONs+Riluzole@F127/PVA57kDa_1 sample, showing the original size distribution and the following data extrapolation using Gaussian fitting. (Right) Dimensional characteristics overview for the principal size populations.

In contrast with the usual trend, the shell thickness that can be calculated (22 nm) is very similar to the one obtained for the similar nanosystem with PVA 13 kDa (24 nm).

At this point, also the nanosystem SPIONs+Riluzole@F127/PVA57kDa was tested for physiological compatibility, being synthesized in Milli-Q water and successively redispersed in PBS. The result was analyzed firstly with TEM, which gave the images and distribution showed in Figure 4.64.

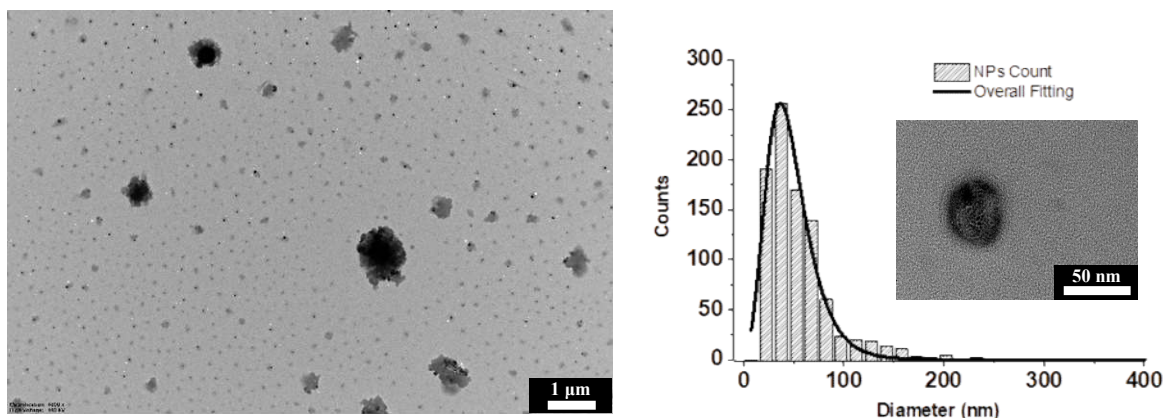


Figure 4.64: (Left) TEM image of SPIONs+Riluzole@F127/PVA57kDa_2 sample re-dispersed in PBS. (Right) Histogram and Extreme fitting showing the size distribution of the inner core, with an insert showing one of the nanosystems prepared, in which the SPIONs in the core are less distinguishable.

The nanosystems that can be detected in the images are similar in shape to the ones in SPIONs+Riluzole@F127/PVA13kDa_2 but completely different from all the other analyzed. The most relevant feature is the average diameter of the inorganic core, with a tailed distribution centered at 37 nm which is even half the already small one calculated for the analogous nanosystems with 13 kDa PVA. Observing more in detail each of these nanosystems, we see that the major part of them has a dark core similar to the other experiments, but with less distinguishable internal SPIONs (insert in **Figure 4.64**), while some others present a very poor contrast. This last feature leads us to suspect that the inorganic content may be scarce or even absent in some of them, which are practically only void polymeric assemble or polymeric structures containing only riluzole molecules (as the crystallization of some cores may indicate). However, regardless of the dry conditions, there are very few aggregates and the nanosystems are well-separated, as was observed in the previous try.

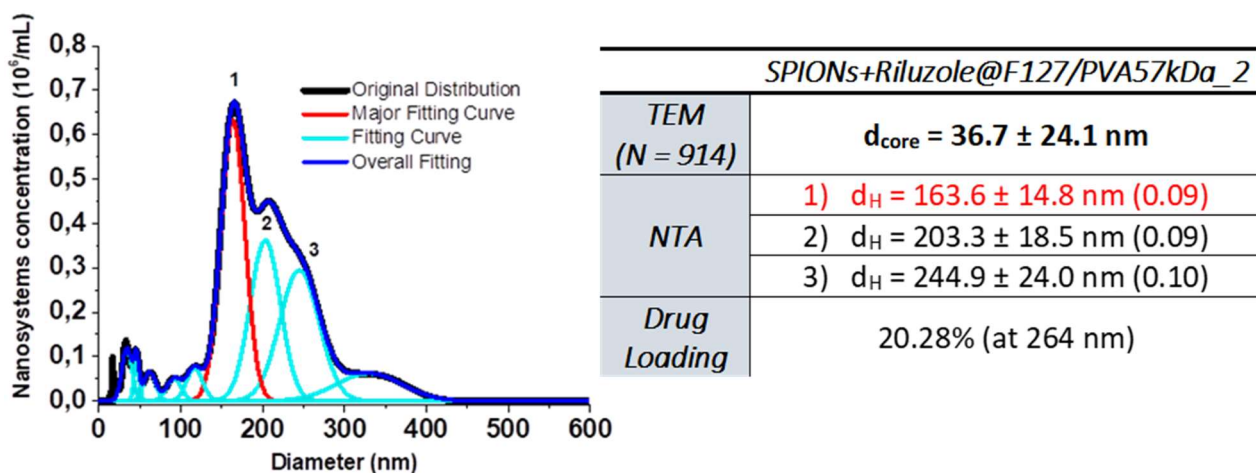


Figure 4.65: (Left) NTA analysis of SPIONs+Riluzole@F127/PVA57kDa_2 sample, showing the original size distribution and the populations extrapolation using Gaussian fitting. (Right) Dimensional characteristics overview for the principal size populations.

We submitted the same sample also to the NTA (**Figure 4.65**), which revealed the presence of three major overlapped populations centered at 164 nm, 203 nm, and 245 nm. By comparison with the SPIONs+Riluzole@F127/PVA13kDa_2 sample, we find a similar trend, but here the overall hydrodynamic diameter is slightly bigger and mostly the shell is much thicker, as could be already assumed by the TEM images.

Finally, we assessed the drug loading of these nanosystems exploiting UV-Vis spectroscopy and the same calibration line we calculated previously. Focusing on the absorbance detected at 264 nm, we estimated a drug loading percentage of 20 %, which is still low, but more than the riluzole content encapsulated in the Pluronic-PVA13 kDa mixture.

Considering these results, before starting with the biological tests, it would be necessary to optimize further the procedure for the nanosystems' preparation in order to convey adequate stability not only in water, but also once they are redispersed in PBS, verifying that this solvent is not detrimental for polymeric shell integrity even worse than in the SPIONs+Riluzole@F127/PVA13kDa_2 case.

The procedure we devised to better emulsify the organic phase containing SPIONs and riluzole and the aqueous phase in which the two polymers are separately dissolved, was used to prepare the next set of SPIONs+Riluzole@F127/PVA57kDa nanosystems. It gave promising results, starting from the appearance of the emulsion, a homogeneous dark brown-grey phase.

TEM was the primary technique used to control the outcome of the synthesis: in the images recorded (**Figure 4.66**), we observed rounded nanosystem definitely more homogeneous in their appearance than all the samples in the previous experiments. However, we also noted the enhanced tendency to agglomerate in big clusters of nanosystems once the solvent is removed, even if each of them maintains its shape and is still clearly distinguishable from the others. The statistical analysis of the core diameters was performed with symmetric a Gaussian fitting, which resulted in an even size distribution of inorganic core centered at 155 nm, therefore bigger than all the rest of the nanosystems characterized so far.

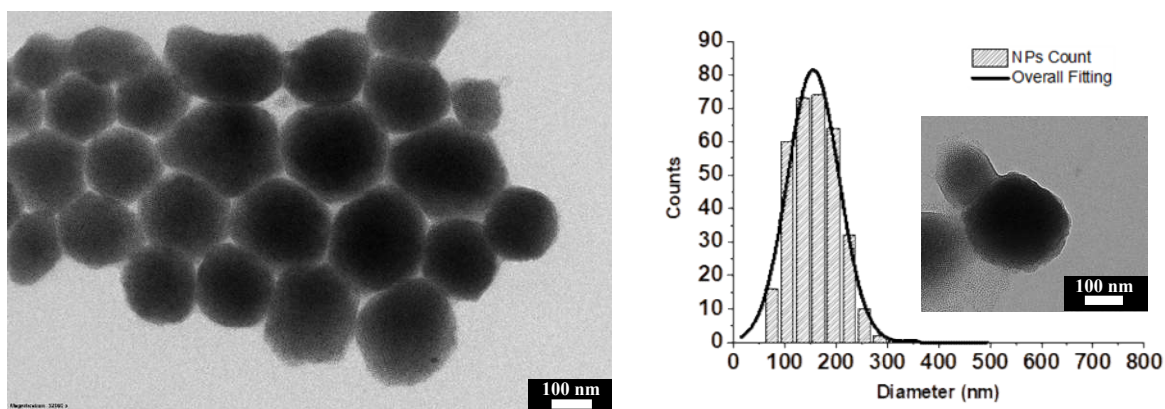


Figure 4.66: (Left) TEM image of SPIONs+Riluzole@F127/PVA57kDa_3 sample. (Right) Histogram and Gaussian fitting showing the size distribution of the inner core, with an insert showing one of the nanosystems prepared.

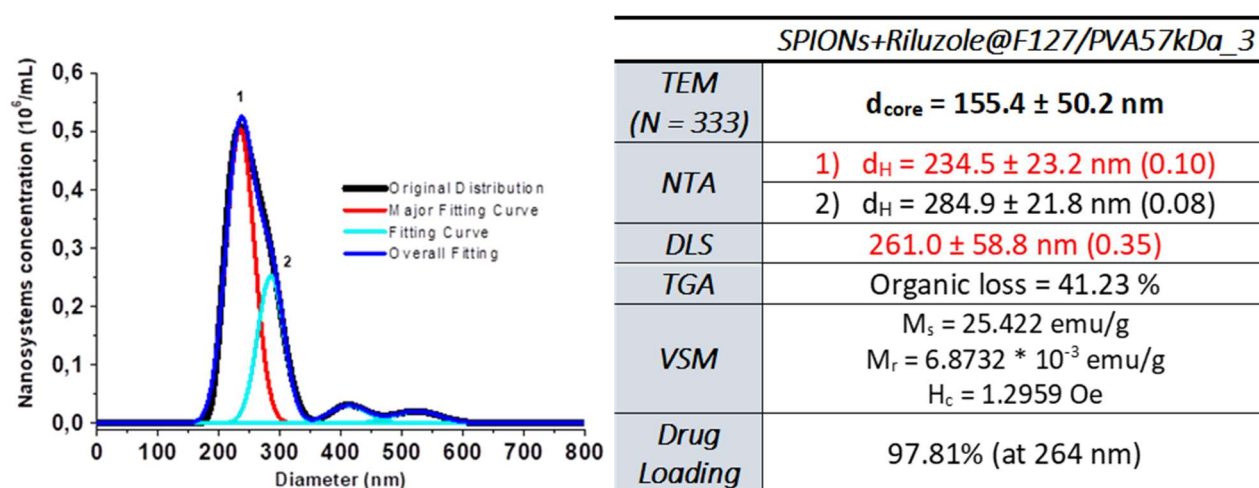


Figure 4.67: (Left) NTA analysis of SPIONs+Riluzole@F127/PVA57kDa_3 sample, showing the original size distribution and the populations extrapolation using Gaussian fitting. (Right) Overview of the dimensional characteristics for the principal size populations, organic content, magnetic properties, and drug loading.

These data can be compared with the results of the NTA, from which we detected few populations, even if they are partially overlapped and the dispersion is significant. Moreover, the hydrodynamic diameter is overall bigger than the previous cases and there are some small aggregates above 400 nm and 500 nm. Considering the polymeric shell, the thickness that can be calculated by operating the difference between the core diameter and the principal hydrodynamic one is around 40 nm in dispersion, once again one of the thicker ever obtained in this syntheses.

To conclude the size characterization, we performed some DLS measurements (**Figure 4.68**) of the sample, obtaining a single distribution, but less broad and polydisperse in respect to the majority of the previous outcomes regarding this particular nanosystem. Even if this structure resulted as one of the largest prepared and the standard deviation is wide, the average hydrodynamic diameter reached is still within the confidence range for biological applications.

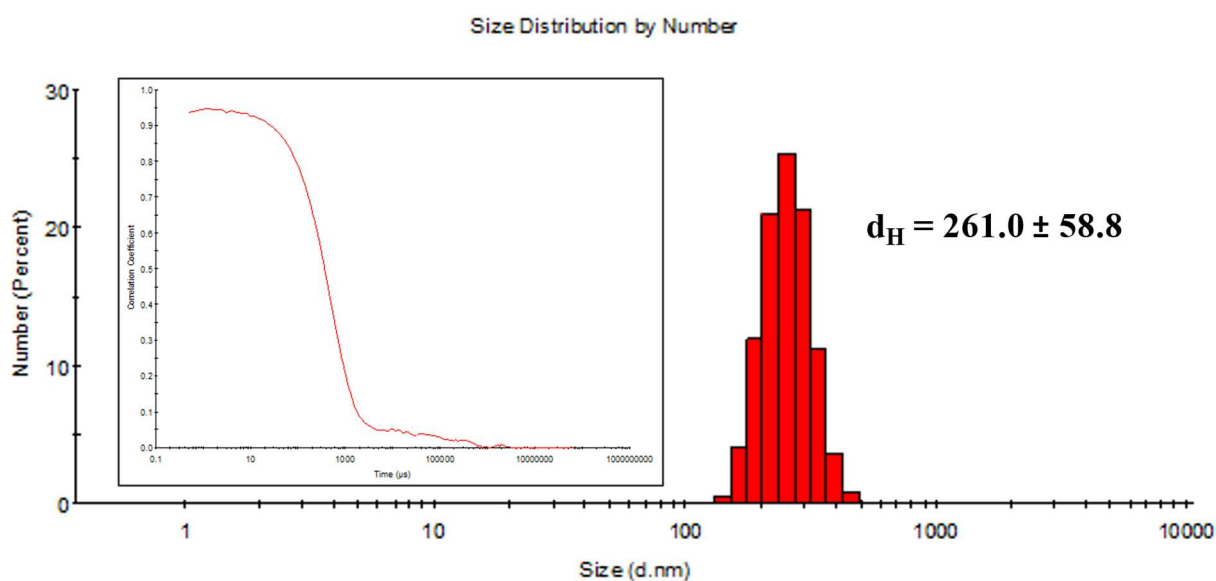


Figure 4.68: DLS analysis of the SPIONs+Riluzole@F127/PVA57kDa_3 sample with the size distribution by number of nanoparticles extrapolated from it and (Insert) the related correlogram.

Also in this case we relied on the riluzole's calibration line at 264 nm for the assessment of the drug loading. The elaboration of the UV-Vis spectra of the yellow supernatant we recorded, gave us a very high percentage of 98 %. The similarity between riluzole inclusion percentages for this sample and the analogous SPIONs+Riluzole@F127/PVA13kDa_3, at a particular fixed synthetic procedure, indicates that the unaltered inner compartment of each nanosystem is the one responsible for the drug payload complexation and protection, regardless of the different external PVA adopted. In addition, the high loading could be also the result of a quick and efficient purification stage, which allowed us to lose the least quantity of riluzole in dispersion that was possible.

The other method by which we can assess the effective riluzole loading inside the nanosystem is the TGA (**Figure 4.69**): it gave an organic loss value of 41.2 %, which is very similar to the 41.6 % of SPIONs+Riluzole@F127/PVA13kDa_3. Based on the previous UV-Vis measurement and considering that we used the same amount of riluzole at the start of the synthesis, if we assume that the percentage of drug molecules encapsulated in SPIONs+Riluzole@F127/PVA13kDa_3 and the present SPIONs+Riluzole@F127/PVA57kDa_3 is the same (above 97 %), then we could conclude that the mass percentage of the polymer is similar, but since PVA 57kDa weights more, we expect to have fewer chains that stabilize the Pluronic micelle and constitute the real outer shell. This could be also the explanation for the smaller hydrodynamic diameter observed in the majority of experiments, with respect to the samples containing PVA 13kDa. Furthermore, the number, position, and shape of the peaks detected in the previous measurement and assigned to the different organic species, are well-preserved and present also in this plot with the characteristic riluzole maximum that appears between PVA and Pluronic maxima.

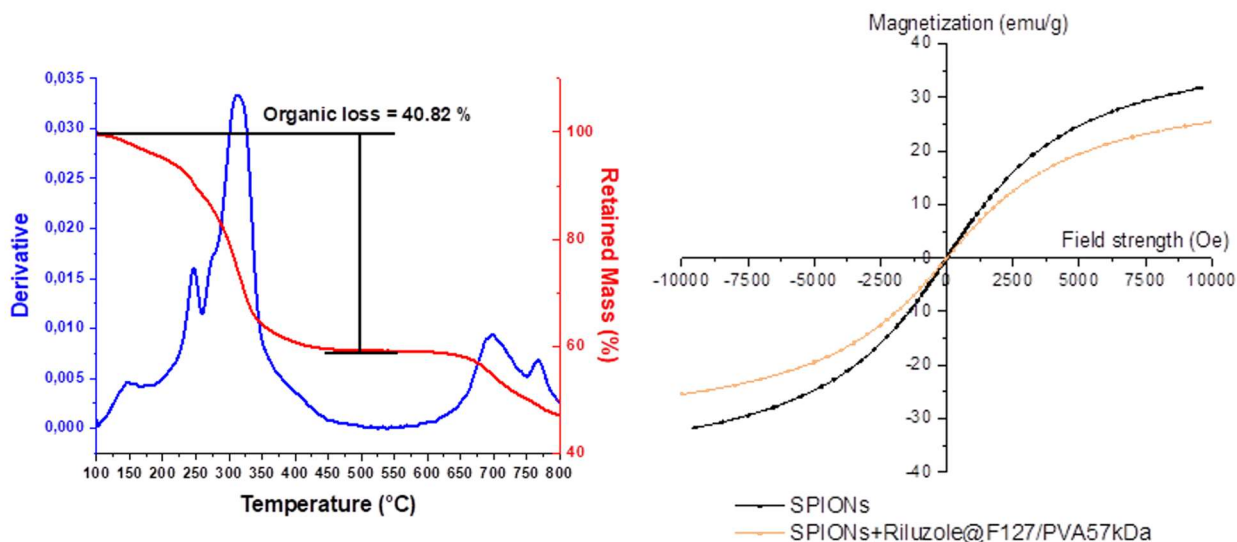


Figure 4.69: (Left) Representative TGA plot of SPIONs+Riluzole@F127/PVA57kDa sample with the derivative of the mass loss and the percentage of the mass that is retained with increasing temperatures. (Right) Magnetization vs. applied field plot showing the superparamagnetic character of (black) the pristine SPIONs and (orange) the same SPIONs encapsulated in the polymeric drug-loaded structure.

Finally, also for this sample, we have measured the magnetization vs. applied field plot (orange line in the plot on the right of **Figure 4.69**) to extrapolate the principal magnetic properties and compare them with the pristine dispersion of SPIONs (black line). The superparamagnetic behavior has been maintained, as the low coercivity of 1.3 Oe and the low remnant field of $6.9 \cdot 10^{-3}$ emu/g demonstrate. However, also in this case we observed a decrease in saturation magnetization from 31.7 emu/g of the SPIONs reference, to 25.4 emu/g. This may be explainable as a concurrent effect of the use of PVA 57 kDa – which stabilizes but separates and exposes the magnetic nanoparticles – and the presence of riluzole molecules that interact with the SPIONs organic layer, hampering the clusterization.

Summing up the experimental results in the assembly and loading of this nanosystem, we achieved and were able to reproduce the nanosystems' assembly and progressively increase the riluzole loading inside them. However, comparing the data with the previous SPIONs+Riluzole@F127/PVA13kDa case, we observed a noticeable increase also in the size of the whole structure which could compromise its biological application. Therefore, for riluzole loading, the nanosystem covered with the lighter PVA is preferred.

4.4.4 Assembly of the polymeric nanosystem – PVA 57kDa + F127 + SF89

The same procedure adopted for SPIONs+Riluzole@F127/PVA57kDa_2 was proposed again with the same assembly and purification steps for the inclusion of SF89, counting on the promising loading percentage obtained for the SPIONs+S89@F127/PVA13kDa_1.

We first characterized these nanosystems by TEM to assess any difference in respect to the previous experiments. An example of the taken TEM images and the deconvolution of the diameter distribution measured are presented in **Figure 4.70**.

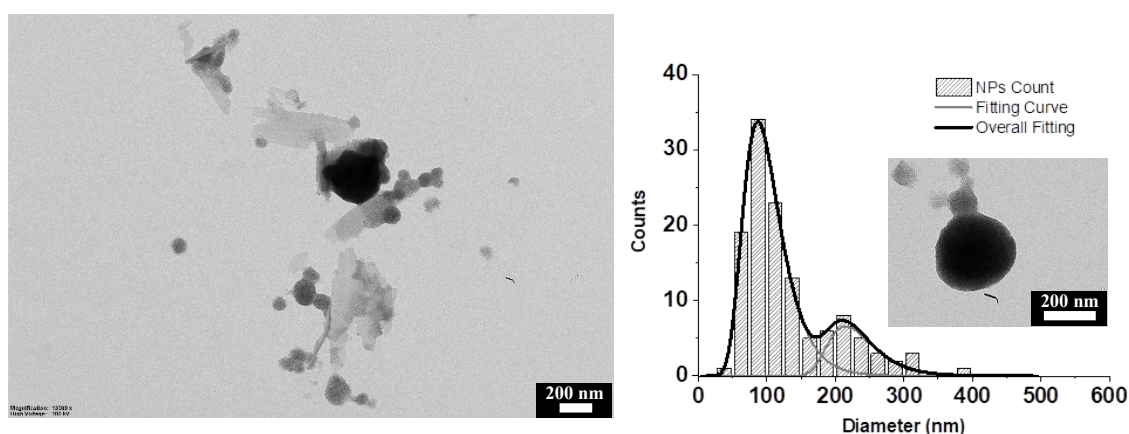


Figure 4.70: (Left) TEM image of SPIONs+SF89@F127/PVA13kDa_1 sample, showing some crystallized unassembled polymer chains. (Right) Histogram and Gaussian fitting showing the size distribution of the inner core, with an insert showing one of the nanosystems prepared.

Unfortunately, the presence of two different size populations that were visible in SPIONs+S89@F127/PVA13kDa_3 is even more marked here: considering almost the same amount of detected nanosystems and the same type of fitting curve, the distribution at 215 nm comprises more elements than the one at 195 nm in the analogous case. However, the major distribution is still found in the 85 - 90 nm range. From the images, it seems that the external coating is more loosely packed around the inorganic cluster and tends to spread more once the water evaporates. This may imply a problem for what concerns the protection of the magnetic and drug payload and the delayed release we seek.

The NTA performed on this sample and showed in **Figure 4.71** confirmed the high dispersity and the multiple populations detected in the TEM images. Possibly, the three major distributions between 139 nm and 230 nm are all related to the major distribution at 87 nm observed with TEM, while the broad population above 300 nm is associated with the one centered at 215 nm in the TEM analysis plot.

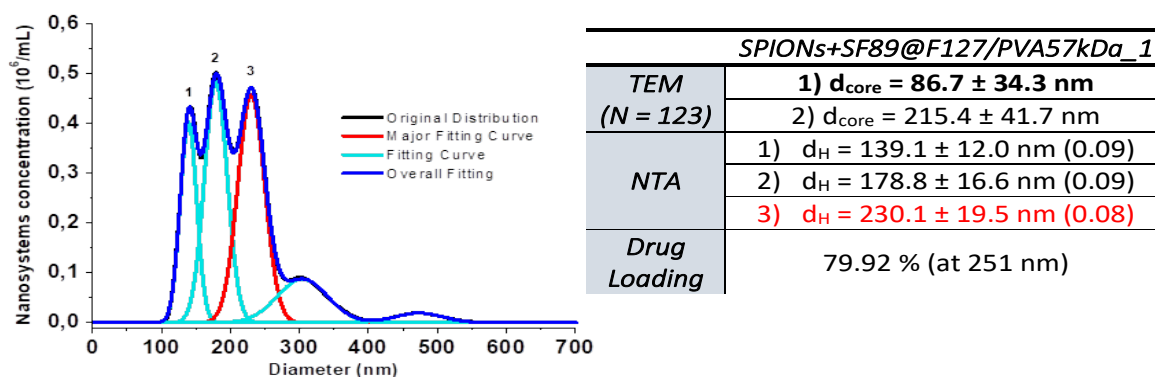


Figure 4.71: (Left) NTA analysis of SPIONs+SF89@F127/PVA57kDa_1 sample, showing the original size distribution and the following data extrapolation using Gaussian fitting. (Right) Overview of the dimensional characteristics for the principal size populations and drug loading.

Overall, the trend highlighted in all the previous cases according to which the hydrodynamic diameter of the nanosystems is smaller when using 57 kDa PVA instead of 13 kDa PVA is also found for this particular nanosystem.

Likewise, the similar experiments, the percentage of SF89 included in the nanosystems in respect to the initial amount used during the synthesis was calculated based on UV-Vis spectra of the yellow supernatant dispersions and the same calibration curve related to the maximum at 251 nm. The result gave a drug loading of 80 %, which is almost identical to the inclusion calculated for SPIONs+SF89@F127/PVA13kDa_1. This fact led us to suspect that the encapsulation does not actually depend on the type of PVA used, which we expected to be an important factor for both the mechanism and the time of the release. Therefore, the encapsulation depends only on the efficient interactions between drug molecules and the hydrophobic portions of SPIONs' coating and Pluronic's intermediate block, species that in fact remained the same for both the experiments, also in terms of quantities and relative weight ratios.

In conclusion, employing the same optimized procedure for the preparation of the polymeric nanosystem, we were able to encapsulate a considerable amount of SPIONs and SF89 molecules within its structure. Despite the greater number of different populations, the nanosystem that resulted the best for SF89 loading was the one covered by the PVA with higher molecular weight.

5.1 GENERAL INFORMATION

All reagents employed were bought from Merck and Alfa Aesar and used without purification, unless where indicated. Solvents were purchased from Merck and VWR. All the glassware employed for the synthesis of SPIONs and polymeric nanosystems was cleaned with aqua regia and copiously rinsed with Milli-Q water before use.

Transmission Electron Microscopy images were collected by means of a Philips EM 208 Electron Microscope operating at 100 kV equipped with 11 MegaPixel bottom-mounted CCD Olympus Quemesa camera by Dr. Paolo Bertocin or Dr. Paolo Pengo at the University of Trieste. Samples for TEM were prepared employing carbon-coated 200 Mesh copper grids and depositing 5 μl of the sample. All TEM images were analyzed through ImageJ software.

X-Ray Absorption Near-Edge Structure spectra were recorded at the SOLEIL synchrotron in Saint-Aubin, France by Prof. Tiziano Montini of the University of Trieste, Italy.

Thermogravimetric Analyses were carried out on a TA instrument TGA Q-500 using platinum pans and with a heating rate of $10\text{ }^{\circ}\text{C}\cdot\text{min}^{-1}$ up to $830\text{ }^{\circ}\text{C}$, previous equilibration at $100\text{ }^{\circ}\text{C}$ for 20 minutes and recorded by Prof. Tatiana Da Ros at the Department of Chemical and Pharmaceutical Sciences of the University of Trieste, Italy.

Vibrating Sample Magnetometry measurements were performed on a Lake Shore 7307 VSM at room temperature ($25\text{ }^{\circ}\text{C}$) and recorded by Dr. Slavko Kralj at the Department for Materials Synthesis of the Jožef Stefan Institute in Ljubljana, Slovenia.

Nanoparticle Tracking Analyses were performed on NanoSight LM10 (NanoSight Ltd, UK) equipped with a 20 mW red laser operating at 655 nm, a Marlin F-033B ASG CCD Camera (Allied Vision Technologies GmbH, Germany), and a PL L 20/0.40 objective. The video data were collected for 60 seconds (1800 frames) and processed through NanoSight NTA software vers. 2.0.

Dynamic Light Scattering analyses were carried out on a Malvern Zetasizer Nano ZS ZEN3600 (Malvern Instruments, Worcestershire, UK) equipped with a 4 mW He-Ne red laser operating at 632.8 nm and a scattering detector at 173° , using disposable polyethylene cuvettes whose optical path was 10 mm. The data were processed employing Zetasizer Software version 8.00.4813.

UV-Visible spectroscopy analyses were carried out on a Perkin Elmer Lambda 35 spectrophotometer having a scanning speed of $240\text{ nm}\cdot\text{min}^{-1}$ and a slit amplitude of 2 nm, or on a Shimadzu UV-2450 having a scanning speed of $210\text{ nm}\cdot\text{min}^{-1}$ and a slit amplitude of 2 nm, using quartz cuvettes with an optical path of 10 mm.

5.2 SYNTHESIS OF SPIONS

Synthesis of SPIONs with hydrothermal synthesis and microwave heating

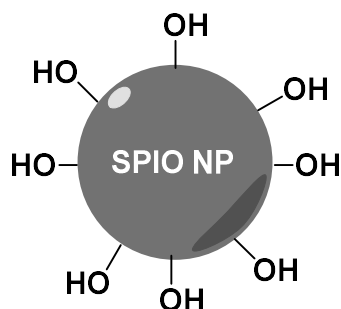


Figure 5.1: Graphical representation of a hydrophilic “naked” SPION, presenting only hydroxyl groups on its surface.

Ferric chloride (quantities in **Table 5.1**) was dissolved in water (2.5 mL) in a 10 mL microwave glass reactor vessel, then hydrazine monohydrate (0.33 mL, 6.79 mmol) was added at room temperature causing the solution to become immediately orange or brown-orange. The mixture was then shaken and heated by microwave without stirring and different reaction times and temperatures were explored. In the end, the black magnetic product was washed with water (5 x 5 mL): between each cycle, the solution is sonicated for several seconds then centrifuged (6000 rpm at 20 °C for 10 minutes with 15 cm rotor). Finally, the mixture is freeze-dried to obtain a black magnetic powder. The specific synthetic conditions employed for the relevant trials are reported in **Table 5.1**.

Table 5.1: Reaction conditions used for the preparation of SPIONs with hydrothermal synthesis and microwave heating. The bold font indicates the significant variation between different representative experiments.

Run	$FeCl_3$ (mg)	$N_2H_4 \cdot H_2O$ (mL)	H_2O (mL)	Time (min)	Temperature (°C)	Final mass (mg)
1	15.1	0.33 (1:70)	2.5	10	100	7.2
2	15.3	0.33 (1:70)	2.5	20	100	0.6
3	15.0	0.33 (1:70)	2.5	10	200	6.7
4	11.11	0.33 (1:100)	2.5	10	100	5.4
$FeCl_3 \cdot 6 H_2O$ (mg)						
5	30.6	0.220 (1:40)	2.5	10	100	9.1
6	30.2	0.380 (1:70)	2.5	10	100	8.6
7	30.9	0.555 (1:100)	2.5	10	100	9.6

All the samples have been analyzed using TEM and some representative images are presented in the previous relative subchapter, but neither of the samples met the desired characteristics.

Synthesis of SPIONs with thermal decomposition and conventional heating

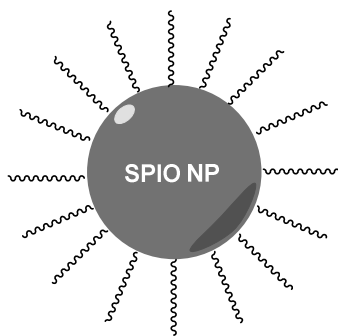


Figure 5.2: Graphical representation of a hydrophobic SPION, coated and passivated by alkyl chains on its surface.

In a round bottom flask, iron(III) acetylacetonate (300.0 mg, 0.824 mmol), 1,2-hexadecanediol (1.10 g, 4.25 mmol), oleic acid (719.8 mg, 2.55 mmol) and oleylamine (681.7 mg, 2.55 mmol) were inserted in this precise order and dispersed in diphenyl ether (8.60 mL). The red-brown solution was magnetically stirred under a flow of argon and then firstly heated at 200 °C for 30 minutes. The solution was then heated to reflux at 265 °C for 30 minutes always under a blanket of argon.

In the end, the mixture was cooled down and EtOH (40 mL) was added to promote nanoparticles precipitation. The sample is then purified by centrifugation (4200 rpm at 15 °C for 10 minutes) and the supernatant solution was removed. The black product was dispersed in hexane (10 mL) in presence of oleic acid (~ 0.05 mL) and oleylamine (~ 0.05 mL). The dispersion was centrifuged again (4200 rpm at 15 °C for 10 minutes) to remove any undispersed residue and the nanoparticles were re-precipitated with EtOH (20 mL). The sample was centrifuged again (4200 rpm at 15 °C for 10 minutes), the supernatant removed and the black product dispersed again in hexane (10 mL).

TEM (hexane): $d_{\text{core}} = 3.22 \pm 1.04$ nm ($\sigma^* = 0.324$); Extreme fitting; over 800 NPs.

Synthesis of SPIONs with thermal decomposition and microwave heating

Iron(III) acetylacetonate ($\text{Fe}(\text{acac})_3$, 500.0 mg, 1.42 mmol), 1,2-hexadecanediol (1,2-C16OH, 1.83 g, 7.08 mmol), oleic acid (C18COOH, 1.23 g, 4.25 mmol), and oleylamine (C18NH₂, 1.14 g, 4.25 mmol) were inserted in a 30 mL microwave tube in this precise order and dispersed in diphenyl ether (Ph₂O, 10 mL) to form a dark red solution. The mixture was deoxygenated for 15 minutes with a constant bubbling of argon, then heated in a microwave instrument firstly at 200 °C for 30 minutes, then at 250 °C for another 30 minutes, always under magnetic stirring (800 rpm).

In the end, the mixture was cooled down, divided into two aliquots, and deoxygenated EtOH (20 mL in each) was added to promote nanoparticles precipitation. The samples were then purified by

centrifugation (4200 rpm at 15 °C for 10 minutes) and the supernatant solution was removed. The black products were dispersed in deoxygenated hexane (10 mL for each aliquot) in presence of oleic acid (~ 0.05 mL) and oleylamine (~ 0.05 mL). The dispersions were centrifuged again (4200 rpm at 15 °C for 10 minutes) to remove any undispersed residue and the nanoparticles were partially dried under a flow of argon and re-precipitated with deoxygenated EtOH (10 mL in each). The samples were finally centrifuged (4500 rpm at 15 °C for 10 minutes), the supernatant was removed and the black product dried under vacuum and stored under argon atmosphere.

Table 5.2: Reaction conditions used for the preparation of SPIONs with thermal decomposition method and microwave heating. The bold font indicates the significant variation between different representative experiments.

Run	<i>Fe(acac)₃</i> (mg)	<i>1,2-C16OH</i> (mg)	<i>C18COOH</i> (mg)	<i>C18NH₂</i> (mg)	Ph ₂ O (mL)	Deox.	Heating ramp	Final mass (mg)
1	100.0	365.9	239.9	227.2	2.86	NO	200 °C for 30 min 265 °C for 30 min	60.8
2	150.0	548.8	359.9	340.8	3.0	YES	200 °C for 30 min 265 °C for 30 min	53.1
3	500.0	1830.0	1200.0	1140.0	10.0	YES	200 °C for 30 min 265 °C for 30 min	194.7

- *SPIONs_1*

TEM (hexane): $d_{\text{core}} = 3.88 \pm 0.78$ nm ($\sigma^* = 0.201$); Gaussian fitting; over 850 NPs.

- *SPIONs_2*

TEM (hexane): $d_{\text{core}} = 4.05 \pm 0.97$ nm ($\sigma^* = 0.238$); Gaussian fitting; over 550 NPs.

XANES: LCF based on the reference spectra gave Fe₃O₄ = 90 % (± 5 %), Fe₂O₃ = 10 % (± 5 %) and a negligible percentage of FeO.

- *SPIONs_3*

TEM (hexane): $d_{\text{core}} = 3.47 \pm 0.66$ nm ($\sigma^* = 0.190$); Gaussian fitting; over 450 NPs.

TGA: organic loss = 33.48 %; $T_{\text{max}} = 325$ °C.

VSM: $M_s = 31.748$ emu/g; $M_r = 1.7561 \cdot 10^{-3}$ emu/g; $H_c = 0.22790$ Oe.

5.3 ASSEMBLY OF THE POLYMERIC STRUCTURE AND SPIONS LOADING

Assembly of the polymeric structure using PVA with Mw = 13 kDa

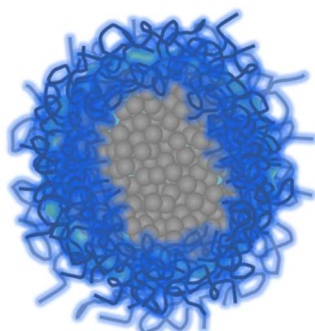


Figure 5.3: Graphical representation of SPIONs (grey spheres) included in a polymeric coating of PVA (blue coils).

Two dispersions were prepared by dissolving PVA 13kDa (20.0 mg) in Milli-Q H₂O (1 mL) and SPIO NPs (quantities in **Table 5.3**) in an appropriate organic solvent. The two dispersions were poured in a vial and the resulting two phases were emulsified with a tip ultrasonicator for 1 minute. At the end of the sonication, the organic solvent was removed by slow evaporation under stirring and the resulting products were purified through several steps of centrifugation or sedimentation, discarding the supernatant dispersion. The precise quantities and operating conditions used in the representative experiments performed are reported in **Table 5.3**.

Table 5.3: Reaction conditions used for the preparation and purification of SPIONs@PVA13kDa nanosystems. The bold font indicates the significant variation between different representative experiments.

<i>Run</i>	<i>SPIONs (mg)</i>	<i>DCM (mL)</i>	<i>PVA 13kDa (mg)</i>	<i>H₂O (mL)</i>	<i>Sonication</i>	<i>Evaporation</i>	<i>Purification</i>
1	8.0	0.4*	20.0	1.0	RT, 1 min, 150 W	60 °C, 5 h	Centrifugation 8500 rpm, 10 min, 20 °C (x3)
2C	8.0	0.4*	20.0	1.0	RT, 1 min, 150 W	60 °C, 5 h	Centrifugation 8500 rpm, 1 min, 20 °C (x3)
2D							Magnetic decantation, washed with H₂O (x3)
3	4.0	0.2	20.0	1.0	RT, 1 min, 150 W	RT, 3 h	Centrifugation 8500 rpm, 1 min, 20 °C (x3)
4	4.0	0.2	20.0	1.0	RT, 1 min, 150 W	RT, 1 h	Centrifugation 8500 rpm, 1 min, 20 °C (x2)
4B	/	/	20.0	1.0	RT, 1 min, 150 W	RT, 1 h	Centrifugation 8500 rpm, 1 min, 20 °C (x2)

*CHCl₃ instead of DCM.

- ***SPIONs@PVA13kDa_1***

Precipitated

NTA (Milli-Q H₂O): $d_H^1 = 42.9 \pm 3.9$ nm ($\sigma^* = 0.091$) (0.6 %), $d_H^2 = 58.5 \pm 4.5$ nm ($\sigma^* = 0.076$) (0.9 %), $d_H^3 = 72.7 \pm 12.8$ nm ($\sigma^* = 0.175$) (2.8 %), $d_H^4 = 128.5 \pm 12.8$ nm ($\sigma^* = 0.100$) (2.9 %), **$d_H^5 = 248.9 \pm 40.5$ nm ($\sigma^* = 0.163$) (53.6 %)**, **$d_H^6 = 302.3 \pm 26.4$ nm ($\sigma^* = 0.087$) (31.7 %)**, $d_H^7 = 418.8 \pm 42.3$ nm ($\sigma^* = 0.101$) (7.4 %); Gaussian fitting; $1.64 \cdot 10^8$ NPs/mL.

Supernatant

TEM (Milli-Q H₂O): $d_{core} = 71.4 \pm 48.1$ nm; Gaussian fitting; 23 NPs.

NTA (Milli-Q H₂O): $d_H^1 = 53.3 \pm 2.8$ nm ($\sigma^* = 0.053$) (0.1 %), $d_H^2 = 71.1 \pm 4.0$ nm ($\sigma^* = 0.056$) (0.1 %), $d_H^3 = 101.7 \pm 7.3$ nm ($\sigma^* = 0.072$) (0.4 %), **$d_H^4 = 217.2 \pm 33.2$ nm ($\sigma^* = 0.153$) (99.4 %)**; Gaussian fitting; $2.33 \cdot 10^8$ NPs/mL.

- ***SPIONs@PVA13kDa_2***

Centrifuged (2C)

NTA (Milli-Q H₂O): $d_H^1 = 32.9 \pm 1.2$ nm ($\sigma^* = 0.036$) (0.2 %), $d_H^2 = 37.1 \pm 5.8$ nm ($\sigma^* = 0.157$) (1.4 %), $d_H^3 = 53.2 \pm 2.9$ nm ($\sigma^* = 0.055$) (0.9 %); $d_H^4 = 70.0 \pm 3.2$ nm ($\sigma^* = 0.045$) (0.4 %), $d_H^5 = 79.0 \pm 10.0$ nm ($\sigma^* = 0.127$) (4.3 %), $d_H^6 = 126.5 \pm 19.0$ nm ($\sigma^* = 0.150$) (7.3 %), **$d_H^7 = 162.2 \pm 11.0$ nm ($\sigma^* = 0.068$) (18.5 %)**, **$d_H^8 = 195.2 \pm 29.9$ nm ($\sigma^* = 0.153$) (34.6 %)**, **$d_H^9 = 292.3 \pm 26.7$ nm ($\sigma^* = 0.092$) (19.0 %)**, $d_H^{10} = 409.7 \pm 38.5$ nm ($\sigma^* = 0.094$) (13.4 %); Gaussian fitting; $2.28 \cdot 10^7$ NPs/mL.

Decanted (2D)

NTA (Milli-Q H₂O): $d_H^1 = 56.9 \pm 3.1$ nm ($\sigma^* = 0.055$) (0.2 %), $d_H^2 = 87.3 \pm 9.6$ nm ($\sigma^* = 0.110$) (2.6 %), $d_H^3 = 124.9 \pm 9.3$ nm ($\sigma^* = 0.075$) (4.2 %), **$d_H^4 = 198.4 \pm 14.8$ nm ($\sigma^* = 0.075$) (15.1 %)**, **$d_H^5 = 271.7 \pm 27.3$ nm ($\sigma^* = 0.100$) (46.2 %)**, **$d_H^6 = 392.3 \pm 33.8$ nm ($\sigma^* = 0.086$) (31.6 %)**; Gaussian fitting; $9.8 \cdot 10^7$ NPs/mL.

- ***SPIONs@PVA13kDa_3***

TEM (Milli-Q H₂O): $d_{core} = 54.0 \pm 21.7$ nm; Gaussian fitting; 35 NPs.

NTA (Milli-Q H₂O): $d_H^1 = 57.5 \pm 2.6$ nm ($\sigma^* = 0.045$) (0.4 %), **$d_H^2 = 121.3 \pm 20.9$ nm ($\sigma^* = 0.173$) (95.2 %)**, $d_H^3 = 188.3 \pm 12.0$ nm ($\sigma^* = 0.063$) (4.4 %); Gaussian fitting; $3.57 \cdot 10^8$ NPs/mL.

- ***SPIONs@PVA13kDa_4***

TEM (Milli-Q H₂O): $d_{core} = 55.5 \pm 18.6$ nm; Gaussian fitting; 109 NPs.

NTA (Milli-Q H₂O): $d_H^1 = 38.6 \pm 4.1$ nm ($\sigma^* = 0.106$) (0.6 %), $d_H^2 = 56.8 \pm 6.6$ nm ($\sigma^* = 0.1115$) (1.9 %), **$d_H^3 = 132.6 \pm 21.9$ nm ($\sigma^* = 0.165$) (90.3 %)**, $d_H^4 = 242.4 \pm 32.5$ nm ($\sigma^* = 0.134$) (7.2 %); Gaussian fitting; $3.64 \cdot 10^8$ NPs/mL.

Blank (4B)

NTA (Milli-Q H₂O): $d_H^1 = 67.4 \pm 6.0$ nm ($\sigma^* = 0.089$) (2.0 %), **$d_H^2 = 130.3 \pm 23.8$ nm ($\sigma^* = 0.183$) (30.2 %)**, $d_H^3 = 172.7 \pm 11.4$ nm ($\sigma^* = 0.066$) (8.2 %), $d_H^4 = 209.6 \pm 27.8$ nm ($\sigma^* = 0.133$) (19.3 %); $d_H^5 = 285.2 \pm 27.4$ nm ($\sigma^* = 0.096$) (15.1 %), $d_H^6 = 370.5 \pm 31.2$ nm ($\sigma^* = 0.084$) (20.2 %), $d_H^7 = 498.7 \pm 46.5$ nm ($\sigma^* = 0.093$) (5.0 %); Gaussian fitting; $1.49 \cdot 10^8$ NPs/mL.

Assembly of the polymeric structure using PVA with Mw = 57 - 66 kDa

Two dispersions were prepared by dissolving PVA 57-66kDa (20.0 mg) in Milli-Q H₂O (1 mL, or PBS) and SPIO NPs (4.0 mg) in DCM (0.2 mL). To favor the complete solubilization of PVA, the dispersion was alternatively sonicated and heated at 80 °C until complete dissolution. The two dispersions were poured in a vial and the resulting two phases were emulsified with a tip ultrasonicator for 1 minute. At the end of the sonication, the organic solvent was removed by slow evaporation under stirring and the resulting products were purified through several steps of centrifugation or filtration, discarding the supernatant dispersion. The precise quantities and operating conditions used in the representative experiments performed are reported in **Table 5.4**.

Table 5.4: Reaction conditions used for the preparation and purification of SPIOs@PVA57kDa nanosystems. The bold font indicates the significant variation between different representative experiments.

Run	SPIOs (mg)	DCM (mL)	PVA 57kDa (mg)	H ₂ O (mL)	Sonication	Evaporation	Purification
1NF	4.0	0.2	20.0*	1.0	RT, 1 min, 150 W	RT, 3 h	Centrifugation 8500 rpm, 1 min, 20 °C (x3)
1F							Filtration 0.2 µm PTFE filter (13 mm)
1B	/	/	20.0*	1.0	RT, 1 min, 150 W	RT, 3 h	Centrifugation 8500 rpm, 1 min, 20 °C (x3)
2NF	4.0	0.2	20.0	1.0	RT, 1 min, 150 W	RT, 3.5 h	Centrifugation 8500 rpm, 1 min, 20 °C (x3)
2F							Filtration 0.2 µm PTFE filter (13 mm)
3	4.0	0.2	20.0	1.0**	RT, 1 min, 150 W	RT, 3 h	Centrifugation 8500 rpm, 1 min, 20 °C (x3)

*Dispersion neither sonicated nor heated; **PBS as solvent

- ***SPIONs@PVA57kDa_1***

Not filtered (1NF)

NTA (Milli-Q H₂O): $d_H^1 = 120.0 \pm 9.8$ nm ($\sigma^* = 0.082$) (1.2 %), **$d_H^2 = 190.3 \pm 35.2$ nm ($\sigma^* = 0.185$) (70.2 %)**, **$d_H^3 = 277.9 \pm 46.5$ nm ($\sigma^* = 0.167$) (25.8 %)**, $d_H^4 = 414.4 \pm 45.2$ nm ($\sigma^* = 0.109$) (2.7 %); Gaussian fitting; $5.83 \cdot 10^8$ NPs/mL.

Filtered (1F)

TEM (Milli-Q H₂O): $d_{core}^1 = 28.9 \pm 6.4$ nm, $d_{core}^2 = 49.3 \pm 4.8$ nm; Gaussian fitting; 57 NPs.

NTA (Milli-Q H₂O): $d_H^1 = 72.8 \pm 19.3$ nm ($\sigma^* = 0.265$) (5.0 %), $d_H^2 = 111.3 \pm 9.9$ nm ($\sigma^* = 0.089$) (6.0 %), **$d_H^3 = 145.2 \pm 26.1$ nm ($\sigma^* = 0.180$) (82.6 %)**, $d_H^4 = 221.9 \pm 33.7$ nm ($\sigma^* = 0.152$) (6.4 %); Gaussian fitting; $3.05 \cdot 10^8$ NPs/mL.

Blank (1B)

NTA (Milli-Q H₂O): $d_H^1 = 102.0 \pm 10.4$ nm ($\sigma^* = 0.101$) (9.8 %), **$d_H^2 = 142.5 \pm 12.8$ nm ($\sigma^* = 0.090$) (44.8 %)**, $d_H^3 = 171.8 \pm 12.1$ nm ($\sigma^* = 0.070$) (14.3 %), $d_H^4 = 223.7 \pm 18.9$ nm ($\sigma^* = 0.085$) (10.2 %), $d_H^5 = 289.0 \pm 39.1$ nm ($\sigma^* = 0.135$) (12.5 %), $d_H^6 = 347.4 \pm 30.2$ nm ($\sigma^* = 0.087$) (8.4 %); Gaussian fitting; $0.44 \cdot 10^8$ NPs/mL.

- ***SPIONs@PVA13kDa_2***

Not filtered (2NF)

NTA (Milli-Q H₂O): **$d_H^1 = 150.8 \pm 24.2$ nm ($\sigma^* = 0.161$) (64.2 %)**; **$d_H^2 = 225.6 \pm 23.0$ nm ($\sigma^* = 0.102$) (25.2 %)**, $d_H^3 = 283.8 \pm 30.4$ nm ($\sigma^* = 0.107$) (10.6 %); Gaussian fitting; $3.28 \cdot 10^7$ NPs/mL.

Filtered (2F)

TEM (Milli-Q H₂O): $d_{core} = 33.3 \pm 19.4$ nm; Extreme fitting; 121 NPs.

NTA (Milli-Q H₂O): $d_H^1 = 64.1 \pm 7.5$ nm ($\sigma^* = 0.117$) (1.5 %), $d_H^2 = 88.7 \pm 9.2$ nm ($\sigma^* = 0.104$) (8.3 %), **$d_H^3 = 120.6 \pm 20.0$ nm ($\sigma^* = 0.166$) (57.3 %)**, **$d_H^4 = 167.3 \pm 25.5$ nm ($\sigma^* = 0.153$) (29.5 %)**, $d_H^5 = 299.5 \pm 59.2$ nm ($\sigma^* = 0.198$) (3.5 %); Gaussian fitting; $3.66 \cdot 10^8$ NPs/mL.

- ***SPIONs@PVA13kDa_3***

TEM (PBS): $d_{core} = 76.5 \pm 13.5$ nm; Gaussian fitting; 20 NPs.

NTA (PBS): $d_H^1 = 94.8 \pm 5.0$ nm ($\sigma^* = 0.053$) (1.2 %), $d_H^2 = 119.7 \pm 9.9$ nm ($\sigma^* = 0.082$) (4.4 %), **$d_H^3 = 173.3 \pm 34.5$ nm ($\sigma^* = 0.199$) (83.0 %)**, $d_H^4 = 239.9 \pm 14.4$ nm ($\sigma^* = 0.060$) (3.5 %), $d_H^5 = 288.4 \pm 42.6$ nm ($\sigma^* = 0.148$) (7.9 %); Gaussian fitting; $2.60 \cdot 10^8$ NPs/mL.

Assembly of the polymeric structure using Pluronic F127 and PVA with Mw = 13 kDa

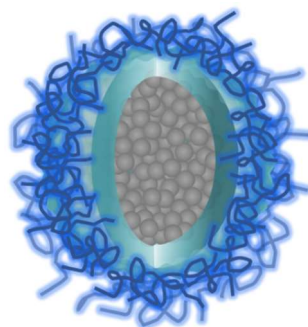


Figure 5.4: Graphical representation of SPIONs (grey spheres) included in a polymeric coating of Pluronic F127 (light blue sphere) and PVA (blue coils).

Three dispersions were prepared by dissolving separately Pluronic F127 in Milli-Q H₂O, PVA 13kDa in Milli-Q H₂O, and SPIO NPs in DCM (all the quantities in **Table 5.5**). To favor the complete solubilization of PVA and Pluronic, the dispersions were alternatively sonicated and heated at 80 °C until complete dissolution. The organic phase containing SPIONs and the aqueous phase containing the Pluronic dispersion were poured in a vial and the resulting two phases were emulsified with a tip ultrasonicator. At the end of the sonication, if other cycles were not needed to better homogenize it, the aqueous phase containing PVA was added to the emulsion and the resulting mixture was emulsified again with a tip ultrasonicator (for more than one cycle, if needed). Subsequently, the organic solvent of the grey emulsion was removed by evaporation under stirring and the resulting products were purified through several steps of centrifugation, discarding the supernatant dispersion. The precise quantities and operating conditions are listed in **Table 5.5**.

Table 5.5: Reaction conditions used for the preparation and purification of SPIONs@F127/PVA13kDa nanosystems. The bold font indicates the significant variation between different representative experiments.

Run	SPIONs (mg)	DCM (mL)	F127 (mg)	H ₂ O (mL)	PVA 13kDa (mg)	H ₂ O (mL)	Sonication	Evaporation	Purification
1	5.0	0.5	30.0	1.0	20.0	1.0	RT, 30s/30s pulse, 5 min, 150 W*	RT, 5 h	Centrifugation 8500 rpm, 1 min, 20 °C (x2)
2	5.0	0.5	30.0	1.0	20.0	1.0	RT, 1 min, 100 W (1+1)	40 °C, 2 h	Centrifugation 8400 rpm, 10 min, 25 °C (x3) + magnetic separation
3	55.0	5.5**	330.0	11.0	220.0	11	RT, 1 min, 100 W (3+3)	40 °C, 2 h	Centrifugation 4400 rpm, 10 min, 30 °C (x2) + magnetic separation

*PVA and Pluonic poured together; **DCM over K₂CO₃

- ***SPIONs@F127/PVA13kDa_1***

TEM (Milli-Q H₂O): $d_{\text{core}}^1 = 46.2 \pm 17.3 \text{ nm}$ (86.7 %), $d_{\text{core}}^2 = 114.4 \pm 15.2 \text{ nm}$ (13.3 %); Extreme fitting; 56 NPs.

NTA (Milli-Q H₂O): $d_{\text{H}}^1 = 40.9 \pm 8.2 \text{ nm}$ ($\sigma^* = 0.202$) (2.8 %), $d_{\text{H}}^2 = 116.9 \pm 23.4 \text{ nm}$ ($\sigma^* = 0.200$) (97.2 %); Gaussian fitting; $2.94 \cdot 10^8$ NPs/mL.

- ***SPIONs@F127/PVA13kDa_2***

TEM (Milli-Q H₂O): $d_{\text{core}} = 122.3 \pm 32.3 \text{ nm}$; Gaussian fitting; 181 NPs.

NTA (Milli-Q H₂O): $d_{\text{H}}^1 = 35.0 \pm 2.1 \text{ nm}$ ($\sigma^* = 0.060$) (0.5 %), $d_{\text{H}}^2 = 50.3 \pm 3.2 \text{ nm}$ ($\sigma^* = 0.064$) (0.5 %), $d_{\text{H}}^3 = 69.1 \pm 4.5 \text{ nm}$ ($\sigma^* = 0.065$) (0.6 %), $d_{\text{H}}^4 = 95.7 \pm 6.6 \text{ nm}$ ($\sigma^* = 0.069$) (1.9 %), $d_{\text{H}}^5 = 160.0 \pm 12.8 \text{ nm}$ ($\sigma^* = 0.080$) (8.4 %), $d_{\text{H}}^6 = 191.9 \pm 14.2 \text{ nm}$ ($\sigma^* = 0.074$) (11.5 %), $d_{\text{H}}^7 = 250.5 \pm 23.4 \text{ nm}$ ($\sigma^* = 0.093$) (56.1 %), $d_{\text{H}}^8 = 316.9 \pm 27.1 \text{ nm}$ ($\sigma^* = 0.086$) (20.3 %); Gaussian fitting; $5.8 \cdot 10^7$ NPs/mL.

- ***SPIONs@F127/PVA13kDa_3***

TEM (Milli-Q H₂O): $d_{\text{core}}^1 = 83.2 \pm 34.2 \text{ nm}$ (85.9 %), $d_{\text{core}}^2 = 181.0 \pm 12.1 \text{ nm}$ (8.8 %), $d_{\text{core}}^3 = 283.3 \pm 44.0 \text{ nm}$ (5.3 %); Extreme fitting; 195 NPs.

NTA (Milli-Q H₂O): $d_{\text{H}}^1 = 129.3 \pm 8.2 \text{ nm}$ ($\sigma^* = 0.063$) (4.2 %), $d_{\text{H}}^2 = 187.1 \pm 20.6 \text{ nm}$ ($\sigma^* = 0.110$) (63.6 %), $d_{\text{H}}^3 = 269.6 \pm 22.8 \text{ nm}$ ($\sigma^* = 0.085$) (27.4 %), $d_{\text{H}}^4 = 485.7 \pm 34.9 \text{ nm}$ ($\sigma^* = 0.072$) (4.8 %); Gaussian fitting; $3.08 \cdot 10^8$ NPs/mL.

DLS (Milli-Q H₂O): $d_{\text{H}} = 197.7 \pm 98.8 \text{ nm}$ (PDI = 0.34).

TGA: organic loss = 30.54 %; $T_{\text{max}}^1 = 240 \text{ }^\circ\text{C}$ $T_{\text{max}}^2 = 303 \text{ }^\circ\text{C}$, $T_{\text{max}}^3 = 601 \text{ }^\circ\text{C}$.

VSM: $M_s = 40.294 \text{ emu/g}$; $M_r = 2.6777 \cdot 10^{-3} \text{ emu/g}$; $H_c = 0.18516 \text{ Oe}$.

Assembly of the polymeric structure using Pluronic F127 and PVA with Mw = 57 - 66 kDa

Three dispersions were prepared by dissolving separately Pluronic F127 in Milli-Q H₂O, PVA 57-66kDa in Milli-Q H₂O, and SPIO NPs in DCM (all the quantities in **Table 5.6**). To favor the complete solubilization of PVA and Pluronic, the dispersions were alternatively sonicated and heated at 80 °C until complete dissolution. The organic phase containing SPIONs and the aqueous phase containing the Pluronic dispersion were poured in a vial and the resulting two phases were emulsified with a tip ultrasonicator. At the end of the sonication, if other cycles were not needed to better homogenize it, the aqueous phase containing PVA was added to the emulsion and the resulting mixture was emulsified again with a tip ultrasonicator (for more than one cycle, if

needed). Subsequently, the organic solvent of the grey emulsion was removed by evaporation under stirring and the resulting products were purified through several steps of centrifugation helped by magnetic separation, discarding the supernatant dispersion. The precise quantities and operating conditions used in the representative experiments performed are reported in **Table 5.6**.

Table 5.6: Reaction conditions used for the preparation and purification of SPIONs@F127/PVA57kDa nanosystems. The bold font indicates the significant variation between different representative experiments.

Run	SPIONs (mg)	DCM (mL)	F127 (mg)	H ₂ O (mL)	PVA 57kDa (mg)	H ₂ O (mL)	Sonication	Evaporation	Purification
1	5.0	0.5	30.0	1.0*	20.0	1.0*	RT, 1 min, 150 W	40 °C, 3 h	Centrifugation 8500 rpm, 1 min, 20 °C (x2) + magnetic separation
2	5.0	0.5	30.0	1.0	20.0	1.0	RT, 1 min, 100 W (1+1)	40 °C, 2 h	Centrifugation 8400 rpm, 10 min, 25 °C (x3) + magnetic separation
3	55.0	5.5**	330.0	11.0	220.0	11	RT, 1 min, 100 W (3+2)	40 °C, 2 h	Centrifugation 4400 rpm, 10 min, 30 °C (x2) + magnetic separation

*PBS as solvent; **DCM over K₂CO₃

- **SPIONs@F127/PVA57kDa_1**

TEM (PBS): $d_{\text{core}} = 116.2 \pm 66.1$ nm; Extreme fitting; 181 NPs.

NTA (PBS): $d_{\text{H}}^1 = 73.6 \pm 7.2$ nm ($\sigma^* = 0.098$) (5.9 %), $d_{\text{H}}^2 = 103.3 \pm 9.6$ nm ($\sigma^* = 0.093$) (12.1 %), **$d_{\text{H}}^3 = 146.0 \pm 12.6$ nm ($\sigma^* = 0.086$) (47.9 %)**, **$d_{\text{H}}^4 = 239.4 \pm 25.2$ nm ($\sigma^* = 0.105$) (28.8 %)**, $d_{\text{H}}^5 = 359.2 \pm 21.3$ nm ($\sigma^* = 0.059$) (5.4 %); Gaussian fitting; $8.7 \cdot 10^7$ NPs/mL.

- **SPIONs@F127/PVA57kDa_2**

TEM (Milli-Q H₂O): $d_{\text{core}} = 131.4 \pm 38.1$ nm; Gaussian fitting; 262 NPs.

NTA (Milli-Q H₂O): $d_{\text{H}}^1 = 103.0 \pm 7.3$ nm ($\sigma^* = 0.071$) (1.8 %), $d_{\text{H}}^2 = 141.9 \pm 10.4$ nm ($\sigma^* = 0.073$) (5.4 %), **$d_{\text{H}}^3 = 193.7 \pm 21.1$ nm ($\sigma^* = 0.109$) (42.2 %)**, **$d_{\text{H}}^4 = 255.4 \pm 31.6$ nm ($\sigma^* = 0.124$) (36.9 %)**, $d_{\text{H}}^5 = 380.7 \pm 33.4$ nm ($\sigma^* = 0.088$) (13.7 %); Gaussian fitting; $9.9 \cdot 10^7$ NPs/mL.

- **SPIONs@F127/PVA57kDa_3**

TEM (Milli-Q H₂O): $d_{\text{core}} = 117.2 \pm 65.5$ nm; Extreme fitting; 354 NPs.

NTA (Milli-Q H₂O): $d_{\text{H}}^1 = 125.9 \pm 8.3$ nm ($\sigma^* = 0.066$) (5.7 %), $d_{\text{H}}^2 = 150.8 \pm 11.7$ nm ($\sigma^* = 0.077$) (12.5 %), $d_{\text{H}}^3 = 201.1 \pm 22.3$ nm ($\sigma^* = 0.111$) (54.2 %), $d_{\text{H}}^4 = 256.5 \pm 29.2$ nm ($\sigma^* = 0.114$) (27.7 %); Gaussian fitting; $1.95 \cdot 10^8$ NPs/mL.

DLS (Milli-Q H₂O): $d_{\text{H}} = 218.2 \pm 88.2$ nm (PDI = 0.33).

TGA: organic loss = 34.72 %; $T_{\text{max}}^1 = 245$ °C $T_{\text{max}}^2 = 307$ °C, $T_{\text{max}}^3 = 628$ °C.

VSM: $M_s = 32.970$ emu/g; $M_r = 4.1747 \cdot 10^{-3}$ emu/g; $H_c = 0.35929$ Oe.

5.4 DRUG LOADING IN THE POLYMERIC NANOSYSTEM

Assembly of the polymeric nanosystem – PVA 13kDa + F127 + Riluzole

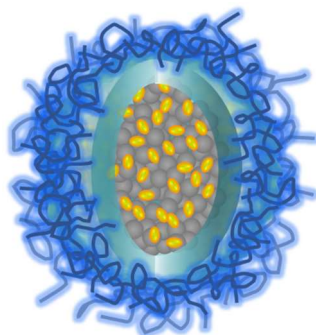


Figure 5.5: Graphical representation of SPIONs (grey spheres) and riluzole molecules (yellow ovals) included in a polymeric coating of Pluronic F127 (light blue sphere) and PVA (blue coils).

Three dispersions were prepared by dissolving separately Pluronic F127 in Milli-Q H₂O, PVA 13kDa in Milli-Q H₂O, and SPIO NPs together with riluzole in DCM (all the quantities in **Table 5.7**). To favor the complete solubilization of PVA and Pluronic, the dispersions were alternatively sonicated and heated at 80 °C until complete dissolution. The organic phase containing SPIONs and riluzole and the aqueous phase containing the Pluronic dispersion were poured in a vial and the resulting two phases were emulsified with a tip ultrasonicator. At the end of the sonication, if other cycles were not needed to better homogenize it, the aqueous phase containing PVA was added to the emulsion and the resulting mixture was emulsified again with a tip ultrasonicator (for more than one cycle, if needed). Subsequently, the organic solvent of the grey emulsion was removed by evaporation under stirring and the resulting products were purified through several steps of centrifugation helped by magnetic separation, discarding the supernatant dispersion. The precise quantities and operating conditions used in the representative experiments performed are reported in **Table 5.7**.

Table 5.7: Reaction conditions used for the preparation and purification of SPIONs+Riluzole@F127/PVA13kDa nanosystems. The bold font indicates the significant variation between different representative experiments.

Run	SPIONs (mg)	Riluzole (mg)	DCM (mL)	F127 (mg)	H ₂ O (mL)	PVA 13kDa (mg)	H ₂ O (mL)	Sonication	Evaporation	Purification
1	5.0	3.0	0.5	30.0	1.0	20.0	1.0	RT, 1 min, 100 W (1+1)	40 °C, 2 h	Centrifugation 8400 rpm, 10 min, 20 °C (x2) + magnetic separation
2	5.0	3.0	0.5*	30.0	1.0	20.0	1.0	RT, 1 min, 100 W (1+1)	40 °C, 2 h	Centrifugation 8400 rpm, 10 min, 20 °C + magnetic separation**
3	55.0	33.0	5.5*	330.0	11.0	220.0	11	RT, 1 min, 100 W (3+1)***	40 °C, 2 h	Centrifugation 4400 rpm, 10 min, 30 °C (x2) + magnetic separation

*DCM over K₂CO₃; **Re-dispersed in PBS; ***Solution kept warm between cycles.

- ***SPIONs+Riluzole@F127/PVA13kDa_1***

TEM (Milli-Q H₂O): $d_{\text{core}} = 144.7 \pm 59.6$ nm; Extreme fitting; 272 NPs.

NTA (Milli-Q H₂O): $d_{\text{H}}^1 = 62.1 \pm 6.0$ nm ($\sigma^* = 0.097$) (2.4 %), $d_{\text{H}}^2 = 79.9 \pm 15.5$ nm ($\sigma^* = 0.194$) (5.2 %), $d_{\text{H}}^3 = 130.4 \pm 16.7$ nm ($\sigma^* = 0.128$) (14.3 %), **$d_{\text{H}}^4 = 193.4 \pm 28.6$ nm ($\sigma^* = 0.148$) (60.5 %)**, $d_{\text{H}}^5 = 266.1 \pm 34.9$ nm ($\sigma^* = 0.131$) (15.6 %), $d_{\text{H}}^6 = 447.7 \pm 36.0$ nm ($\sigma^* = 0.080$) (2.0 %); Gaussian fitting; $1.77 \cdot 10^8$ NPs/mL.

- ***SPIONs+Riluzole@F127/PVA13kDa_2***

TEM (Milli-Q H₂O): $d_{\text{core}} = 73.5 \pm 66.8$ nm; Extreme fitting; 1259 NPs.

NTA (Milli-Q H₂O): $d_{\text{H}}^1 = 96.0 \pm 19.8$ nm ($\sigma^* = 0.206$) (12.1 %), $d_{\text{H}}^2 = 117.7 \pm 8.4$ nm ($\sigma^* = 0.071$) (6.6 %), **$d_{\text{H}}^3 = 145.1 \pm 14.1$ nm ($\sigma^* = 0.097$) (33.9 %)**, **$d_{\text{H}}^4 = 178.5 \pm 18.2$ nm ($\sigma^* = 0.102$) (19.2 %)**, **$d_{\text{H}}^5 = 238.0 \pm 26.3$ nm ($\sigma^* = 0.111$) (25.2 %)**, $d_{\text{H}}^6 = 331.9 \pm 35.1$ nm ($\sigma^* = 0.106$) (2.9 %); Gaussian fitting; $1.76 \cdot 10^8$ NPs/mL.

UV-Vis (Milli-Q H₂O): drug loading = 16.61 % (at 264 nm).

- ***SPIONs+Riluzole@F127/PVA13kDa_3***

TEM (Milli-Q H₂O): $d_{\text{core}} = 108.6 \pm 57.0$ nm; Extreme fitting; 368 NPs.

NTA (Milli-Q H₂O): $d_H^1 = 178.3 \pm 15.9 \text{ nm}$ ($\sigma^* = 0.089$) (29.0 %), $d_H^2 = 215.9 \pm 22.2 \text{ nm}$ ($\sigma^* = 0.103$) (41.2 %), $d_H^3 = 288.9 \pm 24.5 \text{ nm}$ ($\sigma^* = 0.085$) (29.9 %); Gaussian fitting; $1.67 \cdot 10^8$ NPs/mL.

DLS (Milli-Q H₂O): $d_H = 187.8 \pm 53.9 \text{ nm}$ (PDI = 0.57).

TGA: organic loss = 41.61 %; $T_{\max}^1 = 248 \text{ }^\circ\text{C}$, $T_{\max}^2 = 275 \text{ }^\circ\text{C}$, $T_{\max}^3 = 308 \text{ }^\circ\text{C}$, $T_{\max}^4 = 695 \text{ }^\circ\text{C}$.

VSM: $M_s = 27.513 \text{ emu/g}$; $M_r = 10.535 \cdot 10^{-3} \text{ emu/g}$; $H_c = 0.57931 \text{ Oe}$.

UV-Vis (Milli-Q H₂O): drug loading = 97.70 % (at 264 nm).

Assembly of the polymeric nanosystem – PVA 13kDa + F127 + SF89

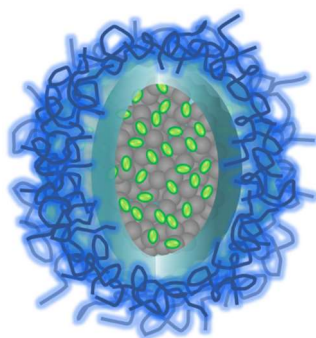


Figure 5.6: Graphical representation of SPIONs (grey spheres) and riluzole molecules (green ovals) included in a polymeric coating of Pluronic F127 (light blue sphere) and PVA (blue coils).

Three dispersions were prepared by dissolving separately Pluronic F127 (30.0 mg) in Milli-Q H₂O (1.0 mL), PVA 13kDa (20.0 mg) in Milli-Q H₂O (1.0 mL) and SPIO NPs (5.0 mg) together with SF89 (4.5 mg) in DCM (0.5 mL, over K₂CO₃). To favor the complete solubilization of PVA and Pluronic, the dispersions were alternatively sonicated and heated at 80 °C until complete dissolution. The organic phase containing SPIONs and SF89 and the aqueous phase containing the Pluronic dispersion were poured in a vial and the resulting two phases were emulsified with a tip ultrasonicator at 100 W and room temperature for 1 minute. At the end of the sonication, PVA was added to the emulsion and the resulting mixture was emulsified again at 100 W and room temperature for 1 minute with a tip ultrasonicator. Subsequently, the organic solvent was removed by evaporation at 40 °C for 2 hours under stirring and the resulting products were purified through two centrifugation steps at 10000 rpm at room temperature for 10 minutes which were helped by magnetic separation, to discard the supernatant dispersion.

- *SPIONs+SF89@F127/PVA13kDa_1*

TEM (Milli-Q H₂O): $d_{\text{core}}^1 = 85.1 \pm 30.0 \text{ nm}$ (91.8 %), $d_{\text{core}}^2 = 195.4 \pm 18.4 \text{ nm}$ (8.2 %); Extreme fitting; 158 NPs.

NTA (Milli-Q H₂O): $d_H^1 = 75.0 \pm 9.6$ nm ($\sigma^* = 0.127$) (1.3 %), $d_H^2 = 104.1 \pm 5.2$ nm ($\sigma^* = 0.050$) (0.4 %), **$d_H^3 = 206.9 \pm 39.8$ nm ($\sigma^* = 0.192$) (55.0 %)**, $d_H^4 = 271.2 \pm 39.2$ nm ($\sigma^* = 0.144$) (36.6 %), $d_H^5 = 349.6 \pm 47.3$ nm ($\sigma^* = 0.135$) (6.7 %); Gaussian fitting; $4.42 \cdot 10^8$ NPs/mL.

UV-Vis (Milli-Q H₂O): drug loading = 78.96 % (at 251 nm).

Assembly of the polymeric nanosystem – PVA 57-66kDa + F127 + Riluzole

Three dispersions were prepared by dissolving separately Pluronic F127 in Milli-Q H₂O, PVA 57-66kDa in Milli-Q H₂O, and SPIO NPs together with riluzole in DCM (all the quantities in **Table 5.8**). To favor the complete solubilization of PVA and Pluronic, the dispersions were alternatively sonicated and heated at 80 °C until complete dissolution. The organic phase containing SPIONs and riluzole and the aqueous phase containing the Pluronic dispersion were poured in a vial and the resulting two phases were emulsified with a tip ultrasonicator. At the end of the sonication, if other cycles were not needed to better homogenize it, the aqueous phase containing PVA was added to the emulsion and the resulting mixture was emulsified again with a tip ultrasonicator (for more than one cycle, if needed). Subsequently, the organic solvent was removed by evaporation under stirring and the resulting products were purified through several steps of centrifugation helped by magnetic separation, discarding the supernatant dispersion. The precise quantities and operating conditions used in the representative experiments performed are reported in **Table 5.8**.

Table 5.8: Reaction conditions used for the preparation and purification of SPIONs+Riluzole@F127/PVA57kDa nanosystems. The bold font indicates the significant variation between different representative experiments.

Run	SPIONs (mg)	Riluzole (mg)	DCM (mL)	F127 (mg)	H ₂ O (mL)	PVA 57kDa (mg)	H ₂ O (mL)	Sonication	Evaporation	Purification
1	5.0	3.0	0.5	30.0	1.0	20.0	1.0	RT, 1 min, 100 W (1+1)	40 °C, 2 h	Centrifugation 8400 rpm, 10 min, 20 °C (x3) + magnetic separation
2	5.0	3.0	0.5*	30.0	1.0	20.0	1.0	RT, 1 min, 100 W (1+1)	40 °C, 2 h	Centrifugation 8400 rpm, 10 min, 20 °C (x2) + magnetic separation**
3	55.0	33.0	5.5*	330.0	11.0	220.0	11	RT, 1 min, 100 W (3+2)***	40 °C, 2 h	Centrifugation 4400 rpm, 10 min, 30 °C (x2) + magnetic separation

*DCM over K₂CO₃; **Re-dispersed in PBS; ***Solution kept warm between cycles.

- ***SPIONs+Riluzole@F127/PVA57kDa_1***

TEM (Milli-Q H₂O): $d_{\text{core}} = 130.0 \pm 39.8$ nm; Gaussian fitting; 139 NPs.

NTA (Milli-Q H₂O): $d_{\text{H}}^1 = 96.9 \pm 14.8$ nm ($\sigma^* = 0.153$) (4.0 %), $d_{\text{H}}^2 = 125.0 \pm 12.2$ nm ($\sigma^* = 0.098$) (6.6 %), **$d_{\text{H}}^3 = 174.7 \pm 28.1$ nm ($\sigma^* = 0.161$) (57.2 %)**, **$d_{\text{H}}^4 = 253.3 \pm 35.5$ nm ($\sigma^* = 0.140$) (32.2 %)**; Gaussian fitting; $2.40 \cdot 10^8$ NPs/mL.

- ***SPIONs+Riluzole@F127/PVA57kDa_2***

TEM (Milli-Q H₂O): $d_{\text{core}} = 36.7 \pm 24.1$ nm; Extreme fitting; 914 NPs.

NTA (Milli-Q H₂O): $d_{\text{H}}^1 = 34.3 \pm 6.1$ nm ($\sigma^* = 0.176$) (2.5 %), $d_{\text{H}}^2 = 46.0 \pm 3.1$ nm ($\sigma^* = 0.066$) (1.0 %), $d_{\text{H}}^3 = 62.1 \pm 7.3$ nm ($\sigma^* = 0.118$) (1.7 %), $d_{\text{H}}^4 = 91.6 \pm 9.0$ nm ($\sigma^* = 0.098$) (1.6 %), $d_{\text{H}}^5 = 116.8 \pm 9.8$ nm ($\sigma^* = 0.084$) (2.6 %), **$d_{\text{H}}^6 = 163.6 \pm 14.8$ nm ($\sigma^* = 0.091$) (33.1 %)**, **$d_{\text{H}}^7 = 203.3 \pm 18.5$ nm ($\sigma^* = 0.091$) (23.7 %)**, **$d_{\text{H}}^8 = 244.9 \pm 24.0$ nm ($\sigma^* = 0.098$) (25.0 %)**, $d_{\text{H}}^9 = 330.2 \pm 40.0$ nm ($\sigma^* = 0.121$) (8.8 %); Gaussian fitting; $1.02 \cdot 10^8$ NPs/mL.

UV-Vis (Milli-Q H₂O): drug loading = 20.28 % (at 264 nm).

- ***SPIONs+Riluzole@F127/PVA57kDa_3***

TEM (Milli-Q H₂O): $d_{\text{core}} = 155.4 \pm 50.2$ nm; Gaussian fitting; 333 NPs.

NTA (Milli-Q H₂O): **$d_{\text{H}}^1 = 234.5 \pm 23.2$ nm ($\sigma^* = 0.099$) (61.6 %)**, **$d_{\text{H}}^2 = 284.9 \pm 21.8$ nm ($\sigma^* = 0.077$) (29.0 %)**, $d_{\text{H}}^3 = 412.2 \pm 31.1$ nm ($\sigma^* = 0.075$) (5.0 %), $d_{\text{H}}^4 = 523.7 \pm 39.2$ nm ($\sigma^* = 0.075$) (4.3 %); Gaussian fitting; $2.27 \cdot 10^8$ NPs/mL.

DLS (Milli-Q H₂O): $d_{\text{H}} = 261.0 \pm 58.8$ nm (PDI = 0.35).

TGA: organic loss = 41.23 %; $T_{\text{max}}^1 = 247$ °C $T_{\text{max}}^2 = 274$ °C, $T_{\text{max}}^3 = 312$ °C, $T_{\text{max}}^4 = 698$ °C.

VSM: $M_s = 25.422$ emu/g; $M_r = 6.8732 \cdot 10^{-3}$ emu/g; $H_c = 1.2959$ Oe.

UV-Vis (Milli-Q H₂O): drug loading = 97.81 % (at 264 nm).

Assembly of the polymeric nanosystem – PVA 57-66kDa + F127 + SF89

Three dispersions were prepared by dissolving separately Pluronic F127 (30.0 mg) in Milli-Q H₂O (1.0 mL), PVA 57-66kDa (20.0 mg) in Milli-Q H₂O (1.0 mL) and SPIO NPs (5.0 mg) together with SF89 (4.5 mg) in DCM (0.5 mL, over K₂CO₃). To favor the complete solubilization of PVA and Pluronic, the dispersions were alternatively sonicated and heated at 80 °C until complete dissolution. The organic phase containing SPIONs and SF89 and the aqueous phase containing the Pluronic dispersion were poured in a vial and the resulting two phases were emulsified with a tip ultrasonicator at 100 W and room temperature for 1 minute. At the end of the sonication, PVA was

added to the emulsion and the resulting mixture was emulsified again at 100 W and room temperature for 1 minute with a tip ultrasonicator. Subsequently, the organic solvent of the grey emulsion was removed by evaporation at 40 °C for 2 hours under stirring and the resulting products were purified through two centrifugation steps at 10000 rpm at room temperature for 10 minutes which were helped by magnetic separation, to discard the supernatant dispersion.

- ***SPIONs+SF89@F127/PVA57kDa_1***

TEM (Milli-Q H₂O): $d_{\text{core}}^1 = 86.7 \pm 34.3 \text{ nm}$ (83.7 %), $d_{\text{core}}^2 = 215.4 \pm 41.7 \text{ nm}$ (16.3 %); Extreme fitting; 123 NPs.

NTA (Milli-Q H₂O): $d_H^1 = 139.1 \pm 12.0 \text{ nm}$ ($\sigma^* = 0.086$) (18.9 %), $d_H^2 = 178.8 \pm 16.6 \text{ nm}$ ($\sigma^* = 0.093$) (31.3 %), $d_H^3 = 230.1 \pm 19.5 \text{ nm}$ ($\sigma^* = 0.085$) (34.8 %), $d_H^4 = 304.4 \pm 36.4 \text{ nm}$ ($\sigma^* = 0.119$) (12.4 %), $d_H^5 = 473.4 \pm 34.8 \text{ nm}$ ($\sigma^* = 0.074$) (2.6 %); Gaussian fitting; $4.02 \cdot 10^8$ NPs/mL.

UV-Vis (Milli-Q H₂O): drug loading = 79.92 % (at 251 nm).

CHAPTER 6: SPIONs@POLYMER: CONCLUSIONS & OUTLOOK

This project required an initial literature search for feasible design and materials comprising iron oxide nanoparticles and polymers for their encapsulation.

Considering the first synthetic part of the project related to the preparation of magnetic nanoparticles, after the preliminary attempts with the hydrothermal method, we discovered a particularly reliable, fast, and reproducible approach for the preparation of hydrophobic SPIONs based on the thermal decomposition of $\text{Fe}(\text{acac})_3$ promoted by microwave heating. With this method, we were able to prepare very small iron oxide nanoparticles with a core diameter determined by TEM below 4 nm and a composition that is consistent with the presence of magnetite as the principal crystal phase. The superparamagnetic behavior – fundamental for the intended clinical applications – was verified by VSM and found to be in keeping with the literature. Given the dimension, the chemical composition, and the magnetic properties, these SPIONs should fulfill exactly the requirements set for their application in nanomedicine as positive contrast agents for ^1H -MRI and a mean to support magnetic drug targeting. To resume, we accomplished to tailor the properties of this known magnetic nanomaterial in order to diverge from its usual application of ^1H -MRI negative contrast agent in favor of a more efficient and innovative positive one. This was achieved by exploiting a well-known synthetic approach as thermal decomposition, using microwaves as a pioneering way of heating.

The first attempts on the preparation of a suitable polymeric scaffold for the hosting of SPIONs were performed using a specific type of polymer, polyvinyl alcohol (PVA), selecting two species of different molecular weight that were tested in parallel. The procedure adopted for the preparation of the polymeric structure was the emulsion-solvent evaporation approach mediated by tip ultrasonication. This allowed the emulsification of the polymeric aqueous phase with the organic one containing SPIONs and the formation of a polymeric matrix that captured and hosted the hydrophobic magnetic nanoparticles. In particular, as previously reported in literature with similar species, we demonstrated that PVA with a molecular weight of 13 kDa is suitable to obtain W/O/W-type nanosystem, while with the 57-65 kDa PVA an O/W-type structure can be prepared. Moreover, we confirmed that both the PVA polymers used were able to store the hydrophobic SPIONs synthesized previously in their inner compartments, and we collected interesting and new evidence supporting the role of these magnetic nanoparticles in the formation of more stable and less disperse nanosystems with respect to polymeric matrix prepared without them.

However, some critical points make this type of nanosystem not completely suitable for theranostic purposes: in particular, the elimination of the unassembled polymer from the dispersion is

cumbersome and the room available on the polymeric structure for hosting SPIONs is small and these remain mostly outside the nanosystem.

To improve the stability of the nanosystem toward the biological environment and increase the amount of SPIONs encapsulated, we changed the structure of the nanosystem by introducing the block-copolymer Pluronic F127, which can form micelles. In this system, we maintained the use of PVA to stabilize the hydrophilic shell of the Pluronic micelle. With this combination of polymeric components and using a procedure consisting of two sonication steps, the first needed to form the Pluronic micelles and the second needed for their stabilization with PVA, we managed to prepare a more stable nanostructure that was easily re-dispersible in water once collected by centrifugation and was able to host the SPIONs tightly. The reason for this enhanced stability is due also to the external PVA, which in some TEM images we saw forming a crystallized corona around the inorganic core held together by SPIONs clusterization and Pluronic micellization.

The progress in emulsion formation and stabilization were evident for both the two PVA used, even if the lighter one was demonstrated to be more tightly bonded to the micelle, thus protecting the hosted nanoparticles better and reducing their magnetic properties less than the higher molecular weight one. We then managed to improve further the emulsification of the polymeric component, by favoring the micellization before the first sonication and increasing the amount of SPIONs encapsulated, still forming nanosystems in the desired range of dimension, with only minor populations of bigger structures and with a polymeric composition that was clear from TGA. Moreover, also the purification steps were refined by exploiting magnetic separation: this permitted a faster and more complete removal of the unassembled non-magnetic polymer or non-magnetic nanosystems.

Resuming the research work of this part of the project, we expanded the possible combinations of nanosystems prepared with polymers, by employing mixtures of Pluronic and PVA with an improved emulsification approach. Furthermore, we exploited the peculiar compartmentalization of these nanosystems to encapsulate SPIONs and achieve state-of-the-art features of combined imaging and drug delivery. Comparing the two nanosystems prepared, we observed that, even with a greater dispersion, the nanosystem prepared with the PVA of lower molecular weight is the most promising foreseeing the desired theranostic purposes because it results in a more stable structure able to encapsulate and protect the magnetic payload better than the nanosystem composed of PVA only.

With these optimized procedures for nanosystem preparation and purification, we studied the loading of the selected drug molecules, riluzole and the triazole-triazinic SF89. Concerning the

loading of riluzole, we exploited the same optimized emulsifying procedure, putting in contact SPIONs and riluzole from the very beginning: after some optimization, this guaranteed the formation of a bigger inorganic core comprising a significant amount of drug molecules, as it was measured by the UV-Vis analysis and confirmed by TGA. The experiments performed in PBS to simulate the dispersion of these species in biological conditions gave well-dispersed nanosystems, however, some evidence suggests that the interactions with phosphate ions could weaken the external polymeric shell. Overall, with an improved ultrasonication method, we were able to encapsulate for the first time riluzole molecules in nanosystems with ideal size below 250 nm in hydrodynamic diameter and optimal SPIONs content, to combine drug therapy with MRI imaging potentially suited for the treatment of ALS. In the preparation of these drug-loaded nanosystems, the low molecular weight PVA performed better than the higher molecular weight one in endowing the nanosystem with properties such as core diameter of 109 nm, hydrodynamic diameter of 216 nm, and magnetic properties suitable for practical applications with a drug loading of 98 %.

The inclusion of the triazole-triazinic SF89 proceeded similarly to the case of riluzole. However, by comparison with the previous drug-loaded nanosystems, we noticed that in this case, the nanosystems obtained were unfortunately more dispersed and with a greater number of populations of different core and shell sizes, even if the trend of having a more expanded shell with the lighter PVA is maintained. Moreover, the lower drug loading obtained with respect to riluzole is in accordance with the lower hydrophobic character of SF89, which we expect to be placed more within the interface between the two layers than in the inorganic core. An interesting aspect that arises from these observations is that the drug encapsulation depends strongly on its interaction between the hydrophobic moiety (inorganic core and hydrophobic compartment of the micelle), since it is the most protected section of the nanosystems, while the drug molecules placed differently would be probably released earlier. Despite results that may still be improved, we managed to apply the novel hybrid polymeric-SPIONs nanosystem whose synthesis we master in the previous parts of the project, for the same theranostic approach, but with an original drug molecule for ALS. In the opposite way to the case of riluzole inclusion, based on the comparison between the physical characteristics and the stability of both these nanosystems, we observed that the most favorable structure for SF89 loading is the one composed by Pluronic F127 and the PVA with higher molecular weight.

In perspective, these nanosystems will be tested for their theranostic properties. In particular, we plan to submit all the nanoplatfoms containing either riluzole or SF89 to the Parallel Artificial

Membrane Permeability Assay (PAMPA), in order to assess the release of the drug in the environment and the efficiency in passing through a simulated biological membrane. Besides this, there is also the need to control the imaging properties of the SPIONs encapsulated in the polymer through phantom MRI experiments.

PART III



FLUORINATED GOLD NANOPARTICLES

7.1 MONOLAYER-PROTECTED GOLD NANOPARTICLES

Noble metal Au nanoparticles have attracted extensive interests in the past decades, due to their size and morphology dependent localized surface plasmon resonances. Their unique optical property, high chemical stability, good biocompatibility, and easy functionalization make them promising candidates for a variety of biomedical applications, including bioimaging, biosensing, and cancer therapy.

— from Ding et al.³⁴⁷, *Theranostics* **2020**, *10*, 8061-8079

Among the different materials that have been previously described as suitable systems for nanomedicine applications, **gold nanoparticles** are undoubtedly one of the most considered and explored³⁴⁸.

Gold in the nanoscale regime has peculiar physical-chemical properties that differ from both those in bulk state and their molecular derivatives. These properties are strictly related to the **size** and cause the appearance of peculiar optical phenomena like the surface plasmon band (SPB)³⁴⁹, the high X-ray attenuation³⁵⁰, and the ability to convert NIR light to heat³⁵¹ to mention a few.

Gold nanoparticles have also interesting **surface electronic features**: while the atoms at the core are surrounded by others and thus with complete coordination, the ones at the surface lack this condition, making them more reactive and prone to soft coordination with organic ligand ends. This noble metal shows inertness not only to a variety of harsh chemical reagents, but also towards biological interactions: being biocompatible and not immunogenic, it is fundamentally non-toxic and can be released from the organism.

The reasons for the widespread interest reside in a series of unique properties that make gold nanoparticles an outstanding working material in the nanotechnology field³⁵². Moreover, size, shape, dispersity, and shell composition can be all finely controlled exploiting various synthetic conditions and functionalization strategies, leading to stable and well dispersible NPs for manifold applications.

Accordingly, this material constitutes a valuable platform for proof-of-concept and preliminary development of many devices: once the system is tested and optimized, changes in material composition can be introduced to achieve different aims or search for other properties.

All these qualities make gold nanoparticles excellent resources in the biomedical field, where the use of hybrid nanostructures (inorganic core and organic shell) opens for applications in advanced treatments of cancer (RT, PTT,³⁵³ drug and biomolecules delivery³⁵⁴), clinical imaging (exploiting different shapes³⁵⁵ and techniques^{356,357}) and biosensors^{358–360}.

Even if there isn't any gold-based nanomedicine approved neither by FDA nor EMA for clinical use yet, there are several promising nanoplatforms currently under trials: a colloidal gold dispersion functionalized with both thiolated PEG chains and recombinant human tumor necrosis factor alpha (rh-TNF, a protein showing antitumoral effects) has been developed by Libutti and co-workers under the name of **Aurimune™ (CYT-6091)** (**Figure 7.1**) that has passed positively the first trials of clinical studies in the phase I³⁶¹. Another promising clinical pilot application in cancer therapy exploits gold-silica nanoshell for the photothermal ablation of prostate tumours³⁶². Kharlamov and co-workers instead are taking at the phase I core/shell silica-gold nanoparticles supported on a bioengineered patch to treat coronary atherosclerosis through plasmonic photothermal therapy³⁶³. In addition, a novel nanotherapeutic compound formed by siRNA oligonucleotides covalently conjugated to a gold nanoparticle (NU-0129) for the treatment of recurrent glioblastoma is at phase I at the Northwestern University³⁶⁴.

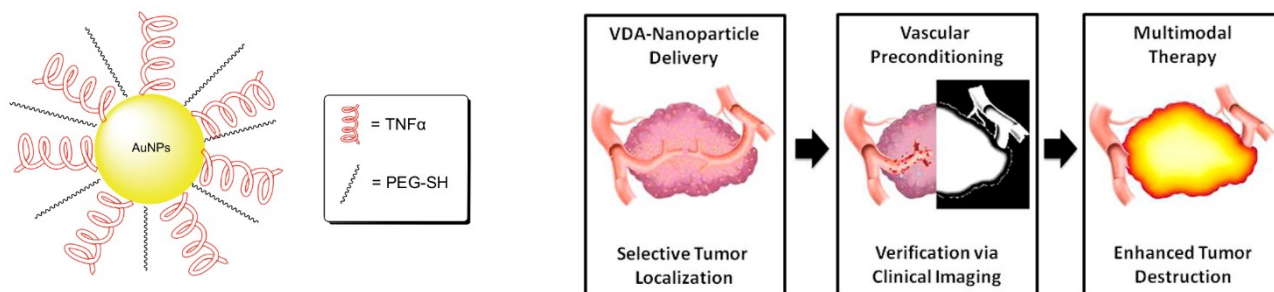


Figure 7.1: (Left) Illustration of functionalizations present on the gold surface of Aurimune™ (CYT-6091) where TNF α means Tumor Necrosis Factor α . (Right) Steps representing the application of a Vasculature Disrupting Agent (VDA) as Aurimune, comprising nanoparticles localization, imaging check, and therapeutic action. Images from references ³⁶⁵ and ³⁶⁶. Copyright © 2008 Chen et al. and © 2013 American Chemical Society.

7.1.1 Synthesis of AuNPs

In the nanomedicine field, the synthetic method that is usually employed for the AuNPs synthesis is the bottom-up method, since it permits finer control over size, shape, dispersion and because NPs stabilization is easier. This type of approach is carried out in a solution (either aqueous or organic) through the reduction of ions to gold(0) by means of chemical, electrochemical or biological

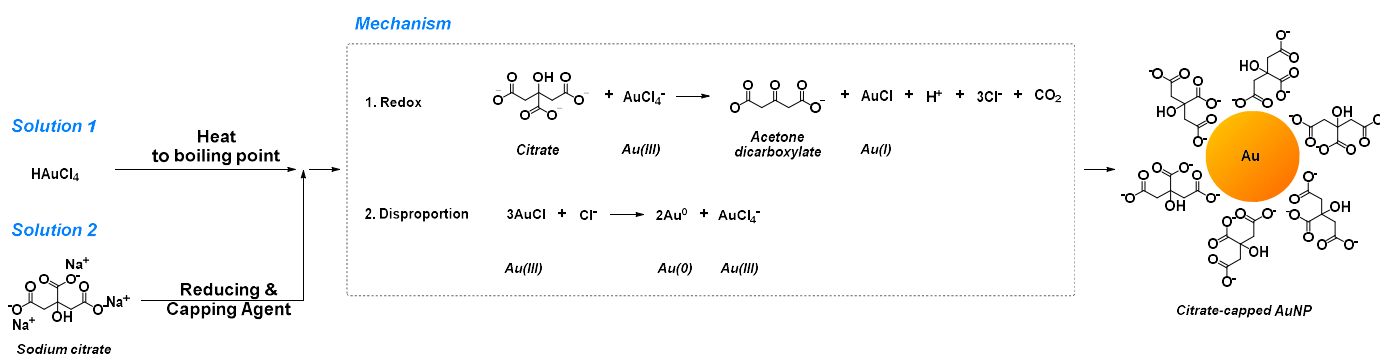
processes³⁶⁷. Some chemical syntheses of gold nanoparticles will be described more in detail in the following section.

7.1.1.1 Gold nanoparticle formation via chemical processes

Among the previous strategies, the **chemical method** (“wet chemistry”) is surely the most popular one and consists in reducing a precursor with gold in +1 or +3 oxidation states to gold(0) by means of an appropriate reducing agent (borohydrides or citric acid, to name the most common); this process may occur in either aqueous phase or organic media, and the gold nanoparticles thus formed have to be stabilized to avoid aggregation. To this end, many capping agents can be used: amines, N-heterocycles, oxygen, alcohols, carboxylic acids, phosphines, but mostly **sulfur-containing ligands as thiols and disulfides**. Moreover, polymers such as polyethylene glycol (PEG) or polyvinylpyrrolidone (PVP) have been used.

Ligands with functional groups containing sulfur, give rise to the strongest bond with gold, of about 40-50 kcal/mol³⁶⁸. In particular, thiols are the most used ones in analogy to many studies carried out on self-assembled monolayers on metal flat surfaces³⁶⁹.

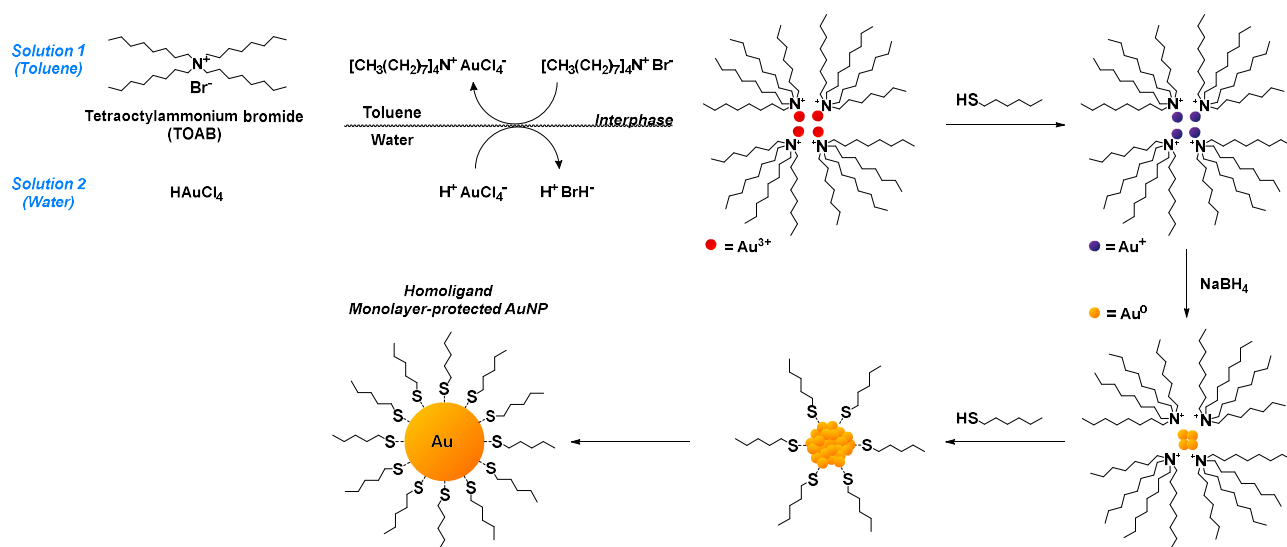
The first synthesis of gold colloids in aqueous solution and CS₂ was reported by Michael Faraday in 1857, using white phosphorous as reducing agent³⁷⁰. The procedure was revisited by **Turkevich in 1951**³⁷¹ (**Scheme 7.1**), then optimized by Frens³⁷², and is currently the most employed one for the preparation of colloidal gold, following a recently unraveled mechanism³⁷³. The gold precursor is always tetrachloroauric acid (HAuCl₄), which is reduced by **sodium citrate** in a water solution brought to the boiling temperature. The excess of citrate works also as the capping agent, creating a coating based on electrostatic interactions that can be easily removed in a subsequent functionalization step, using ligands such as thiols.



Scheme 7.1: Reaction scheme illustrating the synthesis of gold nanoparticles by Turkevich et al., complete with the intermediate mechanism of gold reduction.

Typically, this procedure enables the preparation of nanoparticles with a diameter ranging from 12 to 64 nm, depending on the reaction conditions³⁶⁷. Ascorbic acid may be used to form gold colloids of 12 nm³⁷⁴ whereas stronger reducing agents as sodium borohydride favor the formation of NP with diameters lower than 10 nm or below³⁷⁵.

In 1993 Giersig and Mulvaney proposed for the first time, the stabilization of citrate-gold colloids with alkanethiols³⁷⁶. The first procedure for the preparation of small gold NPs protected by dodecanethiolates was reported in 1994 by **Brust and Schiffrin**³⁷⁷ (**Scheme 7.2**), following a two-phase protocol:



Scheme 7.2: Reaction scheme illustrating the synthesis of gold nanoparticles by Brust and Schiffrin, complete with the intermediate mechanisms for the stabilization and the reduction of gold atoms by the surfactant and the thiol ligand.

Briefly, the tetrachloroaurate anion is transferred from an aqueous solution to the organic layer of toluene using **tetraoctylammonium bromide (TOAB) as the phase transfer reagent**. Alkanethiol is added to the organic layer and subsequently the addition of an aqueous solution of sodium borohydride promotes the reduction of the gold precursor. This process occurs at the toluene/water interface, promoting first the nucleation and then the growth of the gold NPs³⁷⁸.

The very small size of gold nanoparticles that can be obtained, smaller than 5 nm, is due to the formation of small inverse micelles of the surfactant in the organic phase. Inside these micelles, the nucleation and the growth of the gold core takes place when the reducing agent (sodium borohydride) is added.

The **self-assembled monolayers (SAM)** on a three-dimensional structure (3D-SAM) are composed by thiolates that are absorbed spontaneously on the gold core surface and being tightly packed, provide passivation thanks to the strong Au-S bond and Van der Waals interactions among

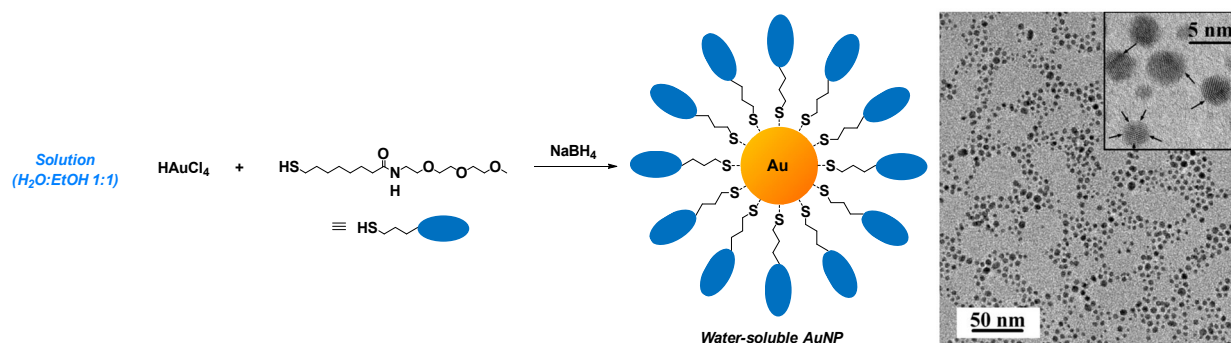
the alkyl chains. These AuNPs are stable in solution over a long period, bearing greatly the exposure to air and thermal changes, as well as multiple cycles of drying and re-dispersion without aggregation or shell deterioration.

Of course, for the progress of gold nanoparticles technology and the easier translation into the biological and medical fields, it is essential to find an approach that could combine the stability of a thiol-protected gold core with the solubility in an aqueous environment.

Murray and colleagues proposed **thiol-ending PEG ligands** to confer water solubility³⁷⁹. Unfortunately, the use of PEG polymer with a high molecular weight (5000 Da), prevents further modification of the monolayer.

In the following years, a variety of ligands were proposed for the synthesis of water-soluble monolayer protected gold NPs, such as small peptides³⁸⁰, glutathione³⁸¹, glycosides³⁸², short PEG-ending chains with thiol groups³⁸³.

An interesting approach was reported by **Pengo et al.**³⁸⁴ (**Scheme 7.3**), using a ligand composed of a **short alkyl chain** (to convey stability), conjugated to a **short PEG (triethyleneglycol monomethylether)**, to impart solubility in water), through an amide bond which increases the stability of the monolayer by forming inter-ligand H bonds.



Scheme 7.3: (Left) Reaction scheme illustrating the synthesis of gold nanoparticles by Pengo et al. (Right) HRTEM image of gold nanoparticles obtained with this method, complete of an inset in which the gold lattice can be seen. Image from reference³⁸⁴. Copyright © 2003 The Royal Society of Chemistry.

NPs' size can be controlled by tuning the Au/thiol molar ratio and the rate of addition of sodium borohydride as reducing agent, obtaining nanoparticles with diameters between 1.5 and 5.0 nm.

Given its structural and synthetical simplicity, these SAM protected NPs established an ideal starting point to reach a further degree of shell complexity and functionalization: a straightforward ligand exchange reaction³⁸⁵ performed directly in a solution of the new incoming thiol species can be employed to introduce for example ligands bearing targeting molecules or reactive functional groups. Additionally, the presence of the short PEG on the NP surface may be particularly useful from the clinical point of view, since it has been demonstrated to prevent nonspecific binding with

biological molecules³⁸³ thus contributing to the making of a “stealth” nanosystem toward possibly immune responses¹⁸³.

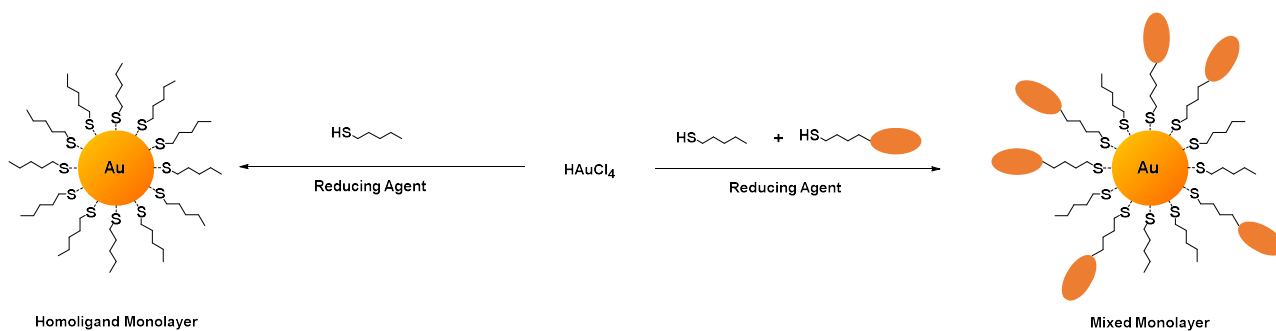
Recent studies of Dawson’s group show that the formation of **protein corona** is sensitive to NP size and functions. Moreover, AuNPs with a gold core lower than 5 nm display long-lived interaction between particles and the biomolecular environment³⁸⁶.

7.1.1.2 Functionalization of gold nanoparticles

The methods that make it possible to build and modify the monolayer around the gold core can be classified in four groups, based on the moment in which the functionalization takes place effectively:

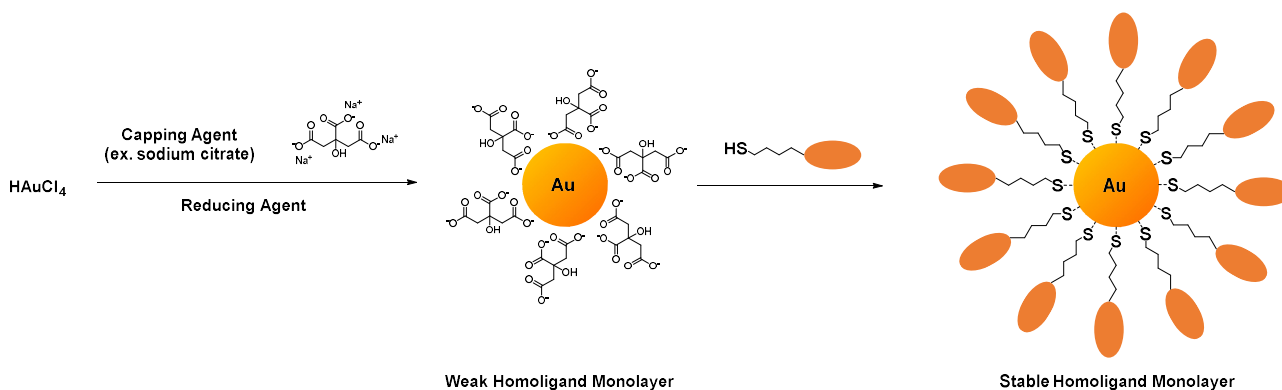
- **Direct synthesis** or “**grafting to**”: the gold nanoparticle is synthesized in presence of a thiol ligand to obtain the complete system with the final and stable monolayer already in place (**Scheme 7.4**);
- **Ligand displacement**: the core is firstly grown and stabilized in presence of ligands that bond the gold surface loosely and successively displaced by thiol ligands (**Scheme 7.5**);
- **Ligand exchange**: the thiol ligands that passivate the core are partially or completely substituted by different thiol ligands; once the core is already passivated by thiol ligands, is still possible (**Scheme 7.6**);
- **Ligand modification (“post-modification”)**: the active ending groups of the ligands are further functionalized or used as a linking point for the covalent insertion of molecules or macromolecules of interest (**Scheme 7.7**).

The first direct possibility (**Scheme 7.4**) requires that some in literature conveniently name also “**grafting to**”, allows forming the nanosystem grafting the ligands that will constitute the final monolayer, **directly on the growing gold nanoparticle** conveying stability and helping the growing process. The synthesis is performed with a reducing species in an aqueous mixture of gold ions (usually HAuCl_4) and the ligand (or more of them, if the aim is to obtain a mixed monolayer)³⁶⁷. The only caution is the compatibility of the functional groups with the reaction conditions, namely, the presence of (strong) reducing agents.



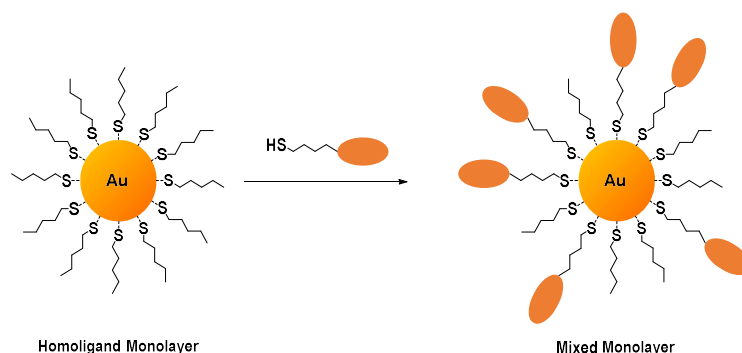
Scheme 7.4: Reaction scheme illustrating the direct synthesis of gold nanoparticles, with the two possible outcomes based on the types of ligands used: one ligand leads to an homoligand monolayer, two or more to a mixed monolayer.

Sometimes these conditions hamper the possibility to insert the thiol ligand in the first step, hence the need for a **ligand displacement approach (Scheme 7.5)**: the objective of this strategy is to form the gold core with a temporary ligand and successively displace it with the final ligand presenting the desired functional group. Usually, preformed AuNPs are protected weakly by electrostatic interactions or ligands such as citrate, amines, or phosphines³⁸⁷ that may be easily replaced completely by one or a mixture of functional thiolates.



Scheme 7.5: Reaction scheme illustrating the ligand displacement approach, starting with a weak capping agent (sodium citrate) that is replaced by a thiol ligand.

A third approach for nanoparticles' functionalization is performing what is called a **“ligand exchange” (Scheme 7.6)**, where the thiolates of the monolayer are partially or completely replaced by different thiols.



Scheme 7.6: Reaction scheme illustrating the ligand exchange approach, in which a thiolate ligand is replaced with a different thiol ligand.

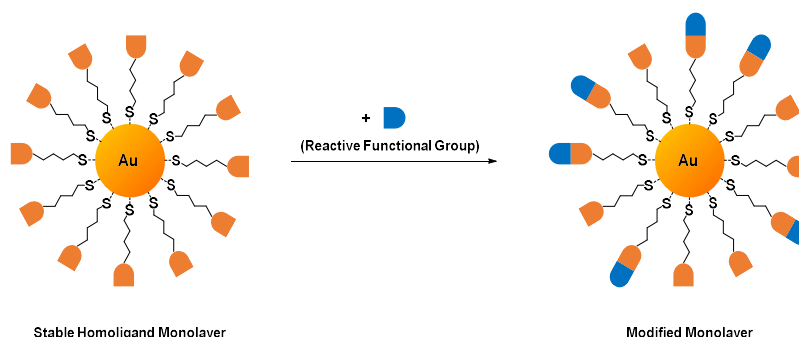
The first example of exchange reaction was performed by Hostetler and colleagues, displacing C8 and C12 thiol chains with a series of different thiol ligands containing useful functional groups³⁸⁸.

Since then, different groups have tried to unveil the mechanism of this process, discovering that the entering ligand place-exchange the exiting one, with a rate that depends on their molar ratio, their relative steric hindrance, and chain length³⁸⁹. In particular, the empirical rule discovered is that the less the thiol is substituted and bulky, the more it is reactive in the exchange reaction.

Generally, what is observed is that the exchange rates are higher than in 2D SAM, due to the presence of vertex and defects on the nanoparticle's surface that favor the substitution^{390,391}.

Usually, the ligand exchange can be adopted to form both homoligand or mixed-ligand monolayers and is particularly useful when the final ligand is not compatible with the reacting conditions for the gold core formation.

Monolayer-protected gold NPs can be further functionalized by **covalent modification** of the functional groups already present on the NP surface with more complex molecules or polymers (**Scheme 7.7**). An example of extreme functionalization was reported by the group of Murray³⁷⁹. In that case, a tripeptide was built step by step on the NP monolayer.



Scheme 7.7: Reaction scheme illustrating the ligand modification after the preparation of gold monolayer-protected nanoparticles.

Interestingly, Xu and colleagues were able to functionalize asymmetrically with a precise nucleotide sequence only a portion of gold nanoparticles covered with oligonucleotides, using

magnetic beads coated with complementary chains as a geometric restriction template and the magnetic separation to help the sample purification³⁹².

Additionally, **polymer-protected gold NPs** may be obtained through this strategy³⁹³. To make this approach possible, it is essential to start with a proper initiator grafted onto the surface: this intermediate state can be achieved using one of the approaches formerly described. Considering the related literature, the types of polymerization that have been tried and can efficiently take place on the gold surface are the surface-initiated atom transfer radical polymerization (SI-ATRP) and the reversible addition-fragmentation chain transfer (RAFT). As an example, the group of Kim and colleagues prepared a siRNA delivery system for the treatment of tumors starting from gold nanoparticles. The nanosystem had a poly(DAMA-HEMA)-multilayered coverage whose cationic charges can incorporate the siRNA strands by electrostatic interaction; in this case, the shell has been grown via SI-ATRP starting from disulfide initiators that were previously grafted on the gold surface³⁹⁴. This strategy has numerous advantages ranging from the fine control over the thickness of the shell (adjusting parameters such as monomer concentration, polymerization time, and temperature), to the possibility of cover the gold core with a layer even denser than the one obtained with the previous methods, counting on the high number of small initiators that can be grafted on the surface. However, this is the least frequent method employed in SAM gold nanoparticles preparation, since it requires a lot of synthetic and purification work to obtain a well compact monolayer.

7.1.1.3 Purification of gold nanoparticles

An efficient **purification method** in the preparation process is fundamental to get rid of the impurities that can accumulate during the synthetic steps (free ligands, unreacted species) but can be very useful also to narrow the nanoparticle size distribution, to separate populations characterized by different mean size or eliminate possible aggregates. This step is even more important for applications in nanomedicine, since the final nanosystem has to be studied in its pure form to avoid any misleading result due to impurities³⁹⁵.

The simplest method of purification is the **extraction** using two immiscible liquids in case the solubility of product and impurities are very different, but also the **centrifugation** (or ultracentrifugation) is a very helpful method to separate nanoparticles from aggregates and small molecules or small particles according to their density and their solubility in the chosen solvent.

Membranes with a precise cut-off can be used to retain a certain nanoparticle population or eliminate aggregates. Besides classic filtration, there is also the possibility to combine it with

centrifugation: the result is **ultrafiltration**, in which the smaller nanoparticles pass the membrane helped by the centrifugal force, while the longer species are retained and can be isolated or dispersed again in fresh solvent.

Dialysis instead is considered a soft purification approach based solely on the concentration gradient between a bag having chosen cut off, filled with the sample, and the outside solution which must be periodically changed since it collects the impurities that pass through the bag membrane. It is particularly useful to remove salts.

Other chromatographic purification techniques are employed, the principals being the **size exclusion chromatography (SEC)**³⁹⁶ and the **gel electrophoresis**³⁹⁷: the first is based on an inert porous stationary phase in which the smaller nanoparticles are retained longer, bigger nanoparticles elute first, while aggregate bigger than the pores are stuck at the head of the column. The second instead relies on a gel matrix across which an electric potential is applied that forces the deposited nanoparticles to migrate accordingly to their charge density and size.

7.1.2 Characterization of AuNPs

The characterization process is of paramount importance while developing a novel theranostic nanosystem. It aims primarily to control the outcome of a new procedure and tune the experimental conditions in order to form nanoparticles with the desired properties. Moreover, since the nanodevice has a clinical finality, a vital part of the analytical process in this field is to verify that the interactions with the biological substrates don't lead to unwanted toxicity and at the same time adequate therapy and imaging capacities are fulfilled, first *in vitro*, then *in vivo*. Ultimately, the characterization process aims to optimize the synthetic steps and to guarantee the reproducibility of the protocol. An increasing number of dedicated techniques have been made available to characterize hybrid organic-inorganic nanoparticles as coated gold nanoparticles, with the purpose to study the metal core and the organic shell separately³⁹⁸.

7.1.2.1 Characterization of the core

The information about the gold core that are commonly investigated are mostly related to its shape, dimension, dispersion, structural composition, and optical properties which, however, are influenced by the organic protective layer.

X-ray techniques are also used for the analysis of the core composition, since the wavelength of excitation has adequate energy to interact with the electronic levels of the material and sense

directly the crystal structure of the sample. For the characterization of gold nanoparticles, one of the most widespread analysis is the **X-ray diffraction (XRD)**, that relies on the Bragg's law to reconstruct the crystallographic structure from the diffraction images and the unique pattern of position, intensity and peaks' profile. With this technique, in 2007 Kornberg and colleagues³⁹⁹ for the first time were able to visualize a high-resolution x-ray structure of a thiol monolayer-protected gold nanoparticle described by the formula $\text{Au}_{102}\text{SR}_{44}$, while Jin and co-workers⁴⁰⁰ succeeded in determining the structural pattern of the thiol ligands disposition on the surface of an $\text{Au}_{133}\text{SR}_{52}$.

Another type of analysis that employs this type of wavelength but in a different way is **X-ray photoemission spectroscopy (XPS)**. Here, exploiting the photoelectric effect, a focused X-ray beam is used to induce the emission of electrons whose kinetic energy is measured to obtain the strength of their binding energy in the atom: this is a useful technique not only to understand what the chemical elements in the sample are, but also to establish their oxidation state, the electronic structure and density. For example, Luo and colleagues were able to verify the conversion of Au^{3+} ions in $\text{Au}(0)$ for amphiphilic Janus gold nanoparticles, identifying the characteristic double signal (at the binding energies of 83.9 and 87.6 eV) in the XPS spectrum of Au_{4f} and also the monolayer composition⁴⁰¹.

Finally, the dimension, the shape, and the preliminary optical properties can be inferred through a **UV-Vis analysis** with the detection of the **surface plasmon band (SPB)**. The average size of the nanoparticles in the dispersion can be extrapolated with Mie theory^{402,403}, whether they are in the 10 - 100 nm range, which corresponds to a maximum of the band between 519 - 569 nm⁴⁰⁴ (**Figure 7.2**).

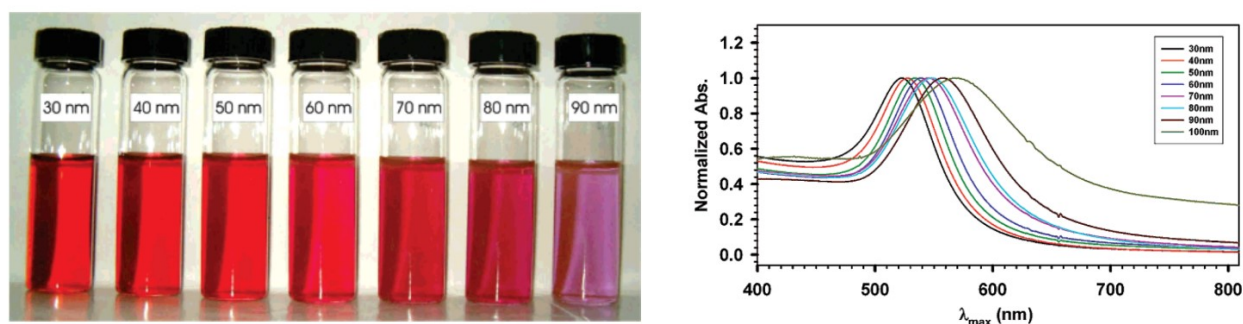


Figure 7.2: (Left) Colloidal dispersions of gold nanoparticles with different colors due to their different average dimension with (Right) the related UV-Vis spectra showing a shift of the maximum absorption peak. Images from reference ⁴⁰⁴. Copyright © 2007 American Chemical Society.

7.1.2.2 Characterization of the organic monolayer

Beside the characterization of the gold core, what is also essential for applications in nanomedicine is knowing precisely the properties and the **physical characteristics of the monolayer**, since it is

the part that effectively will interact with elements like drug molecules, receptors, or cells and determines the real behavior of the nanosystem in the biological environment.

In a preliminary assessment, **UV-Vis spectroscopy** can be used as a qualitative analysis to verify the effective functionalization of the core and the degree of aggregation (and thus the stability) of the sample, studying respectively the shift of the maximum absorbance of the surface plasmon band (SPB) and its broadening, which can be even integrated to obtain the aggregation parameter⁴⁰⁵.

For NPs with a gold core smaller than 5 nm, many of the characterization techniques used for large organic compounds may be used. **IR** and **high-resolution infrared (HR-IR)** offer a qualitative indication of the presence of the desired ligands, even if distinctions between free ligands and the ones chemisorbed on the gold surface cannot be made.

NMR spectroscopy offers much information on the self-assembled monolayer thanks to a different type of experiments⁴⁰⁶. The first important data obtained from a simple ¹H-NMR spectrum is the presence of impurities or free ligands. In this case, sharp signals are present, in contrast to the broad signals pertaining to the thiolates of the monolayer. The broadening is a peculiar feature that can be detected in both ¹H-NMR and ¹³C-NMR spectra of these AuNPs, since with the involvement of the thiolate/Au interface comes a series of factors that depend on³⁷⁵:

- The **packing**: methylene groups closer to the gold surface are more solidly packed and therefore their spin relaxation from dipolar interactions is faster, causing a broad signal;
- The **binding site**: the chemical shift of each thiolate's sections depends slightly on the type of binding site involved (edge, vertex, face) which produces a distinct environment (Knight shifts). For clusters that have many of them, the sum of the relative peaks forms a single broad signal, even if this effect loses quickly its power with distance from the core or with nanoparticle's dimension;
- The **tumbling rate**: thiolates linked to gold surfaces reflect the nanoparticle's behavior in solution and in particular the tumbling speed that is related to the T2 spin-spin relaxation time of the ligand. Large nanoparticles' tumbling is slow and that provokes a reduction of the T2 (a reduced correlation time), which causes the broadening of the signal: this leads to a direct proportion between the width of the peak and the gold core size.

For these reasons, the study of peak broadening can also serve as a mean to infer the core size, even if with small sensitivity and overestimation issues that becomes challenging with increasing dimensions³⁷⁵. However, for quantitative results regarding the ligands, is better to remove the peak broadening through chemical digestion.

Diffusion ordered spectroscopy (DOSY) experiments enable to determine the hydrodynamic diameter of the NPs⁴⁰⁷. Moreover, ¹H-NMR of decomposed mixed-monolayer protected gold NPs allows to determine the ratio between the different ligands and at this point even quantitative determination is possible if a standard is added to the sample.

A notable difference between techniques for the assessment of the dimension regards the type of result in respect to the degree of resolution and the physics behind the measurement: single-particle techniques such as HRTEM and NTA can provide a number-based average dimension of the particle distribution, where each nanoparticle has equal weight, regardless of its size. On the contrary, scattering techniques such as DLS and static light scattering (SLS) base their measurement on the scattered light which is proportional to the particle volume. This result is therefore an intensity-weighted (for DLS) or a volume-weighted average (for SLS), which are often bias to larger values⁴⁰⁸. However, it is always possible to operate a conversion between these average values if the weighting factor is known.

Another important data for the characterization of the monolayer that is always acquired is the number of ligands that have been grafted on the surface during the assembly. **Thermogravimetric analysis (TGA)** can be a very helpful technique: the basic principle is to weigh the mass of the sample before and after heating it up to 800 – 1000 °C. If the procedure is applied to SAM-protected gold nanoparticles, this means that the initial measured mass decreases because of the transformation of the organic monolayer in volatile compounds, while what remains at the end is only relatable to the inorganic metal core which is not affected by the rising temperature.

Inductively coupled plasma mass spectrometry (ICP-MS) in this sense could be an alternative type of analysis to gain similar information since is capable to detect the ratio between core Au atoms and S atoms present on the ligand⁴⁰⁹.

At this point, the results of TGA (or ICP-MS), TEM, and DLS (or NTA) can be combined to obtain the monolayer density, hence the degree of coverage by the ligands grafted on the gold core.

Regarding mixed SAM-protected AuNPs, what is also interesting and useful to know in terms of biological interactions concerns the density, the disposition, and the morphology of the domains formed by each of the different types of ligands on the gold surface. Different types of domains have been identified: “**Janus**”, for a nanoparticle divided in two halves with complete phase segregation, “**stripe**”, for elongated domains, “**patchy**”, if the segregation gives rise to spots of one ligand or “**random**” if the distribution of ligands has a casual organization.

Either direct or indirect characterization methods can be employed to investigate the surface morphology of the monolayer.

Considering the direct methods, the technique that has been proposed is the **scanning tunneling microscopy (STM)**, since it allows to collect an “image” of the monolayer organization with high resolution and even detect and differentiate sub-nanometer ordered domains in the monolayer, such as in the stripe-like fashion⁴¹⁰. STM can be possibly coupled with power spectral density (PSD) to obtain the characteristic spacing of the ligands and quantitative information on domains where the contribution of ligands with different lengths is more visible⁴¹¹. However, some restrictions in the use of this technique have been encountered in terms of sample cleanliness, deposition of the NPs, and ligand length.

Other techniques which can be employed are the **atomic force microscopy (AFM)** or the **small-angle neutron scattering (SANS)**: the first one sense directly the surface of the nanoparticle coming in contact with the monolayer with a small tip on a cantilever, the second instrument provides structural information as a reconstructed 3D comparing hydrogenated and deuterated species in the ligand shell, from which is possible to extrapolate the degree of solvation and the ligand ratio. However, this technique requires NPs samples with dispersion lower than 10% and a significant part of data elaboration.

Focusing on indirect methods instead, several techniques have been optimized to obtain data on the morphology of the mixed monolayer.

Once the chemical information has been collected and the characteristic signals have been detected, **NMR** can be helpful once again, this time to reveal what is the pattern on the shell, as has been reported for example by Stellacci's⁴¹² and our group⁴¹³. In particular, the chemical shifts are influenced by the neighboring ligand species: different organizations of the monolayer produce different behaviors of the chemical shifts vs. the monolayer composition. For random mixtures, the ligand's chemical shift shows a linear dependence on the shell composition, due to the equivalence between the global and the local composition. For Janus morphologies instead, the shift is proportional to the inverse of the composition. For patchy particles, the situation becomes more complex and the trend depends on the evaluation of the shape of those separated domains. This technique has been used both for mixtures of different hydrogenated ligands using ¹H-NMR spectra or mixtures of hydrogenated and fluorinated ligands exploiting ¹⁹F-NMR which is one order of magnitude more sensitive than proton NMR.

Another type of experiment that can be used is **NOESY or HOESY**, even if the effects on which are based can be only observed when the nucleus spins are close enough (less than 0.5 nm):

therefore, the observance of cross-peaks can distinguish Janus particles from other types of morphologies^{412,414}.

Other techniques for obtaining data regarding the type of phase segregation and organization of the mixed monolayer are the **matrix-assisted laser desorption/ionization (MALDI)** coupled with mass spectrometry⁴¹⁵ and measurements of contact angle⁴¹⁶. In particular the MALDI-IM-MS (Ion mobility-mass spectrometry) coupled technique has been demonstrated as particularly useful to detect the type of phase segregation on the surface of gold nanoparticles with mixed thiolate monolayer. The MALDI process generates fragments of Au₄L₄ ions (where L is the thiolate ligand) which are detected by the mass spectrometer: the relative amount of the possible fragments indicates the degree of domain separation (random, patchy, or Janus) (**Figure 7.3**).

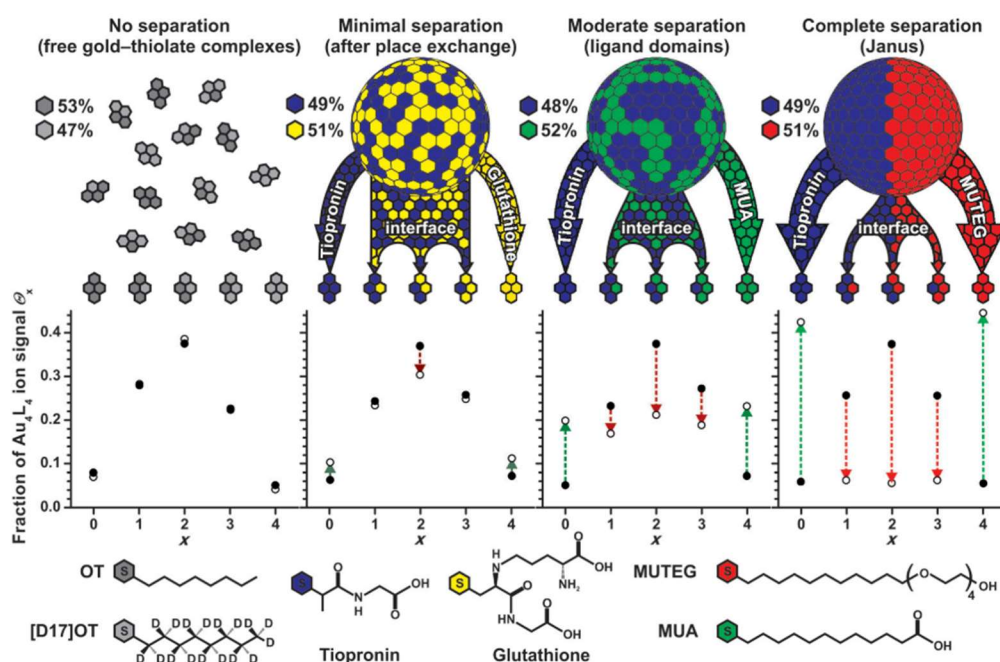


Figure 7.3: Different degrees of phase separation obtained by comparison of experimental (MALDI) and theoretical ligand distributions for free gold-thiolate complexes and three mixed-ligand AuNPs obtained by ligand-exchange reactions of tiopronin AuNPs with free glutathione, 11-mercaptoundecanoic acid (MUA), or mercaptoundecyltetraethylene glycol (MUTEG). Image from reference⁴¹⁵. Copyright © 2011 Wiley-VCH

What has been generally discovered (with also the help of computational simulations) is that the precise type of surface organization in mixed monolayers is highly dependent on a series of factors such as the core dimension (small nanoparticles below 2 nm are more prone to be Janus-type), the length of the ligands and their relative number.

7.2 FLUORINATED LIGANDS

In 1938, R. J. Plunkett, a DuPont chemist, was using tetrafluoroethylene (TFE) as an intermediate in a program aimed at the synthesis of new refrigerants. [...] Plunkett was not expecting the TFE to polymerize [...]. His discovery – of such great importance to mankind, for PTFE now touches peoples' everyday lives in numerous ways – is one of the best known examples of scientific serendipity.

– from “Organofluorine Chemistry: Principles and Commercial Applications”⁴¹⁷

As reported in section 1.4, gold nanoparticles can be functionalized with an extensive variety of alkanethiol ligands. The structure of the ligand may present an alkyl chain (more or less branched) or aromatic rings or more complex units like peptides³⁸¹.

One of the innovative alternatives that has been studied in the last decades comprises the presence of a **perfluorinated moiety** in the structure of the ligand and in the section below the rationale behind this choice will be explained.

Even if the start of fluorine chemistry can be dated back to 1886 with the isolation of elemental fluorine by Henri Moissan⁴¹⁸, only the discovery of Teflon by Roy J. Plunkett at DuPont in 1938 triggered the research and applications of organofluorine compounds.

Since the ligands that are employed in nanomedicine are often not fully fluorinated, for the sake of inclusivity, also compounds with some hydrogen left would be categorized as “fluorinated” or simply “fluorocarbons” and here considered. A rigorous classification is presented in **Figure 7.4**.

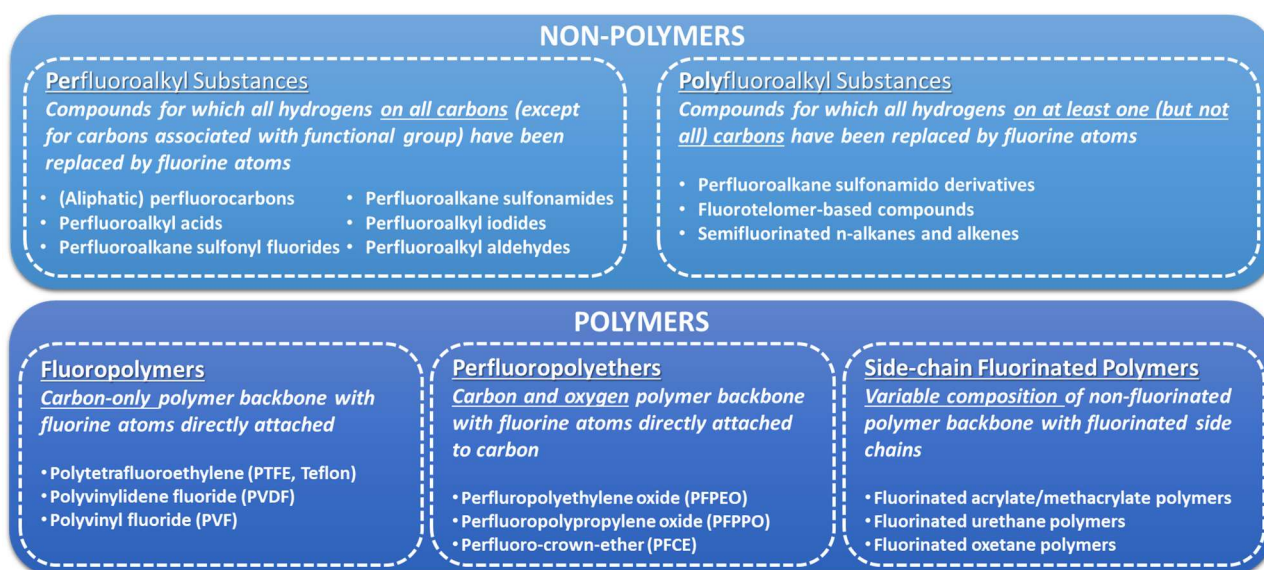


Figure 7.4: Scheme for the definition and the classification of the most common fluorinated species. Adapted from reference⁴¹⁹.

7.2.1 Properties

Perfluorinated compounds present **physicochemical properties** that are extremely different in comparison with the parent hydrogenated chains. Fluorine has a bigger van der Waals radius – 1.47 Å with respect to 1.20 Å for H – and the highest value of electronegativity among all the elements of the Periodic Table, which led to a high ionization potential and very low polarizability⁴²⁰. The presence of a dense electron distribution is the reason why perfluorocarbons are bulkier – the cross-section is around 30 Å² with respect to 20 Å² of the analogous hydrogenated chain)⁴²¹ – and with a more rigid structure⁴²², to the point that the axial rotation is sterically hindered and the conformation with the lowest energy is helical, instead of the gauche or “zig-zag” folding adopted by alkyl chains⁴²³.

Due to the orbital energy levels and their overlapping, the C-F link is the strongest single carbon-heteroatom bond in organic molecules with an energy up to 130 kcal/mol in CF₄ molecules⁴²⁴ while the H-F link is the strongest single bond of all with an energy of 136 kcal/mol (for comparison, the C-H bond is up to 104 kcal/mol in CH₄) and increases with increasing C substitution. Consequently, fluorocarbons are relatively inert species, being chemically and thermally stable and not flammable: the electron cloud is once more determinant, since it shields effectively the carbon backbone and prevents the interaction with any reagent (acids, bases, reducing or oxidizing agents)⁴²⁵.

These features, along with the low polarizability, lead to weak van der Waals intermolecular forces, **fluorophobic interactions** (meaning both hydrophobic and lipophobic, thanks to the bulky structure and the low polarizability combined), and low cohesive energy densities⁴²⁶. The translation in terms of physical states is that fluorocarbons have high vapor pressure and higher melting points in respect to hydrocarbons with the same number of C atoms, while the boiling points could be higher or lower if the number of C atoms is below or above 4 respectively⁴²⁷. Inserting some branch in the structure lowers both the boiling and the melting points.

In relation with other substances, they thus present very low surface tension (even below 20 mN/m), high density, high compressibility and fluidity, anti-friction and spreading abilities, which could be turned useful in material and interface sciences⁴²⁸.

Notably, for a variety of applications in electronics and medicine, they present also low dielectric constants, low refractive index, gas-dissolving capacity (especially in binding oxygen⁴²⁹), and a low critical micellar concentration (CMC) if compared with the analogous hydrogenated surfactants⁴³⁰.

Since these molecules are exploited also in the biomedical field, they have been extensively tested with cells, tissues, or organisms and their biocompatibility has been proved thoroughly. The results indicate that the majority of perfluorinated species are **biologically inert** and physiologically

inactive, since they don't take part in any metabolic process. Notable exceptions being the structures presenting double bonds⁴²⁰ and carboxylic groups⁴³¹, which are extremely reactive in the first case, strongly acidic in the second, and overall toxic.

No carcinogenic, mutagenic, or teratogenic effects have been discovered for the rest of the perfluorocarbon class in the range of 460-520 Da⁴³².

Once inside the bloodstream through ingestion, inhalation, or injection, the emulsion droplets are opsonized, taken by the macrophages of the reticuloendothelial system, and stored for a variable time in the liver, spleen, or bone marrow. Then they are excreted through the bowel or introduced again in the cardiovascular system thanks to lipid carriers and eliminated through expiration or in small amounts through the skin^{433,434}. All these passages do not involve breaks or transformations of their chemical structure. The half-life in the organism can vary from minutes to years and depends principally on the molecular weight, lipophilicity, and volatility; indeed, for several species, there are some pieces of evidence of bioaccumulation in human tissues.

A class of perfluorochemicals which are studied since the 1960s and applied in the biological field as well and will be considered more extensively are **perfluoroethers** (linear or cyclic, such as crown-ethers) or perfluoropolyether (PFPE). They differ from the perfluoroalkyl structures described so far in the extent that they contain oxygen atoms between the $-CF_2-$ units: in the project described in the following section, we will focus on polymers containing **perfluoroethylene oxide units** ($-[CF_2-CF_2-O]_n$), whose geometry, conformation and charge distribution have been already calculated⁴³⁵.

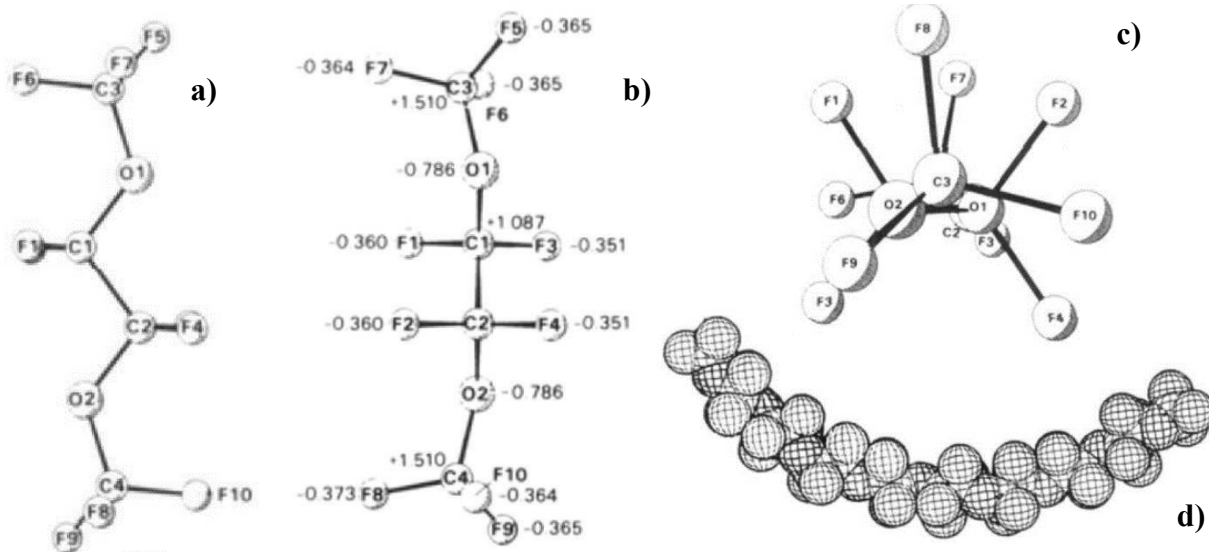


Figure 7.5: Computer drawing of (a) the optimized geometry for the backbone, (b) the net charge distribution, (c) the optimized conformational geometry along the backbone, and (d) the conformation calculated with molecular dynamics for the poly(perfluoroethylene oxide) (PPFEO) model compound. Images from reference ⁴³⁵. Copyright © 1991 American Chemical Society.

Their structure has the peculiar PFCs helical conformation but is generally more flexible, they are soluble in polar solvents and have lower melting points in respect to perfluoroalkanes⁴³⁶, with a very low glass transition point that makes them behave like a liquid in a wide range of temperatures⁴³⁷. Moreover, the thermal and chemical stability which are lead features of PFCs are preserved. This means that PFPE are a more favorable option when looking for longer inert hydrophobic or lipophobic chains.

The **synthesis of perfluoroalkyl (PFA)** is one of the pioneering discoveries done during the Second World War and since the 40s two procedures are still in use for their production: the **Fowler process** and the **electrochemical fluorination** (or Simon process). The Fowler process adopts CoF_3 as a source of fluorine to convert hydrocarbons into fluorocarbons with the creation of HF as co-product⁴³⁸, while the electrochemical fluorination is based on the electrolysis of particular substrates (usually ethers or tertiary amines) in presence of HF and low voltages⁴³⁹.

Later on, DuPont started to investigate and commercialize the **telomerization process** to produce perfluoroalkyl iodides which could be further functionalized^{440,441}; with many optimizations implemented during the years, this radical polymerization is still adopted to produce reactive perfluorochemicals (called also “fluorotelomers” for this reason) with controlled length and variably functionalized.

For what concern the synthesis of **perfluoroethers** instead, the synthetic method that should be adopted depends on the final outcome that is desired, but usually they are carried on using **photooxidation** of tetrafluoroethylene or hexafluoropropylene with UV light⁴⁴² or other radical initiators⁴⁴³ or the (poly)ethylene oxide treatment with elemental fluorine (**direct fluorination**⁴⁴⁴ or **electrochemical fluorination**⁴¹⁷). Different perfluorinated crown ethers have been prepared by controlled elemental fluorination at low temperature, starting from the hydrogenated species^{445,446}.

Considering the synthetic ways proposed, perfluorochemicals have generally high prices, but fortunately only small quantities of them are needed to provide the material or the dispersion with their peculiar properties described.

7.2.2 Applications

The properties of perfluorinated compounds have been exploited for applications in a variety of fields: considering perfluoroalkyl chains with various ending functional groups, in industry they are often used in fire-fighting foams⁴⁴⁷, paints, pesticides⁴⁴⁸, or anti-adherent coatings (the most known being Teflon). Modified perfluoroethers have been patented as well as oil- and water- repellents

coatings for surfaces⁴⁴⁹ or fibers⁴⁵⁰, proton conductor in electronics and fuel cell design (under the commercial name “Nafion”)^{451,452} or as liquid lubricants (Krytox) or sealants in the aerospace industry⁴⁵³.

Apart from materials, this class of perfluorocarbon compounds has been exploited also for **biomedical applications**: since the 60s, perfluorocarbons enriched in oxygen have been investigated as a mean to preserve organs, oxygen carrier, or blood substitute^{429,454} or even to allow total or partial liquid ventilation of the lungs⁴⁵⁵. Indeed, the solubility of oxygen in perfluorohexane is greater than the solubility in n-hexane under identical conditions⁴⁵⁶. With a focus on the nanomedicine field, PFC chains have been used for decades to support and enhance both the diagnostic efforts in pathologies identification and the subsequent request for adequate therapies. While there are some examples of their use in **X-ray imaging** (especially for the gastrointestinal tract)⁴⁵⁷, they are better known in the most widely used imaging method in the world, namely **ultrasound imaging** or ultrasonography. The technique is commonly available, non-invasive, versatile, and cost-effective and allows a real-time analysis with deep tissue penetration and a high degree of safety, since it uses harmless mechanical waves^{458,459}. However, the diagnostic power is often limited by the low imaging resolution, thus the need for a contrast agent that could be capable of scattering ultrasound energy more effectively, given the optimal range of bubble dimension and stability⁴⁶⁰. Beside other gases that can be used as an effective contrast agent such as air⁴⁶¹, N₂⁴⁵⁸, or SF₆⁴⁶², different species belonging to PFCs have been successfully tried like gaseous perfluoropropane⁴⁶³ or perfluorobutane⁴⁶⁴ or liquid perfluoropentane⁴⁶⁵, or perfluorohexane⁴⁶⁶. The preparation of these agents requires the formation of nanobubbles which are often structured by proteins (i.e. albumin), lipids, or polymers (**Figure 7.6**) to pursue stability, biological safety, easy injection, and capillary permeation⁴⁶⁷.

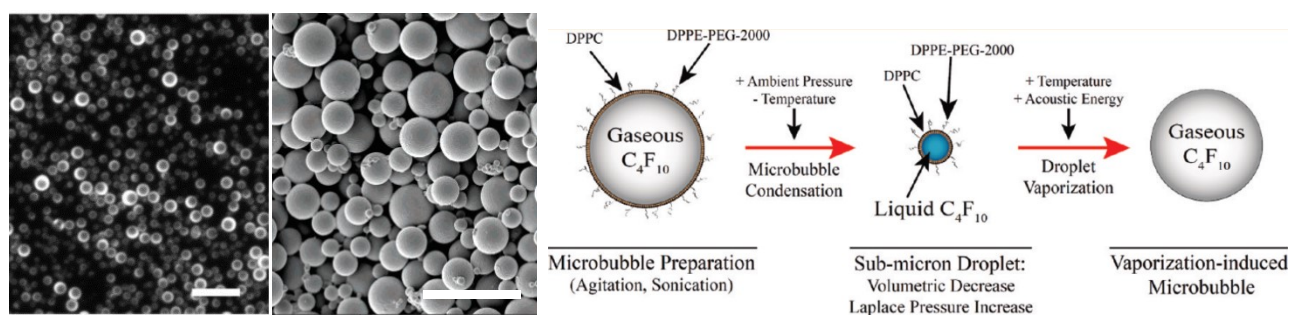


Figure 7.6: (Left) Bright-field microscopy image of liquid perfluorocarbon (dark) encapsulated in a polymeric structure (bright contour) (scale bar = 20 μm) and (Centre) SEM image of the same microcapsule (scale bar = 10 μm). (Right) Representation of the Acoustic Droplet Vaporization (ADV) mechanism used for ultrasound contrast in lipid-encapsulated nanodroplets of decafluorobutane. Images adapted from references ⁴⁶⁶ and ⁴⁶⁸. Copyright © 2006 American Chemical Society and © 2011 American Chemical Society.

The pathologies which benefit from the adoption of this imaging system are prevalently related to the cardiovascular system^{464,469}, since the bubbles remain inside the blood vessels. However, also the oncological application of nanomedicine has taken advantage of it: in this case, smaller bubbles in the nanometre range could extravasate towards the tumor tissue and accumulate in it, where they are converted in microbubbles through **acoustic droplet vaporization (ADV)** (Figure 7.6) in order to become an effective contrast agent for ultrasound imaging^{470,471}.

Coupling PFCs with ultrasounds is beneficial also in terms of therapy: here particular perfluorinated structures can be exploited to favor the accumulation of oxygen near cancer cells, in order to contrast the tumor cells' hypoxia and enhance the **sonodynamic treatment (SDT)**⁴⁷², the **photodynamic treatment (PDT)**^{473,474} or the **radiotherapy**⁴⁷⁵ that work through the formation of reactive oxygen species (ROS), created by chemical species named sonosensitizers⁴⁷⁶.

Another type of treatment in which perfluorocarbons have been demonstrated to enhance efficiency is high intensity **focused ultrasound (HIFU)**⁴⁷⁷, which involves the conversion of acoustic energy in thermal energy that ablate cancer cells in different districts of the body⁴⁷⁸.

The application which is currently one of the most promising in the diagnostic field comprises the use of perfluorinated compounds as **contrast agents for ¹⁹F-MRI**. Comparing it with the most exploited technique in this field, namely ¹H-MRI, several technical similarities can be pointed out that make this technique a trustworthy alternative. The F nucleus has an even higher relative abundance in respect to the H nucleus (basically 100% instead of 99.98%) and a very high and comparable gyromagnetic ratio ($\gamma^{1\text{H}} = 267.5 \text{ rad s}^{-1} \text{ T}^{-1}$, while $\gamma^{19\text{F}} = 251.7 \text{ rad s}^{-1} \text{ T}^{-1}$). This is translated in a **relative sensitivity of 83% compared to proton's**, since the intensity of the collected signal is directly proportional to the number of nuclei and the gyromagnetic ratio.

The signals related to ¹⁹F nuclei can be detected in a wider range of chemical shift, spanning from 550 ppm to -250 ppm, thanks to the higher number of electrons in the outer shell and their higher susceptibility and sensitivity towards the external environment in respect to the single electron of the ¹H nucleus⁴⁷⁹. In respect to the narrower range of 12 ppm of ¹H-NMR, this enables a clearer distinction of the different functional groups even if more perfluorocarbon molecules are used simultaneously in combination with multiple biochemical markers⁴⁷⁹.

Moreover, the **endogenous content of ¹⁹F in our body is negligible**: these atoms are prevalently in the form of fluorapatite $\text{Ca}_5(\text{PO}_4)_3\text{F}$ that can be found in teeth or bones in a concentration above the detection limit estimated around $10^{-3} \mu\text{mol/g}$ wet tissue weight⁴³². However, the nuclei are fixed in the crystalline lattice, so the visible signal is practically inexistent due to the very short spin-spin relaxation time T₂. This means that every fluorine nucleus that is injected in the body as drug or

contrast agent, could be detected and give a reliable qualitative and most of all quantitative response, which is fundamental to have a proper sensitivity.

On the downside of the paucity of ^{19}F nuclei, the requirements needed to have an image with comparable quality in respect to ^1H -MRI, are the high density of F nuclei in the contrast agents' chemical structure and an elevated local concentration of them. The first necessity has been overcome implementing linear perfluorocarbons like the ones in **Figure 7.7** such as perfluorooctylbromide^{480,481} (PFOB, also known commercially as LiquiVent® or Oxygent™ and already used as blood substitute), emulsions of perfluorodecalin and perfluorotributylamine (known as Fluosol-DA)⁴⁸², crown ether such as perfluoro 15-crown-5-ether (which is perfect since it has a single sharp signal)⁴⁸³ or branched structures such as PERFECTA (suPERFluorinatEd ContrAsT Agent) by Metrangolo's group^{484,485}. The second need can be achieved by exploiting nanosystems containing the contrast agent and an active targeting system to focus the accumulation on a precise surface or tissue⁴⁸⁶ (**Figure 7.7**, on the right).

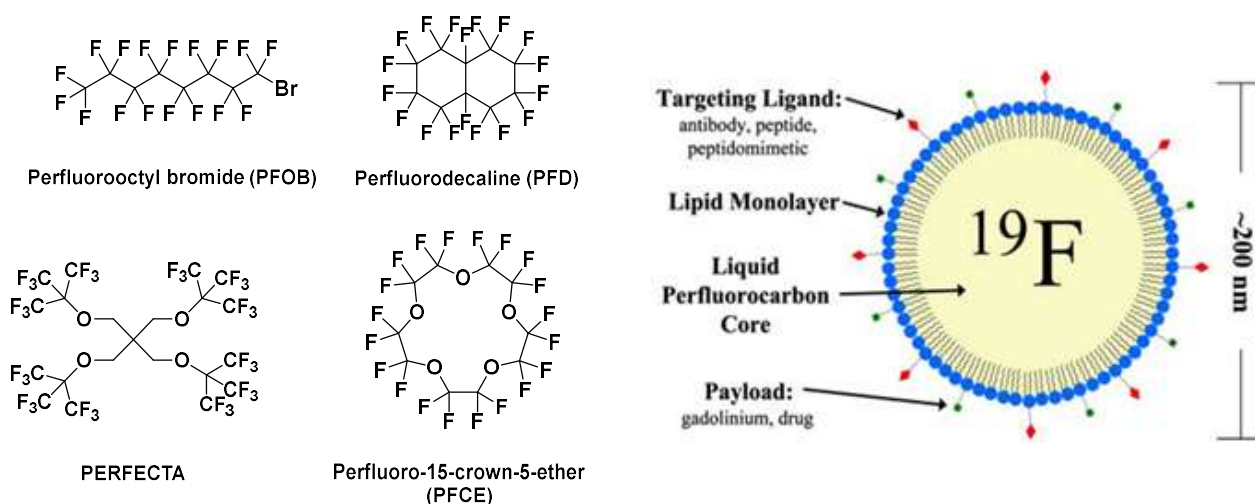


Figure 7.7: (Right) Examples of chemical structures for ^{19}F molecular tracers. (Left) Schematic representation of a functionalized liquid perfluorocarbon nanoemulsion, in which the lipid monolayer functionalized with target ligands contains the liquid perfluorocarbon core and possibly drug molecules. Images from references ⁴⁸⁵ and ⁴⁸⁷. Copyright © 2014 American Chemical Society and © 2009 Biomedical Engineering Society.

Given the efficiency and versatility, several studies have also addressed the possibility to use these perfluorocarbons in a **multimodal imaging** system that works with both ultrasound and ^{19}F -MRI, in order to combine the versatility and ease of use of the former, with the high spatial resolution of the latter^{470,488}.

Besides the applications in the diagnostic area, fluorinated ligands can be efficiently adopted as a mean to **collect and store different drug molecules**: many authors have demonstrated that perfluorocarbons are capable of establishing fluorophilic or non-covalent interactions not only with

molecules containing F nuclei, but also with molecules that have none. Moreover, these bonds are even stronger than an analogous, fully hydrogenated chain could form⁴⁸⁹.

This ability can be extremely useful while designing a complex system that must act as a storage and subsequent release device for precise chemotherapy.

In fact, thanks to their low CMC, **perfluorinated surfactants are known to self-aggregate easily in aqueous media** in order to create structured and thermodynamically stable supramolecular assemblies like films, micelles, fibers, and vesicles⁴²⁵. The formation of these colloidal systems (emulsions, dispersions, or gels) driven by the simultaneous lipophobicity and hydrophobicity of the species, could be exploited as a mean to **deliver drugs**. Moreover, these surfactants or the droplets they form can be further functionalized externally with various species for imaging, targeting, or therapeutic purposes. Then, the carried drug can be linked to the surface, disperse in the coating, or stored internally within the emulsion^{470,487}.

In this case, the outstanding sensitivity of the ¹⁹F MRI technique (eventually enhanced with frequency-selective excitation) can be coupled with the delivery and exploited to have a **quantitative assessment of the drug** that effectively reaches the desired site⁴⁷⁹ or the presence of a particular molecule or epitope in the organism (quantitative imaging), even with complex samples⁴⁹⁰.

Still taking advantage of the high signal-to-noise ratio and the absence of endogenous species, tailored ¹⁹F probes can be successfully used also to **label and track particular cells** (such as stem cells⁴⁸¹ or macrophages⁴⁹¹) or to probe and **verify the activity of specific enzymes**⁴⁹² *in vivo* or *in vitro*.

7.2.3 Fluorinated gold nanoparticles

The fluorinated species which plays the diagnostic or therapeutic roles described in the previous section can be used directly to form the carrier structure that is then stabilized for its use in aqueous environments. Rather than finding their optimal micellization conditions, fluorinated assemblies can be designed by grafting suitable fluorinated structures on a single or multiple cores made of carbon, silica, metal, or metal oxides.

Along this line, gold as a material for nanoparticles is largely considered an ideal option in the preliminary phases of a project, since the result can be achieved through a wide variety of synthetic procedures that allow fine control over size, shape, and dispersion of the nanoparticle's core. It is also a rapid way to investigate the interaction with the biological environment and eventually the suitability of targeting methods, having a scaffold that can be easily tailored.

Considering the chemistry of gold, the **fluorinated ligands** are required to **present a thiol function** at one of the ends to ensure the formation of a strong gold-sulfur bond which guarantees a homogenous and stable monolayer: the preferred structures that are recurrent in literature range from perfluorinated alkyl- or arylthiols to amphiphilic fluorinated thiols⁴⁹³.

Moreover, this particular strategy opens to the possibility of modifying the monolayer with different thiol chains that substitute completely or partially the original thiolates through a **place exchange reaction**³⁸⁵, thus shaping overall nanoparticle's properties and imparting different characteristics.

The **arrangement of a mixture of ligands** that form the monolayer can be random or lead to phase segregation, in which surface morphologies or areas formed by a single type of ligand can be detected, especially when geometric or thermodynamic constraints are introduced in their structures⁴¹⁰ (**Figure 7.8**).

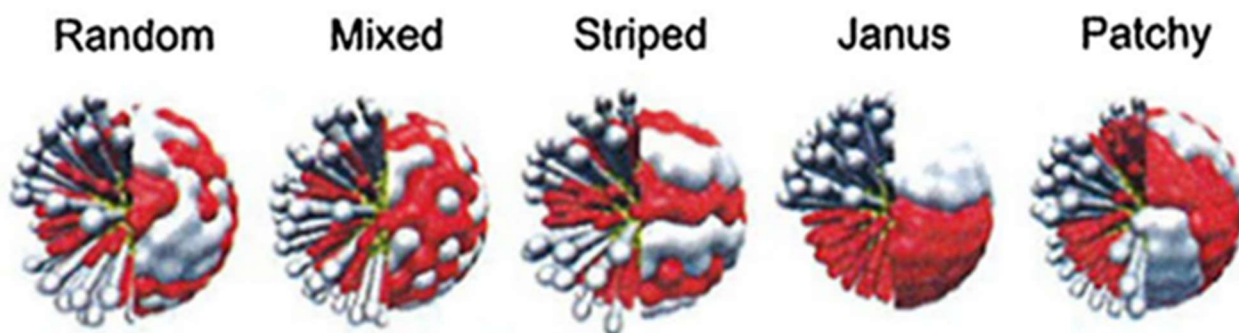


Figure 7.8: Different simulated nanoscale morphologies for a 1:1 mixture of 11-mercapto-1-undecanesulfonate (MUS, hydrophilic, white color) and 1-octanethiol (OT, hydrophobic, red color). Image from reference⁴⁹⁴. Copyright © 2014 The Royal Society of Chemistry.

One of the first attempts in the preparation of fluorinated NPs was performed by the group of **Murray** through a Brust-Schiffrin synthesis, using **fluorinated alkyl and aryl thiolates**⁴⁹⁵. However, the problem with this preparation is that the nanoparticles resulted to be soluble only in perfluorocarbon solvents, thus hardly applicable for further studies.

A step forward for the translation of fluorinated gold NPs in aqueous environments was taken preparing **amphiphilic thiolates which feature polyethyleneglycol (PEG) units**: with the optimal length of the hydrophilic moiety that is exposed and forms the nanoparticles' shell, it was possible to form stable nanostructures and disperse them in water⁴⁹⁶.

Later on, Niikura and co-workers were able to induce a further level of self-assembly of similar NPs that were larger in size, exploiting halogen bonds and inducing the formation of vesicles made of semi-fluorinated gold nanoparticles in THF to use the overall structure as SERS-active drug delivery system in aqueous solutions⁴⁹⁷.

Trying to understand the feasibility of the **fluorinated ligand in drug delivery**, several complexation studies with aromatic, fluorescent, or fluorinated probes have been performed.

Exploiting the Electron Spin Resonance (ESR) setup, the binding constants of a radical probe for gold nanoparticles monolayers carrying flexible fluorinated PEG ligands have been discovered to be significantly higher in respect to their hydrogenated or more rigid fluorinated analogous⁴⁸⁹. This enhanced binding was observed not only for species containing fluorine nuclei, but also for hydrophobic non-fluorinated molecules as a combined effect of the increased hydrophobicity of the fluorinated ligand and de-solvation energy gained from water to fluorinated environment. Combining these properties with the possibility to have the segregation of the phases, it is clear that these nanosystems have the potential to bind and carry even two or more different species at once⁴⁹⁸.

In parallel with these studies, the possibility to exploit these fluorinated gold nanoparticles as **contrast agents for ¹⁹F-MRI** has been deeply investigated. Extensive MRI phantoms experiments have been performed on an aqueous dispersion of gold nanoparticles protected with ligand ending with a perfluoro tert-butoxy head⁴⁹⁹ or presenting perfluorinated ethylene oxide units⁶⁴. The results demonstrated how these nanoplatforms can be efficient contrast agents with comparable features in terms of fluorine loading, signal intensity, and narrowness in respect to the perfluorocarbon emulsions and micelles used so far.

The adaptable design of this type of self-assembled nanoparticles permits even to build **multimodal nanoplatforms**: the MR imaging power of the most sensible nuclei (¹H and ¹⁹F) can be combined using a thiol ligand bearing a Gd(III) chelating unit and another ligand functionalized with a fluorinated moiety on the surface of a gold nanoparticle that is overall water soluble and biocompatible⁵⁰⁰. This strategy has been demonstrated to have a synergic effect, reducing the T1 of the fluorinated moiety, thus speeding up the acquisition and overall enabling the tracing of specific targets or species marked with fluorine nuclei with the sensitivity of ¹⁹F-MRI, while performing also anatomical imaging with ¹H-MRI on the same imaging setup.

A slightly different application that involves fluorinated gold nanoparticles equipped with perfluorooctanethiol or perfluorodecanethiol ligands is the support of **nanostuctured imaging mass spectrometry (NIMS)**, a nanoparticle-assisted soft laser desorption or ionization approach that have the aim of keeping intact the molecular ions, thus assuring high sensitivity even with fragile species^{501,502}.

Since these nanosystems are designed to be implemented in *in vivo* applications, the assessment of their **biocompatibility** is a crucial study that has to be performed carefully. Since all the experiments and the nanosystems proposed are still at the early stage of their development, the information related to their toxicity are mainly based on *in vitro* studies. However, from the

information related to the perfluorinated building blocks used for the preparation of the ligands, is already possible to extrapolate some general guidelines: in particular, perfluorocarbons already used in medicine⁴³², block copolymers containing perfluorinated moieties⁵⁰³ and perfluoropolyethers⁵⁰⁴ show limited toxicity, while for the sulfonate and acid fluorinated derivatives the long term toxicity is not negligible^{505,506} and therefore should be avoided, preventing also the risk of generating them as products of degradation or metabolism. Regarding the preliminary biocompatibility tests performed directly with the nanosystems, all reported **scarce or nil cytotoxicity to HeLa cell lines** in the absence of the drug or when their therapeutic function is not triggered^{64,497,499}.

Another analysis that is fundamental for future *in vivo* applications involves the **interaction with biological membranes**: Marson and co-workers have performed *in silico* and *in vitro* studies for gold nanoparticles protected with a mixed self-assembled monolayer prepared with combinations of hydrogenated and fluorinated ligands⁵⁰⁷. The computational calculations on the monolayer provided the distribution of the ligands in the shell, while its dynamic contact with a simulated lipid bilayer, gave information on the interaction energies. On the other hand, *in vitro* experiments were performed with surface plasmon resonance (SPR) on gold nanoparticles in contact with phospholipid membranes or cells which allowed to obtain comparable values of affinity constants. Overall, the study shows that **nanoparticles with fluorinated amphiphilic ligands possess an enhanced binding ability and cellular uptake** in respect to the gold nanoparticles covered with hydrogenated ligands only and that a minimal variation in the coating composition could be translated in a different mechanism of interaction with cellular membranes.

The contribution this PhD project is bringing consists in the exploration of a different fluorinated moiety originate from the perfluorination of polyethylene oxide. The aim is to prepare novel gold nanoparticles with improved flexibility of the monolayer and a bigger number of fluorine nuclei in order to enhance both the ability to host drug molecules and the ¹⁹F-MRI response of the single nanosystem to improve even more the theranostic approach.

Another approach for the development of a theranostic device pursued in this thesis regards the synthesis of gold nanoparticles covered with a fluorinated monolayer for *in vivo* imaging and drug delivery purposes. The aim is to guarantee a non-invasive method to discern healthy and diseased tissues through the ^{19}F -MRI technique and provide a way to administer drugs to the desired site, forecasting a method to achieve selective cellular targeting and uptake.

A possible medical application for this kind of system is the accurate identification and treatment of specific brain pathologies such as glioblastoma (a brain tumor) or diseases related to leukemia and lymphoma.

8.1 NANOSYSTEM'S DESIGN

This project is built on a series of studies undertaken by our research group on homogeneous or mixed monolayers^{508,509} gold nanoparticles that have led to significant conceptual and practical results in terms of nanoparticle³⁸⁴ and ligand synthesis⁶⁴, morphological analysis^{510,511} and study of interactions with other molecules^{489,496}. These achievements have been extremely important for devising proof-of-concept nanoparticle systems, one of the more pertinent to this thesis is depicted below in **Figure 8.1**.

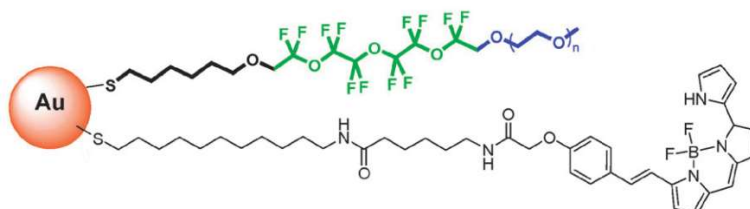


Figure 8.1: Graphical representation of a gold nanoparticle bearing fluorinated and fluorescent ligands previously synthesized by the group of prof. Pasquato. Image from reference ⁶⁴. Copyright © 2013 The Royal Society of Chemistry.

This system proved to represent a starting point for the development of a **contrast agent for ^{19}F -MRI** given its promising performance in ^{19}F -MRI phantom experiments and low toxicity to HeLa cells. In this thesis, we aimed at developing a nanoparticle system with improved performance by increasing the amount of quasi-equivalent fluorine nuclei per nanoparticle thus reducing the nanoparticle dose required to achieve effective contrast in ^{19}F -MRI. In addition, instead of using gold nanoparticles with a core size of 2 nm in diameter, we aimed at preparing larger ones (3 - 4 nm), due to the favorable number of passivating ligands, and smaller tendency to aggregation due to the possible exposition of fluorinated chains in NPs with a high curvature radius.

Moreover, what we want to achieve is a higher number of fluorine nuclei, in order to boost up both the therapeutic and the imaging features: in the first case, a longer chain enriched with fluorine atoms would create a **fluorophobic intermediate layer as a simple hosting system (Figure 8.3)**. Within this layer, we exploit non-covalent interaction to de-solvate, complexing, and trap active drugs, with the following release that is defined only by the monolayer characteristics and the external environment in which the nanoparticle will be immersed.

From the imaging point of view instead, driven by the clinical need for a high sensible contrast agent, our scope is hence to create a monolayer that contains the greatest amount of chemically and magnetically equivalent fluorine nuclei, in order to produce a measurable signal even in case of low concentrations. Looking at future clinical applications, it has to be considered that the necessary concentration of equivalent fluorine nuclei in the biological system for a good MRI signal is very high, in the range of 10^{16} - 10^{19} atoms per voxel (volumetric picture element)⁴⁹³. For this reason, keeping fixed the core dimension and thus the available surface for coating, the intention was first to elongate the fluorinated portion of the ligand, then to insert more of them in a single molecule of ligand, for example with a branched ligand.

For now, the nanosystem is meant to work thanks to a passive targeting scheme based on the EPR effect mentioned above. In the future plan, we do not exclude converting the nanoparticle in an active drug delivery system, to pass easily the blood-brain barrier (BBB) or exploiting, for example, the recognition route of some receptors that are expressed or overexpressed onto the tumor cells' surface to boost up their internalization. This will mean modify the fluorinated ligand or create new ones containing a specific peptide as targeting moiety.

These considerations called for the design of novel ligands based on the use of an extended **perfluoropolyether (PFPE) block**; in this thesis, we implemented this idea in the development of two types of ligands, the first one linear and in two versions (on the left in **Figure 8.2**), the second type branched (on the right in **Figure 8.2**), thus allowing a further increase of the amount of ^{19}F nuclei.

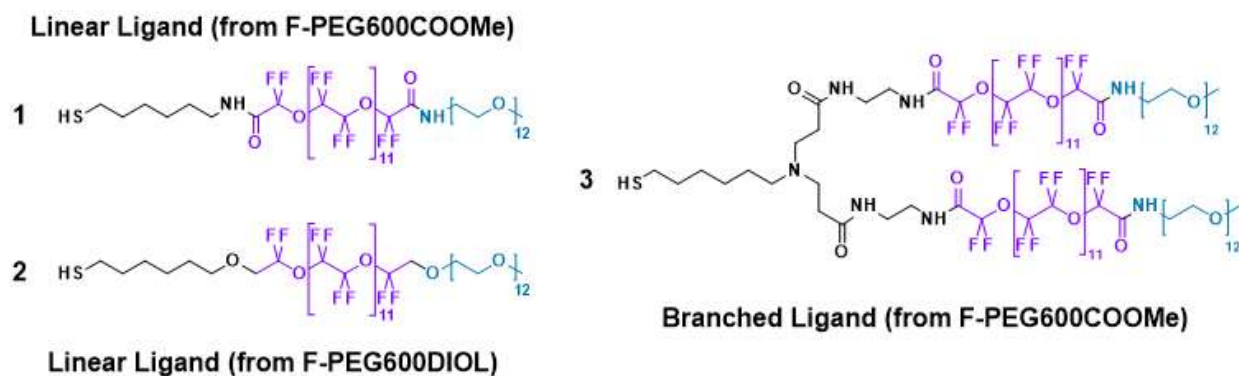


Figure 8.2: Representation of the structure of the fluorinated linear ligands derived (Top left, 1) from F-PEG600COOMe and (Bottom left, 2) from F-PEG600DIOL. (Right, 3) Representation of the structure of the fluorinated branched ligand.

Besides their potential for ^{19}F -MRI, the nanoparticles derived from these ligands are also expected to be useful vectors for hydrophobic drugs because of the inherent hydrophobicity of the fluorinated moiety⁴⁸⁹.

Our choice of perfluoropolyester (PFPE) blocks rather than a simple fluorocarbon (FC) was dictated by former studies that have evidenced how the structure becomes more stable and the chains more flexible in the presence of PFPE⁴⁸⁹. Furthermore, the division in small $-\text{OCF}_2\text{CF}_2-$ domains, guarantees a higher level of nuclear chemical equivalence (only one strong signal, while for FC would be three).

Flexibility and stability reasons have been also at the center of the decision to insert a short alkyl portion between the PFPE moiety and the core, rather than putting the fluorinated layer in its immediate vicinity as we already did⁴⁹⁶. The C6 unit can passivate efficiently the gold surface, providing protection and stabilization from the outer environment. Without this spacer, the presence of gold would make the chemical shift of fluorine atoms different along the chain and broad, with a decreasing effect while moving away from the surface.

Finally, the PFPE function has been chosen for its great oxygen atoms content, which makes the layer more “hydrophilic” than an FC chain and capable of accepting H-bond, thus expanding the variability of interactions. In fact, in respect to a hydrogenated chain of the same length that passivates the gold surface, PFPE should be superior also for therapeutic purposes because it acts as a better host for both hydrogenated and fluorinated drug molecules, thanks to numerous different interactions and the wider space between the chains, as demonstrated for two perfluoroethylene oxide units (**Figure 8.3**)⁴⁸⁹.

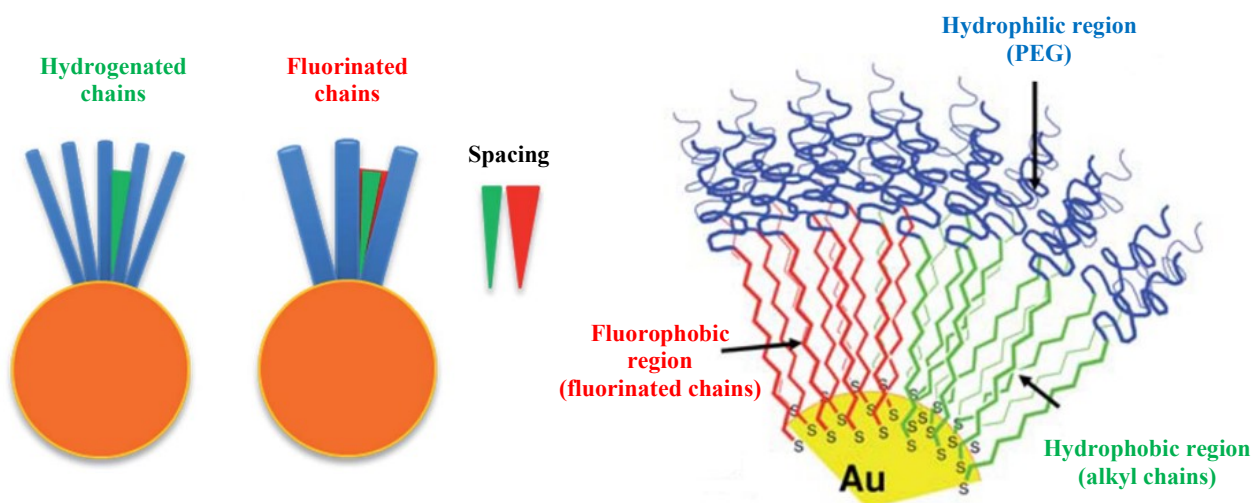


Figure 8.3: (Left) Graphical representation of the space available to host molecules between hydrogenated (green) or fluorinated (red) ligands. (Right) Graphical representation of regions with different polarities in mixed PEGylated monolayer of alkyl and fluoroalkyl ligands. Adapted from references ⁴⁸⁹ and ⁵¹⁰. Copyright © 2015 The Royal Society of Chemistry and © 2010 The Royal Society of Chemistry.

Working with oxyfluorinated chains involves unfortunately a series of issues, related to their solubility properties that differ from those of hydrophilic and lipophilic chains. Since the final purpose of these nanoparticles is to be used *in vivo*, we have to take into account the urge to make them hydrophilic and compatible with the physiological medium. The solution we decide to exploit is to insert a PEGylated chain (PEG₅₅₀ in particular) at the end of the fluorinated ligand to provide water solubility to the nanoparticle and slow down the recognition by the immune system as a non-self element. The length of the polymeric chain is essential to mask the fluorophobic inner part and stabilize the system. The final polyethylene glycol portion is introduced without increasing too much the overall dimension of the structure, maintaining a size in the low nanometers' regime for simpler and more capillary diffusion, even within small vasculature vessels.

Again, focusing on the possible toxicity of the system, it has to be taken into account that the fluorinated molecules proposed as imaging agents usually contain blocks or complete chains of fluorocarbons (FC) or perfluorocarbons, as in the case of the perfluoropolyether (PFPE) in our system. The acute and long-term toxicity that arise in diagnostic and therapeutic fields respectively are currently under study: the preliminary results on cell and animal models display that both FC and PFPE have a low or limited toxicity^{485,512,513}.

8.2 SYNTHESIS OF GOLD NANOPARTICLES PROTECTED BY FLUORINATED THIOLATES

The synthesis of these fluorinated hybrid nanoparticles starts with the preparation of the related fluorinated ligand. We have split our efforts on different structures that had the common feature of presenting a thiol function for the passivation of the gold core, an alkyl spacer, a fluorinated moiety for theranostic purposes, and a PEG tail for water solubility and biocompatibility (**Figure 8.4**). Furthermore, the synthetic pathways proposed keeps the further functionalization a viable option for dual-imaging, active targeting, or drug loading features.

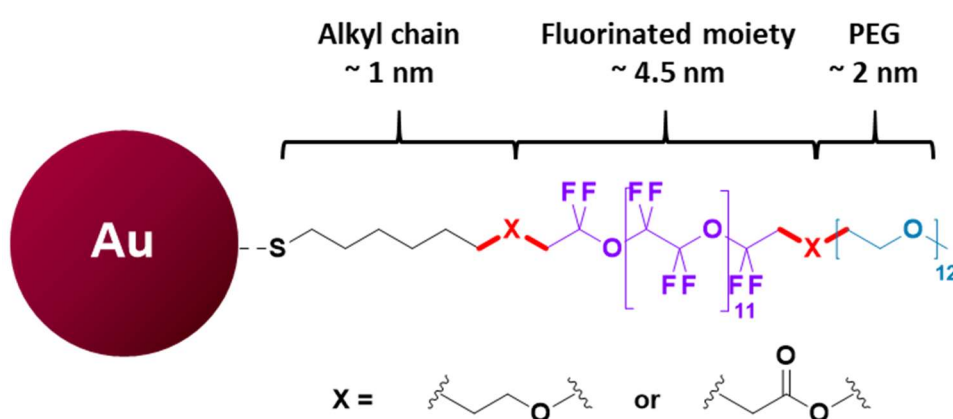


Figure 8.4: General structure of the fluorinated ligands we have synthesized in this project, along with the approximative length estimation of the different parts.

The length of the complete ligand can be estimated considering separately its three portions: the alkyl part before the ramification that starts with the thiol group is around 1 nm, while the fluorinated moiety is around 4.5 nm long. Finally, the PEG₅₅₀ portion has a total length of 2 nm⁵¹¹, considering that the chain is usually coiled up instead of presenting a straight structure.

8.2.1 Synthesis of the linear ligand with F-PEG600COOMe

The first linear fluorinated ligand we have synthesized is characterized by a 6-carbon atoms spacer, a perfluoropolyether moiety containing about 11 perfluoroethylene oxide units, and a PEG portion of M_w 550 Da (hence possessing 12 or 13 ethylene oxide units), all covalently linked together by amide bonds.

chain to convert the terminal hydroxyl group into an amine one with a similar approach, step 3, described for the protected thiol moiety, foreseeing the following insertion of this hydrophilic moiety at the end of the ligand, step 4. Finally, right before the synthesis of gold NPs, the ligand is deprotected to free thiol, step 5. The building blocks TrtSC6OTs and PEG₅₅₀-NH₂ have been prepared according to literature procedures^{64,489} with minor optimization as described in the experimental section.

In the following paragraphs, the relevant synthetic steps to the preparation of ligand HSC6NHOF11CONHPEG **1** and HSC6N(C2CONHC2NHCOOF11CONHPEG)**2** (**Figure 8.2**) will be briefly discussed, along with the principal characterization analysis to verify the achievement of the desired products and intermediates.

Synthesis of 6-tritylthiol-1-hexanol (TrtSC6OH)

The first step is the introduction of a protected thiol function to the 6-bromo-1-hexanol.

The choice for the protecting group has fallen on the trityl species, which can resist basic conditions and is removed with acids or through hydrogenolysis⁵¹⁴. Therefore, the protection is stable in the conditions of the following reaction steps.

The length of 6 carbon atoms in this alkyl chain is essential for the properties of the monolayer that we seek, because it assures stable protection of the gold core, since the alkyl moieties are tightly packed thanks to intermolecular hydrophobic interactions and the additional H-bond among amide groups⁵¹⁵.

The synthesis in this step is a nucleophilic substitution of the bromide group by the thiol function: this action is preceded by the deprotonation of the HS function in the triphenylmethanethiol by K₂CO₃, to enhance the nucleophilicity of the species.

In comparison to the spectra of the precursor, the ¹H-NMR presents a shifted triplet at 2.14 ppm which is associated to the -CH₂- group in alpha to the new tritylthio- group. This is confirmed by the presence of the signal pertaining to the aromatic proton at 7.42-7.20 ppm and from the ¹³C-NMR spectrum which displays the signals related to aromatic carbons at 145 ppm and at 129-127 and 126 ppm. Another characteristic peak of the product is the signal at 66.56 ppm pertaining to the carbon in alpha position to the sulfur atom of the -S-CH₂- group. The ESI-MS analysis confirms the achievement of the desired chemical species, giving an m/z ratio of 399.2, corresponding to the species [M+Na⁺]. The compound is a light yellow amorphous solid obtain with a maximum yield of 98 %.

Synthesis of 6-(tritylthiol)hexyl-4-methylbenzenesulfonate (TrtSC6OTs)

In the following step, the alcoholic group was activated for an S_N2 reaction by conversion to the tosyl leaving group following a standard procedure.

The $^1\text{H-NMR}$ and $^{13}\text{C-NMR}$ spectra recorded helped to control the product formation and the degree of purity. In particular, we noted the disappearance of the peaks at 3.59 ppm ($^1\text{H-NMR}$) and at 63.04 ppm ($^{13}\text{C-NMR}$) related to the methylene group in alpha to the hydroxyl group and the appearance of the signals consistent with the methylene group in alpha to the tosyl moiety at 3.96 ppm ($^1\text{H-NMR}$) and 70.59 ppm ($^{13}\text{C-NMR}$). Additionally, the tosyl group presents the signals in the 7.2-7.5 ppm region in the proton NMR spectrum and between 126-130 ppm in the $^{13}\text{C-NMR}$ spectrum and a singlet at 2.43 ppm pertaining to the methyl group and the corresponding 21.79 ppm peak in the $^{13}\text{C-NMR}$ spectrum. For the correct assignment of certain peaks, we took advantage of some 2D NMR spectroscopy techniques such as gCOSY and gHSQC. The MS spectrum displays both the $[\text{M}+\text{Na}^+]$ and the $[\text{M}+\text{K}^+]$ peaks at 553.2 m/z and 569.2 m/z respectively.

The compound was obtained with a maximum yield of 61 % as a white crystalline solid.

Synthesis of (6-azidohexyl)(trityl)sulfane (TrtSC6N3)

The excellent leaving group we introduced in the previous step is replaced by the azide function provided by sodium azide in an S_N2 reaction carried out in DMF under reflux.

In this case, the formation of the azide was verified by the disappearance of the signals related to the methyl group and the ones in the aromatic region of $^1\text{H-NMR}$ and $^{13}\text{C-NMR}$ spectra belonging to the tosyl group, and the subsequent shift of the signals pertaining to the methylene group in alpha to the azido group at 3.21 ppm in the $^1\text{H-NMR}$ spectrum and 51.45 ppm in the $^{13}\text{C-NMR}$ spectrum.

The MS spectrum displays the $[\text{M}-\text{H}^+]$ peak at 400.4 m/z and the $[\text{M}+\text{Na}^+]$ ion at 424.2 m/z, while the first fragmentation at 359.2 m/z is related to the loss of the whole azide group. The yield of this vitreous light-yellow solid was 80 %.

Synthesis of 6-(tritylthio)hexan-1-amine (TrtSC6NH2)

In this step, the azide function is converted in a primary amine group exploiting a Staudinger reaction with phosphines for its reduction. Briefly, triphenylphosphine is used in THF to form an imide through nucleophilic addition that causes the elimination of a molecule of nitrogen. The

following step is the hydrolysis of the iminophosphorane to form the phosphine oxide as a by-product and the desired amine.

Considering the NMR analysis, even if some minor unidentified impurities can be detected at 5.30 ppm and at 1.91 ppm in the proton NMR spectrum, the formation of the product is clearly verified by the shift of the methylene group in alpha to the nitrogen at 2.67 ppm in the ^1H -NMR spectrum and at 41.53 ppm in the ^{13}C -NMR spectrum. Moreover, we assume that the broad signal in the proton NMR spectrum centered at 3.42 ppm belongs to the two amine protons. ESI-MS spectrum shows the peak related to the $[\text{M}+\text{H}^+]$ ion at 376.0 m/z. The yield of this light-yellow oil was 93 %.

Synthesis of TrtSC₆NHCOOF11OCOOMe

Since the perfluorinated precursor is symmetrical, the reaction we intend to perform is a de-symmetrization, with the aim to maintain one of the methyl ester functions for the following reaction with another species. The approach to guarantee this result is to work with an excess of fluorinated precursors, in order to decrease drastically the option of double addition to both the ester termini. These ester functions are indeed particularly activated by the presence of the perfluoromethylene groups in alpha position to the carbonyl. On the other hand, the disadvantage is that we must be careful to avoid the hydrolysis of the activated ester, therefore it is mandatory to operate in dry conditions and under inert atmosphere. The reaction was initially performed in trifluoroethanol to improve solubility but unfortunately in this solvent, we observed some transesterification, *vide infra*. For this reason, later, this reaction was carried out in methanol, since we found that the trifluoroethoxy moiety, once is linked to the carbonyl group, can be hardly substituted, while with methanol the transesterification leads to a virtual reaction. Since we have used an excess of fluorinated reactant, at the end of the synthesis a purification step through flash chromatography was necessary to separate the product from the unreacted methyl ester and the eventual hydrolyzed derivatives.

The characteristic signal in the proton spectrum is a peak at 8.43 ppm pertaining to the amide proton, while the signal of the methylene group in alpha to the carbonyl group shifts from 2.67 ppm to 3.26 ppm. Moreover, the successful de-symmetrization of the reagent can be verified with the maintenance of the signal at 4.05 ppm that in the product integrates for one methyl ester group only.

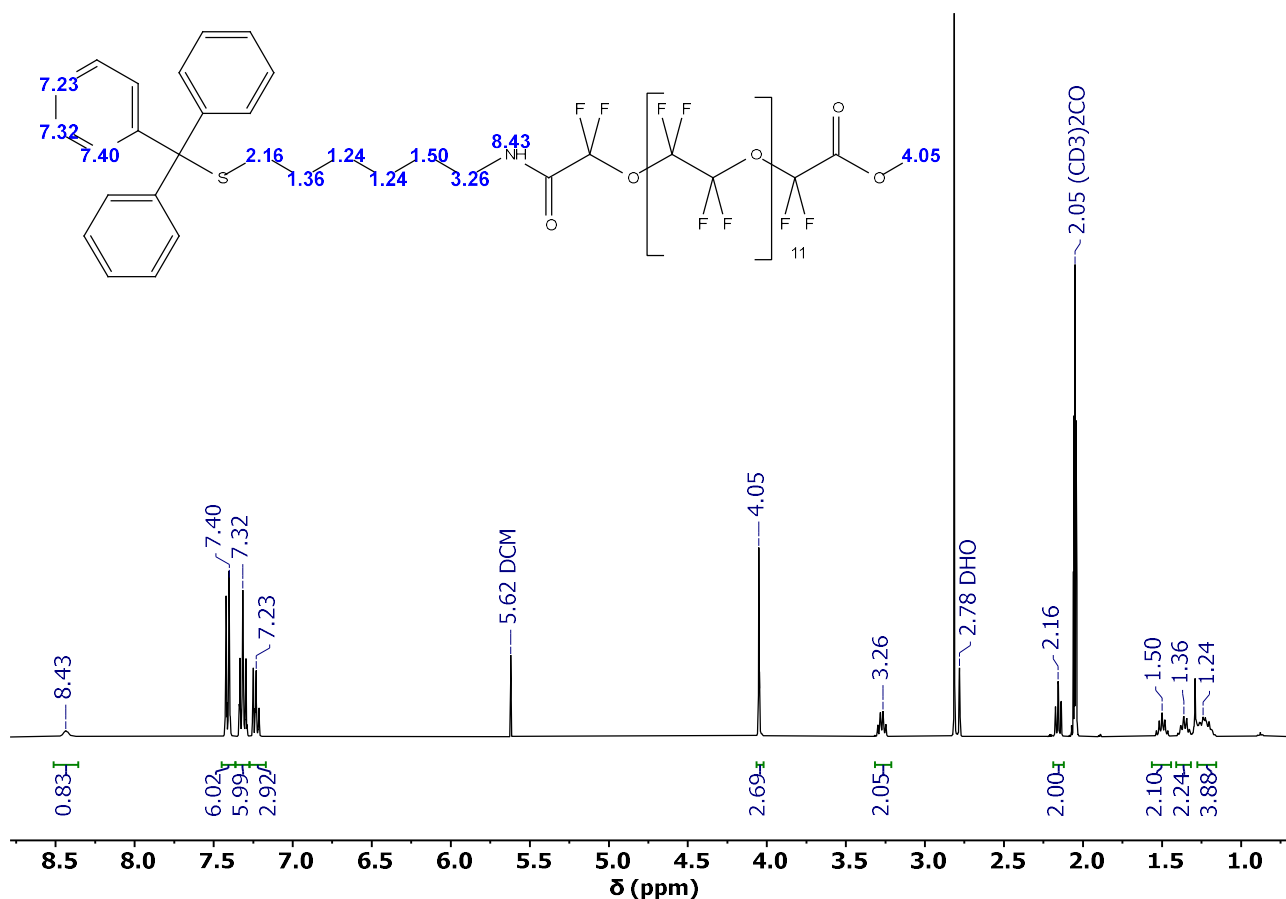


Figure 8.5: ¹H-NMR spectrum (400 MHz, acetone-d₆) of compound TrtSC6NHCOOF11OCOOMe.

In addition, some changes can be observed also in the ¹³C-NMR spectrum, in particular in the region around 157 ppm where the carbonyl group of the amide can be detected at 54.14 ppm and 40.60 ppm, pertaining to the terminal methyl and the methylene in alpha to the amide bond respectively. Moreover, diagnostic is the presence of triplet located between 112.74-118.10 ppm, which corresponds to all the carbons of fluorinated methylene groups.

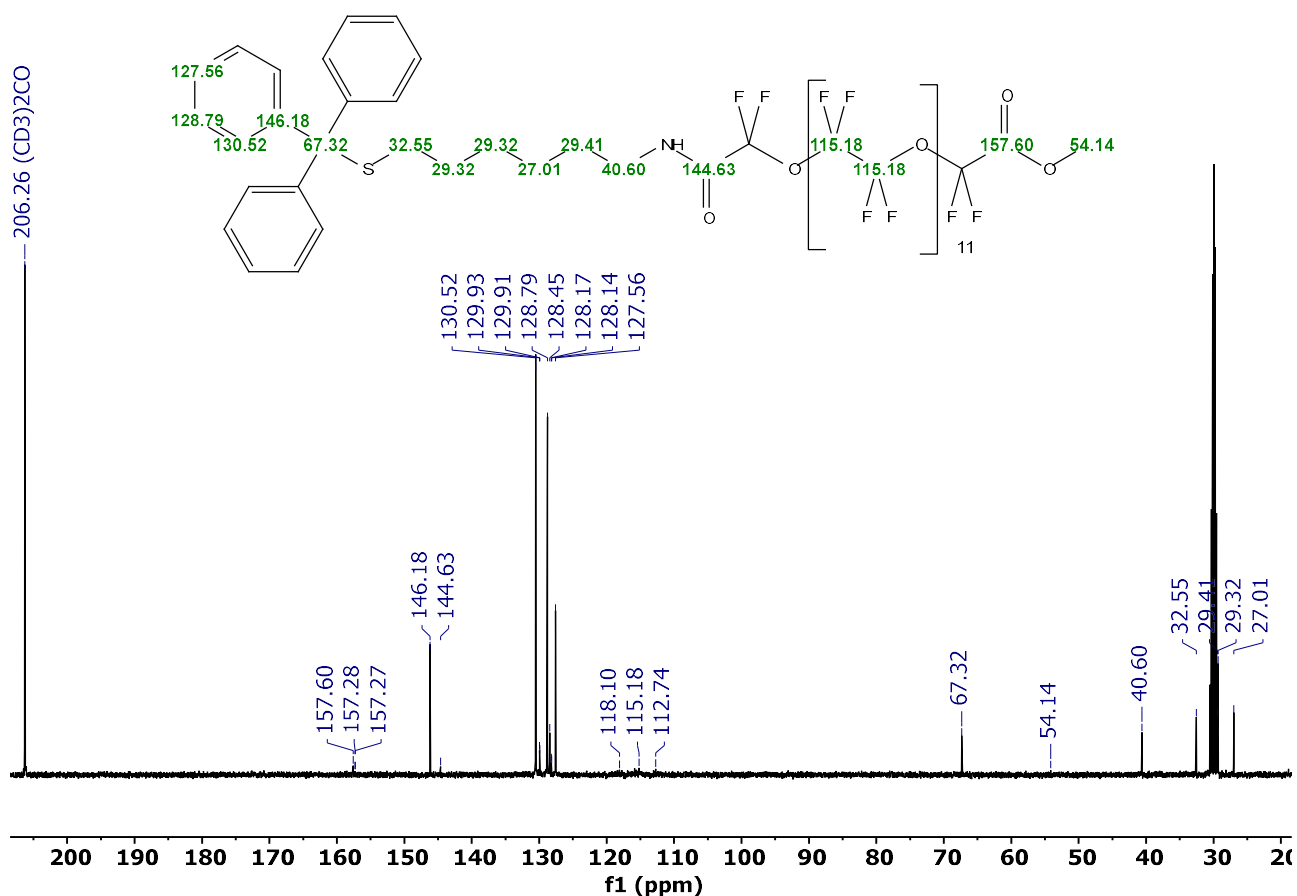


Figure 8.6: ^{13}C -NMR spectrum (101 MHz, acetone- d_6) of compound TrtSC6NHCOOF11OCOOME.

Finally, this compound can be analysed also with ^{19}F -NMR spectroscopy to characterize the fluorinated moiety. Perfluoropolyester has fundamentally two different types of signals: one belongs to the outer $-\text{OCH}_2\text{CF}_2\text{O}-$ fragments, the other to the inner $-\text{OCF}_2\text{CF}_2\text{O}-$ portion that contains nuclei that have a similar surrounding. The relative chemical shifts recorded in a previous work are displayed in **Figure 8.7**.

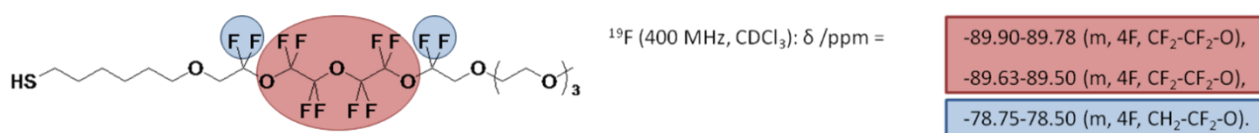


Figure 8.7: (Left) Fluorine atoms detected in ^{19}F -NMR and (Right) chemical shifts of the relative atoms.

The spectrum shows the presence of four different groups of signals: two at -78.59 ppm and a complex one at -89.79 ppm that pertains to the $-\text{CF}_2-$ in alpha to the ester and the $-\text{OCF}_2-$ group. The other signals are slightly shifted in respect to the previous couple due to the presence of the amide group and are centered at -79.13 ppm for the $-\text{CF}_2-$ in alpha position to the amide and -89.32 ppm for the most external perfluoroethylene unit of the product.

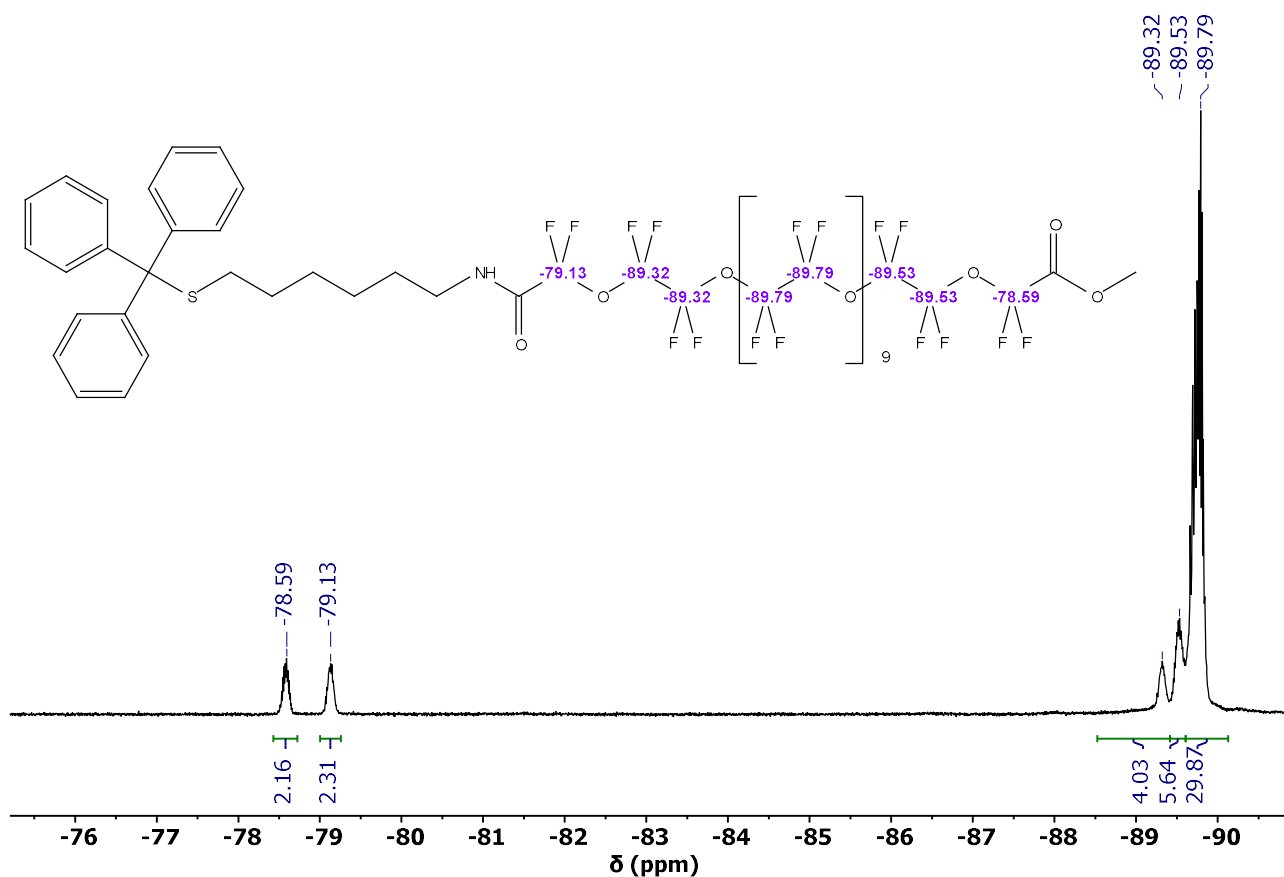


Figure 8.8: ¹⁹F-NMR spectrum (376 MHz, acetone-d₆) of compound TrtSC6NHCOOF11OCOOME.

The MS spectrum analysis of this sample showed more signals than expected, but they can be easily identified as structures analogous to the original one but containing more than 11 perfluoromethylene oxide units. In particular, the signal at 2103.5 m/z belongs to the [OF13+NH₄⁺] ion, the one at 1987.5 m/z to the [OF12+NH₄⁺] ion and finally the signal at 1871.5 m/z is related to the ion [OF11+NH₄⁺] which is the major constituent of the polymeric mixture. Moreover, also the analogous structure with 10 (1755.6 m/z, [OF10+NH₄⁺]) and 9 (1639.5 m/z, [OF9+NH₄⁺]) perfluorinated PEG units can be detected. Finally, at 1528.3 m/z we identified the first fragmentation of the major species, with a loss of 93 m/z, corresponding to the fragment [-CF₂-COOH]. The product was obtained as a viscous solid with a yield of 39 %.

Synthesis of PEG₅₅₀-OTs

In parallel with the preparation of the fluorinated protected thiol moiety, we needed to functionalize one PEG hydroxy group to activate it. Also in this case, we decided to employ the tosyl group as leaving group.

The ^1H -NMR and ^{13}C -NMR spectra allowed us to demonstrate the obtainment of the desired product. Since we are dealing with a polymeric species, rather than identifying all the peaks, the more efficient approach is to determine the ratio between integrals of the tosyl function and the integral of the protons in the ethylene oxide units. This analysis showed a very good agreement with the structure proposed. Indeed, considering 12 repetitive units of ethylene oxide for an MW of 550 g/mol and the insertion of the tosyl group, the final molecular weight calculated is 714.86 g/mol, corresponding to the chemical formula $\text{C}_{32}\text{H}_{58}\text{O}_{15}\text{S}$. Subtracting the four aromatic protons (two in ortho-position to the sulfur at 7.78 ppm and two in meta-position at 7.33 ppm) and the terminal methyl group at 2.44 ppm, 51 protons are left, which is exactly the number of the integral of the signals in the 3.50-3.80 ppm range for the oxo-ethylene groups.

The ^{13}C -NMR spectrum has been recorded to verify the presence of the functional groups and to help with the assignment of each peak. Also in this case it was possible to identify the principal carbon nuclei that are chemically different, while the ones pertaining to the oxo-ethylene carbons resonate all at 70.64 ppm.

The mass spectrum obtained with ESI-MS presents clearly the $[\text{M}+\text{Na}^+]$ ion at 737.3 m/z, from which a series of peaks separated each other by 44 m/z (loss of ethylene oxide fragments) are visible forming the typical Gaussian profile. The product was obtained as a viscous solid with a yield of 85 %.

Synthesis of PEG₅₅₀-N₃

The tosyl leaving group was replaced by the azide function via an $\text{S}_{\text{N}}2$ reaction.

The formation of the azide was verified by the disappearance of the signal pertaining to the methyl group and to the protons of the aromatic ring and the presence of the signal pertaining to the methylene in alpha position to the azide group at 3.38 ppm.

The ^{13}C -NMR gave us little more information on the structure of the compound. We were able to identify only the peaks of chemically different carbons: the methyl group at 59.16 ppm and the methylene group closest to it at 72.06 ppm. More importantly, we detected the disappearance of all the signals related to the presence of the tosyl group in favor of the appearance of the one at 50.82 ppm related to the methylene in alpha position to the azide group. The correct assignment of each signal was helped by the recording of the 2D spectra gHSQC.

The ESI-MS spectrum displays both the $[\text{M}+\text{Na}^+]$ and the $[\text{M}+\text{K}^+]$ ions for the species containing 12 ethylene oxide units, respectively at 608.4 m/z and 624.3 m/z. Starting from these signals, we

can detect also the species presenting more or less oxo-ethylene units as expected, up to 828.4 m/z (17 units) and down to 404.2 m/z.

The product was obtained as an orange-brown oil with a yield of 81 %.

Synthesis of PEG₅₅₀-NH₂

The Staudinger reaction was used for the reduction of the azide to amine group with triphenylphosphine.

Considering the NMR analysis, the diagnostic signals for the occurred reaction are the triplet at 2.85 ppm pertaining to the methylene in alpha position to the amine and the triplet at 3.50 ppm for the β -methylene protons. One more characteristic signal is the broad singlet at 1.80 ppm assigned to the protons of the amine group.

The ¹³C-NMR spectrum confirms the preparation of the PEG-amine species since we can identify the appearance of the peaks at 41.91 ppm related to the methylene carbon directly linked to the amine group and the singlet at 73.55 ppm for the β -methylene carbon.

The MS spectrum displays the [M+H⁺] ion at 560.4 m/z and all the other signals for the polymeric structure of the compound. The final product was obtained as an orange oil with a yield of 94 %.

Synthesis of TrtSC₆NHCOOF₁₁OCONHPEG

In this step, the fluorinated intermediate is conjugated with the modified PEG chain. The reaction performed is an amide bond formation between the amine on the PEG active terminus and the activated ester on the fluorinated ligand.

The critical point of this conjugation is the preservation of the activated ester until its reaction with the amine. Being more electrophilic because of the proximity of a -CF₂- group, this ester function is very sensitive to the presence of water, leading to hydrolysis to carboxylic acid and deactivating the group toward the reaction with amines. A first attempt was unsatisfactory because of the hydrolysis of the reagent in the reaction conditions. Furthermore, we observed that upon chromatographic purification of the crude, the large majority of the product was already hydrolyzed to the corresponding carboxylic acid. Therefore, strictly anhydrous solvents were used in the processes. We were particularly careful not to put in contact this reactant with moisture or not-dried solvents. Regardless, the first tries performed with only the two reactants in anhydrous DMF were unsuccessful. Because of this, the hydrophilic PEG-NH₂ was dissolved in anhydrous diethyl ether

and then in anhydrous methanol, stripping traces of water by rotor evaporation and repeating this step for many cycles.

After we performed another try with the dehydrated PEG-NH₂, obtaining only a small improvement, we understood that a major part of the fluorinated reactant was already hydrolyzed (probably due to its purification via flash chromatography).

To overcome this problem, we decided to rely on activating species that are specific for carbonyl compounds. We used both *N*-(3-dimethylaminopropyl)-*N'*-ethylcarbodiimide hydrochloride (EDC · HCl) and hydroxybenzotriazole (HOBt). With this procedure, we were able to obtain the desired product with a higher yield and purity. However, we used an excess of PEG-NH₂ to assure the complete functionalization of the activated esters available: this implied a further step of purification through flash chromatography, which unfortunately we were not able to optimize for a complete separation.

However, NMR characterization of the product confirmed the formation of the amide bond. Indeed in the proton NMR spectrum, we were able to detect the presence of the PEG moiety, identifying the appearance of the intense signal at 3.58 ppm integrating for 40 protons and the presence of the satellite signals belonging to the protons of more external methylene groups. More importantly, we identified two signals that are particularly diagnostic for the new amide bond formation: the one at 3.62 ppm pertaining to the methylene protons of the PEG alpha to the nitrogen and the singlet at 8.48 ppm belonging to the amide proton, which is distinguishable from the analogous amide proton of the other end that resonates at 8.43 ppm. However, the integral value of these latter signals is 1.44 ppm with respect to the protons of the aromatic system. This is a clear indication that conjugation did not proceed to completion.

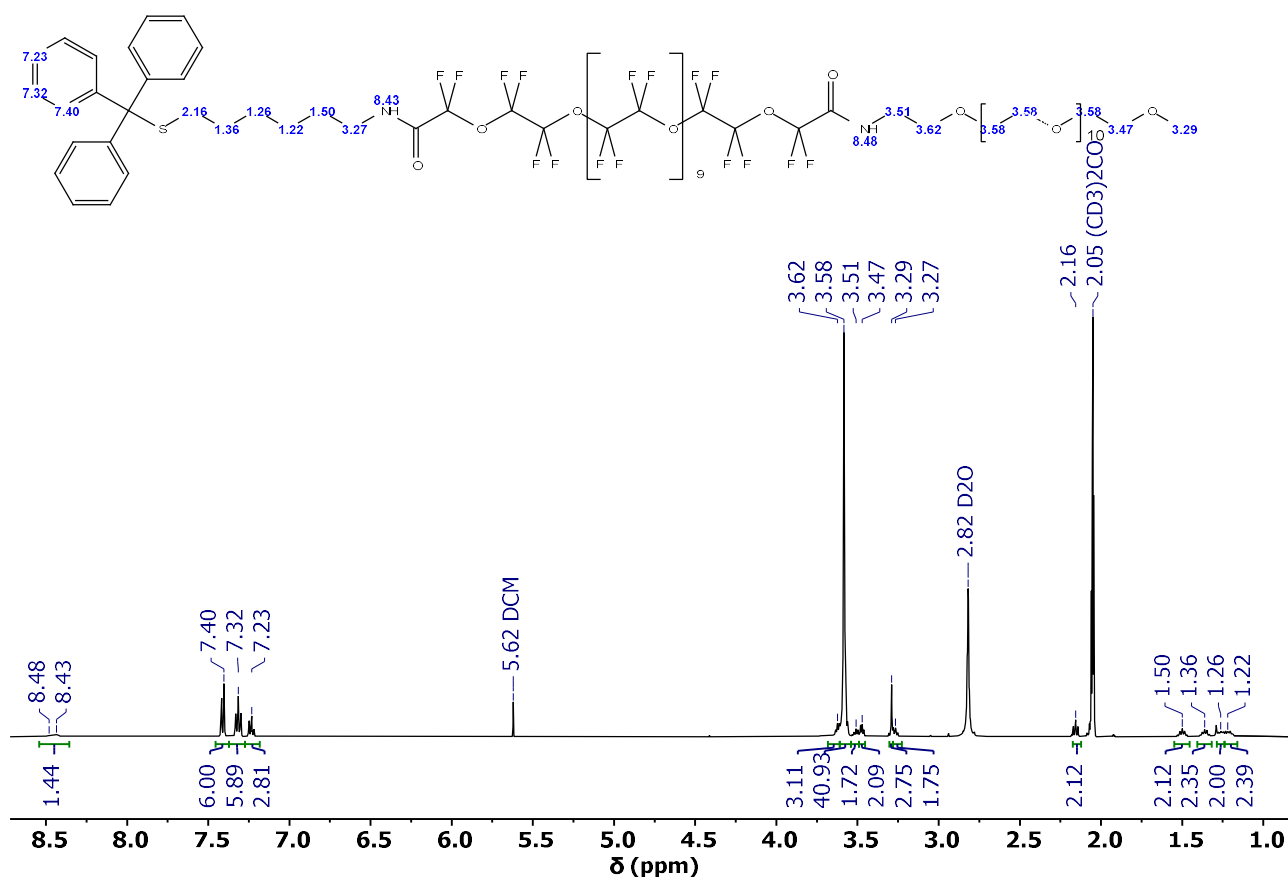


Figure 8.9: ^1H -NMR spectrum (500 MHz, acetone- d_6) of compound TrtSC6NHCOOF11OCONHPEG.

The ^{19}F -NMR spectrum provided very useful information about the effective conjugation, even if the number of nuclei from the integration is lower than the ones expected for the pure desired product. In particular, along with the signals at -89.07 ppm and -89.48 ppm that we assigned to the perfluoroethylene oxide units at the center of the polymeric chain, two close signals can be detected at -78.80 ppm and -78.90 ppm. By comparison with the ^{19}F -NMR spectrum of the reagent, we assume that the most de-shielded nuclei (-78.80 ppm) are the ones in alpha to the amide carbonyl close to the PEG, while the more shielded ones (-78.90 ppm) pertain to the fluorinated methylene alpha the carbonyl amide linked to the alkyl chain.

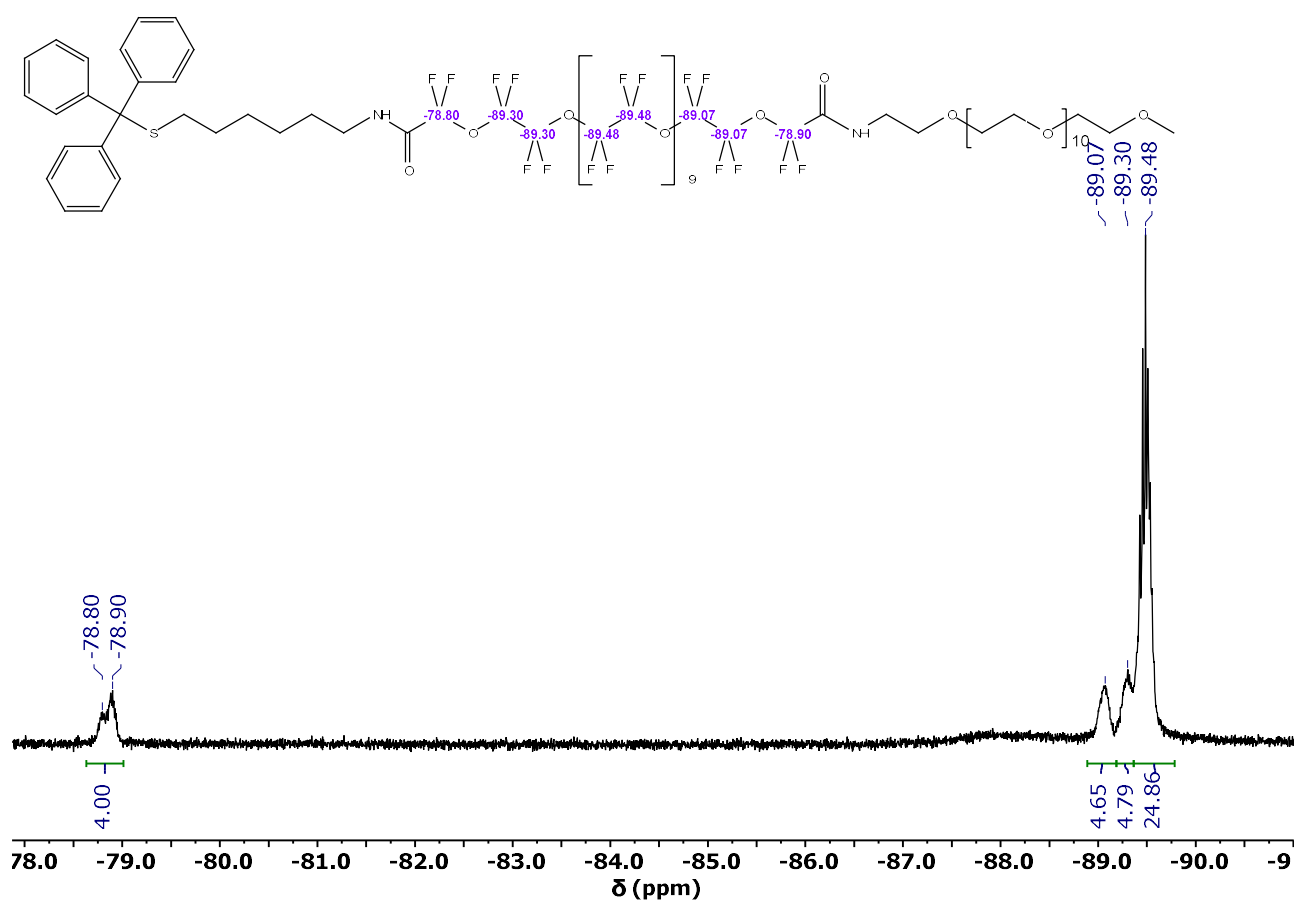


Figure 8.10: ^{19}F -NMR spectrum (376 MHz, acetone- d_6) of compound TrtSC6NHCOOF11OCONHPEG.

From the ESI-MS spectrum, we were not able to detect the molecular peak, but we observed both the typical signal distancing of 44 m/z (ethylene oxide) and 116 m/z (perfluoroethylene oxide), indicating that both the polymeric moieties are present in the final product.

After the purification, a viscous orange oil with a yield of 78 % was obtained.

Synthesis of HSC6NHOF11CONHPEG

The last step for the preparation of this linear fluorinated ligand consists in the deprotection of the thiol, hence removing the trityl group introduced in the first step. This reaction is typically performed using triisopropylsilane (TIPS) and trifluoroacetic acid (TFA) in dry and deoxygenated conditions to avoid the oxidation of the free thiol to disulfide.

After the extraction in organic solvent to remove the triphenylmethane, the crude was analyzed by ^1H -NMR spectroscopy.

In the proton NMR spectrum reported below, the disappearance of the aromatic protons related to the trityl functional group can be appreciated. At the same time, the presence of the signals related

to the amide protons is detected at 8.49 ppm. Another diagnostic signal is the one belonging to the alpha-methylene near the thiol group, a quadruplet at 2.50 ppm in the spectrum recorded. The signal at 2.61 ppm is related instead to the methylene protons alpha to the disulfide. The presence of traces of disulfide is not a problem because the preparation of gold nanoparticles will be carried out under reducing conditions with sodium borohydride.

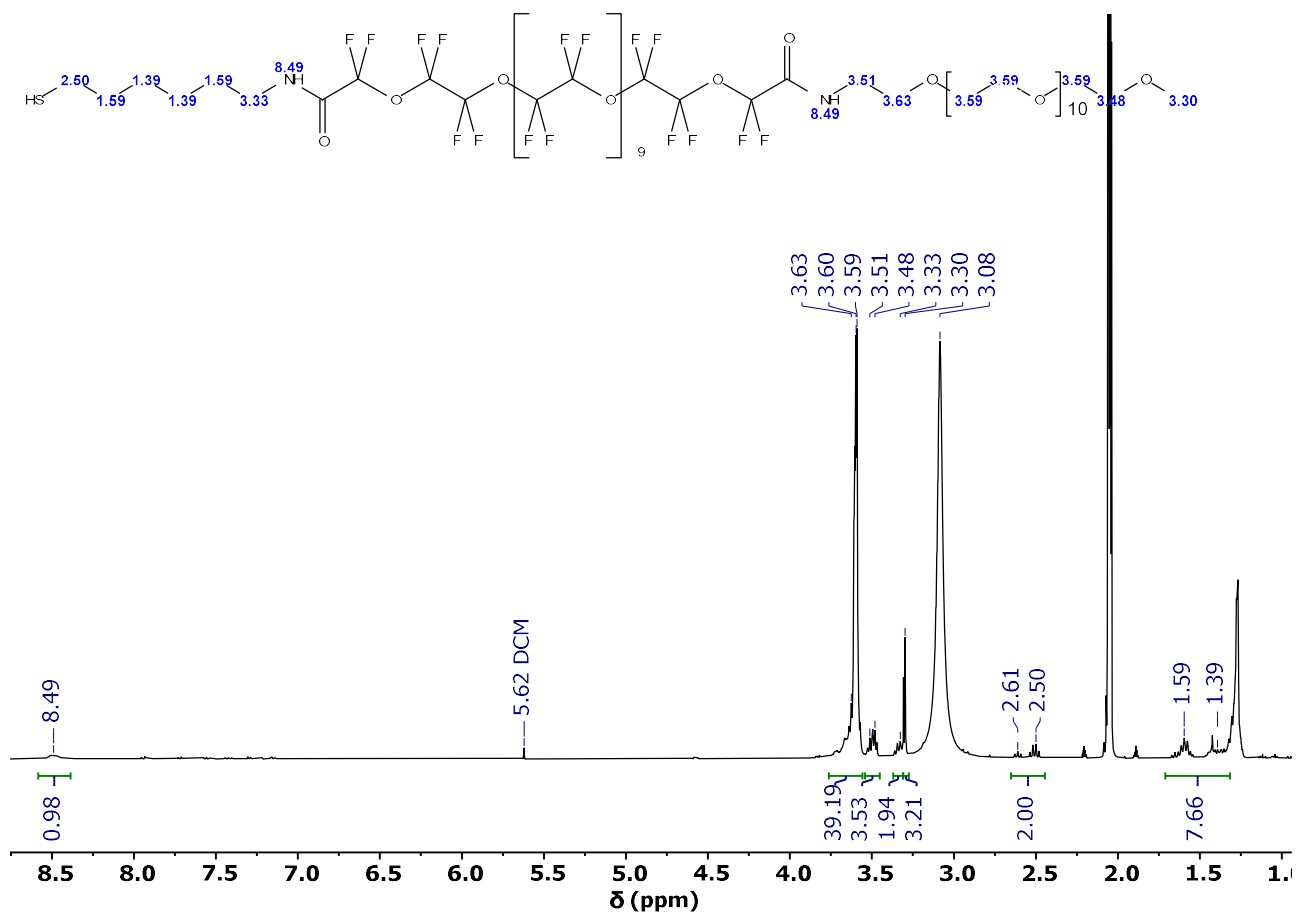


Figure 8.11: ¹H-NMR spectrum (400 MHz, acetone-d₆) of compound HSC6NHCOOF11OCONHPEG.

The ¹⁹F-NMR spectrum confirms that the fluorinated portion of the compound was preserved and still intact after the deprotection.

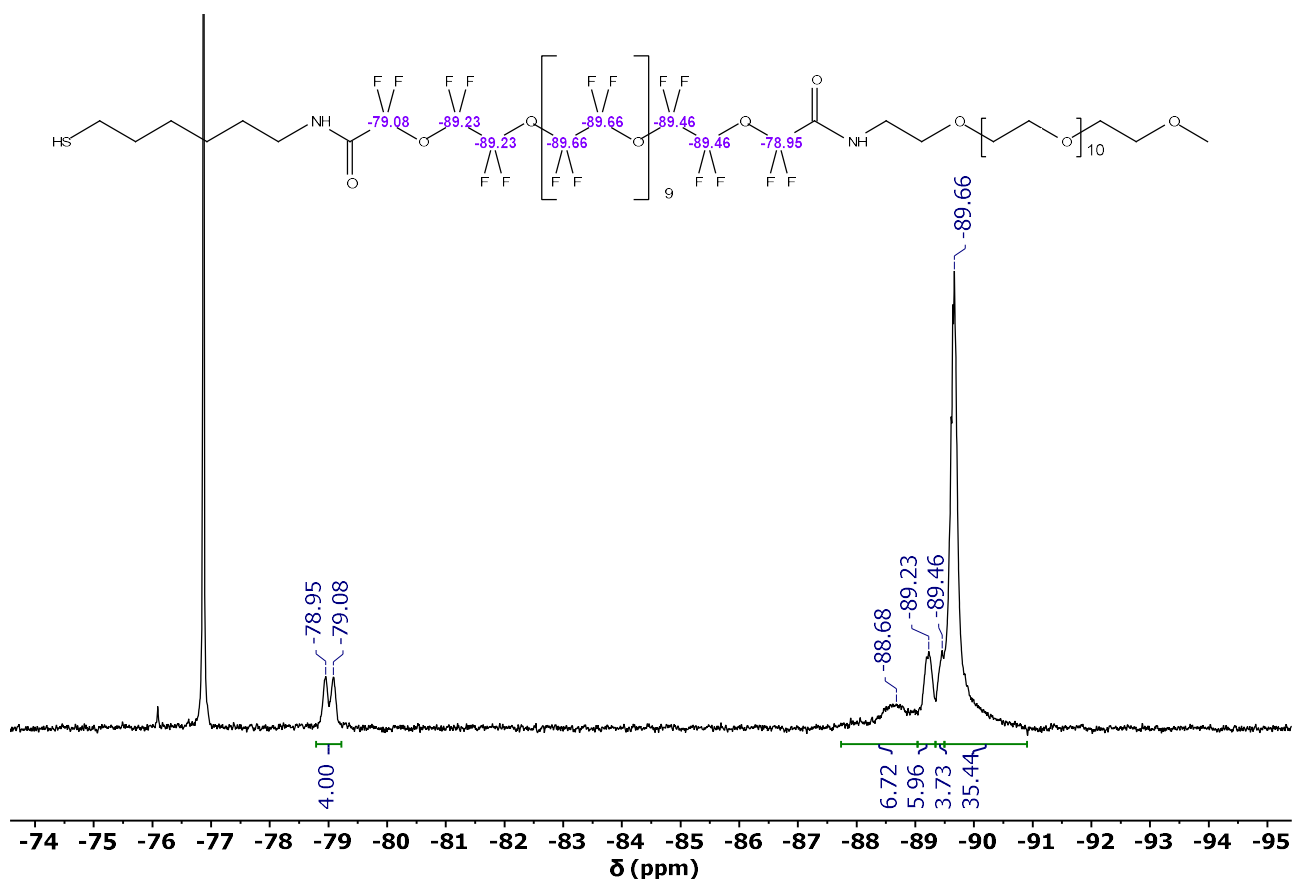


Figure 8.12: ^{19}F -NMR spectrum (376 MHz, acetone- d_6) of compound HSC6NHCOOF11OCONHPEG.

For this ligand, we also measured the ^{19}F T1 and T2 relaxation times. For this purpose, we set an inversion recovery experiment to measure the transversal magnetization after a 180° impulse, followed by a 90° pulse. By plotting the intensity of the major group of peaks at -89.66 ppm at different intervals between these pulses, a T1 relaxation time value of 1.148 s was obtained.

For what concerns the T2 relaxation time instead, we adopted the Carr-Purcell-Meiboom-Gill (CPMG) pulse sequence that provides a method to assess the decay of the transverse magnetization due to field inhomogeneities and the molecular environment causing spin dephasing^{516,517}. Always focusing on the variation of the same group of signals, the intensity data were fitted with an exponential curve to obtain a value of 777 ms for the T2 relaxation time.

These results are in agreement with the long relaxation times fluorinated compounds generally have, especially in the case of long chains. Once this ligand will be bonded to gold nanoparticles, both the T1 and T2 should be considerably shorter because of the slower molecular tumbling rate⁵⁰⁰, increasing its efficiency as a ^{19}F -MRI contrast agent. These measurements were carried out in D_2O at a thiol concentration of around 10^{-6} mol/L.

At the end of the synthetic pathway, we can conclude that the fluorinated linear ligand prepared starting from the fluorinated methyl ester has been effectively synthesized, even if the overall

strategy for the insertion of the F-PEG600COOMe portion was not fully optimized. We still need to improve both the yield of the single synthetic steps and the subsequent purification of the crude, discovering an efficient separation method that could work especially when the mixture becomes more complex due to the presence of different polymeric species of similar polarity.

Moreover, we collected evidence that led us to question the strength of the amide bonds we formed, since both the amide groups are in close proximity to a perfluoromethylene group, which is a strong electron-withdrawing group, making more labile the amide conjugation.

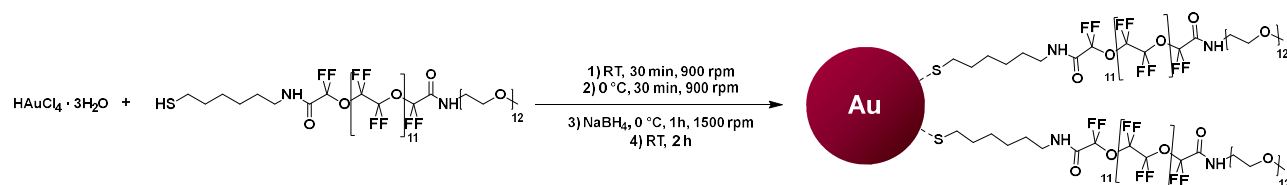
Despite these critical issues, the product of the last step was employed for the synthesis of gold nanoparticles described in the following section.

From the analysis of the ESI-MS spectra, we were not able to find the molecular peak. However, with the instruments set to detect the positive ions, we identified many signals in the 1400-2000 m/z interval that were separated by 44 m/z: we suspect they could be related to the loss of $(\text{OCH}_2\text{CH}_2)_x$ fragment of increasing mass. Moreover, in the 800-1400 m/z range, we identified signals separated by 116 m/z, hence indicating the possible loss of $(\text{OCF}_2\text{CF}_2)_y(\text{OCH}_2\text{CH}_2)_x$ fragments.

8.2.2 Synthesis of AuNPs with F-PEG600COOMe-derivate ligand (Au@SC6NHOF11CONHPEG)

The next step in the preparation of the second hybrid organic-inorganic nanosystem proposed in this thesis is to exploit the first linear fluorinated ligand described to form a stable 3D self-assembled monolayer on gold nanoparticles.

The method used for the preparation of gold nanoparticles with fluorinated thiols is a homogenous phase synthesis reported by our group³⁸⁴ and previously adopted for the synthesis of variously functionalized gold nanoparticles⁵⁰⁰, also with different core sizes⁴⁸⁹. **Scheme 8.2** illustrates the reaction we performed.



Scheme 8.2: Synthetic scheme for the preparation of gold nanoparticles with homoligand monolayer made by fluorinated linear thiolates (Au@SC6NHOF11CONHPEG).

The few important components of the synthesis are the gold precursor, tetrachloroauric acid, dissolved in Milli-Q water, the reducing agent in the form of sodium borohydride, and the thiol ligand in deoxygenated methanol to avoid the formation of the disulfide species.

Several synthetic conditions affect the result in terms of nanoparticle core size and dispersion, but the most relevant ones are the initial molar ratio between the gold precursor and the thiol and the time for the addition of sodium borohydride solution³⁸⁴.

In our case, the aim is to obtain nanoparticles with a core size of 3 nm. For this reason, we used an Au/thiol ratio of 3:2 and we added the reducing agent slowly in 3.5 minutes at 0 °C to avoid the risk of aggregates formation. In the purification, the crude nanoparticle preparation was washed with hexane and then purified through size exclusion chromatography, using Sephadex as stationary phase. This step had the primary aim to remove the small unreacted species, the bigger nanoparticles that eluate first, and the aggregates that remain on top of the column.

The sample collected from the column was analyzed first by TEM reported in **Figure 8.13** to retrieve the average core size and the dispersion. The images recorded show an even distribution of spherical nanoparticles well separated from each other. The analysis of the size distribution was performed using Lorentzian functions to take into account the bimodal distribution observed in **Figure 8.13**. Comparing the integrals of the areas beneath each of these two distributions gave us a sample composed for the 71 % of the desired gold nanoparticles of 3.39 ± 1.94 nm and a minor population (29 %) of smaller nanoparticles with a gold core of 1.67 ± 0.60 nm.

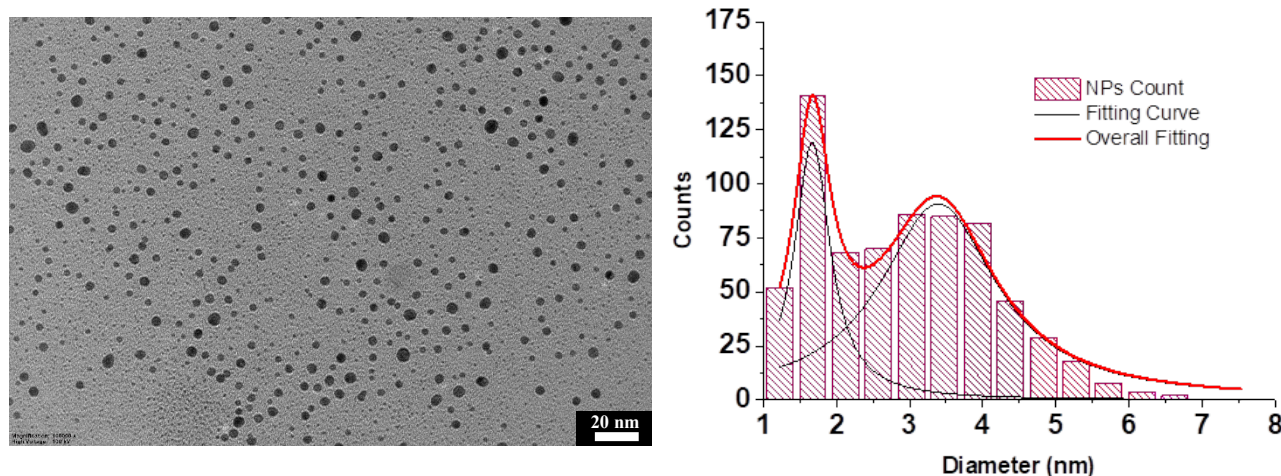


Figure 8.13: (Left) TEM image of the Au@SC6NHOF11CONHPEG. (Right) Histogram and Lorentzian fitting indicating the two size distributions.

Another analysis that can confirm qualitatively the information obtained with TEM is the UV-Vis spectroscopy (**Figure 8.14**). We analyzed a dispersion of these gold nanoparticles in water, obtaining a relative maximum of absorbance at 505 nm. This is also in accordance with the literature, since it has been largely demonstrated how the surface plasmon band (SPB) decreases in intensity and energy with decreasing gold nanoparticle size⁵¹⁸.

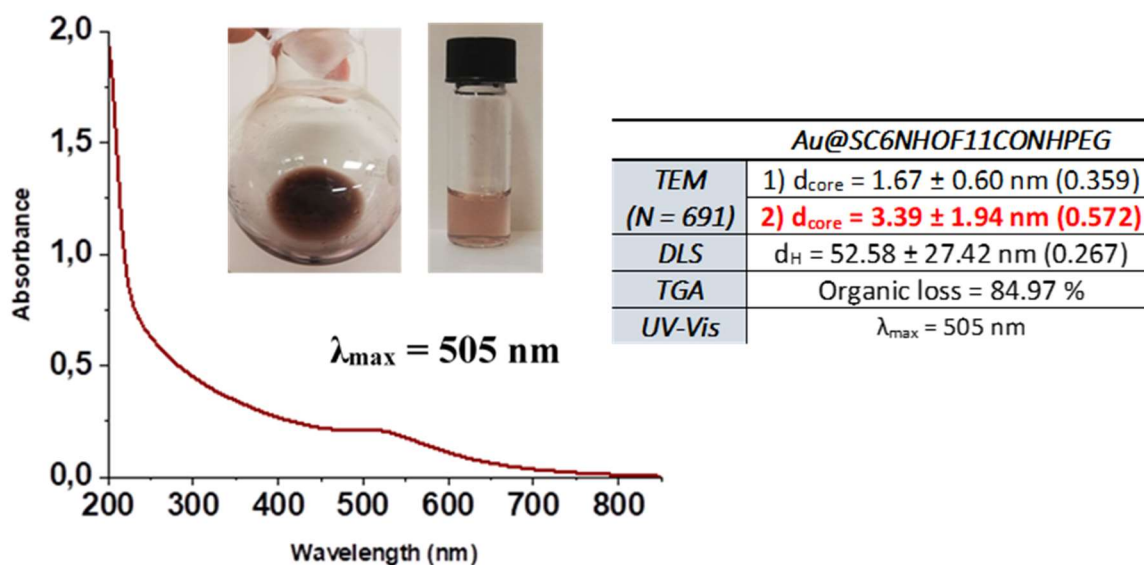


Figure 8.14: (Left) UV-Vis spectrum of fluorinated AuNPs in water with insets showing the nanoparticles' dispersion appearance at different concentrations. (Right) Overview of dimensional, composition, and optical characteristics of the sample.

Once the size of the core has been assessed, we aimed to obtain also the overall dimension of the nanosystem, evaluating the hydrodynamic diameter. For this purpose, we analyzed the sample with DLS, see **Figure 8.15**.

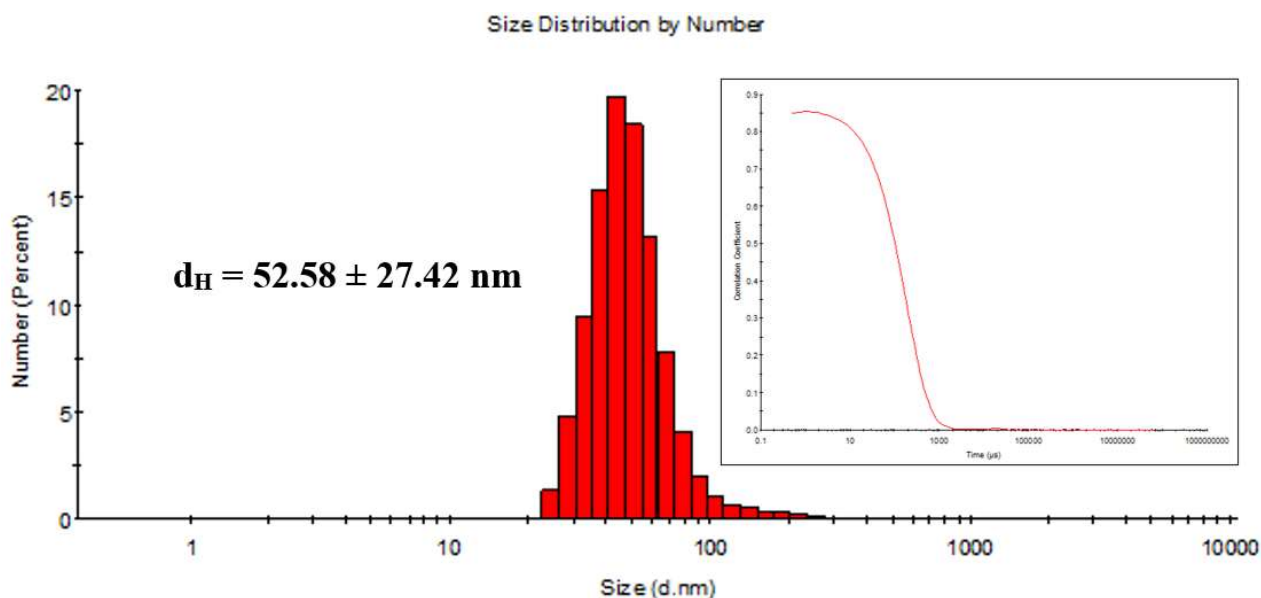


Figure 8.15: DLS analysis of the gold nanoparticles dispersion in water with the size distribution by number of nanoparticles extrapolated from it and (Insert) the related correlogram.

The result obtained displays a d_{H} above the value expected, considering that the bigger population of nanoparticles has an inorganic core of 3.4 nm. By consequence, the shell should be almost 25 nm thick, even if we estimated that the entire stretched structure of the ligand does not reach 10 nm.

This could mean that either the solvation sphere is exceedingly large or, more probable, that the external PEG tends to interact strongly with the hydrophilic chain of other nanoparticles, forming inter-particles non-covalent bonds that result in small aggregates. The TGA, **Figure 8.16**, indicates a loss of organic with the major peak of the first derivative at 319 °C, which is associated to the desorption of the PEG-bearing fluorinated thiol with an organic loss of 85 %.

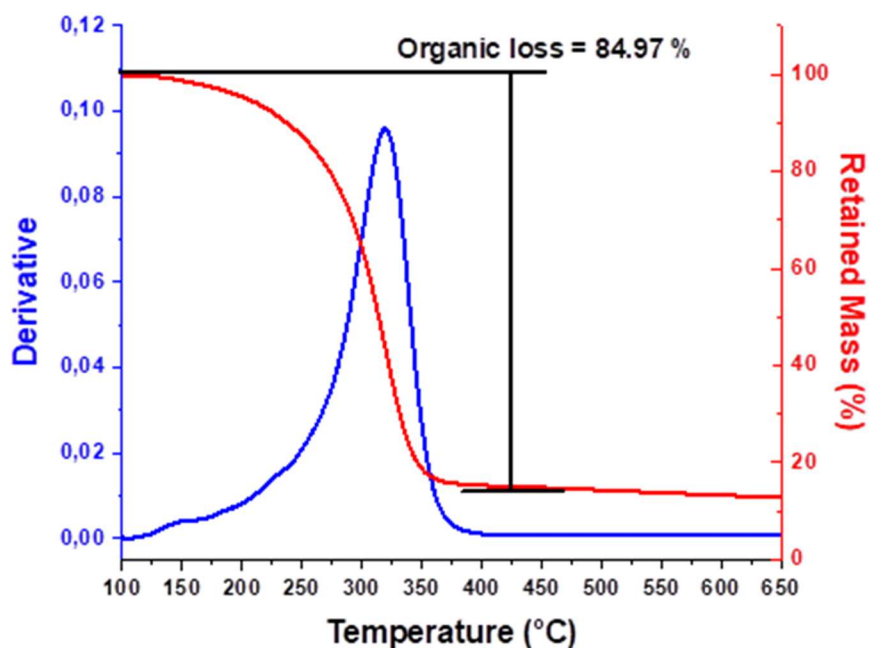


Figure 8.16: TGA plot of the gold nanoparticles sample comprising (left) the derivative of the and (right) the percentage of the mass that is retained with increasing temperatures.

Finally, we characterized these functionalized gold nanoparticles with different NMR experiments to verify that the thiol was bound on the nanoparticle surface with no more free ligand in dispersion. The $^1\text{H-NMR}$ spectrum was compared with that of the thiol ligand (**Figure 8.17**). It is possible to notice that many signals have disappeared and those still present significantly broadened. In particular, only the signals related to the more external part of the PEG moiety – the group of internal ethylene oxide units centered at 3.68 ppm (green dots), the most external methylene at 3.51 ppm (blue dots), and the terminal methyl group at 3.37 ppm (red dots) – can be detected, while the multiplets of the alkyl protons in the 1.25-1.75 ppm range (black dots) are only a very weak and broad signal that is hardly distinguishable from the baseline. This is due to several factors that the ligand linked to gold nanoparticles always suffers. In particular, the portion that is more in proximity to the surface, which experiments a quasi-solid state^{519,520}. Moreover, these protons experience fast spin relaxation from dipolar interactions, the heterogeneity of the binding sites (especially for small clusters), which causes a distribution of chemical shifts, and finally the slow rotational diffusion of the nanoparticle that scales with its size^{375,521}.

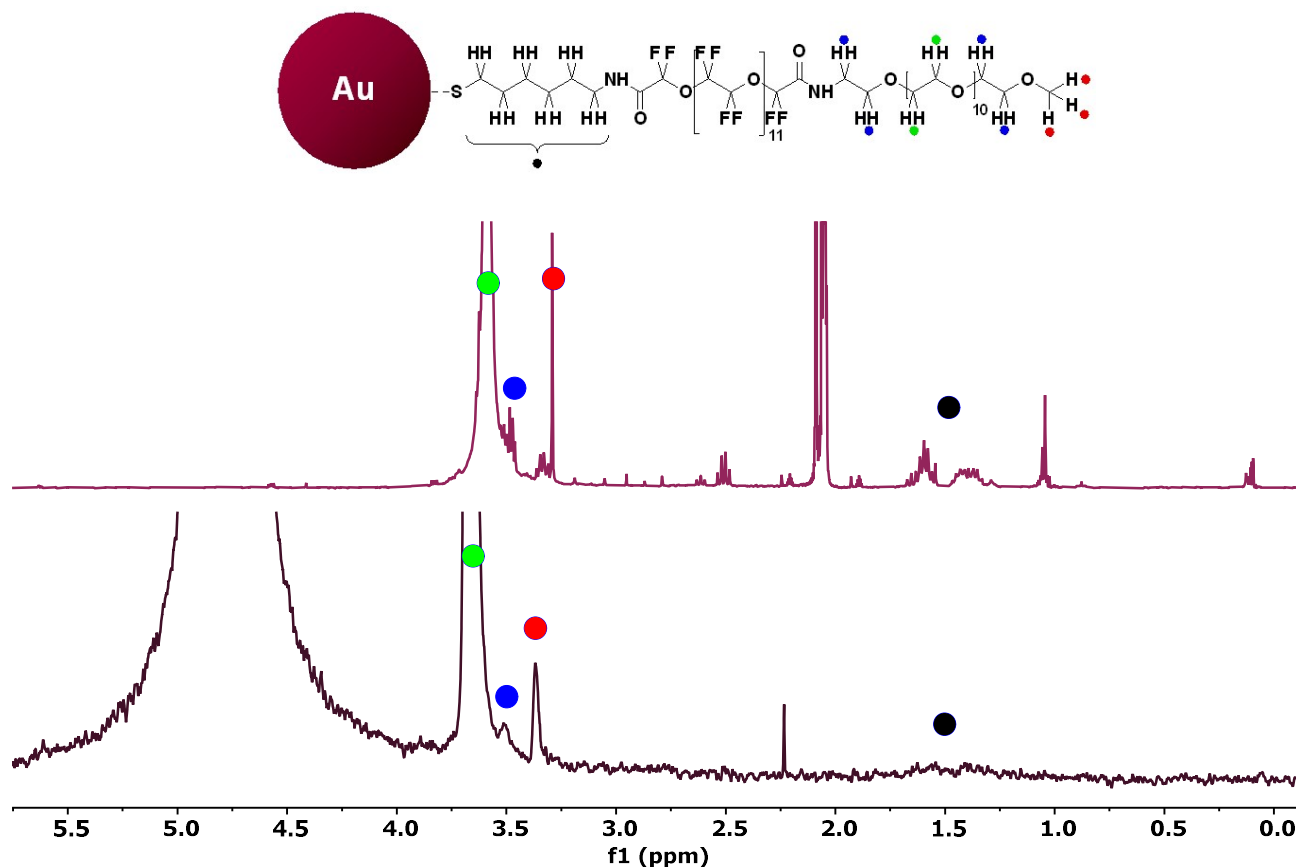


Figure 8.17: Comparison between the ^1H -NMR spectra of the (top) free thiol ligand (HSC6NHOF11CONHPEG) and (bottom) the same ligand when grafted to the gold surface (Au@SC6NHOF11CONHPEG).

The ^{19}F -NMR spectrum shows a similar behavior observed for the ^1H -NMR. Signal broadening characterizes the spectrum, especially for the major ensemble in the range between -88 and -92 ppm (orange, blue and green dots), where an increased number of different broad peaks can be detected. We explain this phenomenon considering that these signals are related to $-\text{CF}_2-$ groups with very reduced mobility. Moreover, the length of the fluorinated structure causes an inhomogeneity in the packing within the same chain, which is translated in signals with different features with respect to the free ligand in solution.

The comparison with the spectrum of the free ligand (**Figure 8.18**) makes clearer the differences and the transition between the two ends of the fluorinated moiety. In fact, it is very noticeable how the double peak at -79 ppm (black and red dots) is now a very weak and broad signal. Also, this spectrum suggests that the NPs purification steps with Sephadex have eliminated completely the traces of TFA and eventual free ligand.

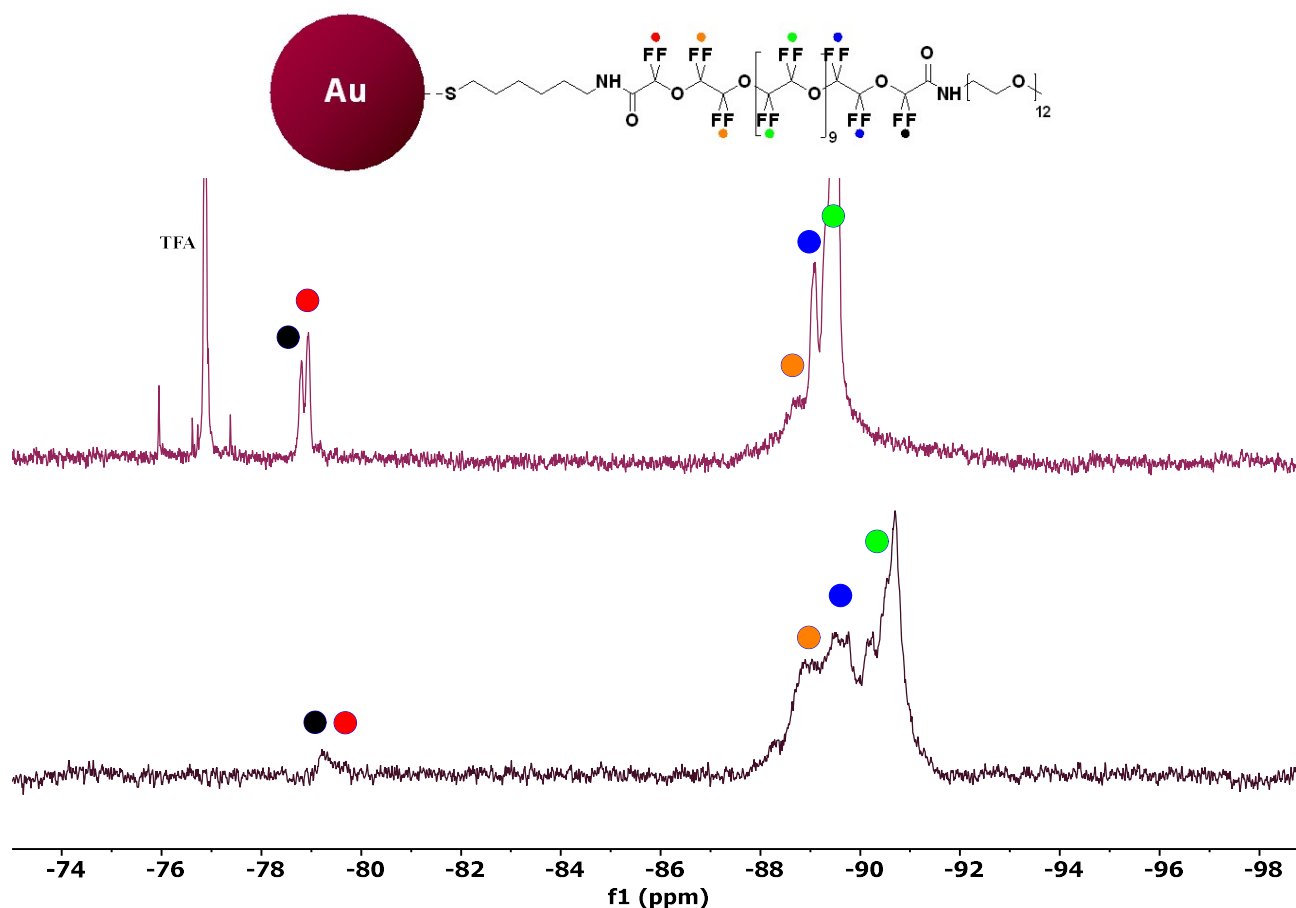


Figure 8.18: Comparison between the ^{19}F -NMR spectra of the (top) free thiol ligand (HSC6NHOF11CONHPEG) and (bottom) gold nanoparticles (Au@SC6NHOF11CONHPEG).

A final experiment performed with these nanoparticles is the extrapolation of the T1 and T2 relaxation times for comparison with the free ligand they carry and to verify their effective applicability in MRI imaging. We performed the same experiments described for the thiol (inversion recovery experiment for T1, Carr-Purcell-Meiboom-Gill sequence for T2), extrapolating the relaxation time values by fitting the points obtained from the series of measurements (**Figure 8.19**). We calculated a T1 of 521 ms and a T2 of 23.5 ms, which are comparable with the values obtained for similar fluorinated nanoparticles we synthesized in a previous work⁶⁴ suitable for their use as MRI contrast agents.

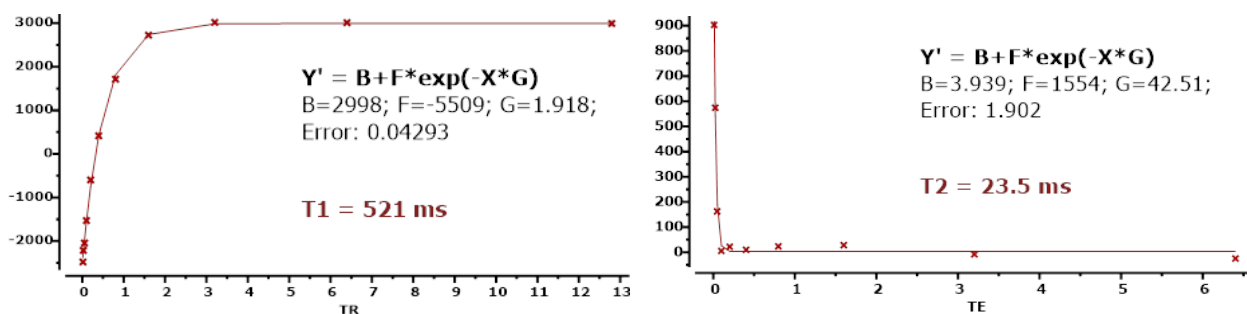


Figure 8.19: Data plot, exponential fitting, function parametrization, and result for (left) the relaxation time T1 and (right) the relaxation time T2.

In respect to the values retrieved previously for the free ligand HSC6NHOF11CONHPEG, we notice a sensible reduction of both the relaxation time T1 and T2, with a consequent increase of relaxivity: this is exactly what we wanted to achieve to obtain a high-performance contrast agent for ^{19}F -MRI and decrease dramatically the long relaxation times fluorinated compounds naturally have in order to reduce the acquisition time it would need for imaging in diagnostics⁵²².

We can conclude that these fluorinated nanoparticles meet the desired requirements of dimension, functionalization, and preliminary imaging features, even if the sample resulted to be polydispersed. The possible aggregation observed with DLS needs to be investigated more deeply at different nanoparticles concentrations.

8.3 SYNTHESIS OF OTHER FLUORINATED LIGANDS

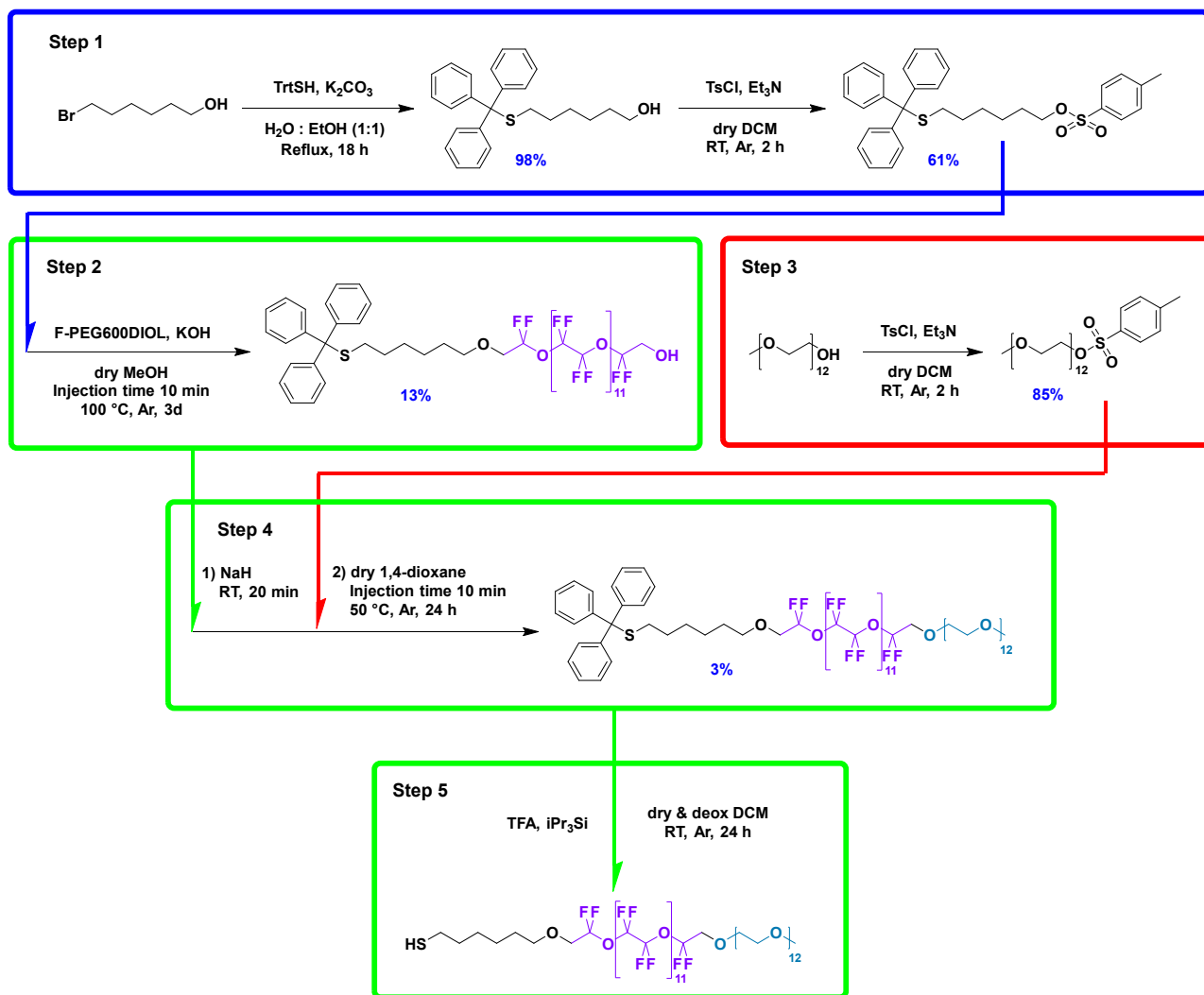
8.3.1 Synthesis of the linear ligand with F-PEG600DIOL

Considering the synthetic issues encountered during the preparation of the linear ligand, because of the labile ester functions in the perfluorinated moiety, we decided to find an alternative that could assure the formation of a similar structure in a faster and less problematic way. To this end we considered the building block F-PEG600DIOL on the right in **Figure 8.20** as a valuable choice.



Figure 8.20: Structural comparison between the previous perfluoropolyether species and the one adopted in the following syntheses.

Besides the intrinsic higher stability of ether groups in respect to the activated ester, the other advantage of this structure is that it requires few or no extra synthetic steps for conjugation with the other parts of the ligand we were preparing. Considering the modified PEG, also in this case a shortening of the synthetic scheme will be possible. The final synthetic approach we devised is presented in **Scheme 8.3**.



Scheme 8.3: Complete synthetic scheme for the preparation of the fluorinated linear starting from the perfluoropolyethylene oxide diol.

Synthesis of TrtSC6OF11OH

The steps for the preparation of the TrtSC6OTs species were immediately followed by the insertion of the fluorinated moiety.

Therefore, the synthetic condition of this step requires only the use of a strong base, KOH in our case, to deprotonate one of the ends of the diol, thus forming a good nucleophile that could replace the tosyl group in an $\text{S}_{\text{N}}2$ reaction. Moreover, the substitution must be performed in an anhydrous solvent and inert atmosphere to avoid the presence of water to preserve the tosyl ester TrtSC6OH.

After the extraction of the product from the crude and the following purification with flash chromatography, the product was sufficiently clean for the subsequent step.

The $^1\text{H-NMR}$ spectrum gave us promising data: apart from the aromatic and alkyl protons whose chemical shifts and integrations were as expected identical to the reagent, we identified the characteristic peaks of the product in the triplet at 3.59 ppm for the CH_2 that previously was in

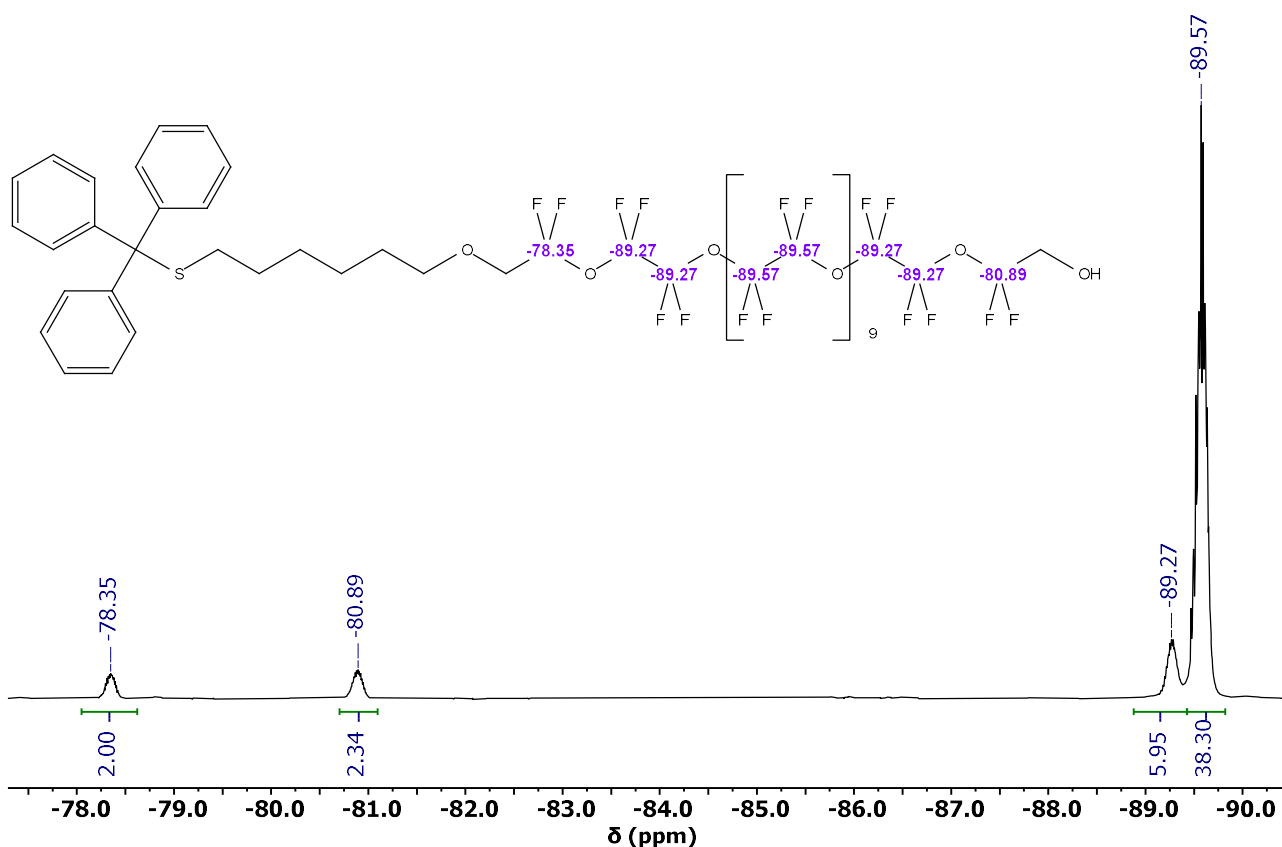


Figure 8.23: ^{19}F -NMR spectrum (376 MHz, acetone- d_6) of compound TrtSC6OF11OH.

Besides the NMR, we performed also the ESI-MS spectrum both in positive and negative mode. In the first case, we were able to identify the $[\text{M}+\text{Na}^+]$ ion at 1834.9 m/z and also the signals of the analogous ions with 12, 13, and 14 perfluoroethylene oxide units, each separated by 116 m/z . We obtained similar results in the negative mode, identifying the $[\text{M}+\text{Cl}^-]$ ion at 1846.8 m/z and the analogous ions pertaining to the species with up to 14 perfluoroethyleneoxide units.

The product was obtained as a transparent oil with a 12 % of overall yield.

Synthesis of TrtSC6OF11OPEG

The same type of reaction exploited in the previous step was used also for the conjugation of the PEG moiety. For this purpose, we needed to modify the PEG structure by converting the hydroxyl group to tosyl group.

In this case, the species we used to deprotonate the terminal alcohol was sodium hydride. The deprotonated alcohol then undergoes the $\text{S}_{\text{N}}2$ reaction, displacing the tosyl group of the modified PEG and forming a new ether bond. After the purification via flash chromatography, the preparation of the desired product was assessed with ^1H -NMR, in which we were able to identify the new

signals related to the presence of the PEG moiety. In particular, the signals at 3.58 ppm of the methylene oxide units and the singlet at 3.29 of the terminal methyl are detected. Moreover, the ether bond formation is confirmed by the presence of the triplets at 4.10 ppm pertaining to the methylene protons of the fluorinated portion near the PEG and at 3.79 ppm for the methylene of the PEG linked to the fluorinated chain.

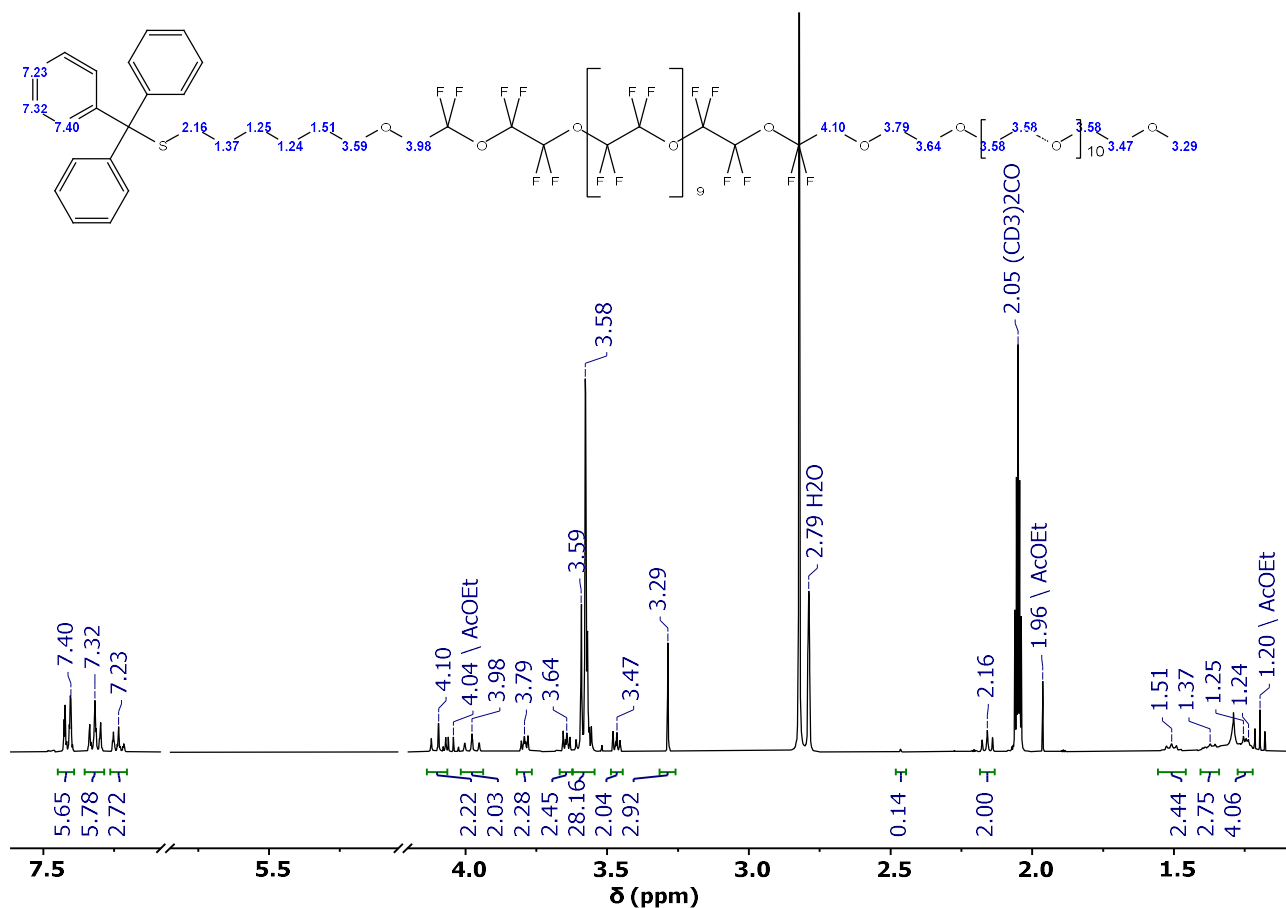


Figure 8.24: ¹H-NMR spectrum (400 MHz, acetone-d₆) of compound TrtSC6OF11OPEG.

Since we have encountered some difficulties in understanding 1D ¹³C-NMR, because of the significant number of coupling that broadens the peaks and makes the interpretation challenging, we assigned the chemical shifts with the help of the heteronuclear 2D spectra gHSQC and gHMBC. The ¹⁹F-NMR spectra confirmed the successful functionalization, since the signal at -80.89 ppm of the reagent is shifted in the product to -78.49 due to the formation of the ether with the PEG moiety.

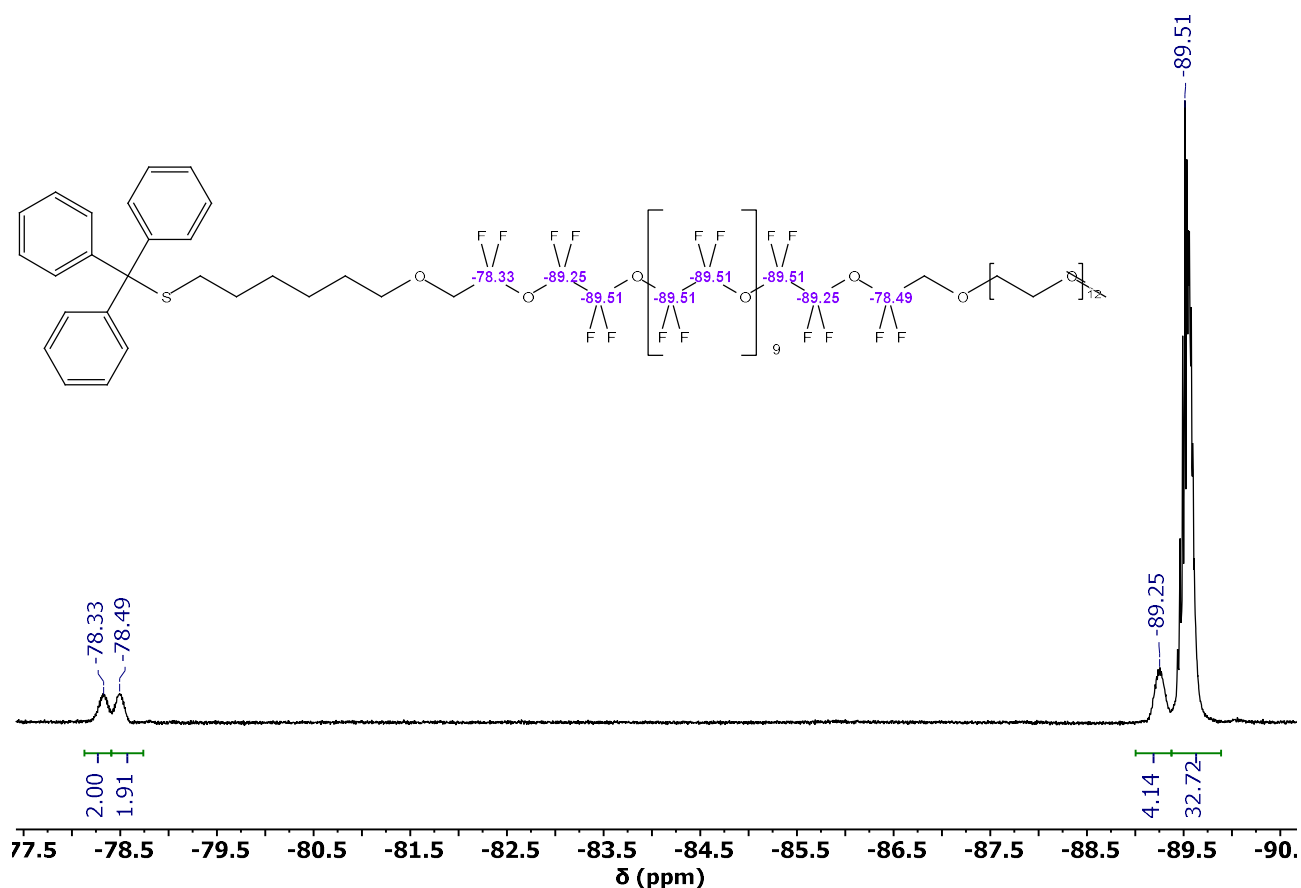


Figure 8.25: ¹⁹F-NMR spectrum (376 MHz, acetone-d₆) of compound TrtSC6OF11OPEG.

The ESI-MS spectra recorded in positive and negative mode gave us respectively the indication of the presence of PEG and -OCF₂CF₂- units with many peaks separated by 44 m/z in the first case or 116 m/z in the second.

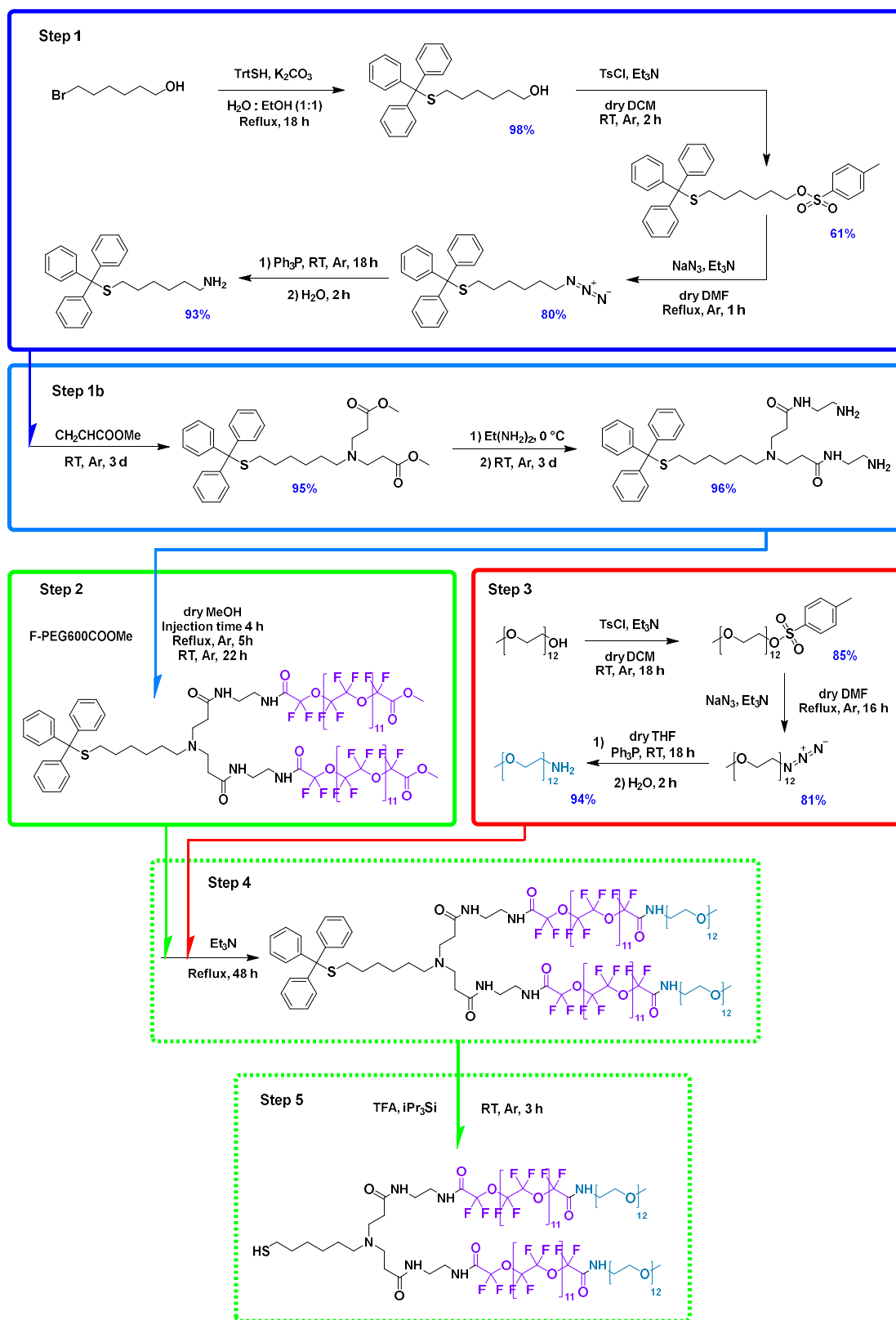
Unfortunately, even if the results related to the last step and in particular to the synthetic pathway chosen were very promising, we were able to obtain only a small amount of purified samples, obtaining a transparent oil after the removal of the solvent with a 3 % yield. This was fundamentally due to the impossibility to separate with a sufficient degree of purity, the unreacted PEG from the product. Therefore, this step needs to be optimized in future work.

8.3.2 Synthesis of the branched ligand with F-PEG600COOMe

After the successful synthesis of the linear ligand with the methyl ester of the perfluoropolyether dicarboxylic acid, we decided to prepare a branched ligand presenting two fluorinated fragments, trying to double the number of fluorine atoms.

This ligand is characterized by a thiol head with the alkyl C6 moiety for a stable monolayer on the gold surface. Then the ramification is imparted by a nitrogen atom and the structure is divided in

two branches, each carrying the PFPE portion with the same length we used for the linear ligand and a PEG₅₅₀ moiety as end group for water solubility. We adopted the synthetic scheme reported in **Scheme 8.4**.



Scheme 8.4: Complete synthetic scheme for the preparation of the fluorinated branched ligand containing two methyl ester perfluoropolyethylene oxide (F-PEG600COOMe) moieties.

Step 1 was maintained as for the linear ligand, as well as the formation of the PEG₅₅₀-NH₂, step 3. The principal modification, which is the key point of this synthesis, is the formation of a branch point starting from the nitrogen atom of the -NH₂ group in the thiol protected alkyl part (step 1b). Then, each of these branches is further modified to bear reactive amine groups (step 1b), which are exploited in the following step 2 for the covalent linkage of the fluorinated moiety. After achieving the fluorinated intermediate, the idea is to attach the modified PEG to both branches (step 4), while step 5 implies the deprotection of the thiol function, removing the trityl group.

Also in this case, we will describe briefly the new steps introduced in the synthesis, presenting the analysis of the data that confirms the preparation of the desired compounds and the attempts performed for the obtainment of the final product.

Synthesis of dimethyl 3,3'-((6-(tritylthio)hexyl)azanediyl)dipropionate (TrtSC₆N(C₂COOMe)₂)

This step has the purpose of introducing the branch point in the alkyl structure. We aim to achieve this functionalization by exploiting two subsequent aza-Michael additions to the methyl acrylate. We expected the first addition to be slower than the second one because of the lower nucleophilicity of the primary amine, with respect to a secondary amine.

The ¹H-NMR and ¹³C-NMR spectra helped to control the effective formation of the desired product. The proton NMR spectrum contains the signal of the methylene in alpha-position to the nitrogen atom in the alkyl chain at 2.75 ppm. Moreover, there are present signals related to the two branches derived from methyl acrylate: the two terminal methyl ester groups at 4.91 ppm. The internal methylene groups instead resonate at 2.75 ppm and 2.45 ppm. The product was also characterized by ¹³C-NMR and HSQCAD spectra which proved crucial for the precise assignment of all resonances.

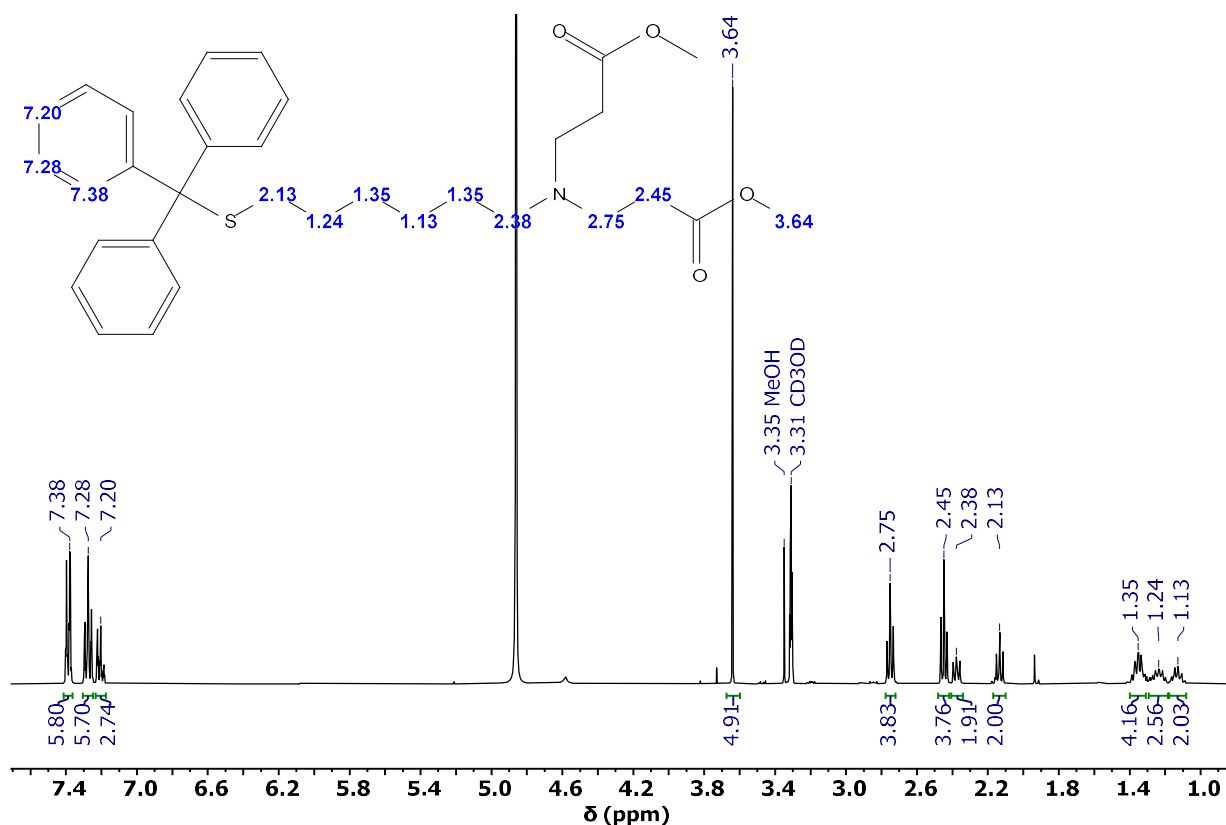


Figure 8.26: ¹H-NMR spectrum (400 MHz, CD₃OD) of compound TrtSC₆N(C₂COOMe)₂.

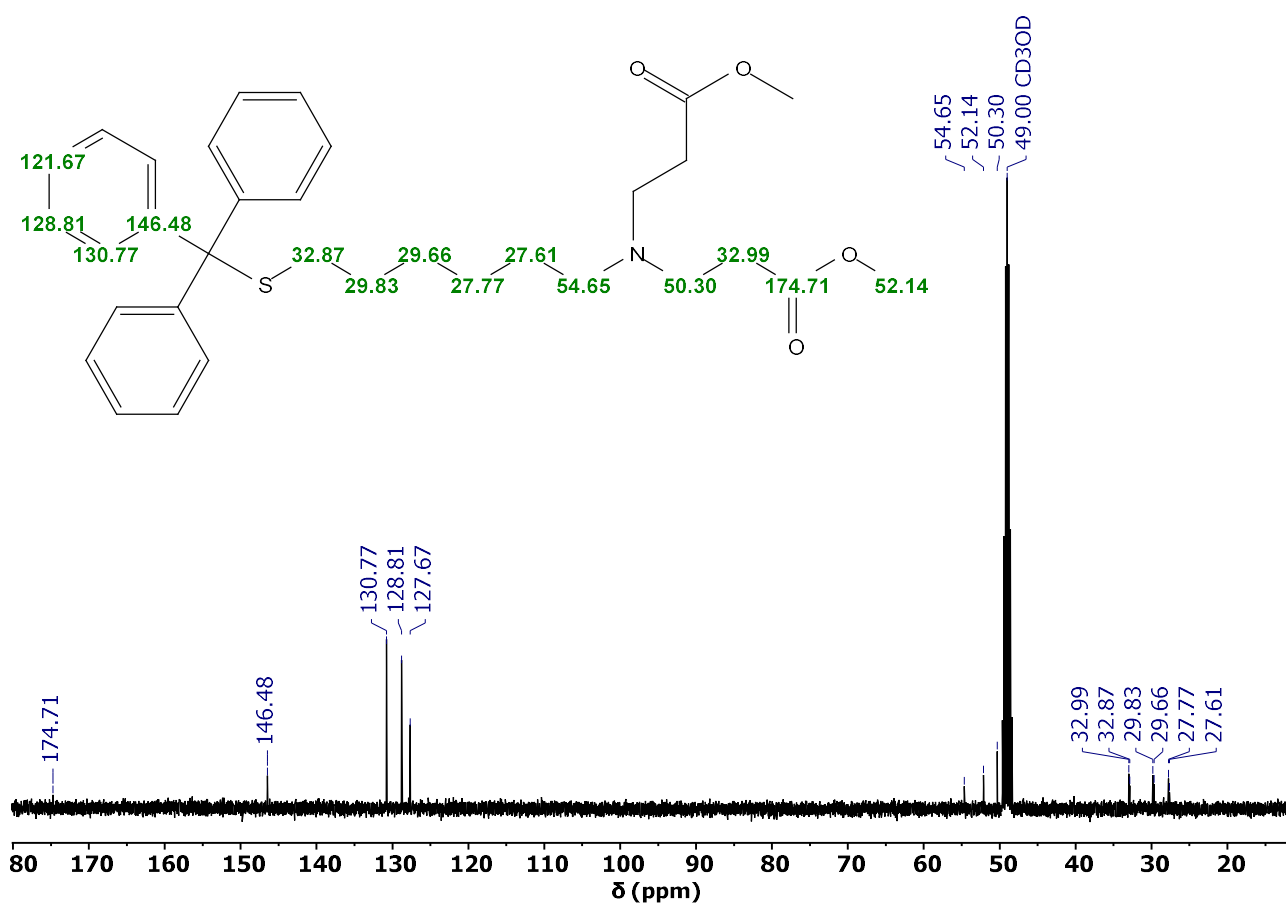


Figure 8.27: ¹³C-NMR spectrum (101 MHz, CD₃OD) of compound TrtSC₆N(C₂COOMe)₂.

The ESI-MS spectrum shows the $[M+H]^+$ and the $[M+K]^+$ ions, detected respectively at 548.3 and 570.3 m/z. The product was obtained as light-yellow oil with a 95 % yield.

Synthesis of 3,3'-((6-(tritylthio)hexyl)azanediyl)bis(*N*-(2-aminoethyl)propionamide) (TrtSC6N(C2CONHC2NH2)2)

The two branches were further functionalized by reaction with ethylenediamine (EDA) to have proper functional groups for further structure modification. Since we had to be sure to elongate both the branches equally, we let the reaction proceed for a prolonged period of time, controlling the progression frequently and eventually inserting additional diamine.

The conjunction could be verified by NMR. The $^1\text{H-NMR}$ spectrum displays amide protons at 8.12 ppm and the methylene groups signals at 2.88 ppm and 3.33 ppm for the added amino-ethylene moiety. In this case, the precise assignment was supported by gCOSY, gHSQC, and gHMBC experiments.

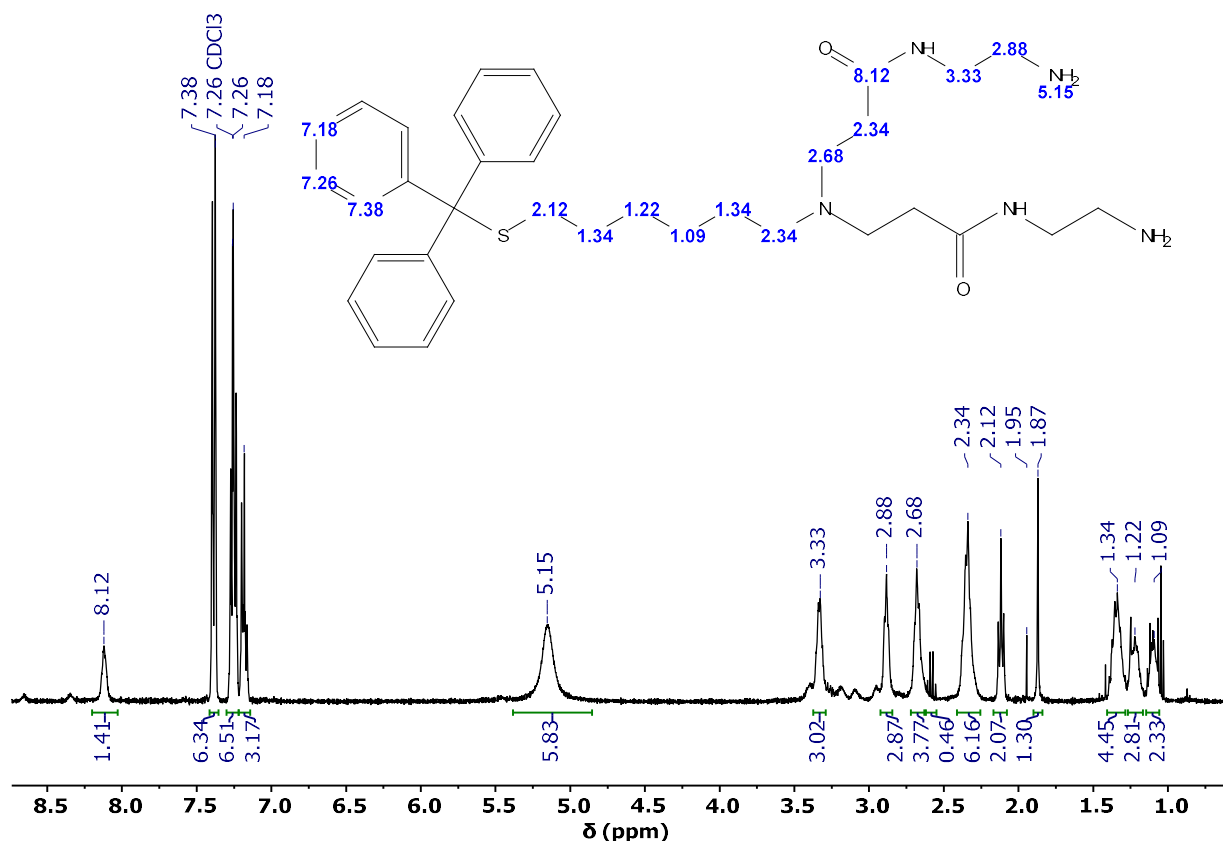


Figure 8.28: $^1\text{H-NMR}$ spectrum (400 MHz, CDCl_3) of compound TrtSC6N(C2CONHC2NH2)2.

The $^{13}\text{C-NMR}$ spectrum presents the chemical shift of the carbonyl carbons at 173.36 ppm and all the signals related to the four carbons of new methylene groups at 39.81 ppm and 40.36 ppm.

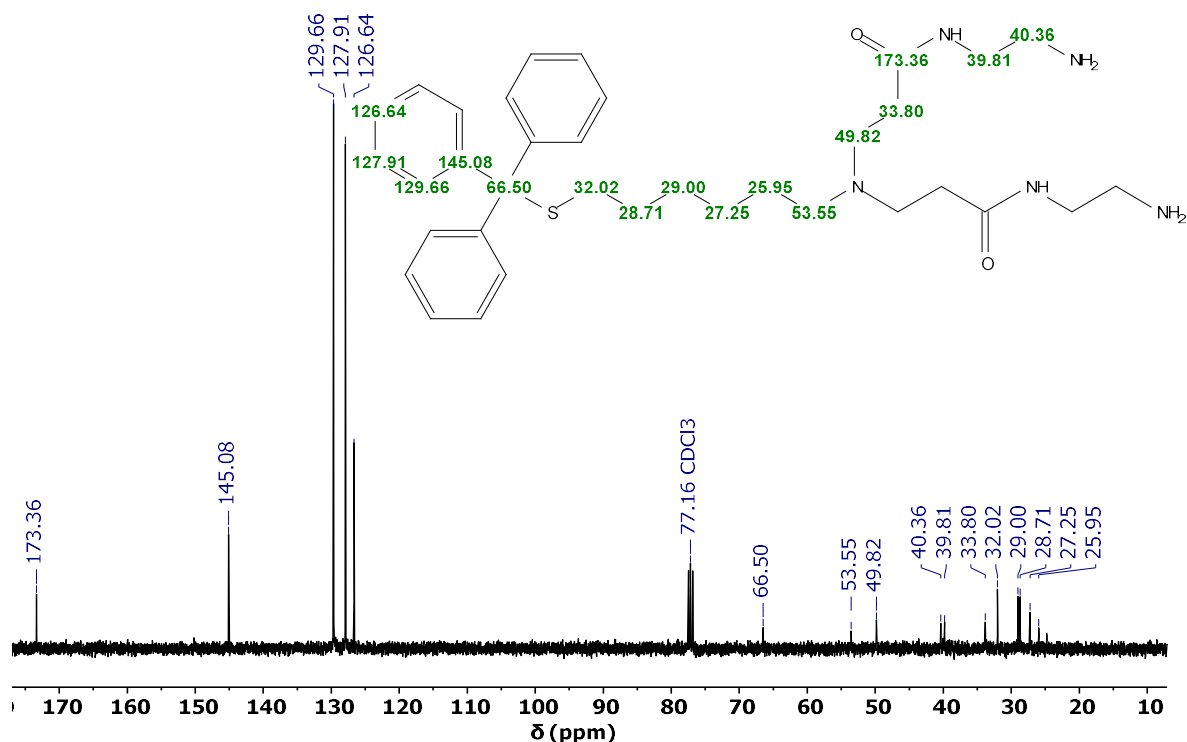


Figure 8.29: ^{13}C -NMR spectrum (101 MHz, CDCl_3) of compound $\text{TrtSC}_6\text{N}(\text{C}_2\text{CONHC}_2\text{NH}_2)_2$.

ESI-MS spectrum displays $[\text{M}+\text{H}^+]$, $[\text{M}+\text{Na}^+]$ and the $[\text{M}+\text{K}^+]$ ions, respectively at 604.4, 626.2 and 644.4 m/z. The yield of the pale-yellow vitreous solid product was 96 %.

Synthesis of the Pre-Y-Framework ($\text{TrtSC}_6\text{N}(\text{C}_2\text{CONC}_2\text{NOF}_{11}\text{COOMe})_2$)

In this step the objective is to insert the fluorinated moiety at the end of each branch, exploiting the coupling of amine functions with the carboxyl methyl ester of the fluorinated F-PEG600COOMe compound.

Considering the analogy with the insertion of the fluorinated moiety on the linear ligand, we started with similar synthetic conditions also in this case. We took advantage of triethylamine as base and amide bond formation promoter, performing the synthesis under reflux, but dispersing the reagents in trifluoroethanol. This solvent was chosen for solubility purposes (considering that the final amount of fluorine nuclei in the product should be doubled), before having understood that its presence is detrimental for the amide bond formation.

The reaction was carried out for 3 days at room temperature and heated to reflux overnight after controlling the crude mixture. In the end, the crude was dried, and the different components were separated by flash chromatography.

The different fractions collected were analyzed by NMR, IR, and ESI-MS. From these analyses, we selected the most promising fraction, even if the interpretation was ambiguous or unexpected for some aspects.

The best result obtained is represented by a species in which only one of the branches has been functionalized with the fluorinated moiety, while the other branch still bears the free amine group likely because of hydrolysis of part of the methyl esters in the perfluorinated building block. We realize the nature of this compound by studying deeply the $^1\text{H-NMR}$ spectrum presented in **Figure 8.30**. By comparison with the spectrum of the reagent (even if in different deuterated solvents), we quickly identified the signals pertaining to the aromatic ring and alkyl chain. Unfortunately, the impurity at 1.29 ppm covers part of the signal of the methylene in γ -position to the tritylthio group. The remaining signals were assigned thanks to different 2D spectra (gCOSY, gHSQC, gHMBC), which were essential to pinpoint the different methylene groups and the interaction between them. In fact, still by comparison with the $\text{TrtSC}_6\text{N}(\text{C}_2\text{CONC}_2\text{NH}_2)_2$ compound, we determined the peaks related to the two methylene groups in alpha position to the tertiary amine in the branching site. At this point, since we have detected a slight splitting of signals (2.89 and 2.93 ppm for the methylene in alpha-position to the tertiary N atom, 2.42 and 2.47 ppm for the β -methylene), we hypothesize the presence of two different branches, one functionalized as desired, one unreacted. The diversity is more evident in the protons of the methylene groups derived from the ethylenediamine part. Indeed, while the ones between the two amide functions are more deshielded and resonate at 3.33 ppm and 3.40 ppm, the 3.05 ppm and 3.44 ppm signals on the branch end with the amine group, are similar to the ones in the reactant's spectrum, notwithstanding the different deuterated solvent.

Even if one of the branches has been functionalized by the perfluoropolyether methyl ester, we do not observe the singlet at 3.99 ppm related to the presence of the methyl ester group: the reason is that the ester has been hydrolyzed in one of the synthetic, work-up or washing steps. An alternative explanation is the occurrence of transesterification with the solvent trifluoroethanol. We hypothesize that the broad signal at 4.60 ppm is maybe due to the protons of the methylene group of the trifluoroethoxyl group, which is broad because of the coupling with the F atoms.

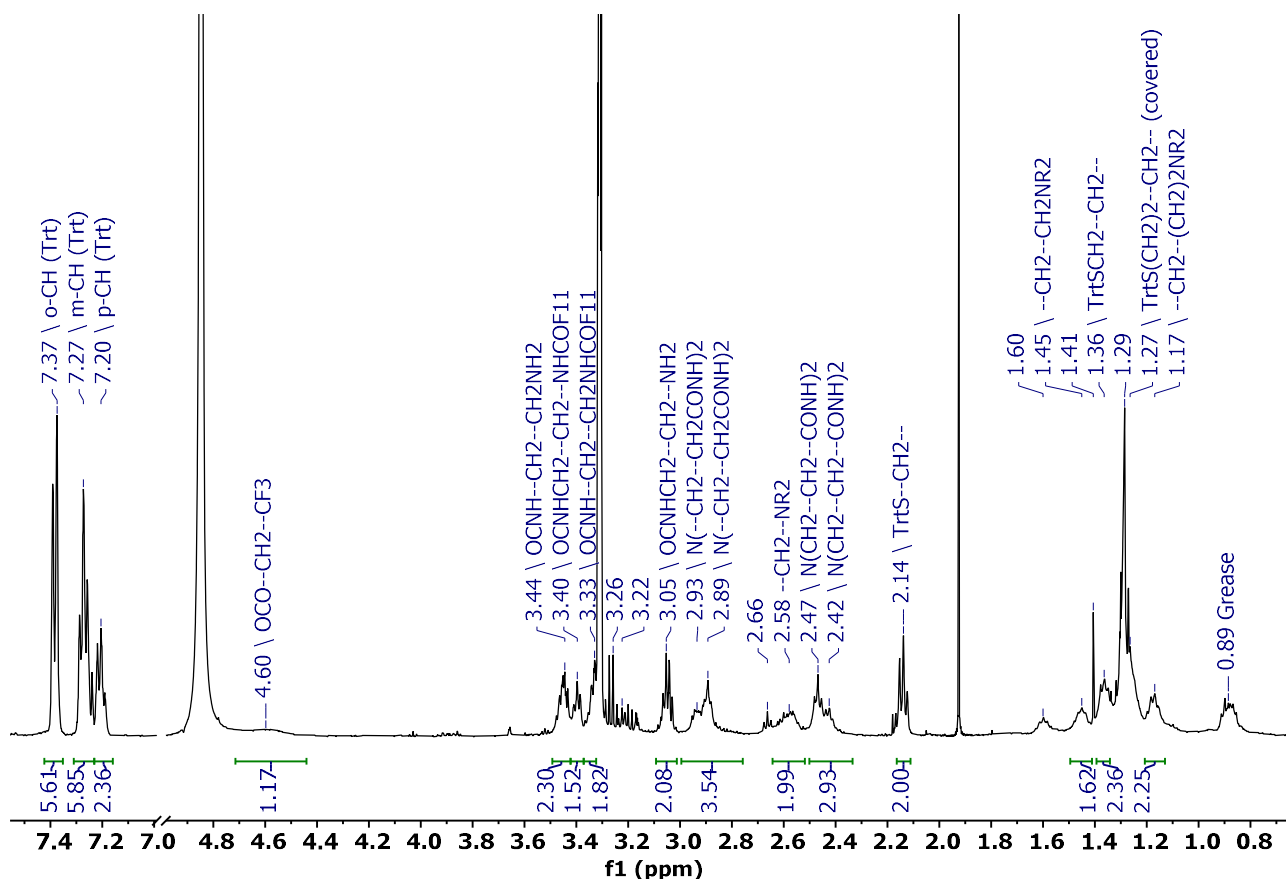


Figure 8.30: ^1H -NMR spectrum (500 MHz, CD_3OD) of the species obtained with the first method tried to prepare $\text{TrtSC}_6\text{N}(\text{C}_2\text{CONC}_2\text{NOF}_{11}\text{COOMe})_2$ compound.

The heteronuclear 2D spectra were also fundamental to determine the chemical shift of each carbon nucleus of the structure (especially the three different carbonyl groups) and their association with the protons.

To have a further verification over the structural hypothesis we proposed, we recorded also the ^{19}F -NMR spectrum of the mono-functionalized species. In the spectrum reported in **Figure 8.31** that we compared with the F-PEG600COOMe spectrum recorded in CD_3OD , we can identify the ensemble of peaks belonging to all the perfluoromethylene groups in the intermediate moiety of the polymer, while the signals in the reagent at -79.05 ppm and -89.90 ppm are shifted at -78.70 ppm and -89.65 ppm respectively. These shifts reflect, for the first signal, the conversion of the methyl ester group to amide, while for the second one may be due to the conversion of the terminal methyl ester to a different ester or to a carboxylic acid function. To better understand this point, we prepared the trifluoromethyl ester of the fluorinated reagent, which displays in the ^{19}F -NMR spectrum a signal at -79.68 ppm pertaining to the terminal CF_3 group. On the other hand, the fluorinated reagent was hydrolyzed to acid on purpose. For this species, a signal at -57.42 ppm assigned to the CF_2 close to the carboxylic groups was found, whereas the signal is at -92.36 ppm in presence of a carboxylate.

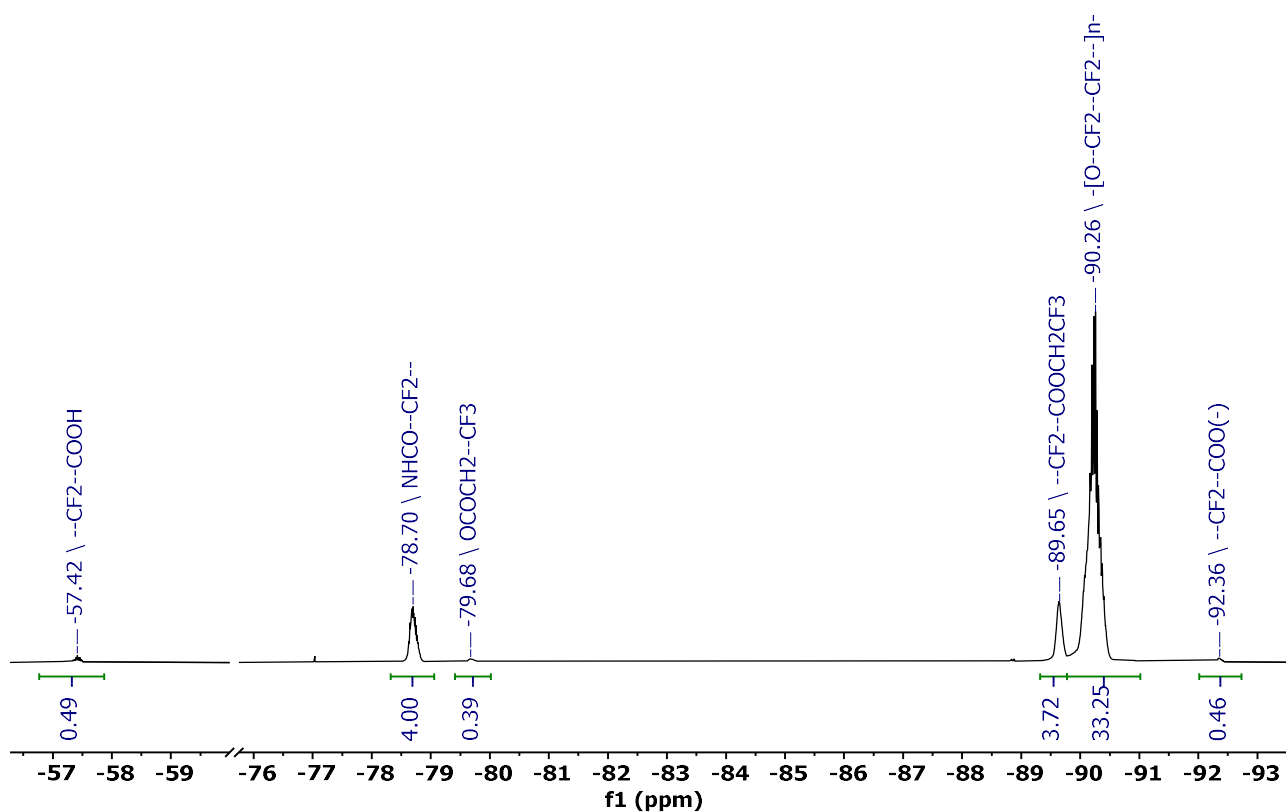


Figure 8.31: ^{19}F -NMR spectrum (376 MHz, CD_3OD) of the species obtained with the first method tried to prepare $\text{TrtSC6N}(\text{C2CONC2NOF11COOMe})_2$ compound.

The IR spectra confirmed the successful conjugation: by comparison with F-PEG600COOMe reference, in the spectrum of the isolated fraction we observed both the intense and broad signals in the $1100\text{--}1250\text{ cm}^{-1}$ range related to C-F bonds stretching^{523,524} and the sharp strong signal at 1681 cm^{-1} assigned to the carbonyl of the amide groups⁵²⁵. However, we expected to maintain the peaks at 1798 cm^{-1} belonging to the methyl ester carbonyl group which are clearly visible in the reference but lacking in the product spectrum. On the contrary, a very broad signal centered at 3380 cm^{-1} is present and we assume this is related both to the high concentrations of carboxylic acid functions and to the presence of the amine group on the unreacted branch. In addition, we also identified a small asymmetry on the right of the 1681 cm^{-1} band and a weak band at 1569 cm^{-1} : they may be assigned respectively to the presence of carboxylates and to the bending of the N-H bond in the amides. Therefore, we concluded that the unreacted terminal methyl ester which we should have preserved for the next step, was hydrolysed either during the synthesis or during flash chromatography separation. This unwanted event could also explain the issues we encountered in eluting the product from the polar stationary phase of the column and the need to use triethylamine to collect the hydrolysed product.

Unfortunately, with the ESI-MS analysis, we were not able to detect the molecular ion $[M+H]^+$, since the calculated molecular weight of the branched product was beyond the instrument range. However, it was possible to identify the characteristic pattern of signals separated by 116 m/z, related to the loss of fragments with an increasing number of perfluoroethylene oxide units.

Given the unsatisfactory results, we decided to repeat the conjugation under different experimental conditions. In particular, we tried to exploit a microwave reactor to speed up the kinetics of the reaction and reduce the risk of hydrolysis and consequent ester functions deactivation which could have occurred in the previous experiment, due to the longer reaction time. Therefore, in a similar approach, we adopted the same reagents ratio and solvent, but limiting the heating to 100 °C for one hour.

The crude mixture was washed with diethyl ether and then analyzed with $^1\text{H-NMR}$, giving the spectrum reported in **Figure 8.32**.

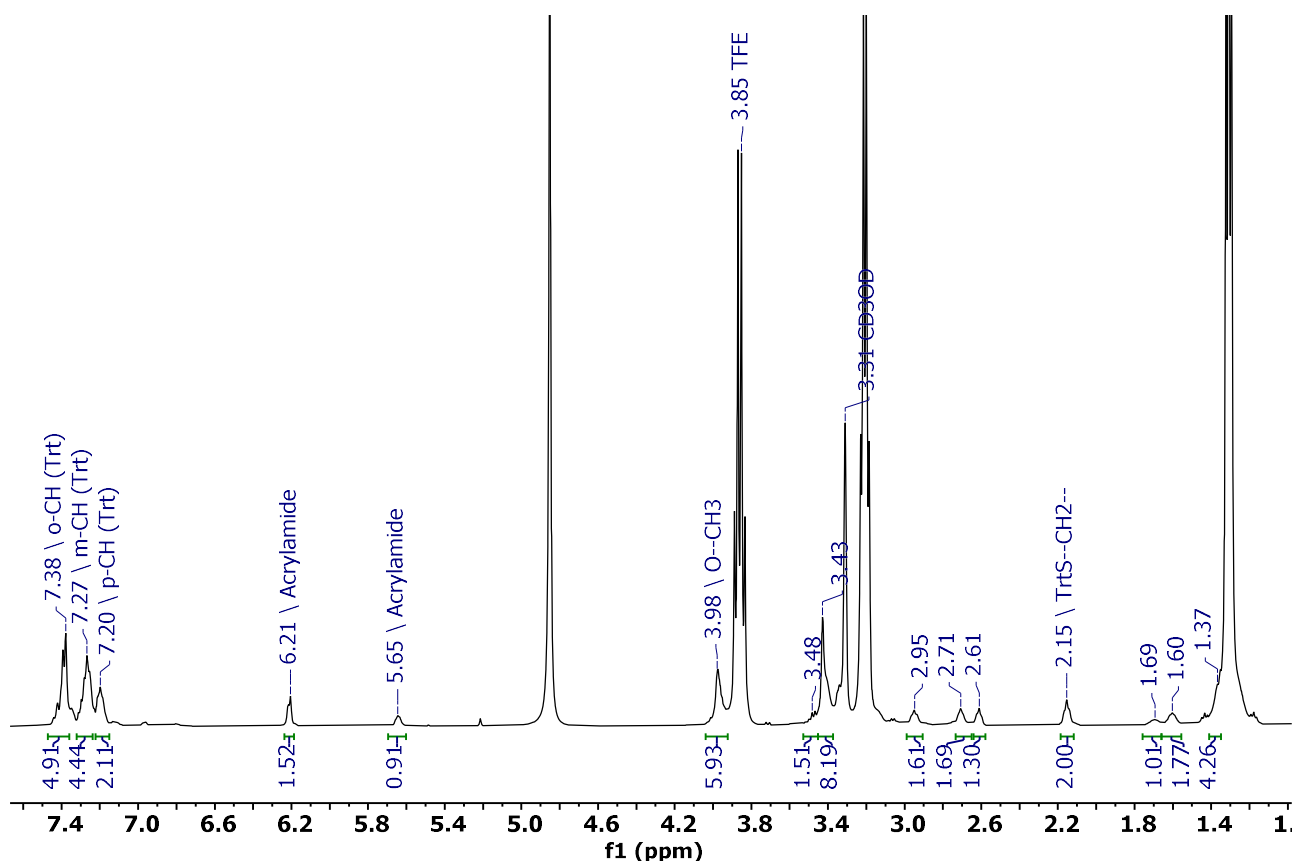


Figure 8.32: $^1\text{H-NMR}$ spectrum (500 MHz, CD_3OD) of the species obtained with the second method tried to prepare $\text{TrtSC}_6\text{N}(\text{C}_2\text{CONC}_2\text{NOF}_{11}\text{COOMe})_2$ compound.

Even if the presence of the singlet at 3.98 ppm integrating for 6 protons with respect to the methylene in alpha to the trityl function could indicate the preservation of the two methyl ester groups after the conjugation, the washing was inefficient in removing completely both the TFE and

the TEA. In addition, the integration is not consistent with the expected number of the aromatic protons and the alkyl one between 1.3 ppm and 1.8 ppm but it is coherent with the methylene groups in the 2-6-3.5 ppm range and the methylene in alpha position to the trityl used as reference. More important, we suspected the peaks at 5.65 ppm and 6.21 ppm that couple in the gCOSY spectrum to be related to the presence of an acrylamide that may have formed from the decomposition of the branches.

Moreover, the ^{19}F -NMR reported in **Figure 8.33** showed a series of numerous different and unexpected signals, which are related neither to the fluorinated reactant nor to the desired product. In addition, chromatographic purification performed on this mixture did not lead to the separation of the fluorinated reagent from the possible products.

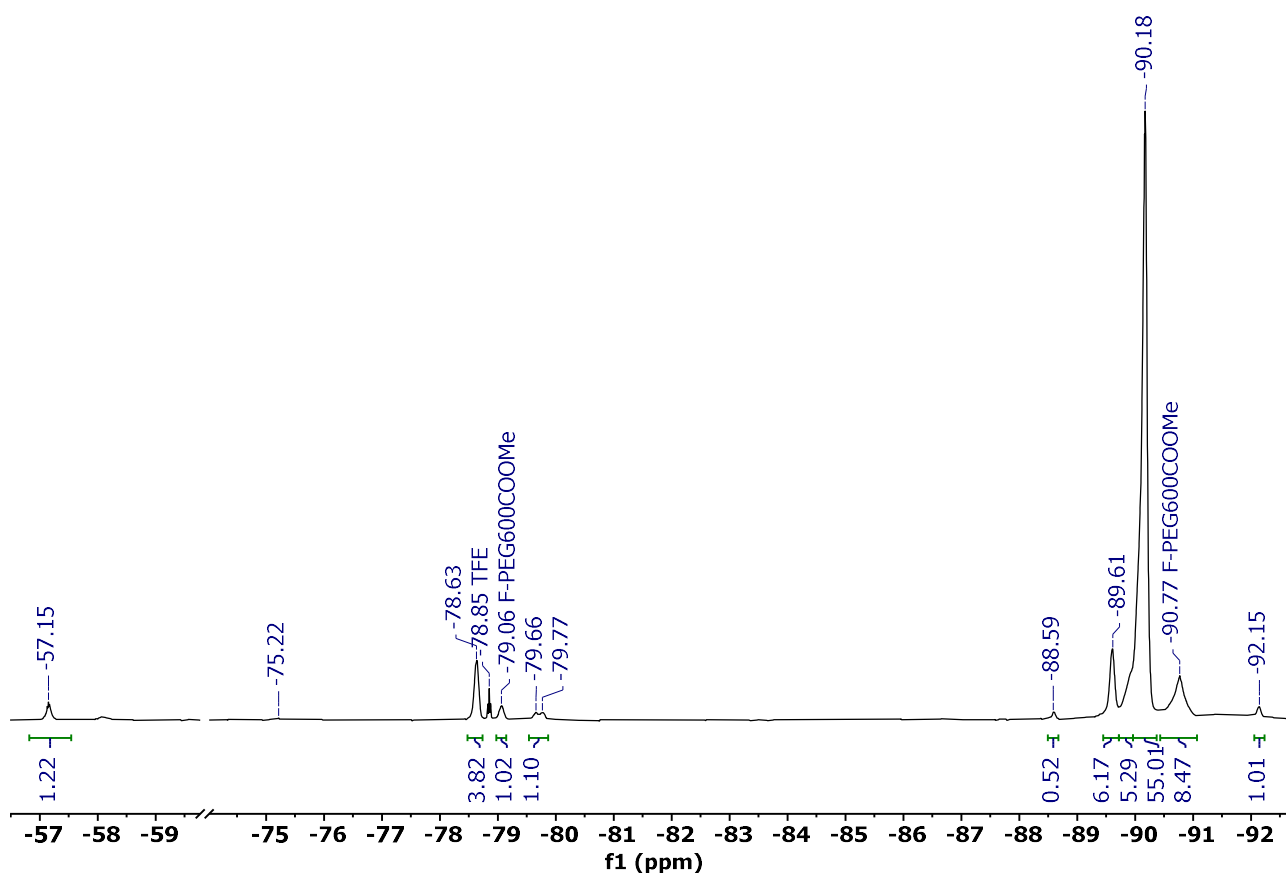


Figure 8.33: ^{19}F -NMR spectrum (376 MHz, CD_3OD) of the species obtained with the second method tried to prepare $\text{TrtSC6N}(\text{C2CONC2NOF11COOMe})_2$ compound.

Suspecting the deactivation of the ester functions as one of the causes for the previous unsatisfactory experiments, in the second series of experiments we relied on a stronger base that is also a well-known activating and coupling agent for carboxylic acids. Indeed, 4-dimethylaminopyridine (DMAP) is generally employed as a catalyst in the Steglich reaction for the preparation of esters, acting as an acyl transfer-reagent. However, it can be employed also for the

preparation of amides, using amines that react even better than alcohols, since they are more nucleophilic than alcohols.

Because of the unfortunate results of the use of microwave, in this experiment the conventional heating was used, with an excess of F-PEG600COOMe and DMAP in respect to the branched reagent. We controlled the reaction with both $^1\text{H-NMR}$ and $^{19}\text{F-NMR}$, obtaining the spectra of **Figure 8.34** and **Figure 8.35**.

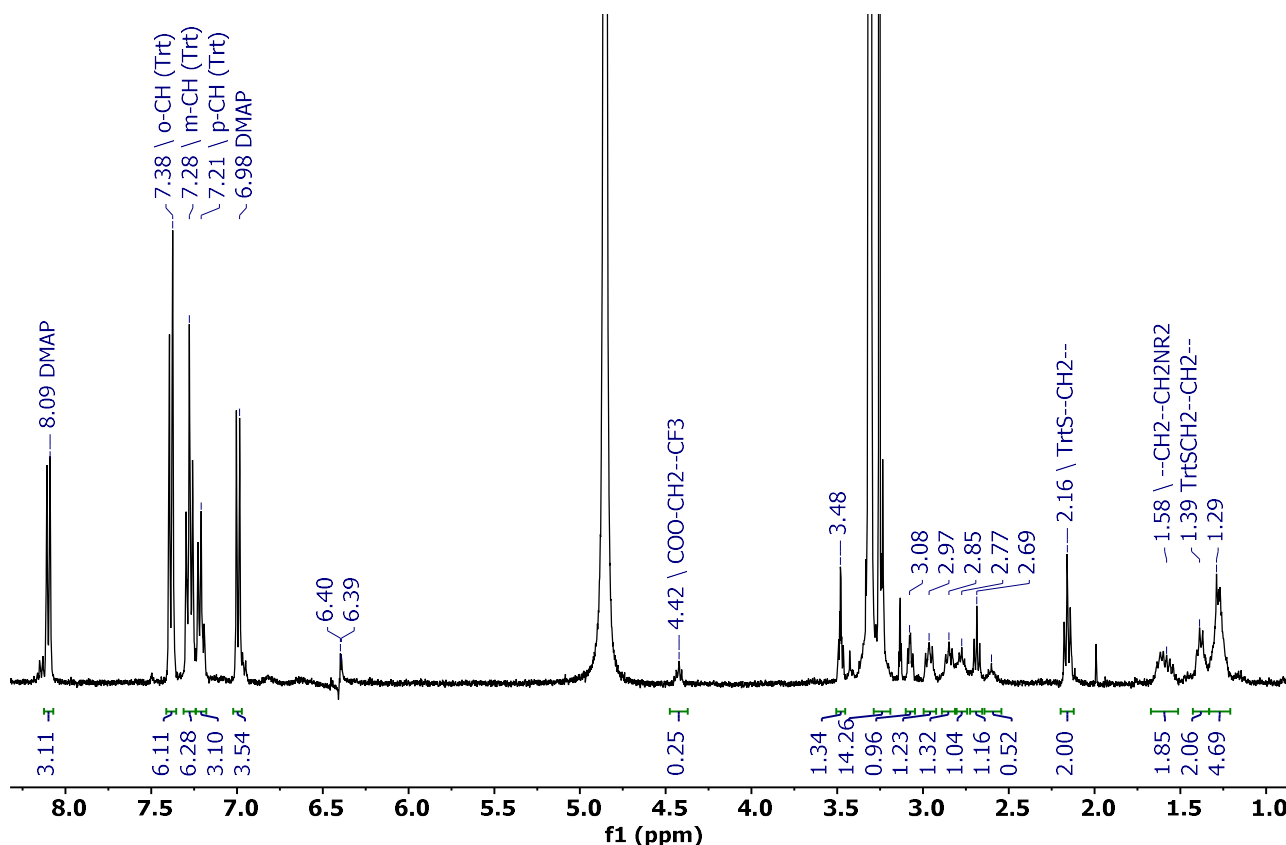


Figure 8.34: $^1\text{H-NMR}$ spectrum (400 MHz, CD_3OD) of the species obtained with the third method tried to prepare $\text{TrtSC}_6\text{N}(\text{C}_2\text{CONC}_2\text{NOF}_{11}\text{COOMe})_2$ compound.

In comparison with the analogous spectrum of the first experiment, we notice similarities only in the alkyl and aromatic regions. The signals belonging to the DMAP indicate that the washing has still to be optimized. Between 2.5 ppm and 3.5 ppm, we observe many triplets which should be related to methylene groups near deshielding nuclei, that however show a low integral value and present a very different multiplicity in respect to the one analyzed previously: this seems a complex sample containing prevalently the unreacted branched precursors, along with mono- and di-substituted fluorinated products.

The $^{19}\text{F-NMR}$ spectrum in **Figure 8.35** is also complex to analyze. The two information that can be deduced from this spectrum regards the partial functionalization of some amine groups as indicated by the single peak at -78.95 ppm which may be assigned to CF_2 in alpha to amide bond and the

complete conversion or hydrolysis of the remaining methyl ester groups, since any other signals are visible within this range.

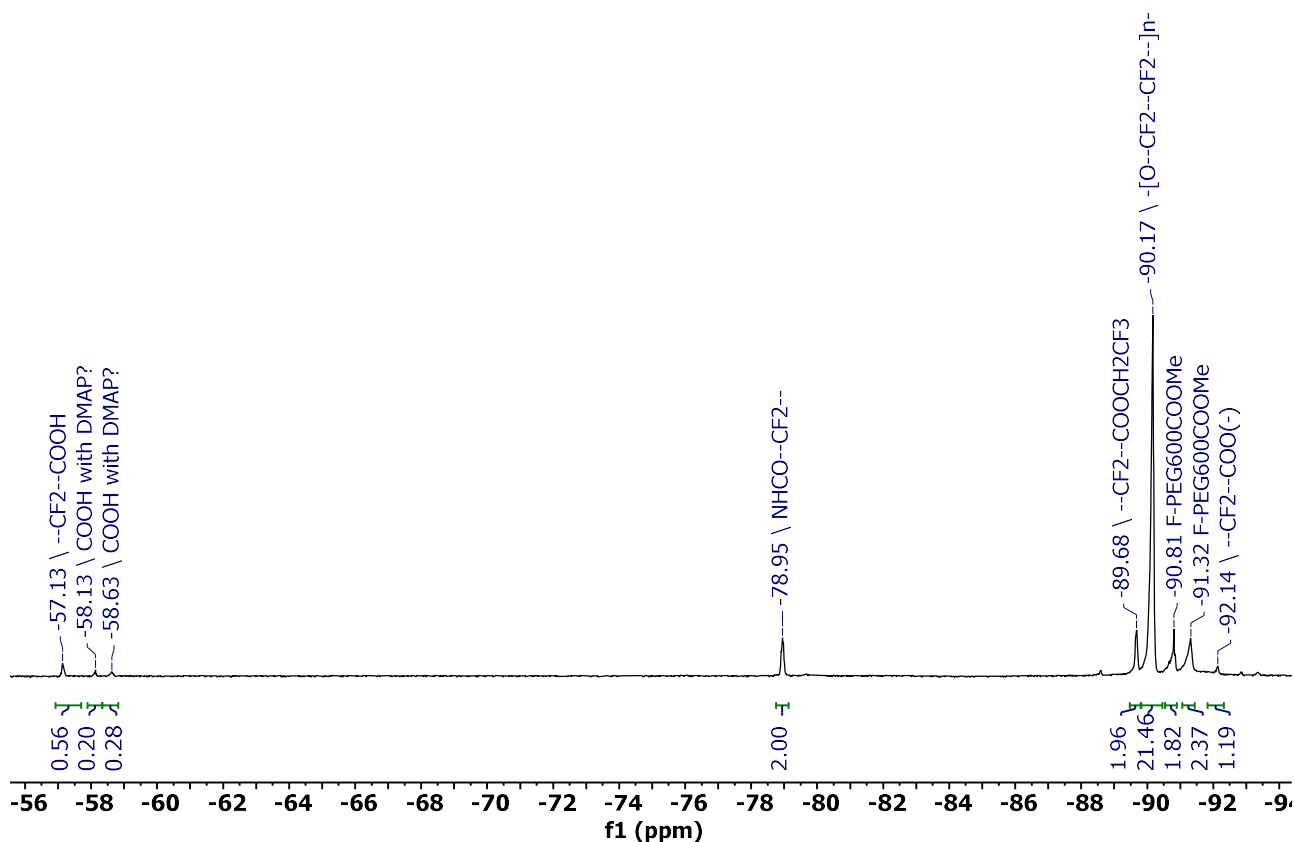


Figure 8.35: ^{19}F -NMR spectrum (376 MHz, CD_3OD) of the species obtained with the third method tried to prepare $\text{TrtSC}_6\text{N}(\text{C}_2\text{CONC}_2\text{NOF}_{11}\text{COOMe})_2$ compound.

At this point, based on the spectra interpretation, neither of the experiments reported here or others performed with this substrate have succeeded in forming the desired compound with an acceptable degree of purity.

The causes we identified vary from the methyl ester hydrolysis to carboxylic group and consequent deactivation toward further modifications, to a possible cyclic structure that follows the formation of the first amide bond and leads to an intramolecular interaction between the other free amine and ester ends.

9.1 GENERAL INFORMATION

All reagents employed were bought from Merck and Alfa Aesar and used without purification, unless where indicated. Fluorinated compounds were bought from ExFluor. Solvents were purchased from Merck and VWR. Deuterated solvents were bought from Merck. Chlorinated solvents employed for dissolving Au NPs were treated with K_2CO_3 before use. Reactions were monitored by TLC on Merck silica gel plates (0.25 mm) and visualized by UV light, $KMnO_4-H_2SO_4$, Ninhydrin, or Pancaldi solution. Flash column chromatography was performed on Normasil silica gel 60® 40-63 mm purchased from VWR. All the glassware employed for the synthesis of Au NPs was cleaned with aqua regia and copiously rinsed with Milli-Q water before use.

Nuclear Magnetic Resonance 1D and 2D spectra were recorded on a Varian 400 spectrometer and/or a Varian 500 spectrometer, operating respectively at 400 MHz and 500 MHz for proton. The NMR spectra were processed using MestReNova software. 1H -NMR spectra were referenced to the residual protons in the deuterated solvent. ^{13}C -NMR spectra were referenced to the solvent chemical shift. ^{19}F -NMR spectra (recorded on Varian 400) were referenced to the fluorine signal of hexafluorobenzene (HFB) added to the sample. Chemical shifts (δ) are reported in ppm and the multiplicity of each signal is described by the conventional abbreviations: s for singlet, d for doublet, t for triplet, q for quartet, qn for quintet, m for multiplet, br for broad peak. Coupling constants (J) are reported in Hertz (Hz).

The longitudinal T1 and the transverse T2 relaxation times measurements were recorded on Varian 400 employing respectively an inversion recovery and a Carr-Purcell-Meiboom-Gill (CPMG) pulse sequences. The data were processed employing MestReNova software using a three-parameter exponential fit.

Mass spectrometry measurements on ligands were performed through electrospray ionization (ESI) technique on a Bruker Esquire 4000 with an ion-trap analyzer or on a Bruker micrOTOF-Q equipped with TOF analyzer and recorded by Dr. Fabio Hollan at the Department of Chemical and Pharmaceutical Sciences of the University of Trieste, Italy. The mass spectra were processed using Bruker or MestReNova software.

UV-Visible spectroscopy analyses were carried out on a Perkin Elmer Lambda 35 spectrophotometer having a scanning speed of $240\text{ nm}\cdot\text{min}^{-1}$ and a slit amplitude of 2 nm, or on a

Shimadzu UV-2450 having a scanning speed of $210 \text{ nm}\cdot\text{min}^{-1}$ and a slit amplitude of 2 nm, using quartz cuvettes whose optical path was 10 mm.

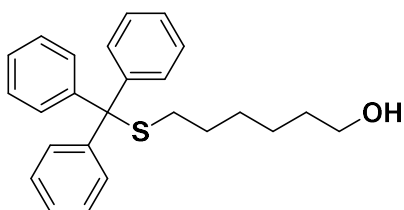
Transmission Electron Microscopy images were collected by means of a Philips EM 208 Electron Microscope operating at 100 kV equipped with 11 MegaPixel bottom-mounted CCD Olympus Quemesa camera by Dr. Paolo Bertocin or Prof. Paolo Pengo at the University of Trieste. Samples for TEM were prepared employing 200 Mesh carbon-coated copper grids and dispersing 5 μl of the sample solutions. All TEM images were analyzed through ImageJ software.

Dynamic Light Scattering analyses were performed on a Malvern Zetasizer Nano ZS ZEN3600 (Malvern Instruments, Worcestershire, UK) equipped with a 4 mW He-Ne red laser operating at 632.8 nm and a scattering detector at 173° , using disposable polyethylene cuvettes whose optical path was 10 mm. The data were processed using Zetasizer software.

Thermogravimetric Analyses were performed on a TA instrument TGA Q-500 using platinum pans and with a heating rate of $10 \text{ }^\circ\text{C}\cdot\text{min}^{-1}$ up to $830 \text{ }^\circ\text{C}$, previous equilibration at $100 \text{ }^\circ\text{C}$ for 20 minutes and recorded by Prof. Tatiana Da Ros at the Department of Chemical and Pharmaceutical Sciences of the University of Trieste, Italy.

9.2 SYNTHESIS OF THE LINEAR LIGAND WITH F-PEG600COOME

Synthesis of 6-tritylthiol-1-hexanol (TrtSC6OH)



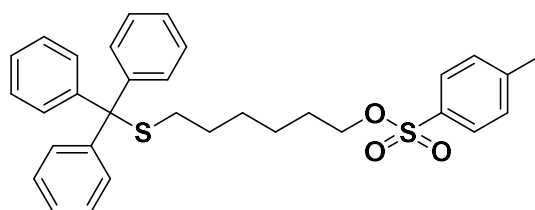
6-bromo-1-hexanol (3.0 mL, 22.86 mmol), triphenylmethanethiol (6.32 g, 22.86 mmol), and potassium carbonate (6.32 g, 45.73 mmol), were solubilized in 250 mL of a mixture of EtOH/H₂O 1:1 giving a white and turbid dispersion. The mixture was then heated under reflux at $90 \text{ }^\circ\text{C}$ for 18 hours, leading to the formation of a limpid yellow solution. At the end of the reaction, the mixture appears clear and light orange. The solution was neutralized with HCl 1 M, then extracted with DCM (3 x 150 mL). The organic phases were collected and washed with distilled water (3 x 150 mL) then brine (1 x 150 mL), dried with Na₂SO₄, filtered with a sintered glass filter, and evaporated in vacuum and finally at the water pump. The product was obtained as a light yellow amorphous solid with a yield of 98 %, 8.44 g.

$^1\text{H-NMR}$ (400 MHz, CDCl_3): δ 7.41 (d, $J = 7.0$ Hz, 5H, Trt, o-CH), 7.28 (t, $J = 7.2$ Hz, 7H, Trt, m-CH + CDCl_3), 7.20 (t, $J = 7.2$ Hz, 3H, Trt, p-CH), 3.58 (t, $J = 6.5$ Hz, 2H, - $\text{CH}_2\text{-OH}$), 2.14 (t, $J = 7.2$ Hz, 2H, TrtS- $\text{CH}_2\text{-}$), 1.48 (q, 2H, - $\text{CH}_2\text{-CH}_2\text{-OH}$), 1.41 (q, 2H, TrtS-(CH_2) $_2$ - $\text{CH}_2\text{-}$), 1.32–1.20 (m, 4H, TrtS- $\text{CH}_2\text{-CH}_2\text{-}$ + - $\text{CH}_2\text{-(CH}_2$) $_2\text{-OH}$) ppm.

$^{13}\text{C-NMR}$ (101 MHz, CDCl_3): δ 145.19 (Trt, C), 129.75 (Trt, o-CH), 127.95 (Trt, m-CH), 126.66 (Trt, p-CH), 66.56 (C-S), 63.04 (- $\text{CH}_2\text{-OH}$), 32.67 (- $\text{CH}_2\text{-CH}_2\text{-OH}$), 32.05 (TrtS- $\text{CH}_2\text{-}$), 28.88 (TrtS- $\text{CH}_2\text{-CH}_2\text{-}$), 28.69 (TrtS-(CH_2) $_2$ - $\text{CH}_2\text{-}$), 25.43 (- $\text{CH}_2\text{-(CH}_2$) $_2\text{-OH}$) ppm.

ESI-MS (MeOH, Positive mode): 399.2 [$\text{M}+\text{Na}^+$] m/z.

Synthesis of 6-(tritylthiol)hexyl-4-methylbenzenesulfonate (TrtSC6OTs)



p-toluensulfonyl chloride (1.39 mg, 7.30 mmol) was solubilized in dry DCM (5 mL) and the mixture cooled at 0 °C under argon atmosphere. A solution of the previous 6-tritylthiol-1-hexanol (TrtSC6OH, 2.5 g, 6.64 mmol) and triethylamine (1.85 mL, 13.28 mmol) in dry DCM (2 mL) was then added dropwise to the mixture. The reaction was stirred at room temperature for two hours.

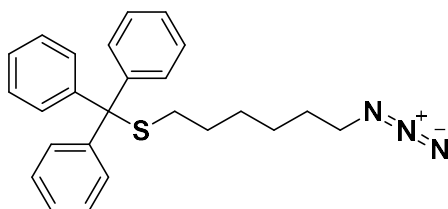
The workup was performed by pouring DCM (40 mL) and water (40 mL) in the mixture, leading to the formation of two layers. The aqueous phase was extracted with DCM (3 x 30 mL), then the organic phases were washed once with HCl 6 N (70 mL), then with a solution of NaHCO_3 5 % (70 mL), and finally water (70 mL). The organic phases were dried with Na_2SO_4 , filtered, and evaporated in vacuum. The crude product was purified by flash chromatography with silica as stationary phase and a solution of CHCl_3/PE 5:5 as eluent (with a gradually increasing of polarity at the end of the column up to 100 % CHCl_3). The separation was controlled with TLC and the desired fraction reunited, obtaining a white crystalline solid after the removal of the solvent with a yield of 61 %, 2.154 g.

$^1\text{H-NMR}$ (500 MHz, CDCl_3): δ 7.77 (d, $J = 8.1$ Hz, 2H, Ts, o-CH), 7.40 (d, $J = 8.3$ Hz, 6H, Trt, o-CH), 7.32 (d, $J = 7.9$ Hz, 2H, Ts, m-CH), 7.27 (m, 8H, Trt, m-CH + CDCl_3), 7.20 (t, $J = 7.5$ Hz, 3H, Trt, p-CH), 3.96 (t, $J = 6.5$ Hz, 2H, - $\text{CH}_2\text{-OTs}$), 2.43 (s, 3H, - CH_3), 2.10 (t, $J = 7.3$ Hz, 2H, TrtS- $\text{CH}_2\text{-}$), 1.55 (m, 5H, - $\text{CH}_2\text{-CH}_2\text{-OTs}$ + D_2O), 1.32 (m, 3H, TrtS- $\text{CH}_2\text{-CH}_2\text{-}$), 1.16 (m, 4H, TrtS-(CH_2) $_2$ - $\text{CH}_2\text{-CH}_2\text{-(CH}_2$) $_2\text{-OTs}$) ppm.

^{13}C -NMR (126 MHz, CDCl_3): δ 145.13 (Trt, C), 144.61 (Ts, C), 129.95 (Ts, m-CH), 129.73 (Trt, o-CH), 128.02 (Ts, o-CH), 127.97 (Trt, m-CH), 126.70 (Trt, p-CH), 70.59 (- CH_2 -OTs), 66.60 (C-S), 31.89 (TrtS- CH_2 -), 28.74 (- CH_2 - CH_2 -OTs), 28.49 (TrtS-(CH_2) $_2$ - CH_2 -), 28.35 (TrtS- CH_2 - CH_2 -), 25.05 (- CH_2 -(CH_2) $_2$ -OTs), 21.79 (- CH_3) ppm.

ESI-MS (MeOH, Positive mode): 569.2 [$\text{M}+\text{K}^+$], 553.2 [$\text{M}+\text{Na}^+$] m/z.

Synthesis of (6-azidohexyl)(trityl)sulfane (TrtSC6N3)



The former 6-(tritylthiol)hexyl-4-methylbenzenesulfonate (TrtSC6OTs, 1.22 g, 2.30 mmol) was solubilized in anhydrous DMF (25 mL) and cooled at 0 °C in argon atmosphere. Sodium azide (1.62 g, 24.92 mmol) was added and the reaction mixture was heated to reflux for 1 hour. In the end, the solution appeared black.

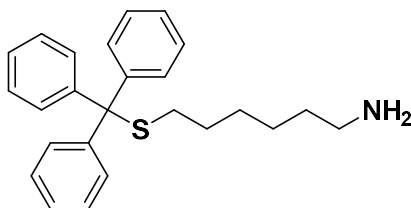
The workup has been carried by pouring the solution in a mixture of AcOEt (150 mL) and water (250 mL), leading to the formation of two layers. The organic phase was washed with water (150 mL, then 8 x 50 mL), then dried in vacuum. The crude product was purified by flash chromatography with silica as the stationary phase and a solution of CHCl_3/PE 3:7 as eluent (with a gradually increasing of polarity at the end of the column up to CHCl_3/PE 5:5). The separation was controlled with TLC and the desired fraction reunited, obtaining a light-yellow oil with a yield of 80 %, 735 mg.

^1H -NMR (400 MHz, CDCl_3): δ 7.43 (d, $J = 7.5$ Hz, 6H, Trt, o-CH), 7.29 (t, $J = 7.5$ Hz, 6H, Trt, m-CH), 7.22 (t, $J = 7.2$ Hz, 3H, Trt, p-CH), 3.21 (t, $J = 7.0$ Hz, 2H, - CH_2 - N_3), 2.17 (t, $J = 7.2$ Hz, 2H, TrtS- CH_2 -), 1.52 (p, $J = 7.0$ Hz, 2H, TrtS- CH_2 - CH_2 -), 1.41 (p, $J = 7.1$ Hz, 2H, TrtS-(CH_2) $_2$ - CH_2 -), 1.27 (m, 4H, - CH_2 - CH_2 - CH_2 - N_3) ppm.

^{13}C -NMR (101 MHz, CDCl_3): δ 145.14 (Trt, C), 129.72 (Trt, o-CH), 127.94 (Trt, m-CH), 126.67 (Trt, p-CH), 66.58 (C-S), 51.45 (- CH_2 - N_3), 31.93 (Trt- CH_2 -), 28.72 (TrtS- CH_2 - CH_2 -(CH_2) $_2$ - CH_2 - CH_2 - N_3), 28.55 (TrtS-(CH_2) $_2$ - CH_2 -), 26.36 (- CH_2 -(CH_2) $_2$ - N_3) ppm.

ESI-MS (MeOH, Positive mode): 424.2 [$\text{M}+\text{Na}^+$], 400.4 [$\text{M}-\text{H}^+$], 359.2, 322.1, 293.0, 243.0, 164.9 m/z.

Synthesis of 6-(tritylthio)hexan-1-amine (TrtSC6NH₂)



The former (6-azidohexyl)(trityl)sulfane (TrtSC₆N₃, 500 mg, 1.25 mmol) was solubilized in anhydrous THF (13 mL) under an argon atmosphere with the following addition of triphenylphosphine (490.0 mg, 1.87 mmol). The reaction mixture was stirred at room temperature for 18 hours. After this time, more triphenylphosphine (163.6 mg, 0.625 mmol) was added and the reaction stirred for another 2 hours. In the end, water (10 mL) was added and the mixture stirred for another 2 hours, leading to a white and turbid liquid with a clear layer on the surface.

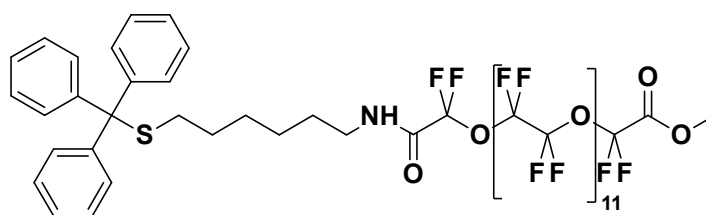
The workup was carried by pouring DCM (20 mL) and water (10 mL) into the mixture, leading to the formation of two layers. The aqueous phase was extracted with DCM (4 x 20 mL), then the organic phases were washed once with water (25 mL). The organic phases were dried with Na₂SO₄, filtered, and evaporated in vacuum, obtaining a light-yellow oil. The crude product was purified by flash chromatography with silica as the stationary phase and a starting solution of DCM/MeOH 95:5 plus 1 % of Et₃N as eluent, which polarity has been progressively increased up to DCM/MeOH 1:1 plus 1 % of Et₃N. The separation was controlled with TLC and the desired fraction reunited, obtaining a light-yellow oil after the removal of the solvent with a yield of 93 %, 435.7 mg.

¹H-NMR (400 MHz, CDCl₃): δ 7.41 (d, *J* = 7.1 Hz, 6H, Trt, o-CH), 7.27 (t, *J* = 7.5 Hz, 6H Trt + CHCl₃), 7.20 (t, *J* = 7.2 Hz, 3H, Trt, p-CH), 3.42 (br, 3H, -NH₂), 2.67 (t, *J* = 7.2 Hz, 2H, -CH₂-NH₂), 2.13 (t, *J* = 7.3 Hz, 2H, TrtS-CH₂-), 1.40 (m, 4H, TrtS-(CH₂)₂-CH₂ + -CH₂-CH₂-NH₂), 1.21 (m, 6H, TrtS-CH₂-CH₂- + -CH₂-(CH₂)₂-NH₂) ppm.

¹³C-NMR (101 MHz, CDCl₃): δ 145.18 (Trt, C), 129.74 (Trt, o-CH), 127.96 (Trt, m-CH), 126.66 (Trt, p-CH), 66.55 (C-S), 41.53 (-CH₂-NH₂), 32.14 (-CH₂-CH₂-NH₂), 32.03 (TrtS-CH₂-), 28.82 (TrtS-CH₂-CH₂-), 28.64 (TrtS-(CH₂)₂-CH₂-), 26.32 (-CH₂-(CH₂)₂-NH₂) ppm.

ESI-MS (MeOH, Positive mode): 376.0 [M+H⁺] m/z.

Synthesis of methyl 11,11,13,13,14,14,16,16,17,17,19,19,20,20,22,22,23,23,25,25,26,26,28,28,29,29,31,31,32,32,34,34,35,35,37,37,38,38,40,40,41,41,43,43,44,44,46,46-octatetracontafluoro-10-oxo-1,1,1-triphenyl-12,15,18,21,24,27,30,33,36,39,42,45-dodecaoxa-2-thia-9-azaheptatetracontan-47-oate (TrtSC₆NHCOOF₁₁OCOOMe)



The fluorinated methyl ester F-PEG600COOMe (3.02 g, 2.00 mmol) was weighed in argon atmosphere and solubilize in anhydrous methanol (5 mL). The former 6-(tritylthio)hexan-1-amine (TrtSC6NH₂, 250 mg, 0.666 mmol) in a 4 mL vial, create vacuum then an Ar atmosphere and solubilize it in anhydrous methanol (1 mL) under argon atmosphere, adding triethylamine (0.093 mL, 0.666 mmol). This yellow solution has been added to the first solution with an injection time of 4 hours and the mixture was stirred for 5 hours under reflux, then 22 hours at room temperature.

At the end of the reaction, the supernatant was collected with a syringe and the bottom phase was washed with anhydrous MeOH (1 mL) and collected. The solvent was evaporated, and the crude was purified by flash chromatography with silica as the stationary phase and a starting solution of DCM/MeOH 95:5 as eluent, which polarity has been increased up to 100% MeOH. The separation has been controlled with TLC and the desired fraction reunited, obtaining a white turbid viscous solid after the removal of the solvent with a yield of 39 %, 483.8 mg.

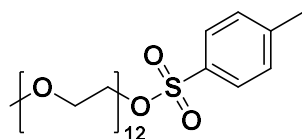
¹H-NMR (400 MHz, acetone-d₆): δ 8.44 (br, 1H, Trt_NHCO), 7.41 (d, *J* = 8.1 Hz, 6H, Trt, o-CH), 7.31 (t, *J* = 7.5 Hz, 6H, Trt, m-CH), 7.23 (t, *J* = 7.3 Hz, 3H, Trt, p-CH), 4.05 (s, 3H, -OCH₃), 3.27 (q, *J* = 6.9 Hz, 2H, -CH₂-NHCO), 2.16 (t, *J* = 7.2 Hz, 2H, TrtS-CH₂-), 1.50 (p, *J* = 7.5 Hz, 2H, -CH₂-CH₂NHCO), 1.36 (p, *J* = 6.9 Hz, 2H, TrtS-CH₂-CH₂-), 1.24 (m, 4H, TrtS-(CH₂)₂-CH₂- + -CH₂-(CH₂)₂-NHCO) ppm.

¹³C-NMR (101 MHz, acetone-d₆): δ 157.60 (C=OOCH₃), 146.18 (Trt, C), 144.63 (NHC=O), 130.52 (Trt, o-CH), 128.79 (Trt, m-CH), 125.56 (Trt, p-CH), 115.18 (t, -[O-CF₂-CF₂]_n-) 67.32 (C-S), 54.14 (COO-CH₃), 40.60 (-CH₂-NHCO), 32.55 (TrtS-CH₂-), 29.41 (-CH₂-CH₂NHCO), 29.32 (TrtS-CH₂-CH₂-CH₂-), 27.01 (-CH₂-(CH₂)₂-NHCO) ppm.

¹⁹F-NMR (376 MHz, acetone-d₆): δ -78.59 (m, 2F, -CF₂-COOMe), -79.13 (m, 2F, NHCO-CF₂-), -89.32 (m, 4F, NHCOCF₂O-CF₂-CF₂-), -89.53 (m, 6F, -CF₂-O-CF₂-CF₂-OCF₂COOMe), -89.79 (m, 30F -[OCF₂-CF₂]_n-) ppm.

ESI-MS (MeOH, Positive mode): 2103.5 [OF13+NH₄⁺]; 1987.5 [OF12+NH₄⁺]; **1871.5** [OF11+NH₄⁺]; 1755.6 [OF10+NH₄⁺]; 1639.5 [OF9+NH₄⁺]; 1528.3 [-CF₂-COOH]; 1412.4 [-OCF₂CF₂)-CF₂-COOH]; 1269.3; 1153.4; . m/z.

Synthesis of 2,5,8,11,14,17,20,23,26,29,32,35-dodecaoxaheptatriacontan-37-yl 4-methylbenzenesulfonate (PEG₅₅₀-OTs)



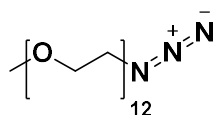
PEG₅₅₀ (2.0 mL, 3.88 mmol) and triethylamine (1.1 mL, 7.89 mmol) were inserted in a flask in which an argon atmosphere was created. A solution of tosylchloride (0.785 g, 4.12 mmol) in dry DCM (5 mL) was added dropwise and the mixture was stirred at room temperature under Ar for 18 hours. The crude solution was diluted with DCM (15 mL) and water (15 mL) to separate the two phases extracted with DCM (3 x 50 mL). The organic phases were collected and washed first with HCl 6 N (100 mL), then with NaHCO₃ 5 % (100 mL), and finally with water (100 mL). In the end, the organic phases were dried with Na₂SO₄, filtered, and evaporated in vacuum. The product was obtained as a transparent oil with a yield of 85 %, 2.36 g.

¹H-NMR (400 MHz, CDCl₃): δ 7.79 (d, *J* = 8.3 Hz, 2H, Ts, o-CH), 7.33 (d, *J* = 8.0 Hz, 2H, Ts, m-CH), 4.15 (dd, *J* = 5.4, 4.3 Hz, 2H, -CH₂-CH₂-OTs), 3.68 (t, *J* = 4.9 Hz, 2H, -O-CH₂-CH₂-OTs), 3.65 (4H, CH₃OCH₂-CH₂-O-CH₂-), 3.64 (30H, -[O-CH₂-CH₂]_n-), 3.61 (4H, -CH₂-CH₂-O-CH₂-CH₂-OCH₂CH₂OTs), 3.57 (4H, -CH₂-CH₂-O-CH₂-CH₂-OCH₂CH₂OTs), 3.54 (dd, 2H, CH₃-O-CH₂-), 3.37 (s, 3H, CH₃-O-), 2.44 (s, 3H, Ts, -C-CH₃) ppm.

¹³C-NMR (126 MHz, CDCl₃): δ 144.87 (Ts, C), 133.11 (Ts, -C-CH₃), 129.92 (Trt, m-CH), 128.07 (Trt, o-CH), 72.02 (CH₃-O-CH₂-), 70.83 (-CH₂-OCH₂-CH₂-OTs), 70.69, 70.68 (CH₃OCH₂CH₂-O-CH₂-), 70.64 (-[O-CH₂-CH₂]_n-), 70.61, 70.59 (CH₃-O-CH₂-CH₂-), 69.35 (-O-CH₂-CH₂-OTs), 68.78 (-O-CH₂-CH₂-OTs), 59.13 (CH₃-O), 21.75 (Ts, -C-CH₃) ppm.

ESI-MS (MeOH, Positive mode): 737.3 [M+Na⁺]; 477.3, 521.3, 561.3, 605.3, 649.3, 693.3, 781.4, 825.4, 869.4, 913.4, 957.5 m/z.

Synthesis of 37-azido-2,5,8,11,14,17,20,23,26,29,32,35-dodecaoxaheptatriacontane (PEG₅₅₀-N₃)



The former PEG₅₅₀-OTs (1.0 g, 1.41 mmol) was inserted in a flask in which an argon atmosphere was created and dissolved in dry DMF (35 mL). This solution was added dropwise in a three-neck flask set up for reflux and filled with argon, containing NaN₃ (910 mg, 14.0 mmol). The resulted mixture was stirred under reflux for 16 hours.

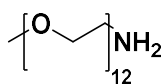
The crude solution was then diluted with water (30 mL) to separate the two phases extracted with DCM (4 x 20 mL). The organic phases were collected and washed abundantly with water (6 x 70 mL). In the end, the organic phases were dried with Na₂SO₄, filtered, and evaporated in vacuum. The product was obtained as an orange-brown oil with a yield of 81 %, 669.6 mg.

¹H-NMR (400 MHz, CDCl₃): δ 3.67 (2H, (-CH₂-CH₂-N₃), 3.66 (4H, -CH₂-CH₂-O-CH₂-CH₂-OCH₂CH₂ON₃), 3.65 (8H, CH₃OCH₂-CH₂-O-CH₂- + -CH₂-CH₂-O-CH₂-CH₂-OCH₂CH₂ON₃), 3.64-3.63 (30H, -[OCH₂-CH₂]_n- + -OCH₂-CH₂-N₃), 3.54 (2H, CH₃O-CH₂-), 3.38 (t, 2H, -CH₂-N₃), 3.37 (s, 3H, CH₃O-) ppm.

¹³C-NMR (101 MHz, CDCl₃): δ 72.07 (CH₃O-CH₂-), 70.83-70.80-70.77 (-CH₂-O-CH₂-CH₂-OCH₂CH₂ON₃), 70.74 (CH₃OCH₂CH₂O-CH₂), 70.70 (-[O-CH₂-CH₂]_n-), 70.65 (CH₃O-CH₂-CH₂-), 70.16 (-CH₂-CH₂-N₃), 59.16 (CH₃O-), 50.82 (-CH₂-N₃) ppm.

ESI-MS (MeOH, Positive mode): 608.4 [M+Na⁺], 624.3 [M+K⁺]; 404.2, 448.3, 476.3, 492.3, 520.3, 536.3, 564.3, 580.3, 652.3 (OC13), 668.3, 696.4 (OC14), 712.3, 740.4 (OC15), 756.4, 784.4 (OC16), 828.4 (OC17), 916.4 m/z.

Synthesis of 2,5,8,11,14,17,20,23,26,29,32,35-dodecaoxaheptatriacontan-37-amine (PEG₅₅₀-NH₂)



The former PEG₅₅₀-N₃ (0.500 g, 0.854 mmol) was solubilized in anhydrous THF (10 mL) in an argon atmosphere with the following addition of triphenylphosphine (335.9 mg, 1.28 mmol). The reaction mixture was stirred at room temperature for 18 hours. In the end, water (3 mL) was added and the mixture stirred for another 2 hours, remaining of the same yellow-orange color.

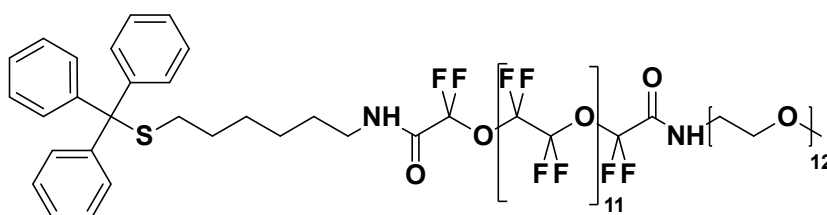
The workup has been carried by evaporating the solvent under reduced pressure and by adding at the residue toluene (20 mL) and water (20 mL), leading to the formation of two layers and stirring to dissolve completely the phosphine oxide. The aqueous phase was washed with toluene (5 x 20 mL), then collected, evaporated, and the yellow solid that appeared dissolved again in DCM (30 mL). The organic phase was dried with Na₂SO₄, filtered, and evaporated in vacuum, obtaining an orange oil with a yield of 94 %, 450.3 mg.

¹H-NMR (400 MHz, CDCl₃): δ 3.65 (9H, CH₃OCH₂-CH₂-O-CH₂- + -CH₂-CH₂-OCH₂CH₂NH₂), 3.64 (8H, CH₃OCH₂CH₂OCH₂-CH₂-O-CH₂- + -CH₂-CH₂-(OCH₂CH₂)₂NH₂), 3.63 (22H, -[OCH₂-CH₂]_n-), 3.62 (4H, -CH₂-CH₂-(OCH₂CH₂)₃NH₂), 3.54 (2H, CH₃O-CH₂-), 3.50 (t, 2H, -OCH₂-CH₂-NH₂), 3.37 (s, 3H, CH₃O-), 2.85 (t, 2H, -CH₂-NH₂), 1.81 (br, 5H, -NH₂) ppm.

^{13}C -NMR (101 MHz, CDCl_3): δ 73.55 ($-\text{CH}_2-\text{CH}_2\text{NH}_2$), 72.06 ($\text{CH}_3\text{O}-\text{CH}_2-$), 70.73 ($\text{CH}_3\text{OCH}_2\text{CH}_2\text{O}-\text{CH}_2-$), 70.71, 70.70 ($-(\text{O}-\text{CH}_2-\text{CH}_2)_n-$), 70.63 ($\text{CH}_3\text{OCH}_2-\text{CH}_2-$), 70.41, 59.15 ($\text{CH}_3\text{O}-$), 41.91 ($-\text{CH}_2-\text{NH}_2$) ppm.

ESI-MS (MeOH, Positive mode): 560.4 $[\text{M}+\text{H}^+]$; 384.3, 428.3, 472.4, 516.4, 604.4, 648.4, 692.4, 736.5, 780.4, 824.5 m/z.

Synthesis of 2,2,4,4,5,5,7,7,8,8,10,10,11,11,13,13,14,14,16,16,17,17,19,19,20,20,22,22,23,23,25, 25,26,26,28,28,29,29,31,31,32,32,34,34,35,35,37,37-octatetrafluoro-N1-(2,5,8,11,14,17,20, 23,26,29,32,35-dodecaoxaheptatriacontan-37-yl)-N38-(6-(tritylthio)hexyl)-3,6,9,12,15,18,21,24) 27,30,33,36-dodecaoxaoctatriacontanediamide (TrtSC6NHCOOF11OCONHPEG)



The former TrtSC6NHCOOF11COOMe (474 mg, 0.256 mmol) was dissolved in anhydrous MeOH (4 mL) under argon atmosphere. The former PEG₅₅₀-NH₂ (143.0 mg, 0.256 mmol) was dried with anhydrous Et₂O (5 x 5 mL) and anhydrous MeOH (3 x 5 mL) and solubilized in anhydrous MeOH (1 mL) under argon and anhydrous Et₃N (42.8 μL , 306.8 μmol) was added. This yellow mixture was added to the first solution with an injection time of 1 minute. The mixture was stirred for 18 hours under reflux. Some DCM over K₂CO₃ (40 mL) was poured into the mixture and the organic phase was washed with water (3 x 20 mL) and dried with Na₂SO₄, filtered, and evaporated to obtain a pale-yellow oil.

At this point, the reaction was pushed forward by stripping the remaining H₂O with anhydrous Et₂O (5 x 3 mL) and anhydrous MeOH (3 x 3 mL). After the solvent removal, the crude was solubilized in anhydrous DMF (1 mL) under argon atmosphere and a solution of the coupling agents EDC·HCl (17.6 mg, 91.75 μmol) and HOBT (6.8 mg, 50.46 μmol) in anhydrous DMF (1 mL) was poured in it. The mixture was stirred for 2 hours at room temperature.

The former dried PEG₅₅₀-NH₂ (25.7 mg, 45.88 μmol) was solubilized in anhydrous DMF (1 mL) and anhydrous Et₃N was added to this yellow solution. This was injected into the solution containing the crude and the coupling agents and the mixture was stirred at 40 °C for 24 hours under argon atmosphere.

Some DCM over K₂CO₃ (20 mL) was poured into the clear orange solution and the organic phase was washed with a 5% p/v citric acid solution (1 x 10 mL) to eliminate the TEAH⁺, then with H₂O

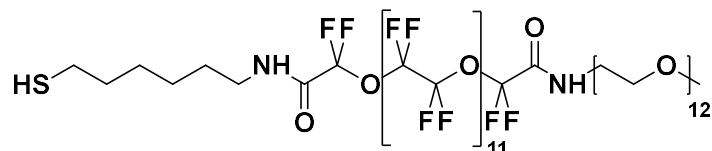
(3 x 10 mL) to remove the DMF. The organic phase was finally dried over Na₂SO₄, filtrated and the solvent was evaporated to obtain a viscous orange oil with a yield of 78 %, 194.5 mg.

¹H-NMR (500 MHz, acetone-d₆): δ 8.48-8.43 (br, 1H, Trt-NHCO + OCNHPEG), 7.41 (d, *J* = 7.4 Hz, 6H, o-CH Trt), 7.32 (t, *J* = 7.7 Hz, 6H, m-CH Trt), 7.23 (t, *J* = 7.3 Hz, 3H, p-CH Trt), 3.62 (t, 3H, OCNHCH₂-CH₂-), 3.58 (41H, -[OCH₂-CH₂]_n-), 3.51 (t, 2H, OCNH-CH₂-), 3.47 (2H, -CH₂-OCH₃) 3.29 (s, 3H, OCH₃), 3.27 (q, *J* = 6.9 Hz, 2H, -CH₂-NHCO), 2.16 (t, *J* = 7.3 Hz, 2H, S-CH₂-), 1.50 (p, *J* = 7.5 Hz, 2H, -CH₂-CH₂NHCO), 1.36 (p, *J* = 6.9 Hz, 2H, TrtSCH₂-CH₂-), 1.24 (m, 4H, TrtS-(CH₂)₂-CH₂- + -CH₂-(CH₂)₂-NHCO) ppm.

¹⁹F-NMR (376 MHz, acetone-d₆): δ -78.80/-78.90 (m, 4F, Trt_NHCO-CF₂- + -CF₂-CONHPEG), -87.92 (6F), -89.07 (m, 5F, NHCOCF₂O-CF₂-CF₂-), -89.30 (m, 5F, -CF₂-O-CF₂-CF₂-OCF₂COOMe), -89.49 (m, 25F -[OCF₂-CF₂]_n-).

ESI-MS (DMF, Negative mode): 1963.3, 1847.3, 1731.3, 1615.3, 1492.2, 1376.2, 1260.2, 1144.2, 1041.0, 925.0, 809.0 **693.0**, 577.0, 461.0, 344.9. 228.8 m/z.

Synthesis of 2,2,4,4,5,5,7,7,8,8,10,10,11,11,13,13,14,14,16,16,17,17,19,19,20,20,22,22,23,23,25, 25,26,26,28,28,29,29,31,31,32,32,34,34,35,35,37,37-octatetracontafluoro-N1-(2,5,8,11,14,17,20, 23,26,29,32,35-dodecaoxaheptatriacontan-37-yl)-N38-(6-mercaptohexyl)-3,6,9,12,15,18,21,24, 27,30,33,36-dodecaoxaoctatriacontanediamide (HSC₆NHCOOF₁₁OCONHPEG)



The former TrtSC₆NHCOOF₁₁OCONHPEG (172.7 mg, 75.52 μmol) was solubilized in deoxygenated anhydrous DCM (7.5 mL, over K₂CO₃) in argon atmosphere with the following addition of TFA (0.133 mL, 1.74 mmol). The formation of a yellow gas was visible, and the solution became transiently bright yellow. After 5 minutes, TIPS (29.7 μL, 145.0 μmol) was added, and the reaction was stirred at room temperature and under Ar for 24 hours. After 8 hours, 10 more equivalent of TFA (0.0851 mL, 0,725 mmol) were added.

The workup was carried out by evaporating the solvent, washing the orange oil with deoxygenated hexane (3 x 10 mL), and evaporating again the residual solvent to obtain an orange oil with a yield of 99 %, 155.0 mg.

¹H-NMR (400 MHz, acetone-d₆): δ 8.49 (br, 1H, Trt-NHCO + OCNHPEG), 3.75-3.55 (40H, OCNHCH₂-CH₂- + -[OCH₂-CH₂]_n-), 3.55-3.45 (m, 4H, OCNH-CH₂- + -CH₂-OCH₃), 3.33 (q, *J*

= 6.9 Hz, 2H, -CH₂-NHCO), 3.30 (s, 3H, OCH₃), 2.61-2.50 (q/t, 2H, S-S-CH₂- + HS-CH₂-), 1.59-1.39 (m, 8H, TrtSCH₂-CH₂- + -CH₂-CH₂NHCO + TrtS-(CH₂)₂-CH₂- + -CH₂-(CH₂)₂-NHCO) ppm.

¹⁹F-NMR (376 MHz, acetone-d₆): δ -78.95/-79.08 (m, 4F, -CF₂-CONHPEG + Trt_NHCO-CF₂-), -88.68 (7F), -89.23/-89.46 (m, 10F, NHCOCF₂O-CF₂-CF₂- + -CF₂-CF₂-OCF₂CONHPEG), -89.66 (m, 35F -[OCF₂-CF₂]_n-).

T1 relaxation time (400 MHz, acetone-d₆, Inversion recovery pulse sequence): T1 = 1.148 s

T2 relaxation time (400 MHz, acetone-d₆, CPMG pulse sequence): T2 = 777 ms

ESI-MS (MeOH, Positive mode): probable loss of (O-CH₂-CH₂-)_y in the 1400-2000 range and loss of (O-CF₂-CF₂-)_x(O-CH₂-CH₂-)_y in the 800-1400 range.

9.3 SYNTHESIS OF AUNPs WITH F-PEG600COOME-DERIVATE LIGAND

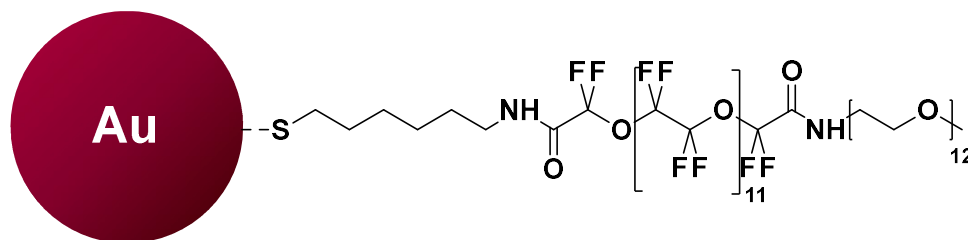


Figure 9.1: Graphical representation of a gold nanoparticle protected by the linear fluorinated ligand containing the F-PEG600COOMe moiety (HSC6NHCOOF11OCONHPEG).

The fluorinated thiol ligand (HSC6NHCOOF11OCONHPEG, 155.0 mg, 72.46 μmol) was dissolved in a round bottom flask in deoxygenated MeOH (20 mL) under an argon atmosphere. In parallel, in a 20 mL vial, tetrachloroauric acid trihydrate (HAuCl₄·3 H₂O, 42.6 mg, 0.108 mmol) was dissolved in 20 mL of deoxygenated Milli-Q water under an argon atmosphere and transferred in a three-neck round bottom flask. The mixture containing the thiolate was poured into the same flask through a cannula system and the mixture was stirred for 30 minutes at RT, then 30 minutes at 0 °C, protected from light and always under argon atmosphere. At the end of that time, a reducing solution of NaBH₄ (45.0 mg, 2 mmol) 0.1 M in 11.9 mL of Milli-Q water was prepared. This solution was then added to the previously prepared mixture in 3.5 minutes at RT. The dark violet mixture obtained was stirred at 0 °C for one hour and successively at RT for 2 hours at RT, always under argon atmosphere. In the end, the reaction was stopped and the solvent was partially removed in vacuum. The crude product in aqueous dispersion was transferred in a 15 mL Falcon tube and the NPs were precipitated by adding hexane (3 mL) and centrifuging (4400 rpm, 10 minutes, 20 °C). The

supernatant was discarded and two more washing cycles of dispersion in hexane and centrifugation were performed. The NPs were finally purified by gel permeation chromatography (Sephadex G-75, Milli-Q H₂O).

TEM (Milli-Q H₂O): $d_{\text{core}}^1 = 1.67 \pm 0.60$ nm ($\sigma^* = 0.359$) (29 %), $d_{\text{core}}^2 = 3.39 \pm 1.94$ nm ($\sigma^* = 0.572$) (71 %); Lorentzian fitting; over 650 NPs.

UV-Vis (Milli-Q H₂O): $\lambda_{\text{max}} = 505$ nm (broad).

DLS (Milli-Q H₂O): $d_{\text{H}} = 52.58 \pm 27.42$ nm (PDI = 0.267).

TGA: organic loss = 84.97 %; $T_{\text{max}} = 319$ °C.

¹H-NMR (400 MHz, D₂O): $\delta = 3.68$ (br, PEG, $-\text{[OCH}_2\text{-CH}_2\text{]}_n\text{-}$), 3.5 (s, $-\text{CH}_2\text{-OCH}_3$), 3.37 (s, O-CH_3) 1.85-1.00 (br, aliphatic H) ppm.

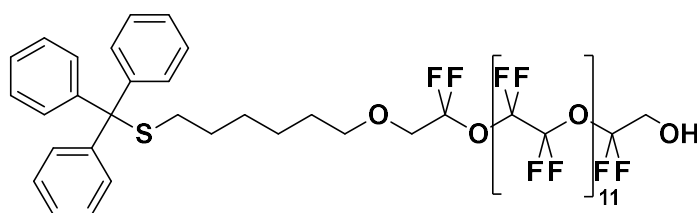
¹⁹F-NMR (376 MHz, D₂O): $\delta = -79.21$ (br, $\text{Trt_NHCO-CF}_2\text{-} + \text{-CF}_2\text{-CONHPEG}$), $-87.50 - -90.30$ (m), -90.69 (m, $-\text{[OCF}_2\text{-CF}_2\text{]}_n\text{-}$) ppm.

T1 relaxation time (400 MHz, D₂O, Inversion recovery pulse sequence): T1 = 521 ms.

T2 relaxation time (400 MHz, D₂O, CPMG pulse sequence): T2 = 23.5 ms.

9.4 SYNTHESIS OF THE LINEAR LIGAND WITH F-PEG600DIOL

Synthesis of 11,11,13,13,14,14,16,16,17,17,19,19,20,20,22,22,23,23,25,25,26,26,28,28,29,29,31,31,32,32,34,34,35,35,37,37,38,38,40,40,41,41,43,43,44,44,46,46-octatetracontafluoro-1,1,1-triphenyl-9,12,15,18,21,24,27,30,33,36,39,42,45-tridecaoxa-2-thiaheptatetracontan-47-ol (TrtC6OF11OH)



The fluorinated PEG diol F-PEG600DIOL (1.5 g, 1.04 mmol) was weighed in argon atmosphere and solubilized in anhydrous 1,4-dioxane (0.6 mL). The former 6-(tritylthiol)hexyl-4-methylbenzenesulfonate (TrtSC6OTs, 250 mg, 0.473 mmol) was solubilized in anhydrous 1,4-dioxane (0.6 mL) and added to the first solution in 10 minutes with the rest of the solvent (1.5 mL). At this double-phase, KOH (42.3 mg, 0.754 mmol) was added and the mixture was stirred at 100 °C for 30 hours argon atmosphere, then one more equivalent of KOH (13.2 mg, 0.235 mmol) was added and the mixture stirred at 100 °C for other 42 hours always under argon atmosphere.

The workup was carried out by pouring H₂O (15 mL) into the mixture and the aqueous phase was extracted with AcOEt (5 x 10 mL), then the organic phases were washed once with water (25 mL), then with brine (25 mL). The organic phases were dried with Na₂SO₄, filtered, and evaporated obtaining a light-yellow oil. The crude product was purified by flash chromatography with silica as the stationary phase and a starting solution of Hexane/AcOEt 9:1 as eluent, which polarity was progressively increased up to Hexane/AcOEt 7:3. The separation was controlled with TLC and the desired fraction reunited, obtaining a transparent oil after the removal of the solvent with a yield of 13 %, 112.4 mg.

¹H-NMR (400 MHz, acetone-d₆): δ 7.41 (d, 6H, Trt, o-CH), 7.32 (t, 7H, Trt, m-CH), 7.23 (t, 3H, Trt, p-CH), 5.27 (t, 1H, -OH), 4.02 (t, 5H_{tot}, -OCF₂-CH₂-OH #1), 4.00 (t, 5H_{tot}, -OCF₂-CH₂-OH #2), 3.98 (t, 5H_{tot}, Trt_O-CH₂-CF₂-O), 3.59 (t, 2H, Trt_-CH₂-OF11), 2.16 (t, 2H, J = 7.2 Hz, Trt-S-CH₂-), 1.51 (m, 2H, -CH₂-CH₂-OF11), 1.37 (m, 2H, TrtS-CH₂-CH₂-), 1.25 (m, 4H, -CH₂-CH₂-(CH₂)₂-OF11) ppm.

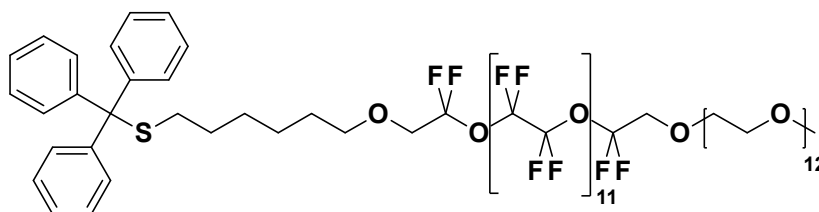
¹³C-NMR (125 MHz, acetone-d₆): δ 146.09 (Trt, C), 130.41 (Trt, o-CH), 128.67 (Trt, m-CH), 127.44 (Trt, p-CH), 115.08 (t, -[O-CF₂-CF₂]_n-), 73.20 (Trt_CH₂-O-), 69.86 (t, Trt_O-CH₂-CF₂-), 67.19 (C-S), 62.47 (t, -O-CF₂-CH₂-OH), 32.45 (TrtS-CH₂-), 29.84 (-CH₂-CH₂-OF11), 29.25 (-CH₂-(CH₂)₃-OF11), 29.16 (TrtS-CH₂-CH₂-), 26.04 (-CH₂-(CH₂)₂-OF11).

¹⁹F-NMR (376 MHz, acetone-d₆): δ -78.35 (m, 2F, Trt_OCH₂-CF₂-), -80.89 (m, 2F, -CF₂-CH₂OH), -89.27 (m, 5F, Trt_OCH₂CF₂O-CF₂-CF₂- + -CF₂-CF₂-OCF₂CH₂OH), -89.57 (m, 39F, [OCF₂-CF₂]_n).

ESI-MS (MeOH, Positive mode): 1834.9 [M+Na⁺], **1603.0**, 1719.0, 1950.9, 2066.8, 2182.8 m/z.

ESI-MS (MeOH, Negative mode): 1846.8 [M+Cl⁻], 1216.9, **1332.8**, 1499.0, 1615.0, 1730.9, 1962.8, 2024.4, 2140.5 m/z.

Synthesis of 40,40,42,42,43,43,45,45,46,46,48,48,49,49,51,51,52,52,54,54,55,55,57,57,58,58,60,60,61,61,63,63,64,64,66,66,67,67,69,69,70,70,72,72,73,73,75,75-octatetrafluoro-85,85,85-triphenyl-2,5,8,11,14,17,20,23,26,29,32,35,38,41,44,47,50,53,56,59,62,65,68,71,74,77-hexacosa-oxa-84-thiapentaoctacontane (TrtSC6OF11OPEG)



The former fluorinated alcohol (TrtSC6OF11OH, 100 mg, 55.16 μmol) was dissolved in anhydrous 1,4-dioxane (0.5 mL) under argon atmosphere. NaH 60% (8.8 mg, 220.65 μmol) was weighted and

washed with hexane (5 x 1 mL), then transferred slowly in the previous dispersion. This dispersion was stirred for 20 minutes at room temperature, during which a vigorous bubbling started, leaving a white precipitate in dispersion afterward. The former PEG₅₅₀-OTs (39.4 mg, 55.16 μmol) was dried with anhydrous 1,4-dioxane (3 x 2 mL), solubilized in anhydrous 1,4-dioxane (0.3 mL) and finally added dropwise to the first dispersion in 10 minutes. The dispersion was heated at 50 °C for 24 hours.

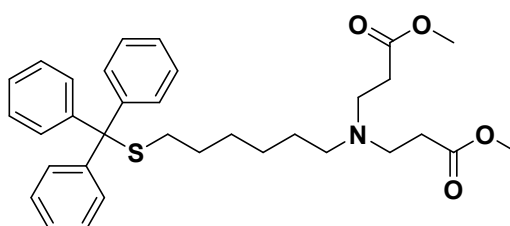
After cooling the dispersion at room temperature, the workup was carried out by pouring CHCl₃ (15 mL) into the mixture and the organic phase was washed with brine (1 x 10 mL), then with H₂O (3 x 10 mL). The organic phases were dried with Na₂SO₄, filtered, and evaporated obtaining a pale yellow-white turbid oil. The crude product was purified by flash chromatography with silica as the stationary phase and a starting solution of CHCl₃/AcOEt 99:1 as eluent, which polarity has been progressively increased, using only AcOEt and 3 % of TEA at the end. The separation was controlled with TLC and the desired fraction reunited, obtaining a transparent oil after the removal of the solvent with a yield of 3 %, 4.1 mg.

¹H-NMR (400 MHz, acetone-d₆): δ 7.40 (d, *J* = 8.3 Hz, 6H, Trt (o-CH)), 7.32 (t, *J* = 7.6 Hz, 6H, Trt (m-CH)), 7.23 (t, *J* = 7.2 Hz, 3H, Trt (p-CH)), 4.10 (t, 2H, *J* = 10.2 Hz OCF₂-CH₂-OPEG), 3.98 (t, 2H, *J* = 10.2 Hz Trt_O-CH₂-CF₂-O), 3.79 (2H, OF11O-CH₂-), 3.64 (2H, OF11OCH₂-CH₂-), 3.62-3.54 (m, 28H, -[O-CH₂-CH₂]_n- + -CH₂-OF11), 3.47 (2H, -CH₂-OCH₃), 3.29 (s, 3H, O-CH₃), 2.16 (t, 2H, *J* = 7.3 Hz, Trt-S-CH₂-), 1.51 (m, *J* = 6.6 Hz, 2H, -CH₂-CH₂-OF11), 1.37 (m, 3H, TrtS-CH₂-CH₂-), 1.26 (m, 4H, -CH₂-CH₂-(CH₂)₂-OF11) ppm.

¹⁹F-NMR (376 MHz, acetone-d₆): δ -78.33 (m, 2F, Trt_OCH₂-CF₂-), -78.49 (m, 2F, -CF₂-CH₂OPEG), -89.25 (m, 4F, Trt_OCH₂CF₂O-CF₂- + -CF₂-OCF₂CH₂OPEG), -89.51 (m, 33F - [OCF₂-CF₂]_n-) ppm.

9.5 SYNTHESIS OF THE BRANCHED LIGAND WITH F-PEG600COOME

Synthesis of dimethyl 3,3'-((6-(tritylthio)hexyl)azanediyl)dipropionate (TrtSC₆N(C₂COOMe)₂)



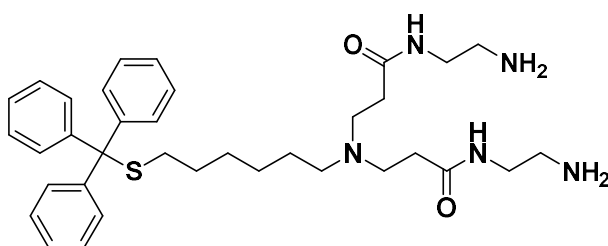
Methyl acrylate (1.68 mL, 18.65 mmol) was dissolved in dry MeOH (5 mL) in a flask in which an argon atmosphere was created. The former 6-(tritylthio)hexan-1-amine (TrtSC₆NH₂, 700.5 mg, 1.87 mmol) was also solubilized in dry MeOH (10 mL) in a vial filled with argon. This solution was then added dropwise at 0 °C in the previous flask and the vial washed with the remaining solvent for the reaction (5 mL). The mixture has been stirred at room temperature under Ar for 3 days. Before the workup steps, the completeness of the reaction has been studied by means of a TLC (DCM/MeOH 9:1, plus 1 % of Et₃N). The product has been finally dried in vacuum, obtaining a light-yellow oil with a yield of 95 %, 986.4 mg.

¹H-NMR (400 MHz, CD₃OD): δ 7.39 (d, *J* = 7.2 Hz, 6H, Trt, o-CH), 7.28 (t, *J* = 7.4 Hz, 6H, Trt, m-CH), 7.20 (t, *J* = 7.2 Hz, 3H, Trt, p-CH), 3.63 (s, 5H, -OCH₃), 2.75 (t, *J* = 7.0 Hz, 4H, -N(CH₂-CH₂)₂), 2.45 (t, *J* = 7.0 Hz, 4H, -N(CH₂-CH₂)₂), 2.38 (t, *J* = 7.3 Hz, 2H, -CH₂-NR₂-), 2.12 (t, *J* = 7.3 Hz, 2H, TrtS-CH₂-), 1.35 (p, 4H, TrtS-(CH₂)₂-CH₂- + -CH₂-CH₂-NR₂), 1.24 (m, 3H, TrtS-CH₂-CH₂-), 1.13 (p, *J* = 7.2 Hz, 2H, -CH₂-(CH₂)₂-NR₂-) ppm.

¹³C-NMR (101 MHz, CD₃OD): δ 174.71 (C=O), 146.48 (Trt, C), 130.77 (Trt, o-CH), 128.81 (Trt, m-CH), 127.67 (Trt, p-CH), 66.40 (C-S), 54.65 (-CH₂-NR₂), 52.14 (-OCH₃), 50.30 (-N(CH₂-CH₂)₂), 32.99 (-N(CH₂-CH₂)₂), 32.87 (TrtS-CH₂-), 29.83 (TrtS-CH₂-CH₂-), 29.66 (TrtS-(CH₂)₂-CH₂-), 27.77 (-CH₂-(CH₂)₂-NR₂), 27.61 (-CH₂-CH₂-NR₂) ppm.

ESI-MS (MeOH, Positive mode): 548.3 [M+H⁺], 570.3 [M+K⁺] m/z.

Synthesis of 3,3'-((6-(tritylthio)hexyl)azanediyl)bis(*N*-(2-aminoethyl)propionamide (TrtSC₆N(C₂CONHC₂NH₂)₂)



Ethylenediamine (4.15 mL, 62.08 mmol) was dissolved in dry MeOH (10 mL) in a flask in which an argon atmosphere was created. A solution of the previous 3,3'-((6-(tritylthio)hexyl)azanediyl)dipropionate (TrtSC₆N(C₂COOMe)₂, 811.3 mg, 1.48 mmol) in dry MeOH (10 mL) was added dropwise at 0 °C, then the container washed with the remaining solvent for the reaction (10 mL). The mixture was stirred at room temperature under Ar for 3 days. The progression has been controlled with a TLC and more ethylenediamine (4 mL) has been added after discovering that the reagent was still present. The mixture has been stirred at room temperature under Ar for another 4 days.

The solvent was removed under reduced pressure and then the crude product was co-evaporated with a solution of toluene/MeOH 9:1 (10 + 10 mL), then eliminating the solvent residual in vacuum.

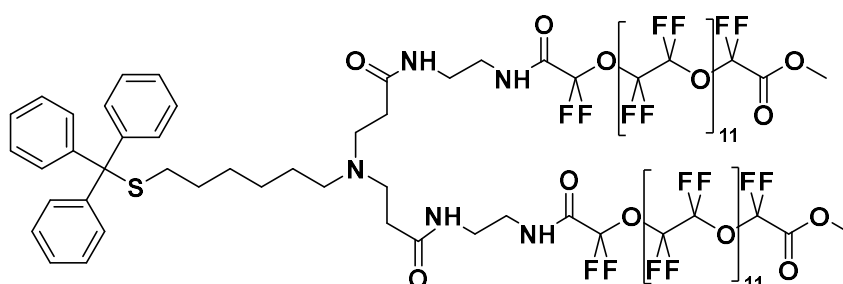
The final product was purified by flash chromatography with silica as the stationary phase and a solution of DCM/MeOH 8:2 and 1 % of Et₃N as eluent. At the end of the column, the product still stuck in the silica was removed using a solution of MeOH and 1 % of Et₃N (around 700 mL). After solvent evaporation, the product was obtained as a pale yellow vitreous solid with a yield of 96 %, 856.4 mg.

¹H-NMR (400 MHz, CDCl₃): δ 8.12 (s, 1H, OCNH-), 7.39 (d, *J* = 7.7 Hz, 6H, Trt, o-CH), 7.26 (t, *J* = 7.5 Hz, 6H, Trt, m-CH), 7.18 (t, *J* = 7.2 Hz, 3H, Trt, p-CH), 5.15 (NH₂), 3.33 (m, 3H, -OCNH-CH₂-CH₂-NH₂), 2.88 (t, *J* = 5.8 Hz, 3H, -OCNH-CH₂-CH₂-NH₂), 2.68 (t, *J* = 6.1 Hz, 4H, -N(CH₂-CH₂)₂), 2.34 (m, 6H, -CH₂-NR₂ + -N(CH₂-CH₂)₂), 2.12 (t, *J* = 7.2 Hz, 2H, TrtS-CH₂-), 1.34 (m, 4H, TrtS-CH₂-CH₂- + -CH₂-CH₂-NR₂), 1.22 (m, 3H, TrtS-(CH₂)₂-CH₂-), 1.09 (m, 2H, -CH₂-(CH₂)₂-NR₂) ppm.

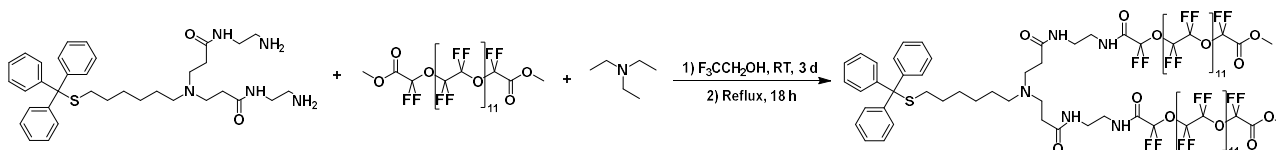
¹³C-NMR (101 MHz, CDCl₃): δ 173.36 (CO), 145.08 (Trt, C), 129.66 (Trt, o-CH), 127.91 (Trt, m-CH), 126.64 (Trt, p-CH), 66.50 (C-S), 53.55 (-CH₂-NR₂), 49.82 (-N(CH₂-CH₂)₂), 40.36 (-OCNH-CH₂-CH₂-NH₂), 39.81 (-OCNH-CH₂-CH₂-NH₂), 33.80 (-N(CH₂-CH₂)₂), 32.02 (TrtS-CH₂-), 29.00 (TrtS-(CH₂)₂-CH₂-), 28.71 (TrtS-CH₂-CH₂-), 27.25 (-CH₂-(CH₂)₂-NR₂), 25.95 (-CH₂-CH₂-NR₂) ppm.

ESI-MS (MeOH, Positive mode): 604.4 [M+H⁺], 626.2 [M+Na⁺], 644.4 [M+K⁺] m/z.

Synthesis of the “Pre-Y-Framework” (Tr tSC6N(C2CONHC2NHCOOF11OCOOME)2)



Try n°1 – Synthesis with triethylamine and conventional heating

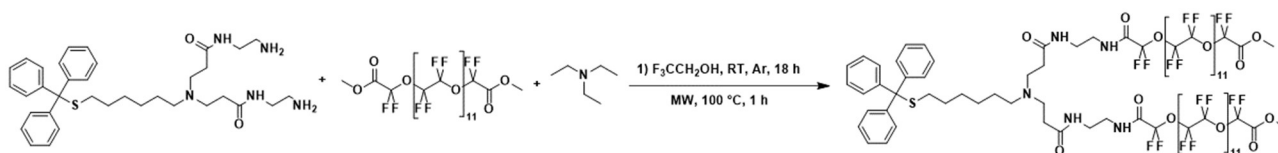


Scheme 9.1: Synthetic scheme for the preparation of the Pre-Y-Framework with triethylamine and conventional heating.

Fluorinated chain methyl ester F-PEG600COOMe (2.81 g, 1.86 mmol) was dissolved in trifluoroethanol (2 mL) in a round bottom flask. A solution of the previous 3,3'-((6-(tritylthio)hexyl)azanediyl)bis(N-(2-aminoethyl)propionamide) (TrtSC6N(C2CONHC2NH2)2, 500 mg, 0.828 mmol) with triethylamine (2 mL) in trifluoroethanol (8 mL) was slowly added, and then the container washed with the remaining solvent for the reaction. The mixture was stirred at room temperature for 3 days then refluxed at 100 °C for 18 hours.

The solvent was removed in vacuum and then the crude product was purified by flash chromatography with silica as the stationary phase and a solution of CHCl₃/MeOH 8:2 as eluent. At the end of the column, the product still stuck in the silica has been removed using a solution of MeOH and 2 % of Et₃N. All the fractions were collected and characterized, obtaining only the mono-functionalized intermediate as the best result (106.6 mg).

Try n°2 – Synthesis with triethylamine and microwave heating

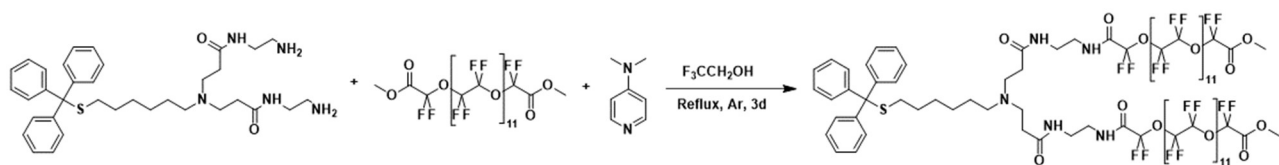


Scheme 9.2: Synthetic scheme for the preparation of the Pre-Y-Framework with triethylamine and microwave heating.

Fluorinated chain methyl ester F-PEG600COOMe (625.2 mg, 0.414 mmol) was dissolved in trifluoroethanol (1 mL) in a microwave vial under argon atmosphere. A solution of 3,3'-((6-(tritylthio)hexyl)azanediyl)bis(N-(2-aminoethyl)propionamide) (TrtSC6N(C2CONHC2NH2)2, 50 mg, 82.8 μmol) with triethylamine (0.25 mL) in trifluoroethanol (1 mL) was slowly added, and then the container washed with the remaining solvent for the reaction. The mixture was stirred at room temperature for 18 hours then heated at 100 °C for 1 hour with a microwave instrument.

The solvent was removed in vacuum and then the crude product was washed with Et₂O (3 x 1 mL) to promote TFE and TEA removal. The crude was purified by flash chromatography with silica as the stationary phase and a solution of CHCl₃/MeOH 8:2 as eluent. At the end of the column, the product still stuck in the silica has been removed using a solution of MeOH and 2 % of Et₃N. All the fractions were collected and characterized, unfortunately obtaining only a decomposed intermediate (81.0 mg).

Try n°3 – Synthesis with DMAP and conventional heating



Scheme 9.3: Synthetic scheme for the preparation of the Pre-Y-Framework with DMAP and conventional heating.

Fluorinated chain methyl ester F-PEG600COOMe (1.25 g, 0.828 mmol) was dissolved in trifluoroethanol (3 mL) in a round bottom flask under argon atmosphere. A solution of 3,3'-((6-(tritylthio)hexyl)azanediyl)bis(N-(2-aminoethyl)propionamide) (TrtSC₆N(C₂CONHC₂NH₂)₂), 100 mg, 0.166 mmol) with DMAP (101.2 mg, 0.828 mmol) in trifluoroethanol (2.5 mL) was slowly added, and then the container washed with the remaining solvent for the reaction (4.5 mL). The mixture has been heated to reflux for 3 days.

The solvent was evaporated under reduced pressure and then the crude product was dissolved in DCM (5 mL) and H₂O (5 mL) and washed by a NH₄Cl 10% m/v solution (5 x 3 mL) with the help of sonication after every addition in order to remove the DMAP and cleaned with H₂O (3 x 3 mL). After the removal of the aqueous phase, and the evaporation of the organic solvent, the crude was checked with NMR and dispersed again in DCM, washed with HCl 0.1 M (2 x 5 mL), and cleaned with H₂O (3 x 1 mL). After the removal of the aqueous phase and the evaporation of the organic solvent, only a complex sample of the mono- and bi-functionalized products as the best result was obtained.

Characterization

The spectra reported (Spectra n°7a-7b) are referred to the crude product obtained after three days under reflux and several washing steps.

¹H NMR (400 MHz, CD₃OD): δ 8.09 (d, N-CH-CH- DMAP), 7.38 (m, H, Trt), 7.27 (m, H, Trt), 7.20 (m, H, Trt), 6.99 (d, N-CH-CH-, DMAP), 4.85 (H₂O), 3.48, 3.30 (Solvent, CD₃OD), 3.25 – 3.23 (-OCNH-CH₂-CH₂-CONH-CF₂-), 3.13 (qt, impurity), 3.08 (-OCNH-CH₂-CH₂-CONH-CF₂-), 2.96 (OCNH-CH₂-CH₂-NH₂-), 2.84 (-N(CH₂-CH₂-)₂), 2.77 (-N(CH₂-CH₂-)₂), 2.68 (t, -CH₂-NR₂-), 2.15 (t, TrtS-CH₂-), 1.98 (AcOH), 1.63 - 1.54 (m, TrtS-CH₂-CH₂-), 1.40 - 1.36 (-CH₂-CH₂-NR₂-), 1.33 – 1.20 (m, -CH₂-CH₂-(CH₂)₂-NR₂).

¹⁹F NMR (376 MHz, CD₃OD): δ -57.13, -58.13, -58.63, -78.95 (TFE or F-PEGCOOMe), -89.68, -90.17 (F-PEGCOOMe), -90.81, -91.32, -92.14.

CHAPTER 10: FLUORINATED AUNPS – CONCLUSIONS & OUTLOOK

For this project, we designed linear and branched PEGylated thiols carrying fluorinated moiety for drug delivery and ^{19}F -MRI. Our initial design relied on the use, as fluorinated moiety, of a perfluoropolyether terminated with carboxymethyl groups (F-PEG600COOMe). However, this was found to present a series of drawbacks due to the lability of the ester functions that are activated towards nucleophilic addition reactions because of the presence of the electron-withdrawing $-\text{CF}_2$ -groups. Indeed, this species is particularly sensitive to water, which can lead to the formation of the carboxylic acid derivative and deactivate the terminus and making overall synthesis cumbersome and low yielding. However, we managed to complete the synthesis and characterization of a first linear ligand. That was used for the synthesis of gold nanoparticles well soluble in aqueous media. Even if the sized dispersity of the sample was not optimal and different populations of nanoparticles were obtained, the dimensional range for the gold core was the designed one, while the hydrodynamic diameter found analyzing the solvation sphere of the ligand, significantly exceed the expectations. Further characterization of the final hybrid nanosystem with NMR allowed us to confirm the effective passivation and verify the complete removal of the free ligand that could have been adsorbed on the monolayer. The particular condition for the extraction and the precipitation of these nanoparticles, followed by size exclusion chromatography, resulted therefore optimal for the purification of this type of gold nanoparticles. The monolayer composition and the degree of passivation were obtained through TGA, finding a considerable amount of organic content, compatible with the unusual length of the final ligand and the extent of the hydrodynamic diameter. Finally, the principal signals in the ^{19}F -NMR spectrum were employed for the extrapolation of the relaxation times T1 and T2, showing a notable reduction of both once the fluorinated ligand is linked to the nanoparticle surface, hence meeting the desired criteria for its use in ^{19}F -MRI. Hence, the first part of this project ended successfully in the synthesis of an original fluorinated ligand for a new combined approach in nanomedicine that combines the innovative and resourceful ^{19}F -MRI with drug-carrying via non-covalent interactions. Moreover, with the synthesis of small gold nanoparticles passivated by this ligand to form a self-assembled monolayer, we created a unique theranostic nanoplatform we foresee to apply in the treatment and diagnosis of glioblastoma. Further research efforts will be put in the search for a suitable drug to include in the novel nanosystem prepared.

The stability issues related to the use of the building block F-PEG600COOMe prompted us to use an alternative species in which the terminal carboxymethyl groups are replaced by alcohol

groups. With this choice, we designed a novel linear ligand whose synthesis was partly optimized. Indeed, we were able to prepare the desired protected ligand. The major critical point we encountered during the synthesis was related to the purification procedures involving the high molecular weight PEG compounds. Optimization of this purification procedure will be dealt with in future work.

The future research work will be devoted to the completion of the other two ligands – the linear one containing the F-PEG600DIOL moiety and the branched one bearing two F-PEG600COOMe units –. For all these species we foresee the implementation with gold nanoparticles for the preparation of monolayer protected fluorinated AuNPs, whose stability, interactions with model drug molecules, and NMR response will be assessed for future theranostic applications.

Moreover, the promising first accomplishments in the synthesis of the linear ligands with the diol precursor, allow us to think of a further alternative: the preparation of the branched ligand carrying two equivalents of the F-PEG600DIOL moiety.

BIBLIOGRAPHY

- (1) Ehrlich, P. *Berichte der Dtsch. Chem. Gesellschaft* **1909**, *42*, 17–47.
- (2) Feynman, R. P. There's Plenty of Room at the Bottom: An Invitation to Enter a New Field of Physics. *Engineering and Science*. 1960, pp 22–36.
- (3) Roco, M. C. *J. Nanoparticle Res.* **2005**, *7*, 707–712, DOI: 10.1007/s11051-005-3141-5.
- (4) Ferrari, M. *Nat. Rev. Cancer* **2005**, *5*, 161–171, DOI: 10.1038/nrc1566.
- (5) Minelli, C.; Lowe, S. B.; Stevens, M. M. *Small* **2010**, *6*, 2336–2357, DOI: 10.1002/smll.201000523.
- (6) Choi, Y. H.; Han, H. K. *J. Pharm. Investig.* **2018**, *48*, 43–60, DOI: 10.1007/s40005-017-0370-4.
- (7) Barenholz, Y.; Gabizon, A. Liposome/Doxorubicin Composition and Method. US4898735A, 1990.
- (8) Barenholz, Y. *J. Control. Release* **2012**, *160*, 117–134, DOI: 10.1016/j.jconrel.2012.03.020.
- (9) Briggs, R. W.; Wu, Z.; Mladinich, C. R. J.; Stoupis, C.; Gauger, J.; Liebig, T.; Ros, P. R.; Ballinger, J. R.; Kubilis, P. *Magn. Reson. Imaging* **1997**, *15*, 559–566, DOI: 10.1016/S0730-725X(97)00020-9.
- (10) Drugs.com. Gastromark - FDA Professional Drug Information Database
www.drugs.com/pro/gastromark.html.
- (11) Min, Y.; Caster, J. M.; Eblan, M. J.; Wang, A. Z. *Chem. Rev.* **2015**, *115*, 11147–11190, DOI: 10.1021/acs.chemrev.5b00116.
- (12) Park, I. H.; Sohn, J. H.; Kim, S. B.; Lee, K. S.; Chung, J. S.; Lee, S. H.; Kim, T. Y.; Jung, K. H.; Cho, E. K.; Kim, Y. S.; Song, H. S.; Seo, J. H.; Ryoo, H. M.; Lee, S. A.; Yoon, S. Y.; Kim, C. S.; Kim, Y. T.; Kim, S. Y.; Jin, M. R.; Ro, J. *Cancer Res. Treat.* **2017**, *49*, 569–577, DOI: 10.4143/crt.2016.289.
- (13) Ma, K.; Mendoza, C.; Hanson, M.; Werner-Zwanziger, U.; Zwanziger, J.; Wiesner, U. *Chem. Mater.* **2015**, *27*, 4119–4133, DOI: 10.1021/acs.chemmater.5b01222.
- (14) Phillips, E.; Penate-Medina, O.; Zanzonico, P. B.; Carvajal, R. D.; Mohan, P.; Ye, Y.; Humm, J.; Gönen, M.; Kalaigian, H.; Schöder, H.; Strauss, H. W.; Larson, S. M.; Wiesner, U.; Bradbury, M. S. *Sci. Transl. Med.* **2014**, *6*, DOI: 10.1126/scitranslmed.3009524.
- (15) Chen, G.; Roy, I.; Yang, C.; Prasad, P. N. *Chem. Rev.* **2016**, *116*, 2826–2885, DOI: 10.1021/acs.chemrev.5b00148.
- (16) Maldiney, T.; Mignet, N. Nanoparticles for Imaging and Imaging Nanoparticles: State of the Art and Current Prospects. In *Pharmaceutical Nanotechnology: Innovation and Production*; Cornier, J., Kwade, A., Owen, A., Van de Voorde, M., Eds.; Wiley-VCH, 2016; pp 533–560.
- (17) Krug, H. F.; Wick, P. *Angew. Chemie - Int. Ed.* **2011**, *50*, 1260–1278, DOI: 10.1002/anie.201001037.
- (18) Sharifi, S.; Behzadi, S.; Laurent, S.; Forrest, M. L.; Stroeve, P.; Mahmoudi, M. *Chem. Soc. Rev.* **2012**, *41*, 2323–2343, DOI: 10.1039/c1cs15188f.
- (19) Nel, A. E.; Mädler, L.; Velegol, D.; Xia, T.; Hoek, E. M. V.; Somasundaran, P.; Klaessig, F.; Castranova, V.; Thompson, M. *Nat. Mater.* **2009**, *8*, 543–557, DOI: 10.1038/nmat2442.
- (20) Hong, G.; Diao, S.; Antaris, A. L.; Dai, H. *Chem. Rev.* **2015**, *115*, 10816–10906, DOI: 10.1021/acs.chemrev.5b00008.
- (21) Marchesan, S.; Melchionna, M.; Prato, M. *Fullerenes, Nanotub. Carbon Nanostructures* **2014**, *22*, 190–195, DOI: 10.1080/1536383X.2013.798726.
- (22) Elsabahy, M.; Heo, G. S.; Lim, S.-M.; Sun, G.; Wooley, K. L. *Chem. Rev.* **2015**, *115*, 10967–11011, DOI:

10.1021/acs.chemrev.5b00135.

- (23) Grimaldi, N.; Andrade, F.; Segovia, N.; Ferrer-Tasies, L.; Sala, S.; Veciana, J.; Ventosa, N. *Chem. Soc. Rev.* **2016**, *45*, 6520–6545, DOI: 10.1039/c6cs00409a.
- (24) Namiki, Y.; Fuchigami, T.; Tada, N.; Kawamura, R.; Matsunuma, S.; Kitamoto, Y.; Nakagawa, M. *Acc. Chem. Res.* **2011**, *44*, 1080–1093, DOI: 10.1021/ar200011r.
- (25) Gradishar, W. J.; Tjulandin, S.; Davidson, N.; Shaw, H.; Desai, N.; Bhar, P.; Hawkins, M.; O’Shaughnessy, J. *J. Clin. Oncol.* **2005**, *23*, 7794–7803, DOI: 10.1200/JCO.2005.04.937.
- (26) Sarmah, J. K.; Mahanta, R.; Bhattacharjee, S. K.; Mahanta, R.; Biswas, A. *Int. J. Biol. Macromol.* **2011**, *49*, 390–396, DOI: 10.1016/j.ijbiomac.2011.05.020.
- (27) Funkhouser, J. *Curr. Drug Discov.* **2002**, *2*, 17–19.
- (28) Jaymand, M. *ACS Biomater. Sci. Eng.* **2020**, *6*, 134–166, DOI: 10.1021/acsbiomaterials.9b00802.
- (29) Fan, W.; Yung, B.; Huang, P.; Chen, X. *Chem. Rev.* **2017**, *117*, 13566–13638, DOI: 10.1021/acs.chemrev.7b00258.
- (30) Qin, S.-Y.; Zhang, A.-Q.; Cheng, S.-X.; Rong, L.; Zhang, X.-Z. *Biomaterials* **2017**, *112*, 234–247, DOI: 10.1016/j.biomaterials.2016.10.016.
- (31) Sun, T.; Zhang, Y. S.; Pang, B.; Hyun, D. C.; Yang, M.; Xia, Y. *Angew. Chemie - Int. Ed.* **2014**, *53*, 12320–12364, DOI: 10.1002/anie.201403036.
- (32) Kanasty, R.; Dorkin, J. R.; Vegas, A.; Anderson, D. *Nat. Mater.* **2013**, *12*, 967–977, DOI: 10.1038/nmat3765.
- (33) Bulaklak, K.; Gersbach, C. A. *Nat. Commun.* **2020**, *11*, 1–4, DOI: 10.1038/s41467-020-19505-2.
- (34) Irvine, D. J.; Hanson, M. C.; Rakhra, K.; Tokatlian, T. *Chem. Rev.* **2015**, *115*, 11109–11146, DOI: 10.1021/acs.chemrev.5b00109.
- (35) Nam, J.; Son, S.; Park, K. S.; Zou, W.; Shea, L. D.; Moon, J. J. *Nat. Rev. Mater.* **2019**, *4*, 398–414, DOI: 10.1038/s41578-019-0108-1.
- (36) Hergt, R.; Dutz, S.; Müller, R.; Zeisberger, M. *J. Phys. Condens. Matter* **2006**, *18*, S2919–S2934, DOI: 10.1088/0953-8984/18/38/S26.
- (37) Laurent, S.; Dutz, S.; Häfeli, U. O.; Mahmoudi, M. *Adv. Colloid Interface Sci.* **2011**, *166*, 8–23, DOI: 10.1016/j.cis.2011.04.003.
- (38) Melamed, J. R.; Edelstein, R. S.; Day, E. S. *ACS Nano* **2015**, *9*, 6–11, DOI: 10.1021/acsnano.5b00021.
- (39) Allison, R. R.; Sibata, C. H. *Photodiagnosis Photodyn. Ther.* **2010**, *7*, 61–75, DOI: 10.1016/j.pdpdt.2010.02.001.
- (40) Lucky, S. S.; Soo, K. C.; Zhang, Y. *Chem. Rev.* **2015**, *115*, 1990–2042, DOI: 10.1021/cr5004198.
- (41) Zhao, N.; Yan, L.; Zhao, X.; Chen, X.; Li, A.; Zheng, D.; Zhou, X.; Dai, X.; Xu, F. J. *Chem. Rev.* **2019**, *119*, 1666–1762, DOI: 10.1021/acs.chemrev.8b00401.
- (42) Kennedy, J. E. *Nat. Rev. Cancer* **2005**, *105*, 4163–4169, DOI: 10.1182/blood-2004-10-4135.
- (43) Al-Bataineh, O.; Jenne, J.; Huber, P. *Cancer Treat. Rev.* **2012**, *38*, 346–353, DOI: 10.1016/j.ctrv.2011.08.004.
- (44) Pan, X.; Bai, L.; Wang, H.; Wu, Q.; Wang, H.; Liu, S.; Xu, B.; Shi, X.; Liu, H. *Adv. Mater.* **2018**, *30*, 1800180, DOI: 10.1002/adma.201800180.

- (45) Zhou, D.; Li, C.; He, M.; Ma, M.; Li, P.; Gong, Y.; Ran, H.; Wang, Z.; Wang, Z.; Zheng, Y.; Sun, Y. *J. Mater. Chem. B* **2016**, *4*, 4164–4181, DOI: 10.1039/c6tb00261g.
- (46) Devarakonda, S. B.; Myers, M. R.; Lanier, M.; Dumoulin, C.; Banerjee, R. K. *Nano Lett.* **2017**, *17*, 2532–2538, DOI: 10.1021/acs.nanolett.7b00272.
- (47) Wang, Z.; Qiao, R.; Tang, N.; Lu, Z.; Wang, H.; Zhang, Z.; Xue, X.; Huang, Z.; Zhang, S.; Zhang, G.; Li, Y. *Biomaterials* **2017**, *127*, 25–35, DOI: 10.1016/j.biomaterials.2017.02.037.
- (48) Wang, X.; Wang, W.; Yu, L.; Tang, Y.; Cao, J.; Chen, Y. *J. Mater. Chem. B* **2017**, *5*, 4579–4586, DOI: 10.1039/c7tb00938k.
- (49) Huang, P.; Qian, X.; Chen, Y.; Yu, L.; Lin, H.; Wang, L.; Zhu, Y.; Shi, J. *J. Am. Chem. Soc.* **2017**, *139*, 1275–1284, DOI: 10.1021/jacs.6b11846.
- (50) Zhang, X.-D.; Luo, Z.; Chen, J.; Shen, X.; Song, S.; Sun, Y.; Fan, S.; Fan, F.; Leong, D. T.; Xie, J. *Adv. Mater.* **2014**, *26*, 4565–4568, DOI: 10.1002/adma.201400866.
- (51) Wen, L.; Chen, L.; Zheng, S.; Zeng, J.; Duan, G.; Wang, Y.; Wang, G.; Chai, Z.; Li, Z.; Gao, M. *Adv. Mater.* **2016**, *28*, 5072–5079, DOI: 10.1002/adma.201506428.
- (52) Hogle, W. P. *Semin. Oncol. Nurs.* **2006**, *22*, 212–220, DOI: 10.1016/j.soncn.2006.07.004.
- (53) Yang, Y.-S.; Carney, R. P.; Stellacci, F.; Irvine, D. J. *ACS Nano* **2014**, *8*, 8992–9002, DOI: 10.1021/nn502146r.
- (54) Phillips, W. T.; Bao, A.; Brenner, A. J.; Goins, B. A. *Adv. Drug Deliv. Rev.* **2014**, *76*, 39–59, DOI: 10.1016/j.addr.2014.07.001.
- (55) Kunjachan, S.; Ehling, J.; Storm, G.; Kiessling, F.; Lammers, T. *Chem. Rev.* **2015**, No. 115, 10907–10937, DOI: 10.1021/cr500314d.
- (56) Huang, J.; Liu, F.; Han, X.; Zhang, L.; Hu, Z.; Jiang, Q.; Wang, Z.; Ran, H.; Wang, D.; Li, P. *Theranostics* **2018**, *8*, 6178–6194, DOI: 10.7150/thno.29569.
- (57) Liu, Y.; Yang, Z.; Huang, X.; Yu, G.; Wang, S.; Zhou, Z.; Shen, Z.; Fan, W.; Liu, Y.; Davisson, M.; Kalish, H.; Niu, G.; Nie, Z.; Chen, X. *ACS Nano* **2018**, *12*, 8129–8137, DOI: 10.1021/acsnano.8b02980.
- (58) Anselmo, A. C.; Mitragotri, S. *Bioeng. Transl. Med.* **2016**, *1*, 10–29, DOI: 10.1002/btm2.10003.
- (59) Chen, H.; Zhang, W.; Zhu, G.; Xie, J.; Chen, X. *Nat. Rev. Mater.* **2017**, *2*, 17024, DOI: 10.1038/natrevmats.2017.24.
- (60) Martins, J. P.; das Neves, J.; de la Fuente, M.; Celia, C.; Florindo, H.; Günday-Türel, N.; Popat, A.; Santos, J. L.; Sousa, F.; Schmid, R.; Wolfram, J.; Sarmiento, B.; Santos, H. A. *Drug Deliv. Transl. Res.* **2020**, *1–4*, DOI: 10.1007/s13346-020-00743-2.
- (61) Björnmalm, M.; Thurecht, K. J.; Michael, M.; Scott, A. M.; Caruso, F. *ACS Nano* **2017**, *11*, 9594–9613, DOI: 10.1021/acsnano.7b04855.
- (62) Stefan Wilhelm; Anthony J. Tavares; Qin Dai; Seiichi Ohta; Julie Audet; Harold F. Dvorak; Chan, W. C. W. *Nat. Rev. Mater.* **2016**, *1*, 16014, DOI: 10.1038/natrevmats.2016.14.
- (63) Ulbrich, K.; Holá, K.; Šubr, V.; Bakandritsos, A.; Tuček, J.; Zbořil, R. *Chem. Rev.* **2016**, *116*, 5338–5431, DOI: 10.1021/acs.chemrev.5b00589.
- (64) Boccalon, M.; Franchi, P.; Lucarini, M.; Delgado, J. J.; Sousa, F.; Stellacci, F.; Zucca, I.; Scotti, A.; Spreafico, R.; Pengo, P.; Pasquato, L. *Chem. Commun.* **2013**, *49*, 8794–8796, DOI: 10.1039/c3cc44572k.
- (65) Du, C.; Liu, X.; Hu, H.; Li, H.; Yu, L.; Geng, D.; Chen, Y.; Zhang, J. *J. Mater. Chem. B* **2020**, *8*, 2296–

2306, DOI: 10.1039/c9tb02391g.

- (66) Elmore, W. C. *Phys. Rev.* **1938**, *54*, 1092–1095, DOI: 10.1103/PhysRev.54.1092.
- (67) Bean, C. P.; Livingston, J. D. *J. Appl. Phys.* **1959**, *30*, S120–S129, DOI: 10.1063/1.2185850.
- (68) Leslie-Pelecky, D. L.; Rieke, R. D. *Chem. Mater.* **1996**, *8*, 1770–1783, DOI: 10.1021/cm960077f.
- (69) Tuček, J.; Kemp, K. C.; Kim, K. S.; Zbořil, R. *ACS Nano* **2014**, *8*, 7571–7612, DOI: 10.1021/nn501836x.
- (70) Liu, X.; Zhang, Y.; Wang, Y.; Zhu, W.; Li, G.; Ma, X.; Zhang, Y.; Chen, S.; Tiwari, S.; Shi, K.; Zhang, S.; Fan, H. M.; Zhao, Y. X.; Liang, X.-J. *Theranostics* **2020**, *10*, 3793–3815, DOI: 10.7150/thno.40805.
- (71) Ling, D.; Lee, N.; Hyeon, T. *Acc. Chem. Res.* **2015**, *48*, 1276–1285, DOI: 10.1021/acs.accounts.5b00038.
- (72) Brown Jr., W. F. *Phys. Rev.* **1963**, *130*, 1677–1686, DOI: 10.1103/PhysRev.130.1677.
- (73) Rügenapp, C.; Gleich, B.; Haase, A. *Pharm. Res.* **2012**, *29*, 1165–1179, DOI: 10.1007/s11095-012-0711-y.
- (74) Nandwana, V.; Ryoo, S.-R.; Kanthala, S.; De, M.; Chou, S. S.; Prasad, P. V.; Dravid, V. P. *ACS Appl. Mater. Interfaces* **2016**, *8*, 6953–6961, DOI: 10.1021/acsami.6b01377.
- (75) Corchero, J. L.; Villaverde, A. *Trends Biotechnol.* **2009**, *27*, 468–476, DOI: 10.1016/j.tibtech.2009.04.003.
- (76) Stirrat, C.; Vesey, A. T.; McBride, O. M. B.; Robson, J. M. J.; Alam, S. R.; Wallace, W. A.; Semple, S. I.; Henriksen, P. A.; Newby, D. E. *J. Vasc. Diagnostics* **2014**, *2*, 99–112, DOI: 10.2147/jvd.s50036.
- (77) Thorek, D. L. J.; Tsourkas, A. *Biomaterials* **2008**, *29*, 3583–3590, DOI: 10.1016/j.biomaterials.2008.05.015.
- (78) Bietenbeck, M.; Florian, A.; Faber, C.; Sechtem, U.; Yilmaz, A. *Int. J. Nanomedicine* **2016**, *11*, 3191–3203, DOI: 10.2147/IJN.S110542.
- (79) Groult, H.; Carregal-Romero, S.; Castejón, D.; Azkargorta, M.; Miguel-Coello, A.-B.; Pulagam, K. R.; Gómez-Vallejo, V.; Cousin, R.; Muñoz-Caffarel, M.; Lawrie, C. H.; Llop, J.; Piot, J.-M.; Elortza, F.; Maugard, T.; Ruiz-Cabello, J.; Fruitier-Arnaudin, I. *Nanoscale* **2021**, *13*, 842–861, DOI: 10.1039/d0nr06378a.
- (80) Cornell, R. M.; Schwertmann, U. *The Iron Oxides: Structure, Properties, Reactions, Occurrence and Uses*; Wiley-VCH: Weinheim, Germany, 2003.
- (81) Pankhurst, Q. A.; Connolly, J.; K, J. S.; Dobson, J. J. *Phys. D. Appl. Phys.* **2003**, *36*, R167–R181, DOI: 10.1088/0022-3727/36/13/201.
- (82) Gupta, A. K.; Gupta, M. *Biomaterials* **2005**, *26*, 3995–4021, DOI: 10.1016/j.biomaterials.2004.10.012.
- (83) Kaittanis, C.; Naser, S. A.; Perez, J. M. *Nano Lett.* **2007**, *7*, 380–383, DOI: 10.1021/nl062553z.
- (84) Ramírez-Navarro, R.; Polesnak, P.; Reyes-Leyva, J.; Haque, U.; Vazquez-Chagoyán, J. C.; Pedroza-Montero, M. R.; Méndez-Rojas, M. A.; Angulo-Molina, A. *Nanoscale Adv.* **2020**, *2*, 3017–3026, DOI: 10.1039/d0na00251h.
- (85) Yu, C.; Zhao, J.; Guo, Y.; Lu, C.; Ma, X.; Gu, Z. *J. Biomed. Mater. Res. - Part A* **2008**, *87*, 364–372, DOI: 10.1002/jbm.a.31786.
- (86) Huang, S.-H.; Chen, D.-H. *J. Hazard. Mater.* **2009**, *163*, 174–179, DOI: 10.1016/j.jhazmat.2008.06.075.
- (87) Melnik, K.; Nakamura, M.; Comella, K.; Lasky, L. C.; Zborowski, M.; Chalmers, J. J. *Biotechnol. Prog.*

- 2001**, *17*, 907–916, DOI: 10.1021/bp010079r.
- (88) Hola, K.; Markova, Z.; Zoppellaro, G.; Tucek, J.; Zboril, R. *Biotechnol. Adv.* **2015**, *33*, 1162–1176, DOI: 10.1016/j.biotechadv.2015.02.003.
- (89) Palanisamy, S.; Wang, Y. M. *Dalt. Trans.* **2019**, *48*, 9490–9515, DOI: 10.1039/c9dt00459a.
- (90) Frantellizzi, V.; Conte, M.; Pontico, M.; Pani, A.; Pani, R.; De Vincentis, G. *Nucl. Med. Mol. Imaging (2010)*. **2020**, *54*, 65–80, DOI: 10.1007/s13139-020-00635-w.
- (91) Sharifi, S.; Seyednejad, H.; Laurent, S.; Atyabi, F.; Saei, A. A.; Mahmoudi, M. *Contrast Media Mol. Imaging* **2015**, *10*, 329–355, DOI: 10.1002/cmml.1638.
- (92) Zhang, L.; Gu, F. X.; Chan, J. M.; Wang, A. Z.; Langer, R. S.; Farokhzad, O. C. *Clin. Pharmacol. Ther.* **2008**, *83*, 761–769, DOI: 10.1038/sj.clpt.6100400.
- (93) Bobo, D.; Robinson, K. J.; Islam, J.; Thurecht, K. J.; Corrie, S. R. *Pharm. Res.* **2016**, *33*, 2373–2387, DOI: 10.1007/s11095-016-1958-5.
- (94) Drugs.com. Feridex - FDA Professional Drug Information Database
<https://www.drugs.com/pro/feridex.html>.
- (95) Ling, D.; Hyeon, T. *Small* **2013**, *9*, 1450–1466, DOI: 10.1002/sml.201202111.
- (96) Briley-Saebo, K.; Bjørnerud, A.; Grant, D.; Ahlstrom, H.; Berg, T.; Kindberg, G. M. *Cell Tissue Res.* **2004**, *316*, 315–323, DOI: 10.1007/s00441-004-0884-8.
- (97) Longmire, M.; Choyke, P. L.; Kobayashi, H. *Nanomedicine* **2008**, *3*, 703–717, DOI: 10.2217/17435889.3.5.703.
- (98) Weissleder, R.; Stark, D. D.; Engelstad, B. L.; Bacon, B. R.; Compton, C. C.; White, D. L.; Jacobs, P.; Lewis, J. *Am. J. Roentgenol.* **1989**, *152*, 167–173, DOI: 10.2214/ajr.152.1.167.
- (99) Patil, R. M.; Thorat, N. D.; Shete, P. B.; Bedge, P. A.; Gavde, S.; Joshi, M. G.; Tofail, S. A. M.; Bohara, R. A. *Biochem. Biophys. Reports* **2018**, *13*, 63–72, DOI: 10.1016/j.bbrep.2017.12.002.
- (100) Jeng, H. A.; Swanson, J. J. *Environ. Sci. Heal. Part A Toxic/Hazardous Subst. Environ. Eng.* **2006**, *41*, 2699–2711, DOI: 10.1080/10934520600966177.
- (101) Mornet, S.; Vasseur, S.; Grasset, F.; Duguet, E. *J. Mater. Chem.* **2004**, *14*, 2161–2175, DOI: 10.1039/b402025a.
- (102) Massart, R. *IEEE Trans. Magn.* **1981**, *17*, 1247–1248, DOI: 10.1109/TMAG.1981.1061188.
- (103) Wu, K. T.; Kuo, P. C.; Yao, Y. D.; Tsai, E. H. *IEEE Trans. Magn.* **2001**, *37*, 2651–2653, DOI: 10.1109/20.951263.
- (104) Demirer, G. S.; Okur, A. C.; Kizilel, S. *J. Mater. Chem. B* **2015**, *3*, 7831–7849, DOI: 10.1039/c5tb00931f.
- (105) Zheng, Y.; Cheng, Y.; Bao, F.; Wang, Y. *Mater. Res. Bull.* **2006**, *41*, 525–529, DOI: 10.1016/j.materresbull.2005.09.015.
- (106) Wang, J.; Sun, J.; Sun, Q.; Chen, Q. *Mater. Res. Bull.* **2003**, *38*, 1113–1118, DOI: 10.1016/S0025-5408(03)00129-6.
- (107) Ali, S.; Khan, S. A.; Eastoe, J.; Hussaini, S. R.; Morsy, M. A.; Yamani, Z. H. *Colloids Surfaces A Physicochem. Eng. Asp.* **2018**, *543*, 133–143, DOI: 10.1016/j.colsurfa.2018.02.002.
- (108) Hyeon, T.; Su Seong Lee; Park, J.; Chung, Y.; Hyon Bin Na. *J. Am. Chem. Soc.* **2001**, *123*, 12798–12801, DOI: 10.1021/ja016812s.

- (109) Chen, Z. P.; Zhang, Y.; Zhang, S.; Xia, J. G.; Liu, J. W.; Xu, K.; Gu, N. *Colloids Surfaces A Physicochem. Eng. Asp.* **2008**, *316*, 210–216, DOI: 10.1016/j.colsurfa.2007.09.017.
- (110) Li, Y.; Zhang, H. *Nanomedicine* **2019**, *14*, 1493–1512, DOI: 10.2217/nnm-2018-0346.
- (111) Khandhar, A. P.; Keselman, P.; Kemp, S. J.; Ferguson, R. M.; Goodwill, P. W.; Conolly, S. M.; Krishnan, K. M. *Nanoscale* **2017**, *9*, 1299–1306, DOI: 10.1039/c6nr08468k.
- (112) Wu, W.; He, Q.; Jiang, C. *Nanoscale Res. Lett.* **2008**, *3*, 397–415, DOI: 10.1007/s11671-008-9174-9.
- (113) Okoli, C.; Sanchez-Dominguez, M.; Boutonnet, M.; Järås, S.; Civera, C.; Solans, C.; Kuttuva, G. R. *Langmuir* **2012**, *28*, 8479–8485, DOI: 10.1021/la300599q.
- (114) Chin, A. B.; Yaacob, I. I. *J. Mater. Process. Technol.* **2007**, *191*, 235–237, DOI: 10.1016/j.jmatprotec.2007.03.011.
- (115) Sahoo, Y.; Pizem, H.; Fried, T.; Golodnitsky, D.; Burstein, L.; Sukenik, C. N.; Markovich, G. *Langmuir* **2001**, *17*, 7907–7911, DOI: 10.1021/la010703+.
- (116) Sahoo, Y.; Goodarzi, A.; Swihart, M. T.; Ohulchanskyy, T. Y.; Kaur, N.; Furlani, E. P.; Prasad, P. N. *J. Phys. Chem. B* **2005**, *109*, 3879–3885, DOI: 10.1021/jp045402y.
- (117) Sousa, M. H.; Rubim, J. C.; Sobrinho, P. G.; Tourinho, F. A. *J. Magn. Magn. Mater.* **2001**, *225*, 67–72, DOI: 10.1016/S0304-8853(00)01229-4.
- (118) Bonacchi, D.; Caneschi, A.; Dorignac, D.; Falqui, A.; Gatteschi, D.; Rovai, D.; Sangregorio, C.; Sessoli, R. *Chem. Mater.* **2004**, *16*, 2016–2020, DOI: 10.1021/cm034948e.
- (119) Lewin, M.; Carlesso, N.; Tung, C.-H.; Tang, X.-W.; Cory, D.; Scadden, D. T.; Weissleder, R. *Nat. Biotechnol.* **2000**, *18*, 410–414, DOI: 10.1038/74464.
- (120) Mikhaylova, M.; Kim, D. K.; Berry, C. C.; Zagorodni, A.; Toprak, M.; Curtis, A. S. G.; Muhammed, M. *Chem. Mater.* **2004**, *16*, 2344–2354, DOI: 10.1021/cm0348904.
- (121) McCarthy, J. R.; Weissleder, R. *Adv. Drug Deliv. Rev.* **2008**, *60*, 1241–1251, DOI: 10.1016/j.addr.2008.03.014.
- (122) Anbarasu, M.; Anandan, M.; Chinnasamy, E.; Gopinath, V.; Balamurugan, K. *Spectrochim. Acta - Part A Mol. Biomol. Spectrosc.* **2015**, *135*, 536–539, DOI: 10.1016/j.saa.2014.07.059.
- (123) Chastellain, M.; Petri, A.; Hofmann, H. *J. Colloid Interface Sci.* **2004**, *278*, 353–360, DOI: 10.1016/j.jcis.2004.06.025.
- (124) Chen, F.; Gao, Q.; Hong, G.; Ni, J. *J. Magn. Magn. Mater.* **2008**, *320*, 1921–1927, DOI: 10.1016/j.jmmm.2008.02.132.
- (125) Veloso, C. H.; Filippov, L. O.; Filippova, I. V.; Ouvreard, S.; Araujo, A. C. *J. Mater. Res. Technol.* **2020**, *9*, 779–788, DOI: 10.1016/j.jmrt.2019.11.018.
- (126) Arkles, B.; Steinmetz, J. R.; Zazyczny, J.; Mehta, P. *J. Adhes. Sci. Technol.* **1992**, *6*, 193–206, DOI: 10.1163/156856192X00133.
- (127) Shen, X.-C.; Fang, X.-Z.; Zhou, Y.-H.; Liang, H. *Chem. Lett.* **2004**, *33*, 1468–1469, DOI: 10.1246/cl.2004.1468.
- (128) Shaghghi, B.; Khoei, S.; Bonakdar, S. *Int. J. Pharm.* **2019**, *559*, 1–12, DOI: 10.1016/j.ijpharm.2019.01.020.
- (129) Mandal, M.; Kundu, S.; Ghosh, S. K.; Panigrahi, S.; Sau, T. K.; Yusuf, S. M.; Pal, T. *J. Colloid Interface Sci.* **2005**, *286*, 187–194, DOI: 10.1016/j.jcis.2005.01.013.

- (130) Teng, X.; Black, D.; Watkins, N. J.; Gao, Y.; Yang, H. *Nano Lett.* **2003**, *3*, 261–264, DOI: 10.1021/nl025918y.
- (131) Fan, H.; Pan, Z. Q.; Gu, H. Y. *Microchim. Acta* **2010**, *168*, 239–244, DOI: 10.1007/s00604-009-0279-3.
- (132) Zhao, L.; Zheng, K.; Tong, J.; Jin, J.; Shen, C. *Catal. Letters* **2019**, *149*, 2607–2613, DOI: 10.1007/s10562-019-02829-0.
- (133) Wang, Z.; Guo, H.; Yu, Y.; He, N. *J. Magn. Magn. Mater.* **2006**, *302*, 397–404, DOI: 10.1016/j.jmmm.2005.09.044.
- (134) Li, Y.; Liu, Y.; Tang, J.; Lin, H.; Yao, N.; Shen, X.; Deng, C.; Yang, P.; Zhang, X. *J. Chromatogr. A* **2007**, *1172*, 57–71, DOI: 10.1016/j.chroma.2007.09.062.
- (135) Chen, C.-T.; Chen, Y.-C. *Anal. Chem.* **2005**, *77*, 5912–5919, DOI: 10.1021/ac050831t.
- (136) Hong, R. Y.; Zhang, S. Z.; Di, G. Q.; Li, H. Z.; Zheng, Y.; Ding, J.; Wei, D. G. *Mater. Res. Bull.* **2008**, *43*, 2457–2468, DOI: 10.1016/j.materresbull.2007.07.035.
- (137) Natile, M. M.; Glisenti, A. *Chem. Mater.* **2003**, *15*, 2502–2510, DOI: 10.1021/cm031019e.
- (138) Sodipo, B. K.; Aziz, A. A. *J. Magn. Magn. Mater.* **2016**, *416*, 275–291, DOI: 10.1016/j.jmmm.2016.05.019.
- (139) Ding, H. L.; Zhang, Y. X.; Wang, S.; Xu, J. M.; Xu, S. C.; Li, G. H. *Chem. Mater.* **2012**, *24*, 4572–4580, DOI: 10.1021/cm302828d.
- (140) Thorek, D. L. J.; Elias, D. R.; Tsourkas, A. *Mol. Imaging* **2009**, *8*, 221–229, DOI: 10.2310/7290.2009.00021.
- (141) Laurent, S.; Forge, D.; Port, M.; Roch, A.; Robic, C.; Elst, L. Vander; Muller, R. N. *Chem. Rev.* **2008**, *108*, 2064–2110, DOI: Doi 10.1021/Cr900197g.
- (142) Grüttner, C.; Müller, K.; Teller, J.; Westphal, F.; Foreman, A.; Ivkov, R. *J. Magn. Magn. Mater.* **2007**, *311*, 181–186, DOI: 10.1016/j.jmmm.2006.10.1151.
- (143) Meng, X.; Wan, J.; Jing, M.; Zhao, S.; Cai, W.; Liu, E. *Acta Pharmacol. Sin.* **2007**, *28*, 2019–2026, DOI: 10.1111/j.1745-7254.2007.00661.x.
- (144) Guan, X.; Su, Z. *Polym. Adv. Technol.* **2008**, *19*, 385–392, DOI: 10.1002/pat.1021.
- (145) Xu, C.; Xu, K.; Gu, H.; Zheng, R.; Liu, H.; Zhang, X.; Guo, Z.; Xu, B. *J. Am. Chem. Soc.* **2004**, *126*, 9938–9939, DOI: 10.1021/ja0464802.
- (146) Song, H. T.; Choi, J. S.; Huh, Y. M.; Kim, S.; Jun, Y. W.; Sun, J. S.; Cheon, J. *J. Am. Chem. Soc.* **2005**, *127*, 9992–9993, DOI: 10.1021/ja051833y.
- (147) Na, H. Bin; Lee, I. S.; Seo, H.; Park, Y. Il; Lee, J. H.; Kim, S. W.; Hyeon, T. *Chem. Commun.* **2007**, No. 48, 5167–5169, DOI: 10.1039/b712721a.
- (148) Park, W.; Yang, H. N.; Ling, D.; Yim, H.; Kim, K. S.; Hyeon, T.; Na, K.; Park, K. H. *Biomaterials* **2014**, *35*, 7239–7247, DOI: 10.1016/j.biomaterials.2014.05.010.
- (149) Lee, N.; Choi, Y.; Lee, Y.; Park, M.; Moon, W. K.; Choi, S. H.; Hyeon, T. *Nano Lett.* **2012**, *12*, 3127–3131, DOI: 10.1021/nl3010308.
- (150) Bae, K. H.; Park, M.; Do, M. J.; Lee, N.; Ryu, J. H.; Kim, G. W.; Kim, C.; Park, T. G.; Hyeon, T. *ACS Nano* **2012**, *6*, 5266–5273, DOI: 10.1021/nn301046w.
- (151) Tong, S.; Hou, S.; Zheng, Z.; Zhou, J.; Bao, G. *Nano Lett.* **2010**, *10*, 4607–4613, DOI: 10.1021/nl102623x.

- (152) Feld, A.; Koll, R.; Fruhner, L. S.; Krutyeva, M.; Pyckhout-Hintzen, W.; Weiß, C.; Heller, H.; Weimer, A.; Schmidtke, C.; Appavou, M. S.; Kentzinger, E.; Allgaier, J.; Weller, H. *ACS Nano* **2017**, *11*, 3767–3775, DOI: 10.1021/acsnano.6b08441.
- (153) Thünemann, A. F.; Rolf, S.; Knappe, P.; Weidner, S. *Anal. Chem.* **2009**, *81*, 296–301, DOI: 10.1021/ac802009q.
- (154) Zeng, L.; Ren, W.; Zheng, J.; Cui, P.; Wu, A. *Phys. Chem. Chem. Phys.* **2012**, *14*, 2631–2636, DOI: 10.1039/c2cp23196d.
- (155) Patterson, A. L. *Phys. Rev.* **1939**, *56*, 978–982, DOI: 10.1103/PhysRev.56.978.
- (156) Ge, S.; Shi, X.; Sun, K.; Li, C.; Uher, C.; Baker, J. R.; Banaszak Holl, M. M.; Orr, B. G. *J. Phys. Chem. C* **2009**, *113*, 13593–13599, DOI: 10.1021/jp902953t.
- (157) Di Marco, M.; Port, M.; Couvreur, P.; Dubernet, C.; Ballirano, P.; Sadun, C. *J. Am. Chem. Soc.* **2006**, *128*, 10054–10059, DOI: 10.1021/ja061674y.
- (158) Li, X.; Iocozzia, J.; Chen, Y.; Zhao, S.; Cui, X.; Wang, W.; Yu, H.; Lin, S.; Lin, Z. *Angew. Chemie - Int. Ed.* **2018**, *57*, 2046–2070, DOI: 10.1002/anie.201705019.
- (159) Lukins, R. E. *AIP Adv.* **2017**, *7*, 056801, DOI: 10.1063/1.4973750.
- (160) Fagaly, R. L. *Rev. Sci. Instrum.* **2006**, *77*, 1–45, DOI: 10.1063/1.2354545.
- (161) Buchner, M.; Höfler, K.; Henne, B.; Ney, V.; Ney, A. *J. Appl. Phys.* **2018**, *124*, 161101, DOI: 10.1063/1.5045299.
- (162) Huang, C.; Zhou, Y.; Jin, Y.; Zhou, X.; Tang, Z.; Guo, X.; Zhou, S. *J. Mater. Chem.* **2011**, *21*, 5660–5670, DOI: 10.1039/c0jm04264a.
- (163) Liu, Y.; Hughes, T. C.; Muir, B. W.; Waddington, L. J.; Gengenbach, T. R.; Easton, C. D.; Hinton, T. M.; Moffat, B. A.; Hao, X.; Qiu, J. *Biomaterials* **2014**, *35*, 378–386, DOI: 10.1016/j.biomaterials.2013.09.079.
- (164) Lak, A.; Kraken, M.; Ludwig, F.; Kornowski, A.; Eberbeck, D.; Sievers, S.; Litterst, F. J.; Weller, H.; Schilling, M. *Nanoscale* **2013**, *5*, 12286, DOI: 10.1039/c3nr04562e.
- (165) Schmidtke, C.; Eggers, R.; Zierold, R.; Feld, A.; Kloust, H.; Wolter, C.; Ostermann, J.; Merkl, J. P.; Schotten, T.; Nielsch, K.; Weller, H. *Langmuir* **2014**, *30*, 11190–11196, DOI: 10.1021/la5021934.
- (166) Amiri, H.; Bordonali, L.; Lascialfari, A.; Wan, S.; Monopoli, M. P.; Lynch, I.; Laurent, S.; Mahmoudi, M. *Nanoscale* **2013**, *5*, 8656–8665, DOI: 10.1039/c3nr00345k.
- (167) Koenig, S. H.; Kellar, K. E. *Magn. Reson. Med.* **1995**, *34*, 227–233, DOI: 10.1002/mrm.1910340214.
- (168) de la Presa, P.; Luengo, Y.; Multigner, M.; Costo, R.; Morales, M. P.; Rivero, G.; Hernando, A. *J. Phys. Chem. C* **2012**, *116*, 25602–25610, DOI: 10.1021/jp310771p.
- (169) Jitkang, L.; Pin, Y. S.; Xin, C. H.; Chun, L. S. *Nanoscale Res. Lett.* **2013**, *8*, 381, DOI: 10.1186/1556-276X-8-381.
- (170) Roonasi, P.; Holmgren, A. *Appl. Surf. Sci.* **2009**, *255*, 5891–5895, DOI: 10.1016/j.apsusc.2009.01.031.
- (171) Butter, K.; Hoell, A.; Wiedenmann, A.; Petukhov, A. V.; Vroege, G. J. *J. Appl. Crystallogr.* **2004**, *37*, 847–856, DOI: 10.1107/S0021889804018564.
- (172) Chen, S.; Li, Y.; Guo, C.; Wang, J.; Ma, J.; Liangs, X.; Yang, L.-R.; Liu, H.-Z. *Langmuir* **2007**, *23*, 12669–12676, DOI: 10.1021/la702049d.
- (173) Speranza, G.; Minati, L.; Torrenzo, S.; Rossi, B.; Migliaresi, C.; Maniglio, D.; Dalbosco, L. *Adv. Sci.*

Technol. **2010**, *76*, 165–170, DOI: 10.4028/www.scientific.net/ast.76.165.

- (174) Kreller, D. I.; Gibson, G.; Novak, W.; Van Loon, G. W.; Horton, J. H. *Colloids Surfaces A Physicochem. Eng. Asp.* **2003**, *212*, 249–264, DOI: 10.1016/S0927-7757(02)00325-4.
- (175) Delgado, A. V.; González-Caballero, F.; Hunter, R. J.; Koopal, L. K.; Lyklema, J. *Pure Appl. Chem.* **2005**, *77*, 1753–1805, DOI: 10.1351/pac200577101753.
- (176) Di Marco, M.; Guilbert, I.; Port, M.; Robic, C.; Couvreur, P.; Dubernet, C. *Int. J. Pharm.* **2007**, *331*, 197–203, DOI: 10.1016/j.ijpharm.2006.11.002.
- (177) Arias, J. L.; Ruiz, A. M.; Gallardo, V.; Delgado, Á. V. *J. Control. Release* **2008**, *125*, 50–58, DOI: 10.1016/j.jconrel.2007.09.008.
- (178) Weissleder, R.; Bogdanov, A.; Neuwelt, E. A.; Papisov, M. *Adv. Drug Deliv. Rev.* **1995**, *16*, 321–334, DOI: 10.1016/0169-409X(95)00033-4.
- (179) Abdolahi, M.; Shahbazi-Gahrouei, D.; Laurent, S.; Sermeus, C.; Firozian, F.; Allen, B. J.; Boutry, S.; Muller, R. N. *Contrast Media Mol. Imaging* **2013**, *8*, 175–184, DOI: 10.1002/cmimi.1514.
- (180) Corot, C.; Robert, P.; Idée, J.-M.; Port, M. *Adv. Drug Deliv. Rev.* **2006**, *58*, 1471–1504, DOI: 10.1016/j.addr.2006.09.013.
- (181) Maeda, H. *Bioconjug. Chem.* **2010**, *21*, 797–802, DOI: 10.1021/bc100070g.
- (182) Senyei, A.; Widder, K.; Czerlinski, G. *J. Appl. Phys.* **1978**, *49*, 3578–3583, DOI: 10.1063/1.325219.
- (183) Arruebo, M.; Fernández-Pacheco, R.; Ibarra, M. R.; Santamaría, J. *Nano Today* **2007**, *2*, 22–32, DOI: 10.1016/S1748-0132(07)70084-1.
- (184) Widder, K. J.; Senyei, A. E.; Scarpelli, D. G. *Proc. Soc. Exp. Biol. Med.* **1978**, *158*, 141–146, DOI: 10.3181/00379727-158-40158.
- (185) Rosen, J. E.; Chan, L.; Shieh, D. Bin; Gu, F. X. *Nanomedicine Nanotechnology, Biol. Med.* **2012**, *8*, 275–290, DOI: 10.1016/j.nano.2011.08.017.
- (186) Lübbe, A. S.; Bergemann, C.; Riess, H.; Schriever, F.; Reichardt, P.; Possinger, K.; Matthias, M.; Dörken, B.; Herrmann, F.; Gürtler, R.; Hohenberger, P.; Haas, N.; Sohr, R.; Sander, B.; Lemke, A.-J.; Ohlendorf, D.; Huhnt, W.; Huhn, D. *Cancer Res.* **1996**, *56*, 4686–4693.
- (187) Meyers, P. H.; Nice, C. M.; Meckstroth, G. R.; Becker, H. C.; Moser, P. J.; Goldstein, M. *Am. J. Roentgenol.* **1966**, *96*, 913–921, DOI: 10.2214/ajr.96.4.913.
- (188) Dames, P.; Gleich, B.; Flemmer, A.; Hajek, K.; Seidl, N.; Wiekhorst, F.; Eberbeck, D.; Bittmann, I.; Bergemann, C.; Weyh, T.; Trahms, L.; Rosenecker, J.; Rudolph, C. *Nat. Nanotechnol.* **2007**, *2*, 495–499, DOI: 10.1038/nnano.2007.217.
- (189) Shao, D.; Li, J.; Zheng, X.; Pan, Y.; Wang, Z.; Zhang, M.; Chen, Q. X.; Dong, W. F.; Chen, L. *Biomaterials* **2016**, *100*, 118–133, DOI: 10.1016/j.biomaterials.2016.05.030.
- (190) Rosensweig, R. E. *J. Magn. Magn. Mater.* **2002**, *252*, 370–374, DOI: 10.1016/S0304-8853(02)00706-0.
- (191) Carrey, J.; Mehdaoui, B.; Respaud, M. *J. Appl. Phys.* **2011**, *109*, 083921, DOI: 10.1063/1.3551582.
- (192) Amstad, E.; Kohlbrecher, J.; Müller, E.; Schweizer, T.; Textor, M.; Reimhult, E. *Nano Lett.* **2011**, *11*, 1664–1670, DOI: 10.1021/nl2001499.
- (193) Purushotham, S.; Chang, P. E. J.; Rumpel, H.; Kee, I. H. C.; Ng, R. T. H.; Chow, P. K. H.; Tan, C. K.; Ramanujan, R. V. *Nanotechnology* **2009**, *20*, DOI: 10.1088/0957-4484/20/30/305101.

- (194) Cervadoro, A.; Giverso, C.; Pande, R.; Sarangi, S.; Preziosi, L.; Wosik, J.; Brazdeikis, A.; Decuzzi, P. *PLoS One* **2013**, *8*, 1–14, DOI: 10.1371/journal.pone.0057332.
- (195) Rao, W.; Deng, Z.-S.; Liu, J. *Crit. Rev. Biomed. Eng.* **2010**, *38*, 101–116, DOI: 10.1615/CritRevBiomedEng.v38.i1.80.
- (196) Ling, Y.; Tang, X.; Wang, F.; Zhou, X.; Wang, R.; Deng, L.; Shang, T.; Liang, B.; Li, P.; Ran, H.; Wang, Z.; Hu, B.; Li, C.; Zuo, G.; Zheng, Y. *RSC Adv.* **2017**, *7*, 2913–2918, DOI: 10.1039/c6ra20860f.
- (197) Bloch, F. *Phys. Rev.* **1946**, *70*, 460–474, DOI: 10.1103/PhysRev.70.460.
- (198) Bloembergen, N.; Purcell, E. M.; Pound, R. V. *Phys. Rev.* **1948**, *73*, 679–712, DOI: 10.1103/PhysRev.73.679.
- (199) Ohgushi, M.; Nagayama, K.; Wada, A. *J. Magn. Reson.* **1978**, *29*, 599–601, DOI: 10.1016/0022-2364(78)90018-5.
- (200) Taboada, E.; Rodríguez, E.; Roig, A.; Oró, J.; Roch, A.; Muller, R. N. *Langmuir* **2007**, *23*, 4583–4588, DOI: 10.1021/la063415s.
- (201) Zhou, Z.; Bai, R.; Munasinghe, J.; Shen, Z.; Nie, L.; Chen, X. *ACS Nano* **2017**, *11*, 5227–5232, DOI: 10.1021/acsnano.7b03075.
- (202) Peng, Y.-K.; Lui, C. N. P.; Chen, Y.-W.; Chou, S.-W.; Raine, E.; Chou, P.-T.; Yung, K. K. L.; Tsang, S. C. E. *Chem. Mater.* **2017**, *29*, 4411–4417, DOI: 10.1021/acs.chemmater.7b00884.
- (203) Li, Z.; Yi, P. W.; Sun, Q.; Lei, H.; Li Zhao, H.; Zhu, Z. H.; Smith, S. C.; Lan, M. B.; Lu, G. Q. *Adv. Funct. Mater.* **2012**, *22*, 2387–2393, DOI: 10.1002/adfm.201103123.
- (204) Shin, T.-H.; Choi, J.-S.; Yun, S.; Kim, I.-S.; Song, H.-T.; Kim, Y.; Park, K. I.; Cheon, J. *ACS Nano* **2014**, *8*, 3393–3401, DOI: 10.1021/nn405977t.
- (205) Pablico-Lansigan, M. H.; Situ, S. F.; Samia, A. C. S. *Nanoscale* **2013**, *5*, 4040–4055, DOI: 10.1039/c3nr00544e.
- (206) Gleich, B.; Weizenecker, J. *Nature* **2005**, *435*, 1214–1217, DOI: 10.1038/nature03808.
- (207) Shen, Z.; Chen, T.; Ma, X.; Ren, W.; Zhou, Z.; Zhu, G.; Zhang, A.; Liu, Y.; Song, J.; Li, Z.; Ruan, H.; Fan, W.; Lin, L.; Munasinghe, J.; Chen, X.; Wu, A. *ACS Nano* **2017**, *11*, 10992–11004, DOI: 10.1021/acsnano.7b04924.
- (208) Barrow, M.; Taylor, A.; Murray, P.; Rosseinsky, M. J.; Adams, D. J. *Chem. Soc. Rev.* **2015**, *44*, 6733–6748, DOI: 10.1039/c5cs00331h.
- (209) Strobel, K.; Hoerr, V.; Schmid, F.; Wachsmuth, L.; Löffler, B.; Faber, C. *Magn. Reson. Med.* **2012**, *68*, 1924–1931, DOI: 10.1002/mrm.24180.
- (210) Hoerr, V.; Tuchscher, L.; Hüve, J.; Nippe, N.; Loser, K.; Glyvuk, N.; Tsytsyura, Y.; Holtkamp, M.; Sunderkötter, C.; Karst, U.; Klingauf, J.; Peters, G.; Löffler, B.; Faber, C. *BMC Biol.* **2013**, *11*, 1–13, DOI: 10.1186/1741-7007-11-63.
- (211) Arbab, A. S.; Frank, J. A. *Regen. Med.* **2008**, *3*, 199–215, DOI: 10.2217/17460751.3.2.199.
- (212) Choi, J.; Park, J. C.; Nah, H.; Woo, S.; Oh, J.; Kim, K. M.; Cheon, G. J.; Chang, Y.; Yoo, J.; Cheon, J. *Angew. Chemie* **2008**, *120*, 6355–6358, DOI: 10.1002/ange.200801369.
- (213) Jaffer, F. A.; Nahrendorf, M.; Sosnovik, D.; Kelly, K. A.; Aikawa, E.; Weissleder, R. *Mol. Imaging* **2006**, *5*, 85–92, DOI: 10.2310/7290.2006.00009.
- (214) Santra, S.; Kaittanis, C.; Grimm, J.; Perez, J. M. *Small* **2009**, *5*, 1862–1868, DOI: 10.1002/smll.200900389.

- (215) Xu, H.-L.; Mao, K.-L.; Huang, Y.-P.; Yang, J.-J.; Xu, J.; Chen, P.-P.; Fan, Z.-L.; Zou, S.; Gao, Z.-Z.; Yin, J.-Y.; Xiao, J.; Lu, C.-T.; Zhang, B.-L.; Zhao, Y.-Z. *Nanoscale* **2016**, *8*, 14222–14236, DOI: 10.1039/c6nr02448c.
- (216) Shapiro, E. M. *Magn. Reson. Med.* **2015**, *73*, 376–389, DOI: 10.1002/mrm.25263.
- (217) Aryal, S.; Key, J.; Stigliano, C.; Ananta, J. S.; Zhong, M.; Decuzzi, P. *Biomaterials* **2013**, *34*, 7725–7732, DOI: 10.1016/j.biomaterials.2013.07.003.
- (218) Li, K.; Nejadnik, H.; Daldrup-Link, H. E. *Drug Discov. Today* **2017**, *22*, 1421–1429, DOI: 10.1016/j.drudis.2017.04.008.
- (219) Deng, Y.; Ling, J.; Li, M. H. *Nanoscale* **2018**, *10*, 6781–6800, DOI: 10.1039/c8nr00923f.
- (220) Gros, L.; Ringsdorf, H.; Schupp, H. *Angew. Chemie - Int. Ed.* **1981**, *20*, 305–325, DOI: 10.1007/978-1-4615-7643-3_2.
- (221) Cohen Stuart, M. A.; Huck, W. T. S.; Genzer, J.; Müller, M.; Ober, C.; Stamm, M.; Sukhorukov, G. B.; Szleifer, I.; Tsukruk, V. V.; Urban, M.; Winnik, F.; Zauscher, S.; Luzinov, I.; Minko, S. *Nat. Commun.* **2010**, *9*, 101–113, DOI: 10.1038/nmat2614.
- (222) Kabanov, A. V.; Vinogradov, S. V. *Angew. Chemie - Int. Ed.* **2009**, *48*, 5418–5429, DOI: 10.1002/anie.200900441.
- (223) Zhou, Q.; Zhang, L.; Yang, T. H.; Wu, H. *Int. J. Nanomedicine* **2018**, *13*, 2921–2942, DOI: 10.2147/IJN.S158696.
- (224) Discher, D. E.; Ahmed, F. *Annu. Rev. Biomed. Eng.* **2006**, *8*, 323–341, DOI: 10.1146/annurev.bioeng.8.061505.095838.
- (225) Rička, J.; Tanaka, T. *Macromolecules* **1984**, *17*, 2916–2921, DOI: 10.1021/ma00142a081.
- (226) Xu, D.-M.; Yao, S.-D.; Liu, Y.-B.; Sheng, K.-L.; Hong, J.; Gong, P.-J.; Dong, L. *Int. J. Pharm.* **2007**, *338*, 291–296, DOI: 10.1016/j.ijpharm.2007.01.050.
- (227) Varga, I.; Szalai, I.; Mészáros, R.; Gilányi, T. *J. Phys. Chem. B* **2006**, *110*, 20297–20301, DOI: 10.1021/jp064282m.
- (228) Vinogradov, S. V.; Zeman, A. D.; Batrakova, E. V.; Kabanov, A. V. *J. Control. Release* **2005**, *107*, 143–157, DOI: 10.1016/j.jconrel.2005.06.002.
- (229) Lee, H.; Mok, H.; Lee, S.; Oh, Y. K.; Park, T. G. *J. Control. Release* **2007**, *119*, 245–252, DOI: 10.1016/j.jconrel.2007.02.011.
- (230) Jin, W.; Xu, P.; Zhan, Y.; Shen, Y.; Van Kirk, E. A.; Alexander, B.; Murdoch, W. J.; Liu, L.; Isaak, D. D. *Drug Deliv.* **2007**, *14*, 279–286, DOI: 10.1080/10717540601036856.
- (231) Xue, Y.; Xia, X.; Yu, B.; Tao, L.; Wang, Q.; Huang, S.-W.; Yu, F. *ACS Appl. Mater. Interfaces* **2017**, *9*, 30253–30257, DOI: 10.1021/acsami.7b06818.
- (232) Wang, X.; Niu, D.; Li, P.; Wu, Q.; Bo, X.; Liu, B.; Bao, S.; Su, T.; Xu, H.; Wang, Q. *ACS Nano* **2015**, *9*, 5646–5656, DOI: 10.1021/nn5068094.
- (233) Bronich, T. K.; Vinogradov, S. V.; Kabanov, A. V. *Nano Lett.* **2001**, *1*, 535–540, DOI: 10.1021/nl0100365.
- (234) Lee, S. H.; Choi, S. H.; Kim, S. H.; Park, T. G. *J. Control. Release* **2008**, *125*, 25–32, DOI: 10.1016/j.jconrel.2007.09.011.
- (235) Oh, J. K.; Siegwart, D. J.; Lee, H.; Sherwood, G.; Peteanu, L.; Hollinger, J. O.; Kataoka, K.; Matyjaszewski, K. *J. Am. Chem. Soc.* **2007**, *129*, 5939–5945, DOI: 10.1021/ja069150l.

- (236) Tyrrell, Z. L.; Shen, Y.; Radosz, M. *Prog. Polym. Sci.* **2010**, *35*, 1128–1143, DOI: 10.1016/j.progpolymsci.2010.06.003.
- (237) Sutton, D.; Nasongkla, N.; Blanco, E.; Gao, J. *Pharm. Res.* **2007**, *24*, 1029–1046, DOI: 10.1007/s11095-006-9223-y.
- (238) Zhou, Q.; Zhang, Z.; Chen, T.; Guo, X.; Zhou, S. *Colloids Surfaces B Biointerfaces* **2011**, *86*, 45–57, DOI: 10.1016/j.colsurfb.2011.03.013.
- (239) Glover, A. L.; Bennett, J. B.; Pritchett, J. S.; Nikles, S. M.; Nikles, D. E.; Nikles, J. A.; Brazel, C. S. *IEEE Trans. Magn.* **2013**, *49*, 231–235, DOI: 10.1109/TMAG.2012.2222359.
- (240) Beltrán-Gracia, E.; López-Camacho, A.; Higuera-Ciapara, I.; Velázquez-Fernández, J. B.; Vallejo-Cardona, A. A. *Nanomedicine Review: Clinical Developments in Liposomal Applications*; Springer Vienna, 2019; Vol. 10, DOI: 10.1186/s12645-019-0055-y.
- (241) Mai, Y.; Eisenberg, A. *Chem. Soc. Rev.* **2012**, *41*, 5969–5985, DOI: 10.1039/c2cs35115c.
- (242) Leong, J.; Teo, J. Y.; Aakalu, V. K.; Yang, Y. Y.; Kong, H. *Adv. Healthc. Mater.* **2018**, *7*, 1701276, DOI: 10.1002/adhm.201701276.
- (243) Yokoyama, M. *J. Drug Target.* **2014**, *22*, 576–583, DOI: 10.3109/1061186X.2014.934688.
- (244) Le Meins, J.-F.; Schatz, C.; Lecommandoux, S.; Sandre, O. *Mater. Today* **2013**, *16*, 397–402, DOI: 10.1016/j.mattod.2013.09.002.
- (245) Liu, G.-Y.; Chen, C.-J.; Ji, J. *Soft Matter* **2012**, *8*, 8811–8821, DOI: 10.1039/c2sm25721a.
- (246) Rideau, E.; Dimova, R.; Schwille, P.; Wurm, F. R.; Landfester, K. *Chem. Soc. Rev.* **2018**, *47*, 8572–8610, DOI: 10.1039/c8cs00162f.
- (247) van Hest, J. C. M.; Delnoye, D. A. P.; Baars, M. W. P. L.; van Genderen, M. H. P.; Meijer, E. W. *Science (80-.)*. **1995**, *268*, 1592–1595, DOI: 10.1126/science.268.5217.1592.
- (248) Zhang, L.; Eisenberg, A. *Science (80-.)*. **1995**, *268*, 1728–1731, DOI: 10.1126/science.268.5218.1728.
- (249) Chang, H.-Y.; Lin, Y.-L.; Sheng, Y.-J.; Tsao, H.-K. *Macromolecules* **2013**, *46*, 5644–5656, DOI: 10.1021/ma400667n.
- (250) Lin, Y.-L.; Chang, H.-Y.; Sheng, Y.-J.; Tsao, H.-K. *Soft Matter* **2013**, *9*, 4802–4814, DOI: 10.1039/c3sm00051f.
- (251) He, P.; Li, X.; Deng, M.; Chen, T.; Liang, H. *Soft Matter* **2010**, *6*, 1539–1546, DOI: 10.1039/b926370e.
- (252) Hu, X.; Zhang, Y.; Xie, Z.; Jing, X.; Bellotti, A.; Gu, Z. *Biomacromolecules* **2017**, *18*, 649–673, DOI: 10.1021/acs.biomac.6b01704.
- (253) Kauscher, U.; Holme, M. N.; Björnmalm, M.; Stevens, M. M. *Adv. Drug Deliv. Rev.* **2019**, *138*, 259–275, DOI: 10.1016/j.addr.2018.10.012.
- (254) Sanson, C.; Diou, O.; Thévenot, J.; Ibarboure, E.; Soum, A.; Brulet, A.; Miraux, S.; Thiaudière, E.; Tan, S.; Brisson, A.; Dupuis, V.; Sandre, O.; Miraux, S.; Thiaudi, E.; Lecommandoux, S. *ACS Nano* **2011**, *5*, 1122–1140.
- (255) Kania, G.; Kwolek, U.; Nakai, K.; Yusa, S.; Bednar, J.; Wójcik, T.; Chłopicki, S.; Skórka, T.; Szuwarzyński, M.; Szczubiałka, K.; Kepczynski, M.; Nowakowska, M. *J. Mater. Chem. B* **2015**, *3*, 5523–5531, DOI: 10.1039/c5tb00182j.
- (256) Qin, J.; Liu, Q.; Zhang, J.; Chen, J.; Chen, S.; Zhao, Y.; Du, J. *ACS Appl. Mater. Interfaces* **2015**, *7*, 14043–14052, DOI: 10.1021/acsami.5b03222.

- (257) Liu, Q.; Song, L.; Chen, S.; Gao, J.; Zhao, P.; Du, J. *Biomaterials* **2017**, *114*, 23–33, DOI: 10.1016/j.biomaterials.2016.10.027.
- (258) Nasir, A.; Kausar, A.; Younus, A. *Polym. - Plast. Technol. Eng.* **2015**, *54*, 325–341, DOI: 10.1080/03602559.2014.958780.
- (259) Qin, B.; Yin, Z.; Tang, X.; Zhang, S.; Wu, Y.; Xu, J.-F.; Zhang, X. *Prog. Polym. Sci.* **2020**, *100*, 101167, DOI: 10.1016/j.progpolymsci.2019.101167.
- (260) Galindo-Rodriguez, S.; Allémann, E.; Fessi, H.; Doelker, E. *Pharm. Res.* **2004**, *21*, 1428–1439, DOI: 10.1023/B:PHAM.0000036917.75634.be.
- (261) Crucho, C. I. C.; Barros, M. T. *Mater. Sci. Eng. C* **2017**, *80*, 771–784, DOI: 10.1016/j.msec.2017.06.004.
- (262) Lee, J. C. M.; Bermudez, H.; Discher, B. M.; Sheehan, M. A.; Won, Y.-Y.; Bates, F. S.; Discher, D. E. *Biotechnol. Bioeng.* **2001**, *73*, 135–145, DOI: 10.1002/bit.1045.
- (263) Jeong, Y.-I.; Cho, C.-S.; Kim, S.-H.; Ko, K.-S.; Kim, S.-I.; Shim, Y.-H.; Nah, J.-W. *J. Appl. Polym. Sci.* **2001**, *80*, 2228–2236, DOI: 10.1002/app.1326.
- (264) Liu, C.; Hong, C.-Y.; Pan, C.-Y. *Polym. Chem.* **2020**, *11*, 3673–3689, DOI: 10.1039/d0py00455c.
- (265) Rao, J. P.; Geckeler, K. E. *Prog. Polym. Sci.* **2011**, *36*, 887–913, DOI: 10.1016/j.progpolymsci.2011.01.001.
- (266) Hennink, W. E.; van Nostrum, C. F. *Adv. Drug Deliv. Rev.* **2002**, *54*, 13–36, DOI: 10.1016/S0169-409X(01)00240-X.
- (267) Pottanam Chali, S.; Ravoo, B. J. *Angew. Chemie - Int. Ed.* **2020**, *59*, 2962–2972, DOI: 10.1002/anie.201907484.
- (268) Wang, S.; Zhang, S.; Liu, J.; Liu, Z.; Su, L.; Wang, H.; Chang, J. *ACS Appl. Mater. Interfaces* **2014**, *6*, 10706–10713, DOI: 10.1021/am502579e.
- (269) Rolland, J. P.; Maynor, B. W.; Euliss, L. E.; Exner, A. E.; Denison, G. M.; DeSimone, J. M. *J. Am. Chem. Soc.* **2005**, *127*, 10096–10100, DOI: 10.1021/ja051977c.
- (270) Che, H.; Van Hest, J. C. M. *J. Mater. Chem. B* **2016**, *4*, 4632–4647, DOI: 10.1039/c6tb01163b.
- (271) Hickey, R. J.; Haynes, A. S.; Kikkawa, J. M.; Park, S.-J. *J. Am. Chem. Soc.* **2011**, *133*, 1517–1525, DOI: 10.1021/ja1090113.
- (272) Petit, J.; Polenz, I.; Baret, J.-C.; Herminghaus, S.; Bäumchen, O. *Eur. Phys. J. E* **2016**, *39*, 1–6, DOI: 10.1140/epje/i2016-16059-8.
- (273) Poschenrieder, S. T.; Hanzlik, M.; Castiglione, K. *J. Appl. Polym. Sci.* **2018**, *135*, 46077, DOI: 10.1002/app.46077.
- (274) Wang, X.; Niu, D.; Wu, Q.; Bao, S.; Su, T.; Liu, X.; Zhang, S.; Wang, Q. *Biomaterials* **2015**, *53*, 349–357, DOI: 10.1016/j.biomaterials.2015.02.101.
- (275) Ge, J.; Hu, Y.; Biasini, M.; Beyermann, W. P.; Yin, Y. *Angew. Chemie - Int. Ed.* **2007**, *46*, 4342–4345, DOI: 10.1002/anie.200700197.
- (276) Lecommandoux, S.; Sandre, O.; Chécot, F.; Rodriguez-Hernandez, J.; Perzynski, R. *Adv. Mater.* **2005**, *17*, 712–718, DOI: 10.1002/adma.200400599.
- (277) Vauthier, C.; Bouchemal, K. *Pharm. Res.* **2009**, *26*, 1025–1058, DOI: 10.1007/s11095-008-9800-3.
- (278) Hu, S. H.; Liu, D. M.; Tung, W. L.; Liao, C. F.; Chen, S. Y. *Adv. Funct. Mater.* **2008**, *18*, 2946–2955, DOI:

10.1002/adfm.200800428.

- (279) Kocbek, P.; Kralj, S.; Kreft, E. M.; Kristl, J. *Eur. J. Pharm. Sci.* **2013**, *50*, 130–138, DOI: 10.1016/j.ejps.2013.04.004.
- (280) Fang, J. H.; Lai, Y. H.; Chiu, T. L.; Chen, Y. Y.; Hu, S. H.; Chen, S. Y. *Adv. Healthc. Mater.* **2014**, *3*, 1250–1260, DOI: 10.1002/adhm.201300598.
- (281) Oliveira, H.; Pérez-Andrés, E.; Thevenot, J.; Sandre, O.; Berra, E.; Lecommandoux, S. *J. Control. Release* **2013**, *169*, 165–170, DOI: 10.1016/j.jconrel.2013.01.013.
- (282) Carregal-Romero, S.; Guardia, P.; Yu, X.; Hartmann, R.; Pellegrino, T.; Parak, W. J. *Nanoscale* **2015**, *7*, 570–576, DOI: 10.1039/C4NR04055D.
- (283) Yang, X.; Chen, Y.; Yuan, R.; Chen, G.; Blanco, E.; Gao, J.; Shuai, X. *Polymer (Guildf)*. **2008**, *49*, 3477–3485, DOI: 10.1016/j.polymer.2008.06.005.
- (284) Yoon, H. Y.; Saravanakumar, G.; Heo, R.; Choi, S. H.; Song, I. C.; Han, M. H.; Kim, K.; Park, J. H.; Choi, K.; Kwon, I. C.; Park, K. *J. Control. Release* **2012**, *160*, 692–698, DOI: 10.1016/j.jconrel.2012.04.012.
- (285) Hu, S. H.; Liao, B. J.; Chiang, C. S.; Chen, P. J.; Chen, I. W.; Chen, S. Y. *Adv. Mater.* **2012**, *24*, 3627–3632, DOI: 10.1002/adma.201201251.
- (286) Vinogradov, S. V.; Batrakova, E. V.; Kabanov, A. V. *Bioconjug. Chem.* **2004**, *15*, 50–60, DOI: 10.1021/bc034164r.
- (287) Feng, L.; Liu, L.; Lv, F.; Bazan, G. C.; Wang, S. *Adv. Mater.* **2014**, *26*, 3926–3930, DOI: 10.1002/adma.201305206.
- (288) Hole, P.; Sillence, K.; Hannell, C.; Maguire, C. M.; Roesslein, M.; Suarez, G.; Capracotta, S.; Magdolenova, Z.; Horev-Azaria, L.; Dybowska, A.; Cooke, L.; Haase, A.; Contal, S.; Manø, S.; Vennemann, A.; Sauvain, J. J.; Staunton, K. C.; Anguissola, S.; Luch, A.; Dusinska, M.; Korenstein, R.; Gutleb, A. C.; Wiemann, M.; Prina-Mello, A.; Riediker, M.; Wick, P. *J. Nanoparticle Res.* **2013**, *15*, 2101, DOI: 10.1007/s11051-013-2101-8.
- (289) Kaszuba, M.; McKnight, D.; Connah, M. T.; McNeil-Watson, F. K.; Nobbmann, U. *J. Nanoparticle Res.* **2008**, *10*, 823–829, DOI: 10.1007/s11051-007-9317-4.
- (290) Jarzębski, M.; Bellich, B.; Białopiotrowicz, T.; Śliwa, T.; Kościński, J.; Cesàro, A. *Food Hydrocoll.* **2017**, *68*, 90–101, DOI: 10.1016/j.foodhyd.2016.09.037.
- (291) Stetefeld, J.; McKenna, S. A.; Patel, T. R. *Biophys. Rev.* **2016**, *8*, 409–427, DOI: 10.1007/s12551-016-0218-6.
- (292) Filipe, V.; Hawe, A.; Jiskoot, W. *Pharm. Res.* **2010**, *27*, 796–810, DOI: 10.1007/s11095-010-0073-2.
- (293) Palomba, R.; Palange, A. L.; Rizzuti, I. F.; Ferreira, M.; Cervadoro, A.; Barbato, M. G.; Canale, C.; Decuzzi, P. *ACS Nano* **2018**, *12*, 1433–1444, DOI: 10.1021/acsnano.7b07797.
- (294) Liu, X.; Kaminski, M. D.; Chen, H.; Torno, M.; Taylor, L.; Rosengart, A. J. *J. Control. Release* **2007**, *119*, 52–58, DOI: 10.1016/j.jconrel.2006.11.031.
- (295) Vijayan, V. M.; Beeran, A. E.; Shenoy, S. J.; Muthu, J.; Thomas, V. *ACS Appl. Bio Mater.* **2019**, *2*, 757–768, DOI: 10.1021/acsbm.8b00616.
- (296) Yang, H. Y.; Jang, M. S.; Li, Y.; Lee, J. H.; Lee, D. S. *ACS Appl. Mater. Interfaces* **2017**, *9*, 19184–19192, DOI: 10.1021/acsbm.7b03747.
- (297) Jain, T. K.; Reddy, M. K.; Morales, M. A.; Leslie-Pelecky, D. L.; Labhasetwar, V. *Mol. Pharm.* **2008**, *5*, 316–327, DOI: 10.1021/mp7001285.

- (298) Ignjatović, A.; Stević, Z.; Lavrnić, S.; Daković, M.; Bačić, G. *J. Magn. Reson. Imaging* **2013**, *38*, 1472–1479, DOI: 10.1002/jmri.24121.
- (299) Meadowcroft, M. D.; Mutic, N. J.; Bigler, D. C.; Wang, J.; Simmons, Z.; Connor, J. R.; Yang, Q. X. *J. Magn. Reson. Imaging* **2015**, *41*, 665–675, DOI: 10.1002/jmri.24582.
- (300) Distaso, E.; Milella, G.; Mezzapesa, D. M.; Introna, A.; D’Errico, E.; Fraddosio, A.; Zoccolella, S.; Dicuonzo, F.; Simone, I. L. *J. Neurol.* **2021**, DOI: 10.1007/s00415-021-10495-9.
- (301) FDA. Rilutek (Riluzole) - FDA Approval
<https://www.accessdata.fda.gov/scripts/cder/daf/index.cfm?event=overview.process&ApplNo=020599>.
- (302) Miller, R. G.; Mitchell, J. D.; Moore, D. H. *Riluzole for Amyotrophic Lateral Sclerosis (ALS)/Motor Neuron Disease (MND)*; 2012, DOI: 10.1002/14651858.CD001447.pub3.
- (303) Barrow, M.; Taylor, A.; Fuentes-Caparrós, A. M.; Sharkey, J.; Daniels, L. M.; Mandal, P.; Park, B. K.; Murray, P.; Rosseinsky, M. J.; Adams, D. J. *Biomater. Sci.* **2018**, *6*, 101–106, DOI: 10.1039/C7BM00515F.
- (304) Krishnan, K. M. *IEEE Trans. Magn.* **2010**, *46*, 2523–2558, DOI: 10.1109/TMAG.2010.2046907.
- (305) Kim, B. Y. S.; Rutka, J. T.; Chan, W. C. W. *N. Engl. J. Med.* **2010**, No. 363, 2434–2443, DOI: 10.1056/NEJMra0912273.
- (306) Lux, J.; Sherry, A. D. *Curr. Opin. Chem. Biol.* **2018**, *45*, 121–130, DOI: 10.1016/j.cbpa.2018.04.006.
- (307) Coriasco, M.; Rampado, O.; Bradac, G. B. *Elementi Di Risonanza Magnetica - Dal Protone Alle Sequenze per Le Principali Applicazioni Diagnostiche*, 1st ed.; Springer-Verlag Italia: Milano, 2014, DOI: 10.1007/978-88-470-5641-1.
- (308) Shin, T.; Choi, Y.; Kim, S.; Cheon, J. *Chem. Soc. Rev.* **2015**, *44*, 4501–4516, DOI: 10.1039/C4CS00345D.
- (309) Kim, B. H.; Lee, N.; Kim, H.; An, K.; Park, Y. Il; Choi, Y.; Shin, K.; Lee, Y.; Kwon, S. G.; Na, H. Bin; Park, J.-G.; Ahn, T.-Y.; Kim, Y.-W.; Moon, W. K.; Choi, S. H.; Hyeon, T. *J. Am. Chem. Soc.* **2011**, *133*, 12624–12631, DOI: 10.1021/ja203340u.
- (310) Roch, A.; Muller, R. N.; Gillis, P. *J. Chem. Phys.* **1999**, *110*, 5403–5411, DOI: 10.1063/1.478435.
- (311) Singh, N.; Jenkins, G. J. S.; Asadi, R.; Doak, S. H. *Nano Rev.* **2010**, *1*, 5358, DOI: 10.3402/nano.v1i0.5358.
- (312) Hong, R. Y.; Li, J. H.; Li, H. Z.; Ding, J.; Zheng, Y.; Wei, D. G. *J. Magn. Magn. Mater.* **2008**, *320*, 1605–1614, DOI: 10.1016/j.jmmm.2008.01.015.
- (313) Osborne, E. A.; Atkins, T. M.; Gilbert, D. A.; Kauzlarich, S. M.; Liu, K.; Louie, A. Y. *Nanotechnology* **2012**, *23*, 215602–215610, DOI: 10.1088/0957-4484/23/21/215602.
- (314) Sun, S.; Zeng, H.; Robinson, D. B.; Raoux, S.; Rice, P. M.; Wang, S. X.; Li, G. *J. Am. Chem. Soc.* **2004**, *126*, 273–279, DOI: 10.1021/ja0380852.
- (315) Xu, Z.; Shen, C.; Hou, Y.; Gao, H.; Sun, S. *Chem. Mater.* **2009**, *21*, 1778–1780, DOI: 10.1021/cm802978z.
- (316) Roca, A. G.; Morales, M. P.; Serna, C. J. *IEEE Trans. Magn.* **2006**, *42*, 3025–3029, DOI: 10.1109/TMAG.2006.880111.
- (317) Liu, X.; Kaminski, M. D.; Guan, Y.; Chen, H.; Liu, H.; Rosengart, A. J. *J. Magn. Magn. Mater.* **2006**, *306*, 248–253, DOI: 10.1016/j.jmmm.2006.03.049.
- (318) Bronstein, L. M.; Huang, X.; Retrum, J.; Schmucker, A.; Pink, M.; Stein, B. D.; Dragnea, B. *Chem.*

Mater. **2007**, *19*, 3624–3632, DOI: 10.1021/cm062948j.

- (319) Effenberger, F. B.; Couto, R. A.; Kiyohara, P. K.; Machado, G.; Masunaga, S. H.; Jardim, R. F.; Rossi, L. M. *Nanotechnology* **2017**, *28*, 115603, DOI: 10.1088/1361-6528/aa5ab0.
- (320) Schütz, M. B.; Xiao, L.; Lehnen, T.; Fischer, T.; Mathur, S. *Int. Mater. Rev.* **2018**, *63*, 341–374, DOI: 10.1080/09506608.2017.1402158.
- (321) Kuzmin, A.; Chaboy, J. *Int. Union Crystallogr. J.* **2014**, *1*, 571–589, DOI: 10.1107/S2052252514021101.
- (322) Yang, K.; Peng, H.; Wen, Y.; Li, N. *Appl. Surf. Sci.* **2010**, *256*, 3093–3097, DOI: 10.1016/j.apsusc.2009.11.079.
- (323) Shen, L.; Laibinis, P. E.; Alan Hatton, T. *Langmuir* **1999**, *15*, 447–453, DOI: 10.1021/la9807661.
- (324) Ayyappan, S.; Gnanaprakash, G.; Panneerselvam, G.; Antony, M. P.; Philip, J. J. *Phys. Chem. C* **2008**, *112*, 18376–18383, DOI: 10.1021/jp8052899.
- (325) Bao, Y.; Sherwood, J. A.; Sun, Z. *J. Mater. Chem. C* **2018**, *6*, 1280–1290, DOI: 10.1039/c7tc05854c.
- (326) Zuluaga-Parra, J. D.; Sánchez-Valdés, S.; Ramos-deValle, L. F.; Beltrán-Ramírez, F. I.; Da-Silva, L.; Ramírez-Vargas, E.; Vázquez-Rodríguez, S.; Flores-Gallardo, S.; Méndez-Nonell, J.; Valera-Zaragoza, M.; Cabrera-Álvarez, E. N. *J. Magn. Magn. Mater.* **2020**, *514*, 167169, DOI: 10.1016/j.jmmm.2020.167169.
- (327) Wei, H.; Bruns, O. T.; Kaul, M. G.; Hansen, E. C.; Barch, M.; Wiśniowska, A.; Chen, O.; Chen, Y.; Li, N.; Okada, S.; Cordero, J. M.; Heine, M.; Farrar, C. T.; Montana, D. M.; Adam, G.; Ittrich, H.; Jasanoff, A.; Nielsen, P.; Bawendi, M. G. *Proc. Natl. Acad. Sci. U. S. A.* **2017**, *114*, 2325–2330, DOI: 10.1073/pnas.1620145114.
- (328) Vanderhoff, J. W.; El-Aassar, M. S.; Ugelstad, J. Polymer Emulsification Process. US 4177177, 1979.
- (329) Anton, N.; Benoit, J. P.; Saulnier, P. *J. Control. Release* **2008**, *128*, 185–199, DOI: 10.1016/j.jconrel.2008.02.007.
- (330) Bilati, U.; Allémann, E.; Doelker, E. *Pharm. Dev. Technol.* **2003**, *8*, 1–9, DOI: 10.1081/PDT-120017517.
- (331) Louisnard, O.; González-García, J. Acoustic Cavitation. In *Ultrasound Technologies for Food and Bioprocessing*; Feng, H., Barbosa-Canovas, G., Weiss, J., Eds.; Springer, New York, NY: New York, NY, 2011; pp 13–64, DOI: 10.1007/978-1-4419-7472-3_2.
- (332) Shuai, X.; Ai, H.; Nasongkla, N.; Kim, S.; Gao, J. *J. Control. Release* **2004**, *98*, 415–426, DOI: 10.1016/j.jconrel.2004.06.003.
- (333) Huang, H. Y.; Hu, S. H.; Hung, S. Y.; Chiang, C. S.; Liu, H. L.; Chiu, T. L.; Lai, H. Y.; Chen, Y. Y.; Chen, S. Y. *J. Control. Release* **2013**, *172*, 118–127, DOI: 10.1016/j.jconrel.2013.07.029.
- (334) Batrakova, E. V.; Kabanov, A. V. *J. Control. Release* **2008**, *130*, 98–106, DOI: 10.1016/j.jconrel.2008.04.013.
- (335) Chatterjee, S.; Hui, P. C.; Kan, C.; Wang, W. *Sci. Rep.* **2019**, *9*, 11658, DOI: 10.1038/s41598-019-48254-6.
- (336) Alexandridis, P.; Alan Hatton, T. *Colloids Surfaces A Physicochem. Eng. Asp.* **1995**, *96*, 1–46, DOI: 10.1016/0927-7757(94)03028-X.
- (337) Ma, W.-D.; Xu, H.; Wang, C.; Nie, S.-F.; Pan, W.-S. *Int. J. Pharm.* **2008**, *350*, 247–256, DOI: 10.1016/j.ijpharm.2007.09.005.
- (338) Chun, K. W.; Lee, J. B.; Kim, S. H.; Park, T. G. *Biomaterials* **2005**, *26*, 3319–3326, DOI:

10.1016/j.biomaterials.2004.07.055.

- (339) Huang, H.-Y.; Hu, S.-H.; Chian, C.-S.; Chen, S.-Y.; Lai, H.-Y.; Chen, Y.-Y. *J. Mater. Chem.* **2012**, *22*, 8566–8573, DOI: 10.1039/c2jm00032f.
- (340) El-Aassar, M. R.; El fawal, G. F.; El-Deeb, N. M.; Hassan, H. S.; Mo, X. *Appl. Biochem. Biotechnol.* **2016**, *178*, 1488–1502, DOI: 10.1007/s12010-015-1962-y.
- (341) Kurchania, R.; Sawant, S. S.; Ball, R. J. *J. Am. Ceram. Soc.* **2014**, *97*, 3208–3215, DOI: 10.1111/jace.13108.
- (342) Ramírez, L. P.; Landfester, K. *Macromol. Chem. Phys.* **2003**, *204*, 22–31, DOI: 10.1002/macp.200290052.
- (343) Nabi, B.; Rehman, S.; Fazil, M.; Khan, S.; Baboota, S.; Ali, J. *Drug Dev. Ind. Pharm.* **2020**, *46*, 471–483, DOI: 10.1080/03639045.2020.1730396.
- (344) Raju, K. N.; Sunitha, T.; Babu, I. S. *Int. J. Appl. Pharm.* **2014**, *6*, 4–5, DOI: 10.22159/ijap.2014v6i3.3750\.
- (345) Storch, A.; Burkhardt, K.; Ludolph, A. C.; Schwarz, J. *J. Neurochem.* **2000**, *75*, 2259–2269, DOI: 10.1046/j.1471-4159.2000.0752259.x.
- (346) Bryson, H. M.; Fulton, B.; Benfield, P. *Drugs* **1996**, *52*, 549–563, DOI: 10.2165/00003495-199652040-00010.
- (347) Ding, X.; Li, D.; Jiang, J. *Theranostics* **2020**, *10*, 8061–8079, DOI: 10.7150/thno.42284.
- (348) Dreaden, E. C.; Alkilany, A. M.; Huang, X.; Murphy, C. J.; El-Sayed, M. A. *Chem. Soc. Rev.* **2012**, *41*, 2740–2779, DOI: 10.1039/c1cs15237h.
- (349) Daniel, M.-C.; Astruc, D. *Chem. Rev.* **2004**, *104*, 293–346, DOI: 10.1021/cr030698.
- (350) Cole, L. E.; Ross, R. D.; Tilley, J. M. R.; Vargo-Gogola, T.; Roeder, R. K. *Nanomedicine* **2015**, *10*, 321–341, DOI: 10.2217/nnm.14.171.
- (351) Zhao, T.; Li, L.; Li, S.; Jiang, X.-F.; Jiang, C.; Zhou, N.; Gao, N.; Xu, Q.-H. *J. Mater. Chem. C* **2019**, *7*, 14693–14700, DOI: 10.1039/c9tc04429a.
- (352) Yeh, Y.-C.; Creran, B.; Rotello, V. M. *Nanoscale* **2012**, *4*, 1871–1880, DOI: 10.1039/c1nr11188d.
- (353) Thorat, N. D.; Tofail, S. A. M.; Von Rechenberg, B.; Townley, H.; Brennan, G.; Silien, C.; Yadav, H. M.; Steffen, T.; Bauer, J. *Appl. Phys. Rev.* **2019**, *6*, DOI: 10.1063/1.5049467.
- (354) Ghosh, P.; Han, G.; De, M.; Kim, C. K.; Rotello, V. M. *Adv. Drug Deliv. Rev.* **2008**, *60*, 1307–1315, DOI: 10.1016/j.addr.2008.03.016.
- (355) Xia, Y.; Li, W.; Cobley, C. M.; Chen, J.; Xia, X.; Zhang, Q.; Yang, M.; Cho, E. C.; Brown, P. K. *Acc. Chem. Res.* **2011**, *44*, 914–924, DOI: 10.1021/ar200061q.
- (356) Qian, X.; Peng, X.-H.; Ansari, D. O.; Yin-Goen, Q.; Chen, G. Z.; Shin, D. M.; Yang, L.; Young, A. N.; Wang, M. D.; Nie, S. *Nat. Biotechnol.* **2008**, *26*, 83–90, DOI: 10.1038/nbt1377.
- (357) Kim, C. S.; Wilder-Smith, P.; Ahn, Y.-C.; Liaw, L.-H. L.; Chen, Z.; Kwon, Y. J. *J. Biomed. Opt.* **2009**, *14*, 034008, DOI: 10.1117/1.3130323.
- (358) Nam, J.-M.; Park, S.-J.; Mirkin, C. A. *J. Am. Chem. Soc.* **2002**, *124*, 3820–3821, DOI: 10.1021/ja0178766.
- (359) Maiti, S.; Prins, L. J. *Tetrahedron* **2017**, *73*, 4950–4954, DOI: 10.1016/j.tet.2017.05.028.
- (360) Salvia, M.-V.; Ramadori, F.; Springhetti, S.; Diez-Castellnou, M.; Perrone, B.; Rastrelli, F.; Mancin, F. J.

Am. Chem. Soc. **2015**, *137*, 886–892, DOI: 10.1021/ja511205e.

- (361) Libutti, S. K.; Paciotti, G. F.; Byrnes, A. A.; Alexander, H. R.; Gannon, W. E.; Walker, M.; Seidel, G. D.; Yuldasheva, N.; Tamarkin, L. *Clin. Cancer Res.* **2010**, *16*, 6139–6149, DOI: 10.1158/1078-0432.CCR-10-0978.
- (362) Rastinehad, A. R.; Anastos, H.; Wajswol, E.; Winoker, J. S.; Sfakianos, J. P.; Doppalapudi, S. K.; Carrick, M. R.; Knauer, C. J.; Taouli, B.; Lewis, S. C.; Tewari, A. K.; Schwartz, J. A.; Canfield, S. E.; George, A. K.; West, J. L.; Halas, N. J. *Proc. Natl. Acad. Sci. U. S. A.* **2019**, *116*, 18590–18596, DOI: 10.1073/pnas.1906929116.
- (363) Kharlamov, A. N.; Tyurnina, A. E.; Veselova, V. S.; Kovtun, O. P.; Shur, V. Y.; Gabinsky, J. L. *Nanoscale* **2015**, *7*, 8003–8015, DOI: 10.1039/c5nr01050k.
- (364) Anselmo, A. C.; Mitragotri, S. *Bioeng. Transl. Med.* **2019**, *4*, e10143, DOI: 10.1002/btm2.10143.
- (365) Chen, P. C.; Mwakwari, S. C.; Oyelere, A. K. *Nanotechnol. Sci. Appl.* **2008**, *1*, 45–66, DOI: 10.2147/nsa.s3707.
- (366) Shenoi, M. M.; Iltis, I.; Choi, J.; Koonce, N. A.; Metzger, G. J.; Griffin, R. J.; Bischof, J. C. *Mol. Pharm.* **2013**, *10*, 1683–1694, DOI: 10.1021/mp300505w.
- (367) Mao, W.; Son, Y. J.; Yoo, H. S. *Nanoscale* **2020**, *12*, 14996–15020, DOI: 10.1039/d0nr01690j.
- (368) Pensa, E.; Cortés, E.; Corthey, G.; Carro, P.; Vericat, C.; Fonticelli, M. H.; Benítez, G.; Rubert, A. A.; Salvarezza, R. C. *Acc. Chem. Res.* **2012**, *45*, 1183–1192, DOI: 10.1021/ar200260p.
- (369) Love, J. C.; Estroff, L. A.; Kriebel, J. K.; Nuzzo, R. G.; Whitesides, G. M. *Chem. Rev.* **2005**, *105*, 1103–1169, DOI: 10.1021/cr0300789.
- (370) Faraday, M. *Philos. Trans. R. Soc. London* **1857**, *147*, 145–181, DOI: 10.1098/rstl.1857.0011.
- (371) Turkevich, J.; Stevenson, P. C.; Hillier, J. *Discuss. Faraday Soc.* **1951**, *11*, 55–75, DOI: 10.1039/DF9511100055.
- (372) Frens, G. *Nat. Phys. Sci.* **1973**, *241*, 20–22, DOI: 10.1038/246421a0.
- (373) Gao, Y.; Torrente-Murciano, L. *Nanoscale* **2020**, *12*, 2740–2751, DOI: 10.1039/c9nr08877f.
- (374) Slot, J. W.; Geuze, H. J. *J. Cell Biol.* **1981**, *90*, 533–536, DOI: 10.1083/jcb.90.2.533.
- (375) Hostetler, M. J.; Wingate, J. E.; Zhong, C.-J.; Harris, J. E.; Vachet, R. W.; Clark, M. R.; Londono, J. D.; Green, S. J.; Stokes, J. J.; Wignall, G. D.; Glish, G. L.; Porter, M. D.; Evans, N. D.; Murray, R. W. *Langmuir* **1998**, *14*, 17–30, DOI: 10.1021/la970588w.
- (376) Giersig, M.; Mulvaney, P. *Langmuir* **1993**, *9*, 3408–3413, DOI: 10.1021/la00036a014.
- (377) Brust, M.; Walker, M.; Bethell, D.; Schiffrin, D. J.; Whyman, R. *J. Chem. Soc. Chem. Commun.* **1994**, 801–802, DOI: 10.1039/C39940000801.
- (378) Li, Y.; Zaluzhna, O.; Xu, B.; Gao, Y.; Modest, J. M.; Tong, Y. Y. *J. Am. Chem. Soc.* **2011**, *133*, 2092–2095, DOI: 10.1021/ja1105078.
- (379) Wuelfing, W. P.; Gross, S. M.; Miles, D. T.; Murray, R. W. *J. Am. Chem. Soc.* **1998**, *120*, 12696–12697, DOI: 10.1021/ja983183m.
- (380) Higuchi, M.; Ushiba, K.; Kawaguchi, M. *J. Colloid Interface Sci.* **2007**, *308*, 356–363, DOI: 10.1016/j.jcis.2006.12.069.
- (381) Schaaff, T. G.; Knight, G.; Shafiqullin, M. N.; Borkman, R. F.; Whetten, R. L. *J. Phys. Chem. B* **1998**, *102*, 10643–10646, DOI: 10.1021/jp9830528.

- (382) Jung, J.; Park, S.; Hong, S.; Ha, M. W.; Park, H.; Park, Y.; Lee, H.-J.; Park, Y. *Carbohydr. Res.* **2014**, *386*, 57–61, DOI: 10.1016/j.carres.2013.12.012.
- (383) Zheng, M.; Davidson, F.; Huang, X. *J. Am. Chem. Soc.* **2003**, *125*, 7790–7791, DOI: 10.1021/ja0350278.
- (384) Pengo, P.; Polizzi, S.; Battagliarin, M.; Pasquato, L.; Scrimin, P. *J. Mater. Chem.* **2003**, *13*, 2471–2478, DOI: 10.1039/b306366f.
- (385) Ingram, R. S.; Hostetler, M. J.; Murray, R. W. *J. Am. Chem. Soc.* **1997**, *119*, 9175–9178, DOI: 10.1021/ja971734n.
- (386) Boselli, L.; Polo, E.; Castagnola, V.; Dawson, K. A. *Angew. Chemie - Int. Ed.* **2017**, *56*, 4215–4218, DOI: 10.1002/anie.201700343.
- (387) Nicol, J. R.; Dixon, D.; Coulter, J. A. Gold Nanoparticle Surface Functionalization: A Necessary Requirement in the Development of Novel Nanotherapeutics. *Nanomedicine*. 2015, pp 1315–1326, DOI: 10.2217/nnm.14.219.
- (388) Hostetler, M. J.; Green, S. J.; Stokes, J. J.; Murray, R. W. *J. Am. Chem. Soc.* **1996**, *118*, 4212–4213, DOI: 10.1021/ja960198g.
- (389) Donkers, R. L.; Song, Y.; Murray, R. W. *Langmuir* **2004**, *20*, 4703–4707, DOI: 10.1021/la0497494.
- (390) Häkkinen, H.; Barnett, R. N.; Landman, U. *Phys. Rev. Lett.* **1999**, *82*, 3264–3267, DOI: 10.1103/PhysRevLett.82.3264.
- (391) Luedtke, W. D.; Landman, U. *J. Phys. Chem. B* **1998**, *102*, 6566–6572, DOI: 10.1021/jp981745i.
- (392) Xu, X.; Rosi, N. L.; Wang, Y.; Huo, F.; Mirkin, C. A. *J. Am. Chem. Soc.* **2006**, *128*, 9286–9287, DOI: 10.1021/ja061980b.
- (393) Shan, J.; Tenhu, H. *Chem. Commun.* **2007**, No. 44, 4580–4598, DOI: 10.1039/B707740H.
- (394) Kim, H. S.; Son, Y. J.; Mao, W.; Leong, K. W.; Yoo, H. S. *Nano Lett.* **2018**, *18*, 314–325, DOI: 10.1021/acs.nanolett.7b04183.
- (395) Hühn, J.; Carrillo-Carrion, C.; Soliman, M. G.; Pfeiffer, C.; Valdeperez, D.; Masood, A.; Chakraborty, I.; Zhu, L.; Gallego, M.; Yue, Z.; Carril, M.; Feliu, N.; Escudero, A.; Alkilany, A. M.; Pelaz, B.; Pino, P. Del; Parak, W. J. *Chem. Mater.* **2017**, *29*, 399–461, DOI: 10.1021/acs.chemmater.6b04738.
- (396) Novak, J. P.; Nickerson, C.; Franzen, S.; Feldheim, D. L. *Anal. Chem.* **2001**, *73*, 5758–5761, DOI: 10.1021/ac010812t.
- (397) Parak, W. J.; Pellegrino, T.; Micheel, C. M.; Gerion, D.; Williams, S. C.; Alivisatos, A. P. *Nano Lett.* **2003**, *3*, 33–36, DOI: 10.1021/nl025888z.
- (398) Ong, Q.; Luo, Z.; Stellacci, F. *Acc. Chem. Res.* **2017**, *50*, 1911–1919, DOI: 10.1021/acs.accounts.7b00165.
- (399) Jadzinsky, P. D.; Calero, G.; Ackerson, C. J.; Bushnell, D. A.; Kornberg, R. D. *Science (80-.)*. **2007**, *318*, 430–433, DOI: 10.1126/science.1148624.
- (400) Zeng, C.; Chen, Y.; Kirschbaum, K.; Appavoo, K.; Sfeir, M. Y.; Jin, R. *Sci. Adv.* **2015**, *1*, e1500045, DOI: 10.1126/sciadv.1500045.
- (401) Luo, K.; Hu, C.; Luo, Y.; Li, D.; Xiang, Y.; Mu, Y.; Wang, H.; Luo, Z. *RSC Adv.* **2017**, *7*, 51605–51611, DOI: 10.1039/c7ra10323a.
- (402) Mie, G. *Ann. Phys.* **1908**, *330*, 377–445.

- (403) Link, S.; El-Sayed, M. A. *Shape and Size Dependence of Radiative, Non-Radiative and Photothermal Properties of Gold Nanocrystals*; 2000; Vol. 19, DOI: 10.1080/01442350050034180.
- (404) Njoki, P. N.; Lim, I. I. S.; Mott, D.; Park, H. Y.; Khan, B.; Mishra, S.; Sujakumar, R.; Luo, J.; Zhong, C. J. *J. Phys. Chem. C* **2007**, *111*, 14664–14669, DOI: 10.1021/jp074902z.
- (405) Lévy, R.; Thanh, N. T. K.; Christopher Doty, R.; Hussain, I.; Nichols, R. J.; Schiffrin, D. J.; Brust, M.; Fernig, D. G. *J. Am. Chem. Soc.* **2004**, *126*, 10076–10084, DOI: 10.1021/ja0487269.
- (406) Marbella, L. E.; Millstone, J. E. *Chem. Mater.* **2015**, *27*, 2721–2739, DOI: 10.1021/cm504809c.
- (407) Morris, K. F.; Johnson Jr., C. S. *J. Am. Chem. Soc.* **1993**, *115*, 4291–4299, DOI: 10.1021/ja00063a053.
- (408) Modena, M. M.; Rühle, B.; Burg, T. P.; Wuttke, S. *Adv. Mater.* **2019**, *31*, 1901556, DOI: 10.1002/adma.201901556.
- (409) Hinterwirth, H.; Kappel, S.; Waitz, T.; Prohaska, T.; Lindner, W.; Lämmerhofer, M. *ACS Nano* **2013**, *7*, 1129–1136, DOI: 10.1021/nn306024a.
- (410) Jackson, A. M.; Myerson, J. W.; Stellacci, F. *Nat. Mater.* **2004**, *3*, 330–336, DOI: 10.1038/nmat1116.
- (411) Biscarini, F.; Ong, Q. K.; Albonetti, C.; Liscio, F.; Longobardi, M.; Mali, K. S.; Ciesielski, A.; Reguera, J.; Renner, C.; De Feyter, S.; Samorì, P.; Stellacci, F. *Langmuir* **2013**, *29*, 13723–13734, DOI: 10.1021/la403546c.
- (412) Liu, X.; Yu, M.; Kim, H.; Mamei, M.; Stellacci, F. *Nat. Commun.* **2012**, *3*, 1182, DOI: 10.1038/ncomms2155.
- (413) Şologan, M.; Marson, D.; Polizzi, S.; Pengo, P.; Boccardo, S.; Pricl, S.; Posocco, P.; Pasquato, L. *ACS Nano* **2016**, *10*, 9316–9325, DOI: 10.1021/acsnano.6b03931.
- (414) Pradhan, S.; Brown, L. E.; Konopelski, J. P.; Chen, S. *J. Nanoparticle Res.* **2009**, *11*, 1895–1903, DOI: 10.1007/s11051-008-9543-4.
- (415) Harkness, K. M.; Balinski, A.; McLean, J. A.; Cliffel, D. E. *Angew. Chemie - Int. Ed.* **2011**, *50*, 10554–10559, DOI: 10.1002/anie.201102882.
- (416) Pradhan, S.; Xu, L.-P.; Chen, S. *Adv. Funct. Mater.* **2007**, *17*, 2385–2392, DOI: 10.1002/adfm.200601034.
- (417) Banks, R. E.; Smart, B. E.; Tatlow, J. C. *Organofluorine Chemistry: Principles and Commercial Applications*, 1st ed.; Banks, R. E., Smart, B. E., Tatlow, J. C., Eds.; Springer Science+Business Media: New York, 1994.
- (418) Dolbier Jr., W. R. *J. Fluor. Chem.* **2005**, *126*, 157–163, DOI: 10.1016/j.jfluchem.2004.09.033.
- (419) Buck, R. C.; Franklin, J.; Berger, U.; Conder, J. M.; Cousins, I. T.; de Voogt, P.; Jensen, A. A.; Kannan, K.; Mabury, S. A.; van Leeuwen, S. P. J. *Integr. Environ. Assess. Manag.* **2011**, *7*, 513–541, DOI: 10.1002/ieam.258.
- (420) Kissa, E. *Fluorinated Surfactants and Repellents*, 2nd ed.; Marcel Dekker, Inc.: New York, 2001.
- (421) Tiddy, G. J. T. *Concentrated Surfactant Systems*, 1st ed.; Eicke, H.-F., Ed.; Springer Basel AG: Interlaken, Switzerland, 1985.
- (422) Eaton, D. F.; Smart, B. E. *J. Am. Chem. Soc.* **1990**, *112*, 2821–2823, DOI: 10.1021/ja00163a065.
- (423) Furukawa, G. T.; McCoskey, R. E.; King, G. J. *J. Res. Natl. Bur. Stand. (1934)*. **1952**, *49*, 273–278, DOI: 10.6028/jres.049.029.
- (424) Lemal, D. M. *J. Org. Chem.* **2004**, *69*, 1–11, DOI: 10.1021/jo0302556.

- (425) Krafft, M. P. *Adv. Drug Deliv. Rev.* **2001**, *47*, 209–228, DOI: 10.1016/S0169-409X(01)00107-7.
- (426) Riess, J. G. *Colloids Surfaces A Physicochem. Eng. Asp.* **1994**, *84*, 33–48, DOI: 10.1016/0927-7757(93)02696-C.
- (427) Hudlický, M.; Pavlath, A. E. *Chemistry of Organic Fluorine Compounds II - A Critical Review [ACS Monograph 187]*; Hudlický, M., Pavlath, A. E., Eds.; American Chemical Society: Washington, DC, 1995.
- (428) Krafft, M. P.; Riess, J. G. *Biochimie* **1998**, *80*, 489–514, DOI: 10.1016/S0300-9084(00)80016-4.
- (429) Castro, C. I.; Briceno, J. C. *Artif. Organs* **2010**, *34*, 622–634, DOI: 10.1111/j.1525-1594.2009.00944.x.
- (430) Shinoda, K.; Hato, M.; Hayashi, T. *J. Phys. Chem.* **1972**, *76*, 909–914, DOI: 10.1021/j100650a021.
- (431) Olson, C. T.; Andersen, M. E. *Toxicol. Appl. Pharmacol.* **1983**, *70*, 362–372, DOI: 10.1016/0041-008X(83)90154-0.
- (432) Ruiz-Cabello, J.; Barnett, B. P.; Bottomley, P. A.; Bulte, J. W. M. *NMR Biomed.* **2011**, *24*, 114–129, DOI: 10.1002/nbm.1570.
- (433) Riess, J. G. *Biomater. Artif. Cells Immobil. Biotechnol.* **1992**, *20*, 183–202, DOI: 10.3109/10731199209119635.
- (434) Flaim, S. F. *Artif. Cells, Blood Substitutes, Biotechnol.* **1994**, *22*, 1043–1054, DOI: 10.3109/10731199409138801.
- (435) Pacansky, J.; Miller, M.; Hatton, W.; Liu, B.; Scheiner, A. *J. Am. Chem. Soc.* **1991**, *113*, 329–343, DOI: 10.1021/ja00001a047.
- (436) Ishikawa, N.; Sasabe, M. *J. Fluor. Chem.* **1984**, *25*, 241–253, DOI: 10.1016/S0022-1139(00)80953-7.
- (437) Lopez, G.; Ameduri, B.; Habas, J. P. *Macromol. Rapid Commun.* **2016**, *37*, 711–717, DOI: 10.1002/marc.201500658.
- (438) Fowler, R.; Buford III, W. B.; Hamilton, Jr., J. M.; Sweet, R. G.; Weber, C. E.; Kasper, J. S.; Litant, I. *Ind. Eng. Chem.* **1947**, *39*, 292–298, DOI: 10.1021/ie50447a612.
- (439) Simons, J. H.; Harland, W. J. *J. Electrochem. Soc.* **1949**, *95*, 55–59, DOI: 10.1149/1.2776735.
- (440) Brace, N. O. Addition of Polyfluoroalkyl Iodides to Unsaturated Compounds and Products Produced Thereby. US 3145222, 1964.
- (441) Blanchard, W. A.; Rhode, J. C. Process for Preparing Perfluoroalkyl Iodides. US 3226449, 1965.
- (442) Sianesi, D.; Pasetti, A.; Belardinelli, G. Perfluorinated Copolyethers. GB 1370050 A, 1974.
- (443) Marchionni, G.; Pagano, E.; Guarda, P. A. Process for Preparing Perfluoropolyethers. US 2005/0075517 A1, 2005.
- (444) Gerhardt, G. E.; Lagow, R. J. *J. Org. Chem.* **1978**, *43*, 4505–4509, DOI: 10.1021/jo00417a026.
- (445) Lin, W.-H.; Bailey Jr., W. I.; Lagow, R. J. *Pure Appl. Chem.* **1988**, *60*, 473–476, DOI: 10.1351/pac198860040473.
- (446) Lin, T. Y.; Lin, W. H.; Clark, W. D.; Larson, S. B.; Simonsen, S. H.; Lynch, V. M.; Brodbelt, J. S.; Maleknia, S. D.; Liou, C. C.; Lagow, R. J. *J. Am. Chem. Soc.* **1994**, *116*, 5172–5179, DOI: 10.1021/ja00091a022.
- (447) Lehmler, H.-J. *Chemosphere* **2005**, *58*, 1471–1496, DOI: 10.1016/j.chemosphere.2004.11.078.
- (448) Key, B. D.; Howell, R. D.; Criddle, C. S. *Environ. Sci. Technol.* **1997**, *31*, 2445–2454, DOI:

10.1021/es961007c.

- (449) Dams, R. J.; Martin, S. J. Coating Compositions with Perfluoropolyetherisocyanate Derived Silane and Alkoxysilanes. US 2005/0121644 A1, 2005.
- (450) Peng, S.; Getty, S. J.; Hopkins, T. E.; Wang, Y. Perfluoroether Based Polymers. US 2008/0113199 A1, 2008.
- (451) Harth, R.; Mor, U.; Ozer, D.; Bettelheim, A. J. *Electrochem. Soc.* **1989**, *136*, 3863–3867, DOI: 10.1149/1.2096564.
- (452) Enea, O.; Duprez, D.; Amadelli, R. *Catal. Today* **1995**, *25*, 271–276, DOI: 10.1016/0920-5861(95)00076-R.
- (453) Cai, J.; Lin, R.; Rao, C. Perfluoroether Sealant Compositions. US 2014/0027057 A1, 2014.
- (454) Riess, J. G. *J. Fluor. Chem.* **2002**, *114*, 119–126, DOI: 10.1016/S0022-1139(02)00017-9.
- (455) Hirschl, R. B.; Croce, M.; Gore, D.; Wiedemann, H.; Davis, K.; Zwischenberger, J.; Bartlett, R. H. *Am. J. Respir. Crit. Care Med.* **2002**, *165*, 781–787, DOI: 10.1164/ajrccm.165.6.2003052.
- (456) Dias, A. M. A.; Bonifácio, R. P.; Marrucho, I. M.; Pádua, A. A. H.; Costa Gomes, M. F. *Phys. Chem. Chem. Phys.* **2003**, *5*, 543–549, DOI: 10.1039/b207512c.
- (457) Wootton, S. L.; Coley, B. D.; Hilton, S. V. W.; Edwards, D. K.; Amberg, J. R.; Mattrey, R. F. *Am. J. Roentgenol.* **1993**, *161*, 409–416, DOI: 10.2214/ajr.161.2.8333387.
- (458) Yang, F.; Li, Y.; Chen, Z.; Zhang, Y.; Wu, J.; Gu, N. *Biomaterials* **2009**, *30*, 3882–3890, DOI: 10.1016/j.biomaterials.2009.03.051.
- (459) Yang, J. M.; Favazza, C.; Chen, R.; Yao, J.; Cai, X.; Maslov, K.; Zhou, Q.; Shung, K. K.; Wang, L. V. *Nat. Med.* **2012**, *18*, 1297–1302, DOI: 10.1038/nm.2823.
- (460) Schutt, E. G.; Klein, D. H.; Mattrey, R. M.; Riess, J. G. *Angew. Chemie - Int. Ed.* **2003**, *42*, 3218–3235, DOI: 10.1002/anie.200200550.
- (461) Smith, M. D.; Kwan, O. L.; Reiser, H. J.; DeMaria, A. N. *J. Am. Coll. Cardiol.* **1984**, *3*, 992–998, DOI: 10.1016/S0735-1097(84)80358-7.
- (462) Schneider, M.; Arditi, M.; Barrau, M.-B.; Brochot, J.; Broillet, A.; Ventrone, R.; Yan, F. *Invest. Radiol.* **1995**, *30*, 451–457, DOI: 10.1097/00004424-199508000-00001.
- (463) Podell, S.; Burrascano, C.; Gaal, M.; Golec, B.; Maniquis, J.; Mehlhaff, P. *Biotechnol. Appl. Biochem.* **1999**, *30*, 213–223, DOI: 10.1111/j.1470-8744.1999.tb00773.x.
- (464) Nakatsuka, M. A.; Mattrey, R. F.; Esener, S. C.; Cha, J. N.; Goodwin, A. P. *Adv. Mater.* **2012**, *24*, 6010–6016, DOI: 10.1002/adma.201201484.
- (465) Forsberg, F.; Roy, R.; Merton, D. A.; Rawool, N. M.; Liu, J. Bin; Huang, M.; Kessler, D.; Goldberg, B. B. *Ultrasound Med. Biol.* **1998**, *24*, 1143–1150, DOI: 10.1016/S0301-5629(98)00062-3.
- (466) Pisani, E.; Tsapis, N.; Paris, J.; Nicolas, V.; Cattel, L.; Fattal, E. *Langmuir* **2006**, *22*, 4397–4402, DOI: 10.1021/la0601455.
- (467) Correias, J. M.; Bridal, L.; Lesavre, A.; Méjean, A.; Claudon, M.; Hélénon, O. *Eur. Radiol.* **2001**, *11*, 1316–1328, DOI: 10.1007/s0033001100940.
- (468) Sheeran, P. S.; Luois, S.; Dayton, P. A.; Matsunaga, T. O. *Langmuir* **2011**, *27*, 10412–10420, DOI: 10.1021/la2013705.
- (469) Porter, T. R.; Xie, F.; Kricsfeld, D.; Armbruster, R. W. *J. Am. Coll. Cardiol.* **1996**, *27*, 1497–1501, DOI:

10.1016/0735-1097(96)00017-4.

- (470) Rapoport, N.; Nam, K. H.; Gupta, R.; Gao, Z.; Mohan, P.; Payne, A.; Todd, N.; Liu, X.; Kim, T.; Shea, J.; Scaife, C.; Parker, D. L.; Jeong, E. K.; Kennedy, A. M. *J. Control. Release* **2011**, *153*, 4–15, DOI: 10.1016/j.jconrel.2011.01.022.
- (471) Zhou, L. Q.; Li, P.; Cui, X. W.; Dietrich, C. F. *Cancer Lett.* **2020**, *470*, 204–219, DOI: 10.1016/j.canlet.2019.11.034.
- (472) Sun, L.; Xu, Y.; Zhang, X.; Gao, Y.; Chen, J.; Zhou, A.; Lu, Q.; Wang, Z.; Shao, K.; Wu, H.; Ning, X. *Adv. Mater.* **2020**, *32*, DOI: 10.1002/adma.202005295.
- (473) Cheng, Y.; Cheng, H.; Jiang, C.; Qiu, X.; Wang, K.; Huan, W.; Yuan, A.; Wu, J.; Hu, Y. *Nat. Commun.* **2015**, *6*, 6–13, DOI: 10.1038/ncomms9785.
- (474) Song, X.; Feng, L.; Liang, C.; Yang, K.; Liu, Z. *Nano Lett.* **2016**, *16*, 6145–6153, DOI: 10.1021/acs.nanolett.6b02365.
- (475) Zhou, Z.; Zhang, B.; Wang, H.; Yuan, A.; Hu, Y.; Wu, J. *Theranostics* **2018**, *8*, 4898–4911, DOI: 10.7150/thno.27598.
- (476) Wan, G. Y.; Liu, Y.; Chen, B. W.; Liu, Y. Y.; Wang, Y. S.; Zhang, N. *Cancer Biol. Med.* **2016**, *13*, 325–338, DOI: 10.20892/j.issn.2095-3941.2016.0068.
- (477) Zhou, Y.; Wang, Z.; Chen, Y.; Shen, H.; Luo, Z.; Li, A.; Wang, Q.; Ran, H.; Li, P.; Song, W.; Yang, Z.; Chen, H.; Wang, Z.; Lu, G.; Zheng, Y. *Adv. Mater.* **2013**, *25*, 4123–4130, DOI: 10.1002/adma.201301655.
- (478) Bailey, M. R.; Khokhlova, V. A.; Sapozhnikov, O. A.; Kargl, S. G.; Crum, L. A. *Acoust. Phys.* **2003**, *49*, 437–464, DOI: 10.11477/mf.1416200967.
- (479) Tran, T. D.; Caruthers, S. D.; Hughes, M.; Marsh, J. N.; Cyrus, T.; Winter, P. M.; Neubauer, A. M.; Wickline, S. A.; Lanza, G. M. *Int. J. Nanomedicine* **2007**, *2*, 515–526.
- (480) Mattrey, R. F. *Am. J. Roentgenol.* **1989**, *152*, 247–252, DOI: 10.2214/ajr.152.2.247.
- (481) Partlow, K. C.; Chen, J.; Brant, J. A.; Neubauer, A. M.; Meyerrose, T. E.; Creer, M. H.; Nolte, J. A.; Caruthers, S. D.; Lanza, G. M.; Wickline, S. A. *FASEB J.* **2007**, *21*, 1647–1654, DOI: 10.1096/fj.06-6505com.
- (482) Mason, R. P.; Antich, P. P.; Babcock, E. E.; Gerberich, J. L.; Nunnally, R. L. *Magn. Reson. Imaging* **1989**, *7*, 475–485, DOI: 10.1016/0730-725X(89)90402-5.
- (483) Dardzinski, B. J.; Sotak, C. H. *Magn. Reson. Med.* **1994**, *32*, 88–97, DOI: 10.1002/mrm.1910320112.
- (484) Tirota, I.; Mastropietro, A.; Cordiglieri, C.; Gazzera, L.; Baggi, F.; Baselli, G.; Bruzzone, M. G.; Zucca, I.; Cavallo, G.; Terraneo, G.; Bombelli, F. B.; Metrangolo, P.; Resnati, G. *J. Am. Chem. Soc.* **2014**, *136*, 8524–8527, DOI: 10.1021/ja503270n.
- (485) Tirota, I.; Dichiarante, V.; Pigliacelli, C.; Cavallo, G.; Terraneo, G.; Bombelli, F. B.; Metrangolo, P.; Resnati, G. *Chem. Rev.* **2015**, *115*, 1106–1129, DOI: 10.1021/cr500286d.
- (486) Caruthers, S. D.; Neubauer, A. M.; Hockett, F. D.; Lamerichs, R.; Winter, P. M.; Scott, M. J.; Gaffney, P. J.; Wickline, S. A.; Lanza, G. M. *Invest. Radiol.* **2006**, *41*, 305–312, DOI: 10.1097/01.rli.0000199281.60135.6a.
- (487) Kaneda, M. M.; Caruthers, S.; Lanza, G. M.; Wickline, S. A. *Ann. Biomed. Eng.* **2009**, *37*, 1922–1933, DOI: 10.1007/s10439-009-9643-z.
- (488) Koshkina, O.; Lajoinie, G.; Baldelli Bombelli, F.; Swider, E.; Cruz, L. J.; White, P. B.; Schweins, R.;

- Dolen, Y.; van Dinther, E. A. W.; van Riessen, N. K.; Rogers, S. E.; Fokkink, R.; Voets, I. K.; van Eck, E. R. H.; Heerschap, A.; Versluis, M.; de Korte, C. L.; Figdor, C. G.; de Vries, I. J. M.; Srinivas, M. *Adv. Funct. Mater.* **2019**, *29*, 1806485, DOI: 10.1002/adfm.201806485.
- (489) Boccalon, M.; Bidoggia, S.; Romano, F.; Gualandi, L.; Franchi, P.; Lucarini, M.; Pengo, P.; Pasquato, L. *J. Mater. Chem. B* **2015**, *3*, 432–439, DOI: 10.1039/C4TB01536C.
- (490) Morawski, A. M.; Winter, P. M.; Crowder, K. C.; Caruthers, S. D.; Fuhrhop, R. W.; Scott, M. J.; Robertson, J. D.; Abendschein, D. R.; Lanza, G. M.; Wickline, S. A. *Magn. Reson. Med.* **2004**, *51*, 480–486, DOI: 10.1002/mrm.20010.
- (491) Nöth, U.; Morrissey, S. P.; Deichmann, R.; Jung, S.; Adolf, H.; Haase, A.; Lutz, J. *Artif. Cells. Blood Substit. Immobil. Biotechnol.* **1997**, *25*, 243–254, DOI: 10.3109/10731199709118914.
- (492) Mizukami, S.; Takikawa, R.; Sugihara, F.; Shirakawa, M.; Kikuchi, K. *Angew. Chemie - Int. Ed.* **2009**, *48*, 3641–3643, DOI: 10.1002/anie.200806328.
- (493) Pengo, P.; Pasquato, L. *J. Fluor. Chem.* **2015**, *177*, 2–10, DOI: 10.1016/j.jfluchem.2015.03.005.
- (494) Van Lehn, R. C.; Alexander-Katz, A. *Soft Matter* **2014**, *10*, 648–658, DOI: 10.1039/c3sm52329b.
- (495) Dass, A.; Guo, R.; Tracy, J. B.; Balasubramanian, R.; Douglas, A. D.; Murray, R. W. *Langmuir* **2008**, *24*, 310–315, DOI: 10.1021/la702651y.
- (496) Gentilini, C.; Evangelista, F.; Rudolf, P.; Franchi, P.; Lucarini, M.; Pasquato, L. *J. Am. Chem. Soc.* **2008**, *130*, 15678–15682, DOI: 10.1021/ja8058364.
- (497) Niikura, K.; Iyo, N.; Higuchi, T.; Nishio, T.; Jinnai, H.; Fujitani, N.; Ijiro, K. *J. Am. Chem. Soc.* **2012**, *134*, 7632–7635, DOI: 10.1021/ja302122w.
- (498) Gentilini, C.; Franchi, P.; Mileo, E.; Polizzi, S.; Lucarini, M.; Pasquato, L. *Angew. Chemie - Int. Ed.* **2009**, *48*, 3060–3064, DOI: 10.1002/anie.200805321.
- (499) Michelena, O.; Padro, D.; Carrillo-Carrión, C.; Del Pino, P.; Blanco, J.; Arnaiz, B.; Parak, W. J.; Carril, M. *Chem. Commun.* **2017**, *53*, 2447–2450, DOI: 10.1039/c6cc08900c.
- (500) Sologan, M.; Padelli, F.; Giachetti, I.; Aquino, D.; Boccalon, M.; Adami, G.; Pengo, P.; Pasquato, L. *Nanomaterials* **2019**, *9*, 879, DOI: 10.3390/nano9060879.
- (501) Kurczyk, M. E.; Zhu, Z. J.; Ivanisevic, J.; Schuyler, A. M.; Lalwani, K.; Santidrian, A. F.; David, J. M.; Giddabasappa, A.; Roberts, A. J.; Olivos, H. J.; O'Brien, P. J.; Franco, L.; Fields, M. W.; Paris, L. P.; Friedlander, M.; Johnson, C. H.; Epstein, A. A.; Gendelman, H. E.; Wood, M. R.; Felding, B. H.; Patti, G. J.; Spilker, M. E.; Siuzdak, G. *Nat. Commun.* **2015**, *6*, 1–8, DOI: 10.1038/ncomms6998.
- (502) Palermo, A.; Forsberg, E. M.; Warth, B.; Aisporna, A. E.; Billings, E.; Kuang, E.; Benton, H. P.; Berry, D.; Siuzdak, G. *ACS Nano* **2018**, *12*, 6938–6948, DOI: 10.1021/acsnano.8b02376.
- (503) Krafft, M. P.; Riess, J. G. *Chem. Rev.* **2009**, *109*, 1714–1792, DOI: 10.1021/cr800260k.
- (504) Srinivas, M.; Turner, M. S.; Janjic, J. M.; Morel, P. A.; Laidlaw, D. H.; Ahrens, E. T. *Magn. Reson. Med.* **2009**, *62*, 747–753, DOI: 10.1002/mrm.22063.
- (505) Post, G. B.; Cohn, P. D.; Cooper, K. R. *Environ. Res.* **2012**, *116*, 93–117, DOI: 10.1016/j.envres.2012.03.007.
- (506) Scialli, A. R.; Iannucci, A.; Turim, J. *Regul. Toxicol. Pharmacol.* **2007**, *49*, 195–202, DOI: 10.1016/j.yrtph.2007.08.003.
- (507) Marson, D.; Guida, F.; Sologan, M.; Boccardo, S.; Pengo, P.; Perissinotto, F.; Iacuzzi, V.; Pellizzoni, E.; Polizzi, S.; Casalis, L.; Pasquato, L.; Pacor, S.; Tossi, A.; Posocco, P. *Small* **2019**, *15*, 1–12, DOI:

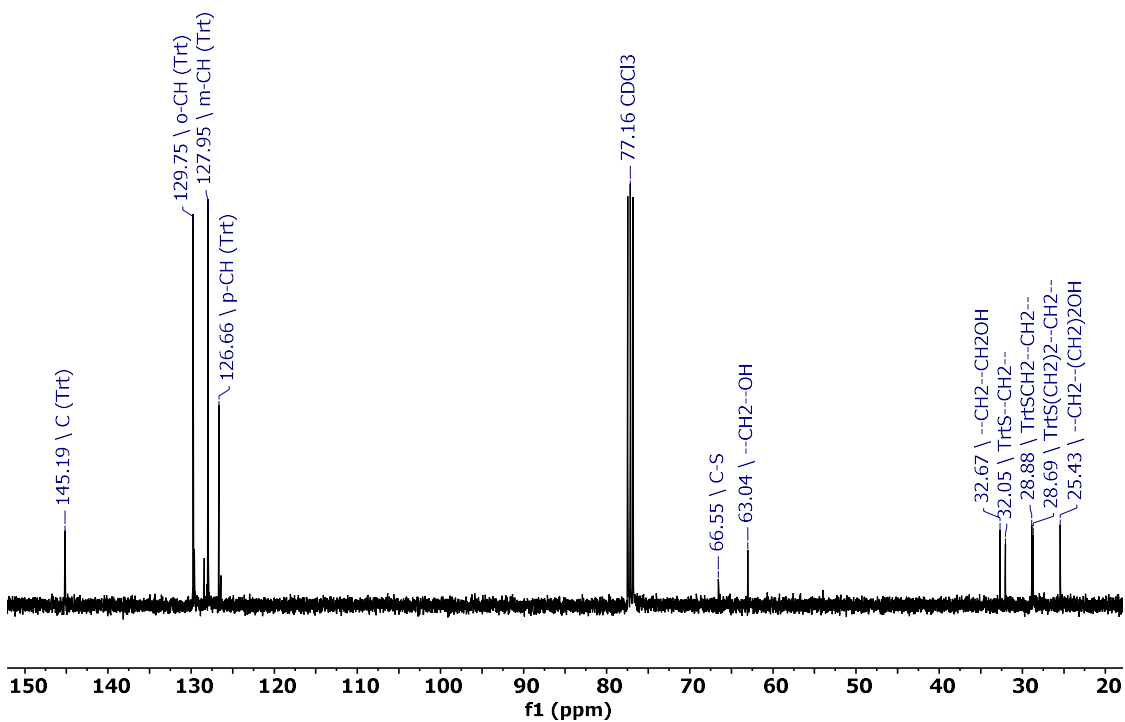
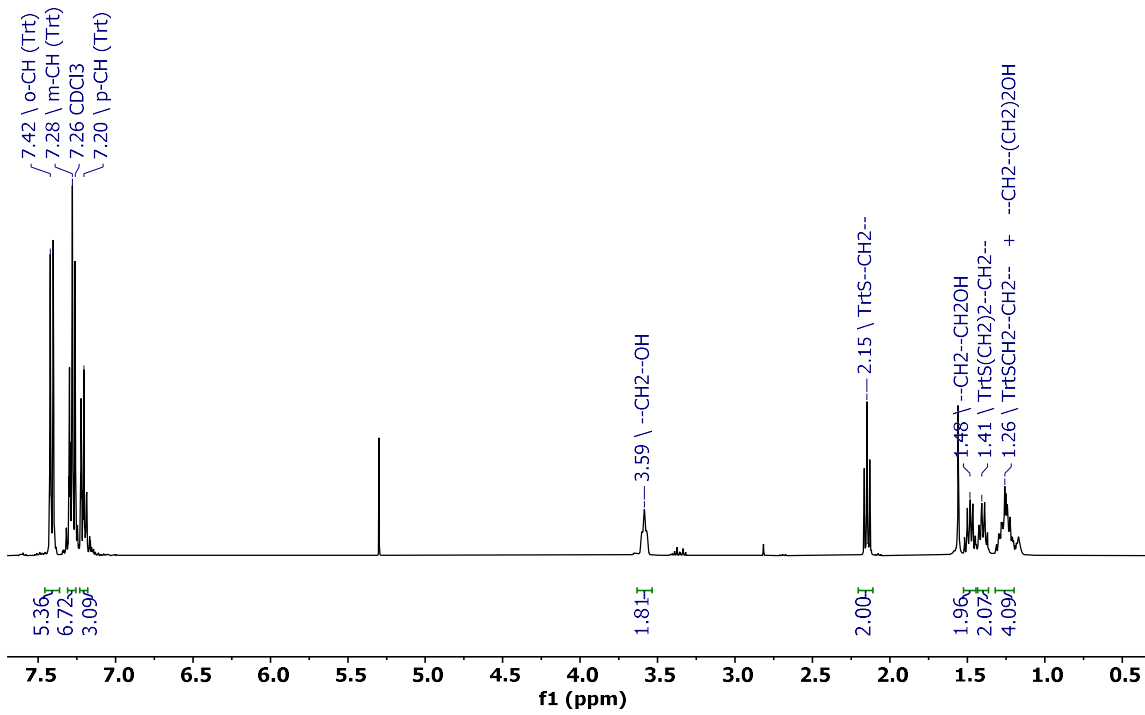
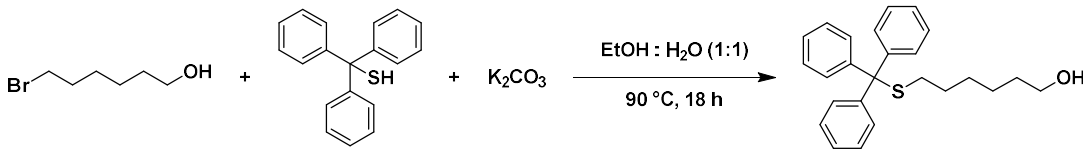
10.1002/sml.201900323.

- (508) Bidoggia, S.; Milocco, F.; Polizzi, S.; Canton, P.; Saccani, A.; Sanavio, B.; Krol, S.; Stellacci, F.; Pengo, P.; Pasquato, L. *Bioconjug. Chem.* **2017**, *28*, 43–52, DOI: 10.1021/acs.bioconjchem.6b00585.
- (509) Sologan, M.; Cantarutti, C.; Bidoggia, S.; Polizzi, S.; Pengo, P.; Pasquato, L. *Faraday Discuss.* **2016**, *191*, 527–543, DOI: 10.1039/C6FD00016A.
- (510) Gentilini, C.; Pasquato, L. *J. Mater. Chem.* **2010**, *20*, 1403–1412, DOI: 10.1039/B912759C.
- (511) Posocco, P.; Gentilini, C.; Bidoggia, S.; Pace, A.; Franchi, P.; Lucarini, M.; Fermeglia, M.; Pricl, S.; Pasquato, L. *ACS Nano* **2012**, *6*, 7243–7253, DOI: 10.1021/nn302366q.
- (512) Wallace, K. B.; Kissling, G. E.; Melnick, R. L.; Blystone, C. R. *Toxicol. Lett.* **2013**, *222*, 257–264, DOI: 10.3174/ajnr.A1256.Functional.
- (513) Janjic, J. M.; Srinivas, M.; Kadayakkara, D. K. K.; Ahrens, E. T. *J. Am. Chem. Soc.* **2008**, *130*, 2832–2841.
- (514) Kim, B.; Han, G.; Toley, B. J.; Kim, C. K.; Rotello, V. M.; Forbes, N. S. *Nat. Nanotechnol.* **2010**, *5*, 465–472, DOI: 10.1038/nnano.2010.58.
- (515) Boal, A. K.; Rotello, V. M. *Langmuir* **2000**, *16*, 9527–9532, DOI: 10.1021/la0012384.
- (516) Carr, H. Y.; Purcell, E. M. *Phys. Rev.* **1954**, *94*, 630–638, DOI: 10.1103/PhysRev.94.630.
- (517) Meiboom, S.; Gill, D. *Rev. Sci. Instrum.* **1958**, *29*, 688–691, DOI: 10.1063/1.1716296.
- (518) Vezmar, I.; Alvarez, M. M.; Khoury, J. T.; Salisbury, B. E.; Shafigullin, M. N.; Whetten, R. L. *Zeitschrift fur Phys. D - Atoms Mol. Clust.* **1997**, *40*, 147–151, DOI: 10.1007/s004600050180.
- (519) Badia, A.; Gao, W.; Singh, S.; Demers, L.; Cuccia, L.; Reven, L. *Langmuir* **1996**, *12*, 1262–1269, DOI: 10.1021/la9510487.
- (520) Terrill, R. H.; Postlethwaite, T. A.; Chen, C.; Poon, C.-D.; Terzis, A.; Chen, A.; Hutchison, J. E.; Clark, M. R.; Wignall, G.; Londono, J. D.; Superfine, R.; Falvo, M.; Johnson Jr., C. S.; Samulski, E. T.; Murray, R. W. *J. Am. Chem. Soc.* **1995**, *117*, 12537–12548, DOI: 10.1021/ja00155a017.
- (521) Song, Y.; Harper, A. S.; Murray, R. W. *Langmuir* **2005**, *21*, 5492–5500, DOI: 10.1021/la0503606.
- (522) Lee, H.; Price, R. R.; Holburn, G. E.; Partain, C. L.; Adams, M. D.; Cacheris, W. P. *J. Magn. Reson. Imaging* **1994**, *4*, 609–613, DOI: 10.1002/jmri.1880040416.
- (523) Shen, J.; Bai, Y.; Yin, Q.; Wang, W.; Ma, X.; Wang, G. *J. Ind. Eng. Chem.* **2017**, *56*, 82–89, DOI: 10.1016/j.jiec.2017.06.048.
- (524) Tuazon, E. C.; Fateley, W. G.; Bentley, F. F. *Appl. Spectrosc.* **1971**, *25*, 374–375, DOI: 10.1366/000370271779949230.
- (525) Piacenti, F.; Camaiti, M. *J. Fluor. Chem.* **1994**, *68*, 227–235, DOI: 10.1016/0022-1139(93)03045-N.

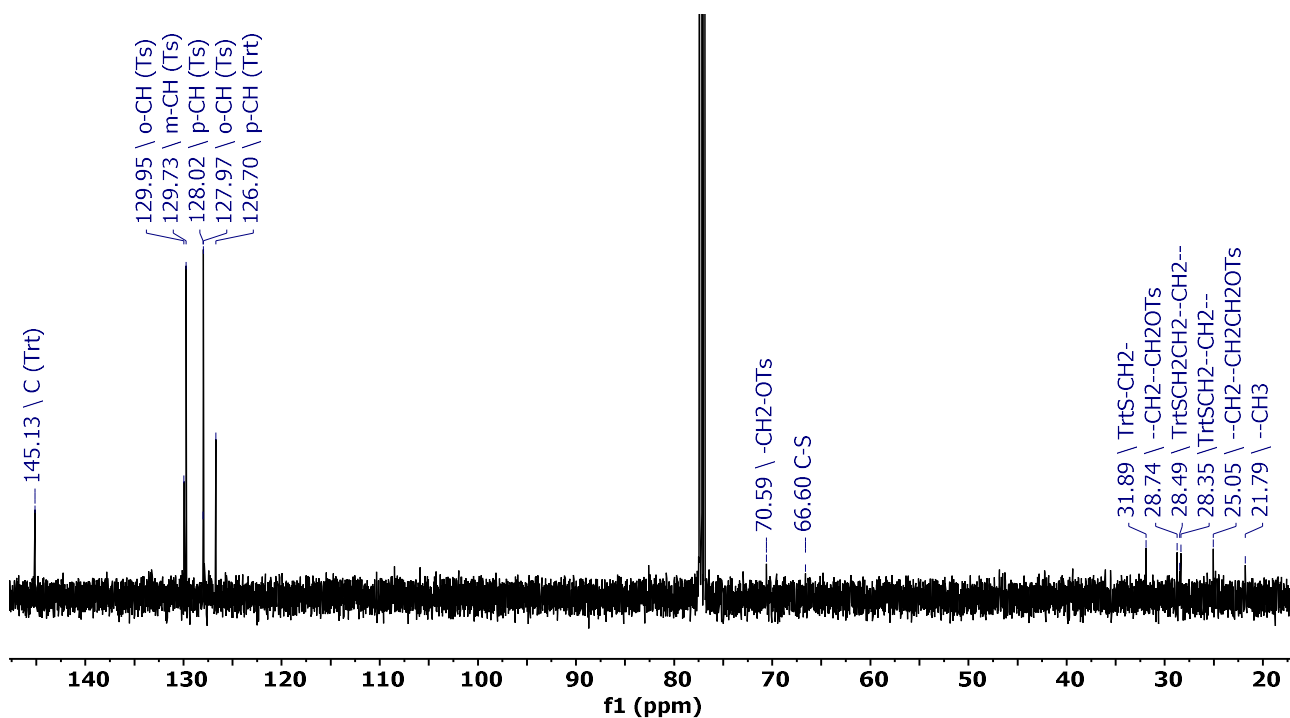
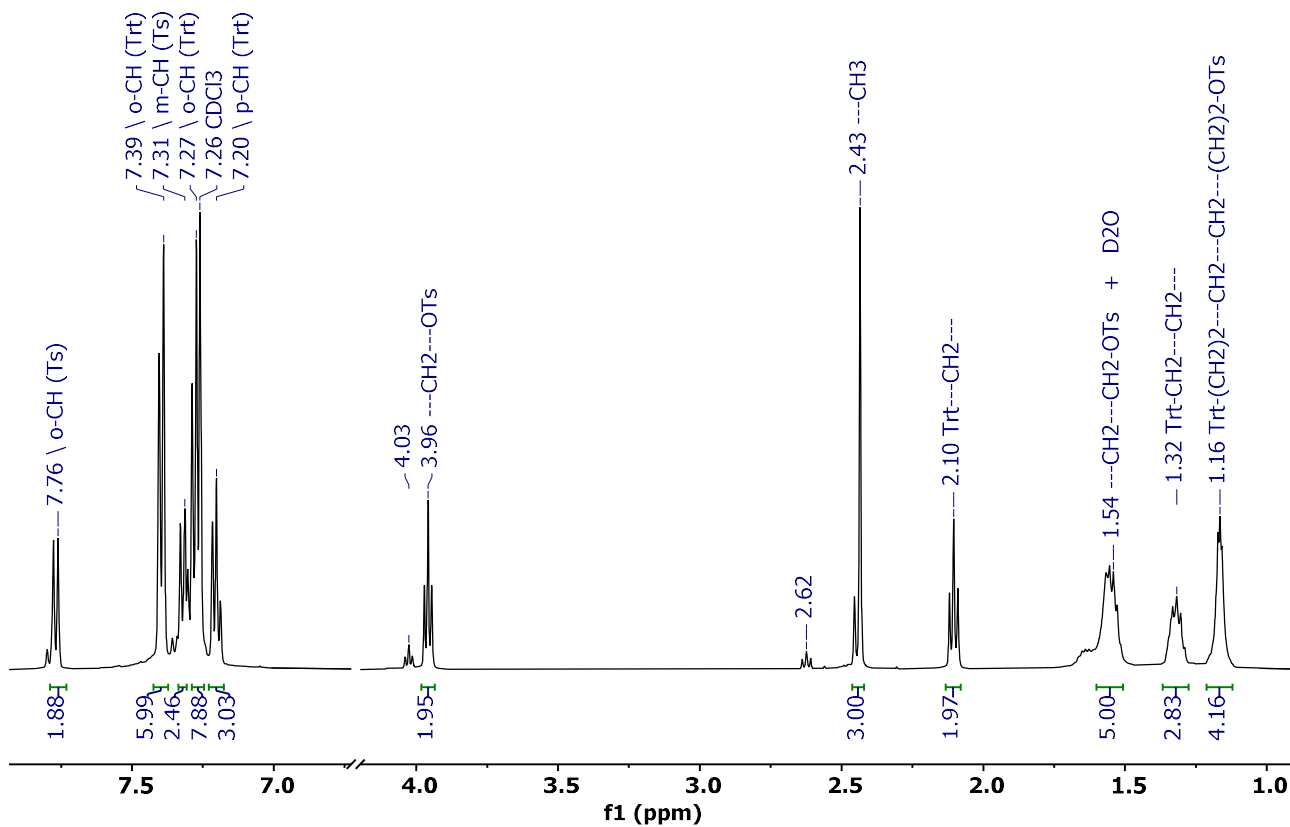
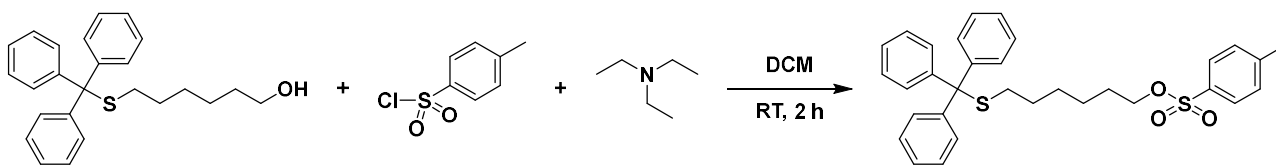
APPENDIX

APPENDIX: NMR SPECTRA (CHAPTERS 8 - 9)

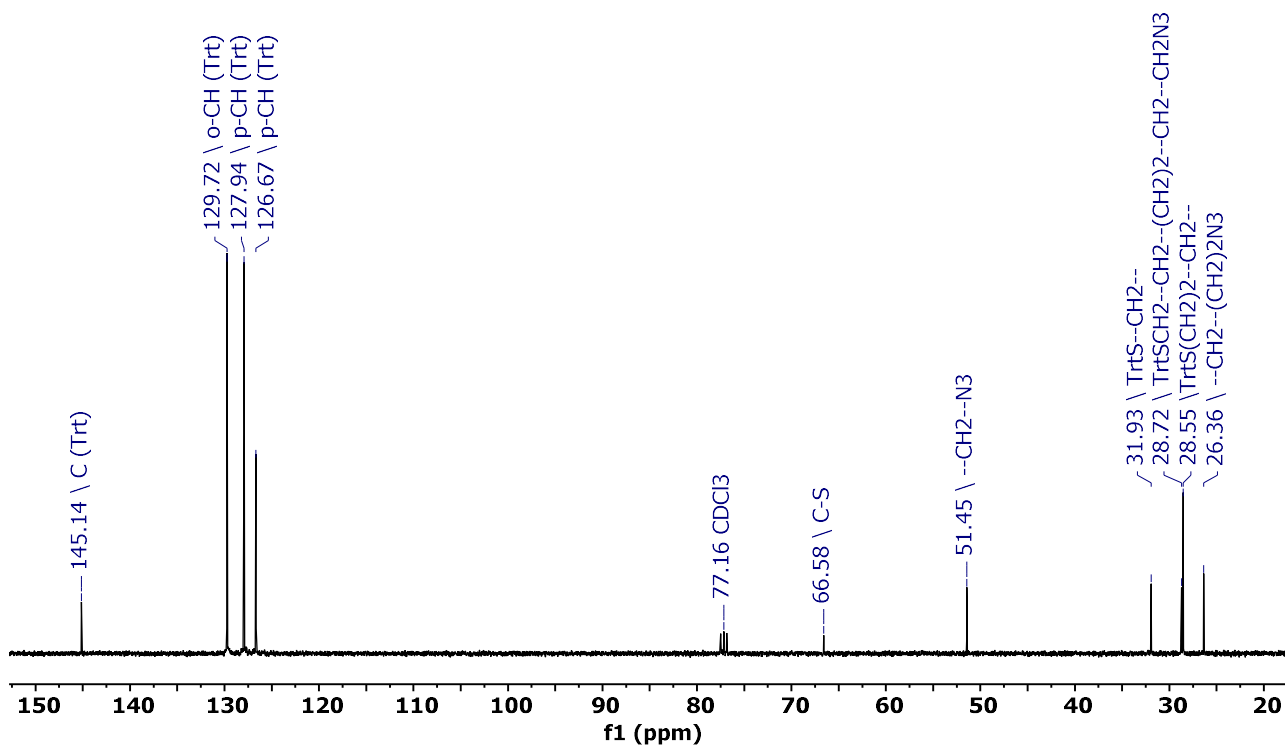
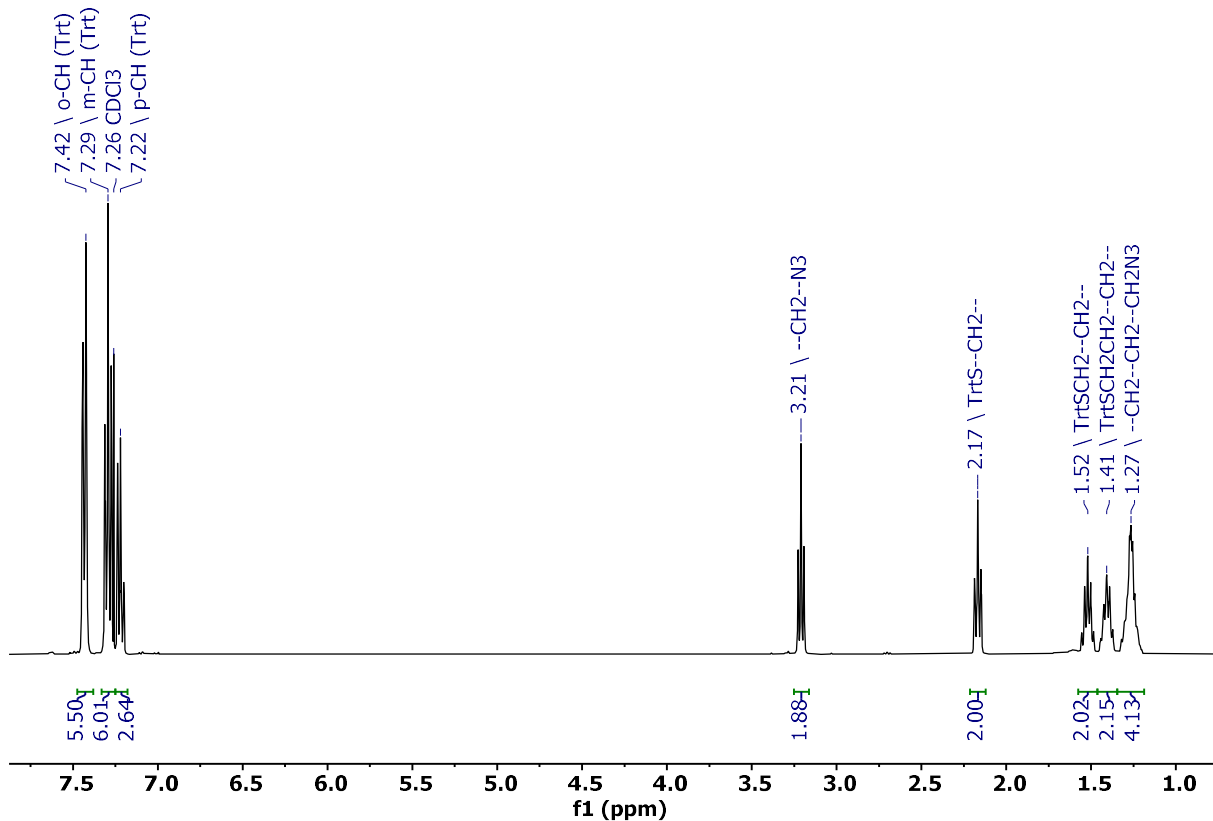
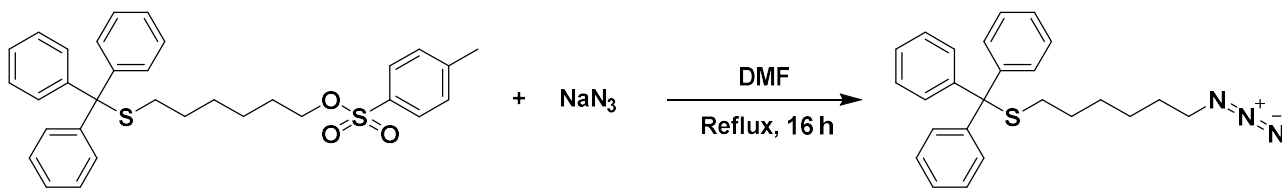
Synthesis of 6-tritylthiol-1-hexanol (TrtSC6OH)



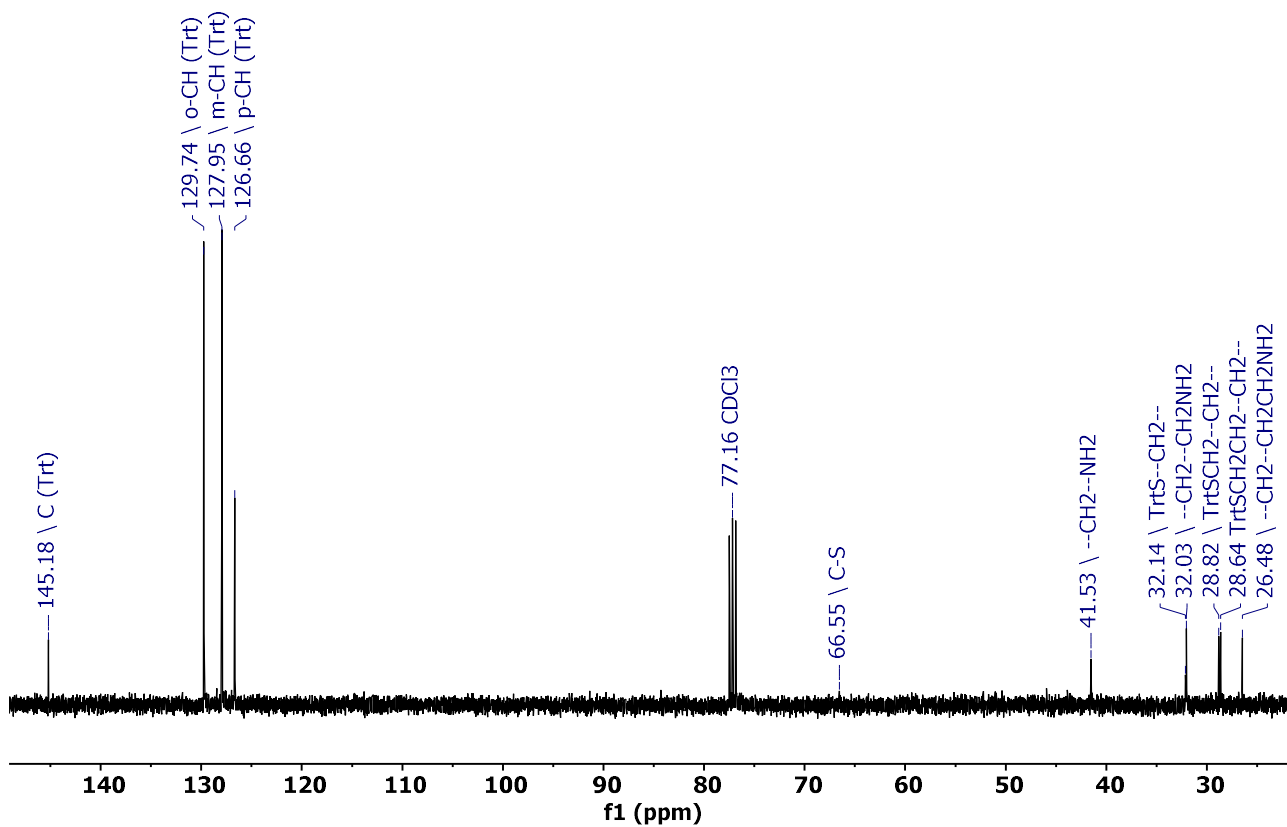
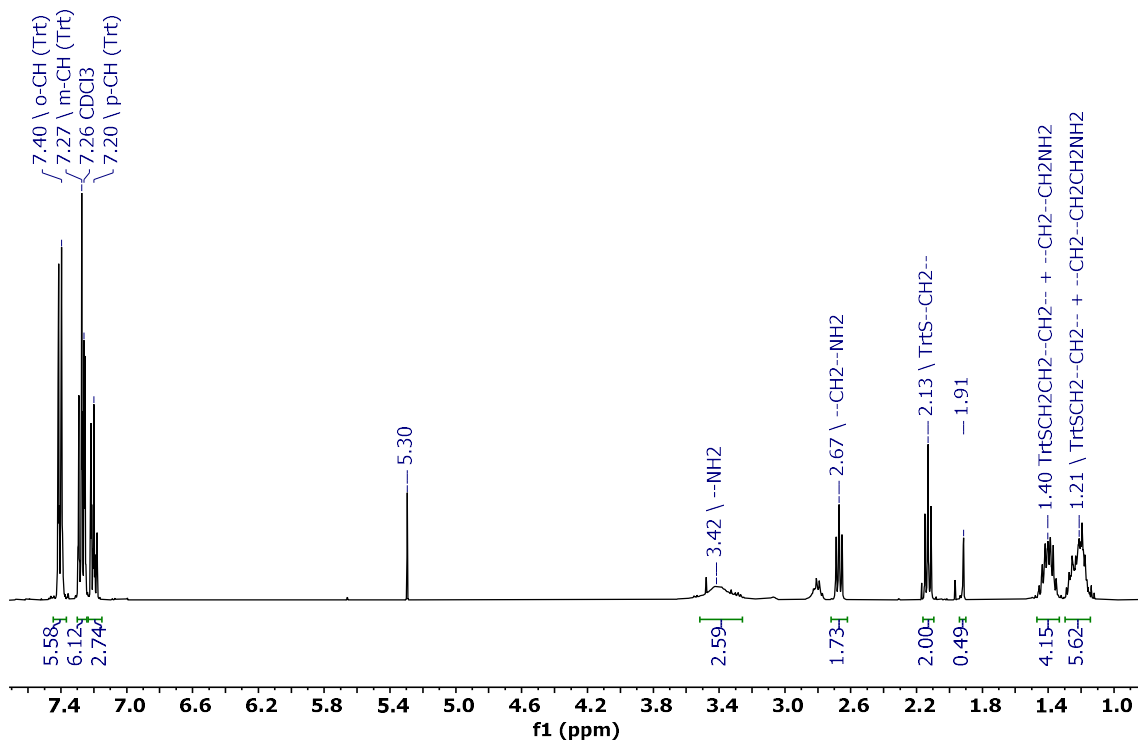
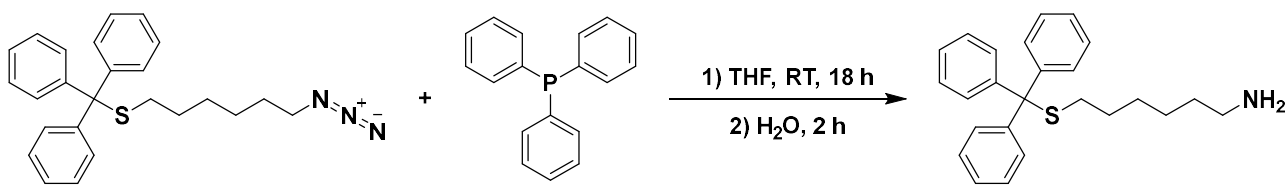
Synthesis of 6-(tritylthiol)hexyl-4-methylbenzenesulfonate (TrtSC6OTs)



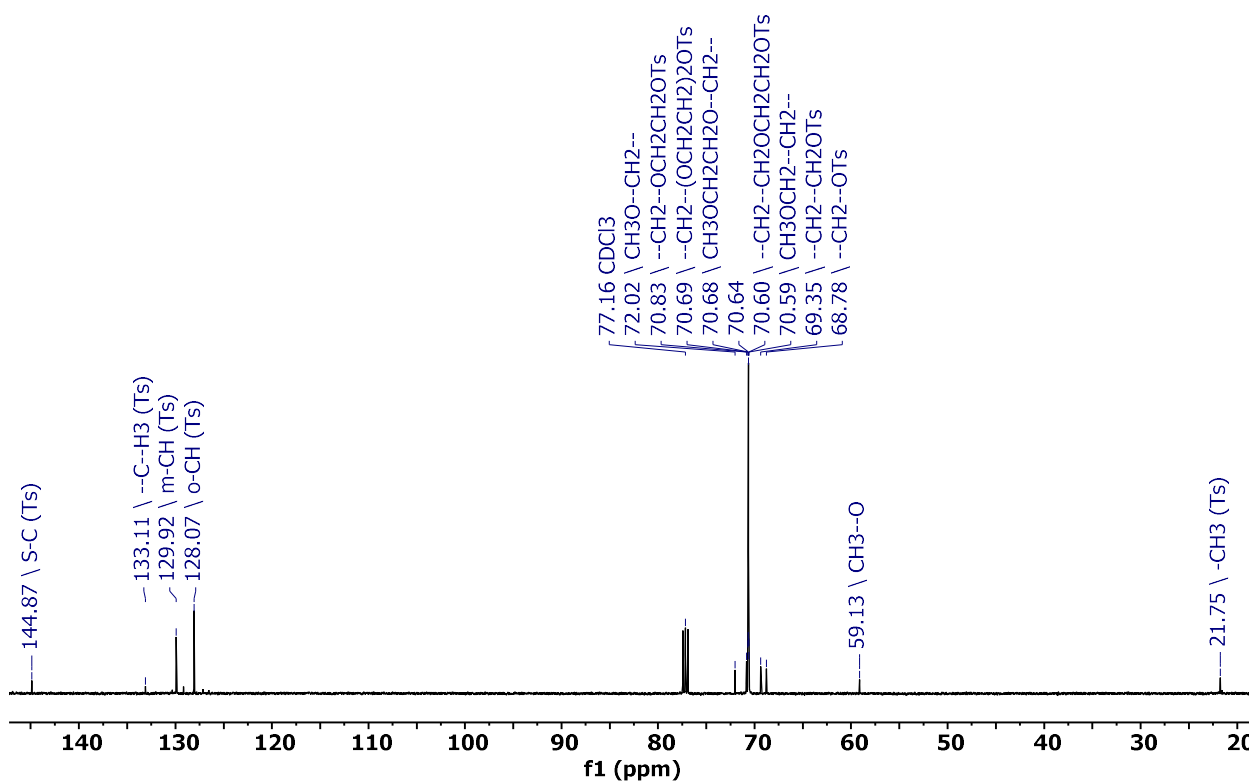
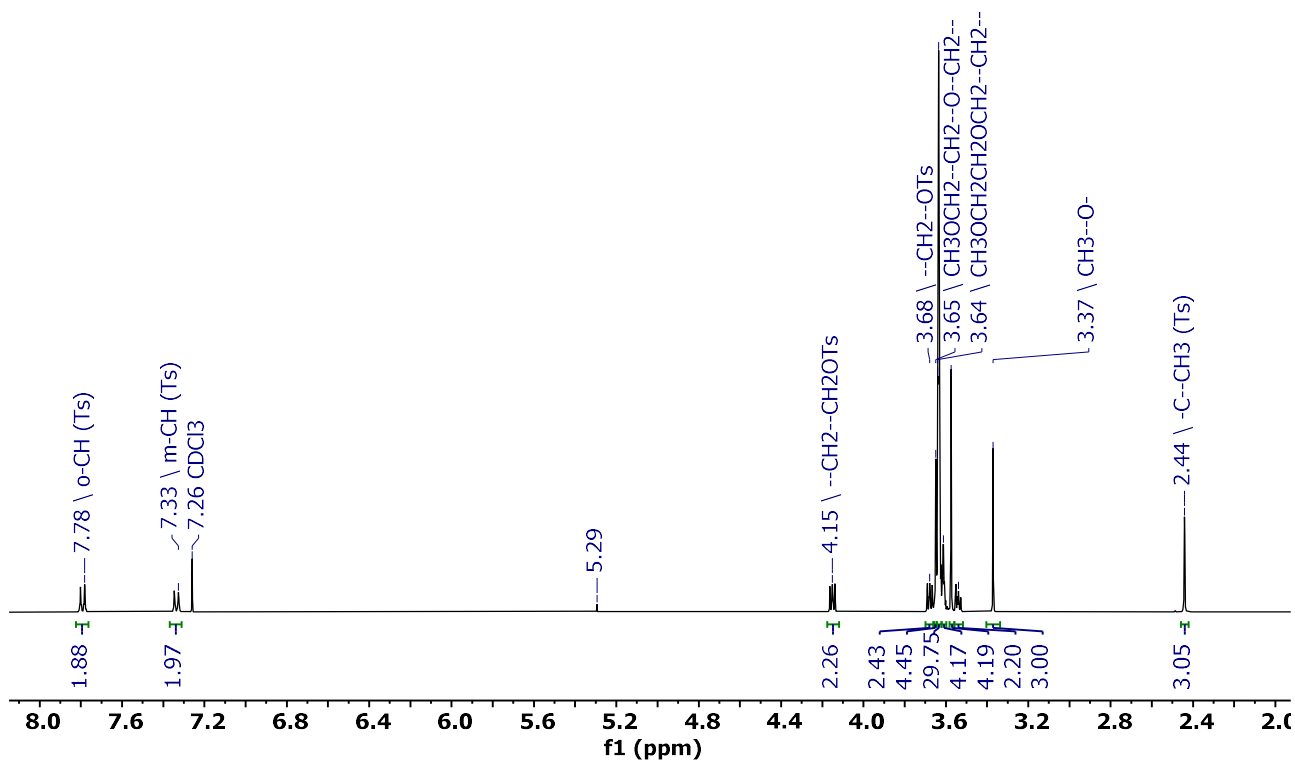
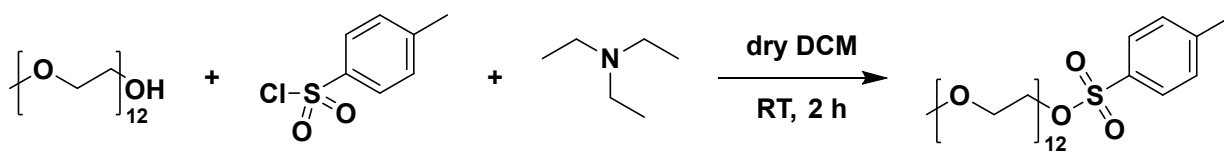
Synthesis of (6-azidoheptyl)(trityl)sulfane (TrtSC6N3)



Synthesis of 6-(tritylthio)hexan-1-amine (TrtSC6NH2)



Synthesis of PEG₅₅₀-OTs



Synthesis of PEG₅₅₀-NH₂

